DOE/ER-0313/13

Fusion Reactor Materials

Semiannual Progress Report for Period Ending Sept. 30, 1992

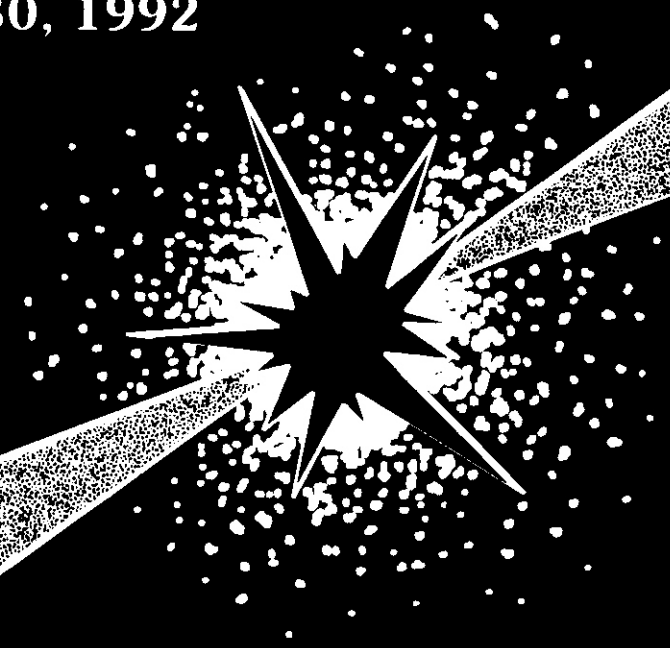

U. S. Department of Energy
Office of Fusion Energy

DOE/ER-0313/13
Distribution
Categories
UC-423. -424

FUSION REACTOR MATERIALS
SEMIANNUAL PROGRESS REPORT
FOR THE PERIOD ENDING
SEPTEMBER 30, 1992

Prepared for
DOE Office of Fusion Energy
(AT 15 02 03 A)

Prepared for
OAK RIDGE NATIONAL LABORATORY
Oak Ridge, Tennessee 37831
Managed by
MARTIN MARIETTA ENERGY SYSTEMS, INC.
for the
U.S. DEPARTMENT OF ENERGY
under Contract DE-AC05-84OR21400

FOREWORD

This is the thirteenth in a series of semiannual technical progress reports on fusion reactor materials. This report combines research and development activities which were previously reported separately in the following progress reports:

- Alloy Development for Irradiation Performance
- Damage Analysis and Fundamental Studies
- Special Purpose Materials

These activities are concerned principally with the effects of the neutronic and chemical environment on the properties and performance of reactor materials; together they form one element of the overall materials programs being conducted in support of the Magnetic Fusion Energy Program of the U.S. Department of Energy. The other major element of the program is concerned with the interactions between reactor materials and the plasma and is reported separately.

The Fusion Reactor Materials Program is a national effort involving several national laboratories, universities, and industries. The purpose of this series of reports is to provide a working technical record for the use of the program participants. and to provide a means of communicating the efforts of materials scientists to the rest of the fusion community, both nationally and worldwide.

This report has been compiled and edited under the guidance of A. F. Rowcliffe, G. L. Burn, and S. S. Knee', Oak Ridge National Laboratory. Their efforts, and the efforts of the many persons who made technical contributions. are gratefully acknowledged. F. W. Wiffen, Reactor Technologies Branch, has responsibility within DOE for the program reported on in this document.

R. Price, Chief
Reactor Technologies Branch

Reports previously listed in this series are as follows:

DOE/ER-0313/1	Period ending September 30, 1986
DOWER-03132	Period ending March 31, 1987
DOE/ER-0313/3	Period ending September 30, 1987
DOE/ER-0313/4	Period ending March 31, 1988
DOE/ER-0313/5	Period ending September 30, 1988
DOWER-0313/6	Period ending March 31, 1989
DOE/ER-0313/7	Period ending September 30, 1989
DOWER-031348	Period ending March 31, 1990
DOE/ER-0313/9	Period ending September 30, 1990
DOWER-0313/10	Period ending March 31, 1991
DOE/ER-0313/11	Period ending September 30, 1991
DOE/ER-0313/12	Period ending March 31, 1992

CONTENTS

*Inadvertantly omitted from DOE/ER/12

A complete description and details of the design, construction, and installation of capsules JP-9 through JP-16 has been previously reported. The capsules were installed in the High Flux Isotope Reactor (HFIR) target July 20, 1990 for irradiation beginning with HFIR fuel cycle 289. The capsules were removed and stored in the reactor pool during HFIR cycle 292 (11/25/90 - 12/10/90) to provide room for required isotope production. They were reinstalled for HFIR cycle 293 for continued irradiation. Of these eight target capsules, JP-10, 11, 13, and 16 completed their scheduled number of cycles (11) and were removed from the reactor in September 1991. In addition, JP-14 was removed from the reactor at the end of cycle 310 (9/18/92) after 21 cycles.

Three new capsules in this series, JP-20, 21, and 22, are currently being designed. These capsules were added to the program in order to complete the experimental matrix included in the JP-9 through JP-16 capsules. The new capsules will contain transmission electron microscope (TEM) disks and SS-3 flat tensile specimens at 300-600°C and will achieve doses of 8, 18 and 40 dpa, respectively. The preliminary experiment matrix is described in detail in a previous report.

Fabrication and operation of four HFIR-MFE RB' capsules (60, 200, 330, and 400°C) to accommodate MFE specimens previously irradiated in spectrally tailored experiments in the ORR are proceeding satisfactorily. With the exception of the 60°C capsule, where the test specimens are in direct contact with the reactor cooling water, specimen temperatures (monitored by 21 thermocouples) are controlled by varying the thermal conductance of a thin gas gap region between the specimen holder outer sleeve and containment tube.

Irradiation of the 60 and 330°C capsules was started on July 17, 1990. As of September 30, 1992, these two capsules had completed 22 cycles of their planned 24-cycle (formerly 22-cycle) irradiation to a damage level of approximately 18.3 displacements per atom (dpa). Assembly of the 200 and 400°C capsules is scheduled for completion in November 1992; operation of these two capsules will follow the first two (60 and 330°C).

Calculations of neutron displacement damage cross-sections for SiC are presented. We use Biersack and Haggmark's empirical formula in constructing the electronic stopping power, which combines the Lindhard's model at low PKA energies and the Bethe-Bloch's model at high PKA energies. The electronic stopping power for polyatomic materials is computed on the basis of Bragg's Additivity Rule. A continuous form of the inverse power law potential is used for nuclear scattering. Coupled intergro-differential equations for the number of displaced atoms *j*, caused by PKA *i*, are then derived. The procedure outlined above gives partial displacement cross-sections, displacement cross-sections lor each specie of the lattice, and for each PKA type. The corresponding damage rates for several fusion and fission neutron spectra are calculated. The stoichiometry of the irradiated material is investigated by finding the ratio of displacements among various atomic species. The role of each specie in displacing atoms is also investigated by calculating the fraction of displacements caused by each PKA type. The study shows that neutron displacement damage rates of *SiC* in typical magnetic fusion reactor first wall will be ~10-15 [dpa] $[MW]^{-1}[m]^2$, that in typical lead-protected inertial confinement fusion reactor first walls to be ~15-20 [dpa]$[MW]^{-1}[m]^2$. For fission spectra, we find that the neutron displacement damage rate of *SiC* is ~74 [dpa] per 10^{27} n/m^2 in FFTF. ~39 [dpa] per 10^{27} in HFIR, and 25 [dpa] per 10^{27} in NRU. Approximately 80% of displacement atoms are shown to be of the carbon-type.

Based on a preliminary survey of more than 15 oxides and nitrides, four ceramic materials (CaO, MgO, Y_2O_3, and BN) were identified as candidates for insulator coating development. These compounds were fabricated by various techniques and exposed to flowing Li at 400-410" to assess chemical compatibility. Yttrium oxide exhibited excellent corrosion resistance in flowing liquid Li at 400°C; its corrosion rate was calculated to be 0.042 μm/hr. Resistivity measurements by a standard four-probe method on Y_2O_3 in air at temperalures between −450 and 1000°C. before and after exposure to Li for 675 h at 410°C, indicated no deterioration in resistivity. The resistivity of in-situ-formed $(V,Ti)_XN$ reaction-product layers on V-20Ti and TiN on Ti was determined at room temperature and 80°C by a two-probe method. The resistivity of the film on the V-20Ti alloy was low (−20 Ωm) and the film on Ti exhibited metallic conduction. Adhesion bonding between Y_2O_3 and Y, V, Ti, Y, V-20Ti, V-3Ti-1Si, and Types 304 and 316 stainless steel was investigated in reducing and oxidizing gaseous environments at 927°C. Except for the V-20Ti alloy, the V-base alloys, Ti, and Type 304 stainless steel were well bonded to Y_2O_3 in the reducing atmosphere. In the oxidizing atmosphere, bond regions of Types 304 and 316 stainless steel were better than in the reducing atmosphere because of reaction between the oxide scale on the steels (Cr_2O_3) and Y_2O_3 to form $YCrO_3$. Neither V, Ti, nor the V-alloys bonded with Y_2O_3. These results suggest that a low-melting eutectic layer forms between Y_2O_3 and the oxides layers present on V, Ti, and V-alloys.

Suscept bility of Types 316NG ano sens t zed 304 stain ess stee s (SS) to SCC was invest gatec at temperatures of 60-289°C in slow-stra n-rate-lens le (SSRT) tests .n oxygenated water that s mulates mportant parameters anticipated in I rst-wal /b anket systems. Severa aod tiona SSRT tests were performed on crevice specimens of Type 316NG SS .n oxygenated water contain ng 100 ppb su.fate at steel exnib ts good resistance to SCC under crevice anc noncrevice conditions at temperat.res <150°C n a nominal ITER coolant chemistry. In contrast. sensitized Type 304 SS exn bited intergran.ar stress corrosion cracking (IGSCC) at <100°C unoer crevice conditions. SSRT tests have been conducted on weldment specimens of Type 316L SS with matching f ller meta .nder crevice conditions .n oxygenate0 water contain ng 0.06-6 0 ppm ch oride at 150-225°C Most specimens fract.rec n the base metal. and severa others fract.red n the neat-attected zone (HAZ) of the weld. bat none failed n the weld metal.

Various intermetallic films were produced on vanadium, vanadium-base alloys, and Types 304 and 316 stainless steel (SS) by exposing the materials to liquid- and/or vapor-phase lithium containing dissolved elements (3-5 at. %) in sealed capsules at temperatures between 600 and 775°C. After each test, the capsules were opened and the samples were examined by optical and scanning electron microscopy; they were then analyzed by electron-energy-dispersive and X-ray diffraction techniques. The nature of the coatings. i.e., surface coverage, thickness, and composition, varied with exposure time and temperature, solute in lithium, and alloy composition. Solute elements that yielded adherent coatings on various substrates provide a means of developing in-situ electrical insulator coatings by oxidation of the reactive layers with dissolved oxygen andlor nitrogen in liquid lithium.

Research has been conducted to develop a diffusion coating of Y_2O_3 on the surface of V, which could help eliminate the MHD effect. The process involves yttriding, in which a diffusion coating of Y is formed on the surface of V by immersing the samples in a molten salt and applying a potential. The yttrium layer can then be oxidized to form the electrical insulator Y_2O_3. An yttrium coating up to 10 μm in thickness with a diffusion zone of ~1 μm has been produced.

The radiation enhanced conductivity (REC) in four types of silicon carbide based materials was measured. As expected, the material with the highest initial conductivity showed the lowest conductivity enhancement. Chemically vapor deposited material showed only a few percent change at ionizing fluxes of several Gy/s. Two materials with higher initial resistivities demonstrated significant REC, the highest resistivity of the two changing by more than a factor of thirty for a dose of **4.2** Gy/s.

1.0 IRRADIATION FACILITIES, TEST MATRICES, AND EXPERIMENTAL METHODS

BEAM-TARGET INTERACTION IN AN ACCELERATOR-BASED NEUTRON SOURCE FOR A FUSION MATERIAL TEST FACILITY -
A. Hassanein and D. Smith (Argonne National Laboratory)

OBJECTIVE

To provide a high neutron flux for testing and evaluation of candidate materials for fusion environment. The beam-target interaction is analyzed.

SUMMARY

High-current linear-accelerators have increased the attractiveness of a deuterium-lithium neutron source for fusion materials testing and evaluation. Detailed beam-target interaction and the resulting energy deposited and the jet thermal response are analyzed. Issues relating to jet instabilities, nozzle erosion rates, and the impact of thicker jets on the neutron spectrum at the testing area need further analysis.

PROGRESS AND STATUS

This report concerns the development of a high flux neutron source for fusion material testing using a high current linear accelerator. A high energy (35 MeV) deuteron beam is bombarded into a lithium target to produce the high energy neutrons needed to simulate the fusion environment via the Li(d,n) nuclear stripping reaction. This neutron spectrum, which peaks near a neutron energy of 14 MeV, produces atomic displacements and transmutation products in irradiated materials similar to those in real fusion reactors.

The deposition and the response of the lithium jet due to the bombardment of high energy deuterons is modeled and simulated using the A*THERMAL computer code. The code is modified to handle the deposition of high energy ions into different target materials. The code calculates, using several analytical models, the energy loss of the incident ion beam through both the electronic and nuclear stopping powers of the target atoms long its path. The analytical models use stopping cross-sections which incorporate some experimental data to accurately model the deposition profile. This code is much faster and more reliable than using Monte Carlo codes which require extensive running time and careful statistical interpretations of the result. The code then calculates the detailed spatial thermal response of the jet using both finite element and finite difference techniques with advanced numerical methods. The detailed analysis and the specific models used in the calculations for the D-Li system are discussed elsewhere[1]. The analysis of using a water jet system instead of the lithium jet bombarded by a triton beam to produce the required neutron flux and the advantages/disadvantages of such a system are described elsewhere[3].

As an example, the power deposited from a 35 MeV deuteron beam into a lithium jet is shown in Fig. 1. The beam produced by the accelerator is not expected to be a mono-energetic beam, but has a Gaussian energy distribution with an rms width of 0.5 - 1.0 MeV. The peak power deposited is substantially reduced by increasing the rms width of the profile. Following the energy deposition, the jet thermal hydraulic response is evaluated. Liquid lithium at a bulk temperature of about 500 K is accelerated vertically downward from a nozzle at a velocity of about 17 m/s. The spatial temperature profile for the mono-energetic beam is shown in Fig. 2. The temperature at the jet surface is only around 600 K which is very low for any significant evaporation into the accelerator chamber to interfere with the deuteron beam.

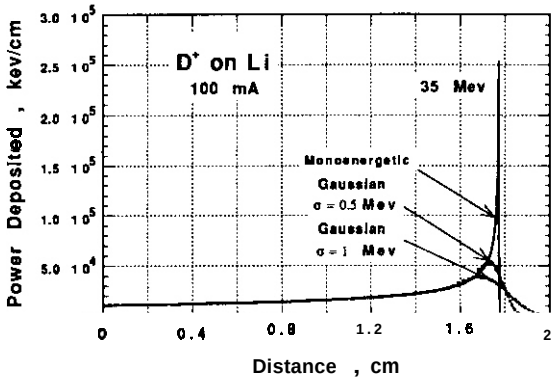

Fig. 1. Power deposited In the lithium jet lor different beam profiles.

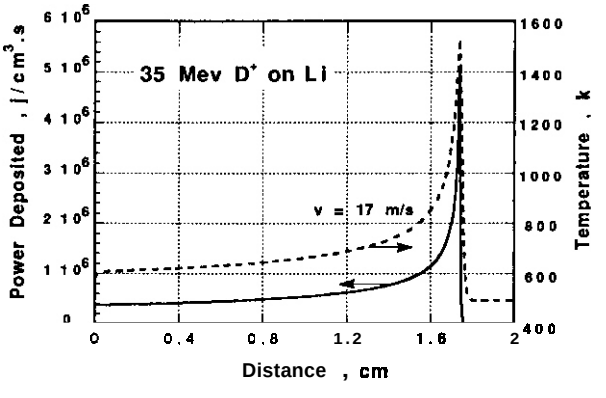

Fig. 2. Lithium jet temperature profile due to mono-energetic beam deposition.

Future issues that need to be analyzed are the resulting radiation damage and activation to the accelerator chamber and other components, the erosion rate of the nozzle and down stream components, jet instabilities, and the effect of using thicker jet thicknesses on the resulting neutron spectrum at the test area.

REFERENCES

1. A. Hassanein, J. Nuclear Materials, 122/123 (1984).
2. A. Hassanein, to be published.
3. A. Hassanein, D.L. Smith, D.K. Sze, and C.B. Reed, "Analysis of the Tritium-Water ($T-H_2O$) System for a Fusion Material Test Facility," ANL/FPP/TM-261, April 1992.

LIQUID LITHIUM TARGET DEVELOPMENT FOR AN ACCELERATOR-BASED NEUTRON SOURCE - 8. F. Picologlou and D. L. Smith (Argonne National Laboratory)

OBJECTIVE

The objective of this task is the development of a liquid lithium target for the Fusion Material Test Facility.

SUMMARY

A proposed high-flux high energy fusion materials irradiation facility uses a deuteron beam impinging on a lithium target to produce neutrons with a spectrum that peaks around 14 MeV. The lithium target consists of a jet of liquid lithium of appropriate thickness. The lithium target development activity is examining the possibility of creating a stable planar free jet of desirable thermal hydraulic characteristics through magnetohydrodynamic body forces created by a DC magnetic field.

PROGRESS AND STATUS

Introduction

The lithium jet target characteristics for the proposed accelerator-based neutron source should be such that the deposition of essentially the entire deuteron beam energy in the jet does not result in unacceptable temperatures and lithium vapor generation rates. Past designs of the lithium jet target utilized a curved jet on a backing plate. The jet curvature results in centrifugal forces that tend to stabilize the jet and generate a pressure field in the bulk of the jet that increases lithium saturation temperature and, thus, decreases lithium vapor generation rates. However, the backing plate will be subjected to liquid metal corrosion and high energy neutron flux and its lifetime is likely to be short. A planar jet that does not require a backing plate will be clearly more desirable **if it** can be made stable and **if it** can be shown that any bubble generation in the bulk of the fluid as a result of the superheat is of no consequence. To achieve the former, the magnetohydrodynamic interaction of a DC magnetic field with the jet nozzle flow or the liquid metal jet itself will be used. Effort to date has been devoted to consideration of the different possible orientations of the magnetic field in terms of their possible effectiveness and adaptability to the geometric and operational constraints of the device.

Discussion

It is known that the application of a magnetic field in the nozzle area of a liquid metal jet stabilizes the jet and delays downstream jet breakdown. The most probable mechanism for this effect is damping of turbulence in the nozzle by the magnetic field. **It** is also known that application of a magnetic field in a free surface flow tends to eliminate ripples on the free surface through the same mechanism of turbulence suppression. These effects are expected to depend on the orientation of the magnetic field, the conductance of the nozzle, suitable non-dimensional parameters for magnetohydrodynamic flows (Hartmann number and interaction parameter) and, of course, flow geometry and upstream conditions. Because no experimental or analytical treatment of the problem for the high velocity, high aspect jet ratios of interest for this application have been found, an assessment of the required analytical development **and/or** experimental investigations has started. Since this assessment is at its very early stages, only general statements can be made at this time. Because the effect on a magnetic field applied at a jet nozzle is understood only qualitatively, the possible effect of a uniform magnetic field on the jet itself was considered first.

There are three possible orientations of the magnetic field relative to the jet. Axial, transverse to the long side of the jet, and transverse to the short side. Without any consideration on the adaptability of a given orientation to the geometric constraints of the device, **it** can be stated that all three orientations will tend to retard the evolution of the rectangular jet to a jet of a circular cross section. Since this evolution is a likely mode of jet breakdown, **it** follows that all three orientations will tend to delay jet instabilities. However, because only deviations from uniform jet velocities produce any magnetohydrodynamic forces in a uniform magnetic field, the relative efficiency of the different orientations can only be ascertained after considerable analysis. This analysis would involve the following steps: 1) determination of steady-state jet evolution without a magnetic field; 2) determination of steady state evolution with a uniform magnetic field; **3)** linear stability analysis for the three orientations of and comparison of results.

The above approach will provide a measure of the relative efficiency of the three possible field orientations. However, because a linear stability analysis is not valid up to jet breakdown, the actual jet behavior will have to be experimentally determined. The same can be said of the effect of magnetic field applied at the nozzle.

An interesting option involves the use of a magnetic field parallel to the long side of the jet that varies in the flow direction. Such a field will induce current eddies which, upon interaction with the applied field, will cause forces that oppose the transition from rectangular to circular jet.

CONCLUSIONS

The use of magnetic fields to stabilize the lithium jet target appears to be feasible. The various options of the use of magnetic fields for jet stabilization have been considered and the approach needed to evaluate their relative efficiency has been laid out.

FUTURE WORK

The assessment of the relative efficiency of the different field orientations will continue. The resources required to carry out a detailed analytical assessment will be estimated and the scope of the activity will be defined on the basis of available resources. An experimental program to study jet stabilization under relevant conditions will be formulated. Bubble formation in the jet bulk will be investigated through a scoping type of analysis, and a more detailed approach will be formulated, if required.

CONCEPTUAL DESIGNS OF SUPERCONDUCTING ACCELERATORS FOR A FUSION MATERIALS IRRADIATION FACILITY. - R. B. Clare. J. R. Delayen, and B. J. Micklich (Argonne National Laboratory)

OBJECTIVE

The International Fusion Materials Irradiation Facility (IFMIF) will require an accelerator capable of delivering reliably a continuous beam of 35 MeV, 250 mA deuterons to a liquid lithium target. Such an accelerator has never been built either as a room temperature or superconducting device. There are reasons to believe that rf superconductivity has distinct advantages for the design and development of cw, high-current accelerators. The objective of this research is to identify all the issues associated with a superconducting accelerator for an IFMIF, to do a conceptual design, and to formulate a development plan.

SUMMARY

This research has been of a theoretical and analytical nature. We have investigated the dynamics of high-current beams with the goal of identifying possible instabilities and their cures, and also the causes of emittance growth and halo formation which would lead to activation of the accelerator. We have also done conceptual designs of some of the critical components of the accelerator, and we have developed a model for the control and stabilization of heavily beam loaded superconducting cavities.

PROGRESS AND STATUS

Beam Breakup in High-Current Superconducting Accelerators

The equation of motion governing cumulative beam breakup has been solved analytically using Fourier analysis. This technique enables the investigation of the effect of non-zero bunch length on beam breakup, which is an especially relevant consideration for low-velocity linacs. It also simplifies the calculation of the transverse dynamics of unbunched particles which constitute a diffuse longitudinal halo between bunches. Simulations illustrating the salient features of cumulative beam breakup with finite bunch length both with and without focusing have been performed.

Halo Formation and Emittance Growth

Charge redistribution in transversely focused space-charge dominated beams occurs on a time scale of the order of a quarter of the plasma period and results in a nearly uniform beam. It is characterized by laminar flow and reversible dynamics, but it can terminate with shock-like behavior and wave breaking. The ensuing turbulence is the signature of irreversible dynamics which will convert available free energy into thermal energy on a time scale which is much less than the relaxation time associated with binary coulomb collisions. In turn, this turbulent heating leads to rapid emittance growth and halo formation. We have done a calculation of the resulting transverse dynamics of a beam in a continuous linear focusing channel. The calculation is based on the Fokker-Planck equation which is used to describe the evolution of the beam following the charge-redistribution phase. Turbulence is assumed to be the principal effect of nonlinear space-charge forces. A model of turbulent heating is used to calculate the Fokker-Planck coefficients, and the particle orbits are modeled as harmonic oscillators with a linear restoring force equal to the net transverse focusing force. These simplifications allow for an analytic, closed-form solution of the Fokker-Planck equation, yielding the evolution of the coarse-grained distribution function of particles in the transverse phase space of a single particle. The results are applied to the one-dimensional sheet beam which provides a sufficient example of the qualitative beam dynamics, and for which the evolution of all of the salient beam properties can be described in terms of well-known functions.

Based on this analysis, an estimate of the ratio of accelerator aperture to beam diameter necessary to keep the activation of the cavities due to beam halo impingement can be obtained. While this work is still in progress, it appears that a ratio of 8 would be sufficient at the beam energy and current of an IFMIF.

Phase and Amplitude Stabilization of Beam-Loaded Superconducting Cavities

A model has been developed to analyze the static and dynamic behavior of superconducting accelerating cavities operated in self-excited loops in the presence of phase and amplitude feedback, ponderomotive effects and beam loading. This is an extension of an earlier analysis of the stabilization of superconducting cavities which has been the basis of the control system of several superconducting accelerators but did not include beam loading. Conditions have been derived to ensure static and dynamic stability in the presence of ponderomotive effects (coupling between the mechanical and electromagnetic modes of the cavity through the radiation pressure). Expressions for the effect of fluctuations of cavity frequency and beam amplitude and phase on the cavity field amplitude and phase and beam energy gain have been obtained.

*Work supported by the Office of Fusion Energy, U.S. Department of Energy, under Contract W-31-109-ENG-38.

Jnvestisations of Superconducting RFQs for the Acceleration of Hiah-Current Beams

Tests of the first superconducting RFQ structure indicated that high surface electric fields could be sustained in a quadrupole geometry. However, the geometry used in those tests was not appropriate for an accelerating structure, and the area sustaining the high electric field was too small to assume that such fields could be achieved in actual RFQ structures. We have initiated a program to analyze and model a variety of geometries suitable for superconducting RFQ structures. We are also designing a niobium RFQ sparker to experimentally measure the surface electric fields that can be achieved on large areas in an actual RFQ structure.

Additionally, we have designed a series of superconducting RFQs based on surface fields which can reasonably be expected to be achieved. These studies are still in progress, but it appears that superconducting RFQs would be able to efficiently accelerate the beam required for an IFMIF.

Niobium Activation Analysis

Work is also under way to estimate the neutron yield and long-term radioactivity generated by deuteron beam interactions with niobium. Deuteron interactions do not appear to create much long-lived radioactivity directly but do create a significant neutron source. Of particular concern are the isotopes ^{92}Nb and ^{91}Nb, which are produced by (n,2n) and (n,3n) reactions.

CONCLUSIONS

We have begun to address what appeared to be the most fundamental and difficult issues related to the application of rf superconductivity to an accelerator for an IFMIF. In all cases, we have found that the issues could be resolved easily and that superconducting accelerators have features which make them particularly attractive for this application.

FUTURE WORK

All of the issues which have been addressed so far need to be pursued in greater depth before a conceptual design can be produced. Once some of the aspects of the design have been finalized, other aspects can be addressed. Additionally, experimental work to test some of the concepts, assumptions, and designs will need to be started as soon as possible.

NEUTRONICS ANALYSIS OF A D-Li NEUTRON SOURCE - I. Gomes, Y. Gohar, and D. Smith (Argonne National Laboratory)

OBJECTIVE

The objective in this preliminary phase is to analyze the neutron flux distribution and nuclear responses that can be achieved inside the test cell. Analysis of the influence of several parameters as deuteron incident energy, lithium target thickness, and beam profile and configuration are to be performed. Also, nuclear responses, such as helium production, nuclear heating, and others, are to be evaluated and roughly estimate the uncertainties of these responses at the high energy tail (above 20 MeV neutrons).

SUMMARY

Results from preliminary calculations for one beam and dual beam configurations are presented. The influence of the lithium target thickness on the neutron economy of the system has been addressed. The nuclear responses induced by the neutron source has been calculated and a brief discussion about the lack of evaluated nuclear cross section data above 20 MeV is presented.

PROGRESS AND STATUS

Discussion

Several parameters are considered in the neutronics performance evaluation of a neutron source. The first parameter is the beam current to which the neutron flux is directly proportional. The second parameter is the number and geometrical spatial positions of the deuteron beams as well as the beam cross sectional area and the deuteron density distribution across the same area. Another parameter is the deuteron energy in the beam which defines the required lithium target thickness for optimum neutron production.

1. Preliminary Uncollided Neutron Flux Results for Single and Dual Beam Configurations

Table 1 presents results of the available volume with uncollided neutron flux above an indicated threshold for three incident deuteron energies for a 2 cm lithium target. The dual beam cases have two separated beam lines perpendicular to each other and positioned at different distance relative to the corner of the test cell. The total deuteron current (200 mA) is maintained constant in all cases and the beams have a flat deuteron density distribution across a 3 by 1 cm area. It can be noticed that the dual beam configuration only presents advantages in terms of available volume when the threshold considered is low enough and/or the distance to the corner is short enough to permit a significant interference between the two beams. The dual beam cases do not produce any gain for a threshold of 10^{15} neutrons/cm^2.sec in terms of volume, since the available volume is reduced significantly. Also, in terms of the flux uniformity, the flux is basically only uniform at the surface which encloses that volume. Once inside that volume, the flux may vary one or more orders of magnitude in a very few centimeters. Figures 1 and 2 display a 3D view of the surface enclosing fluxes above 10^{14} and 10^{15} neutrons/cm^2.sec, respectively.

An alternative to avoid the design complexity of having two separate beam lines and to having a large area with uniform flux is to vary the beam cross sectional area. Studies to quantify and to establish the trends between the two options are underway.

Table 1. Volume with Neutron Flux Above Indicated Threshold

Configuration Type	volume (cm^3)					
	Uncollided Neutron Flux Threshold Value					
	10^{15} n/cm^2.sec			10^{14} n/cm^2.sec		
	Deuteron Energy (MeV)			Deuteron Energy (MeV)		
	30	35	40	30	35	40
Single Beam	19	38	66	930	1550	2400
Dual Beam Cases (position relative to the cell corner, cm)						
20	7	20	40	690	1290	2370
15	7	20	41	830	1610	2650
10				1020	1700	----

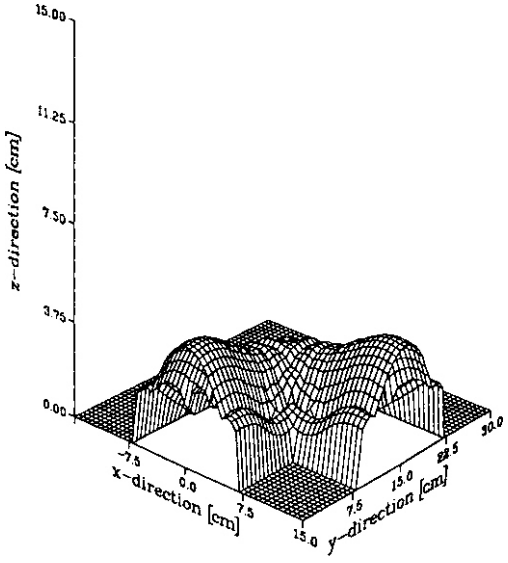

Fig. 1. Surface enclosing total neutron fluxes above 10^{14} neutrons/cm^2.sec for a 3 by 1 cm from a 35 MeV deuteron beam.

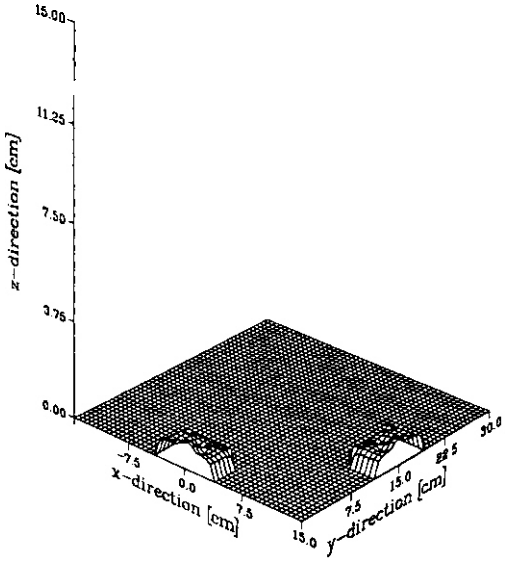

Fig. 2. Surface enclosing total neutron fluxes above 10^{15} neutrons/cm^2.sec for a 3 by 1 cm from a 35 MeV deuteron beam.

2. Neutron Source Strength

Table 2 presents results for the neutron production based on the cross section datal for the Deuteron-Lithium reaction. It can be noticed that most of the neutrons are produced in the energy interval between 0 (zero) and 15 MeV. It also can be noticed that as the deuteron incident energy increases, more neutrons are produced with energies above 20 MeV. On the other hand, increasing the incident deuteron energy of 30 MeV to 35 and to 40 MeV increases the total neutron production by 30% and 63%. respectively. Figure 3 displays the neutron energy spectrum of a 35 MeV incident deuteron beam neutron source.

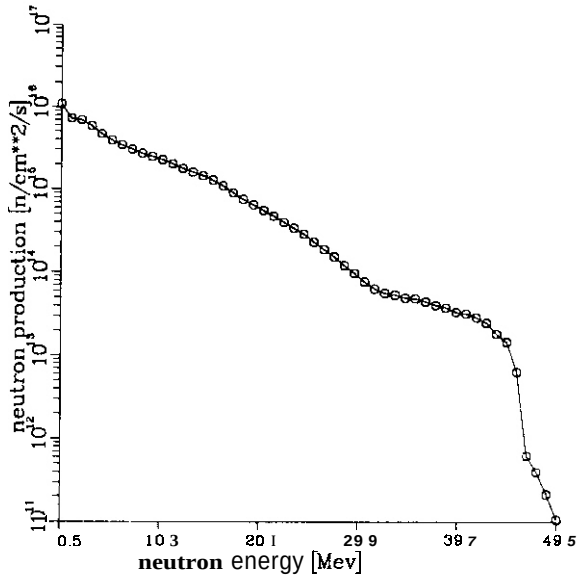

Fig. 3. Neutron energy spectrum for a 35 MeV deuteron beam.

Table 2. Comparison of Neutron Production and Energy Distribution for Three Incident Deuteron Energies

Percentage of Neutrons in Each Energy (MeV) Group	Deuteron Incident Energy 30 MeV	35 MeV	40 MeV
0 to 13	87.10	83.69	79.71
13 to 15	4.84	4.43	4.62
15 to 21	5.51	7.63	9.28
21 to 50	2.54	4.26	6.39
Total Neutron Production	5.226e+16	6.822e+16	8.516e+16
Average Neutron Energy (Mev)	5.59	6.34	7.04

3. Analysis of Nuclear Responses

The analysis of the neutron induced nuclear response is an ongoing task. Preliminary results are presented in this section. The calculation of the nuclear responses was performed with the MCNP[2] Monte Carlo code. For neutrons above 20 MeV, an approximation was used due to the lack of evaluated nuclear data at that energy range. The transport cross section and the nuclear response functions are assumed constant above 20 MeV. It is important to improve this approximation in the future analysis.

Table 3 presents results for nuclear heating and helium production for a 200 mA current of 30, 35, and 40 MeV deuteron beams. The lithium target thickness is taken to be equal to the optimum thickness for the maximum neutron production. The results represent the maximum response values, for a 0.16 cm thick stainless steel plate located at the back of the lithium target. Despite the fact that only 2.54% of the neutrons produced from a 30 MeV deuteron beam have energies above *20* MeV (see Table *2).* the total neutron induced helium production has about 17% of its value due to neutrons with energy above 20 MeV and about 23% of the neutron heating is due to neutrons with energy greater than 20 MeV. For 35 and 40 MeV deuteron beams, about 30% and 37% of the nuclear heating are due to neutrons above 20 MeV, respectively.

Table 3. Nuclear Responses for a 200 mA Beam Current

Energy (MeV)	Neutron Heating (watts/cm^3)			Helium Production (appm/yr)			Hydrogen Production (appm/yr)			Tritium Production (appm/yr)		
	Deuteron Energy (MeV)			Deuteron Energy (MeV)			Deuteron Energy (MeV)			Deuteron Energy (MeV)		
	30	35	40	30	35	40	30	35	40	30	35	40
0 to 20	122	159	197	5,900	7,700	9,400	30,000	38,000	45,000	35	58	84
20 to 50	36	68	114	1,200	2,300	3,900	5,400	10.000	17,000	57	105	178
TOTAL	158	227	311	7,100	10,000	13,300	35,400	48,000	62,000	92	163	262

CONCLUSION

Preliminary neutronics results were obtained for the target area where the effect of energy, geometry, and particle density of the deuteron beam were analyzed.

REFERENCES

1. F.M. Mann, F. Schmittroth, and L.L. Carter. "Neutrons from d + Li and the FMIT Irradiation Environment', HEDL-TC-1459, Westinghouse Hanford Company, Richland. WA.

2. J.F. Briesmeister, ed, MCNP4 - Monte Carlo Neutron and Photon Transport Code", Los Alamos National Laboratory Report LA-7396-M Rev 4.

THE INFLUENCE OF SPECIMEN SIZE ON MEASUREMENT OF THERMAL OR IRRADIATION CREEP IN PRESSURIZED TUBES

F. A. Garner and M. L. Hamilton, (Pacific Northwest Laboratory)', R. J. Puigh, C. R. Eiholzer and D. R. Duncan, (Westinghouse Hanford Company), M. 8. Toloczko, (University of California) and A. S. Kumar, (University of Missouri-Rolla)

OBJECTIVE

The objective of this effort is to determine the impact of specimen miniaturization on measurement of irradiation creep using pressurized tubes.

SUMMARY

Thin-walled pressurized tubes have been developed for measurement of thermal creep and irradiation creep. Miniaturization of these tubes allows more tests to be conducted in the limited reactor space available and decreases the impact of displacement rate gradients and temperature gradients. Studies conducted on a variety of tube sizes show that, when specimen fabrication history and irradiation conditions are controlled. miniaturization can be successfully achieved and valid data produced.

PROGRFSS AND STATUS

Introduction

There is a very limited amount of fission reactor test space available at high neutron fluxes in which to conduct irradiation experiments with well-defined temperatures and well-characterized neutron flux/spectra. The various advanced neutron source concepts currently being proposed for fusion-relevant irradiations will involve even smaller test volumes with larger gradients in displacement rate and possibly temperature. These ronsiderations provide an incentive to miniaturize irradiation test specimens in order to maximize the amount of data obtained and to avoid gradients in both neutron exposure and temperature across a specimen. This in turn requires that detailed studies be conducted to determine the effect of size reductions on the validity of the measurements obtained.

Although a significant amount of progress has been made for tensile and fracture properties (see refs. 1-4, for example), no comparative studies have been published on the miniaturization of the thin-walled pressurized tubes used to study irradiation creep. This paper outlines the results of a number of size effects studies on both thermal and irradiation creep that were conducted under the sponsorship of the U.S. Liquid Metal Reactor (LMR) and fusion reactor programs.

As shown in figure 1, the LMR program eventually centered its research on two standard "NCD" sizes: (5.84 mm and 4.57 mm OD) which are shown compared with the more conventional uniaxial creep specimens that are very difficult to test in reactor. Also shown in figure 1 is a smaller (2.54 mm OD) pressurized tube that was previously under development for the Fusion Materials Irradiation Test (FMIT) facility[5]. When the FMIT project was discontinued, the development effort on this tube was also stopped. This effort may be resurrected if a fusion-relevant neutron source is eventually built. Table 1 compares the dimensions of these three pressurized tubes. Figure 2 shows details of tube construction.

Whatever size is employed, pressurized tubes have inherent advantages for irradiation creep studies. Not only are they relatively small in mass and volume, but the stress is maintained without attachments within the reactor or to its externals. Additionally, the nearly biaxial stress state is almost an exact simulation of the stress state found in the fuel cladding used in the LMR program and the resultant strains are easily applied to other stress states[6]. Lastly, the stress is maintained at a nearly constant value even for relatively large creep-induced strains ($\leq$20%). This is due to the fact that the drop in gas pressure with creep strain is almost exactly offset by the thinning of the tube wall. It should be noted that swelling-induced dimensional changes lead to a drop in gas pressure that is not compensated by wall thinning. Changes in stress, however, are negligibly small for swelling levels less than 10%.

When considering the use of pressurized tubes to study creep, other factors become important and can impact the validity of using these miniature specimens. Whereas solid tensile specimens must meet certain minimum dimensional tolerances, thin-walled pressurized tubes require even more stringent tolerances to avoid introducing large uncertainties in the stress level, especially at temperatures where the strain rate is nonlinear with stress. For example, a 10% variation in wall thickness of a thin-walled tube, with a stress exponent n=4, translates into a large change in stress dependence of creep; $(1.1)^4 = 1.46$. Thin-walled tubes will also have a much more pronounced deformation-induced texture in their grain orientations than

---

'Pacific Northwest Laboratory is operated for the U.S. Department of Energy by Battelle Memorial Institute under Contract DE-AC06-76RLO 1830.

-NCD = National Cladding and Duct

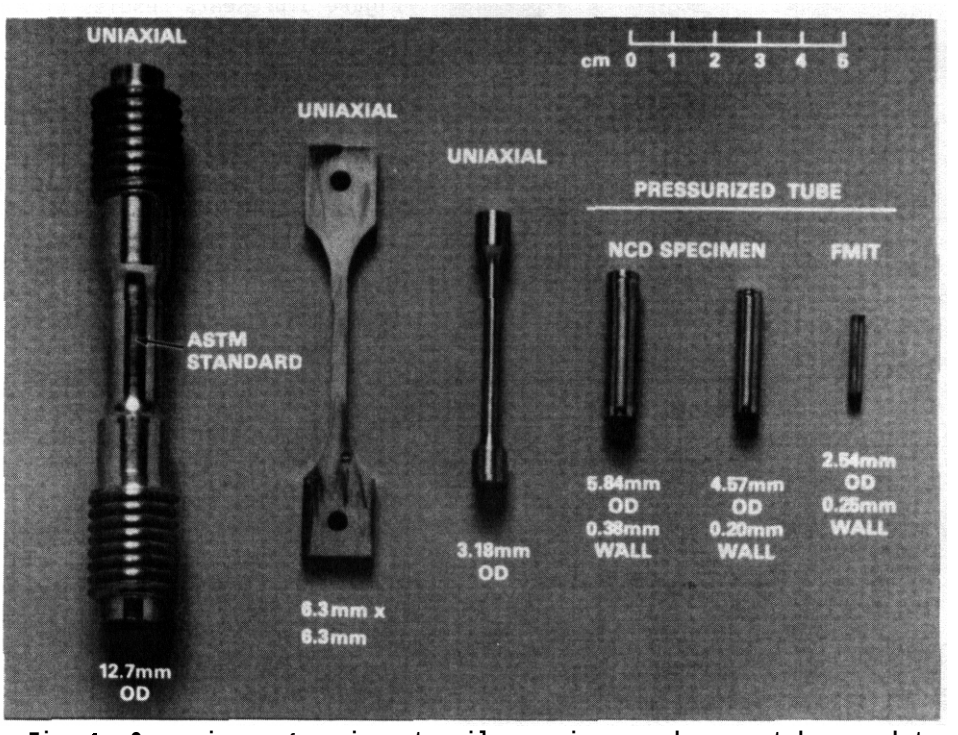

Fig. 1. Comparison of various tensile specimens and creep tubes used to study thermal or irradiation creep in the LMR and fusion reactor materials programs.

Table I--Dimensions of Small Tubes Employed in Current Studies

	Outer Diameter	Length	Wall Thickness
LMR "NCD" Tubes	5.84 mm (0.230 in)	2.82 cm	0.38 mm
	4.57 mm (0.180 in)	2.24 cm	0.20 mm
"FMIT" Tube	2.54 mm (0.100 in)	1.44 cm	0.25 mm

will larger solid tensile specimens, and the uniformity of the cold-work level across the specimen can be significantly different in the two specimen types

When analyzing the performance of miniature tubes. there are two types of size effects to be considered: direct and indirect. Direct size effects concern the influence of end effects and diameter-to-thickness ratios. Both of these influence the degree of triaxiality of the stress state. Indirect size effects arise from the trade-offs sometimes made in constructing smaller tubes. For instance, heating effects associated with the welding of end-caps to the tube may change the microstructure of a relatively larger fraction of the length of smaller tubes. Second, a reduction of the tube diameter may require some changes in processing history, and these changes are not always negligible. Finally, irradiation creep is strongly dependent on the void swelling rate[7-10], and void swelling is often strongly dependent on processing variables[11-13].

The majority of the studies reported here were conducted as thermal creep (constant stress) tests or stress rupture (constant pressure) tests in order to define optimum size ranges. A wider variety of sizes was employed in the early LMR studies, and although these appear in various figures in this paper they were not listed in Table 1 since they were discontinued early in the program. The most pertinent studies will be reported last and concern the in-reactor creep behavior of the two NCD tube sizes.

Experimental Details

The construction of the pressurized tubes has been described elsewhere[14] and is shown schematically in figure 2. In the earliest of the studies described in this paper, the diameter of the tubes were measured at five equidistant locations using differential LVDT probes[15]. The center three measurements were used to assure the absence of end effects, and the average of the three measurements is shown in various figures to follow. In the more recent studies these measurements were made using a non-contacting laser system[16]. Stress rupture tests were conducted at constant internal pressure in a furnace under argon cover gas. Irradiations were conducted under sodium in the Fast Flux Test Facility (FFTF), with the specimens maintained at ±5°C of their target temperature in the Materials Open Test Assembly (MOTA)[14].

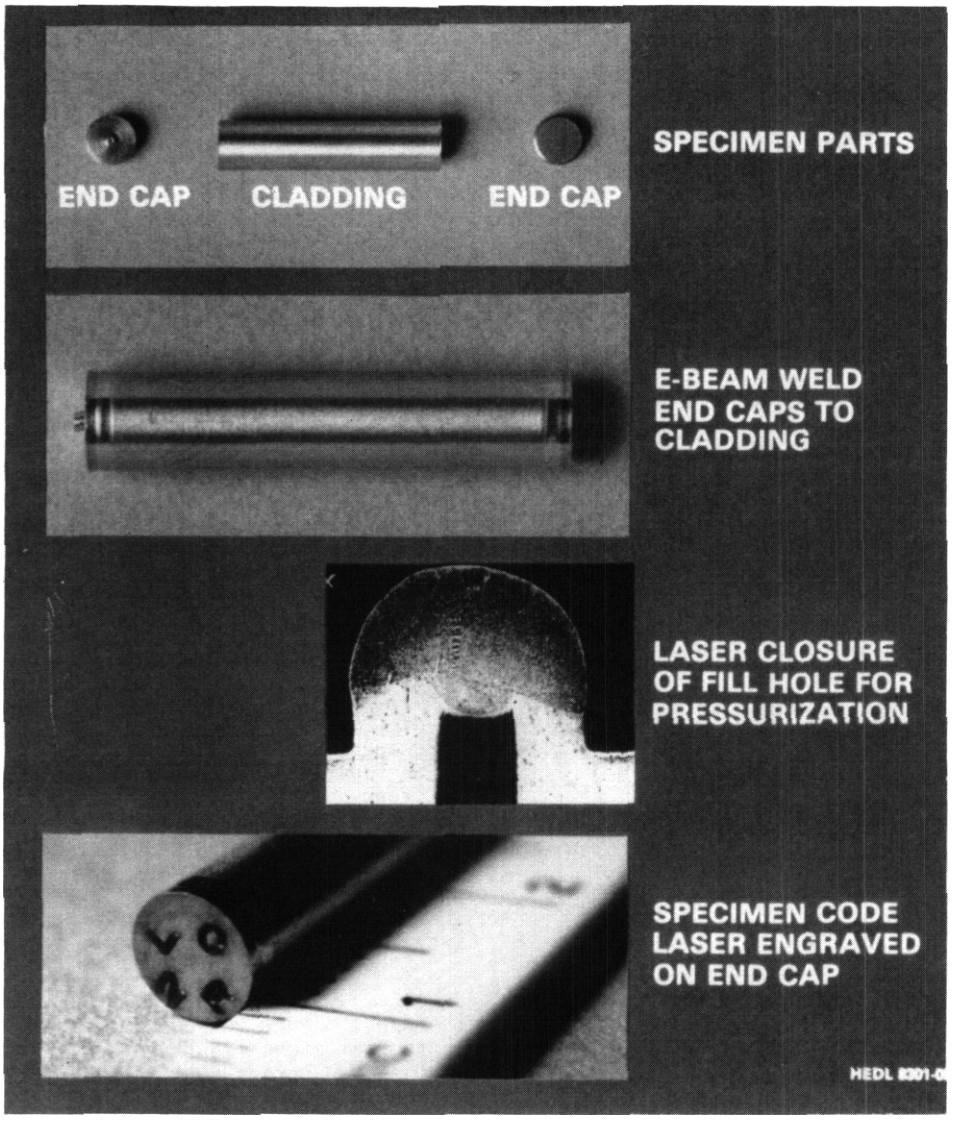

Fig. 2. Details of pressurized tube fabrication.

Results: Out-of-Reactor Tests

Figure 3 presents results of a comparison of the thermal creep response of cold-worked 316 stainless steel for three different stress states in the regime of nonlinear response to stress. Note that two of these stress states involve the use of tubes and the other is a rod specimen. In spite of the different stress states and specimen geometries, relatively good reproducibility between identical specimens and relatively good agreement between differing stress states was obtained when compared on the basis of effective stress and effective strain.

In the current studies, the effect of tube length was investigated. Figure 4 shows a comparison of strain data for nominally identical tubes varying only in their length. It was determined that lengths in excess of 1" (2.54 cm) were unnecessary. It was also determined that the influence of end effects in these tubes was easily avoided by the diameter measurement technique described earlier.

A variety of thermal creep and stress rupture tests have been conducted out of reactor to determine the influence of both tube diameter and length. Figures 5 and 6 show the results of both types of tests conducted on the FFTF first core heats of 20% cold-worked 316 stainless steel. demonstrating no effects of either variable. As shown in figure 7, an even wider range of tube diameters'were tested in a study on the LMR improved D9-type steel based on titanium-modified 316 stainless steel. While the D9 heat used to produce the data in figure 7 does not appear to respond to size differences, another group of silicon and molybdenum modified D9 heats appears to show a pronounced effect of tube size (figure 8). This effect appears to be relatively insensitive to variations in Si and Mo content. As shown in figure 9, the differences in rupture behavior were mirrored in the hardness measurements performed on the two specimen sizes after thermal aging.

When the differences in data between the various heats in figure 8 and 9 are examined in detail, it becomes obvious that some chemical variations are more sensitive to processing history than others. It appears, however, that the differences in rupture behavior for the 5.84 and 4.57 mm (5.84 and 4.57) diameter tubes are illusory and reflect only slight differences in processing history as shown in Table 2.

The only in-reactor size effects tests were conducted on D9 heat 83508 and are described in the next section. As shown in figures 10 and 11, the effect of specimen size, if any, on the thermal creep of these tubes is relatively small at 550 and 750°C. The apparent differences at 575 and 605°C for some pressures are thought to reflect undetected loss of tube pressure prior to the start of the final segment of the aging and measurement sequence.

Results: In-Reactor Tests

Figures 12 and 13 present the irradiation creep and void swelling strains. The differences in deformation behavior for the two tube sizes are relatively small. Upon closer comparison it is obvious that the largest of these relatively small differences occur when the two sizes of specimens were irradiated at significantly different positions in core, as evidenced by measurable differences in their dpa levels.

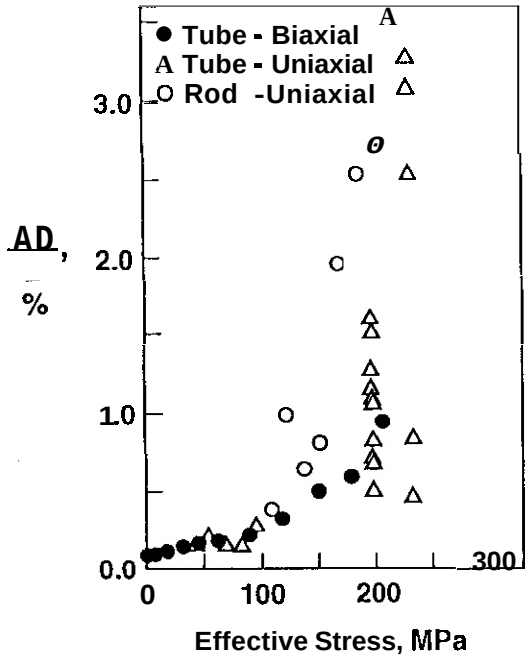

Fig. 3. Effect of geometry and stress state on thermal creep at 650°C of 20% cold-worked 316 stainless steel after 100 hours[15].

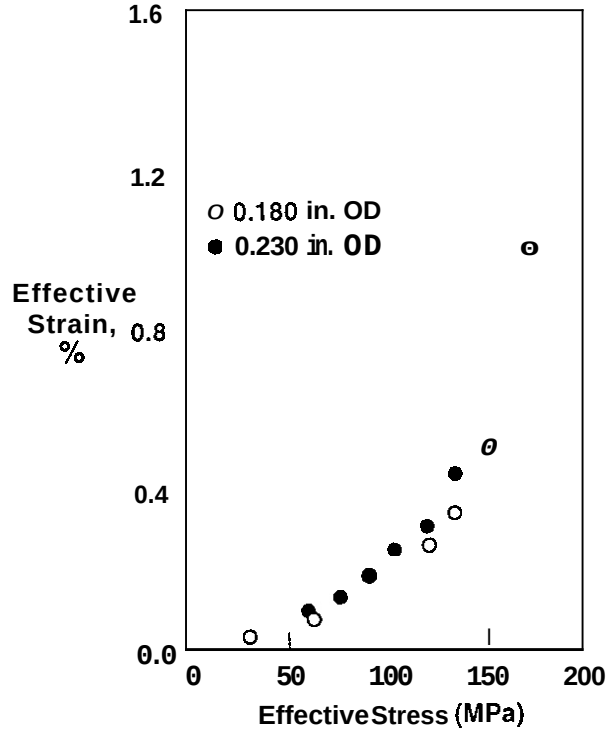

Fig. 5. Effect of tube diameter on thermal creep at 575°C of 20% cold-worked 316 stainless steel after 3,000 hours. (NCD tubes described in table 1.)

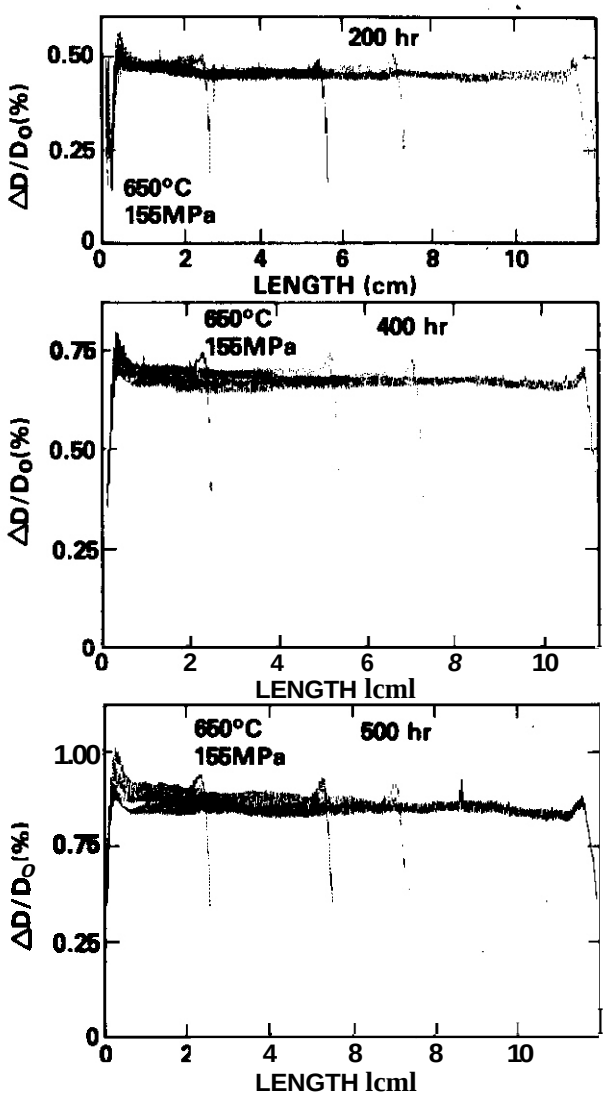

Fig. 4--Effect of tube length on thermal creep of 20% cold-worked 316 stainless steel at 650°C.

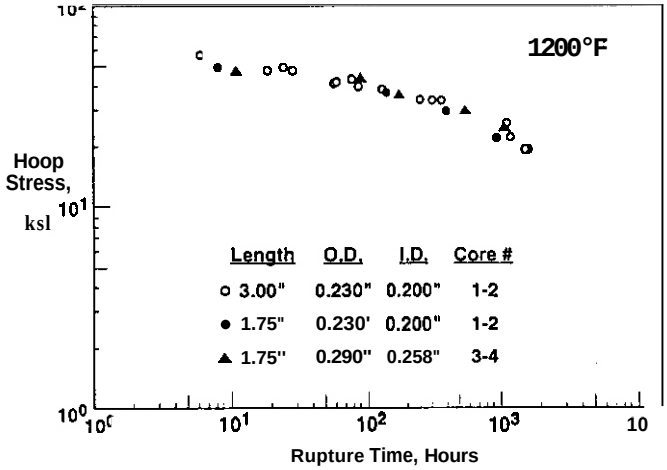

Fig. 6. Influence of tube size on stress rupture behavior at 650°C of 20% cold-worked 316 stainless steel used in the first several core loadings of FFTF.

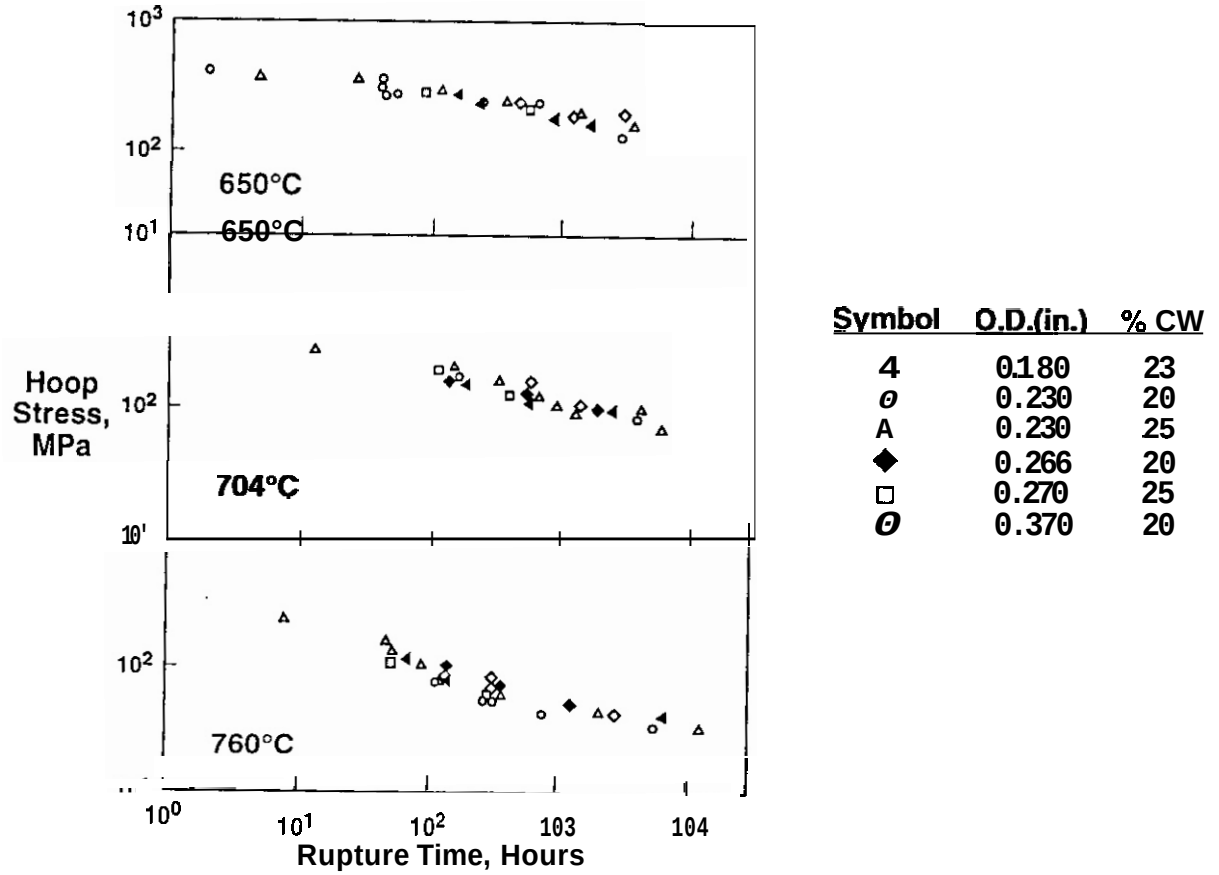

Fig. 7. Influence of tube diameter and cold-work level on the stress rupture behavior of titanium modified alloy D9-C1.

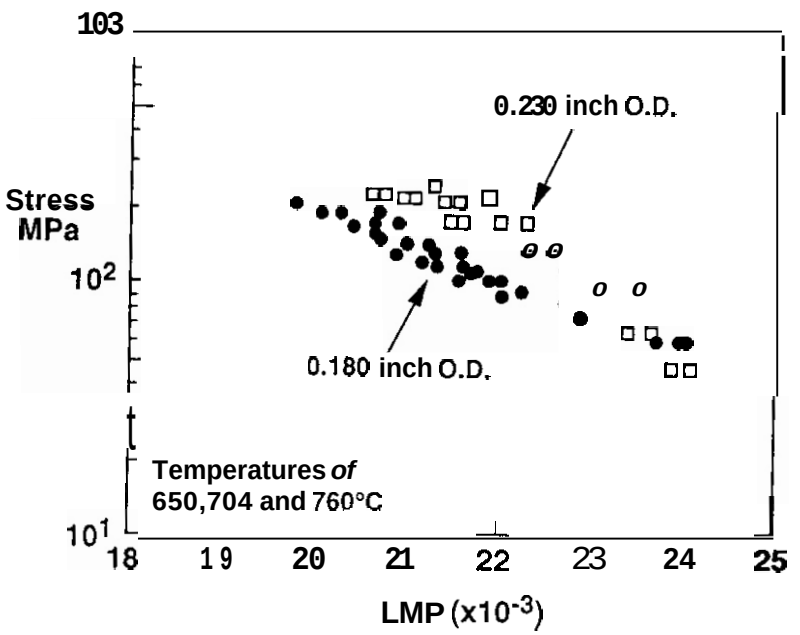

Fig. 8. Stress rupture behavior of chemical variations (Si and Mo) of 20% cold-worked D9 alloy. The apparent size effect is an artifact of differences in production history. LMP is the Larson-Miller parameter.

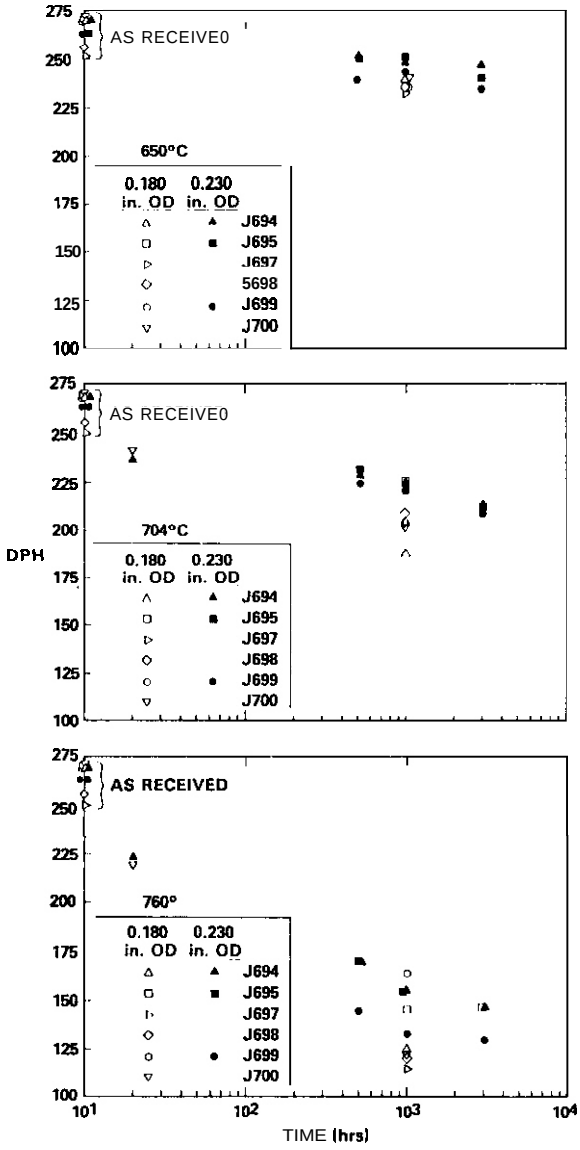

Fig. 9. Hardness of the chemical variable heats of D9 following aging at 650, 704 and 760°C, showing different behavior at two tube sizes. The range of hardness response reflect: the individual sensitivity of each variant to processing and aging history.

Thus, even these relatively small differences probably arise from the flux and temperature sensitivity of void swelling and its very large impact on irradiation creep.

Discussion

The experimental results presented in this paper clearly indicate that, within the range of sizes explored in these studies, there are no significant effects of specimen size on thermal creep or irradiation creep. It is possible, however, to produce the appearance of a size effect if some other variable is inadvertently introduced into the comparison. Relatively small changes in heat treatment and radiation environment, for example, have been shown to produce such a result.

The role of heat treatment is known to be particularly strong. In a recent study[17] it was shown that small differences in radiation variables could produce significant differences in swelling behavior, but even larger changes could be induced by variables that are normally thouqht unnecessary to control. The interpass annealing or 'temper" anneaiing temperature between' successive cold-work reductions exerts a particularly large effect on void swelling, primarily by affecting the duration of the transient regime of swelling[13]. The influence of the temper annealing temperature on recrystallization has also been found to be unexpectedly strong, overshadowing the influence of minor variations in alloy composition[18]. The processes involved in recrystallization are also invoived in determining the high temperature behavior of thermal and irradiation creep.

CONCLUSIONS

It appears that thin-walled pressurized tubes can be reduced in size without introducing any problems in data generation or creep analysis. Care must be taken, however, to avoid the inadvertent introduction of other uncontrolled variations in tube manufacture or irradiation environment.

FUTURE WORK

This effort is complete.

Table 2--Processing History of Pressurized Tubes Constructed From the Chemical Variable Heats of D9

Tube O.D.	Homogenization Temperature	Interpass Anneal Temperature
0.230 in (5.84 mm)	1175°C (5 hrs)	~1070°C
0.180 in (4.57 mm)	1175°C (5 hrs)	~1070°C
	1200°C (24 hrs)*	one intermediate solution treatment at 1175°C

*hot rolled at 1175°C and annealed (1025°C/1 hr/WQ) between homogenization treatments.

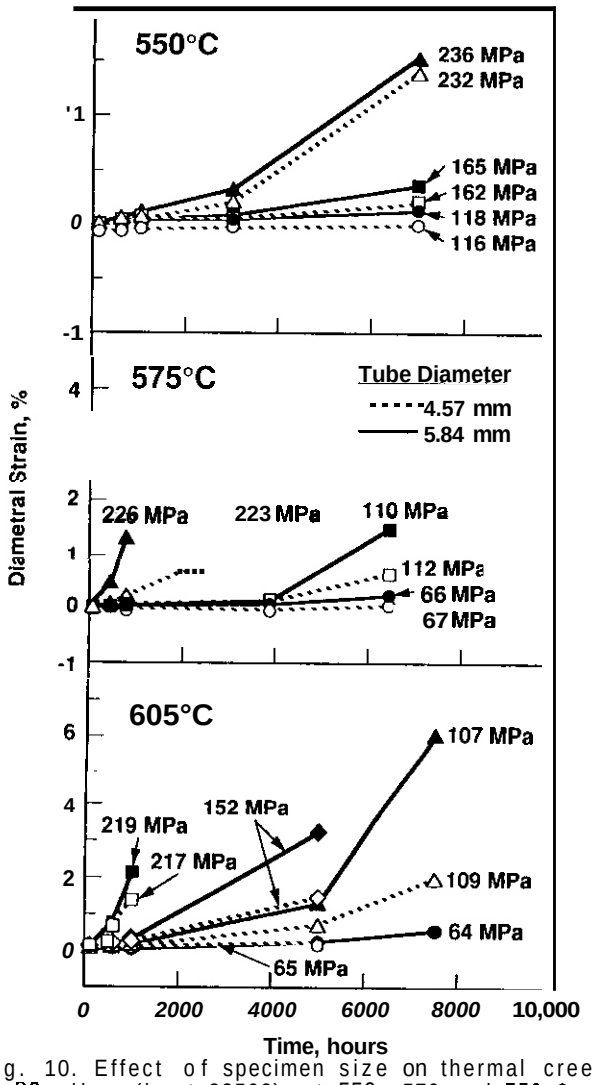

Fig. 10. Effect of specimen size on thermal creep of D9 alloy (heat 83508) at 550, 570 and 750°C.

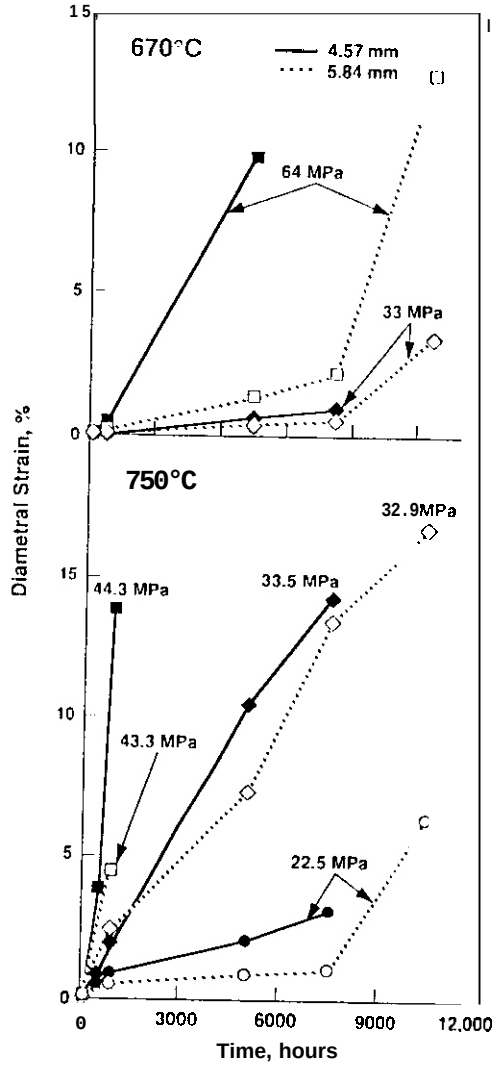

Fig. 11. Effect of specimen size on thermal creep of 09 alloy (heat 83508) at 670-750°C.

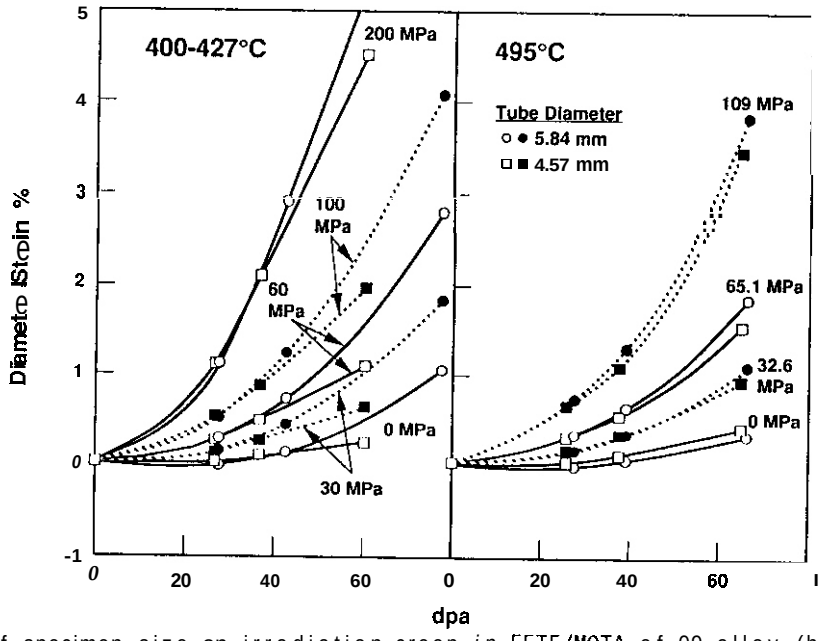

Fig. 12. Influence of specimen size on irradiation creep *in* FFTF/MOTA of 09 alloy (heat 83508) at 400 at 495°C.

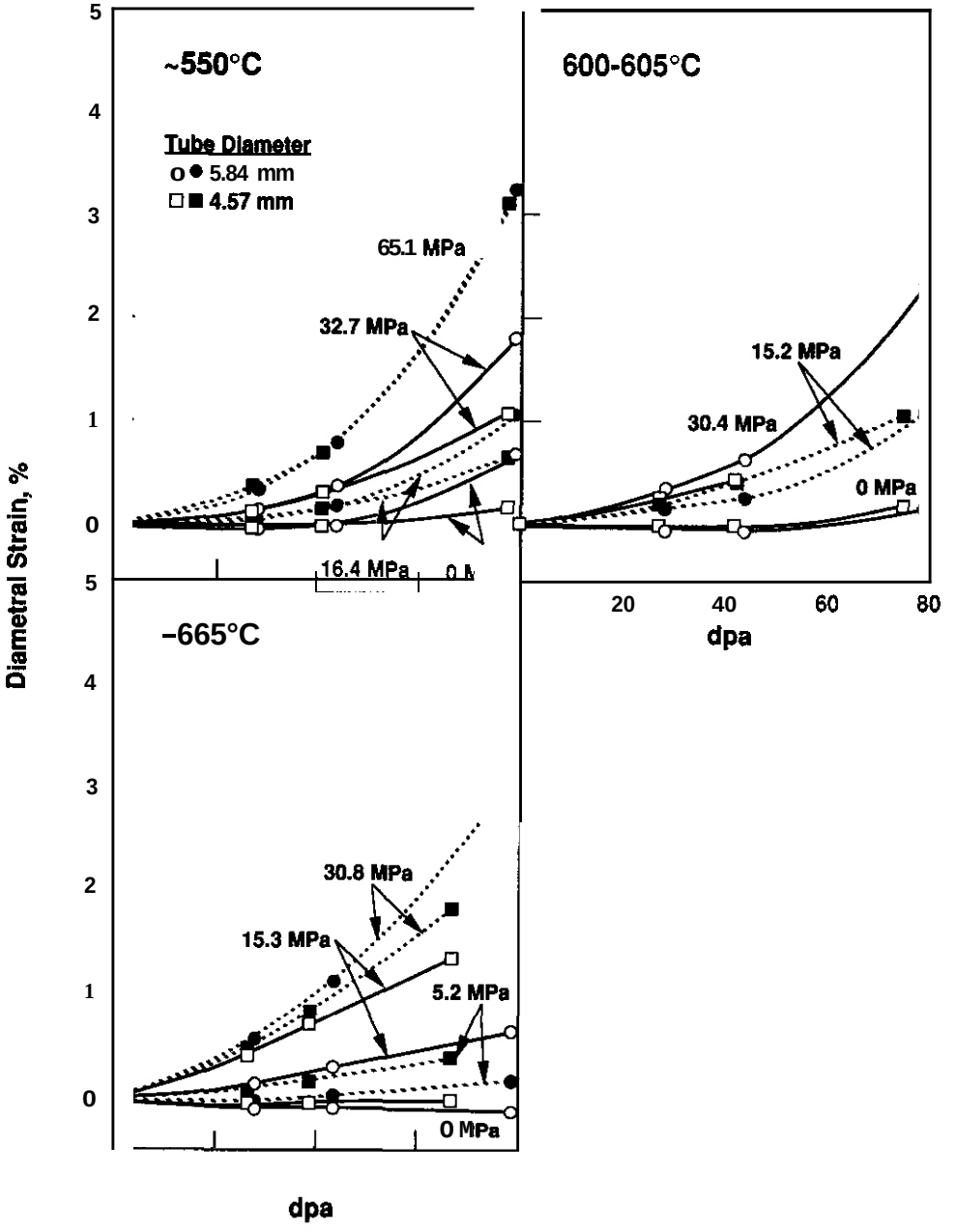

Fig. 13. Influence of specimen size on irradiation creep in FFTF/MOTA of D9 alloy (heat 835081 at 550 to 665°C.

ACKNOWLEDGEMENTS

This work was supported by the U.S. Department of Energy under Contracts DE-AC06-76RLO 1830 and DE-AC06-76FF02170. The participation of M. B. Toloczko and A. S. Kumar was supported by the Northwest College and University Association for Science (Washington State University) under Grant DE-FG06-89ER-75522 with the U.S. Department of Energy.

REFERENCES

1. Kumar, A. S., Garner, F. A., Hamilton, M. L., and Louden, B. S., "Recent Improvements in Size Effects Correlations for DBTT and Upper Shelf Energy of Ferritic Steels", ASTM International Symposium on Small Specimen Test Technology and Their Application to Nuclear Reactor Pressure Vessel Annealing and Plant Life Extension, New Orleans LA, January 29-30, 1992 (in press).

2. Garner, F. A., Hamilton M. L., Heinisch H. L., and Kumar, A. S., "Application of Miniature Tensile Specimens to Studies of Radiation Damage in Metals", ibid.

3. Lucas, G. E., Metallurgical Transactions 21A(1990)1105.

4. "The Use of Small-Scale Specimens for Testing Irradiated Material," ASTM STP 888, W. R. Corwin and G. E. Lucas, Eds., American Society for Testing and Materials, Philadelphia, 1983.

5. Hagan, J. W., Opperman, E. K., and Trego, A. L., Journal of Nuclear Materials 122 & 123 (1984) 958.

6. Malvern, L. E., "Introduction to the Mechanics of a Continuous Medium", Prentice-Hall, Inc., 1969, pg. 364-366.

7. Garner, F. A. and Gelles, D. S., Journal of Nuclear Materials 159 (1988) 286.

8. Garner, F. A. and Porter, D. L., Journal of Nuclear Materials 155-157 (1988) 1006.

9. Toloczko, M. E., Garner, F. A., and Eiholzer, C. R., Journal of Nuclear Materials 191-194 (1992) in press.

10. Woo, C. H., Garner, F. A., and Holt, R. A., Proceedings of 16th International Symposium on Effects of Radiation on Materials, Denver CO, 1992, in press.

11. Erager, H. R., and Garner, F. A., "Dependence of Void Formation on Phase Stability in Neutron-Irradiated Type 316 Stainless", Effects of Radiation on Structural Materials, ASTM STP 683, J. A. Sprague and D. Kramer, Eds., American Society for Testing and Materials, 1979, pp. 207-232.

12. Garner, F. A., Journal of Nuclear Materials 122 & 123 (1984) 459.

13. Garner, F. A., Bates, J. F., and Mitchell, M. A., Journal of Nuclear Materials, 189(1992)201.

14. Puigh, R. J. and Schenter, R. E., "In-Reactor Stress Rupture Experiment in the Materials Open Test Assembly (MOTA)", Effects of Radiation on Materials: Twelfth International Symposium, ASTM STP 870, F. A. Garner and J. S. Perrin, Eds., American Society for Testing and Materials, Philadelphia, 1985, pp. 795-802.

15. Gilbert, E. R. and Blackburn, L. D., Transaction of the ASME (1977) 168.

16. Gilbert, E. R. and Chin, B. A. "Irradiated Materials Measurement Technology", Effects of Radiation on Materials: Tenth conference, ASTM STP 725, D. Kramer, H. R. Erager and J. S. Perrin, Eds., American Society for Testing and Materials, 1981, pp. 665-679.

17. Garner, F. A., Heinisch, H. L., Simons, R. L. and Mann, F. M., Radiation Effects and Defects in Solids, 113 (1990) 229.

18. Paxton, M. M., Knecht, R. L., and Holmes, J. J., IERSM Semiannual Progress Report, HEDL TME 74-51, Hanford Engineering Development Laboratory (1974) pp. HEDL:58-61.

19. Garner, F. A., Hamilton, M. L., Eiholzer, C. R., Tolocrko, M. E., and Kumar, A. S., Journal of Nuclear Materials 191-194 (1992) in press.

20. Garner, F. A., Hamilton, M. L., Eiholrer, C. R., Toloczko, M. E., and Kumar, A. S., Proceedings of 16th International Symposium on Effects of Radiation on Materials, Denver CO, 1992, in press.

STATUS OF U.S./JAPAN COLLABORATIVE PROGRAM PHASE II HFIR TARGET CAPSULES - J. E. Pawel and R. L. Senn (Oak Ridge National Laboratory)

OBJECTIVE

The objective of this program is to determine the response of various U.S. and Japanese austenitic and ferritic stainless steels with different pretreatments and alloy compositions to the combined effects of displacement damage and helium generation at temperatures in the range of 300 to 600°C and doses of 18 to 70 dpa.

SUMMARY

A complete description and details of the design, construction, and installation of capsules JP-9 through JP-16 has been previously reported.[1] The capsules were installed in the High Flux Isotope Reactor (HFIR) target July 20, 1990 for irradiation beginning with HFIR fuel cycle 289. The capsules were removed and stored in the reactor pool during HFIR cycle 292 (11/25/90 - 12/10/90) to provide room for required isotope production. They were reinstalled for HFIR cycle 293 for continued irradiation. Of these eight target capsules, JP-10, 11, 13, and 16 completed their scheduled number of cycles (11) and were removed from the reactor in September 1991. In addition, JP-14 was removed from the reactor at the end of cycle 310 (9/18/92) after 21 cycles.

Three new capsules in this series, JP-20, 21, and 22, are currently being designed. These capsules were added to the program in order to complete the experimental matrix included in the JP-9 through JP-16 capsules. The new capsules will contain transmission electron microscope (TEM) disks and SS-3 flat tensile specimens at 300-600°C and will achieve doses of 8, 18 and 40 dpa, respectively. The preliminary experiment matrix is described in detail in a previous report.[1]

PROGRESS AND STATUS

Capsules JP-9 throueh JP-16

The as-built specimen matrix for the JP-9 through JP-16 series capsules can be found in a previous report[2] These capsules contain TEM disks, bar and flat (SS-3) tensile specimens, hourglass fatigue specimens, and sheet specimens. A wide variety of alloys and thermomechanical conditions are included. Many of the TEM disks were made from isotopically tailored alloys to produce a range of He/dpa ratios (<0.1, 10, 20, 70). The experiment addresses long-standing basic questions on the role of helium in microstructural evolution and will explore the high fluence swelling behavior of the most swelling-resistant materials currently available. Details of the irradiation history of these capsules is shown in Table 1.

During this reporting period, JP-14 was removed from the reactor after completing the scheduled number of cycles (21) and having accumulated a total dose of 38905 MWd or 34 dpa. It will remain stored in the reactor pool for a cool-down period before disassembly in early 1993.

Causules JP-20 throueh 22

Three new capsules have been added to the US/Japan collaborative testing of Phase II HFIR target capsules, identified as JP-20, 21, and 22. These capsules are designed to complete the original experiment matrix of the JP-9 through JP-16 series capsules. It is planned to irradiate the three capsules in inner target positions for 5, 11, and 22 cycles, respectively, to achieve peak doses of approximately 8, 18, and 35 dpa. Specimen temperatures in each capsule will be 300, 400, 500, or 600°C.

PRESENT STATUS

Parts for JP-20, 21, and 22 that were the same as previous capsules have been received and subassemblies completed where possible. Assembly drawings will be issued in November 1992. Loading lists are being finalized.

TABLE 1. IRRADIATION HISTORY - JP-9, -10, -11, -12, -13, -14, -15, -16

HFIR OPERATION				JP 10,-11,-13,-16		JP-14		JP-P,. -12, -15	
CYCLE YO.	START DATE	END DATE	MWd/ Cycle	IRR. TO 20 DPA MWd	dpa*	IRR. TO 40 DPA MWd	dpa*	IRR. TO 70 MWd	A dpa*
289	07-20-W	09-07-K	1879	1879	1.64	1879	1.64	1879	1.64
290	w-19-90	10-11-w	1852	3731	3.26	3731	3.26	3731	3.26
291	10-17-90	11-13-90	1838	5569	4.86	5569	4.86	5569	I.M
292	11-25-90	12-10-90	1847	CAPSULES CUT OF REACTOR FOR THIS CYCLE					
293	12-27-PO	01-23-91	1965	7534	6.58	7534	6.58	7534	6.58
291	02-01-91	02-25-91	1906	9440	8.24	9440	8.24	9440	8.21
295	03-01-91	03-21-91	1908 **	11348	9.91	11348	9.91	11348	9.91
296	04-06-91	04-28-91	1871	13222	11.54	13222	11.54	13222	11.51
297	05-19-91	06-15-91	1845 ■■	15067	13.15	15067	13.15	15067	13.15
2P8	06-20-91	07-11-91	1747	16811	14.68	16814	14.68	16811	11.68
299	07-25-91	08-15-91	1711	18555	16.20	18555	16.20	18555	16.20
300	08-28-91	09-17-91	1724	20279	17.70	20279	17.70	20279	17.70
301	09-27-91	10-19-91	1851	JP-10, -11, -13. -16		22130	19.32	22130	19.32
302	10-27-91	11-21-91	1829	removed 9/19/91 at		23959	20.92	23959	20.92
303	12-01-91	12-22-91	1821	end HFIR Cycle 300.		25780	22.51	25780	22.51
304	12-31-91	01-24-92	1826			27606	24.10	27606	21.10
305	01-30-92	02-27-92	1876			29482	25.74	29482	25.74
306	33-31-92	04-27-92	1845 **			31327	27.35	31327	27.35
307	05-01-92	05-28-92	1842			33169	28.96	33169	28.96
308	06-02-92	06-30-92	1938			35107	30.65	35107	30.65
309	07-03-92	08-01-92	1949			37056	32.35	37056	32.35
310	08-27-92	09-18-92	1849			38905	33.96	38905	33.96
311						REMOVED AT EOC 310			

* DPA levels based on achieving 0.000873 dpa/MWd.

** These values were corrected 10/27/92 to reflect values from the most recent HFlR power history as published by RRD.

FUTURE WORK

The required drawing revisions must he completed and the balance of parts ordered so that capsule assembly can begin. Final loading lists and capsule assembly procedures will be developed. Installation in HFIR is planned for early in 1993.

REFERENCES

1. R. L. Senn, "Status of U.S./Japan Collaborative Program Phase II HFIR Target Capsules," pp. 8-20 in Fusion Reactor Materials Semiann. Proe. Rep. Sept. 30, 1987, DOE/ER-0313/3, US. DOE Office of Fusion Energy.

2. R. L. Senn, "Status of U.S./Japan Collaborative Program Phase II HFIR Target Capsules," pp. 7-9 in Fusion Reactor Materials Semiann. Proe. Rep., March 31, 1988, DOE/ER-0313/4, U.S. DOE Office of Fusion Energy.

3. R. L. Senn, "Status of U.S./Japan Collaborative Program Phase II HFIR Target Capsules," pp. 6-13 in Fusion Reactor Materials Semiann. Proc. Rep., Sept. 30, 1988, DOE/ER-0313/5, U. S. DOE Office of Fusion Energy.

4. J. E. Pawel and R. L. Senn, "Status of U.S./Japan Collaborative Program Phase II HFIR Target Capsules," pp. 15-23 in Fusion Reactor Materials Semiann. Proe. Reo., March 31. 1992, DOE/ER-0313/12, U. S. DOE Office of Fusion Energy.

FABRICATION AND OPERATION OF HFIR-MFE RB* SPECTRALLY TAILORED IRRADIATION CAPSULES

A. W. Longest, D. W. Heatherly, E. D. Clemmer (Oak Ridge National Laboratory).

OBJECTIVE

The objective of this work is to fabricate and operate irradiation capsules for irradiating magnetic fusion energy (MFE) candidate first-wall materials in the High Flux Isotope Reactor (HFIR) removable beryllium (RB*) positions. Japanese and U.S. MFE specimens are being transferred to RB* positions following irradiation to 7.5 dpa at temperatures of 60, 200, 330, and 400°C in Oak Ridge Research Reactor (ORR) experiments ORR-MFE-6J and -7J.

SUMMARY

Fabrication and operation of four HFIR-MFE RB* capsules (60, 200, 330, and 400°C) to accommodate MFE specimens previously irradiated in spectrally tailored experiments in the ORR are proceeding satisfactorily. With the exception of the 60°C capsule, where the test specimens are in direct contact with the reactor cooling water, specimen temperatures (monitored by 21 thermocouples) are controlled by varying the thermal conductance of a thin gas gap region between the specimen holder outer sleeve and containment tube.

Irradiation of the 60 and 330°C capsules was started on July 17, 1990. As of September 30, 1992, these two capsules had completed 22 cycles of their planned 24-cycle (formerly 22-cycle) irradiation to a damage level of approximately 18.3 displacements per atom (dpa). Assembly of the 200 and 400°C capsules is scheduled for completion in November 1992; operation of these two capsules will follow the first two (60 and 330°C).

PROGRESS AND STATUS

Introduction

A series of spectrally tailored irradiation capsules are being fabricated and operated as part of the U.S./Japan collaborative program for testing MFE candidate first-wall materials in mixed-spectrum fission reactors. The test specimens are being irradiated in the RB* facility' of the HFIR.

Four HFIR-MFE RB* capsules were designed to accommodate Japanese and U.S. MFE specimens previously irradiated to 7.5 dpa at temperatures of 60, 200, 330, and 400°C in the ORR in spectrally tailored experiments ORR-MFE-6J and -7J. Details of these ORR experiments, including descriptions of the test matrix, mechanical property specimens, and techniques of spectral tailoring, have been reported elsewhere?' Hafnium liners are being used in the HFIR-MFE RB" experiments to tailor the neutron spectrum to closely match the helium production-to-atom displacement ratio (14 appm/dpa) expected in a fusion reactor first wall.

The HFIR-MFE RB* capsules are being irradiated in pairs (first the 60 and 330°C capsules, then the 200 and 400°C capsules) to a damage level of approximately 18.3 dpa. The target exposure level was given as 17.5 dpa (22 HFIR cycles) in the last progress report[4]; however, it was decided to extend the 60 and 330°C irradiations for two additional cycles to 18.3 dpa (24 HFIR cycles), at which time the 200 and 400°C capsules should be assembled and ready to replace them.

60°C Causule

The 60°C capsule, designated HFIR-MFE-60J-1, is an uninstrumented capsule with the test specimens in contact with the reactor cooling water. Capsule design, assembly, and details of the specimen loading were described previously.'

Irradiation of this capsule began July 17, 1990, at the start of HFIR cycle 289. As of September 30, 1992, 22 cycles of its planned 24-cycle irradiation to a damage level of approximately 18.3 dpa had been completed. Specimen operating temperatures in this capsule are predicted to be within 10°C of 60°C.

330°C Causule

The 330°C capsule, designated HFIR-MFE-330J-1, is an instrumented and singly contained capsule where the specimen temperatures are monitored by 21 thermocouples and controlled by adjusting the thermal conductance of a thin gas gap region between the specimen holder outer sleeve and containment tube. This capsule is cooled with 49°C reactor cooling water flowing downward over the containment tube surface. Capsule design, assembly, and details of the specimen loading were described previously.[6,7]

Irradiation of this capsule began on July 17, 1990, at the start of HFIR cycle 289. As of September 30, 1992, 22 cycles of its planned 24–cycle irradiation to a damage level of approximately 18.3 dpa had been completed.

Typical thermal operating data for the 330J-1 experiment were presented in detail previously[8]. During this report period, measured temperatures in the aluminum alloy specimen holder continued to indicate specimen operating temperatures within about 25°C of 330°C, which satisfies the temperature criterion for these experiments.

200 and 400°C Causules

The 200 and 400°C capsule designs were described previously[9] and are basically the same as that of the 330°C capsule. The main differences in the three capsule designs are associated with (1) the number and spacing of the specimen holder slots and holes to accommodate differences in the number of specimens of the various types, (2) the width of the temperature control gas gap region between the specimen holder outer sleeve and containment tube to obtain the desired specimen operating temperatures, and (3) the test piece included in the aluminum plug and holder above the test specimen holder to obtain extra information.

Assembly of the 200 and 400°C capsules was started this report period hut completion was delayed by approximately two months because of aluminum welding difficulties. A defective weld was discovered in both of the aluminum housing tube weldments that were designated for use on these capsules; both welds had passed full inspection (helium leak test, dye-penetrant and radiography) approximately two years earlier when the housing tubes were fabricated. Subsequent inspections revealed cracks in the weld area on the inside of both housing tubes. This problem was solved by replacing the cracked welds with new ones. However, during examination of the replacement welds, porosity was revealed that was borderline with respect to meeting specifications. This porosity could not be eliminated in subsequent test welds. At this point, the replacement welds were evaluated on the basis of updated design requirements and found to be acceptable for the intended use, and assembly of the capsules was resumed.

Assembly of the 200°C capsule was nearing completion at the end of this report period. Assembly of the 400°C capsule is scheduled for completion in November 1992. Operation of these two capsules will follow the first two (60 and 330°C) and is scheduled to start in November 1992.

FUTURE WORK

Assembly of the 200 and 400°C capsules is scheduled for completion in November 1992. These two capsules are to be operated for 24 HFIR cycles.

REFERENCES

1. K. R. Thoms et al., "HFIR Irradiation Facilities Improvements - Completion of the HIFI Project," J. Nucl. Mater., 155-157 (1988) 1340-45.

2. J. L. Scott et al., pp. 12-20 in *ADIP Semiann. Prog. Rep., March 31, 1985,* DOE/ER-0045/14, U.S. DOE, Office of Fusion Energy.

3. J. L. Scott et al., *Second Annual Prog. Rep. on United States-Japan Collaborative Testing in the High Flux Isotope Reactor and the Oak Ridge Research Reactor, Sept. 30, 1985,* ORNL/TM-10102.

4. A. W. Longest et al., "Fabrication and Operation of HFIR-MFE RB* Spectrally Tailored Irradiation Capsules," in *Fusion Reactor Materials Semiann. Prog. Rep., March 31, 1992,* DOE/ER-0313/12, US. DOE, Office of Fusion Energy.

5. **A. W.** Longest et al., "Design and Fabrication **of** HFIR-MFE RB* Spectrally Tailored Irradiation Capsules," in ***Fusion Reacfor Maferials Semiann. Prog. Rep., March 31, 1988,*** DOE/ER-0313/4, U.S. DOE, Office of Fusion Energy.

6. **A. W.** Longest et al., "Design and Fabrication **of** HFIR-MFE RB* Spectrally Tailored Irradiation Capsules," in ***Fusion Reacfor Materials Semiann. Prog. Rep., Sept. 30, 1987,*** DOE/ER-0313/3, U.S. DOE, Office of Fusion Energy.

7. **A. W.** Longest et al., "Design and Fabrication of HFIR-MFE RB* Spectrally Tailored Irradiation Capsules," in ***Fusion Reacfor Maferials Semiann. Bog. Rep., Sept. 30, 1988,*** DOE/ER-0313/5, **U.S.** DOE, Office of Fusion Energy.

8. **A.** W. Longest et al., "Fabrication and Operation **of** HFIR-MFE RB* Spectrally Tailored Irradiation Capsules," in ***Fusion Reacfor Materials Semiann. Prog. Rep., Sept. 30, 1991,*** DOE/ER-0313/11, **U.S.** DOE, Office **of** Fusion Energy.

9. **A.** W. Longest et al., "Design and Fabrication **of** HFIR-MFE RB* Spectrally Tailored Irradiation Capsules," in ***Fusion Reactor Materials Semiann. Bog, Rep., March 31, 1989,*** DOE/ER-0313/6, U.S. DOE, Office of Fusion Energy.

2.0 DOSIMETRY, DAMAGE PARAMETERS, AND ACTIVATION CALCULATIONS

NEUTRON DISPLACEMENT DAMAGE CROSS-SECTIONS FOR SiC*, Hanchen Huang and Nasr Ghoniem, University of California, Los Angeles

OBJECTIVES

The objective of the present study is to develop and apply a computational tool for calculations of neutron displacement cross-sections for ***SIC*** in various fission and fusion neutron spectra.

SUMMARY

Calculations of neutron displacement damage cross-sections for ***SIC*** are presented. We use Biersack and Haggmark's empirical formula in constructing the electronic stopping power, which combines the Lindhard's model at low PKA energies and the Bethe-Bloch' s model at high PKA energies. The electronic stopping power for polyatomic materials is computed **on** the basis of Bragg's Additivity Rule. A continuous form of the inverse power law potential is used for nuclear scattering. Coupled intergro-differential equations for the number of displaced atoms j, caused by PKA i, are then derived. The procedure outlined above gives partial displacement cross-sections, displacement cross-sections for each specie of the lattice, and for each PKA type. The corresponding damage rates for several fusion and fission neutron spectra are calculated. The stoichiometry of the irradiated material is investigated by finding the ratio of displacements among various atomic species. The role of each specie in displacing atoms is also investigated by calculating the fraction of displacements caused by each PKA type. The study shows that neutron displacement damage rates of ***SIC*** in typical magnetic fusion reactor first wall will be ~10-15 $[\text{dpa}][MW]^{-1}[m]^2$, that in typical lead-protected inertial confinement fusion reactor first walls to be ~15-20 $[\text{dpa}][MW]^{-1}[\text{m}]^2$. For fission spectra, we find that the neutron displacement damage rate of ***SIC*** is –74 [dpa] per 10^{27} n/m^2 in FFTF, –39 [dpa] per 10^{27} in HFIR, and ***25*** [dpa] per 10^{27} in NRU. Approximately 80% of displacement atoms are shown to be of the carbon-type.

PROGRESS **AND** STATUS

Introduction

Early calculations of radiation damage rates in monatomic materials have been made **on** the basis of simplifying assumptions. Jenkins [1] and Sheely [2] used the Kinchin-Pease model to account for the displacement efficiency and calculated the displacement cross-sections for iron. Their work was extended and made complete by Doran [3], who used Lindhard's model in accounting for the displacement efficiency and included inelastic (e.g., $(n, 2n)$ and (n,γ)) nuclear reaction channels. Investigation of displacement rates in polyatomic materials **soon** followed. In the works of Baroody [4] and Andersen & Sigmund [5], the contributions of the electronic stopping to the energy loss were omitted. Realizing the importance of this mechanism of energy loss, Parkin and Coulter [6] accounted for the electronic stopping by using Lindhard's model and solving coupled intergro-differential equations for the number of displaced atoms. The investigations were applied to MgO, Al_2O_3 and TaO. Their work was further developed to a computer code by Greenwood [7]. Alberman & Lesueur [8] developed a similar computer code (COMPOSI), on the basis of their own formulation to calculate the displacement damage rates in diatomic materials. However, their formulation is not accurate because they assumed that the energy transferred is fixed after the ion travels a distance in the matrix.

In this paper, we present a calculational method for displacement damage in ***SIC.*** First, we construct the electronic stopping power based on Lindhard's [9,10] and Bethe-Bloch's [11,12] formulations, and **use** Biersack and Haggmark's empirical bridging formula [13]. Secondly, we extend this formulation to polyatomic materials and use Bragg's Additivity Rule, which was experimentally shown to be reasonably accurate within 10-15% [14]. Thirdly, we formulate coupled intergrodifferential equations for the number of displaced atoms. The numerical procedure is an extension of the Runge-Kutta method to coupled differential equations. Following these steps, we calculate the partial displacement cross-sections, the damage rates of each atomic specie, the damage rates caused by each PKA type, the total displacement cross-section, and the total displacement damage rates of ***SIC*** under irradiation conditions of FFTF, HFIR, NRU [15], **PROMETHEUS** [16] and ARIES4 [17]. Finally, conclusions are given in section ***5***, especially the implications of these results to simulation experiments of neutron irradiation in non-fusion facilities

Theory

Electronic Stopping Power in Polyatomic Materials

In the low energy range, Lindhard's theory of electronic stopping for energetic ions is well accepted. Although it is proposed by Ziegler et al. [18] that the electronic stopping power of silicon and carbon may behave as $E^{0.35}$ at very low ion energies, we use the Lindhard formulation. The reasons for this choice are two fold: (1) there is not enough experimental data to give accurate electronic stopping cross-sections in the very low energy range, and (2) electronic stopping in this range ($E \leq 500$ eV) doesn't have a large effect on displacement damage calculations. The Lindhard's electronic stopping cross-section is given by [9,10]

$$S_e = \frac{1}{N_2}\left(\frac{dE}{dx}\right)_e = 8\pi e^2 a_0 \frac{Z_1^{7/6} Z_2}{Z} \frac{v}{v_0} \tag{1}$$

where $Z^{2/3} = Z_1^{2/3} + Z_2^{2/3}$, $v_0 = \frac{2\pi e^2}{h}$, and $a_o = 0.529\,\text{Å}$

Z, and Z_2 are charge numbers of the projectile and the target atoms, respectively e the charge of an electron, v the velocity of the projectile, N_2 the atom density of the target, and h the Planck constant. This formula is valid for PKA energies $E < 25$ KeV/amu [18].

In the case of fusion neutron irradiation of low Z elements, the PKA energy can be high enough so that Lindhard's formulation does not hold anymore. For PKA energies greater than 200 KeV/amu, the Bethe-Bloch's electronic stopping power is in good agreement with experiments. The Bethe-Bloch's stopping cross-section is given by [11,12]:

$$S_e = \frac{1}{N_2}\left(\frac{dE}{dx}\right)_e = \frac{2\pi Z_{eff}^2 Z_2 e^4 (M_1/m_e)}{e} \ln\left(\frac{4E}{(M_1/m_e)\bar{I}}\right) \tag{2}$$

where Z_{eff} is an effective charge of the projectile, given by Bohr [19]. E is the energy of the projectile, M_1 the mass of the projectile, m_e the mass of the electron, N_2 the atomic density of the target, and, $\bar{I}$ the ionization energy of the target atom. This stopping formulation is valid for PKA energies $E > 200$ KeV/amu.

To cover the entire range, we propose to extrapolate the formulation of Bethe-Bloch to low energy by linear extrapolation at the highest stopping energy point. The two stopping powers are then bridged according to Biersack and Haggmark's procedure [13], which is given by:

$$S_e^{-1} = (S_e)_{\text{Lindhard}}^{-1} + (S_e)_{\text{Bethe-Bloch}}^{-1} \tag{3}$$

The theoretical prediction of electronic stopping power based on this equation is compared with the experimental data of electronic stopping power in monatomic materials given by Northcliffe [20], and very good agreement is obtained. Since the Bragg's Additivity Rule has been experimentally shown to be accurate within 10-15% [14], we extend the electronic stopping power obtained above to polyatomic materials based on Bragg's Additivity Rule. This is given by:

$$(S_e)_{composite} = \frac{\sum_i A_i N_i S_{ei}}{\sum_i A_i N_i} \tag{4}$$

where A, N_i and S_{ei} are mass number, atomic density and single element electronic stopping cross-section of specie i, respectively.

Interatomic Potentials & Atomic Scattering Cross-sections

Winterbon[21] compared the accuracy of the atomic scattering cross-section based on the inverse power law potential with that based on the Thomas-Fermi potential, and found that they are in fairly good agreement, provided that several power laws are used to cover the entire energy range. Therefore, the inverse power law potential, which is very simple, is used in this paper. In applying the inverse power law potential, the main problem to be solved is matching potentials of different powers. Here, we are concerned with the energy transfer process. Therefore, we match different powers by requiring that the atomic stopping cross-section is continuous at each transition point. According to Winterbon[21], we have:

$$\sigma(E,T)dT = C_m E^{-m} T^{-1-m} dT \tag{5}$$

where $C_m = \frac{\pi}{2}\lambda_m a^2 \frac{A_1}{A_2}\left(\frac{2Z_1Z_2e^2}{a}\right)^{2m}$ and $a = \frac{0.4683}{\left(Z_1^{2/3}+Z_2^{2/3}\right)^{1/2}}$

The value of the power m, and the constant λ_m are given by:

$$\begin{aligned}(m,\lambda_m) &= (1/3,\ 1.309) && \text{for } \varepsilon \le \varepsilon_2\\ &= (1/2,\ 0.327) && \text{for } \varepsilon_2 \le \varepsilon \le \varepsilon_1\\ &= (1,\ 0.5) && \text{for } \varepsilon_1 \le \varepsilon\end{aligned}$$

where ε is the reduced energy $\varepsilon = E/e_0$ while $e_0 = \frac{Z_1Z_2e^2}{a}$, $(\varepsilon_1, \varepsilon_2)$ are transition energies, and A, and A, are the mass numbers of the projectile and the target respectively.

Chou and Ghoniem [22] modified this cross-section at extremely low energies. They proposed to match the Born-Mayer potential by using an inverse power potential with $m = 0$ and $\lambda_m = 24$ for $\varepsilon < \varepsilon_3$. According to the matching procedure mentioned above, Chou and Ghoniem found that the transition energies should be chosen as $(\varepsilon_1, \varepsilon_2, \varepsilon_3) = (2 - 10, 0.369, 0.0234)$. For SiC, we found that a smoother matching can be obtained if we choose $\varepsilon_1 = 15$. Therefore the values, $(\varepsilon_1, \varepsilon_2, \varepsilon_3) = (15, 0.369, 0.0234)$ are used in this paper. We compared the results based on these two different matching procedures and found that they give similar results, except that the new matching gives smoother dependence of the damage cross-section on energy.

Governing Equations for the Number of Displaced Atoms, ν_{ij}

Assume that the solid contains atoms of type i and j. If a PKA of type i travels a distance dx, it will eventually result in a number of displacements of atoms of type i (ν_i) and a number of atoms of type j (ν_{ij}). Similarly, a PKA of type j will produce ν_{ji} and ν_{jj}. Conservation of atoms implies that each one of these numbers are separately conserved over all possibilities. That is to say that ν_{ij} is conserved before and after interaction. Therefore, we have the following conservation equations

$$\begin{aligned}\nu_{ij}(E) = \sum_k \int_0^{\Lambda_{ik}E} \Big(\Gamma(E - T - E_{jd}/\Lambda_{ij})\nu_{ij}(E - T) + \Gamma(T - E_{kd})(\delta_{kj} + \nu_{kj}(T))\Big) N_k \sigma_{ik}(E,T)dxdT\\ + \int_0^{T_{cm}} \nu_{ij}(E - T_e) N_e \sigma_{ie}(E,T)dxdT + \left(1 - \sum_k N_k \sigma_{ik}(E)dx - N_e \sigma_{ie}(E)dx\right)\nu_{ij}(E)\end{aligned} \tag{6}$$

where ν_{ij} is the number of displaced atoms of type j caused by PKA of type i, excluding the PKA itself, $\Gamma(x)$ is the step function, N_i the atomic density of specie i, $\sigma_{ij}(E,T)$ the differential atomic scattering cross-section of species i and j, $\sigma_{ij}(E)$ the total microscopic atomic scattering cross-section between species i and j, Λ_{ij} the energy transfer efficiency between

species i and j, and δ_{kj} the Kronecker delta function. The first integral represents the number of displacements ν_{ij} if a PKA (of type i) collides with target atoms in traveling through a short distance dx. The contributions to ν_{ij} are the displacements resulting from the collision in dx, the displacements induced by the slowed-down PKA, and the displacements induced by the SKA (Secondary Knock-on Atom). The second integral represents the number of displacements ν_{ij} if the PKA collides with electrons in traveling dx. The last term represents the number of displacements ν_{ij} if nothing happens in traveling the distance dx. The collision cascade model will be discussed in more detail in the next section. The reader is referred to Lindhard's work (e.g. ref **3)** for further explanation of the derivation of equation **(6).**

Approximating $\nu_{ij}(E - T_e) = \nu_{ij}(E) - T_e\left(\frac{d\nu_{ij}(E)}{dE}\right)$ and performing the algebraic manipulations, we obtain the following coupled integro-differential equations:

$$S_{ie}\frac{d\nu_{ij}(E)}{dE} = \sum_k f_k \int_0^{\Lambda_{ik}E} \left\{\left[\Gamma_{ik}E(T - E_{kd})(\delta_{kj} + \nu_{kj}(T))\right]\sigma_{ik}(E,T)dT + \left[\Gamma(E - T - E_{jd}/\Lambda_{ij})\nu_{ij}(E - T) - \nu_{ij}(E)\right]\sigma_{ik}(E,T)dT\right\} \tag{7}$$

where $S_{ie}(E)$ is the electronic stopping cross-section for projectile of specie i, f_k the fraction of atom density of specie i in the composite, E_{jd} the displacement threshold of specie j.

Because there is no resonance in the displacement efficiency and the atomic scattering cross-section, there is little doubt that the integration could be done attaining high accuracy by using any simple integration procedure. **On** the other hand, care must be exercised in solving the coupled integral-differential equations (7). We extended the Runge-Kutta[23] method to two coupled differential equations, and the numerical extension procedure of Runge-Kutta method to **2** coupled differential equations is given in Appendix A.

Collision Cascade Model

A PKA (of type i) traveling a short distance in binary ceramics may have several collision channels. The PKA may collide with an atom of specie k (k may represent **Si** or C) and transfer an amount of energy T to the atom. There will be slowed-down PKA's with energy $(E\text{-}T)$ and SKA's with energy T after the collision. Both the slowed-down PKA's and SKA's will continue to displace lattice atoms as long as they are energetic enough. If the energy of the PKA is high enough, there will be a series of displacements initiated by this single PKA. Since the free path of a heavy ion is small, displacements will occur locally, and a displacement cascade ensues. In this process, the minimum energy transferable is the displacement threshold energy, $E_{\ }$, of the target atom, which is **92.6** eV and **16.3** eV for silicon and carbon, respectively [24]. In order lo transfer this amount of energy from specie i to specie k, the knock-on atom of specie i must have energy no less than E_{kd}/Λ_{ik}. Below this energy, a knock-on atom of specie **i** cannot displace an atom of specie k anymore and the knock-on atom is captured.

Capture events are treated via a threshold capture energy value represented by the step function $\Gamma(E - T - E_{jd}/\Lambda_{ij})$. In the event that $i = j$ (i.e., similar species), $\Lambda_{ij} = 1$ and the minimum energy required for displacement is E_{jd}. When the species are different, the minimum energy required **is** E_{jd}/Λ_{ij}. This procedure is equivalent to the treatment given by Parkin and Coulter [6]. However, in our calculations, the displacement cross-section is found to be insensitive to the capture events.

The PKA may collide only with electrons in dx and not cause displacement. The energy transfered to electrons, T_e, is used in electronic excitations. The PKA is left with energy $E - T_e$, which will be used in displacing lattice atoms or exciting electrons in the subsequent steps.

The PKA may collide with nothing in dx and keep its original energy E, which will then be used in displacing lattice atoms or exciting electrons in the subsequent steps.

The Primary Recoil Spectrum

When a diatomic material is irradiated by a neutron, **PKA's** may be of type i or type j. The primary recoil spectrum (PRS) depends on three factors: (1) the neutron scattering cross-section with each specie, (2) the anisotropy of neutron elastic scattering cross-section, and (3) the neutron spectrum. The number of PKAs of type i per unit energy at energy E is defined as:

$$P_i(E) = \int_{E_n,\min}^{E_n,\max} \Phi(E_n) \sum_{\ell=\text{all channels}} 2\pi\sigma_{\ell,i}(E_n,\theta) \left|\frac{d\cos\theta}{dE}\right| dE_n \qquad (8)$$

where $\Phi(E_n)dE_n$ is the neutron flux from energy E_n to $E_n + dE_n$, $\sigma_{\ell,i}(E,\theta)$ is the differential scattering cross-section of a neutron with specie **i** in nuclear channel ℓ (e.g., elastic, (n,n'), (n,p), (n,α), (n,γ) nuclear reactions). The neutron spectra [15,16,17] for several facilities are shown in figure (1). The neutron elastic cross-section of silicon at low energies ($E_n \leq 2$ MeV) is given by Hughes and Schwanz [26]. Other neutron cross-sections are obtained from the ENDF-V library [25]. The reasons for this choice are two fold: (1) the neutron elastic cross-section of silicon at low energies is not available in ENDF-V, and (2) the neutron elastic cross-section of carbon deducted from the total neutron cross-section given by Hughes and Schwartz[26] is in good agreement with that obtained from ENDF-V [25]. The neutron elastic cross-sections for silicon and carbon are compared in figure (2) [25,26]

For the elastic collision channel, we have:

$$E_{\min} = 0 \qquad E_{\max} = \Lambda_{ni} E_n \qquad \left|\frac{d\cos\theta}{dE}\right| = \frac{2}{\Lambda_{ni} E_n} \qquad (9)$$

where Λ_{ni} is the energy transfer efficiency between a neutron and specie i. For the (n,γ) nuclear reaction channel, we find that the minimum (E_{min}) and maximum (E_{max}) transferred energies are given by:

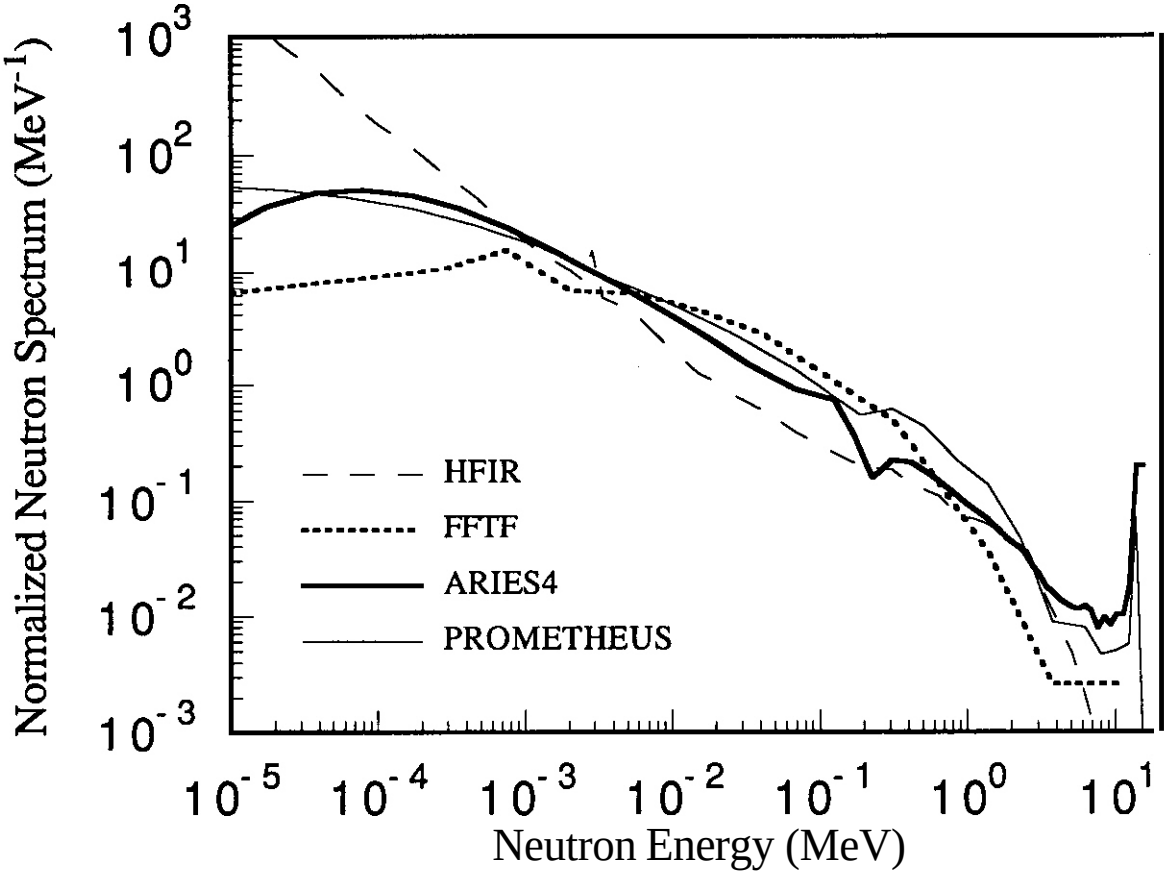

Figure 1: Neutron spectra in several fusion and fission facilities

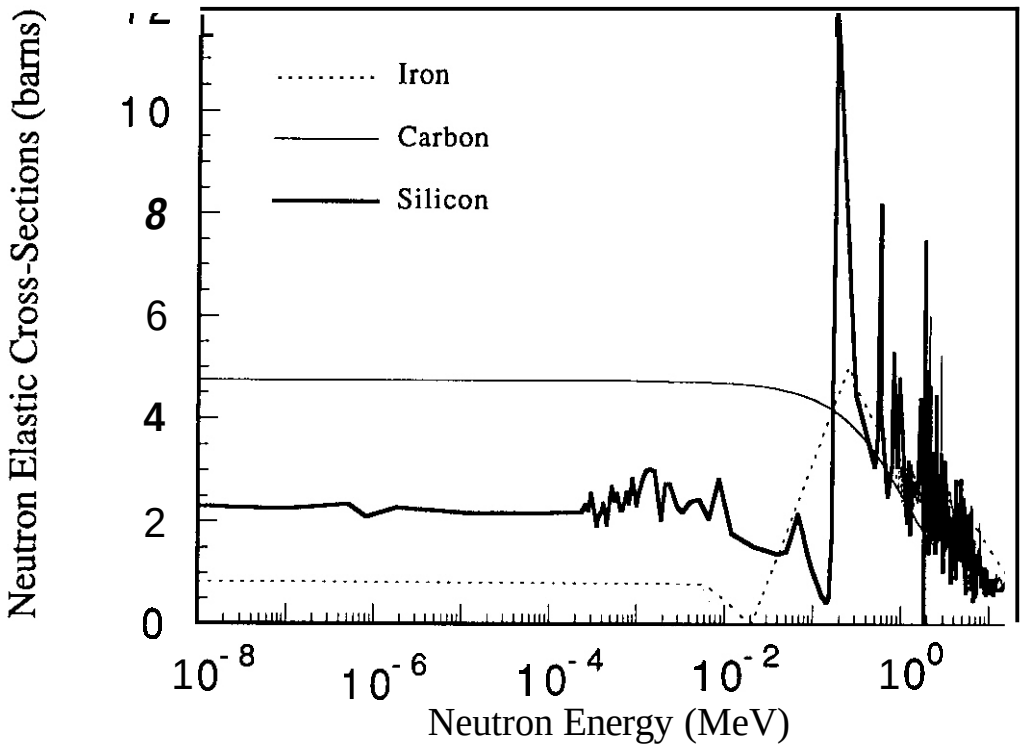

Figure 2: Comparison of neutron elastic scattering cross-sections of carbon and silicon

$$E_{\min/\max} = \frac{E_n}{1+A_i} - \frac{1}{2(1+A_i)}\left(\frac{A_i}{1+A_i}\frac{E_n}{c} - \frac{Q_{i,\gamma}}{c}\right)^2 \mp \frac{\sqrt{2E_n}}{1+A_i}\left(\frac{A_i}{+A_i}\frac{E_n}{c} - \frac{Q_{i,\gamma}}{c}\right) \tag{10}$$

and

$$\left|\frac{d\cos\theta}{dE}\right| = \frac{1+A_i}{\sqrt{2E_n}}\left(\frac{A_i}{1+A_i}\frac{E_n}{c} - \frac{Q_{i,\gamma}}{c}\right)^{-1} \tag{11}$$

For a given (n,x) nuclear reaction channel, ($x = n', p, \alpha$, etc.), we get:

$$E_{\min/\max} = \frac{B_i E_n}{(1+A_i)^2} + \left(\frac{A_i E_n}{1+A_i} - Q_{i,\ell}\right)\left(1+\frac{B_i}{x}\right)^{-1} \mp \frac{2}{1+A_i}\sqrt{\left(\frac{A_i E_n^2}{1+A_i} - Q_{i,\ell}E_n\right)\left(\frac{1}{x}+\frac{1}{B_i}\right)^{-1}} \tag{12}$$

and

$$\left|\frac{d\cos\theta}{dE}\right| = \frac{1+A_i}{2}\sqrt{\left(\frac{1}{x}+\frac{1}{B_i}\right)\left(\frac{A_i E_n^2}{1+A_i}\right)^{-1}}$$

where c is the speed of light, A_i is the mass number of specie i, $B_i = A_i + 1 - x$ the mass number of the resulting atom in reaction, $Q_{i,l}$ the neutron reaction energy of specie i in channel ℓ, $s = \Lambda_{Bj}/\Lambda_{ij}$ a scale factor which accounts for (n,α) and (n,γ) reactions.

There are several reasons of using s to acwunt for (n,α), (n,p) and (n,γ) channels. First, a (n,α) reaction produces a PKA that is dramatically different from the lattice atom. The associated Q-value is large, while the cross-section is small.

Secondly, the PKA is not too much different from the lattice atom in (n,p) and (n,γ) channels, as far as the electronic stopping power and atomic scattering cross-section are concerned. The last and the most important factor is that even for fusion neutron spectra, the neutron elastic collision channel still dominates. All other channels contribute a small fraction of the total cross-section. But if neutron sources with higher neutron energies are used, non-elastic nuclear reaction channels have to be carefully studied.

In the present study, we only consider elastic, (n,n'), (n,p), (n,α) and (n,γ) nuclear reactions channels because other channels have very high Q-values ($\geq$ 10 MeV), small cross-sections or both, for neutrons with energy less than 15 MeV.

The Displacement Cross-section and Damage Rate

We define the partial displacement cross-section as

$$\sigma_{ij}(E_n) = \sum_{t=\text{all channels}} 2\pi \int_{E_{min}}^{E_{max}} s\sigma_{t,i}(E_n,\theta) \left| \frac{d\cos\theta}{dE} \right| [\nu_{ij}(E) + \delta_{ij}]\, dE \tag{14}$$

Because each specie in a polyatomic material has different neutron cross-sections, the probability that a neutron will collide with specie i is $\dfrac{N_i\sigma_{t,i}(E_n)}{\sum_i N_j\sigma_{t,j}(E_n)}$. However, the probability that a PKA will collide with specie i is simply assumed to be proportional to the atomic density of specie i. Based on these arguments, the partial displacement cross-section for lattice atom i is given by:

$$\sigma_{\text{lattice } i} = f_i \sum_k \frac{N_k\sigma_{t,k}(E_n)}{\Sigma_t(E_n)} \sigma_{ki}(E_n) \tag{15}$$

where $\sigma_{t,k}(E_n)$ is the total neutron microscopic cross-section of specie k, $\Sigma_t(E_n)$ the total macroscopic neutron cross-section of the composite.

The displacement damage rate of specie i is given as

$$R_{\text{lattice } i} = \int_{E_{n\,min}}^{E_{n\,max}} \sigma_{\text{lattice } i}(E_n)\Phi(E_n)dE_n \tag{16}$$

The total displacement cross-section and total displacement damage rate are simply given as the summation of the partial displace ment cross-sections and partial damage rates respectively. Similarly we can define the partial displacement cross-section corresponding to PKA of type i as:

$$\sigma_{\text{PKA}\,i}(E_n) = \frac{N_i\sigma_{t,i}(E_n)}{\Sigma_t(E_n)} \sum_k f_k\sigma_{ik}(E_n) \tag{17}$$

The corresponding displacement damage rate $R_{\text{PKA }i}$ can be calculated in the same way as for $R_{\text{lattice } i}$.

Cascade Stoichiometry

It is clear from the formulation presented here that the displacement damage rates of various elements in a polyatomic solid can be vastly different. If the displacement damage rates of various elements are not in proportion to their stoichiometry

in the matrix, the possibility of non-stoichiometric microstructure formation will exist. Asymmetries in displacement threshold energies for various elements in the material, different nuclear reaction cross-sections, and different electronic energy loses for various elements in the material can lead to non-stoichiometric cascades. Let's now define the displacement cascade stoichiometry ratio as:

$$S_{ij} = \frac{R_{\text{lattice } i}}{R_{\text{lattice } j}} - S_{mat} \tag{18}$$

where S_{mat} is the thermodynamic stoichiometric ratio of the matrix, which is 1 for stoichiometric SiC. If S_{ij} is zero, then the cascade stoichiometry **is** the same as that of the matrix, Otherwise, the cascade is considered to be non-stoichiometric.

To gain insight into the type of PKA which results in more damage, we define the PKA damage ratio as:

$$PR_i = \frac{R_{\text{PKA } i}}{\sum_j R_{\text{PKA } j}} \tag{19}$$

Results

The electronic stopping power of carbon in carbon is shown in figure (3), where equations **(1-3)** are used. The general fit given by equation **(3)** gives good agreement with the experimental data reported by Northcliffe[20]. It is noted that the electronic stopping power at high PKA energies deviates substantially from the Lindhard's model. For carbon PKA with energies greater than –*2* MeV, the Lindhard's model would tend to overestimate the electronic energy loss. Thus for fusion neutrons, **this** effect is expected to play an important role. For silicon, however, the deviation from Lindhard's model at PKA energies relevant to fusion applications is small.

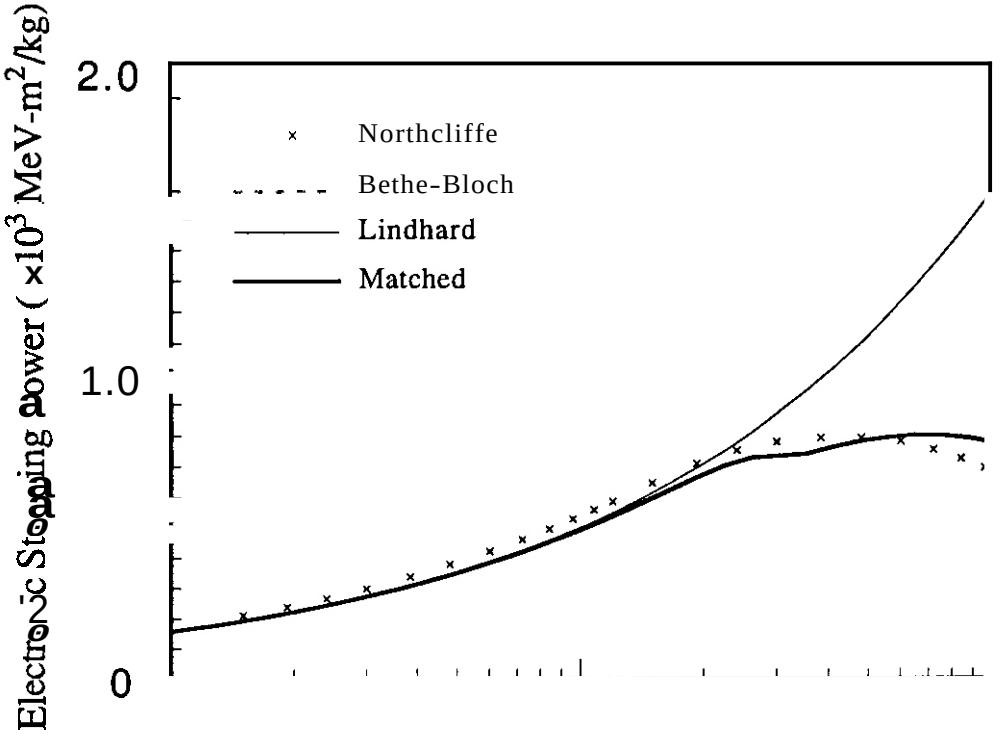

Figure 3: Comparison of experimental and theoretical electronic stopping powers for carbon in carbon.

The primary recoil spectra for carbon and silicon based on equation (8), under several neutron irradiation conditions, are shown in figures (4) and (5). It is seen that the primary recoil spectrum resulting from fusion neutron irradiation and that resulting from fission neutron irradiation are very different at high PKA energies. This fact directly corresponds to the differences of the neutron spectra shown in figure (1). The result may have important implications for the simulation of fusion neutron damage with fission neutrons.

The fraction of energy which is dissipated in atomic displacements rather than heat is defined as the damage efficiency. This fraction is shown in figure (6), where we show ξ_{ij} as the fraction of energy used in displacements in the process that ion i displaces in several fusion and fission facilities lattice atoms j. It is seen that the damage efficiency for carbon is lower than that for silicon, particularly at higher energies, because of the higher electronic stopping power of C in SiC. At high energies, although the electronic energy loss decreases as a function of energy, the scattering cross-section decreases at a faster rate, with the net effect being a decrease in the displacement efficiency. This is exemplified for carbon ions at high PKA energies in figure (6). There are two factors which determine the number of displaced atoms by a given transferred energy: (1) the electronic stopping power, and (2) the displacement threshold. Figure (7) demonstrates the energy dependence of the number of displaced atoms, ν_{ij}, obtained by solving the coupled integro-differential equations.

The partial displacement cross-sections defined in equation (14) and the total displacement cross-section are shown in figure (8). The important fact to mention here is that the displacement cross-section of SiC is very different from that of steel, as calculated by Doran[3]. If the neutron spectrum is composed mainly of fast neutrons (0.1 MeV ≤ E, ≤ 1 MeV), the displacement damage rate of SiC will be larger than that of steel. On the other hand, if the neutron spectrum is composed mainly of fusion neutrons, the damage rate of SiC will be smaller than that of steel. The reasons for these can be seen by referring to figure (2). The nuclear elastic cross-section of *Si* or C is higher than that of iron in the neutron energy range (0.1MeV - 1MeV), and lower than that of iron for fusion neutrons.

Based on equations (15), the partial displacement damage rates of silicon and carbon, the total displacement damage rate and the two fractions defined in section 3 are calculated for typical fusion reactors, a fast fission reactor, a mixed spectrum reactor and a thermal fission reactor. The calculated results are listed in table I below. From the table, one can see

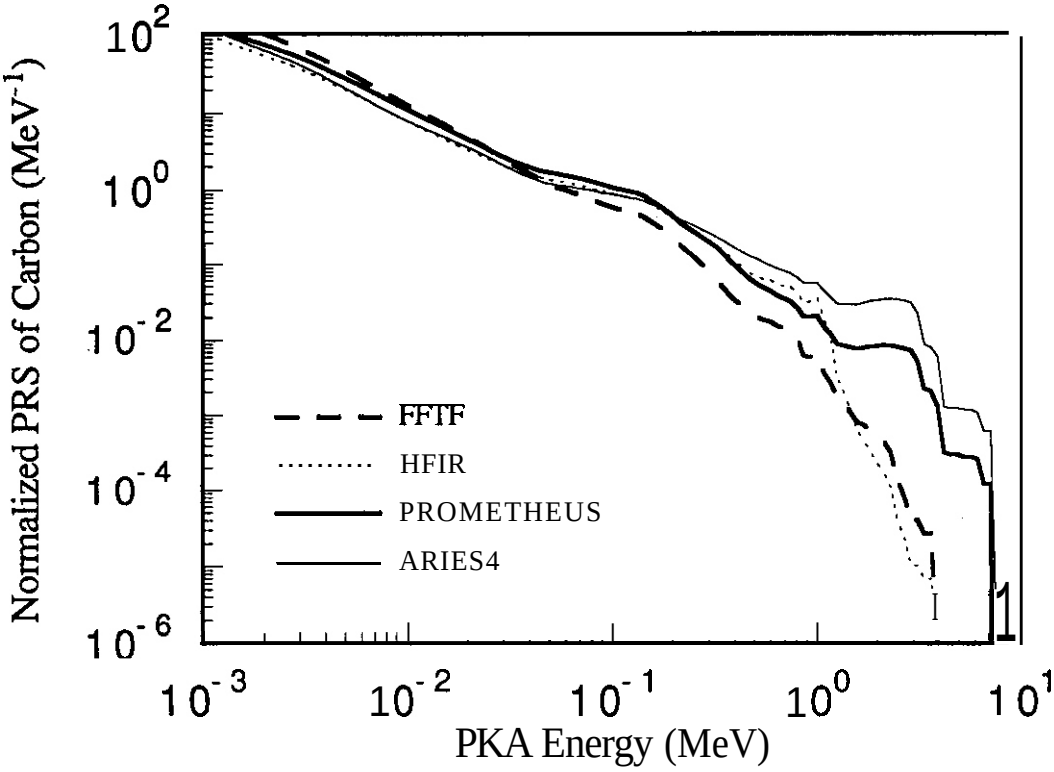

Figure 4 Primary recoil spectra of carbon in several fusion and fission facilities.

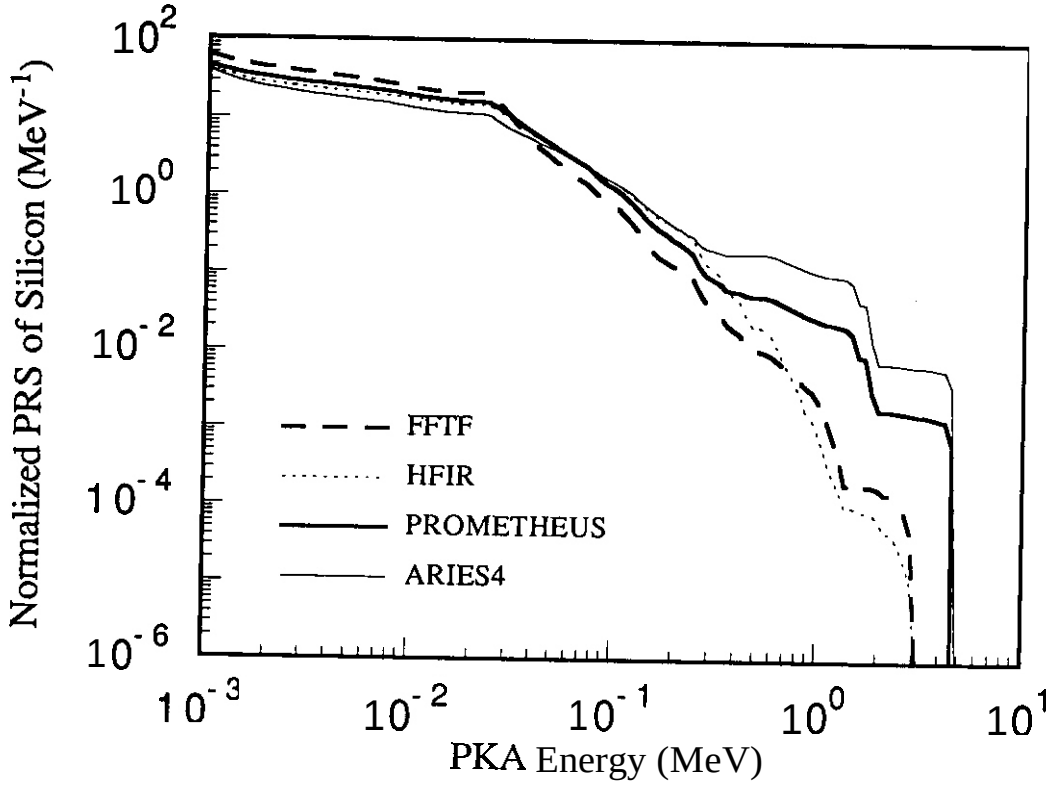

Figure 5: Primary recoil spectra of silicon in several fusion and fission facilities.

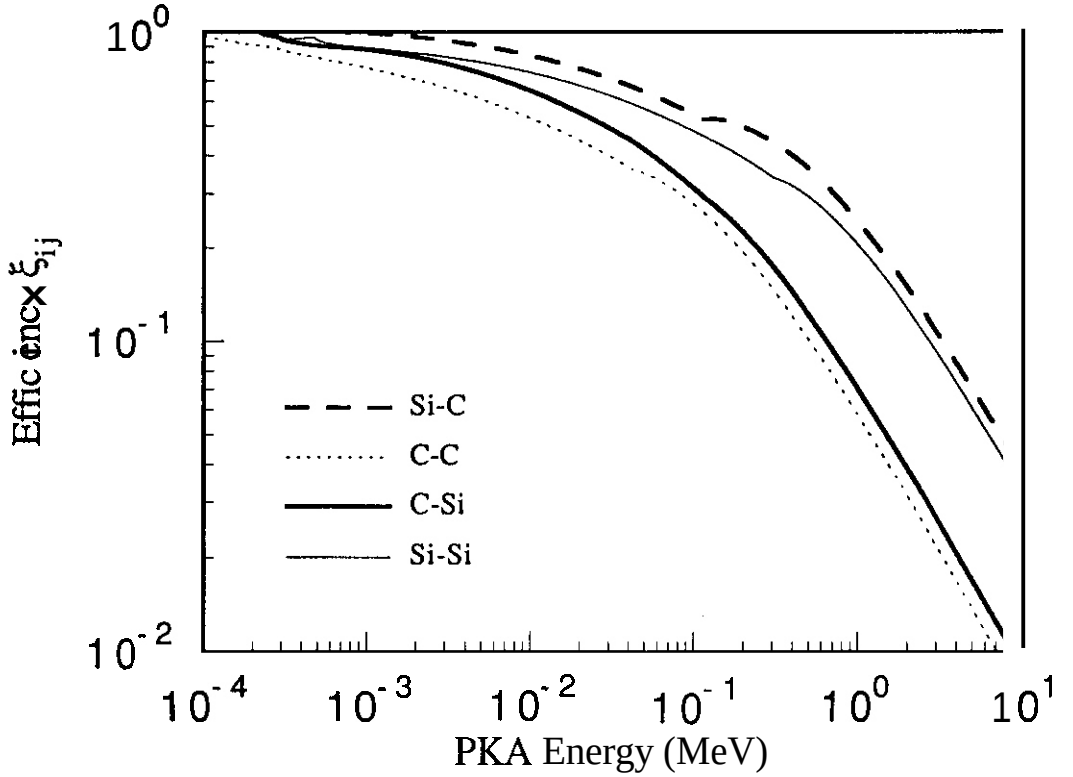

Figure 6 Displacement efficiency ξ_{ij} The first subscript is PKA while the second is the lattice atom being displaced.

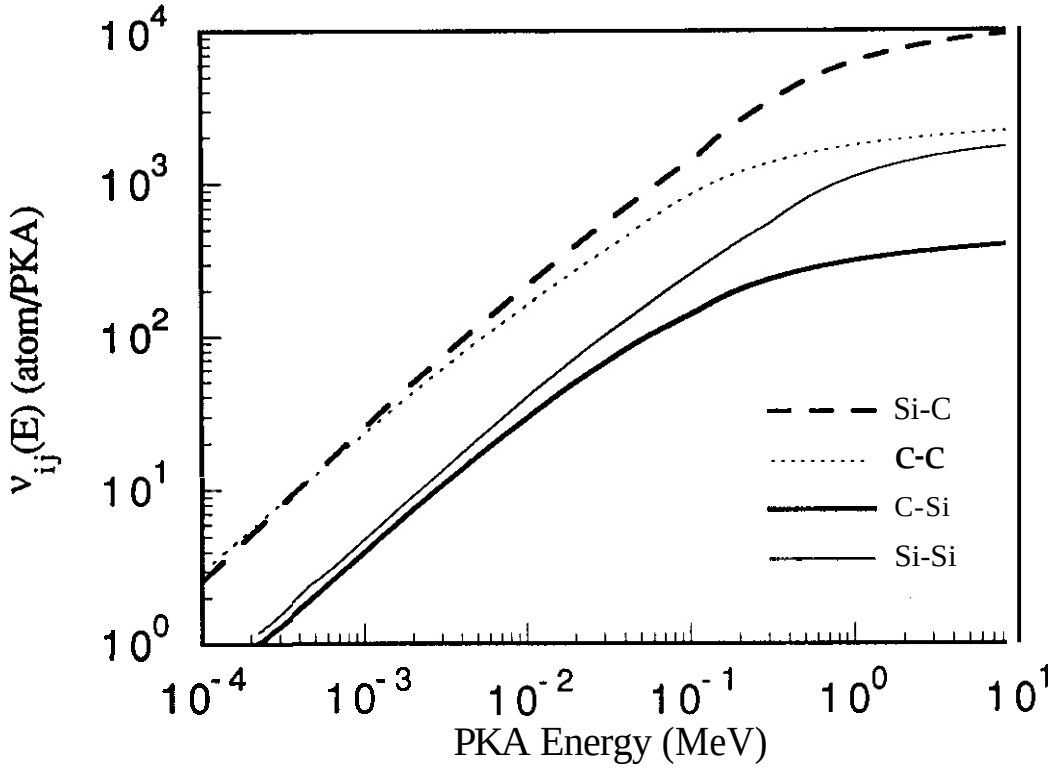

Figure 7: Number **of** displaced atoms of type j caused by PKA of type i, ν_{ij}.

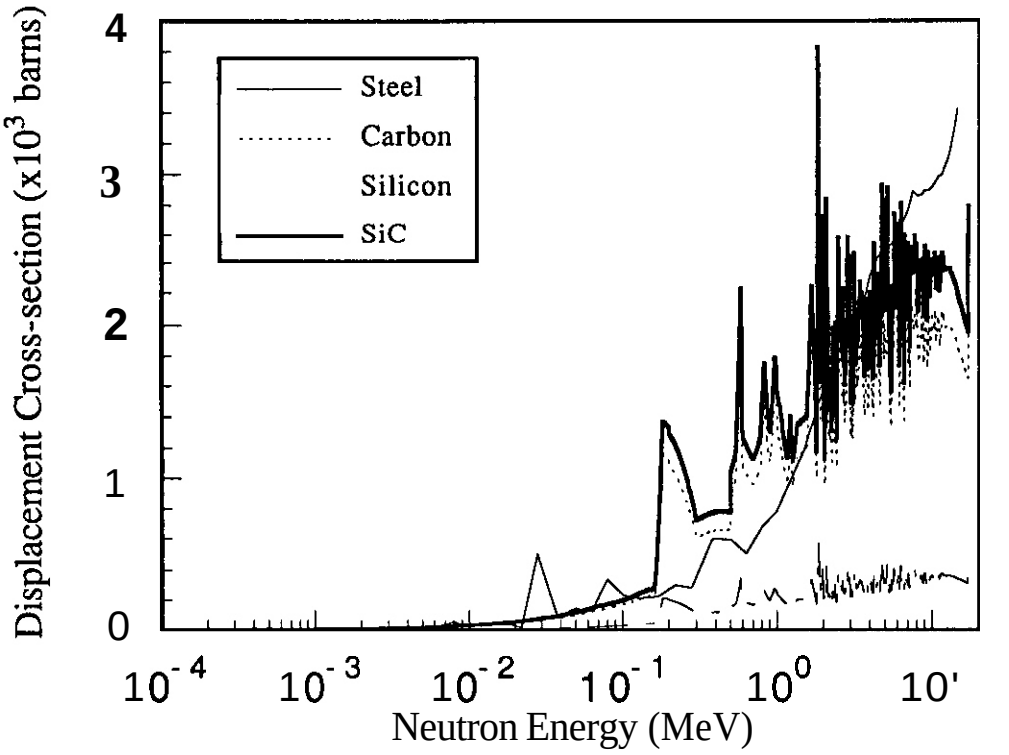

Figure 8: Displacement cross-sections for SiC. Also shown is the displacement cross-section for steel calculated by Doran [3].

that thermal neutrons don not result in significant displacement damage in SiC. The displacement damage rate for a typical fusion reactors is on the order of ~15 dpa/year for 1 MW/m^2 neutron wall loading.

TABLE I

facility / dpa / specie	AREIS-4 [ref 17]	PROMETHEUS [ref 16]	FFTF [ref 15]	HFIR [ref 15]	NRU [ref 15]
Carbon	11.5	13.7	62.5	32.7	21.4
Silicon	2.1	2.5	11.2	5.8	3.8
Total	13.6	16.2	73.7	38.5	25.2
$S_{c\text{-}si}$	4.5	4.5	4.6	4.6	4.6
PR_c	0.27	0.33	0.35	0.34	0.34
Location	first wall	first wall	midplane in MOTA	Instrumented position	Markiv fast neutron rod
Normalization	MW-Y/m^2	MW-Ym^2	10^{27} n/m^2	10^{27} n/m^2	10^{27} n/m^2

CONCLUSION

The results of our calculations reveal many features of the displacement damage process for SiC in a neutron environment. Salient conclusions are given below:

(1) The total displacement cross-section of SiC for epithermal neutrons is small. However, the displacement cross-section for fast neutrons (0.1MeV $\leq$ E, $\leq$ 1 MeV) is larger than that of steel. The damage rate is also smaller than that of steel for fusion neutrons. This may have important implications for the simulation of fusion neutron damage with fission neutrons. Therefore, fast reactor irradiation will accelerate damage production in comparison to fusion reactors.

(2) The local stoichiometry of SiC will be dramatically changed after irradiation, because carbon atoms are easily displaced due to their small displacement threshold. Approximately 80% of the displaced atoms will be carbon-type. It is experimentally found [27] that SiC does not amorphorize if the irradiation temperature is above 650°C. The thermo-chemical driving forces for recrystalization are strong enough to restore the best stoichiometry.

(3) The displacement damage rate for typical magnetic confinement fusion conditions is around 14 dpa/year for 1 MW/m^2 neutron wall loading, that for typical inertial confinement fusion conditions is around 16 dpa/year for 1 MW/m^2 neutron wall loading, that for FFTF is around 74 dpa per 10^{27} n/m^2, that for HFIR is around 39 dpa per 10^{27} n/m^2, and that for NRU is around 25 dpa per 10^{27} n/m^2. The damage rate is sensitive to the neutron spectrum, i.e. the design.

(4) The interpretation of simulation experiments with energetic particles (up to 100 MeV) requires further analysis. Non-elastic neutron scattering channels will become important in this case. Subsequently, the number of PKA species will be larger than the number of lattice species.

ACKNOWLEDGMENTS

The authors would like to thank Dr. M. Yousself at UCLA and Dr. L. El-gubaly at the University of Wisconsin for providing the neutron spectra for PROMETHEUS and ARIES-IV, respectively. Support of the US Department of Energy, Office of Fusion Energy, under grant number DE-FG03-91ER54 115 is greatly acknowledged.

FUTURE WORK

Radiation effects modeling efforts at UCLA will focus on microstructure evolution in irradiated SiC.

REFERENCES

1. J. Jenkins, Nucl. Sci. Eng., **41 (1970) 155**
2. W. Sheely, Nucl. Sei. Eng., **29 (1967) 165**
3. B. Doran, Nucl. Sci. Eng., **49 (1972) 130**
4. E. Baroody, Phys. Rev., **112 (1958) 1571**
5. N. Andersen and P. Sigmund, Mat **Fys.** Medd., **39 (1974) 3**
6. D. Parkin and C. Coulter, J. Nucl. Mater., **85&86 (1979) 611**
7. L. Greenwood, Reactor Dosimetry: Methods, Applications and Standardization, **ASTM** STP **1001,** Harry Ferrar IV and E. Lippincott, Eds., American Society for Testing and Materials, Philadelphia, **1989,** pp. 598-602.
8. **A.** Alberman and D. Lesueur, ibid, pp. 576-591
9. J. Lindhard and M. Scharff, Mat. Fys. Medd., **27 (1953) 15**
10. **J.** Lindhard and M. Scharff, Phys. Rev., **124 (1961) 128**
11. H. Bethe, ***Ann.*** Physik, **5 (1930) 325**
12. F. Bloch, Ann. Physik, **16 (1933) 285**
13. **J.** Biersack and L. Haggmark, J. Nuel. Instr. Meth., **174 (1980) 257**
14. **N.** Ghoniem, "Validity of Brass Stopping Cross-section Additivity Rule for SiC," Master's Thesis, McMaster University, May **1974**
15. M. Ahdou, M. Tillack, A. Raffray, **A.** Hadid, P. Gierszewski, B. Picologlou, R. Puigh, and D. Sze, et al., Modeling, Analysis and Experiments for Fusion Nuclear Technology, PPG-1021, UCLA-ENG-86-44, **FNT-17,** Jan. **1987,** Chap. **2**
16. Personal communications with Dr. M. Youssef at UCLA about PROMETHEUS
17. Personal communications with Dr. L. El-gubaly at Univ. of Wisconsin about **ARIES4**
18. J. Ziegler, **J.** Biersack and U. Littmark, The Stopping and Range of **Ions** in Solids, Chap. **3,** Pergamon Press, **1985**
19. N. Bohr, Phys. Rev., **59 (1941) 270**
20. L. Northcliffe and R. Schilling, Nuclear Data Tables, A7 **(1970) 233**
21. K. Winterbon, P. Sigmund and J. Sanders, Mat. Fys. Medd., **37 (1970) 14**
22. P. Chou, "A Monte Carlo Approach to Ion Transport in Solids and its Applications to Bulk and Surface Damage Analysis," Ph.D. Thesis at **UCLA,** May **1986**
23. K. Atkinson, An Introduction to Numerical Analysis, 2nd Ed., John Wiley and Sons, **1988,** Chap. **7**
24. A. El-Azab and N. Ghoniem, **J.** Nucl. Mater., **191-194 (1992)** unknown
25. ENDF-V, JENDL-3, evaluated by JAERI and TIT, updated on Dec. **19, 1991**
26. D. Hughes and R. Schwartz, Neutron Cross Sections, U.S. Government Printing Office, Washington, DC, **1958**
27. K. Okamura, T. Matsuzawa, M. Sato, H. Kayano, S. Morozum, H. Tezuka and A. Kohyama, **J.** Nuel. Mater., **155-157 (1988) 329**

TRANSMUTATION OF COPPER IN FFTF AND STARFIRE - F. A. Garner and L. R. Greenwood, Pacific Northwest Laboratory[a] and F. M. Mann, Westinghouse Hanford Company

OBJECTIVE

The objective of this effort is to determine the origin of radiation-induced changes in the electrical conductivity of copper alloys in both fission and fusion environments.

SUMMARY

Calculations of the transmutation of pure copper in the recent MOTA-2A out-of-core experiment yield somewhat different values than expected from previous calculations for earlier MOTA in-core experiments. The differences arise not only from position-dependent spectral variations but also from changes in neutron flux and spectrum associated with the placement of the CDE experiment in FFTF. In addition, there has been a re-evaluation of the cross-sections for transmutation. The resulting differences between the current and earlier predictions for the original FFTF core loading are that the zinc concentration is significantly higher and the nickel concentration *is* somewhat lower in the current calculation. Relative to the original core loading, however, the production rate per dpa of both nickel and zinc in the MOTA-2A experiment in the current core loading is increased due to spectral softening arising from both the new CDE core and the out-of-core location.

Although the nickel transmutation rate increases significantly in the STARFIRE first wall neutron spectrum, the nickel-to-zinc transmutation ratio is also reduced compared to that of previous calculations, with the difference arising only from the re-evaluation of the transmutation cross-sections.

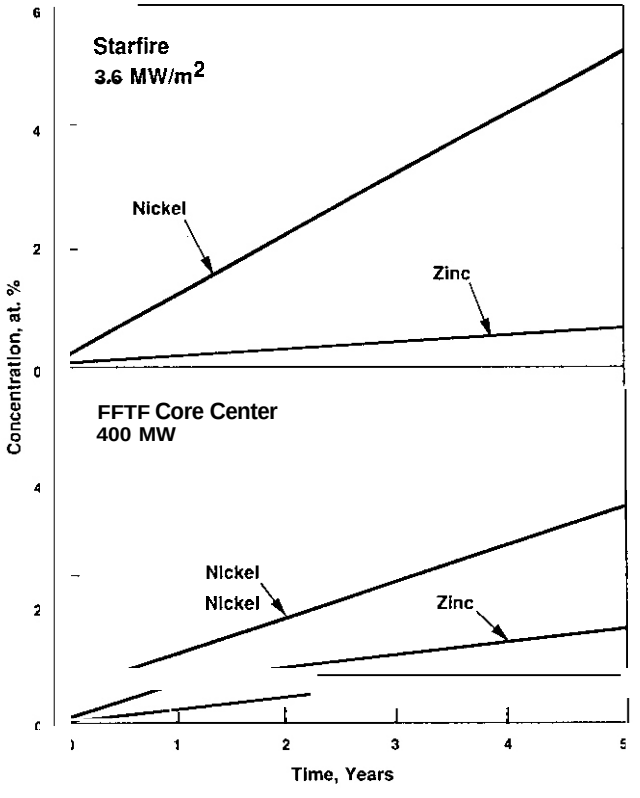

Fig. 1. Previously reported REAC-calculated values of transmutation products of pure copper at core center of the original core of FFTF and the STARFIRE first wall fusion spectra.[3]

PROGRESS AND STATUS

Introduction

In a previous series of calculations using the REAC computer code,[1-3] it was shown that pure copper irradiated in FFTF would develop a significant amount of nickel during a typical irradiation in MOTA, as shown in figure 1. A lesser amount of zinc was calculated to be formed. These reports also showed that the Ni/Zn ratio would increase substantially in a typical fusion reactor (STARFIRE) spectra. These two elements significantly reduce both the electrical and thermal conductivities of copper, with nickel exerting the largest influence on a per atom basis.[3] Thus, irradiations in FFTF produce conductivity changes that are lower than that expected in fusion spectra.

The previous FFTF calculations were based on the assumption of continuous irradiation in the center of the original FFTF core operating at 400 MW. The current core configuration is different, however, and operates at 291 MW with a somewhat softer neutron spectrum.[4] These differences in neutron environment are consequences of core and reflector changes associated with the placement of the Core Demonstration Experiment (CDE) in FFTF Cycle 9. These changes influenced the fluxes and spectra of MOTA-1E and beyond.

The neutron spectrum and flux are also functions of axial position in the MOTA. While early copper irradiations were conducted at in-core locations, most current copper irradiations are being conducted at positions near or below the bottom of the core where the neutron spectrum is softer. Since MOTA 2A contained the most extensive set of

---

[a] Pacific Northwest Laboratory is operated for the U.S. Department of Energy by Battelle Memorial Institute under Contract DE-AC06-76RLO 1830.

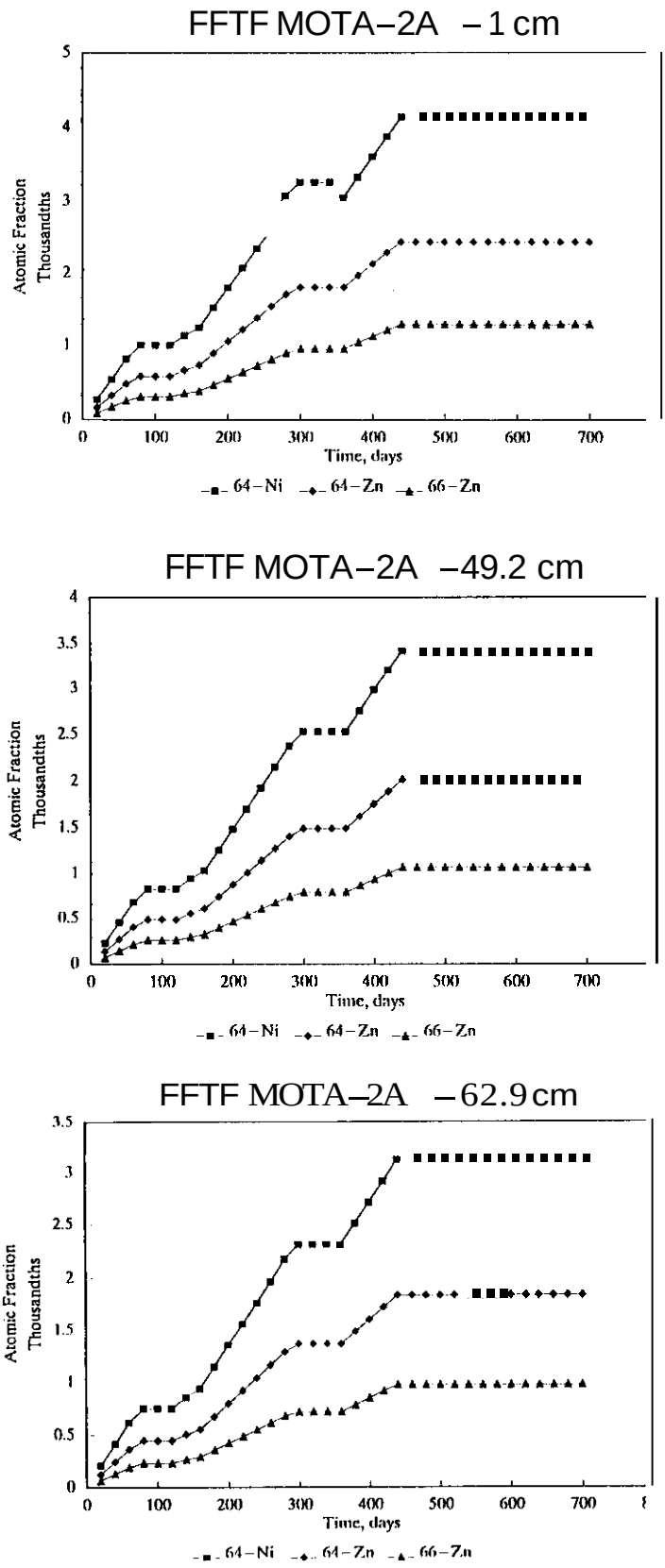

Fig. 2. Current STAY'SL calculations of three major transmutation products in pure copper in MOTA-2A in the current FFTF core loading at (a) -1 cm, (b) **-49.2** cm, (c) **-62.9** cm, measured from the core center.

dosimetry monitors employed in any of the MOTAs, the transmutation of pure copper was recalculated for this MOTA, especially for below-core positions. In order to evaluate the impact of the re-evaluated cross-sections and the various changes in neutron flux and spectra, two sets of calculations were performed.

In the first calculation the reaction rates in MOTA-2A were determined from spectral analyses[5] using the exact run history of 300 EFPD at 291 MW with two shutdown periods between the three reactor cycles of ~100 days each. Calculations were performed at three MOTA positions where spectral measurements were performed; namely, -1 cm, **-49** cm, and **-63** cm, all measured from core center. The **-49** and -63 cm positions define the upper and lower boundaries of the MOTA below-core basket. The most important reaction rates were calculated directly by the STAY'SL computer code.[6] The weaker reaction rates were estimated using ratios of known cross-sections. One of these cross sections, involving the partition of the products of the ^{63}Cu (n,γ) reaction has been re-evaluated, changing significantly since the first set of calculations was performed.

In the second set of calculations, the original set of calculations were repeated using the re-evaluated ^{63}Cu (n,γ) cross section for both the original FFTF core center and the STARFIRE first wall fusion reactor spectra.

The principal reactions considered in both sets of calculations were (n, γ), (n, p), (n, 2n), and (n, a) for the two copper isotopes (^{63}Cu, ^{65}Cu) and (n, γ) on other isotopes as they formed from copper. The calculations were performed by numerically integrating the differential equations for each atomic species, starting with pure, natural copper. The other atomic species considered were ^{64}Cu, ^{66}Cu, ^{60}Ni, ^{62}Ni, ^{63}Ni, ^{64}Ni, ^{64}Zn, ^{65}Zn, ^{66}Zn, and ^{60}Co. This carried the calculations to the second order, which was clearly sufficient, judging by the small production of many of the species.

Four of the transmutants are radioactive with half-lives sufficiently short that they will decay substantially during the MOTA 2A lifetime. They were allowed in the calculation to decay both during and after irradiation. ^{64}Cu decays very quickly to ^{64}Zn and ^{64}Ni, and ^{66}Cu decays rapidly to ^{66}Zn. ^{65}Zn decays back to ^{65}Cu and ^{60}Co decays at a slower rate to ^{60}Ni. ^{63}Ni is also radioactive, but its decay is minimal since its half-life is 100 years.

Results and Discussion

The results of the STAY'SL calculations are shown in figure 2 and listed in tables 1-3. Although calculations were performed for each day of operation, summaries are listed only for intervals of 20 days for a total of 700 days. The MOTA-2A irradiation ended at 439 days including the interim shutdown periods. Only ^{60}Ni, ^{60}Co, and ^{65}Zn are seen to change significantly by decay in the post-shutdown period.

Table 1. STAY'SL-calculated transmutants in pure copper irradiated in FFTF-MOTA 2A at one centimeter below the core center.

Copper Transmutation in FFTF MOTA-2A, -1 cm

Day	Cu63	Cu65	Ni60	Ni62	Ni63	Ni64	Zn64	Zn65	Zn66	Co60
20.	6.913E-01	3.082E-01	6.054E-10	5.583E-08	1.467E-06	2.744E-04	1.618E-04	1.575E-08	8.555E-05	2.132E-07
40.	6.908E-01	3.081E-01	2.137E-09	1.116E-07	2.929E-06	5.485E-04	3.235E-04	6.015E-08	1.711E-04	4.246E-07
60.	6.904E-01	3.080E-01	6.982E-09	1.674E-07	4.388E-06	E.225E-04	4.851E-04	1.313E-07	2.566E-04	6.345E-07
E0.	6.901E-01	3.080E-01	1.222E-08	2.036E-07	5.328E-06	1.000E-03	5.900E-04	1.874E-07	3.121E-04	7.681E-07
100.	6.901E-01	3.080E-01	1.772E-08	2.036E-07	5.328E-06	1.000E-03	5.900E-04	1.770E-07	3.121E-04	7.626E-07
120.	6.901E-01	3.080E-01	2.318E-08	2.036E-07	5.328E-06	1.000E-03	5.900E-04	1.672E-07	3.121E-04	7.571E-07
140.	6.899E-01	3.079E-01	2.865E-08	2.314E-07	6.052E-06	1.137E-03	6.707E-04	2.162E-07	3.549E-04	8.582E-07
160.	6.897E-01	3.079E-01	3.5145-0S	2.537E-07	6.630E-06	1.247E-03	7.352E-04	2.564E-07	3.890E-04	9.373E-07
180.	6.893E-01	3.078E-01	4.265E-08	3.094E-07	8.071E-06	1.520E-03	8.964E-04	3.905E-07	4.745E-04	1.143E-06
Z00.	6.888E-01	3.077E-01	5.164E-08	3.652E-07	9.506E-06	1.793E-03	1.057E-03	5.465E-07	5.599E-04	1.347E-06
220.	6.884E-01	3.077E-01	6.209E-08	4.209E-07	1.094E-05	2.066E-03	1.218E-03	7.202E-07	6.453E-04	1.550E-06
240.	6.880E-01	3.076E-01	7.399E-08	4.768E-07	1.236E-05	2.339E-03	1.379E-03	9.132E-07	7.307E-04	1.751E-06
260.	6.875E-01	3.075E-01	E.733E-08	5.327E-07	1.378E-05	2.612E-03	1.540E-03	1.123E-06	8.160E-04	1.950E-06
280.	6.871E-01	3.074E-01	1.021E-07	5.886E-C7	1.519E-05	2.884E-03	1.700E-03	1.349E-06	9.014E-04	2.148E-06
300.	6.868E-01	3.073E-01	1.182E-07	6.250E-07	1.611E-05	3.061E-03	1.805E-03	1.475E-06	9.568E-04	2.270E-06
320.	6.868E-01	3.073E-01	1.344E-07	6.250E-07	1.611E-05	3.061E-03	1.805E-03	1.393E-06	9.568E-04	2.254E-06
340.	6.868E-01	3.073E-01	1.506E-07	6.250E-07	1.611E-05	3.061E-03	1.805E-03	1.316E-06	9.568E-04	2.238E-06
360.	6.868E-01	3.073E-01	1.666E-07	6.250E-07	1.611E-05	3.061E-03	1.805E-03	1.243E-06	9.568E-04	2.222E-06
380.	6.864E-01	3.072E-01	1.833E-07	6.810E-07	1.751E-05	3.333E-03	1.965E-03	1.510E-06	1.042E-03	2.418E-06
400.	6.859E-01	3.072E-01	2.014E-07	7.370E-07	1.891E-05	3.605E-03	2.125E-03	1.789E-06	1.127E-03	2.612E-06
420.	6.855E-01	3.071E-01	2.209E-07	7.932E-07	2.030E-05	3.877E-03	2.285E-03	2.080E-06	1.213E-03	2.805E-06
440.	6.851E-01	3.070E-01	2.418E-07	8.467E-07	2.162E-05	4.135E-03	2.437E-03	2.359E-06	1.294E-03	2.985E-06
460.	6.851E-01	3.070E-01	2.632E-07	8.467E-07	2.162E-05	4.135E-03	2.437E-03	2.229E-06	1.294E-03	2.964E-06
480.	6.851E-01	3.070E-01	2.844E-07	8.467E-07	2.162E-05	4.135E-03	2.437E-03	2.106E-06	1.294E-03	2.942E-06
500.	6.851E-01	3.070E-01	3.055E-07	8.467E-07	2.162E-05	4.135E-03	2.437E-03	1.989E-06	1.294E-03	2.921E-06
520.	6.851E-01	3.070E-01	3.264E-07	8.467E-07	2.162E-05	4.135E-03	2.437E-03	1.879E-06	1.294E-03	2.900E-06
540.	6.851E-01	3.070E-01	3.472E-07	8.467E-07	2.162E-05	4.135E-03	2.437E-03	1.775E-06	1.294E-03	2.880E-06
560.	6.851E-01	3.070E-01	3.678E-07	8.467E-07	2.162E-05	4.135E-03	2.437E-03	1.677E-06	1.294E-03	2.859E-06
580.	6.851E-01	3.070E-01	3.883E-07	8.467E-07	2.162E-05	4.135E-03	2.437E-03	1.584E-06	1.294E-03	2.839E-06
600.	6.851E-01	3.070E-01	4.086E-07	8.467E-07	2.162E-05	4.135E-03	2.437E-03	1.496E-06	1.294E-03	2.818E-06
620.	6.851E-01	3.070E-01	4.288E-07	8.467E-07	2.162E-05	4.135E-03	2.<:?E-03	1.413E-06	1.294E-03	2.798E-06
640.	6.851E-01	3.070E-01	4.488E-07	8.467E-07	2.162E-05	4.135E-03	2.437E-03	1.335E-06	1.294E-03	2.778E-06
660.	6.851E-01	3.070E-01	4.687E-07	8.467E-07	2.162E-05	4.135E-03	2.437E-03	1.261E-06	1.294E-03	2.758E-06
680.	6.851E-01	3.070E-01	4.885E-07	8.467E-07	2.162E-05	4.135E-03	2.437E-03	1.192E-06	1.294E-03	2.738E-06
700.	6.851E-01	3.070E-01	5.081E-07	8.467E-07	2.162E-05	4.135E-03	2.437E-03	1.126E-06	1.294E-03	2.719E-06

Table 2. STAY'SL-calculated transmutants in pure copper irradiated in FFTF-MOTA 2A at 49 centimeters below the core center.

Copper Transmutation in FFTF MOTA-2A, -49.2 cm

Day	Cu63	Cu65	Ni60	Ni62	Ni63	Ni64	Zn64	Zn65	Zn66	Co60
20.	6.913E-01	3.082E-01	2.281E-10	1.410E-08	4.427E-07	2.262E-04	1.334E-04	1.071E-08	7.055E-05	6.038E-08
40.	6.910E-01	3.082E-01	8.885E-10	2.821E-08	8.840E-07	4.523E-04	2.668E-04	4.094E-08	1.411E-04	1.203E-07
60.	6.906E-01	3.081E-01	1.978E-09	4.231E-08	1.324E-06	6.783E-04	4.000E-04	8.946E-08	2.116E-04	1.797E-07
E0.	6.904E-01	3.080E-01	3.462E-09	5.149E-08	1.609E-06	E.251E-04	4.866E-04	1.277E-07	2.574E-04	2.176E-07
100.	6.904E-01	3.080E-01	5.021E-09	5.149E-08	1.609E-06	8.251E-04	4.866E-04	1.206E-07	2.574E-04	2.160E-07
120.	6.904E-01	3.080E-01	6.568E-09	5.149E-08	1.609E-06	8.251E-04	4.866E-04	1.139E-07	2.574E-04	2.145E-07
140.	6.902E-01	3.080E-01	8.174E-09	5.855E-08	1.828E-06	9.380E-04	5.532E-04	1.474E-07	2.927E-04	2.431E-07
160.	6.901E-01	3.080E-01	9.955E-09	6.421E-08	2.003E-06	1.028E-03	6.064E-04	1.748E-07	3.209E-04	2.655E-07
180.	6.897E-01	3.079E-01	1.208E-08	7.836E-08	2.429E-06	1.254E-03	7.294E-04	2.663E-07	3.913E-04	3.239E-07
200.	6.893E-01	3.078E-01	1.463E-08	9.256E-08	2.874E-06	1.479E-03	8.724E-04	3.722E-07	4.618E-04	3.818E-07
220.	6.890E-01	3.078E-01	1.759E-08	1.068E-07	3.307E-06	1.705E-03	1.005E-03	4.917:-07	5.322E-04	4.392E-07
240.	6.886E-01	3.077E-01	2.096E-08	1.211E-07	3.739E-06	1.930E-03	1.138E-03	6.227E-07	6.027E-04	4.962E-07
260.	6.883E-01	3.076E-01	2.474E-08	1.355E-07	4.170E-06	2.155E-03	1.271E-03	7.676E-07	6.731E-04	5.527E-07
280.	6.879E-01	3.076E-01	2.893E-08	1.499E-07	4.599E-06	2.380E-03	1.403E-03	9.225E-07	7.435E-04	6.089E-07
300.	6.877E-01	3.075E-01	3.349E-08	1.593E-07	4.877E-06	2.526E-03	1.489E-03	1.009E-06	7.892E-04	6.435E-07
323.	6.877E-01	3.075E-01	3.810E-08	1.593E-07	4.877E-06	2.526E-03	1.489E-03	9.527E-07	7.892E-04	6.389E-07
340.	6.877E-01	3.075E-01	4.267E-08	1.593E-07	4.877E-06	2.526E-03	1.489E-03	9.000E-07	7.892E-04	6.343E-07
360.	6.877E-01	3.075E-01	4.721E-08	1.593E-07	4.877E-06	2.526E-03	1.489E-03	8.502E-07	7.892E-04	6.297E-07
380.	6.873E-01	3.074E-01	5.195E-08	1.737E-07	5.304E-06	2.751E-03	1.622E-03	1.003E-06	8.596E-04	6.853E-07
400.	6.870E-01	3.074E-01	5.708E-08	1.883E-07	5.729E-06	2.975E-03	1.754E-03	1.225E-06	9.300E-04	7.403E-07
420.	6.866E-01	3.073E-01	6.261E-08	2.029E-07	6.153E-06	3.199E-03	1.886E-03	1.424E-06	1.000E-03	7.950E-07
440.	6.863E-01	3.072E-01	6.853E-08	2.169E-07	6.554E-06	3.412E-03	2.012E-03	1.616E-06	1.067E-03	8.462E-07
460.	6.863E-01	3.072E-01	7.459E-08	2.169E-07	6.554E-06	3.412E-03	2.012E-03	1.527E-06	1.067E-03	8.402E-07
480.	6.863E-01	3.072E-01	8.061E-08	2.169E-07	6.554E-06	3.412E-03	2.012E-03	1.442E-06	1.067E-03	8.342E-07
500.	6.863E-01	3.072E-01	8.658E-08	2.169E-07	6.554E-06	3.412E-03	2.012E-03	1.362E-06	1.067E-03	8.282E-07
520.	6.863E-01	3.072E-01	9.251E-08	2.169E-07	6.554E-06	3.412E-03	2.012E-03	1.287E-06	1.067E-03	8.222E-07
540.	6.863E-01	3.072E-01	9.840E-08	2.169E-07	6.554E-06	3.412E-03	2.012E-03	1.216E-06	1.067E-03	8.164E-07
560.	6.863E-01	3.072E-01	1.042E-07	2.169E-07	6.554E-06	3.412E-03	2.012E-03	1.148E-06	1.067E-03	8.105E-07
580.	6.863E-01	3.072E-01	1.101E-07	2.169E-07	6.554E-06	3.412E-03	2.012E-03	1.085E-06	1.067E-03	8.047E-07
600.	6.863E-01	3.072E-01	1.158E-07	2.169E-07	6.554E-06	3.412E-03	2.012E-03	1.025E-06	1.067E-03	7.989E-07
620.	6.863E-01	3.072E-01	1.215E-07	2.169E-07	6.554E-06	3.412E-03	2.012E-03	9.681E-07	1.067E-03	7.932E-07
640.	6.863E-01	3.072E-01	1.272E-07	2.169E-07	6.554E-06	3.412E-03	2.012E-03	9.145E-07	1.067E-03	7.875E-07
660.	6.863E-01	3.072E-01	1.329E-07	2.169E-07	6.554E-06	3.412E-03	2.012E-03	8.639E-07	1.067E-03	7.819E-07
680.	6.863E-01	3.072E-01	1.385E-07	2.169E-07	6.554E-06	3.412E-03	2.012E-03	8.161E-07	1.067E-03	7.763E-07
700.	6.863E-01	3.072E-01	1.440E-07	2.169E-07	6.554E-06	3.412E-03	2.012E-03	7.709E-07	1.067E-03	7.707E-07

Table 3. STAY'SL-calculated transmutants in pure copper irradiated in FFTF-MOTA 2A at 63 centimeters below the core center.

copper Transmutation in FFTF MOTA-2A, -62.9 cm

Day	Cu63	Cu65	Ni60	Ni62	Ni63	Ni64	Zn64	Zn65	Zn66	Co60
20.	6.914E-01	3.082E-01	5.265E-11	3.607E-09	1.036E-07	2.059E-04	1.215E-04	8.878E-09	6.422E-05	1.293E-08
40.	6.910E-01	3.082E-01	2.051E-10	7.220E-09	2.069E-07	4.118E-04	2.429E-04	3.394E-08	1.284E-04	2.776E-08
60.	6.907E-01	3.081E-01	4.565E-10	1.084E-08	3.099E-07	6.175E-04	3.642E-04	7.418E-08	1.926E-04	4.148E-08
60.	6.905E-01	3.081E-01	7.991E-10	1.321E-08	3.767E-07	7.511E-04	4.430E-04	1.059E-07	2.343E-04	5.022E-08
100.	6.905E-01	3.081E-01	1.159E-09	1.321E-08	3.767E-07	7.511E-04	4.430E-04	1.000E-07	2.343E-04	4.986E-08
120.	6.905E-01	3.081E-01	1.516E-09	1.321E-08	3.767E-07	7.511E-04	4.430E-04	9.449E-08	2.343E-04	4.950E-08
140.	6.903E-01	3.080E-01	1.867E-09	1.504E-08	4.279E-07	8.539E-04	5.036E-04	1.222E-07	2.664E-04	5.611E-08
160.	6.902E-01	3.080E-01	2.297E-09	1.650E-08	4.689E-07	9.361E-04	5.521E-04	1.450E-07	2.921E-04	6.128E-08
180.	6.899E-01	3.079E-01	2.789E-09	2.018E-08	5.711E-07	1.141E-03	6.732E-04	2.209E-07	3.563E-04	7.475E-08
200.	6.896E-01	3.079E-01	3.377E-09	2.390E-08	6.730E-07	1.347E-03	7.942E-04	3.089E-07	4.204E-04	8.821E-08
220.	6.892E-01	3.078E-01	4.060E-09	2.766E-08	7.746E-07	1.552E-03	9.152E-04	4.081E-07	4.845E-04	1.014E-07
240.	6.889E-01	3.078E-01	4.839E-09	3.147E-08	6.759E-07	1.757E-03	1.036E-03	5.178E-07	5.487E-04	1.145E-07
260.	6.886E-01	3.077E-01	5.711E-09	3.533E-08	9.769E-07	1.962E-03	1.157E-03	6.374E-07	6.128E-04	1.276E-07
280.	6.883E-01	3.076E-01	6.677E-09	3.926E-08	1.078E-06	2.167E-03	1.278E-03	7.662E-07	6.769E-04	1.405E-07
300.	6.880E-01	3.076E-01	7.729E-09	4.184E-08	1.143E-06	2.300E-03	1.356E-03	8.378E-07	7.185E-04	1.485E-07
320.	6.880E-01	3.076E-01	8.793E-09	4.184E-08	1.143E-06	2.300E-03	1.356E-03	7.914E-07	7.185E-04	1.475E-07
340.	6.880E-01	3.076E-01	9.849E-09	4.184E-08	1.143E-06	2.300E-03	1.356E-03	7.476E-07	7.185E-04	1.464E-07
360.	6.880E-01	3.076E-01	1.090E-08	4.184E-08	1.143E-06	2.300E-03	1.356E-03	7.062E-07	7.185E-04	1.454E-07
360.	6.877E-01	3.075E-01	1.199E-08	4.579E-08	1.243E-06	2.505E-03	1.477E-03	8.582E-07	7.826E-04	1.582E-07
400.	6.6-<E-01	3.075E-01	1.318E-08	4.982E-08	1.343E-06	2.709E-03	1.597E-03	1.017E-06	8.467E-04	1.709E-07
620.	6.871E-01	3.074E-01	1.445E-08	5.393E-08	1.4435-06	2.913E-03	1.718E-03	1.183E-06	9.107E-04	1.835E-07
440.	6.868E-01	3.073E-01	1.582E-08	5.791E-08	1.537E-06	3.108E-03	1.632E-03	1.343E-06	9.716E-04	1.954E-07
460.	6.868E-01	3.073E-01	1.722E-08	5.791E-08	1.537E-06	3.108E-03	1.832E-03	1.269E-06	9.716E-04	1.940E-07
480.	6.868E-01	3.073E-01	1.861E-08	5.791E-08	1.537E-06	3.108E-03	1.832E-03	1.199E-06	9.716E-04	1.926E-07
500.	6.868E-01	3.073E-01	1.999E-08	5.791E-08	1.537E-06	3.108E-03	1.832E-03	1.132E-06	9.716E-04	1.912E-07
520.	6.868E-01	3.073E-01	2.135E-08	5.791E-08	1.537E-06	3.108E-03	1.832E-03	1.070E-06	9.716E-04	1.898E-07
540.	6.868E-01	3.073E-01	2.271E-08	5.791E-08	1.537E-06	3.108E-03	1.832E-03	1.010E-06	9.716E-04	1.885E-07
560.	6.868E-01	3.073E-01	2.406E-08	5.791E-08	1.537E-06	3.108E-03	1.832E-03	9.545E-07	9.716E-04	1.871E-07
560.	6.868E-01	3.073E-01	2.540E-08	5.791E-08	1.537E-06	3.108E-03	1.832E-03	9.017E-07	9.716E-04	1.858E-07
600.	6.868E-01	3.073E-01	2.673E-08	5.791E-08	1.537E-06	3.108E-03	1.832E-03	8.518E-07	9.716E-04	1.844E-07
620.	6.868E-01	3.073E-01	2.805E-08	5.791E-08	1.537E-06	3.108E-03	1.832E-03	8.046E-07	9.716E-04	1.831E-07
640.	6.868E-01	3.073E-01	2.937E-08	5.791E-08	1.537E-06	3.108E-03	1.832E-03	7.601E-07	9.716E-04	1.818E-07
660.	6.868E-01	3.073E-01	3.067E-08	5.791E-08	1.537E-06	3.108E-03	1.832E-03	7.180E-07	9.716E-04	1.805E-07
660.	6.868E-01	3.073E-01	3.196E-08	5.791E-08	1.537E-06	3.108E-03	1.832E-03	6.783E-07	9.716E-04	1.792E-07
700.	6.868E-01	3.073E-01	3.324E-08	5.791E-08	1.537E-06	3.108E-03	1.832E-03	6.408E-07	9.716E-04	1.779E-07

As shown in figure 2, the STAY'SL results also show that the only significant species (from the standpoint of conductivity changes) are ^{64}Ni, ^{64}Zn, and ^{66}Zn, all three of which are stable isotopes. At all three positions for which calculations were performed, slightly more nickel than zinc was produced, with the Ni/Zn ratio constant at 1.108.

This invariability of the Ni/Zn ratio with neutron spectrum is a direct consequence of the fact that both elements are produced primarily by (n,γ) reactions involving ^{63}Cu and ^{65}Cu. Both elements exhibit a very similar dependence on neutron energy. The decrease in formation rates of both elements with decreasing height in the core results primarily from the lower neutron flux at these lower levels. Since the primary reaction rates involve (n,γ) reactions, however, the transmutation rates per neutron increase toward the bottom of the core as a consequence of spectral softening. Thus, the production rates do not decrease as fast as either the fast fluence or dpa rates decrease.

Note that the Ni/Zn ratio found in the STAY'SL study is much less than the ~3/1 rates shown in figure 1. This difference is due primarily to the re-evaluated cross-section used for zinc and nickel production from ^{63}Cu in the current calculations. The calculated individual production rates have also changed, however, reflecting the softer spectrum found in the current FFTF core. The 300 day REAC value for nickel production at core center, derived from figure 1 (after correction for the power level difference in the two cases) is 0.359%, which is -14% lower than the current predicted value of 0.416%. A comparable calculation for zinc yields a power-normalized REAC value of 0.120% vs. 0.373% currently predicted. Thus, the levels of nickel and zinc increase significantly relative to those of the previous calculation, leading to a substantial increase (~20%, relative to the earlier calculations) in the predicted loss of electrical conductivity.

As shown in figure 3 and table 4 the REAC calculations were repeated, using the flux/spectrum information employed earlier for the original FFTF core loading and changing only the ^{63}Cu cross-sections for production of nickel and zinc. Note that the original 300-day core center values of 0.379% Ni and 0.165% Zn are different from the current values of 0.359% Ni and 0.373% Zn. The Ni/Zn ratio at core center is calculated to be 1.024 by REAC, and is only slightly different from that calculated by STAY'SL to be 1.108. The bottom-of-core Ni/Zn ratio increases only slightly to 1.034, still somewhat lower than that of the spectrally softer MOTA-2A value, the STAY'SL calculation of which does not allow spectral variations to affect the Ni/Zn ratio.

FFTF Midplane 5.45 X 10^{15} n $cm^{-2}s^{-1}$ Atom %			
Time, days	Ni	Zn	Ni/Zn
20	0.0253	0.0247	1.024
40	0.0506	0.0494	1.024
60	0.0759	0.0741	1.024
80	0.1012	0.0988	1.024
100	0.1264	0.1235	1.023
300	0.3792	0.3705	1.023
FFTF Top of Core 3.04 X 10^{15} n $cm^{-2}s^{-1}$			
20	0.0173	0.0167	1.036
40	0.0346	0.0335	1.033
60	0.0519	0.0502	1.034
80	0.0693	0.0669	1.036
100	0.0865	0.0836	1.035
300	0.2600	0.2510	1.036
20	0.0247	0.0239	1.033
40	0.0493	0.0477	1.034
60	0.0739	0.0715	1.034
80	0.0985	0.0953	1.034
100	0.1231	0.1191	1.034
300	0.3690	0.3570	1.034

Time, years	Ni	Zn	Ni/Zn
0.5	0.517	0.234	2.209
1	1.032	0.466	2.215
2	2.118	0.952	2.225
5	5.455	2.417	2.257

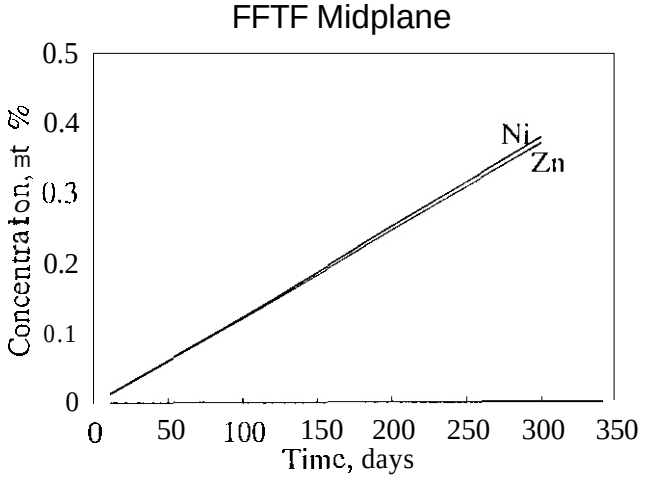

Fig. 3. Revised REAC calculations of the transmutation products of pure copper at core center of the original core of FFTF.

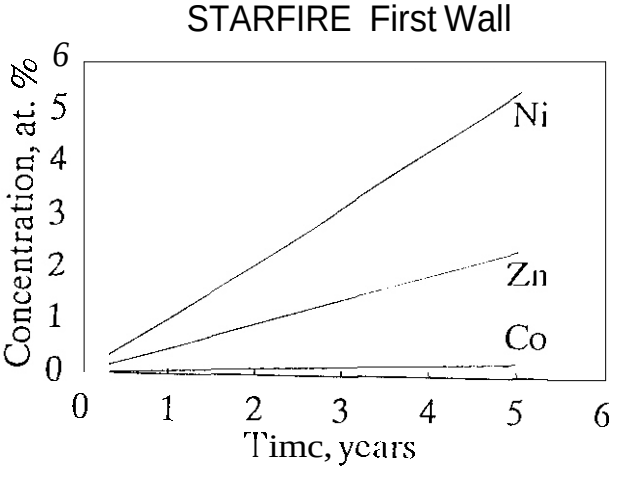

Fig. 4. Revised REAC calculations of the transmutation products of pure copper at the first wall of STARFIRE.

The validity of the revised transmutation rates calculated by REAC has been independently tested by Edwards and Garner using the measured changes in conductivity.[7] It appears that the predicted transmutation rates agree within 15% of those required to produce the observed changes, slightly overpredicting the conductivity changes. This is thought to be excellent agreement considering the impact of calculational uncertainties and local flux and spectra perturbations arising from structural and material discontinuities that cannot be included in the calculational procedure.

Using the REAC code with re-evaluated ^{63}Cu (n,γ) reaction rates, the transmutation rates for the STARFIRE first wall neutron spectrum and flux were calculated and are shown in table 5 and figure 4. The significantly increased production of nickel relative to that in FFTF is primarily a consequence of the contribution of the $^{63}Cu(n, 2n)$ reaction, yielding a Ni/Zn ratio that increases slowly with exposure, reaching 2.26 after 5 years of continuous STARFIRE operation.

REFERENCES

1. F. M. Mann, "Transmutation of Alloys in MFE Facilities as Calculated by REAC (A Computer Code System for Activation and Transmutation)", HEDL-TME-81-37, Westinghouse Hanford Company, 1981,

2. F. M. Mann, in "Damage Analysis and Fundamental Studies Quarterly Progress Report" DOE/ER-0046/24," February 1986, U.S. Department of Energy, pp. 10-20.

3. F. A. Garner, H. L. Heinisch, R. L. Simons, and F. M. Mann, "Radiation Effects and Defects in Solids 113 (1990) 229-255.

4. F. A. Garner and L. R. Greenwood, "Calculation of Displacement Levels for Pure Elements and Most Multicomponent Alloys Irradiated in FFTF MOTA-1F," in Fusion Reactor Materials Semiannual Report DOE/ER-0313/12 (1992) in press.

5. L. R. Greenwood and L. S. Kellogg, "Neutron Dosimetry for the MOTA-2A Experiment in FFTF," in Fusion Reactor Materials Semiannual Progress Report DOE/ER-0313/12 (1992) in press.

6. F. G. Perey, "Least Squares Dosimetry Unfolding: The Program STAY'SL", ORNL-TM-6062, Oak Ridge National Laboratory, 1977.

7. D. J. Edwards and F. A. Garner, "The Influence of Transmutation and Void Swelling on Electrical Properties of Copper and Several Copper Alloys," in this semiannual report.

3.0 MATERIALS ENGINEERING AND DESIGN REQUIREMENTS

No contributions.

4.0 FUNDAMENTAL MECHANICAL BEHAVIOR

No contributions.

5.0 RADIATION EFFECTS, MECHANISTIC STUDIES, THEORY AND MODELING

ANALYSIS OF DISPLACEMENT DAMAGE AND DEFECT PRODUCTION UNDER CASCADE DAMAGE CONDITIONS — S.J. Zinkle (Oak Ridge National Laboratory) and B.N. Singh (Risø National Laboratory)

OBJECTIVE

The objective of this study is to review the available information on production of freely migrating defects, and to introduce a new framework for describing defect production under cascade damage conditions.

SUMMARY

The production. annihilation, and accumulation of point defects in metals during displacive irradiation is dependent on a variety of physical conditions, including the nature and energy of the projectile particles and the irradiation temperature. This paper briefly reviews the evolution of the defect population in an isolated displacement cascade, and outlines a proposed framework for identifying the relevant components of displacement damage and defect production under cascade damage conditions. The most significant aspect of energetic cascades is that the concepts of atomic displacements and residual defect oroduction must be treated separately. An evaluation of experimental and computer defect production studies indicates that the overall fraction of defects surviving correlated annihilation in an energetic displacement cascade in copper decreases from about 30% of the Norgett-Robinson-Torrens (NRT) calculated displacements at **4** K to about 10% of the NRT displacements at 300 K. **Due** to differences in the thermal stability of vacancy versus interstitial clusters, the fractions of freely migrating defects available for inducing microstructural changes at elevated temperatures may be higher for vacancies than for interstitials. The available evidence suggests that the fraction of freely migrating vacancies at temperatures relevant for void swelling in copper is ~5% of the calculated NRT displacements.

PROGRESS AND STATUS

1.0 Introduction

Steady progress has been made over the last **40** years in understanding the physics of displacement damage processes in metals. The number and spatial distribution of displaced atoms in a displacement cascade is dependent on the mass, electrical charge, and energy of the projectile particle. along with the temperature, crystal structure and mass of the host lattice. Early attempts to calculate the number of atomic displacements occuring during irradiation were made by Kinchin and Pease' and Snyder and Neufeld.[2] A modified version of the Kinchin and Pease model known as the NRT model[3] is generally accepted as the international standard for quantifying the number of atomic displacements in irradiated materials. This achievement allowed experimental tests performed in different irradiation sources to be directly compared on a standard basis. According to the NRT model, the number of Frenkel pairs (N_D) generated by a primary **knock-on** atom **(PKA)** of energy E is given by

$$N_D = \frac{\kappa(E - S_e)}{2E_D} = \frac{\kappa S_D}{2E_D}, \qquad S_D > 2E_D/\kappa \tag{1}$$

where κ is the "displacement efficiency,' S_e is the energy lost to electron excitation, S_D is the damage energy, and E_D is the threshold displacement energy.[3] Binary collision calculations indicated that the 'displacement efficiency" was constant. $\kappa \cong 0.8$, for PKA energies above $2E_D$ and extending up to 100 keV if an energy threshold criterion was used to define stable defects.4 Integration of the NRT damage function (Eq. **1)** over recoil spectrum and time yields the calculated atomic concentration of displacements, commonly known as the NRT displacements per atom (dpa).

Application of the NRT model to radiation effects studies requires the implicit assumption that the residual defect concentration is equal (or at least proportional) to the calculated number of displacements. The criterion for the formation of a stable displacement in the NRT model (which is based on a series of isolated binary collisions) is simply whether the struck atom acquires a kinetic energy greater than E_D. The spatial distribution of displaced atoms and the possibility of subsequent interstitial-vacancy annihilation within an energetic displacement cascade are not addressed in the NRT model. Molecular dynamics **(MD)** calculations indicate that the cascade region associated with energetic PKAs consists of a collection of highly agitated atoms in a severely distorted lattice (as opposed to individually resolvable Frenkel pairs).[5-7] These computer simulations suggest that the basic concept of Frenkel pairs is inappropriate for describing defect production in energetic cascades. In addition, numerous computer simulation and

experimental studies have found that, for PKA energies greater than about 0.5 keV, a substantial fraction of the displacement damage is annihilated via interstitial-vacancy recombination as the energetic cascade cools to thermal equilibrium even for irradiations conducted at 4 K.[3-11] This results in a fraction of residual defects (relative to the NRT calculated displacements) that is dependent on the PKA energy. Hence, the NRT model for atomic displacements is not a physically realistic indicator of defect production under cascade conditions. At best, the NRT model is a reasonably good correlation parameter for defect production under certain circumstances, e.g., for comparing radiation effects in two similar PKA irradiation spectra.

This paper briefly reviews the present understanding of the production, annihilation, and accumulation of point defects under cascade damage conditions. As noted by several authors, the NRT dpa unit does not provide sufficient information for accurately modelling radiation damage processes that occur when displacement cascades are present.[12-19] A proposed framework of displacement damage and defect production parameters (scaled as fractions of the NRT calculated displacements) that are useful for describing radiation damage processes is outlined in this paper, with particular emphasis on the migrating defect fraction. All of these damage parameters refer to an isolated displacement cascade; intercascade interactions must be separately accounted for in rate theory models, as discussed in Section 3.1.1. Published experimental and computational results are analyzed to obtain information on the dependence of these damage parameters on PKA spectra and temperature.

2.0 Evolution *Of* An Isolated Displacement Cascade

The creation and subsequent decay of a displacement cascade may be conceptually divided into at least three overlapping stages.[10,20] The collisional phase lasts ~10^{-13}s, during which all of the collisions transferring energy $\geq E_D$ occur. Annihilation, in-cascade clustering, and replacement events occur during the relaxation and cascade cooling phase, which lasts ~10^{-11}s. If the irradiation temperature is sufficiently high to allow thermally-activated defect migration. then a diffusional interaction phase ensues during which the mobile defects interact within and outside of the cascade region to form clusters or annihilate via recombination or at sinks.

2.1 Collisional Phase

Computer simulations have found that displacement cascades are formed in metals for primary knock-on atom energies greater than about 1 keV.[4,7,8,10,16,20,21] According to MD calculations, a high density of displaced atoms are generated in a spatially localized region within a time period of a few tenths of a picosecond.[5,7,10] The number of atoms that are displaced from their lattice site during the collisional phase is much greater than the NRT calculated displacements -- most of the displaced atoms recombine with vacant lattice sites during the subsequent cascade cooling phase.[10,22]

Due to ballistic ejection and replacement collision sequences by interstitials, the distribution of defects in a displacement cascade is spatially segregated into a vacancy rich core and an interstitial-rich periphery.[5,7,10,21,23-25] As discussed later. this high concentration of spatially segregated defects may significantly influence the fraction of clustered or isolated vacancies and interstitials that survive the cascade quench. The size of the displacement cascade increases with increasing PKA energy up to a threshold value.[25] Above this threshold PKA energy, multiple distinct damage regions (subcascades) are produced instead of a single large cascade. Well-defined subcascades begin to form in copper for PKA energies above about 20 keV.[20,25-30]

2.2 Annihilation and Clusterlna of Point Defects durlna the Cascade Quench

At the end of the collisional phase, atoms within the cascade region possess a high mean kinetic energy. The kinetic energy imparted to the atoms by the PKA is subsequently dissipated in the lattice within a time scale of ~10^{-11}s. Figure 1 shows the geometrical distribution of clustered and isolated defects near the end of the cascade quench phase (12.5 ps), as determined from a recent MD simulation of a 25 keV PKA in copper irradiated at a temperature of 10 K.[20] Numerous computer[7,16,20,29] and experimental[31-35] studies have found that a substantial fraction of the vacancies and interstitials present after the cascade quench are in clustered form. The center of the cascade region contains primarily vacancy defects. whereas interstitial defects occur predominantly near the cascade periphery. A recent MD simulation has also reported evidence for punching of an interstitial prismatic dislocation loop from the periphery of a 25 keV cascade core in copper.[20]

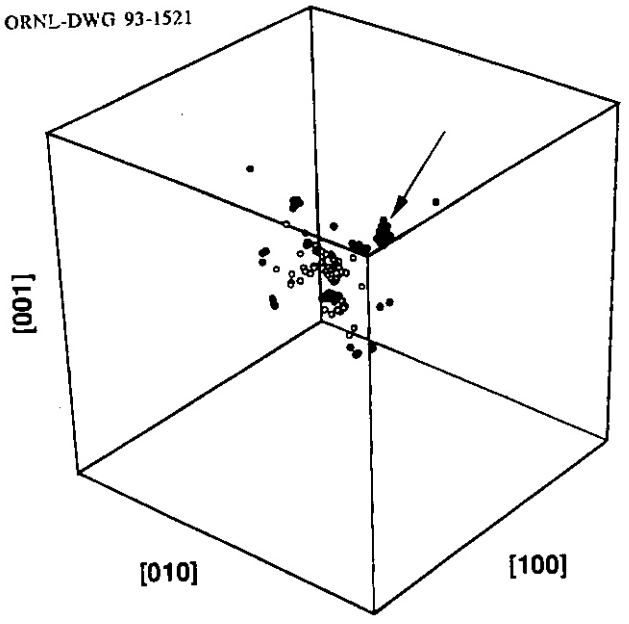

Fig. 1. View of the defect configuration after 12.5 ps for a 25 keV PKA in copper at a lattice temperature of 10 K, according to a recent MD calculation.[20] The filled circles represent interstitials and the open circles represent vacancies. The arrow points to a large prismatic dislocation loop containing 17 interstitials.

Computer simulations have found that residual agitation in the lattice causes considerable rearrangement of the atoms within the cascade region as the cascade approaches thermal equilibrium.[5,10,16,20,36] This atomic mixing may be quantified by the displacement mixing factor (DMF), defined as the number of replacements (lattice site rearrangements) relative to the NRT displacements occurring during the collisional and cascade quench phases. The number of replacements (N_R) is monitored experimentally or by computer simulation by utilizing random walk diffusion theory. The diffusion coefficient for atomic mixing (D_M) after N_R uncorreiated jumps in a time interval t can be approximated for large N_R by

$$D_M = N_R < r^2 > /6t \qquad (2)$$

where $<r^2>$ is the mean square length of the individual jumps, which is approximately equal to the square of the nearest neighbor distance.[6,37,38,39] The DMF includes lattice mixing contributions from both the collisional phase and the subsequent cascade cooling phase. Recoil mixing and order-disorder measurements have found that the number of atomic replacements per dpa is on the order of 100 for energetic PKA cascades.[22,37-40]

Recent molecular dynamics studies have led to a resurgence of the Seitz and Koehler[41] thermal spike model of displacement cascades.[5,7,22,42] According to this model, interstitials which are transported via ballistic ejection or replacement collision sequences to the periphery of the cascade region will preferentially escape recombination during the cooling of the thermal spike. This results in a segregated distribution of clustered and isolated interstitials near the outer boundary of the cascade, and a corresponding fraction of clustered and isolated vacancies near the center of the cascade. Several experimental measurements and MD calculations on atomic mixing support the thermal spike concept. For example, the amount of atomic mixing in Cu has been found to be about three times higher than that in Ni for a 5 keV PKA.[6] This difference has been attributed to the lower melting temperature for Cu. which causes the thermal spike to be larger and of longer lifetime than in Ni. Recent MD calculations have also found that the amount of mixing increases with increasing temperature, due to the longer lifetime of the cascade and an increase in the agitated lattice volume associated with the slower cascade quench rate at high temperatures.[6,43,44] According to calculations by Hsieh et al,[43] the DMF at 700 K is four times the DMF at 0 K for a 3 keV cascade in copper.

For increasingly energetic PKA energies (up to the onset of subcascade formation), the fraction of defects that survive the cascade quench has been found to monotonically decrease relative to the NRT dpa.[6,7,9,11,44-53] This is attributed to two mechanisms. First, the increased mean kinetic energy within the cascade volume causes enhanced annihilation of displacement damage during the thermal spike. More importantly, the larger cascade volume associated with energetic PKAs ensures that fewer interstitials will be transported via ballistic ejection or replacement collision sequences beyond the highly agitated cascade core.[5-7] The defect fraction (relative to the NRT calculated displacements) retained in a quenched cascade is therefore reduced due to the efficient defect recombination that occurs readily within the thermal spike region.

The quenched cascade defect fraction (QDF) is defined to be the fraction of the NRT calculated displacements that survives the cascade quench. The QDF can only be measured for low temperature irradiations, where defect migration does not occur. This defect fraction is often referred to as a 'displacement cascade efficiency" or a 'defect production efficiency' in the literature. However, some confusion has been introduced into the literature because

different research groups have chosen to normalize these "efficiency" factors to either the original Kinchin-Pease expression or the NRT displacement function, which are different from each other by a factor of 0.8 (i.e., by the NRT "displacement efficiency"). We have chosen to adopt a neutral, descriptive terminology to avoid this possible source of confusion.

Electrical resistivity measurements have been performed on several metals during irradiation at temperatures near 4 K (where no long-range point defect migration is possible) in order to determine the quenched cascade defect fraction (QDF).[9,11,45-53] The measured value of the QDF steadily decreases from near unity for electron and proton irradiations (where only isolated Frenkel pairs are produced) to a value of about 0.3 for 5 keV cascades in copper. Multiple subcascades are produced as the PKA energy increases above about 20 keV.[26-30] The formation of subcascades causes the QDF to remain nearly constant for PKA energies between 20 and 500 keV in copper, with a value near 0.3.[11] Recent molecular dynamics calculations of cascades in copper have deduced similar values for the QDF at these low temperatures.[5,7,20,44]

Figure 2 illustrates the recoil energy dependence of the QDF in copper irradiated at low temperature. The filled symbols refer to experimental data,[9,11,45-53] whereas the open symbols are the results of MD calculations.[6,20,54,55] The solid line is an eye guide through the experimental data obtained in nearly monoenergetic irradiation spectra (electron and neutron irradiations). With the exception of the low QDF values computed by King and Benedek,[55] the MD calculations are in reasonably good agreement with the "monoenergetic" experimental data. As has been noted elsewhere,[9,11] defect production measurements made with light ion irradiation sources produce QDF values that are higher than values obtained from "monoenergetic" PKA sources for a given median recoil energy. This occurs because long-range Coulomb interactions by the ions induce a significant number of low energy PKAs, which have an enhanced defect survival rate compared to the median PKA energy. The rapid increase of the QDF from zero to a value >1 at very low recoil energies (E <30 eV) may be attributed to an inability of the modified Kinchin-Pease model to describe displacements in a polycrystalline material at recoil energies near the threshold displacement energy, ED. due to the strong dependence of ED on crystallographic orientation.[55-57]

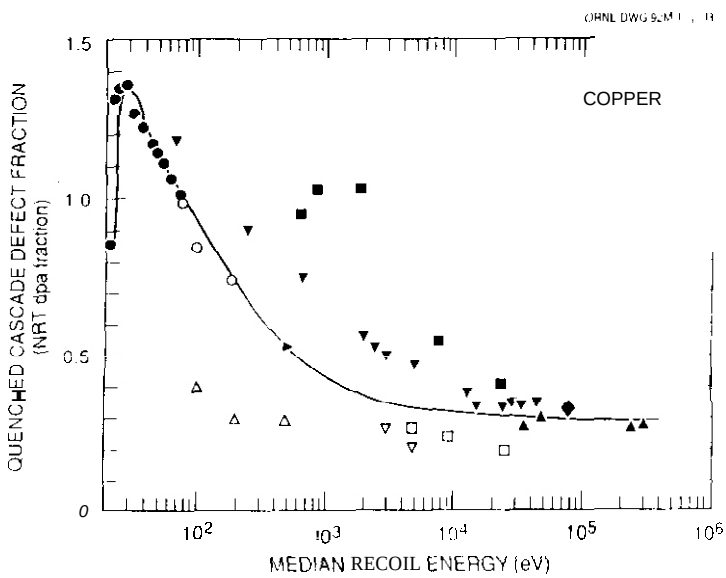

Fig. 2. Dependence of the quenched cascade defect fraction (QDF) on median PKA energy in copper. The open symbols[6,20, 54,55] refer to MD calculations whereas the filled symbols refer to experimental measurements as the result of electron (•),[48] ion (▼■),[9,47] fission fragment (◆),[53] and neutron (► ▲)[11,49-52] irradiation at low temperatures,

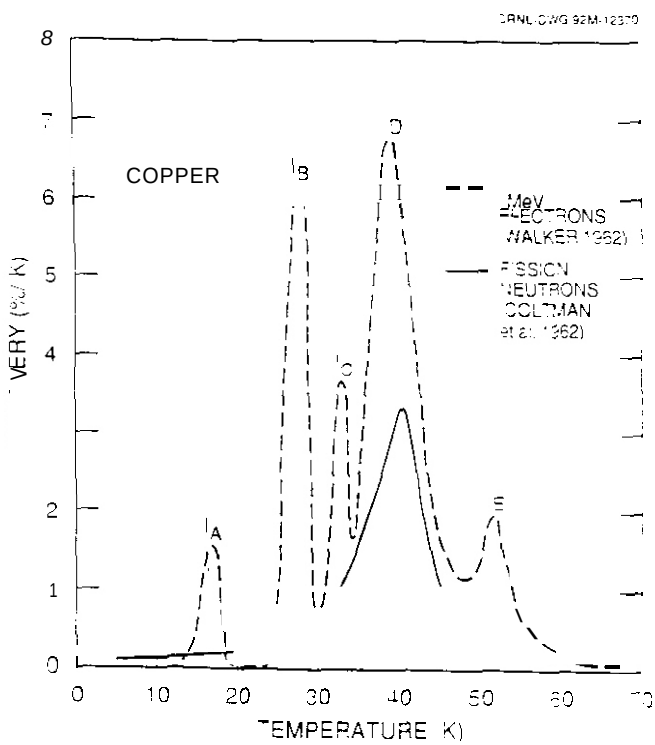

Fig. 3. Differential isochronal annealing curves for electron[58,59] and fast neutron60 irradiated copper showing the Stage I (interstitial) recovery peaks

2.3 Temperature Dependence Of The Survivlna Defect Fraction

Many of the defects which survive the cascade quench are subject to correlated recombination if the irradiation temperature is high enough to allow thermal diffusion. Figure 3 compares the amount of Stage I (interstitial) defect recovery that occurs in copper following low temperature irradiation with electrons[58,59] and neutrons.[60] Five different annealing peaks are observable for the electron irradiation case. Analyses of the annealing kinetics of experiments performed with different irradiation fluxes. fluences and sample purities have allowed the first three stages (I_A to I_C) to be identified as close pair (essentially single jump) recombination events.[58,59,61] Substages I_D and I_E have been found to be due to correlated (recombination with its own vacancy pair) and uncorrelated (recombination with a vacancy from another Frenkel pair) recovery of migrating interstitials. respectively. In contrast to the electron case, the Stage I recovery of neutron irradiated copper generally consists of only one major substage,[60-66] which is centered near the electron irradiation I_D correlated recombination substage. This neutron irradiation recovery stage has been found to be due to interstitial annihilation events within the same parent displacement cascade. Due to the highly disrupted lattice structure associated with an energetic displacement cascade, the concept of correlated recombination of distinct Frenkel pairs is not applicable for neutron irradiation conditions. For the purposes of energetic cascades, we will consider 'correlated recombination' to include all post-quench vacancy or interstitial annihilations involving defects from the same parent cascade.

Numerous studies have established that the amount of correlated recovery (substage I_D) decreases with increasing PKA energy.[34,58-63,67] Approximately 80% of the displacement damage introduced during low temperature irradiation is recovered via correlated recombination in electron-irradiated copper,[58,59,61] compared with ~50% correlated recovery for thermal neutrons[60,61] and only ~30% for fast neutrons.[61-66] Since correlated recombination is a diffusion process, it can be suppressed by solute additions that act as interstitial traps.[61,62,68]

Due to correlated annihilation effects, it is apparent that the fraction of defects surviving both the cascade quench and subsequent correlated in-cascade recombination during irradiation at temperatures above the recovery Stage I wiil be less than the low-temperature QDF. The surviving defect fraction (SDF) is defined to be the fraction of NRT calculated displacements remaining after correlated recombination has occurred in the cascade. For irradiations performed at low temperature (below Stage I), no thermal diffusion occurs and the SDF is equal to the QDF. For radiation effects modelling, the SDF is generally more important than the QDF because it represents the fraction of defects that escape in-cascade annihilation and are capable of interacting with other defects in the matrix.

One approach for estimating the effect of correlated recombination on the SDF is to monitor the annealing behavior of quenched displacement cascades introduced during low temperature irradiation. Computer annealing simulations[12,21,29] of isolated energetic PKA cascades in copper indicate that about 22% of the defects present after the cascade quench recombine within the cascade during short term annealing. Assuming a quenched cascade defect fraction of QDF = 0.3. this indicates that SDF ≅0.23. This estimate agrees well with experimental isochronal annealing data (Fig. 3), where 30% of the defects present in copper after neutron irradiation at 4 K suffer correlated annihilation during Stage I annealing, i.e., SDF (50 K) ≅0.7 QDF (4 K) ~0.21.

A more direct approach for estimating the value of SDF (T) is to perform irradiation tests at elevated temperatures. Dislocation pinning[69] and electrical resistivity[68,70] experiments indicate that only about half of the defects created in electron irradiated copper escape correlated recombination during irradiation at temperatures where interstitials are mobile. The fraction of defects annihilated by correlated recombination in electron irradiated copper decreases slightly with increasing temperature above 50 K, due to a reduced recombination radius at elevated temperatures. The close average spacing between an interstitial and its vacancy pair in electron irradiated copper (~2 nm for 3 MeV electrons)[68] allows temperature to have a significant effect on the drift diffusion of interstitials in the elastic strain field of their correlated vacancy. The fraction of defects surviving correlated recombination in electron-irradiated copper is SDF ~0.35 at 50 K and SDF (200 K) ~0.65. Radiation-induced segregation experiments[71] performed on Ni-Si indicate that about 40% of the displacement damage created during electron irradiation at temperatures near 700 K survives correlated recombination, i.e. SDF (700 K) ~0.4. In summary, the key point is that even in the absence of cascade damage conditions only a fraction of the displacement damage survives correlated recombination and is available for migration and interactions in the lattice.

Electrical resistivity measurements[53,67,72,73] and MD calculations[6,7,43,74] performed at elevated temperatures suggest that the surviving defect fraction (SDF) for energetic PKAs in copper drops rapidly to a value near **0.1** as the irradiation temperature is increased from 0 to 300 K, and then decreases only slightly with further increases in temperature. The temperature-dependent value of the SDF obtained from recent MD calculations is summarized in Fig. 4, along with lower bounds for SDF (T) derived from electrical resistivity measurements. Unfortunately, the precise value of SDF (T) cannot be directly measured by experiment at elevated temperatures where point defects are mobile, because some uncorrelated defect annihilation (at sinks or via recombination in the lattice) will occur along with the correlated intracascade recombination. Nevertheless, the available experimental measurements are in good agreement with the values of SDF (T) obtained by MD calculation: electrical resistivity measurements on copper irradiated with fission fragments at 7 K and **85** K[53] indicate that the surviving defect fractions are SDF (7 K) ≅0.33 and SDF **(85K) 20.14.** A similar analysis of the initial resistivity damage ratios reported by Theis and Wollenberger[72] for neutron irradiated copper suggests that SDF **(55**K)/SDF (4 **K) 20.65,** and SDF **(140**K)/SDF (4 K) **20.52.** Assuming a surviving defect fraction at 4 K of SDF **(4** K) ~ *0.30* this would correspond to SDF (55 K) ≥0.20 and SDF **(140**K) **20.16.** Electrical resistivity and transmission-electron microscopy (TEM) measurements on copper[73] and gold[75] irradiated at room temperature with 14-MeV neutrons indicate that SDF (300 K) **20.12.** Once again, these estimates are lower bounds for the value of SDF (T) since some of the defects that survive correlated recombination will suffer uncorrelated annihilation prior to the measurement. In-situ TEM studies of defect cluster formation in gold and nickel during ion irradiation also suggest that the SDF (defect yield) decreases as the irradiation temperalure is increased from 300 K to 600 K.[35,76]

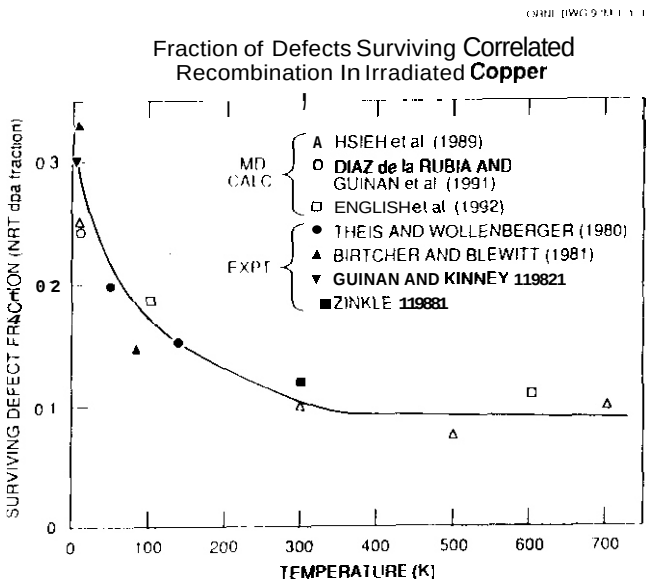

Fig. 4. Temperature-dependent fraction of defects surviving the cascade quench and correlated recornbination (SDF) in copper irradiated under cascade conditions. The open symbols[20,43,74] refer to MD calculations performed with PKA energies of 3 to 5 keV, and the filled symbols[52,53,72,73] refer to lower-bound estimates obtained from electrical resistivity measurements on neutron-irradiated copper (see text).

The decrease in the surviving defect fraction (SDF) with increasing irradiation temperature for energetic cascades (Fig. 4) can be rationalized by considering the influence of correlated annihilation on defect production, and the effect of temperature on the thermal spike. The 30% decrease in the energetic-cascade SDF (from 0.3 to 0.2) as the temperature is increased from 0 to 50 K matches the 30% correlated recovery observed in Stage I annealing tests (Fig. 3), and hence may be attributed primarily to correlated recombination effects. However, the apparent further decrease in the SDF to a value near 0.1 for irradiation at temperatures above 300 K requires additional physical mechanisms to be considered. As the irradiation temperature is increased above **-10** K, the cascade quenching rate is reduced due to a decrease in the lattice thermal conductivity and a reduced temperature gradient between the cascade core and the surrounding lattice. The displacement cascade is therefore at high temperatures for a longer time, which would result in more efficient recombination of displacement damage during the cascade quench. At elevated temperatures, the reduced quenching rate and high lattice temperature also causes an increase in the thermal spike volume.[43] This would reduce the SDF since fewer interstitial?, would be located outside of the highly agitated cascade core region, where recornbination occurs readily.6

2.4 Partitioning of Defects that Survive the Cascade Quench and Correlated Recombination

The relative proportions of isolated and clustered defects remaining after the cascade quench and subsequent correlated recombination stages will generally be different for vacancies and interstitials (Fig. 1), and will depend on parameters such as the PKA energy and the ambient lattice temperature. The surviving defect fraction (SDF) can be broken into two components: the isolated point defect fractions ($IDF_{i,v}$), which consists of monovacancies and

monointerstitials, and the clustered defect fractions ($CDF_{i,v}$), which includes mobile defect clusters such as di-interstitials and divacancies along with larger sessile clusters. The subscripts i,v denote quantities for which the fraction of vacancies and interstitials will generally be unequal. Hence,

$$SDF = CDF_i + IDF_i = CDF_v + IDF_v \quad (3)$$

As with the SDF, both the clustered and isolated point defect fractions are defined relative to the NRT calculated displacements and are expected lo be functions of temperature as well as PKA energy.

Computer annealing calculations,[21,77,78] molecular dynamics calculations,[7,16,20,36,44] and experiments based on X-ray diffuse scattering[31,32] and electrical resistivity measurements[72] indicate that most of the vacancies and interstitials that survive the quench phase of an energetic cascade will be in the form of clusters. According to electrical resistivity measurements[34] and MD calculations,[20,44] the fraction of surviving defects that are clustered in FCC metals during irradiation near 10 K increases with increasing PKA energy. Assuming a constant surviving defect fraction at 10 K of SDF = 0.3 for PKA energies between 5 and 25 keV, the MD calculations indicate CDF_v (10 K) ≅0.06 and CDF_i (10 K) ≅0.07 for 5 keV cascades and CDF_v (10 K) ≅0.14 and CDF_i (10 K) ≅ 0.21 at 25 keV.[20] Other experimental and computer studies suggest similar values for neutron irradiated (>20 keV cascade) copper at low temperature, CDF, ≅0.22[21] and CDF_i ≅0.18,[72] once again assuming a surviving defect fraction of SDF = 0.3. There have been numerous reported TEM observations of direct in-cascade vacancy and interstitial cluster formation in ion and neutron irradiated metals.[35,42,75,76,] 79.80

According to MD calculations performed for energetic cascades in copper near 4 K, the isolated point defect fractions present at the end of the cascade quench stage are ~10% of the NRT calculated displacements for both interstitials and vacancies, i.e. $IDF_{i,v}$ (4 K) ~0.1.[20] This represents an upper limit for $IDF_{i,v}$ at elevated temperatures since some of these point defects would be subsequently annihilated by correlated recombination (Fig. **3).** Theis and Wollenberger[72] deduced that the freely migrating interstitial fraction produced in copper during neutron irradiation at 50 to 170 K was 15% of the interstitial production rate at 4.6 K, which indicates that IDF_i = 0.15 SDF (4 K) ≅4.5%. Computer simulated annealing studies of energetic cascades in copper at 300 K suggest freely migrating defect fractions of about 1% for vacancies and about 4% for interstitials, for PKA cascade energies greater than 20 keV.[21] These calculations agree with order-disorder measurements made on neutron irradiated copper at temperatures below annealing Stage V, which found IDF_v (423 K) ≤2%[81] and IDF_v (414 K) ≤1.5%.[82] The fraction of freely migrating interstitials in nickel irradiated with neutrons at 623 K was estimated from Curie temperature measurements to be about 2.6%.[83] All of these values are upper limits for $IDF_{i,v}$ since the freely migrating defect fractions will also include some contribution from small mobile clusters such as di-interstitials (see Sections 2.5 and 2.6). Data from numerous other experimental studies generally indicate that the fraction of "freely migrating" defects is 1 to 10% of the NRT dpa value.[13] A detailed analysis of these "freely migrating defect" studies is presented in Section 3.2.2.

Table 1 summarizes the available information on the various displacement damage and defect production parameters. It is worth reemphasizing that all of these damage parameters will depend on the PKA cascade energy and probably also irradiation temperature, in a manner analogous to that shown in Figs. 2 and 4 for the quenched cascade and surviving defect fractions. All of the damage parameters are normalized with respect to the NRT calculated displacements. For radiation damage modelling, the most important parameters are the displacement mixing factor (DMF). the clustered defect fractions ($CDF_{i,v}$), and the isolated point defect fractions ($IDF_{i,v}$).

2.5 Thermal Stability and Mobility of Defect Clusters

A complete description of the temporal evolution of a displacement cascade at an elevated temperature (homologous temperature >0.3 T_M) must include evaporation of monodefects from defect clusters that were initially formed during the cascade quench. Figure 5 shows the temperature-dependent density of stacking fault tetrahedra (SFT) observed in a dilute Cu-B alloy following a temperature-controlled reactor irradiation to ~1.2 dpa.[84] According to current thinking, the SFT are formed as a result of collapse of the vacancy-rich core of the displacement cascade during or subsequent to the cascade quench. The rapid decrease in the SFT density for neutron irradiation temperatures higher than 450 K is presumed to be predominantly due to vacancy evaporation from the clusters, and can be models.[85]

Table 1. Summary of proposed displacement damage and defect production parameters

Parameter	Typical values in Cu		
	1 MeV electron	30 keV cascade	Comments
DMF = displacement mixing factor	DMF = 1	DMF ~100	DMF = DMF (T)
QDF = quenched cascade defect fraction	QDF ≅ 1 (all temperatures)	QDF (4 K) ~0.3 QDF (300 K) ≥0.12	$QDF_i = QDF_v$
SDF = correlated recombination surviving defect fraction	SDF (4 K) ≈ 1 SDF (300 K) ~0.5	SDF (4 K) ≅ 0.3 SDF (50 K) ~0.2 SDF (300 K) ~0.1	$SDF_i = SDF_v$ SDF = SDF (T)
clustered defect fractions		CDF_v (4 K) ~0.1	
$IDF_{i,v}$ = isolated point defect fractions	IDF_i (4 K) = IDF_v = 1 IDF_i (300 K) = IDF_v ≅ 0.5	IDF_i (4 K) ~0.1 IDF_v (4 K) ~0.1 IDF_i (300 K) ≤ 0.04 IDF_v (300 K) ~0.02	IDF ≈ IDF (T)

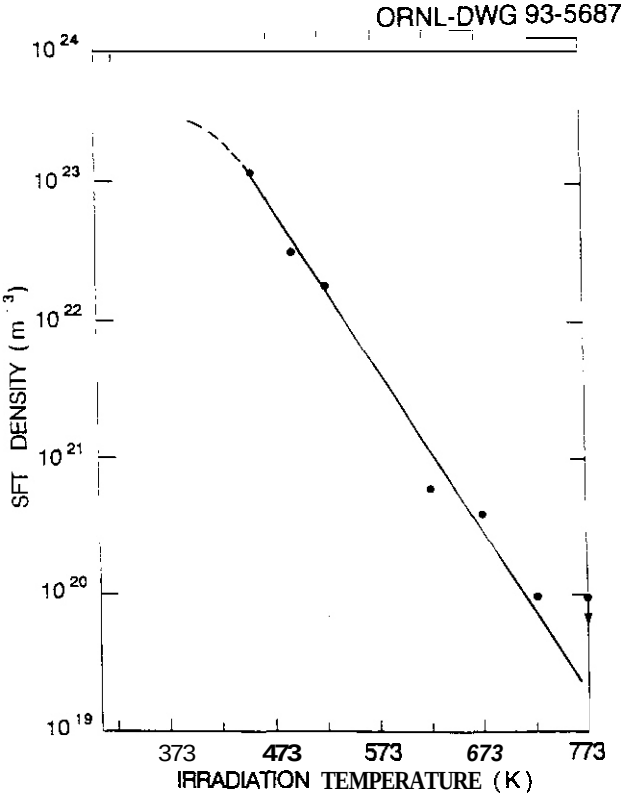

Fig. 5. Density of stacking fault tetrahedra versus irradiation temperature for copper - 100 wl ppm B irradiated with neutrons at ~2 x 10^{-7} dpa/s.[84]

At moderate temperatures and high damage fluxes, the stability of vacancy clusters during irradiation is determined predominantly by interstitial absorption (which induces decomposition of the clusters), instead of thermal evaporation.[76,86-88] Numerous TEM studies have been performed on the production and annealing of vacancy clusters during elevated temperature irradiation.[42,75,76,86-89]

At intermediate temperatures relevant for void swelling (0.3 to 0.6 T_M), vacancy clusters are thermally unstable whereas interstitial clusters are thermally stable. For example, MD calculations have found that the binding energy of a tetra-interstitial cluster in copper is 2.53 eV, whereas the binding energy for a tetra-vacancy cluster is only 0.28 eV; the corresponding binding energy per defect for clusters containing more than 5 point defects is ~0.85 eV/interstitial and ~0.44 eV/vacancy, respectively.[90,91] Even larger differences between the stability of small vacancy and interstitial clusters have been obtained for nickel.[91] As noted by Simons[77] and Woo and Singh,[18,19] this difference in stability between vacancy and interstitial clusters can lead to an excess supply of mobile vacancies relative to the mobile interstitial. population at elevated temperatures and must be considered for the modeling of void swelling and other elevated temperature radiation damage processes. A modified rate theory model has recently been developed that takes into account this asymmetric supply of available point defects, i.e. the so-called "production bias."[19,92,93]

The clustered defect fraction (CDF) includes larger, sessile clusters and small defect clusters that may be mobile at a given irradiation temperature. Recent MD calculations indicate that the migration energies for small clusters containing up to 4 point defects are comparable to the corresponding values for isolated point defects. For example, the migration energy of a tri-interstitial in nickel was calculated to be ~0.50 eV, and divacancy migration energies of 0.47 eV

and 0.55 eV were obtained for nickel and copper, respectively.[90,91] Similar calculations indicate that the migration energies of tri- and tetra-vacancy clusters in copper are 0.56 eV and 0.38 eV, respectively.[94] The mobility of a tetra-interstitial cluster produced directly in a displacement cascade in copper was found to be comparable to that of the metastable crowdion interstitial.[56] Diffuse x-ray scattering measurements performed during isochronal annealing of neutron-irradiated copper indicate that small interstitial clusters become mobile and coarsen at Stage II annealing temperatures, 50 to 170 K.[33]

A further comment is necessary regarding the mobile component of the clustered defect fraction. According to MD calculations, the diffusion of many of the interstitial clusters may be restricted to planar motion or even one-dimensional glide.[56,91,95] The high binding energy of small interstitial clusters compared to their migration energy means that these clusters can be transported long distances (via glide) without breaking apart. Therefore, interstitial clusters generally cannot be treated in the same framework as isolated point defects, which migrate via random walk, three-dimensional diffusion. Small vacancy clusters, on the other hand, pass through several intermediate configurations to complete a migration step[94] and the overall cluster motion is apparently random in the absence of external stress. In addition, the relative thermal instability of small vacancy clusters compared to their migration energy will cause vacancy evaporation from the cluster before it migrates a significant distance.

2.6 Defect Production Resulting from Displacement Damage

Figures 6 and 7 schematically outline the temporal evolution of the vacancy and interstitial population in an isolated energetic displacement cascade at intermediate temperatures relevant for void swelling. A high concentration of defects are created during the collisional phase ($\sim 10^{-13}$ s). Most of these defects are subsequently annihilated during the cascade quench ($\sim 10^{-11}$ s), leaving a collection of isolated and clustered defects. The high degree of atomic mixing during the collisional and cascade quench phases can produce displacement mixing factors (DMFs) of ~100. Short range diffusion of the mobile interstitials and vacancies (and associated small mobile clusters) within the cascade induces further recombination and clustering after the cascade quench. The duration of this intracascade (correlated) recombination phase is dependent on the irradiation temperature (defect mobilities). Finally, thermally activated diffusion induces long-range migration of the mobile portion of the defects that survive the cascade quench and correlated recombination phases.

As outlined in Fig. 7, there are 3 components to the fraction of migrating interstitials or vacancies ($MDF_{i,v}$). The most straightforward component is the isolated point defect fraction ($IDF_{i,v}$), which is produced directly in the displacement cascade. A second component (mobile cluster fraction, $MCF_{i,v}$) is comprised of small defect clusters which are mobile (Section 2.5). The third component is due to thermal annealing of immobile vacancy clusters (and also interstitial clusters at very high temperatures). Mobile vacancies are released by evaporation from the surviving immobile vacancy clusters (which exist predominantly near the center of the displacement cascade, Fig. 1). Some of these evaporating vacancies will be annihilated at the residual immobile interstitial clusters surrounding the displacement cascade core; a recent diffusion calculation[92,93] found that 20% of the initially clustered vacancies associated with a 20 keV cascade in copper will be annihilated during annealing at 523 K.

Unfortunately, the magnitude of the mobile vacancy and interstitial cluster fractions ($MCF_{i,v}$) are not known at the present time. In Fig. 6, we simply denote r as the fraction of the clustered vacancy component CDF_v that is either initially freely migrating (e.g. divacancies), or escapes intracascade (correlated) annihilation following evaporation of the vacancy clusters at elevated temperature. Obviously, the value of r would be dependent on time (until steady state cluster evaporation conditions are achieved). With this simplification, the fraction of freely migrating vacancies at elevated temperature is $MDF_v = IDF_v + r\,CDF_v$, i.e. a mixture of the isolated vacancy fraction (IDF_v) and the initially clustered fraction (CDF_v). The corresponding fraction of freely migrating interstitials at temperatures relevant for void swelling is $MDF_i = IDF_i$ since the interstitial clusters formed in the displacement cascade would be thermally stable. This expression is a lower limit for the migrating interstitial fraction since it excludes mobile clusters (e.g. di-interstitials) that probably should be considered freely migrating. At very high irradiation temperatures, where interstitial clusters are thermally unstable, the fraction of migrating interstitials would become comparable to the vacancy fraction, i.e. $MDF_i \sim IDF_i + r\,CDF_i$. A portion (1-r) of the initially clustered interstitials would be lost due to annihilation by the evaporating vacancy clusters. Table 2 summarizes the temperature-dependent relations for the migrating defect fractions in copper.

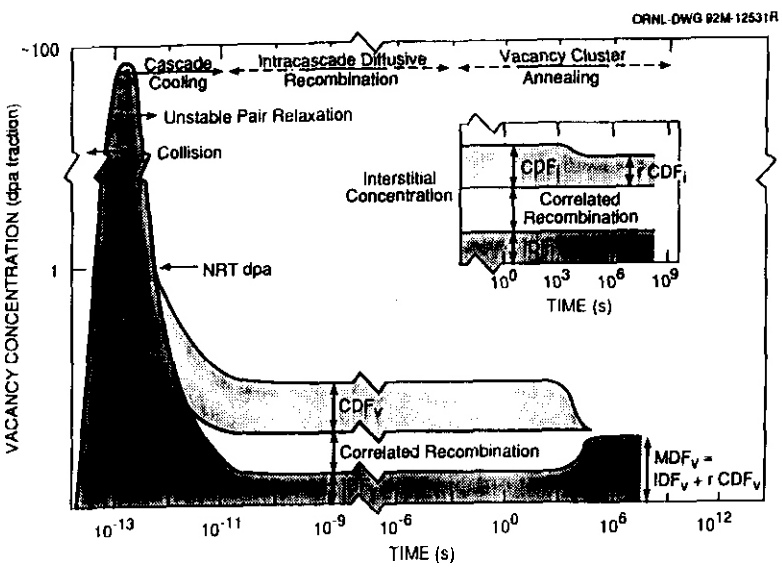

Fig. 6. Evolution of the vacancy and interstitial (inset) defect population in an isolated energetic displacement cascade in copper. The latter stages of the figure (t >1 s) are indicative of an irradiation temperature where vacancy clusters are thermally unstable and interstitial clusters are stable.

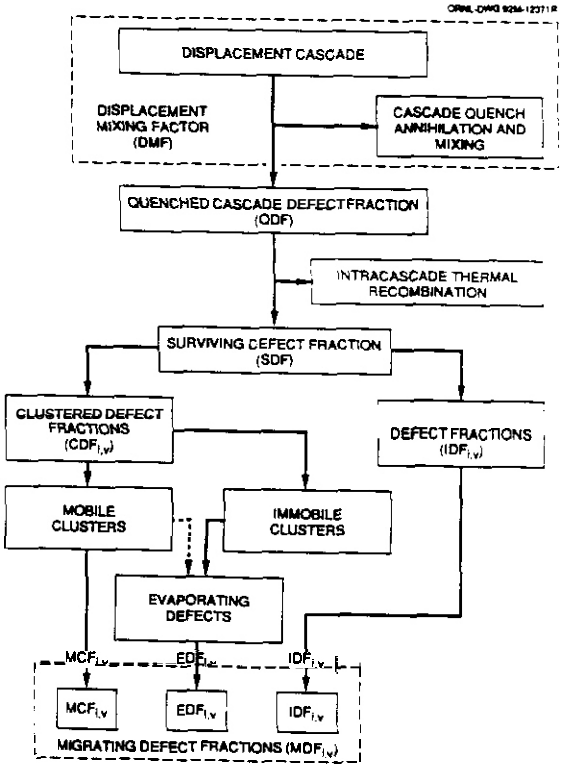

Fig. 7. Flow chart showing the contributions of isolated point defects, mobile defect clusters, and thermally evaporating defects clusters to the fraction of migrating defects.

Table 2. Temperature dependence of the migrating defect fractions ($MDF_{i,v}$) in copper.*

Irradiation Condition	Available migrating defect fraction ($MDF_{i,v}$)	
	Interstitial	Vacancy
Defect clusters stable (T c 450 K)	$MDF_i \geq IDF_i$	$MDF_v > IDF_v$
Vacancy clusters unstable (450 K c T < 900 K)	$MDF_i \geq IDF_i$	$MDF_v = IDF_v + rCDF_v$
Vacancy and interstitial clusters unstable (T > 900 K)	$MDF_i = IDF_i + rCDF_i$	$MDF_v = IDF_v + rCDF_v$

'The inequalities in some of the expressions result from the neglect of mobile defect clusters due to insufficient knowledge about their importance (see **text).**

3.0 DISCUSSION

The calculation of the number of atomic displacements using the NRT model3 has achieved worldwide standardization, which underscores its importance as a "benchmark" for radiation effects studies. However, it is now apparent that a distinction needs to made between the generation of atomic displacements and residual defecf production under cascade damage conditions.[12] Depending on the property of interest, the NRT calculated number of displacements either underestimates (atomic mixing) or overestimates (residual defect production) the relevant radiation effects parameter for cascade conditions. The central concept that emerges from the present analysis is that there is no single unique parameter that adequately describes all of the various defect-induced radiation processes that may occur under cascade damage conditions. Instead, a revised defect production framework is needed that is more flexible and physically descriptive of cascade damage conditions than the NRT model.

One of the intentions of this paper is to propose a standardized notation and terminology for the various displacement damage and defect production parameters that are of interest for radiation effects studies. The proposed

nomenclature is summarized in Table 1. The three fundamental parameters that are most useful for advanced radiation damage models are the displacement mixing factor (DMF), the clustered defect fractions ($CDF_{i,v}$), and the isolated point defect fractions ($IDF_{i,v}$). All of the parameters are essentially independent of dose and microstructure for a given material, since they refer to damage produced by an isolated PKA. and are defined as fractions of the NRT calculated displacements. The possibility of modified damage parameters due to cascade impingement on existing microstructural features such as dislocation loops needs to be separately addressed in rate theory models (see Section 3.1.2). The available evidence discussed in section 2.3 indicates that for cascade damage conditions, all of the defect production parameters should decrease with increasing irradiation temperature. Since vacancies and interstitials are produced in equal numbers during the irradiation, it follows that the fractions of vacancies and interstitials surviving the cascade quench and correlated recombination must be equal, $SDF_v = SDF_i$. However, the partitioning between isolated defects and defect clusters is generally not equal for vacancies and interstitials (Section 2.4).

3.1 Consequences of Intracascade Clusterlna of Vacancies and Interstitials

Section 2 outlined the physical nature of point defects and defect clusters resulting from multi-displacement processes in an isolated collision cascade. In the following, we consider the importance of these characteristics of an isolated displacement cascade on (a) modelling the defect accumulation behavior under cascade damage conditions, and (b) identifying different defect fractions in experiments carried out under multi-cascade damage conditions.

3.1.1 Modeling Of Microstructural Evolution

A key aspect of the defect production in an energetic collision cascade is that a substantial fraction of the interstitials and vacancies surviving intracascade recombination are already in clustered form following the cascade quench ($\sim 10^{-11}$ s). MD simulations of energetic cascades invariably show a vacancy-rich cascade core consisting primarily of clustered vacancies, surrounded by a diffuse shell of clustered and isolated interstitials (Fig. 1). In other words, the damage production is not only inhomogeneous but is also segregated in that the populations of interstitials and vacancies are separated from each other in space. Since the major component of the damage is in the form of clusters (Section 2.4), it is of vital importance to consider the thermal as well as spatial stability of these clusters in radiation effects models. As discussed in Section 2.5, vacancy clusters in the collapsed or uncollapsed state would act as vacancy sources for the matrix at irradiation temperatures above Stage V (i.e., in the void swelling regime). Interstitial clusters, on the other hand, are thermally stable and will not release single interstitials to the matrix. In addition, small interstitial clusters are likely to be efficiently removed from the system by gliding to sinks such as grain boundaries and dislocations.

An accurate physical model of defect production and accumulation under cascade damage conditions must incorporate the following aspects, which are not addressed in traditional rate theory models:

(i) a large proportion of the defects are produced heterogeneously in the form of vacancy and interstitial clusters, with the remainder being isolated vacancies and interstitials

(ii) the bias for absorption of mobile interstitial clusters and freely migrating interstitials at sinks such as dislocations will likely be different

(iii) the fractions of interstitials and vacancies in clustered or isolated forms are not likely to be equal, i.e. there may be an asymmetry in the production of freely migrating fractions of interstitials and vacancies

(iv) vacancy evaporation from clusters formed during the cascade quench will produce a temperature-dependent contribution to the fraction of freely migrating vacancies, MDF_v

The problem of vacancy clustering in the cascade was addressed in the mid 1970s,[96] and has been found to be important for the modeling of the temperature dependence of swelling in metals.[97] Recently, the effects of intracascade recombination as well as in-cascade clustering of interstitials and vacancies have been incorporated into the rate theory treatment of defect accumulation.[18,19] The consideration of intracascade clustering and the thermal stability of interstitial and vacancy clusters yields an asymmetric supply of migrating vacancies versus interstitials ('production bias') which has been found to be a strong driving force for void swelling in the steady state.[19,92,93]

On the basis of the clustering behavior of interstitials and vacancies observed in MD simulations, Singh and Foreman93 have calculated the escape rate of vacancies from cascades. Using this rate as an effective production rate of vacancies, they investigated the time dependence of vacancy accumulation in neutron-irradiated copper during the initial transient regime (10^{-5} to 1 dpa).[92,93] They found that the best fit to the published void swelling data was obtained if about 15% of the interstitials were allowed to escape directly to sinks other than voids. This escape was assumed to occur via one-dimensional glide of small interstitial clusters. Recently the problem of cluster mobility and escape have been treated in detail by Trinkaus and coworkers.98 Their calculations indicate that the combination of production bias and gliding interstitial clusters can yield a high level of vacancy supersaturation, particularly when the density of dislocations is very low ($<10^{12}/m^2$).

Cascade impingement on lattice imperfections becomes more likely at high displacement damage levels, particularly for lower irradiation temperatures due to the increased thermal stability of radiation induced clusters. These cascade overlap effects may modify the values of the defect production parameters compared to their isolated cascade values.[12,99] MD simulations[16] have found that the defect production parameters are greatly reduced if a cascade occurs on or near a pre-existing defect cluster or dislocation loop. Electrical resistivity studies have shown that the defect production rate at low temperatures in metals is dependent on the initial microstructure.34 Stage I annealing results also indicate that the partitioning between isolated and clustered defects may be affected by cascade overlap: The amount of correlated recovery observed during Stage I annealing after ion or neutron irradiation near 4 K decreases with increasing fluence, which suggests that cascade overlap induces a higher proportion of clustered defects (fewer mobile interstitials) compared to an isolated displacement cascade.[62,64,65,67] Therefore, the possibility of fluence-dependent defect production fractions should be incorporated into any comprehensive model of defect accumulation in irradiated metals.

3.1.2 t f Def t r from Ex . t

In view of the preceding discussion, it is apparent that the analysis of the results of experiments aimed at quantifying a well-defined fraction of defects (e.g., migrating defect fractions) produced under cascade damage conditions must include the considerations of intracascade recombination and clustering, thermal stability, and mobility of the resulting clusters, along with the possibility of cascade resolution of existing clusters. The important question is what defect fraction can be extracted from the results of high temperature irradiation experiments in a well-defined form. The schematic flow diagram in Fig. 7 reveals that the fraction of defects responsible for mass transport or void swelling during irradiation at elevated temperatures is composed of three very different components:

(i) as-produced freely migrating isolated interstitials and vacancies ($IDF_{i,v}$)

(ii) mobile interstitial and vacancy clusters ($MCF_{i,v}$), which includes freely migrating clusters such as di-interstitials and divacancies, and larger interstitial clusters which most likely will migrate via one-dimensional glide

(iii) a strongly temperature dependent contribution from vacancies evaporating from vacancy clusters (EDF_v)

Experimental mass transport measurements such as radiation-induced segregation or radiation-enhanced diffusion can monitor the aggregate value of the fraction of mobile defects participating in mass transport. It must be emphasized, however, that correct values of the migrating defect fractions ($MDF_{i,v}$) can be derived only if a rate theory model that considers all three components of the MDFs is employed. Unfortunately, the data from all existing migrating defect fraction measurements have been analyzed with traditional rate theories using assumptions that are only pertinent to the homogeneous Frenkel pair production case. These derived values cannot be related to fundamental damage parameters such as $IDF_{i,v}$ and $MDF_{i,v}$.

Since the time-dependent response of the 3 components of the migrating defect fraction ($IDF_{i,v}$, $EDF_{i,v}$, $MCF_{i,v}$) is not well known, there is a strong need to obtain defect production data as a function of fluence at elevated temperatures in order to verify what conditions produce a steady-state behavior. In analogy with void swelling studies, the transient regime may extend to damage levels much greater than a few dpa. Valuable information on the temperature dependence of various defect production fractions (Table 1) could be obtained from a systematic low-dose investigation at temperatures above and below the Stage I, Stage III, and Stage V temperatures associated with interstitial migration, vacancy migration, and vacancy cluster evaporation, respectively.

3.2 REVIEW OF DEFECT PRODUCTION MEASUREMENTS

3.2.1 Quenched Cascade Defect Fraction

The data obtained from the quenched cascade defect fraction (QDF) measurements near 4 K (Figure 2) are in good agreement that QDF(4 K) decreases from a value near 1 for low energy PKAs to a saturation value of ~0.3 for cascade energies ≥30 keV in copper.[9,11,47-53] There is some evidence that the saturation value of QDF (4 K) decreases slightly with increasing atomic mass of the irradiated metal,[28,47] which may be expected on the basis of cascade density effects: higher density cascades are created in the higher mass targets, which may cause increased in-cascade recombination. However, other studies have found no significant effect of atomic mass on the QDF.[50-52] The crystal structure apparently exerts a strong influence on the saturation value of the QDF; hexagonal close-packed metals have the highest values (~0.8), body centered cubic metals are intermediate and face centered cubic metals have the lowest values (~0.3) for the saturation value of the QDF.[50-52] Several experimental studies suggest that the proportion of clustered defects in a displacement cascade increases with increasing mass.[34,63-66] For example, the decrease in the amount of correlated Stage I recombination in neutron irradiated metals with increasing mass[63-66] is evidence for enhanced clustering in the displacement cascades of the high-mass metals (fewer mobile interstitials available for correlated recombination).

One recurring concern in the quenched cascade defect fraction (QDF) measurements is the applicability of electrical resistivity analyses for cases where defect clustering is known to occur.[9,34,100] The effective specific resistivity of vacancies or interstitials in a large cluster that has collapsed into a dislocation loop will depend on the size of the loop; the resistivity per defect for a *5.5* nm diameter faulted loop in copper is about half the Frenkel pair specific resistivity.[100] Some studies have concluded that electrical resistivity measurements in copper may underestimate the number of surviving defects in clustered form by as much as a factor of 2 or 3.[101,102] These results would suggest that the apparent decrease in the QDF for energetic cascades in copper may be largely due to the decreased resistivity per defect associated with defect clustering. Other experimental and theoretical analyses have found that the resistivity per defect for clusters formed from cascade collapse in neutron-irradiated copper is essentially the same as the Frenkel pair value.[34,53,100] A recent analysis combining resistivity and TEM techniques concluded that the mean size of clusters produced in copper irradiated with neutrons at room temperature resulted in a resistivity per defect that was fortuitously comparable to the Frenkel pair specific resistivity.[100] Computer calculations of the quenched cascade defect fraction in copper and nickel generally support the electrical resistivity results.[20,21,36,77] However, the validity of using resistivity measurements to monitor defect production under cascade clustering conditions remains in question for other metals.

3.2.2 Migrating Defect Fractions ($MDF_{i,v}$)

There have been numerous attempts to experimentally determine migrating defect fractions following irradiation at elevated temperature (see reviews in refs. 13.14). The deduced values for $MDF_{i,v}$ obtained from experimental studies and computer simulations on face centered cubic metals are summarized in Table 3.[21,29,39,72,74,81-83,103-115] The measurements are in apparent agreement that the fraction of 'freely migrating defects" for energetic cascades is ~1 to 10% of the NRT dpa, which is significantly less than the quenched cascade defect fraction at 4 K of QDF (4 K) ~0.3, but still an appreciable amount compared to the apparent elevated temperature surviving defect fraction (Fig. 4) of SDF (300 K) ~0.1. Unfortunately, it is difficult to obtain a more precise evaluation of the individual components of freely migrating vacancies and interstitials because the migrating defect fractions cannot be directly measured, but instead have been deduced from fits to simple homogeneous rate theory models that did not include treatment of the three individual components of the $MDF_{i,v}$. Many of the measurements were performed at elevated temperatures where vacancy clusters are thermally unstable and would act as internal sources of free vacancies. The analyses generally assumed that the mobile defect fraction was constant over the range of temperatures investigated and ignored consideration of the thermal stability of defect clusters, which depends on both temperature and irradiation time (damage rate). Measurements were often made at irradiation temperatures or damage levels which produced significant transient changes in the irradiation-induced microstructure during part of the measurement, but the data analysis assumed steady state conditions. Almost all of the studies failed to differentiate between the fractions of mobile vacancies and interstitials ($MDF_{i,v}$) and did not consider the possible presence of mobile defect clusters (which may not exhibit random walk, three-dimensional migration). As discussed later, some of the scatter in the deduced migrating defect fractions is also due to differences in the definition of "freely migrating defects" by different research groups.[107,111] In the following. the suitability of several experimental methods for estimating migrating defect fractions is analyzed in more detail.

deduced from experimental data or computer simulations on fcc metals.*

Metal	Temperature	Method	MDF_i	MDF_v	Ref.
Cu	100 K, 600 K	MD calc.	<6%		74
Cu	670 K	Void swelling		>5%	103-106
Cu_3Au	423 K	Ordering		≤2%	81
Cu	414 K	Ordering		≤1.5%	82
Cu	330 K	Disln. pinning	1%		113, 114
Cu	300 K	Computer Anneal	4%	1%	21, 29
Cu	170 K	Resistivity	4.5%		72
Cu	400 to 800 K	Diffusion	FMD ~1.5%		111
Cu-1% Au	623 K	Segregation	FMD ~1%		109
Ag-24% Zn	310 to 410 K	Ordering	10%	10%	115
Ni-4% Si	623 K	Curie temp.	2.6%		83
Ni-13% Si	623 to 923 K	Segregation	FMD ~2%		107
Ni	650 to 950 K	Diffusion	FMD ~1.5%		39
Ni-P	770 K	Segregation	FMD ~1 to 10%		110
Ni-Al	700 K	Segregation	FMD ~2.5%		112
Fe-Cr-Ni	700 to 950 K	Segregation	FMD ~3 to 17%		107

Perhaps the most direct approach to estimate the fraction of freely migrating vacancies (MDF_i) is to analyze the void swelling behavior of irradiated metals. Since the void swelling is due to the difference in the accumulation of vacancies and interstitials at void embryos, the void swelling rate yields a lower limit for MDF_i. The swelling rate is an absolute lower limit for MDF_v because it neglects uncorrelated recombination in the lattice and annihilation at sinks. Several low-dose (<1 dpa) neutron irradiation studies on copper and nickel[79,116-118] have observed an 'S-shaped" swelling behavior versus dose, with transient swelling rates equal to or greater than 2%/dpa. A more definitive lower limit for the MDF_v is obtained by examining the steady state swelling rate produced after higher dose irradiations. Figure 8 shows several recent void swelling results for copper irradiated with fast neutrons at temperatures near 400 C.[103-106] Most studies have found that the steady state swelling rate of neutron-irradiated copper at this temperature is near 0.5%/dpa. However, several studies[103,106] have found that the swelling rate of oxygen-bearing copper is dramatically higher, with values as high as 5%/dpa. Oxygen is known to stabilize void swelling in metals by a chemisorption reaction, which reduces the surface energy and thereby suppresses the evaporation of vacancies from small voids.[119] Since the presence of small quantities of impurity oxygen should not modify the number of displacements (NRT dpa) introduced during neutron irradiation, these results[103,106] suggest that the lower limit for the freely migrating vacancy fraction at 400 C in fast neutron irradiated copper is MDF_i ~5%.

Data derived from radiation induced segregation (RIS) measurements have been instrumental in establishing that the fraction of freely migrating defects for energetic cascades at elevated temperatures is significantly less than the quenched cascade defect fraction measured near 4 K.[13,107] As summarized in Table 3, these measurements indicate that the migrating defect fraction is between 1 and 17% of the NRT calculated displacements.[107-110] (The Kr+ ion data reported in ref. 107 has been ignored because it could not be consistently fitted to the computer model).[121] Most of the RIS measurements have monitored the interstitial component of the migrating defect fraction since the observed solute segregation was due to preferential solute binding to mobile interstitials. The quantitative accuracy of the RIS studies is dependent on the applicability of several simplifying assumptions employed in the data analysis,[120,121] including the assumptions that steady state conditions prevail and that point defect loss occurs predominantly via recombination. The freely migrating defect fraction derived in most of the RIS studies was defined to be the fraction of defects that migrate over distances that are large compared to typical cascade dimensions.[107,121] This definition includes not only losses from correlated recombination within the displacement cascade, but also uncorrelated defect annihilation at clusters produced in adjoining displacement cascades. Hence, their derived values ara dependent on the details of the

surrounding microstructure. Recent estimates suggest the fraction of migrating defects that suffer uncorrelated recombination may be very large,[122,123] which may partly explain the low deduced 'freely migrating defect" values obtained from most of the RIS studies compared to the higher MDF, values obtained from void swelling.

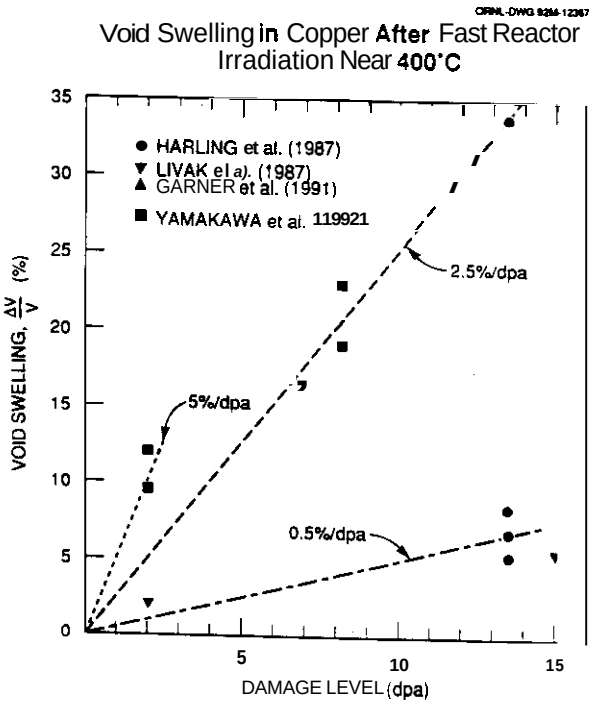

Fig. 8. Void swelling rates observed in oxygen-bearing and oxygen-free copper after fast reactor irradiation near 400°C.[103-106] The dpa conversion for the data from Ref. [106] assumed 1×10^{26} n/m^2 (E >0.1 MeV) = 6.5 dpa.

Another experimental technique that has been used to estimate freely migrating defect fractions is based on radiation-enhanced diffusion (RED) measurements.[38,39,111] This technique has the advantage that relatively short-range diffusion (~20 nm) is sufficient to produce measurable results. Conventional steady-state rate theory was used to extract estimates of the irradiation-induced sink concentration and the freely migrating defect fraction from RED data on ion irradiated Ni and Cu.[39,111] The freely migrating defect fraction was defined to be the mobile fraction that survived correlated (in-cascade) recombination, but unfortunately the analysis assumed that the vacancy and interstitial fractions were equal at all temperatures. As summarized in Table 3, the deduced freely migrating defect fraction in both metals was ~1.5% of the NRT calculated displacements for irradiation temperatures relevant for void swelling. The sink concentrations determined from the analyses were an order of magnitude higher than that measured by TEM at a comparable damage rate, which is presumably due to the large surface sink effect[120] associated with the short distance (50 nm) between the diffusion marker layer and the free surface of the specimen. The authors also deduced that the irradiation-induced sink density was independent of irradiation flux, which is in contrast to TEM observations and simple rate theory arguments. An accurate assessment of the sink strength is essential, since the freely migrating defect fractions in their analysis were deduced from the fitting of a parameter proportional to the square of the sink strength Low-energy ions with a mean range comparable to the depth of the marker layer have been utilized in the RED studies reported to date. The possible effect of these injected ions on enhancing interstitial clustering and vacancy annihilation (and thereby suppressing the migrating defect fraction) should be investigated.

Several other experimental techniques have also been used for obtaining estimates of the migrating fractions of vacancies and interstitials, $MDF_{i,v}$. Dislocation pinning measurements were analyzed to deduce that the fraction of migrating interstitials produced during 0.9 to 23 MeV neutron irradiation of copper at 330 K was ~2% of the 1 MeV electron value, i.e. MDF_i (330 K) ≅1%.[113,114] However, the authors did not demonstrate in convincing fashion that the observed pinning was due solely to freely migrating interstitials (as opposed to interstitials plus vacancies), as assumed in their data analysis. Hence, the quantitative value of their derived migrating defect fraction must be viewed with caution. Several researchers have estimated migrating defect fractions at temperatures below annealing Stage V from irradiation-induced ordering reactions, using strain relaxation[115] or electrical resistivity[81,82] measurements. Huang and coworkers[82] determined that the fraction of freely migrating vacancies in copper during neutron irradiation at 414 K was 55% of the defect production rate at 4 K, i.e. IDF_v (414 K) 51.5%. Kirk and Blewitt[81] derived a similar value for reactor irradiated copper of IDF_v (423 K) 52%. The study by Beretz et al.[115] is commendable because their analysis considered both the transient buildup of radiation-produced sinks and their thermal instability at elevated temperatures. Their analysis also attempted to separately determine the vacancy and interstitial components of the available defect fraction. They concluded that the migrating fractions of vacancies and interstitials at 310 to 410 K in a neutron-irradiated Ag-Zn alloy were both ~10%. Huang, Guinan and Hahn[83] recently employed measurements of the Curie temperature of a Ni-Si alloy to estimate the fraction of available migrating interstitials during neutron irradiation at 623 K. They deduced that the freely migrating interstitial fraction was 6 to 7% of the corresponding value for electron irradiation. This implies that MDF_i ~2.6%, assuming that 40% of the defects in electron-irradiated nickel escape correlated recombination at elevated temperatures (ref. [71], see Section 2.3).

The advantages of experimental techniques such as order-disorder or Curie temperature measurements tor determining fundamental defect production parameters are: (1) the measurements are sensitive Io a specific type of point defect (vacancy vs. interstitial), and (2) the measurements are sensitive to defect migration over distances that are comparable to the size of a displacement cascade. Measurements that require defect migration over large distances become increasingly susceptible to large errors in the data analysis due to uncertainties in the precise magnitude of point defect loss terms at sinks and via recombination.

Finally, it must be kept in mind that the values of the various defect production parameters will depend on the metal being irradiated. Most of the defect production measurements available in the literature have been performed on two face-centered cubic metals, Cu and Ni. The results obtained from these two metals may not be applicable to other metals with different atomic mass, crystal structure, or physical properties. Even the results obtained on copper and nickel suggest a difference in the cascade quench behavior of these similar-mass materials, with Ni having a higher calculated quenched cascade defect fraction and less atomic mixing.[5,6,20] This has been attributed to a difference in the electronic thermal conductivity of these two metals.[124]

4. CONCLUSIONS

The number of disolacements calculated according to models such as NRT does not directly correlate with the number of residual defects as the PKA energy is increased from values producing isolated Frenkel pairs to values producing dense displacement cascades. There is no unique damage parameter that adequately describes all of the various physical processes associated with cascade damage. It is proposed that three fundamental damage parameters should be used to characterize radiation effects under cascade damage conditions: the displacement mixing factor (DMF). the clustered defect fractions ($CDF_{i,v}$), and the isolated point defect fractions ($IDF_{i,v}$), all of which are defined in terms of the NRT calculated displacements. There is substantial evidence from experimental and computer simulation studies that the DMF increases with increasing temperature, whereas the residual defect fractions decrease with increasing temperature.

Experimental results and MD calculations suggest that the fraction of defects (relative to the NRT calculated displacements) surviving the cascade quench and subsequent correlated recombination tor energetic cascades in copper decreases from SDF −0.3 at 4 K to SDF −0.1 at 300 K. Measurements at elevated temperatures are in general agreement that the fraction of migrating defects is 1 to 10% of the calculated NRT displacements. Unfortunately, the quantitative values reported in these studies are not reliable due to shortcomings in the rate theory models used to deduce the defect parameters from the experimental data. Void swelling results indicate that the lower bound for the fraction of migrating vacancies in neutron-irradiated copper at temperatures near 400°C is MDF_v −5%. New single-variable experimental studies are needed to investigate the fluence dependence of defect accumulation through the transient and steady-state dose regimes at various temperatures and fluxes.

Consideration must be given to the basic features of cascade damage in both the design of defect production experiments and in the analysis of experimental data aimed at determining specific defect tractions. Only a fraction of the displacement damage induced by an energetic cascade escapes correlated annihilation within the cascade and is available for inducing microstructural change in the matrix. The determination of defect production parameters from the experimental data must include an explicit treatment of intracascade recombination and clustering of interstitials and vacancies, and the thermal stability and mobility of these clusters. Clearly, an analysis based on conventional rate theory and the assumption of homogeneous production of isolated vacancies and interstitials at an equal rate is not appropriate for this purpose.

ACKNOWLEDGEMENTS

The authors would like to thank H.L. Heinisch and R.E. Stoller for their stimulating comments on the general topic of displacement damage and defect production. This work was performed while one of the authors (S. J. Zinkle) was a visiting scientist at Risø National Laboratory, and the hospitality displayed during this visit is gratefully acknowledged. This work was also partially supported by the Office of Fusion Energy, U.S. Department of Energy, under contract DE-AC05-84OR21400 with Martin Marietta Energy Systems, Inc.

REFERENCES

1. G.H. Kinchin and R.S. Pease, Rep. Prog. Phys. 18 (1955) 1.
2. W.S. Snyder and J. Neufeld, Phys. Rev. 97 (1955) 1636.
3. M.J.Norgett, M.T. Robinson, and I.M. Torrens, Nucl. Engr. Des. 33 (1975) 50.
4. M.T. Robinson and I.M.Torrens, Phys. Rev. B 9 (1974) 5008.
5. T. Diaz de la Rubia, R.S.Averback, H. Hsieh. and R. Benedek, J. Mater. Res. 4 (1989) 579.
6. R.S. Averback. H. Horngming, T. Diaz de la Rubia and R. Benedek, J.Nucl. Mater. 179-181 (1991) 87.
7. A.J.E. Foreman, W.J. Phythian. and C.A. English, Harwell AEA Technology Report AEA-TRS-2031 (1991).
8. J.R. Beeler, Phys. Rev. 150 (1966) 470.
9. R.S. Averback. R. Benedek and K.L. Merkle, Phys. Rev. B 18 (1978) 4156.
10. M.W. Guinan and J.H. Kinney, J. Nucl. Mater. 103&104 (1981) 1319
11. J.H. Kinney, M.W. Guinan and Z.A. Munir. J. Nucl. Mater. 122&123 (1984) 1028.
12. D.G. Doran, Nucl. Eng. Des. 33 (1975) 55.
13. L.E. Rehn and P.R. Okamoto, Mat.Sci.Forum 15-18 (1987) 985.
14. L.E. Rehn, J. Nucl. Mater. 174 (1990) 144.
15. L.K. Mansur and K. Farrell, J. Nucl. Mater. 170 (1990) 236.
16. C.A. English, W.J. Phythian and A.J.E. Foreman, J. Nucl. Mater. 174 (1990) 135.
17. V. Naundorf and H. Wollenberger, J. Nucl. Mater. 174 (1990) 141.
18. C.H. Woo and B.N. Singh. Phys. Stat. Sol. (b) 159 (1990) 609.
19. C.H. Woo and B.N. Singh. Phil. Mag. A, 65 (1992) 889.
20. T. Diaz de la Rubia and M.W. Guinan, Mat. Sci. Forum 97-99 (1992) 23.
21. H.L. Heinisch, Rad. Eff. Def. Solids 113 (1990) 53.
22. R.S. Averback and D.N. Seidman, Mat. Sci. Forum 15-18 (1967) 963.
23. J.A. Brinkman, J. Appl. Phys. 25 (1954) 961.
24. A. Seeger, in Proc. 2nd UN Conf on Peaceful Uses of Atomic Energy, Geneva, Vol. *6* (United Nations, New York. 1958) p. 250
25. H.L. Heinisch and B.N. Singh, Phil. Mag. A (1992) in press
26. K.L. Merkle, Phys. Stat. Sol. 18 (1966) 73.
27. T. Muroga, K. Kitajima and S. Ishino. S., J. Nucl. Mater. 133-134 (1985) 378.
28. H.L. Heinisch and B.N. Singh. J. Nucl. Mater. 179-181 (1991) 893.
29. H.L. Heinisch, J. Nucl. Mater. 117 (1983) 46.
30. M. Alurralde, A. Caro and M. Victoria, J. Nucl. Mater. 183 (1991) 33.
31. B. von Guerard and J. Peisl, J. Appl. Cryst. 8 (1975) 161.
32. R. Rauch, J. Peisl, A. Schmalzbauer and G. Wallner. J. Nucl. Mater. 168 (1989) 101.
33. R. Rauch, J. Peisl, A. Schmalzbauer and G. Wallner. J. Phys: Condens. Matter 2 (1990) 9009.
34. R.S. Averback, K.L. Merkle and L.J. Thompson, Rad. Effects 51 (1980) 91.
35. M.A. Kirk, I.M. Robertson. M.L. Jenkins, C.A. English, T.J. Black and J.S. Vetrano, J.S.. J. Nucl.Mater. 149 (1987) p. 21.
36. T. Diaz de la Rubia, R.S. Averback, R. Benedek. and I.M. Robertson, Rad. Eff. Def. Solids 113 (1990) 39.
37. H. Wiedersich, Nucl. Instr. Meth. B 7/8 (1985) 1.
38. M.P. Macht, A. Muller, V. Naundorf and H. Wollenberger, Nucl. Instr. Meth. Phys. Res. B. 16 (1986) 146.
39. A. Muller, V. Naundorf and M-P Macht. J. Appl. Phys. 64 (1988) 3445.
40. R.H. Zee, M.W. Guinan and G.L. Kulcinski. J. Nucl. Mater 114 (1983) 190.
41. F. Seitz and J.S. Koehler, Solid State Physics 2 (1956) 327.
42. C.A. English and M.L. Jenkins, Mat. Sci. Forum 15-18 (1987) 1003.
43. H. Hsieh. T. Diaz de la Rubia. R.S. Averback, and R. Benedek, Phys. Rev. B 40 (1989) 9986.
44. T. Diaz de la Rubia and W. Phythian. J. Nucl. Mater. 191-194 (1992) in press
45. P. Jung. B.R. Nielsen. H.H. Andersen, J.F. Bak. H. Knudsen. R.R. Coltman, Jr., C.E. Klabunde. J.H. Williams, M.W. Guinan and C.E. Violet, ASTM STP 782 Eds. H.R. Brager and J.S. Perrin (ASTM, Philadelphia, 1982) p. 963
46. P. Jung. J. Nucl. Mater. 117 (1983) 70.
47. T. Iwata and A. Iwase. Rad. Eff. Def. Solids 113 (1990) 135.
48. G.W. Iseler, H.I. Dawson. A.S. Mehner and J.W. Kauffmann, Phys. Rev. 146 (1966) 468.
49. R.R. Coltman, Jr., C.E. Klabunde and J.K. Redman, Phys. Rev. 156 (1967) 715.
50. R.R. Coltman, Jr.. C.E. Klabunde and J.M. Williams, J. Nuci. Mater. 99 (1981) 284.
51. C.E. Klabunde and R.R. Coltman. Jr., J. Nucl. Mater. 108&109 (1982) 183.

52. M.W. Guinan and J.H. Kinney, J. Nucl. Mater. 108&109 (1982)95.
53. R.C. Birtcher and T.H. Blewitt, J. Nucl. Mater. 98 (1981)63.
54. J.O. Schiffgens and R.D. Bourquin, J.Nucl.Mater. 69&70(1978) 790.
55. W.E. King and R. Benedek, R.. J. Nucl. Mater. 117 (1983)26.
56. A.J.E. Foreman, C.A. English and W.J. Phythian, Harwell AEA Technology Report AEA-TRS-2028 (1991).
57. P. Jung, Phys. Rev. B 23 (1981)664.
58. J.W. Corbett, R.B. Smith and R.M. Walker, Phys. Rev. 114 (1959)1460.
59. R.M. Walker, in Radiation Damage in Solids, Proc. Int. School of Physics 'Enrico Fermi' XVIII Course, D.S. Billington, Ed. (Academic Press, New York, 1962)p. 594
60. R.R. Coltman, Jr., C.E. Klabunde, D.L. McDonald and J.K. Redman, J. Appl. Phys. 33 (1962)3509.
61. M.W. Thompson, Defects and Radiation Damage in Metals (Cambridge Univ. Press, London, 1969)
62. T.H. Blewitt, in Radiation Damage in Solids, D.S. Billington. Ed. (Academic Press, New York. 1962) p. 630
63. J.A. Horak and T.H. Blewitt, J. Nucl. Mater. 49 (1973) 161.
64. M. Nakagawa, K. Boening, P. Rosner and G. Vogl, Phys. Rev. B 16 (1977)5285.
65. M. Nakagawa, J. Nucl. Mater. 108&109 (1982) 194.
66. M.W. Guinan, J.H. Kinney and R.A. Van Konynenburg. J.Nucl.Mater. 133 & 134 (1985)357.
67. M. Lehmann, G. Saemann-Ischenko, H. Adrian, J. Bieger, and P. Muller, Rad. Eff. 46 (1980) 227.
68. R. Lennartz, F. Dworschak. and H. Wollenberger, H., J.Phys.F: Metal Phys. 7 (1977)2011.
69. G. Roth, H. Wollenberger. Chr. Zeckau and K. Lucke. Rad. Effects, 26, (1975) 141.
70. D.E. Becker, F. Dworschak and H. Wollenberger, Phys. Stat. Sol. (b) 54 (1972)455.
71. T. Muroga, S. Ishino. P.R. Okamoto, and H. Wiedersich, J. Nucl. Mater. 122&123 (1984)634.
72. U. Theis and H. Wollenberger, J. Nucl. Mater. 88 (1980) 121.
73. S.J. Zinkle. J. Nucl. Mater. 155-157 (1988) 1201.
74. C.A. English, A.J.E. Foreman, W.J. Phythian. D.J. Bacon, and M.L. Jenkins in Materials Modeling: From Theory to Technology. Eds. C.A. English, J.R. Matthews. H. Rauh, A.M. Stoneham and R. Thepford (Inst. of Physics Publ., Bristol, 1992)p. 105
75. M. Kiritani, Mat. Sci. Forum 15-18 (1987)1023.
76. N. Sekimura and S. Ishino. J. Nucl. Mater. 155-157 (1988) 1217; Y. Kanzaki, N. Sekimura and S. Ishino. J. Nucl. Mater. 191-194 (1992)in press.
77. R.L. Simons, J. Nucl. Mater. 141-143 (1986)665.
78. C.H. Woo, B.N. Singh and H.L. Heinisch, H.L.. J. Nucl. Mater. 174 (1990) 190.
79. M. Kiritani, T. Yoshiie, S. Kojima, Y. Satoh and K. Hamada, J. Nucl. Mater. 174 (1990)327.
80. Y. Shimomura. H. Fukushima and M.W. Guinan. J. Nucl. Mater. 174 (1990)210.
81. M.A. Kirk and T.H. Blewitt. Met. Trans. A 9 (1978)1729
82. J.S. Huang, M.W. Guinan and M.A. Kirk, M.A., J. Nucl. Mater. 155-157 (1988) 1084.
83. J.S. Huang, M.W. Guinan and P.A. Hahn. J. Nucl. Mater. 155-157 (1988)1227.
84. S.J. Zinkle. K. Farrell and H. Kanazawa. J. Nucl. Mater. 179-181 (1991) 994.
85. C.A. English, B.L. Eyre and J. Summers, Phil. Mag. 34 (1976) 503.
86. R.M.J. Cotterill and M.W. Jones, Proc. Int. Conf. Cryst. Latt. Def.. J. Phys. Soc. Japan 18, Suppl. III (1963)158.
87. S. Ishino. N. Sekimura, K. Hirooka. and T. Muroga, J. Nucl. Mater. 341-143 (1986)776.
88. S. Ishino and N. Sekimura, J. Nucl. Mater. 174 (1990)158.
89. Y. Shimomura. H. Fukushima, M. Kami. T. Yoshiie, H. Yoshida, and M. Kiritani, J. Nucl. Mater. 141-143 (1986) p. 846.
90. N.Q. Lam, N.V. Doan and L. Dagens, J. Phys. F. 5 (1985)799.
91. N.Q. Lam and L. Dagens, J. Phys. F. 16 (1986) 1373.
92. B.N. Singh, C.H. Woo and A.J.E. Foreman, Mat. Sci. Forum 97-99 (1992)75.
93. B.N. Singh and A.J.E. Foreman, Phil. Mag. A 66 (1992)in press
94. M.J. Sabochick and S. Yip, J. Phys. F: Metal Phys. 18 (1988)1689.
95. H.R. Schober and R. Zeller. J. Nucl. Mater. 69&70 (1978)341.
96. R. Bullough, B.L. Eyre and K. Krishan, Proc. Roy. Soc. A346 (1975) 81.
97. R.E. Stoller and G.R. Odette. in Radiation Induced Changes in Microstructure, ASTM STP 955, Eds. F.A. Gamer, N.H. Packan and A.S. Kumar (ASTM, Philadelphia, 1987)p. 371.
98. H. Trinkaus, B.N. Singh and A.J.E. Foreman, J. Nucl. Mater. in press.

99. I.M. Robertson, J.S. Vetrano, M.A. Kirk and M.L. Jenkins, Phil. Mag. A 63 (1991) 299.
100. S.J. Zinkle, J. Phys. F.: Metal Phys. 18 (1988) 377.
101. B.C. Larson, J. Appl. Crystallogr. 8 (1975)150.
102. P. Ehrhart, B. Schonfeld and K. Sonnenberg, Point Defects and Defect Interactions in Metals, Ed. J. Takamura et al. (Univ. Tokyo Press, Tokyo, 1982) p. 687.
103. O.K. Harling, N.J. Grant, G. Kohse. M. Ames, T-S Lee and L.W. Hobbs, J. Mater. Res. 2 (1987)568.
104. R.J. Livak, T.G. Zocco and L.W. Hobbs, J. Nucl. Mater. 144 (1987)121.
105. F.A. Garner, H.R. Brager and K.R. Anderson, J. Nucl. Mater. 179-181 (1991) 250.
106. K. Yamakawa, I. Mukouda, and Y. Shimomura, J. Nucl. Mater. 191-194 (1992)in press
107. L.E. Rehn. P.R. Okamoto and R.S. Averback. Phys. Rev. B 30 (1984)3073.
108. A.D. Marwick, R.C. Piller and M.E. Horton, in Dimensional Stability and Mechanical Behavior of Irradiated Metals and Alloys (British Nucl. Energy Soc., London, 1984) p. 111
109. T. Hashimoto. L.E. Rehn and P.R. Okamoto, Phys. Rev. B 38 (1988)12868.
110. S.M. Murphyand J.M. Perks, J. Nucl. Mater. 171 (1990) 360.
111. V. Naundorf, M.P. Macht and H. Wolienberger, J. Nucl. Mater. 186 (1992)227.
112. P. Jung. M.I. Ansari, H. Klein and D. Meertens, J. Nucl. Mater. 148 (1987)148.
113. J.A. Goldstone, D.M. Parkin and H.M. Simpson. J. Appl. Phys. 51 (1980) 3690.
114. J.A. Goldstone, D.M. Parkin and H.M. Simpson. J. Appl. Phys. 53 (1982)4189.
115. D. Beretz. M. Halbwachs and J. Hillairet. Rad. Effects 62 (1982)219.
116. J.L. Brimhall and H.E. Kissinger. Rad. Effects 15 (1972)259.
117. C.A. English, B.L. Eyreand J.W. Muncie. Phil. Mag. A 56 (1987) 453.
118. B.N. Singh, T. Leffers. and A. Horsewell. Phil. Mag. A 53 (1986) 233.
119. S.J. Zinkle and E.H. Lee, Met. Trans. A 21 (1990) 1037.
120. R.C. Piller and A.D. Marwick, Dimensional Stability and Mechanical Behaviour of Irradiated Metals and Alloys (British Nuclear Energy Society, London, 1984) p. 25.
121. P.R. Okamoto, L.E. Rehn. and R.S. Averback, J. Nucl. Mater. 133&134 (1985)373.
122. H. Wiedersich, Mat. Sci. Forum 97-99 (1992)59.
123. L.E. Rehn and H. Wiedersich, Mat. Sci. Forum 97-99 (1992)43.
124. C.P. Flynn and R.S. Averback. Phys. Rev. B 38 (1988)7118.

THE RELATIONSHIP BETWEEN THE COLLISIONAL PHASE DEFECT DISTRIBUTION AND CASCADE COLLAPSE EFFICIENCY

K. Morishita, (U. Tokyo), H. L. Heinisch (Pacific Northwest Laboratory)[a] and S. Ishino, (U. Tokyo)

OBJECTIVE

The objective of this work is to determine the spectral dependence of defect production and microstructure evolution for the development of fission-fusion correlations.

SUMMARY

Cascades produced in binary collision simulations of ion-irradiation experiments were analyzed to determine if a correlation exists between the defect distribution in the collisional phase and the number of visible clusters produced directly in cascades (caused by the so-called "collapse" of the cascade defects). The densities of the vacancy distributions in the simulated cascades were compared to the measured cascade collapse efficiencies to obtain the minimum or "critical" vacancy densities required for collapse. The critical densities are independent of the cascade energy for self-ions and exhibit differences with ion mass that are consistent with the cascade energy dissipation characteristics.

PROGRESS AND STATUS

Introduction

Many features of the primary damage state of a displacement cascade are set forth during the collisional phase of the cascade, including those that impact the production of defects that contribute to microstructural changes. The collisional phase begins with the first collision of the irradiating projectile, and it ends when no atom has enough energy to create another stable displaced atom. During the collisional phase, which usually lasts a few tenths of a picosecond, the cascade structure -- the number, size, energy density and spacing of subcascades -- is established. Since the collisional phase consists of relatively high energy atomic collisions, it is well-described using the binary collision approximation (BCA).

The BCA is the basis of the computer simulation code MARLOWE, which was employed by Heinisch and Singh[2] to determine the structure of high energy cascades caused by primary recoil atoms (PKAs) of up to 1 MeV in a number of pure metals. In that work the number and spacing of subcascades was determined as a function of atomic number, atomic mass and crystal structure. The analysis relied heavily on the concept of defect density to define and identify subcascades. The implicit assumption was made that the spatial density of vacant sites at the end of the collisional phase is directly related to the deposited energy density, and that regions of sufficiently high vacancy density correspond to areas where visible clusters are produced. Comparisons were made between the simulation results and transmission electron microscope (TEM) images of 14 MeV neutron-irradiated metal foils. From these comparisons it was concluded that multiple TEM-visible clusters could be associated with a single subcascade. The number of visible clusters per subcascade was found to increase with atomic mass.

Many experiments involving ion-irradiation of thin metal foils have reported the number of TEM-visible clusters produced per incident ion[3-8]. It has been assumed that the vacancy-rich cores of cascades collapse to form visible clusters or loops with an efficiency that depends on the masses of the incident ion and the target atoms, as well as the ion energy. The quoted efficiency factors tell only part of the story, because some cascades might contain multiple subcascades, and some subcascades might contain multiple clusters.

The ion-irradiation experiments offer an opportunity to compare BCA simulations of high energy cascades with TEM observations for heavy-ion irradiations, including self-ions. The present study was undertaken to determine if the vacancy density (hence, energy density) of subcascades in the collisional phase correlates with the production of TEM-visible defect clusters. This includes the possibility that locally dense regions within a single subcascade during the collisional phase correlate with the production of multiple visible clusters. We want to determine if a "critical density" for collapse can be identified, and if so, to study the effects of relative projectile mass on collapse efficiency.

Procedure

Heavy ion and self-ion irradiations in Ag, Cu, Au, Mo and W were simulated using MARLOWE. The irradiations and the measured defect yields are listed in Table 1. The MARLOWE parameter settings were the same as those used in Ref. 2, except that the problem geometry was set up to match the irradiation conditions of

---

'Pacific Northwest laboratory is operated for the U.S. Department of Energy by Battelle Memorial Institute under Contract DE-AC06-76RLO 1830.

the experiments. One hundred ions were followed for each ion-target system, and for each set of incident ions a beam divergence of 5-20 degrees was assumed depending on how precisely the target geometry was described by the experimenter.

Table 1. Experimental Defect Yields and Calculated Critical Densities (CD) for Ion-irradiated Metal Foils.

ION (keV)	TARGET	DEFECT YIELD	CD	REFERENCE
30 Cu	Cu	0.50	1.4	Stathopoulos, 3
90 Cu	Cu	1.1	1.4	Stathopoulos, 4
30 W	Cu	0.60	1.7	Stathopoulos, 3
90 W	Cu	0.95	1.9	Stathopoulos; 4
30 Ag	Ag	0.55	1.6	Schober, 5
50 Ag	Ag	0.95	1.6	Schober, 5
70 Au	Au	1.0	1.9	Merkle, 6
60 Mo	Mo	0.12	3.0	English, 7
60 Sb	Mo	0.15	3.2	English, 7
60 Xe	Mo	0.20	2.6	English, 7
120 Sb	Mo	0.29	2.6	English, 7
180 Sb	Mo	0.35	2.7	English, 7
60 Au	W	0.1	4.3	Hausermann, 8

For each cascade the regions of high vacancy concentration were identified using a modified version of the subcascade identification scheme described in Ref. 2. By simply using different parameter settings, it was possible to identify multiple high density regions (HDRs) within single subcascades. (The irradiations of 90 keV ions on Cu and 180 keV ions on Mo are the only cases where the production of more than one subcascade per cascade is expected to occur.) The density of defects in a HDR is defined as the occupation ratio of vacant sites to lattice sites in a spherical volume. The vacancy densities of the HDRs for 100 simulated ions are distributed over a range of values.

The calculated HDR densities were compared with the collapse efficiencies measured in the experiments. It was assumed that the HDRs of higher density have a higher probability of collapsing. The distribution of the HDR density values for a set of 100 ions is schematically represented in Fig. 1, where the method of determining the critical vacancy density for cascade collapse is illustrated. The experimental defect yield values were converted from a "per ion" basis to a "per HDR" basis, then compared to the distributions. The area under the distribution curve representing the experimental yield fraction of HDRs with the highest densities determines the critical density.

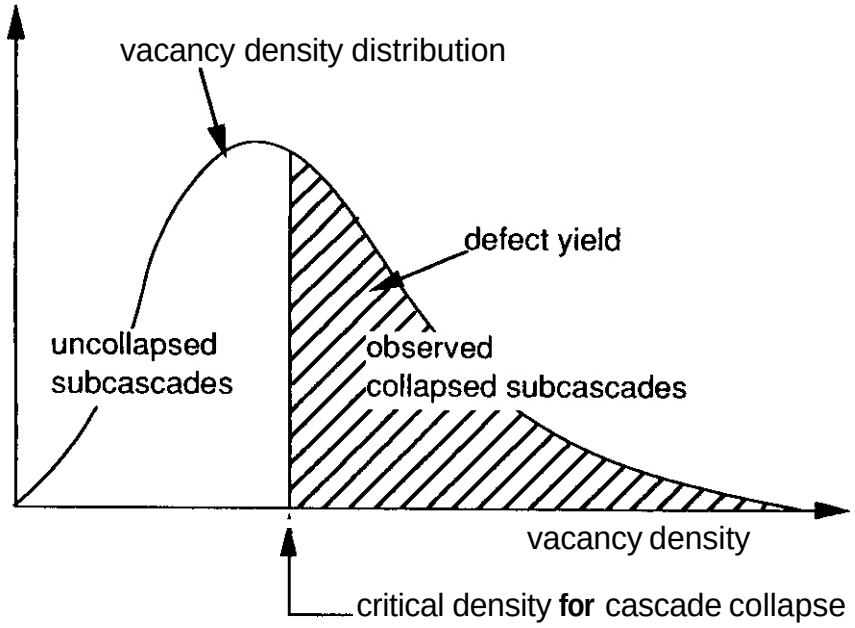

Figure 1. A schematic representation of the distribution of vacancy densities of high density regions in cascades. The area under the curve to the right of the vertical line represents the clusters observed by TEM of ion-irradiated thin foils. The vertical line thus indicates the critical density for production of a visible cluster.

Results

Figure 2 shows the density distributions for the fcc metals list in Table 1. The vertical lines indicate the critical vacancy density values, i.e. the density value above which an HDR is assumed to result in a visible cluster or loop. The values of calculated critical density for each irradiation are given in Table 1.

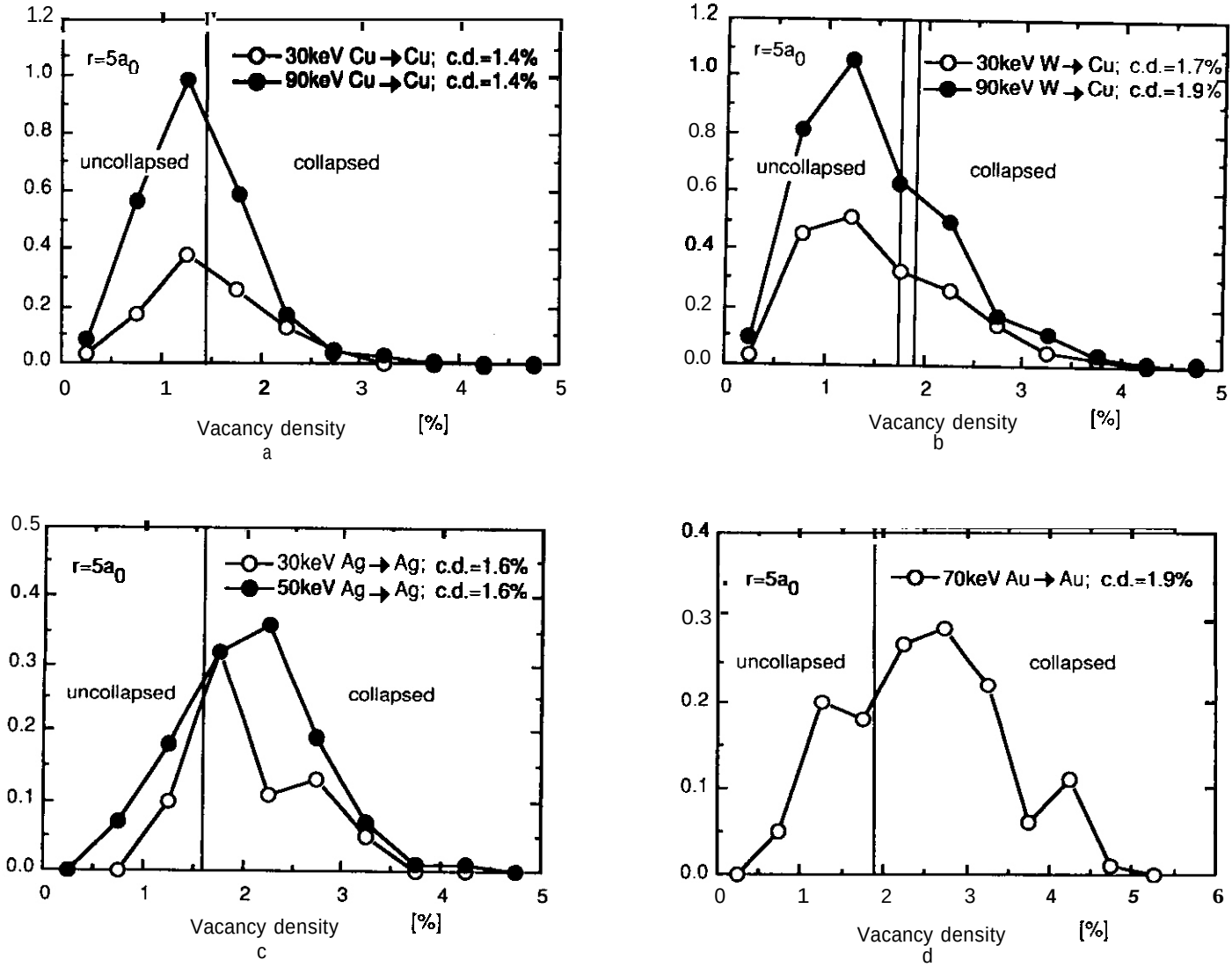

Figure 2. Distributions of vacancy densities in ion-irradiation simulations of a) 30 keV and 90 keV self-ions on Cu, b) 30 keV and 90 keV W-ions on Cu, c) 30 keV and 50 keV self-ions on Ag, and d) 70 keV self-ions on Au. In each case 100 ions were simulated. The vertical lines indicate the critical density values. The y-axis has normalized values.

In the fcc metals the critical densities are independent of self-ion energy. There is a tendency toward increasing critical density with increasing target mass and, in Cu, with increasing ion mass.

The density distributions for the bcc metals are shown in Figure 3. In Mo the variation among relatively similar values shows no clear pattern. However, the density distribution for 60 keV Sb ions has a bimodal distribution that is unlike that of the other Mo results, and it may well be due to statistical fluctuation. If the hump at higher densities is reduced, the critical density will be reduced, and the critical densities in the Sb-ion irradiations will be more nearly independent of ion energy. However, the critical densities for Xe and Sb ions are smaller relative to that for self-ions, which is contrary to the effect of ion mass in Cu. Given the relatively small sample size of 100 ions for each case, perhaps it is best concluded that the critical vacancy density for collapse is about the same in all the irradiations of Mo. The critical density for Au ions on W is considerably higher than that for Mo.

Discussion

It is not surprising that the critical density is independent of self-ion energy in Cu. It is well-documented that cascades do not change their nature with increasing energy. Both point defect production and subcascade production increase linearly with damage energy[9]. It is at first surprising that the critical densities are higher for W-ion irradiation. If the cascades with 1.4% density collapse in self-ion irradiations, why do they not collapse when produced by W ions? Examination of the cascade aspect ratios shows that cascades produced by W ions have somewhat more elongated shape on average. Thus, they

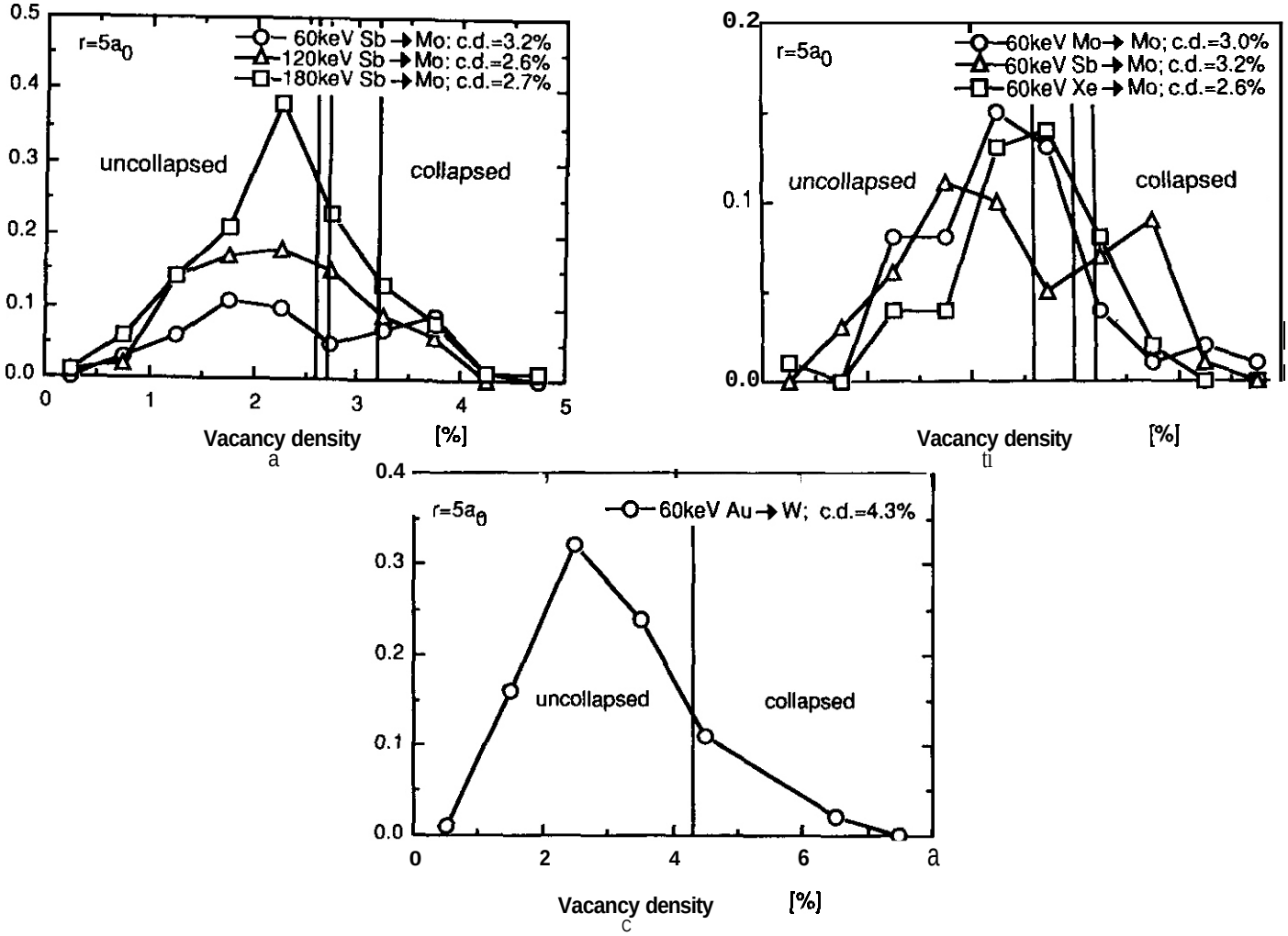

Figure 3. Distributions of vacancy densities in ion-irradiation simulations of a) 60 keV, 120 keV and 180 keV Sh-ions on Mo, b) 60 keV Mo-, Sh- and Xe-ions on Mo, and c) 60 keV Au-ions on W. In each case 100 ions were simulated. The vertical lines indicate the critical density values. The y-axis has normalized values.

may cool off more rapidly than the self-ion cascades, requiring a higher initial density of defects to achieve collapse.

The increase in critical density with increasing target mass in the fcc metals can also be explained by energy dissipation arguments. Only the 90 keV Cu self-ions produce multiple subcascades[2]. In all other cases a single spike is produced, and in Ag and Au these spikes are well below the threshold energy for production of subcascades (the 30 keV Cu self-ion has about three times the reduced energy of the 30 keV Ag self-ion or the 70 keV Au self-ion). The cascades in higher Z elements tend to have more compact cascades with higher energy densities, as illustrated in Figs. 2a, c and d. Having a higher surface to volume ratio, the smaller cascades cool off more rapidly, and a higher critical density is required for collapse (even though a larger total fraction of all HDRs collapse) in Au and Ag than in Cu.

In Mo there is not much variation of the ion masses, and the critical densities are expected to be independent of the Sb ion energy. Thus, one expects all values of the critical density to be about the same in Mo, which they are (within the statistical fluctuations mentioned above).

The critical density values are higher for the bcc metals than the fcc metals. It may not be appropriate to make this comparison because of geometrical factors caused by the differences in crystal structure. However, using the energy dissipation arguments again, one might expect that higher critical density values are necessary for Mo and W because of their much higher melting points (e.g. Cu, 1356 K; W 3683 K). In molecular dynamics (MD) simulations of cascades by Diaz de la Rubia et al.[19] it was shown that the resolidification rates of molten zones in the cascade cores were significantly higher in the metals with higher melting points.

It appears that there is a good correlation between the defect configuration in the collisional phase and the measured efficiency of cascade collapse to TEM-visible clusters. However, one must consider some caveats. The experiments were performed at room temperature (at least), where defects have considerable mobility in some of these systems. Thus, it may be possible that visible clusters nucleate and grow in numbers and locations other than those predicted by the collisional phase distribution of defects. On the other hand, there is a high probability that in the regions of highest energy, stable clusters form directly in the cascades, as observed in MD simulations". Unfortunately, there are not enough MD simulations at high enough energies to verify the direct production of TEM-visible clusters.

The experimental measurements used for determination of the critical densities were not all made at the same time by the same experimenters. In particular, the ability to resolve small clusters varies among observers, and even varies over the years for the same observer. The uncertainties in the measured efficiencies due to this are very difficult to assess. The trends discussed above should be considered in light of this situation.

CONCLUSIONS

The critical densities are independent of the cascade energy for self-ions, and they exhibit differences with ion mass that are consistent with the cascade energy dissipation characteristics. This is good evidence that the density of defects (hence, the density of deposited energy) in the collisional phase is an indicator of the ability to produce a visible cluster or loop. With proper calibration to experimental results and details from MO simulations, binary collision simulations can be a very useful tool for predicting defect production and for interpreting experiments involving high energy cascades.

REFERENCES

1. M. T. Robinson and I. M. Torrens, Phvs. Rev. 8 9, 5008 (1974)

2. H. L. Heinisch and 8. N. Singh, Phil. Mag. in press (1992).

3. A. Y. Stathopaulos, Phil. Mag. A 44, 285 (1981)

4. A. Y. Stathopoulos and C. A. English, J. Nucl. Mater. **108 & 109,** 69 (1985).

5. T. Schober, Phvs. Stat. Sol. (a) 1, 307 (1970).

6. K. L. Merkle, L. R. Singer and J. R. Wrobel, Appl. Phvs. Lett. **17,** 6 (1970).

7. C. A. English and M. L. Jenkins, Mater. Sci. Forum 15-18, 1008 (1987).

8. F. Haussermann, Phil. Mag. 25, 583 (1972).

9. H. L. Heinisch, J. Nucl. Mater. **117,** *46* (1983).

10. T. Diar de la Rubia, R. S. Averback, H. Hsieh and R. Benedek, J. Mater. Res. *4,* 579 (1989)

11. T. Diar de la Rubia and M. W. Guinan, Phvs. Rev Lett. 66 2766 (1991).

Effects of Stress on Microstructural Evolution During Irradiation - D. S. Gelles, Pacific Northwest Laboratory'

OBJECTIVE

The purpose of this work is to summarize the available literature on the subject of microstructural response during irradiation creep to identify areas where further work is needed. This work was presented at the International Conference on Evolution of Microstructure in Metals During Irradiation.

SUMMARY

Many theories have been postulated to describe irradiation creep but few have been supported with microstructural evidence. The purpose of this paper is to review microstructural studies of the effects of stress during irradiation in order to assess the validity of the available irradiation creep theories. Microstructural studies based on high voltage electron, ion, proton and neutron irradiation will be described, with major emphasis placed on interpreting behavior demonstrated in austenitic steels. Special attention will be given to work on fast neutron irradiated Nimonic PE16, a precipitation strengthened superalloy.

PROGRESS *AND STATUS*

Introduction

The effects of stress on microstructure during irradiation is a fitting topic in a conference on evolution of microstructure in metals during irradiation because an understanding of microstructural development due to irradiation has proven to be a valuable tool to predict behavior and optimize materials for irradiation environments. Due to the large financial investment required for reactor construction, and the resultant need for cost-effective design optimization, it is practical to invest a significant effort in microstructural examination and interpretation. However, application of materials in irradiation environments requires not only an understanding of the effects of irradiation on microstructure, but also an understanding of how stress affects that microstructural development. One of the more extensive bodies of literature on effects of irradiation on materials is in the field of irradiation creep.[1,2] A great many theories have been posed to explain irradiation creep response, and yet relatively few efforts have been directed toward understanding the effects of stress on microstructural development during irradiation.

Studies of the effects of stress on microstructure during irradiation are difficult to perform due to a lack of specimen availability. In general, microstructural evolution under stress must be a major experimental objective rather than a postirradiation experiment because the tendency is to reirradiate specimens to higher doses, rather than to perform destructive examinations. Therefore, most microstructural studies of irradiation creep are based on electron and ion irradiation experiments rather than on neutron irradiated material. However, the author has been fortunate to have had the opportunity to examine several specimens that were neutron irradiated under stress to a relatively low dose and then removed for destructive examination. This review will therefore report on microstructural studies of irradiation creep experiments using light ions and electrons, but most of the information will be based on the author's experience. Cubic metal systems will be emphasized and systems such as zirconium alloys (where growth is commonly observed) will be ignored. Also, experiments based on internal stresses due to precipitation, etc. (but involving more complex stress states) will be ignored. Wherever possible, discussion will include the experimental techniques employed.

Irradiation *creep processes* reflected in microstructure

Specimen shape change in response to applied stress during irradiation can occur by a rearrangement of individual grains, by a change in grain shape, or by a combination of these two. Furthermore, change in grain shape can occur by either simple diffusion processes or dislocation evolution.

Diffusion Creep

The earliest example of microstructural evidence for in-reactor creep was probably diffusion creep found in a reactor component made from precipitation strengthened magnesium.[3] Zones denuded of precipitate particles could be identified at low magnification (using optical metallographic techniques) lying parallel to the compressive stress axis. In effect, grains had been elongated to accommodate the stress, by diffusion of the matrix atoms, producing either denuded zones or precipitate pile-ups at grain boundaries. This response was dependent upon the boundary position in relation to the stress axis. Similar response is easily shown during thermal creep. It was later demonstrated, that such denuded zones and pile-ups were,

---

"Pacific Northwest Laboratory is operated for the U.S. Department of Energy by Battelle Memorial Institute under Contract DE-AC06-76RLO 1830.

in effect, consequences of grain boundary sliding.[6] Although it can be argued that this example of diffusion creep does not represent irradiation creep (as the process is probably not significantly accelerated by irradiation), it is included to emphasize that grain boundary sliding may be affected by irradiation. This was demonstrated about a decade later, by showing grain boundary dislocation climb in ion-irradiated gold bicrystals.[7]

Dislocation Evolution in the HVEM

Grain shape change due to dislocation evolution has accounted for the bulk of microstructural studies of effects of stress during irradiation. Earliest work by Buckley and co-workers considered dislocation evolution in stressed ribbon tensile specimens containing a thinned central region during irradiation in a high voltage electron microscope (HVEM).[8] They chose to study the bowing in long perfect dislocation segments in aluminum, and found that the addition of a dispersion of second-phase particles stabilized the structure against surface effects. They observed large fluctuations in the local shear stress (as measured by dislocation bow) as a function of time, even for individual dislocation segments, with no obvious trends toward diminishing local shear stress with increasing displacement dose up to 10 dpa, and no noticeable displacement of the mean local shear stress from zero under external stress sufficient to induce plasticity. It was apparent from their work that elastic strain field perturbations occurred as a result of continually altering spatial distributions of neighboring dislocations. Subsequent experiments, making use of these observations, redefined the experiment to eliminate the applied stress and only considered irradiation induced motion of internal structural defects during observation in the HVEM.[9] Based on observations on a variety of metals and alloys during irradiation at elevated temperature, dislocation movements were of two distinct types: spasmodic, large amplitude jerks corresponding to glide, and relatively slow but progressive unidirectional drifts corresponding to climb. They concluded that irradiation introduces a fluctuating direction and intensity of internal stress derived from the continuously changing separation and elastic interactions between moving dislocations. Irradiation creep rates were therefore directly proportional to the externally applied stress, inversely proportional to the friction stress associated with glide, and usually proportional to swelling rate. Evidence for a climb-glide mechanism for irradiation creep was apparent.

The First Frank Loop Evolution Study

Dislocation evolution studies then shifted to concentrate on Frank loop distributions in austenitic steels following neutron irradiation, starting with the work of Okamoto and Harkness.[10] They examined the Frank loop size distributions in a pressurized tube of annealed 316 stainless steel irradiated with fast neutrons to a moderate dose of 2×10^{21} n/cm^2 ($E > 0.1$ MeV) at 410°C and a hoop stress of 207 MPa. Employing high resolution, dark-field imaging using stacking fault relrods, they were able to show anisotropy in the loop population on the various (111) planes, but the average loop diameter was the same. They concluded that stress-biased loop nucleation was an important mechanism controlling radiation enhanced creep, at least for a dislocation structure composed mainly of faulted interstitial loops.

Other Frank Loop Evolution Studies

These results were followed by a series of papers on loop evolution using neutron,[11,12] helium ion,[13] proton,[14,15] and deuteron[16-18] irradiation in similar materials and electron irradiation in aluminum.[19] Brager and co-workers first examined 20% cold worked 316 stainless steel, comparing microstructural response following irradiation at 450°C to 9×10^{21} n/cm^2 ($E > 0.1$ MeV) for a solid rod in uniaxial tension and for biaxial pressurized tubes, all at stress levels of 138 MPa.[11] They found that the major effect of stress on the uniaxial condition was in Frank loop size as measured in bright-field dislocation contrast images for <110> and <112> crystal directions. Mean loop diameters and maximum loop diameters were found to increase with increasing stress perpendicular to the appropriate (111) plane, loop size was smaller in stressed specimens compared to unstressed specimens, but loop number densities on the different (111) planes could not be correlated with applied stress. Biaxially stressed pressurized tubes differed from the uniaxial condition in both stressed and unstressed cases. In the unstressed case, the mean loop size was 20% smaller, loop number density about a factor of five larger, and the dislocation density about twice that of the unstressed rod. In the stressed case, the density of dislocations and Frank loops was about twice that of the uniaxially stressed sample, and the Frank loop size distribution on the different {111} planes was invariant with the magnitude of the stress normal to the plane of the loop. One additional observation was reported: for a pressurized tube irradiated to 1×10^{21} n/cm^2 at a stress level of 276 MPa, the dislocation density was only slightly higher and mean loop size and density were considerably smaller than at a higher dose. One can therefore conclude that cold worked material responds differently from annealed material, and often in unexpected ways, depending upon fabrication history and stress state.

Brager and co-workers then reported on the microstructures found in a series of both annealed and 20% cold worked 316 stainless steel pressurized tubes irradiated at 500°C to fast neutron fluences ranging from 2.0 to 3.0×10^{22} n/cm^2, ($E > 0.1$ MeV) in order to explore, quantitatively, the stress-coupled relationship of swelling and irradiation creep." In this case, dislocation imaging was based on weak-beam, dark-field contrast encompassing both stacking fault relrods and reciprocal lattice spots, and in situations where foils were thin and showed surface contours, the 2½0 technique was employed to differentiate among individual Frank loops on the different (111) planes. They found that for the solution annealed case, void volume increased approximately linearly with hoop stress, and void number density increased quadratically

with hoop stress to 163 MPa, but that mean void size decreased somewhat with increasing hoop stress due to enhanced nucleation of small voids. Also, Frank loop number density varied with increasing stress normal to the (111) plane of the loop, but the effect was obscured at the lowest stress levels. However, loop size was insensitive to stress state and many loops in the stressed specimen were irregular in shape. For the case of 20% cold worked material at a hoop stress of 327 MPa, no voids were observed, but similar dependencies in Frank loop response were found. Frank loop number density varied with increasing stress normal to the (111) plane of the loop, but loop size was insensitive to stress state and many loops were irregular in shape.

In summary, evidence was found for stress enhanced void nucleation, and for a stress dependence on loop nucleation, the latter in agreement with Okamoto and Harkness.[11] It was also noted that Frank loops could be eliminated by self-unfaulting or intersection with other components of the microstructure, and that as total dislocation density increased, both maximum and mean Frank loop diameter decreased independently of the starting condition, solution treatment, or cold work.

Perfect Loop Evolution

Sokursky and Protsenko considered dislocation loop orientation in helium ion bombarded and annealed nickel,[13] but in this case the Burgers vector was of the type $\frac{a}{2}\langle 110\rangle$. In a preliminary experiment, they had noted that helium ion bombardment black spot damage annealed into unfaulted loops on (111) planes but that not all the possible Burgers vectors occurred with equal probability. The sample of annealed pure nickel foil had been irradiated using 70 keV helium ions at a temperature no higher than 100°C to a dose of 10^{16} ions/cm^2. It was then annealed for 5 h at 500°C, which produced loops of 20 to 40 nm diameter. Analysis was performed on a grain near (130) orientation using bright-field dislocation contrast, with stereo pairs taken for most imaging conditions employed, so that the type and sign of the Burgers vectors of dislocation loops as well as the loop habit plane could be determined. The procedure compared images using 200, 002, and 111 dislocation contrast to assign Burgers vectors for each of the prismatic loops present, and confirmed the assignment for each of the Burgers vectors using 113, 111, and 202 contrast to show disappearance. All loops were found to be prismatic of Burgers vector type $\frac{a}{2}\langle 110\rangle$, the habit plane was (111) and the majority of the loops (73%) were either [101], [10$\bar{1}$] or [01$\bar{1}$], with more than half (62%) of the $\frac{a}{2}\langle 110\rangle$ loops lying on (111). The anisotropy in the loop populations was correctly interpreted as an effect of induced stress due to ion bombardment, which was later shown to be a common difficulty with such experiments,[20] and was therefore a consequence of an effect of stress on microstructural evolution.

Loop evolution Under Proton Bombardment

In two papers, Harwell researchers considered irradiation creep response in thin ribbon samples of pure nickel and both solution treated and cold worked 321 stainless steel under 4 MeV proton irradiation and performed postirradiation microstructural examinations.[14,15] They found that for pure nickel bombarded to 0.2-0.4 dpa in the temperature range 450-500°C under stresses in the range 40-100 MPa, the dislocation structure consisted of long segments intersecting and bowing between a dislocation loop population. Most of the loops were unfaulted and many of the line segments appeared to have originated as large loops, but no preferential alignment of loops was evident. In comparison, unstressed specimens bombarded to similar doses at these temperatures did not show such line segments, but did show a larger proportion of sessile (Frank) loops. This was interpreted as demonstration that dislocation slip provided the overriding contribution to strain.

The results on AISI 321 steel[15] were more complex. An annealed specimen tested at 100 MPa and 400°C to a total dose of 0.23 dpa was found to contain a high density (2×10^{16} cm^{-3}) of small (8.5 nm diameter) dislocation loops, most of which were unfaulted and interstitial in character. No continuous dislocation network was observed; nor was any orientation dependence identified. In comparison, 60% cold worked material irradiated to 0.22 dpa at 150 MPa and 500°C contained an extremely complex dislocation structure, and evidence was found of significant strain-induced martensite formation during cold work. Few signs of radiation damage were visible, indicating that the cold working dislocation network was the dominant point defect sink.

The proton irradiations were continued on dilute nickel alloys by Atkins and McElroy and described in two papers published at five-year intervals.[21,22] The first paper showed that dislocation loop distributions were different for pure nickel, commercial-purity nickel, and a Ni-2.5Si alloy following irradiation to 0.2 dpa at 450°C and 50 MPa.[21] In pure nickel, the structure was very inhomogeneous, consisting of complex arrays of fine dislocation loops surrounded by line dislocations between which were regions essentially free of any visible radiation damage. In commercial nickel, loops were homogeneously distributed with some evidence of rafting occurring behind moving line dislocations, resulting in small localized areas with larger and more densely concentrated dislocation loops. In the Ni-Si alloy, significant differences were found between stressed and unstressed conditions, with larger loops (30 nm) found at lower number density (3.0×10^{15} cm^{-3}) in the stressed case than in the unstressed case (12 nm, 5.6×10^{15} cm^{-3}). No loop orientation dependence was discussed.

Loop orientation was analyzed in the later report[22] for the Ni-Si alloy irradiated to 0.2 dpa at 450°C, comparing an unstressed specimen to one deformed at 50 MPa. Analysis was based on $\vec{g}=\pm020$ bright-field Frank loop dislocation images for foils oriented near [101]. Analysis revealed that applied stress

influenced the partitioning of loops on the different (111) planes but did not influence the overall loop density or size. Frank loop density was highest on (111) planes with the highest normal stress. However, the Frank loop distribution anisotropy only accounted for about 25% of the total strain; the remainder, therefore, was attributed to the unexpectedly high density (5-10% of the total population) and large size (2 to 5 times larger) of unfaulted <110> loops. It was noted that unfaulted loops were randomly distributed (in some cases occurring in small colonies as if some cooperative process had contributed to the unfaulting) and that they were more common in stressed material.

Transient Response

Experiments similar to those done at Harwell were performed by Michel and co-workers[16-18] to study the transient creep behavior of cold worked nickel. High purity nickel sheet tensile specimens in a 95% cold worked condition were stressed and simultaneously irradiated with either 22 MeV deuterons or 70 MeV alpha particles at 224°C to doses of 0.01 to 0.04 dpa for stress at levels of 138 to 345 MPa. Changes in microstructure following irradiation creep were reported for several specimen conditions by making comparison with the starting microstructure.[16,17] Prior to irradiation, the cold worked nickel contained slip traces, deformation bands, and dislocation cells with mean diameters in the range of 0.8 to 1.2 μm. The dislocation cell structure was retained after irradiation creep deformation, but a heterogeneous distribution of defect clusters, small dislocation loops, and random dislocations was also found (as indicated using bright-field dislocation contrast). No substantial difference was found between microstructures from deuteron and alpha particle irradiation experiments. Analysis of the nature and alignment of the defects was inconclusive due to the small defect size, but there was evidence that the defects were effective obstacles to dislocation motion. A subsequent series of examinations considered the effect of dose on microstructure,[18] and determined that with increasing dose from 0.002 to 0.02 dpa, defect cluster density rose modestly from 0.82 to 1.4×10^{16} cm^{-3}, mean defect size rose modestly from 3.0 to 4.3 nm, and dislocation density decreased from 6.6×10^{10} cm^{-2}. Most of the change due to irradiation, howevrer, had been achieved by a dose of 0.002 dpa. Michel and co-workers concluded that the microstructure was primarily influenced by the irradiation and not the stress, in view of the decreased dislocation density and relatively unchanged dislocation cell diameter in comparison to the preirradiation microstructure. The observed transient deformation could only be explained by a climb-controlled glide mechanism.

Several years later, Henager and co-workers performed similar deuteron bombardment experiments on pure nickel in order to assess effects of starting microstructure on response.[23,24] Pure nickel in three initial microstructure conditions (85% cold worked, 25% cold worked, and annealed) was irradiated as stressed foil-tensile specimens with 15 or 17 MeV deuterons at 200°C. Stress levels ranged from 65 to 145 MPa, depending on microstructural condition. The cold worked specimens were either pre-crept thermally for 20 h (85%) or annealed for 20 h at 250°C and then pre-crept thermally for 20 h (25%) prior to irradiation creep testing, and then received postirradiation creep deformation for 20 h prior to microstructural examination. Electron microscopy examination using bright-field dislocation contrast revealed a high density (2×10^{15} cm^{-3}) of dislocation loops throughout the material and voids in recrystallized regions of the 85% cold worked material. Also, in the annealed material, clusters of larger loops were found associated with network dislocation segments in thin foils and, in the 25% cold worked condition, the cell structure became partly unknit during irradiation creep. However, the scale of the microstructure was too fine to allow determination of loop Burgers vectors or orientation dependencies. Therefore, microstructural development was similar to that found by Michel and co-workers. However, the authors concluded that a climb-glide mechanism was not able to explain the observed strain rates and total strains measured. A subsequent paper concluded that their results could be explained by a reaction between gliding dislocations and irradiation induced dislocation loops thereby removing the loops and allowing long range dislocation glide.[25]

Later work by Henager and Simonen expanded their technique to ferritic alloys similar to pressure vessel steels in order to study effects of copper and nickel additions on irradiation hardening kinetics.[26] Two alloys one containing 1.1% nickel and one with 0.29% copper, were irradiated as sheet-tensile specimens at 400°C using 14 MeV deuterons to about 0.05 dpa at stress levels of 35 to 45 MPa. The preirradiation heat treatment involved recrystallization of the hot rolled sheet at 700°C (below the austenite phase field) for 2 h, and thermal creep for 12 h to stabilize the thermal creep microstructure. Irradiation under stress lasted 24 h followed by a further 12 h of thermal creep prior to microstructural examination. Microstructural examination using bright-field dislocation contrast revealed dislocation tangles and small dislocation loops, and one of the tested specimens of the alloy containing negligible copper additions and somewhat higher carbon content (0.054 versus 0.032%) showed an unusually high density of fine carbide particles. The additions of copper resulted in a higher density of loops (7.5 verses 2.0×10^{14} cm^{-3}) but a smaller mean loop diameter (1.0 versus 1.9 nm). The results were found to be consistent with a climb-glide creep model.

HVEM Studies of Frank Loop Anisotropy

The HVEM was a very powerful tool for the study of the development of loop anisotropy during irradiation creep. The first report of this kind described the effect of stress on aluminum during electron irradiation.[19] Aluminum single crystals were irradiated with 2 MeV electrons (from room temperature to 130°C) under constant load conditions and at stress levels as high as the yield stress. Frank loops formed on all {111} planes, isotropically if no stress was applied but anisotropically under stress, with the highest populations appearing on the primary slip plane, or the {111} plane with the highest Schmid factor,

and the lowest populations on planes perpendicular to the tensile axis (so that the normal stress was maximized). However, loop sizes for the different loop orientations were unaffected by applied stress. When the loops reached a certain value, unfaulting occurred, and the loops then moved onto other (111) planes and interacted with Frank loops on those planes, reducing the loop density. However, loop nucleation continued, and nucleation was favored on the same planes as before.

During the next decade, the study of effects of stress on microstructural evolution during irradiation concentrated on loop anisotropy in electron irradiation experiments. In France, 316 stainless steel tensile specimens were thinned to perforation and irradiated with 1 MeV electrons at 350 and 450°C in the Toulouse HVEM.[27] Microstructural examination was based on bright-field dislocation contrast imaging, which provides narrow images and good resolution at an operating voltage of 1 MeV. A specimen was first stressed and examined at low beam intensity to provide thermal creep conditions (at observation imaging intensities on the order of 1% of the irradiation flux), and dislocation evolution was found to be typical of slip deformation from dislocation sources. The electron flux was then increased to standard conditions in an illuminated region 2 μm in diameter, and microstructural development was recorded to a dose on the order of 1.3 dpa. The sample width was about 60 μm, so that only about 3% of the width was irradiated (even less of the cross sectional area). Irradiation to 0.3 dpa was found to cause progressive erasure of the slip dislocation structure because small dislocation loops developed. At the same time, dislocations climbed into helices and then coalesced into loops. For doses on the order of 0.35 dpa, loops remained smaller than 50 nm in diameter and were generallv of a faulted character (ie., Frank loops). Therefore, four sets of Frank loops were present and it was pbssible to demonstrate anisotropy in number density, but size distributions for the different orientations were similar.

The anisotropy in the Frank loop populations did tend to correspond to the maximum normal stress; the highest populations corresponded to loop planes with intermediate or maximum normal stress states. (The angle between the tensile axis and the Burgers vector was a minimum.) At a higher dose, unfaulted loops with parallelogram configdration on (111) planes could be identified, and examples of Frank loop unfaulting could be found where an unfaulted $\frac{a}{2}$<110> loop was generated from an $\frac{a}{3}$<111> Frank loop by formation of an $\frac{a}{6}$<211> partial dislocation. However, the unfaulting process was generally very rapid. This response was interpreted to show that the local stress preferentially induces unfaulting of one of the four (111) loops, producing one type of $\frac{a}{2}$<110> Burgers vector. However, it was not possible to quantify defect densities for the six $\frac{a}{2}$<110> Burgers vectors due to the small loop sizes. The size required for loop unfaulting was found to be a function of irradiation dose and irradiation temperature: ~30 nm for 0.3 dpa, but 80-100 nm for 0.7 dpa at 350°C, and ~50 nm for 0.3 dpa at 450°C. Thermal activation appeared to control the unfaulting process.

Following irradiation to doses above 0.5 dpa after most of the Frank loops had unfaulted, a corduroy contrast effect parallel to (111) plane traces could be observed, most prominently under strong contrast conditions. In general, only one corduroy direction was evident, but on occasion a second was clearly visible. No obvious correlation was found between the (111) corduroy direction and the applied stress, and no evidence of glide could be identified. The corduroy effect is thought to result from reactions between perfect loops of two different Burgers vectors parallel to the (111) plane in question, and may have been due to large anisotropies in the perfect dislocation Burgers vector populations.

In Japan, a number of HVEM irradiation creep studies were reported. Jitsukawa and co-workers irradiated pure nickel ribbon tensile specimens under stress at 450°C to about 1 dpa with 1 MeV electrons and examined the dislocation evolution near a central perforation in bright-field dislocation contrast.[28] When loops grew to about 10 nm, they rotated to {110} planes and grew into rhombus-shaped prismatic loops that eventually coalesced into larger loops. In comparison, the Frank loops were retained when no external stress was applied, but on subsequent application of stress after irradiation, the Frank loops unfaulted. No attempt was made to define anisotropy in the loop populations during irradiation creep, but anisotropy was demonstrated following Frank loop unfaulting due to postirradiation deformation. This work was expanded to include cyclic unloading of stressed pure nickel specimens during irradiation in order to better understand effects of stress on Frank loop unfaulting.[29] Loop unfaulting was only observed for loops in a certain size range; if Frank loops were allowed to grow beyond that size (50 nm) while the stress was removed, those loops were stable against unfaulting.

Loop growth rate measurements were also performed, and it was found that perfect loops grew faster than Frank loops, but under stress, some perfect loops eventually stopped growing and began to shrink, whereas if no stress were applied, Frank loops were found to continue to grow at a uniform rate. The work also was able to demonstrate that growth rates of Frank loops were a function of the stress normal to the loop plane, providing growth rates up to 50% higher for normal stresses on the order of 17 MPa, although this result was not included in the original publication.[30]

Sato and co-workers performed similar experiments on annealed single crystal ribbon specimens of an austenitic steel that had been thinned almost to perforation in the central region.[31] Grips were attached to the single crystals by welding to provide a tensile stress in the [110] direction, and identical irradiations were performed in adjacent regions uiing 1 MeV electrons at 455°C for zero stress and up to 60 MPa (the yield stress for the material). Bright-field dislocation contrast showed that in general, the application of stress resulted in a slightly higher density of faulted loops and that loop orientations favorable with respect to the tensile axis had considerably higher densities than did the (111) planes

containing the tensile direction. A 5° error in tensile axis orientation promoted considerably higher loop densities on one of the two favorably oriented planes.

The work was expanded considerably in a subsequent paper to quantify the result of the internal stress due to anisotropic loop populations on subsequent loop development.[32] Two areas of a specimen were irradiated at 349°C, one unstressed and the other at 50 MPa. Loop development was isotropic in the unstressed case, but anisotropic for a 50 MPa stress, favoring the loops on those planes with the highest resolved tensile stress. The anisotropy was developed before the loops grew to a visible size. Based on studies varying the applied stress, the degree of anisotropy was shown to be a linear function of the stress normal to the loop plane, but extrapolation of the behavior to earlier work by Brager et al.[12] required a bilinear fit, suggesting that a change in controlling mechanism was occurring or that saturation in anisotropy would likely occur at higher stress levels. However, loop growth rate measurements for loops on the different planes of a stressed specimen indicated that growth rate was not altered by application of stress.

Loop Growth in Silver and Copper

Interstitial loop growth under tensile stress in the HVEM has also been studied in silver and copper.[33] Single crystal ribhon specimens were prepared with a (111) foil plane and a <110> tensile axis so that two {111} planes were equally stressed and the other two planes were parallel to the tensile axis. Silver specimens were irradiated with 1 MeV electrons at 85 and 130°C using applied stress levels varying from zero to 53.9 MPa, and copper speciceens-were likewise irradiated at 155°C for stresses between zero and 34.3 MPa. The loops were imaged using g=202, so that only two of the four sets of Frank loops were in strong contrast (but this included one of each of the two types of planes of interest, either parallel or inclined to the tensile axis), and one of the sets of loops out of contrast appeared in weak residual contrast, but perpendicular to the beam so that apparent distortion in shape was a true distortion. No attempt was made to compare anisotropy in the loop populations as a function of orientation with respect to the Burgers vector, but micrographs demonstrated that as the stress was increased, the loops in residual contrast became more elongated, indicating that stress does indeed distort loop growth in the direction of the applied stress. It may be noted that previous studies had effectively assumed that Frank loops were circular, and based analyses on that assumption.

Recent Proton and Ion Irradiation Studies

Finally, in recent years, several papers have been written based on proton or ion irradiation. Jung and co-workers have considered 6.2 MeV proton irradiation of austenitic stainless steel,[34] nickel alloys containing aluminum,[35] and martensitic stainless steel.[36] The austenitic steel study was intended to determine the difference between compressive and tensile stress states on void swelling response, and it was found that neither mean void diameter, void number density, or void volume varied significantly as a result of change in stress direction for stresses as high as 100 MPa over the temperature range 300 to 500°C to doses approaching 0.5 dpa.

Jung and Klein then considered the irradiation creep response in Ni-8.5,-11.1 and -13.1 at.% Al in order to provide understanding of behavior in more complex precipitation strengthened superalloys. Specimens were irradiated under tensile stresses from 10 to 250 MPa at temperatures from 160 to 390°C to doses approaching 0.3 dpa. Starting microstructure included solution annealed, aged, 20% cold worked, and cold worked and aged, and specimens were allowed to creep thermally prior to irradiation, until steady state response was obtained. Creep rates per displacement rate were found to decrease slightly with increasing aluminum content but showed no dependence on pretreatment. Microstructural examination for the solution annealed case showed that precipitates of γ' and dislocation loops grew under irradiation and that these growing dislocation loops were surrounded by precipitate free regions; after doses of about 0.2 dpa, however, the precipitate size stabilized.

In the overaged case, large precipitate particles were dissected by climbing dislocations as precipitation occurred between the large precipitate particles. The cold worked and aged material produced a combination of these responses. However, no comparison was made between the response in stressed and unstressed material (in fact, it was not even clear that microstructural studies were on stressed specimens), so no conclusions could be drawn about the effect of stress on microstructural evolution.

Similar behavior had been observed before in unstressed experiments,[37] and unfortunately, behavior is very different in superalloys, where γ' precipitation occurs on dislocations during irradiation. The studies on martensitic steel were intended to provide microstructural explanation for resistivity changes but no significant change in creep was found comparing thermal response and irradiation creep at 520°C and tensile stresses of 50 and 200 MPa to doses on the order of 0.5 dpa. The major effect of irradiation was found to be a much higher dislocation density.

Katoh and co-workers are completing microstructural examination of 4 MeV nickel ion irradiated ribbon tensile specimens of 316 stainless steel in a solution annealed condition.[38] Following irradiation at 500°C at stress levels of 3, 50, and 100 MPa for doses of 3 dpa, the dislocation structure consisted of mainly faulted loops but with between 10 and 20 percent unfaulted loops. The Frank loops were quantitatively analyzed for five different conditions of stress and orientation to determine anisotropy, but analysis was based on bright field images, and it was not possible to differentiate between (111) and

(11$\bar{1}$) Frank loops for foils oriented near [110]. However, analysis did show that only for stress conditions of 50 or 100 MPa, when loop plane normals were within 5" of the stress axis, loop populations were above 30%, whereas when the angle between the loop plane and the stress axis was 45" or greater, loop populations were sometimes below 20%, and therefore anisotropy could be demonstrated as a function of loop normal stress. Variations in loop size were negligible for the 50 MPa condition but did show slightly larger mean diameter for loops with plane normal 14' from the stress axis In the 100 MPa condition. Irradiation at 600°C to 50 dpa produced a low density of cavities, network dislocations, and needle-like precipitate particles. Application of stress was found to have negligible effect on void number density, but did result in increasing void size with increasing stress and, as a result, increasing swelling with increasing stress for stress levels of 0, 50, 100, and 200 MPa. This is interpreted as a consequence nucleation beginning and ending earlier under the presence of applied stress. Also, precipitate particles appeared to get larger and coarser with increasing applied stress.

Observations bv the Author

Pressurized Tube Examinations

The procedures established by Brager and co-workers for microscopy of pressurized tube specimens[11,12] have been applied to a number of other materials. Thirteen pressurized tubes of several candidate breeder reactor cladding materials were made available for destructive examination following irradiation to 2 or $5x10^{22}$ n/cm^2 (all fluences by the author given as E > 0.1 MeV). Conditions included five unstressed specimens and specimens stressed to approximately 170 MPa hoop stress at temperatures from 430 to 630°C. Alloys included Nimonic PE16, an Ni-34Fe-17Cr-3Mo-1.3Al-1.3Ti y' precipitation strengthened superalloy; M-813, a similar Fe-36Ni-19Cr-4Mo-2.8Ti-1.6Al alloy; Inconel 706, a Ni-37Fe-16Cr-2Nb-1.8Ti-0.3Al y" precipitation strengthened superalloy; and AISI 330, an Fe-36Ni-19Cr1.5Mn-1.3Si austenitic stainless steel. Based primarily on observations of the Nimonic PE16 specimens from this series, it was possible to produce a straightforward description of the evolution of microstructure due to irradiation and the effect of stress on that evolution.[39-41] That description is summarized here, accompanied by selected micrographs.

Two of the pressurized tube specimens examined were foynd to contain unfaulted dislocation networks: 20% cold worked AISI 330 irradiated at 625°C to $5x10^{22}$ n/cm and fully hardened M813 irradiated at 550°C to $2x10^{22}$ n/cm^2. The network in stressed AISI 330 contained a poorly defined subgrain structure on the order of 300 nm in diameter, but the network in M813 contained only individual dislocation segments and tangles, with no cell wall formation. No attempt was made to relate these structures to the stress axis or to zero stress conditions.

The response was quite different in Inconel 706 pressurized tube specimens. Independent of irradiation temperature (430 or 550°C), stress state, or heat treatment condition (fully aged or solution treated), following irradiation to $2x10^{22}$ n/cm^2, the dislocation structure in Inconel 706 consisted almost entirely of Frank loops. Loop densities were significantly higher in the 430°C irradiation condition but mean loop sizes were lower. Loop size was not altered significantly by preirradiation heat treatment. Loop size distributions were quantified in two of the stressed specimens irradiated at 550°C, and it was found that although size distributions were only slightly sensitive to the stress state orientation, large variations in number densities were found but without any straightforward dependence with regard to the normal or shear stresses on the various (111) planes.[39] All conditions of Inconel 706 examined were found to have retained y' and at least some y" precipitation-strengthening phases, but the effect of stress on precipitate microstructural evolution could not be demonstrated except in the case of irradiation at 430°C Following irradiation at 430°C to $2x10^{22}$ n/cm^2 under stress, no evidence of y" was found in diffraction patterns and it was only apparent in superlattice dark-field imaging. In comparison, for the unstressed specimen, weak y" diffraction spots were readily observed, arising from higher number density and larger size. Therefore, the application of stress appears to promote the dissolution of y" phase in Inconel 706.

Frank Loop Growth and Unfaulting in Nimonic PE16

Nimonic PE16 provided examples of both Frank loop development and unfaulted dislocation network tangles. Of particular interest was a sample of solution treated Nimonic PE16 irradiated to $2x10^{22}$ n/cm^2 at 550°C under a hoop stress of 167 MPa, where both Frank loop arrays and unfaulted dislocation tangles could be seen in a single grain, with clearly defined boundaries separating these regions. In comparison, a companion unstressed specimen contained very few unfaulted regions, whereas aged, and cold worked and aged conditions contained very few Frank loops. The Frank loops found in solution treated Nimonic PE16 were very unusual because they were able to grow to very large sizes (on the order of 500 nm) and began impinging on each other without unfaulting. (This delayed unfaulting response is thought to be associated with the decoration of dislocations with y' due to irradiation induced solute segregation.)

An example of the dislocation structure in $\vec{g}$=11$\bar{1}$ contrast for a single grain of a solution treated PE16 pressurized tube near an <011> foil orientation is given in Figure 1. Shawn as a montage, the grain is defined by a twin boundary on the left and high angle grain boundaries on the right. In the lower central part of the figure, an elliptical region can be seen, containing mostly unfaulted dislocation segments and surrounded by regions with only Frank loops. Similar unfaulted regions can be identified along the grain boundary on the right, in a region on the twin boundary at the left and surrounding a large precipitate

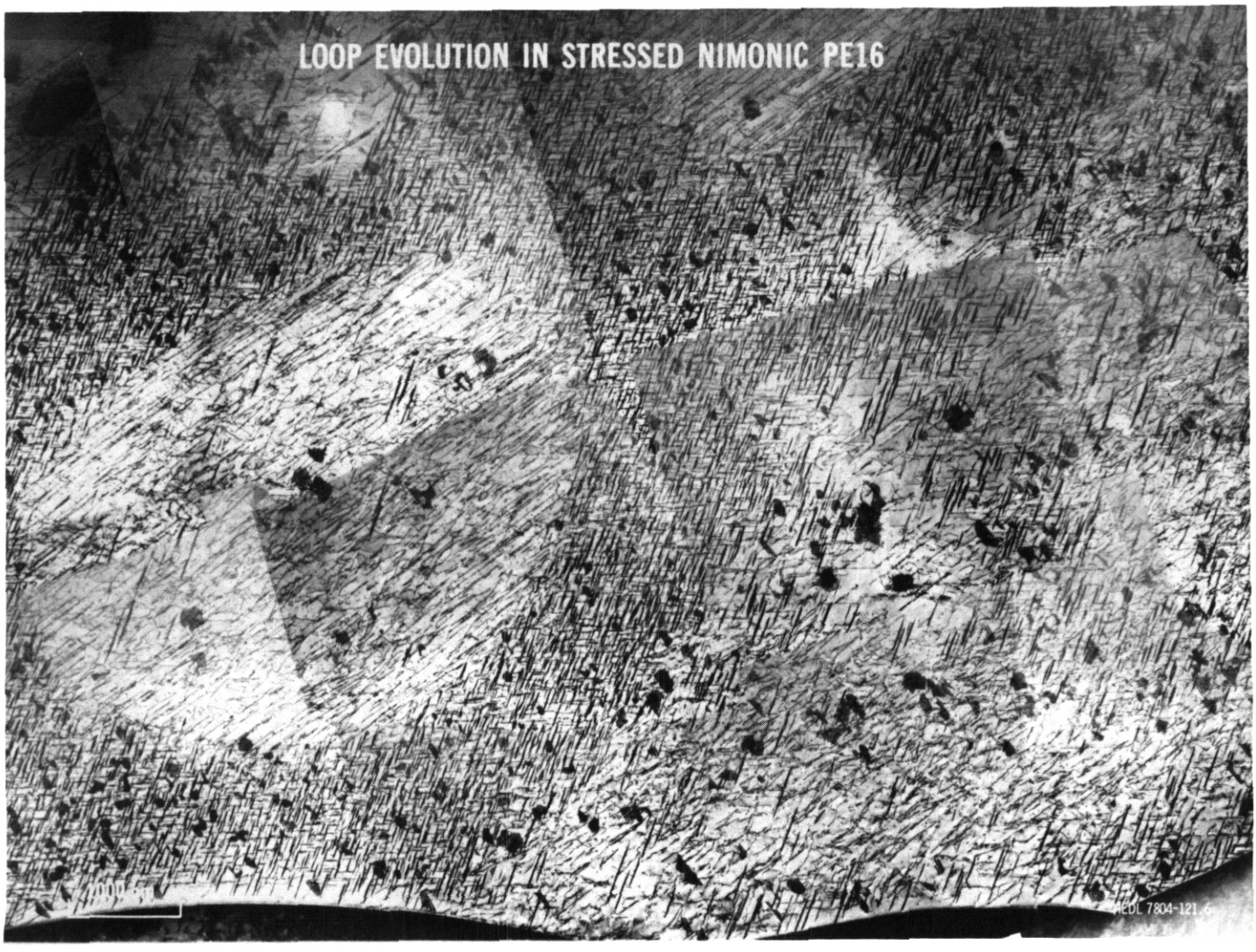

Fig. 1. Montage showing variations in the Dislocation Structure in a Single Grain of Solution Treated Nimonic PE16 After Irradiation to 2×10^{22} n/cm^2 (E>0.1 MeV) at 550°C Under a Hoop Stress of 167 MPa.

particle at the lower left. Three of the four sets of Frank loops are imaged in this figure under strong stacking fault contrast, one steeply inclined and therefore highly elliptical, and the other two less inclined and fairly equiaxed. These two can be differentiated by slightly different fringe direction-and different fringe spacing. The fourth set of Frank loops is exactly edge on, normal to the operating g vector, and therefore appears as individual line segments. From this figure, it is easy to identify a large anisotropy in the Frank loop populations, with the equiaxed loop shapes in much lower concentration for areas without unfaulted dislocations.

The dislocation structures for this irradiation condition are shown at higher magnification in Figure 2. The Frank loop structure in the unstressed pressurized tube specimen is shown using $\vec{g}$=200 contrast for a foil near (001) in Figure 2a. Two sets of loops appear to be horizontal, with different fringe spacing and slightly different fringe directions, and two sets of loops appear to be vertical, also with different fringe spacing and slightly different fringe direction. Measurements confirmed that little anisotropy exists in these loop populations (as shown inset in Figure 2a). Figure 2b provides an example of Frank loops in the stressed condition using similar contrast but for a foil near (011) so that two sets of loops are steeply inclined and appear to be elongated in directions about 70° apart and two sets are equiaxed, one with narrow horizontal fringes, and the other with widely spaced vertical fringes. Visual comparisons of the distributions of the various Frank loop orientations can demonstrate that the equiaxed loops with widely spaced vertical fringes are at lower number density, as demonstrated by quantitative measurement in which it was shown that the distributions were proportional to the normal stress levels for the various {111} loop planes [as shown on inset in Figure 2b).[39] Figures 2c and d provide stereo pair micrographs of a boundary region between Frank loop populations and unfaulted perfect dislocation populations. In this case, imaging is based on $\vec{g}$=111 for a foil orientation near <011>, so that three sets of Frank loops can be seen from stacking fault contrast, and the fourth is only observed edge on appearing as horizontal line

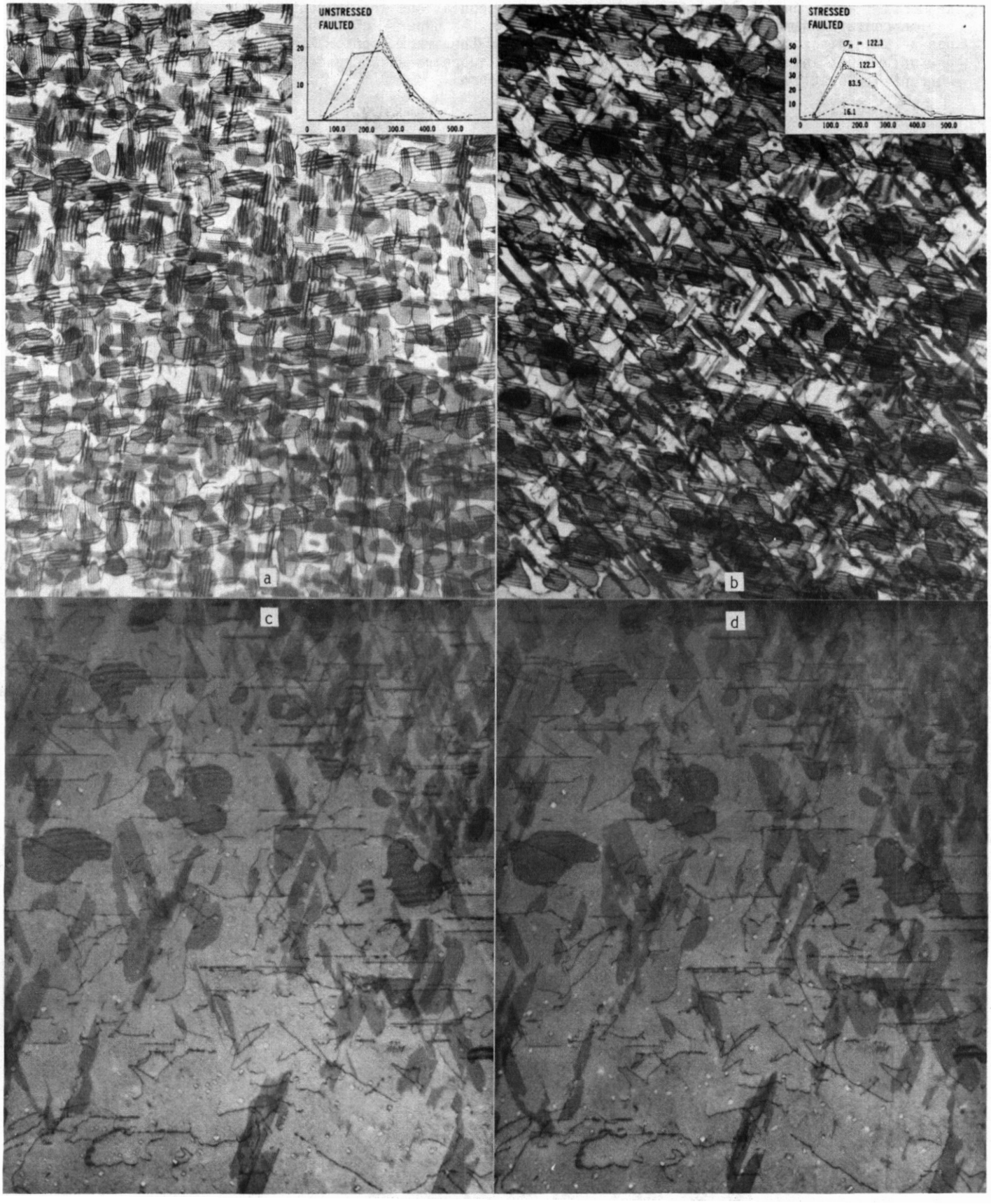

Fig. 2. Dislocation Structures at higher Magnification in Solution Treated Nimonic PE16 Pressurized Tube Specimens Irradiated at 550°C to 2×10^{22} n/cm^2 Frank loops in a) unstressed with $\vec{g}=200$ near <001>, and b) at 167 MPa hoop stress with $\vec{g}=200$ near <011> with size distributions inset, and a transition region between faulted and unfaulted areas, in c) and d) as a stereo pair with $\vec{g}=11\bar{1}$ near <011>.

segments. Also, only half the perfect dislocation populations are in contrast. In this stereo pair, a region containing mainly Frank loops can be found in the upper right, but elsewhere perfect dislocations can be seen dispersed among, and often connected to, the Frank loops. Many of the Frank loops are of unusual shape; in particular, one at the bottom left appears as a crescent, connected at one end to a perfect dislocation and at the other to the top surface.

Frank Loop Unfaulting Mechanism

Based on observations made from Figures 2c and d, a Frank loop unfaulting mechanism was proposed during irradiation in austenitic steels that requires interaction of a perfect dislocation to nucleate the necessary $\frac{a}{6}$<112> Shockley partial dislocation.[40] A perfect dislocation of suitable Burgers vector interacts with a Frank loop on an intersecting plane to produce a Shockley partial according to the reaction:

$$\tfrac{a}{2}[\bar{1}\bar{1}1] + \tfrac{a}{3}[111] \rightarrow \tfrac{a}{6}[\bar{1}\bar{1}2] \qquad (1)$$

The Shockley partial can sweep across the fault plane to unfault it, and then react with the dislocation defining the other side of the Frank loop (and therefore of reverse sense) to reestablish the original perfect dislocation Burgers vector:

$$\tfrac{a}{6}[\bar{1}\bar{1}2] + \tfrac{a}{3}[\bar{1}\bar{1}\bar{1}] \rightarrow \tfrac{a}{2}[\bar{1}\bar{1}1] \qquad (2)$$

The resulting morphology is a coil formed in the perfect dislocation on an intersecting (111) plane Several examples of such coils can be identified in Figures 2c and d. However, the coils rapidly straighten out, as can be demonstrated from Figure 1 in the unfaulted regions.

Recently, Suzuki and co-workers pointed out that Equations (1) and (2) are not applicable for interstitial Frank loops because the loop contains two fault planes, and therefore two Shockley partial dislocations dislocations are required for unfaulting.[42] However, it can be shown that, although not energetically favorable, the two necessary unfaulting dislocations can be created by the reaction:

$$\tfrac{a}{6}[\bar{1}\bar{1}2] \rightarrow \tfrac{a}{6}[\bar{2}11] + \tfrac{a}{6}[1\bar{2}1] \qquad (3)$$

Therefore, for interstitial loops, Equations (1) and (2) should be rewritten:

$$\tfrac{a}{2}[\bar{1}\bar{1}0] + \tfrac{a}{3}[111] \rightarrow \tfrac{a}{6}[\bar{2}11] + \tfrac{a}{6}[1\bar{2}1] \qquad (1a)$$

$$\tfrac{a}{6}[\bar{2}11] + \tfrac{a}{6}[1\bar{2}1] + \tfrac{a}{3}[\bar{1}\bar{1}\bar{1}] \rightarrow \tfrac{a}{2}[\bar{1}\bar{1}1] \qquad (2a)$$

Both Equations (la) and (2a) are energetically favored to proceed, whereas Equation (2) is an energy balance, and the driving force to proceed comes from removal of stacking fault material.

In cases where Frank loops and perfect dislocations coexist in austenitic steels, it can be anticipated that Frank loop unfaulting will be occurring constantly by the above reaction, and when Frank loops are present, they remain because an interaction has not yet occurred. Therefore, the Frank loop populations found in such cases give very little insight into the prior microstructural evolution. Brager and co-workers became aware of this problem by noting that the maximum and mean Frank loop diameters were related to the total dislocation density.[12] Frank loop distributions have been measured in partially unfaulted and fully unfaulted regions of the solution treated pressurized tube of Nimonic PE16 irradiated at 550°C to 2×10^{22} n/cm^2 at a stress of 167 MPa. The results are shown in Figure 3, where each size distribution is labeled with the corresponding normal and shear stresses for the various (111) planes. The loop populations that are most reduced by unfaulting are not a direct function of the corresponding shear stresses, but adjacent regions have similar distributions, as would be expected from the unfaulting mechanism described above.

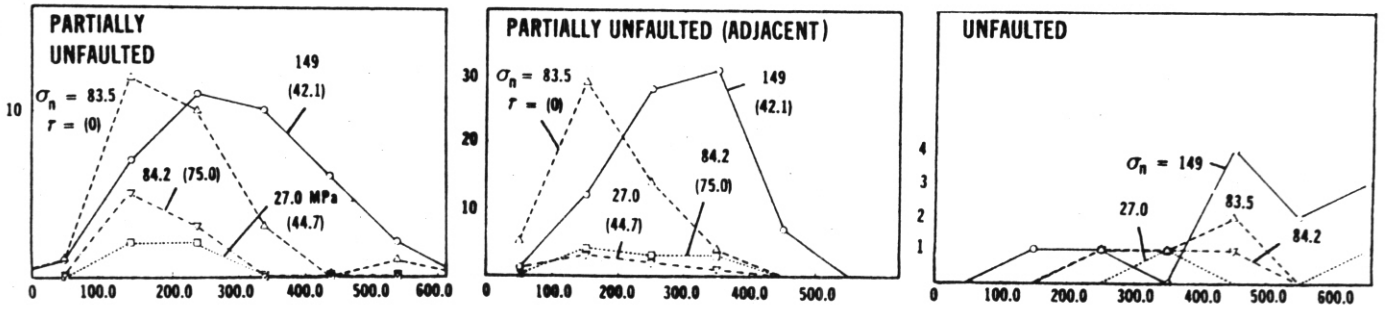

Fig. 3. Frank Loop Size Distributions for Partially Unfaulted a) and b) and an Unfaulted Region c) in a Solution Treated Nimonic PE16 Pressurized Tube Irradiated at 550°C to 2×10^{22} n/cm^2 at a Hoop Stress of 167 MPa.

Burgers Vector Anisotropy for Perfect Dislocations

In consideration of the consequences of this unfaulting mechanism, it became apparent that only dislocations of two orthogonal Burgers vectors were required to unfault all Frank loops present in a microstructure.[40] Therefore, the anisotropy generated in Frank loop populations would not necessarily be retained in perfect dislocation populations, and even larger anisotropies might develop. As a result, procedures were developed to determine the Burgers vectors for all perfect dislocations in a field of view.[41] The procedure was similar to the one used by Sokursky and Protsenko.[13] Stereo pair images using $\vec{g}$ = 200, 002 and 111 were compared to assign Burgers vectors for each of the perfect dislocations present (but no other images were taken to show disappearance; instead it was assumed they were all of $\frac{a}{2}$<110> type). Anisotropy in the perfect dislocation populations was measured for three pressurized tube conditions of Nimonic PE16: solution treated and irradiated to $2x10^{22}$ n/cm^2 at 550°C and 167 MPa hoop stress, overaged and irradiated to $8x10^{22}$ n/cm^2 at 480°C and 331 MPa hoop stress, and fully aged and irradiated to $8x10^{22}$ n/cm^2 at 480°C and 331 MPa hoop stress. Dislocation images used either bright field images or conditions approaching weak beam, dark field contrast in the latter two cases, and it was possible to show that in weak beam imaging, voids, and Frank loops were also in contrast. Analysis of the Burgers vector anisotropy demonstrated variations in dislocation density as large as a factor of 10 to 50. Therefore, anisotropy was generated in the perfect dislocation populations that was significantly larger than that found in the Frank loop populations. Also noteworthy was the observation that the perfect dislocations in these specimen conditions were pure edge in character with a tendency to lie on (100) planes. As a result, the opportunity for the dislocations to glide on (111) planes was not available, and it was therefore unlikely that an irradiation creep mechanism involving glide could be controlling in Nimonic PE16.

These results on anisotropy in perfect dislocation populations were analyzed by Adams[43] in light of the Stress Induced Preferential Absorption (SIPA) irradiation creep theory as it applied to straight edge dislocations by Wolfer[44] to show that the anisotropy tends to scale with the SIPA stress parameter, the parameter comparable to the normal stress for Frank loops. However, in the data sets for the higher fluence conditions, significant scatter was found, suggesting that self-stress fields from the dislocation populations themselves may begin to impact the local SIPA state.

Burgers vector anisotropy measurements were then attempted on two lots of 316 stainless steel pressurized tubes irradiated in the FFTF to $8x10^{22}$ n/cm^2 at 450°C and hoop stresses of zero or 138 MPa and at 650°C and hoop stresses of zero or 68.9 MPa. One lot was in a solution annealed condition and the other at 20% cold work prior to irradiation. Following irradiation at 450°C, both lots of material were found to contain both Frank loops and unfaulted dislocation segments. Following irradiation at 650°C, the solution annealed material developed a microstructure characteristic of climb dominated behavior whereas the cold worked material developed well defined subgrains with moderate dislocation density within subgrains. Measurements were not attempted in the cold worked material, but Frank loop anisotropy measurements for the 450°C condition and perfect dislocation anisotropy measurements for the 650°C condition were made for both stressed and unstressed samples of the annealed material. Results for 450°C Frank loop populations were representative of similar measurements, showing some anisotropy in the unstressed condition but somewhat more in the stressed condition, with the highest number densities for the loop plane with the highest normal stress. It could also be noted that the loop population with the lowest normal stress contained the loops with largest diameters. Results for 650°C demonstrated perfect dislocation Burgers vector anisotropy for both the unstressed and stressed conditions. The variation was somewhat lower in the unstressed case, a maximum variation of a factor of 4.3 compared to 5.3 for the stressed case. Of the possible explanations for this result, the most reasonable cause was that internal stresses can develop in unpressurized tubes approaching those of a tube pressurized to 69 MPa.

Perfect dislocation Burgers Vector Anisotropy in Ferritics

Most recently, the analysis of perfect dislocation Burgers vector anisotropy has been extended to ferritic alloys.[45] Ferritic qlloys are found to develop both $\frac{a}{2}$<111> and a<100> dislocations during irradiation, so that a complete analysis of Burgers vector anisotropy required determinations for dislocations with all seven possible Burgers vectors. A procedure was possible based on stereo pairs for three imaging conditions, g=200, 011, and 101 or 110, assuming only $\frac{a}{2}$<111> and a<100> dislocations were present, and using to advantage the fact that a<100> dislocations show stronger contrast in 200 imaging than do $\frac{a}{2}$<111> dislocations. A duplex ferrite/martensite alloy of composition Fe-10Cr-2Mo-0.9Ni-0.7Si-0.05C-0.12V-0.06Nb was irradiated as pressurized tubes in FFTF at 407 and 520°C to $7.5x10^{22}$ n/cm^2 with stress levels ranging from zero to -90 MPa, but dislocation anisotropy analysis was limited to a 407°C irradiation condition with an 86 MPa hoop stress. Only a delta ferrite region was analyzed to reduce complications from martensite lath boundaries, and weak beam, dark field contrast imaging was used. It was found that anisotropy could be as large as a factor of 7.6 among different Burgers vector possibilities (variations of a factor of 7.3 for $\frac{a}{2}$<111> dislocations and 2.7 for a<100> dislocations). This was surprising because the creep strain corresponding to this anisotropy was only 0.15% diametral (with 0.11% diametral strain measured in the unstressed specimen). However, it may be noted that deformations in Nimonic PE16 ranged from -0.02 to 1.255% diametral strain, so that anisotropy in dislocation populations had previously been demonstrated in cases of small creep strains.

Discussion

This review clearly shows the evolution in our understanding of irradiation creep toward a concentration on dislocation Burgers vector anisotropy. Initially, a mechanism based on climb controlled glide was forwarded by Harwell workers.[8,9,14,15] However, the attention of experimenters was diverted to anisotropy in Frank loop populations where clear effects of stress on loop populations could be identified,[10-13,19,21,22,27-29,31-33,38] and a glide based creep mechanism generally could not apply. Examples could be found where glide was clearly dominating such as in cold worked material irradiated to low dose.[16-18,23-26] Our observations on Nimonic PE16, a well studied material with irradiation creep response similar to austenitic steels, appear to indicate that a glide based mechanism cannot apply, which is a further indication that the climb controlled glide interpretation for irradiation creep has limited applicability.

Although the data are not completely consistent, Frank loop populations appear to develop anisotropy under stress without significant variation in loop size. This suggests a mechanism controlled by stress affected nucleation. However, it has been argued that, in fact, loop anisotropy is controlled by growth rates at very small loop sizes[39,46] and that therefore SIPA rather than stress-induced preferential nucleation (SIPN) applies.

Studies of Frank loop anisotropy often gave contradictory response. Sometimes, populations were enhanced in proportion to the normal stress on the loop plane, sometimes not. The disparity may exist because Frank loop populations generally coexist with perfect dislocations, and a perfect dislocation unfaulting mechanism was not fully appreciated. In other words, unfaulting destroyed the Frank loop historical record and left anisotropy reflecting internal stresses rather than the externally applied stress. Alternatively, the concern can be raised that irradiation creep experiments that irradiate only a small portion of the cross section of the specimen really represent irradiation creep stress relaxation experiments in the irradiated region. This concern generally was applicable to HVEM experiments. In this case, the remainder of the specimen cross section must bear the load that was relaxed in the irradiated region, thereby producing a much more complex stress state in the irradiated region.

Given the rambling nature of a historical review, it is appropriate to summarize the important concepts controlling dislocation evolution during irradiation creep. Stress has been shown to affect dislocation evolution in several ways. If, at the start of irradiation, there are few point defect sinks, loops will nucleate and grow, whereas if the sink density is high from, for example, cold worked dislocations, loop nucleation may be averted and dislocation glide encouraged. Loop distributions generally develop anisotropy in the populations on their different habit planes due to applied stress. The anisotropy appears to be generated when loops are small, and then all loops grow at the same rate. It may seem surprising that SIPA does not encourage loop growth in the most favorable orientations, but in fact, as the loops all grow at the same rate, the internal stress will continue to build up, counter balancing the external stress and turning off SIPA. After the initial nucleation of a stable loop population, further loop nucleation is discouraged until unfaulting reduces dislocation densities to allow enhancements of point defect concentrations to levels required for further nucleation. When perfect dislocations are present, application of stress does encourage dislocation climb for dislocations with favorably oriented Burgers vectors, leading to enhanced Frank loop unfaulting and reduced void swelling incubation. Perfect dislocation populations also develop anisotropic Burgers vector populations in response to applied stress. The level of anisotropy can be very large, greater than an order of magnitude in dislocation density for different Burgers vectors. Also, the anisotropy can develop quickly, within *10* dpa, but at a higher dose, SIPA response is distorted, with some favorably oriented Burgers vectors developing.

Once anisotropy is generated, several consequences can be envisioned. Further irradiation will tend to propagate the anisotropy as a result of continued climb of dislocation. Unless a simple mechanism exists for rebalancing the anisotropy (such as dislocation network node rearrangement), anisotropy will grow with increasing irradiation. If the external stress is then removed, the Burgers vector anisotropy must lead to irradiation growth (but measurements indicate that the amount of growth measured is small so the anisotropy must quickly disappear[41]).

The anisotropy can be thought of as generation of an internal stress. Adams has tried to estimate the internal stress buildup from SIPA creep." He estimated that for the data of Brager and co-workers,[12] where the ratio of vacancies in voids to atoms in loops was 4, the internal stress buildup would only reduce the unconstrained creep rate due to loop growth by 12 to 18%. Unfortunately, he failed to realize that the remaining atoms were combined into the perfect dislocation populations, which also contained anisotropy; hence his estimate was probably off by a factor of four. Therefore, the levels of internal stress can approach those of the externally applied stress, and creep is, in effect, a measure of the climb in the anisotropic dislocation populations, the anisotropy being produced in response to the external stress. Experiments by Buckley and Manthorpe[8,9] gave an early indication of just how large the internal stresses can be. When contributions to internal stress such as irradiation driven grain boundary migration and grain boundary sliding are taken into account, it is not difficult to understand why there can be such large deviations from the SIPA description of Burgers vector anisotropy.

Recommended future work should consider such issues as reconfirming Burgers vector anisotropy in perfect dislocation populations, and determining states of internal stress resulting from such anisotropy. For

example, a change in the internal stress state from the presence of a high volume fraction of voids may explain creep cessation.

CONCLUSIONS

Microstructural studies of effects of stress during irradiation have been ongoing for about twenty years. Early efforts appeared to confirm the climb glide mechanism, but it was later learned that climb glide was most important at low dose where prior cold work was introduced. Instead, the major effect is now found to be caused by development of anisotropy in Burgers vector populations, most easily observed in Frank loop populations but also found in perfect dislocation populations. The effect of stress on Frank loop populations can be wiped out by loop unfaulting and perfect dislocation network development. Stress accelerates network development because dislocation velocities are increased, leading to reductions in swelling incubation. The concept of internal stress should be examined in greater detail, and consideration given to stress relaxation experiments in order to better understand internal stress states.

FUTURE WORK

This work is completed.

REFERENCES

1. Irradiation Embrittlement and Creeo in fuel cladding and core components, (British Nuclear Energy Society, London, 1973).

2. Measurement of Irradiation-Enhanced Creeo in Nuclear Materials, M. R. Cundy, P. Von Der Hardt, and R. H. Loelgen, Eds. (North-Holland, Amsterdam, 1977), published in J. Nucl. Mater., Vol. 65.

3. Fundamental Mechanisms of Radiation Induced Creep and Growth, C. J. C. Carpenter, C, E. Coleman, and S. R. MacEwen, Eds. (North-Holland, Amsterdam, 1980), published in J. Nucl. Mater., Vol. 90.

4. Fundamental Mechanisms of Radiation-Induced Creep and Growth, C. H. Woo and R. J. McElroy, Eds. (North-Holland, Amsterdam, 1988), published in J. Nucl. Mater., Vol. 159.

5. V. J. Haddrell, J. Nucl. Mater., 18 (1966) 231.

6. R. Raj and M. F. Ashby, Met. Trans., 2 (1971) 1113.

7. Y. Komem, P. Pétroff, and R. W. Balluffi, Phil. Mag., (1972) 239.

8. S. N. Buckley and S. A. Manthorpe, in Irradiation Embrittlement and Creeo in Fuel Cladding and Core Components (British Nuclear Energy Society, London, 1973) 253.

9. S. N. Buckley and S. A. Manthorpe, Ibid. reference 2, 295.

10. P. K. Okamoto and S. D. Harkness, J. Nucl. Mater., 48 (1973) 204.

11. H. R. Brager, E. R. Gilbert, and J. L. Straalsund, Rad. Eff., 21 (1974) 37.

12. H. R. Brager, F. A. Garner, and G. L. Guthrie, J. Nucl. Mater., 66 (1977) 301.

13. Yu. N. Sokursky and L. N. Protsenko, J. Br. Nucl. Enersv Soc., 14 (1975) 137.

14. R. J. McElroy, J. A. Hudson, and R. S. Nelson, in Radiation Effects and Tritium Technology for Fusion Reactors, J. S. Watson and F. W. Wiffen, Eds., CONF-750989 Vol. 2 (1976) II-72.

15. J. A. Hudson, R. S. Nelson, and R. J. McElroy, Ibid reference 2, 279.

16. P. L. Hendrick, D. J. Michel, A. G. Pieper, R. E. Sarratt, and A. L. Bement, Jr., Ibid reference 14, II-84.

17. D. J. Michel, P. L. Hendrick, and A. G. Pieper, in Irradiation Effects on the Microstructure and Properties of Metals, ASTM STP 611 (ASTM, Philadelphia, PA, 1976) 284.

18. D. J. Michel, P. L. Hendrick, and A. G. Pieper, J. Nucl. Mater., 75 (1978) 1

19. T. Tabata, Y. Nakajima, T. Kida, and H. Fujita, in High Voltase Electron Microscoov 1977, supplement to J. Electron Microscopy, 26 (1977) 519.

20. W. G. Wolfer and F. A. Garner, J. Nucl. Mater., 85 & 86 (1979) 583

21. T. Atkins and R. J. McElroy, in Effects of Radiation on Materials: Eleventh Conference, ASTM STP 782, H. R. Brager and J. S. Perrin, Eds. (ASTM, Philadelphia, 1982) 841.

22. T. Atkins and R. J. McElroy, in Radiation-Induced Changes in Microstructure: 13th International Symposium (Part I, ASTM STP 955, F. A. Garner, N. H. Packan and A. S. Kumar, Eds. (ASTM, Philadelphia, 1987) 447.

23. C. H. Henager, Jr., PhD. Dissertation Thesis "Low Dose Irradiation Creep of Pure Nickel," University of Washington, 1983.

24. C. H. Henager, Jr., E. P. Simonen, E. R. Bradley, and R. G. Stang, J. Nucl. Mater., 117 (1983) 250.

25. C. H. Henager, Jr., E. P. Simonen, and E. R. Bradley, J. Nucl. Mater., 122 & 123 (1984) 413.

26. C. H. Henager, Jr. and E. P. Simonen, in Influence of Radiation on Material Properties: 13th International Symposium (Part II, ASTM STP 956, F. A. Garner, C. H. Henager, Jr., and N. Igata, Eds., (ASTM, Philadelphia, 1987) 69.

27. D. Caillard, J. L. Martin, and B. Jouffrey, Acta Met., 28 (1980) 1059.

28. S. Jitsukawa, Y. Katano, and K. Shiraishi, J. Nucl. Sci. and Tech., 21 (1984) 671.

29. S. Jitsukawa, Y. Katano, K. Shiraishi, and F. A. Garner, to be published in ASTM STP 1125, in press.

30. F. A. Garner and D. S. Gelles, Ibid reference 4, 286.

31. A. Sato, C. Ikeda, S. Nakamura, M. Suzuki, and T. Mori, Scripta Met., 20 (1986) 1119.

32. M. **Suzuki** and A. Sato, J. Nucl. Mater., 172 (1990) 97.

33. H. Saka, K. Kawamura, Y. Morozumi, and H. Teshima, J. Nucl. Mater., 179-181 (1991) 966.

34. H. K. Sahu and P. Jung, J. Nucl. Mater., 136 (1985) 154.

35. P. Jung and H. Klein, J. Nucl. Mater., 159 (1988) 360.

36. P. Jung, Ibid reference 33, 745.

37. D. I. Potter and A. W. McCormick, Acta Met., 27 (1979) 933.

38. Y. Katoh, Y. Kohno, and A. Kohyama, submitted for publication in Effects of Radiation on Materials: 16th International Symposium, ASTM STP 1175, A. S. Kumar, D. S. Gelles and R. K. Nanstad, Eds. (ASTM, Philadelphia, PA 1993).

39. D. S. Gelles, F. A. Garner, and H. R. Brager, in Effects of Radiation on Materials: Tenth Conference, ASTM STP 725, D. Kramer, H. R. Brager and J. S. Perrin, Eds. (ASTM, Philadelphia, PA, 1981) 735.

40. D. S. Gelles, in Dislocation Modellins of Phvsical Svstems, M. F. Ashby, R. Bullough, C. S. Hartley, and J. P. Hirth, Eds. (Pergamon Press, Elmsford, NY 1981) 158.

41. D. S. Gelles, in Effects of Radiation on Materials: Twelfth International Conference, ASTM STP 870, F. A. Garner, and J. S. Perrin, Eds. (ASTM, Philadelphia, PA, 1985) 98.

42. M. Suzuki, A. Sato, T. Mori, J. Nagakawa, N. Yamamoto, and H. Hiraishi, Phil. Mag. A, 65 (1992) 1309.

43. D. S. Gelles, F. A. Garner, and B. L. Adams in Damase Analysis and Fundamental Studies Quarterly Progress Report July-September 1982, DOE/ER-0046/11 (USDOE, Washington, DC 1982) 81. Also reviewed in reference 30.

44. W. G. Wolfer, Scripta Met., 9 (1975) 801.

45. D. S. Gelles, A. Kimura, A. Kohyama, and R. J. Puigh, to be included in Fusion Reactor Materials Semiannual Progress Report for the Period Ending March 31, 1992, DOE/ER-0313/12, PNL-SA-20994.

46. F. A. Garner, W. G. Wolfer, and H. R. Brager, in Effects of Radiation on Structural Materials, ASTM STP 683, J. A. Sprague and D. Kramer, Eds., (ASTM, Philadelphia, PA, 1979) 160.

47. B. L. Adams, J. Nucl. Mater., 115 (1983) 49.

IRRADIATION CREEP DUE TO SIPA UNDER CASCADE DAMAGE CONDITIONS - C. H. Woo, (Whiteshell Laboratories), F. A. Garner, (Pacific Northwest Laboratory)' and R. A. Holt, (Chalk River Laboratories)

OBJECTIVE

The objective of this effort is to determine the interrelationships between void swelling, irradiation creep and the stress state imposed on structural materials for fusion reactors.

SUMMARY

This paper derives the relationships between void swelling and irradiation creep due to SIPA and SIG under cascade damage conditions in an irradiated pressurized tube. It is found that at low swelling rates irradiation creep is a major contribution to the total diametral strain rate of the tube, whereas at high swelling rates the creep becomes a minor contribution. The anisotropy of the corresponding dislocation structure is also predicted to decline as the swelling rate increases. The theoretical predictions are found to agree very well with experimental results.

PROGRESS AND STATUS

Introduction

An awareness has developed recently that irradiation creep mechanisms, operating in response to applied or internal stresses, leave microstructural records of their action.[1] One of the strongest features of this record is an anisotropic distribution of Burger's vectors that is very pronounced prior to the onset of significant void swelling. This anisotropy appears to fade however, as swelling increases in magnitude and rate. Recent studies have also shown that the interaction of void swelling, irradiation creep and stress-affected microstructural development appears to be much more complex than previously envisioned. Creep rates first accelerate with the onset of swelling and then decline as the swelling rate increases.[2,3] Creep equations developed from the data on highly pressurized tubes overpredict the creep observed in fuel pins where the onset of void swelling precedes the development of significant stress levels.[4]

Insights obtained from studying the stress-affected microstructure and the swelling-creep relationship can be combined with the SIPA creep mechanism to produce a new understanding of the phenomenon involved. In this regard, irradiation creep due to Stress-Induced Preferred Absorption (SIPA) has been a subject of active investigation for many years. This mechanism is derived from the difference between the climb rates of the aligned and non-aligned dislocations due to a stress-induced differential bias (with reference to the stress state). The creep stain is caused both directly by SIPA, and indirectly by the anisotropic dislocation structure introduced as a result of SIPA. This indirect mechanism was referred to as SIPA-Induced Growth (SIG).[5]

Traditionally, SIPA creep has been modeled using rate theory in the same way as void swelling and other irradiation damage phenomena. In that treatment, it was implicitly assumed that all the point defects generated by irradiation can migrate freely, and are thus all available for preferential absorption at sinks. However, it was shown recently[6,7] that this approach may not be appropriate for irradiation involving fission neutrons, fusion neutrons and heavy ions. In these cases, the point defects are produced in damage cascades in which extensive recombination and clustering occurs, leaving only a small proportion of the point defects free to migrate. The difference in thermal stability between the interstitial and vacancy clusters has been shown to result in a 'production bias'. This production bias can provide the dominant driving force for void swelling in the high swelling temperature regime (e.g., 720-920K for stainless steels in fast reactors).

At temperatures below the high swelling regime, the observed swelling rate is much lower because both vacancy and interstitial clusters are thermally stable, acting as recombination centers. The steady-state number densities of the clusters are maintained by absorption at moving dislocations. Because both kinds of clusters are swept up in roughly equal proportions by the dislocations, the net void swelling and dislocation climb rates are mostly governed by the biased absorption of the freely migrating point defects. Recently, an analysis has been performed of irradiation creep behavior in pressurized tubes of austenitic and ferritic steels in the EBR-II and FFTF fast reactor in the low swelling regime (~400°C).[8] It was shown that the relatively complicated creep behavior observed in these experiments can be explained very well by a SIPA-based theory including SIG.

At higher temperatures, the vacancy clusters are thermally unstable, and their steady-state number density is thus much lower than that of the interstitial clusters. This creates a bias because the clustered interstitials are mostly immobile and are only accessible to the moving sinks/dislocations, but not to the

---

'Pacific Northwest Laboratory is operated for the U.S. Department of Energy by Battelle Memorial Institute under Contract DE-AC06-76RLO 1830.

immobile sinks such as voids and grain boundaries. The climb of dislocations is thus mainly determined by the net absorption of the interstitial clusters. The dislocation climb velocity and interstitial loop growth rate resulting from this production bias in an unstressed crystal under cascade damage conditions have been derived and shown to explain the large increase in swelling rate in the high temperature regime.[9] To analyze irradiation creep in this temperature range, the effects of an applied stress must also be taken into account. To address this, the climb velocity of dislocations in a stressed crystal under cascade irradiation has been derived and presented separately.[10]

In this paper, using the results from ref. 10, we examine the creep behavior of neutron-irradiated pressurized tubes, in a temperature range that includes the peak swelling regime. The resulting steady-state creep strain rate is calculated and compared with experimental observation.

Steadv-State Dislocation Structure

We consider the steady-state dislocation structure of a neutron-irradiated closed-end pressurized tube. Let σ_H be the hoop stress and K be the displacement damage rate (NRT). We model the dislocation structure by three classes of dislocations, with Burgers vectors aligned, class 1, with the radial direction; class 2, with the hoop direction; and class 3, with the longitudinal direction. We assume that the dislocation line length increases by loop growth and recovers by the cancellation of dipoles by climb.[11] Then the conservation equation of the line density ρ_n of the nth class is given by

$$\dot{\rho}_n = \dot{\lambda}_n - \alpha_D \rho_n^2, \quad n = 1, 2, 3 \ldots \qquad [1]$$

where the dot indicates the derivative with respective to time. In Eqn.(1), $\dot{\lambda}_n$ is the production rate of dislocations of the nth class by the growth of the interstitial loops. The line destruction rate by annihilation of dislocations of the opposite sign is given by $\alpha_D \rho^2$, where α_D is the reaction cross section (and depends on the climb velocity).

The loop line growth rate for cascade damage conditions, including the effect of SIPA due to a deviatoric stress tensor σ_{ij} has been derived as.[10]

$$\dot{\lambda}_n = \frac{\rho_n}{b_n \rho r_n} \{ (1-\epsilon_i) q G \Delta\psi \frac{\sigma_{ij}}{\mu} [\omega_i^n \omega_j^n - \sum_\kappa f_\kappa \omega_i^\kappa \omega_j^\kappa] + \dot{S} \} \qquad [2]$$

where b_n = magnitude of the Bergers vector of the nth class
ρ = total dislocation density
ρ_n = dislocation density of class n
r_n = mean loop radius of the nth class
q = ratio of the dislocation sink strength (i.e., network plus loops) to the total sink strength
ϵ_i = fraction of interstitials immobilized by intracascade clustering
G = effective point-defect production rate after intracascade recombination is taken into account' If a is the fraction of intracascade recombination, then $G = (1-a)K$
$\Delta\psi$ = point-defect property associated with the SIPA effect (see eqn.13 for definition.
μ = shear modulus
ω_i^κ = ith component of the unit burgers vector for loops of the kth class
f_κ = fraction of line density due to the kth class
$\dot{S}$ = net rate of accumulation of interstitials at the interstitial loops and network dislocations = (net rate of accumulation of vacancies at the voids)

We note that eqn.(2) has the same form as the equivalent equation derived in a previous paper' in which irradiation creep in the low swelling rate regime was analyzed and where the swelling is driven only by the dislocation bias. In the following, we assume steady-state conditions (i.e., $\dot{\rho}_n = 0$). Making use of the experimental observation that SIPA mainly affects the steady-state loop-number density, but not so much the size of the loops,[12-14] the relative dislocation densities can be obtained as the solution of the simultaneous algebraic eqns. (1) and (2):

$$f_1 = \frac{1}{3} - \frac{1}{2x} [1 - (1 - \frac{2x^2}{3})^{1/2}] \qquad [3a]$$

$$f_2 = \frac{1}{3} + \frac{1}{2x}\left[1 - \left(1 - \frac{2x^2}{3}\right)^{1/2}\right] \qquad [3b]$$

$$f_3 = \frac{1}{3} \qquad [3c]$$

where

$$x = (1-\epsilon_i)\, qG\Delta\psi \frac{\sigma_H}{\mu \dot{S}} \qquad [4]$$

The solution of eqns (1-2) in eqns (3a-3c) is obtained under the physical condition $f_1 + f_2 + f_3 = 1$ and the condition that the fs are positive definite. This is equivalent to the condition $x \leq 6/5$, or $2/3 > f_1 > 0$, $2/3 > f_2 > 0$, and $f_3 = 1/3$. The possibility of vacancy loop formation is also excluded (see ref. 1) in the present treatment.

Diametral Strain Rate

The deviatoric strain rate in the hoop direction associated with the climb of an anisotropic dislocation structure (i.e., due to SIG) is given by

$$\dot{\epsilon}_H^{SIG} = \left(f_2 - \frac{1}{3}\right)\dot{S}. \qquad [5]$$

The diametral strain rate due to SIPA creep under the biaxial stress condition presently considered can be derived, and is given by

$$\dot{\epsilon}_H^{SIPA} = \tau_H f_2 \left(\frac{5}{6} - f_2\right), \qquad [6]$$

where

$$\tau_H = (1-\epsilon_i)\, qG\Delta\psi \frac{\sigma_H}{\mu} \qquad [7]$$

Thus the total diametral strain rate of an irradiated pressurized tube is given by

$$\dot{\epsilon}_H = \frac{\dot{S}}{3} + \dot{\epsilon}_H^{SIG} + \dot{\epsilon}_H^{SIPA}. \qquad [8]$$

In terms of the effective creep rate and the effective stress,' the creep law can be written as

$$\frac{\bar{\epsilon}}{\bar{\sigma}} = C\frac{4\left(\dot{\epsilon}_H^{SIPA} + \dot{\epsilon}_H^{SIG}\right)}{3\sigma_H} \qquad [9]$$

where C is a geometric constant dependent on the tube diameter and wall thickness (=1.15 for the present case'). Eqn.(9) can be put in exactly the same form as the empirical relation proposed by Garner et.al.[1,15].

$$\frac{\dot{\epsilon}}{\sigma} = D\dot{S} + B_o \qquad [10]$$

where D is the creep swelling coupling coefficient, given by

$$D = \frac{4C}{3\sigma_e}\left(f_2 - \frac{1}{3}\right) \qquad [11]$$

and B_o is given by

$$B_0 = \frac{4C\tau_H}{3\sigma_H} f_2 \left(\frac{5}{6} - f_2\right) \qquad [12]$$

Values of D and B_o can be evaluated using eqns. (3b) and (7), provided the value of $\Delta\psi$ is known. For SIPA due to elastodiffusion,[16] $\Delta\psi$ is given by

$$\Delta\psi = \frac{3}{16}\beta\left[P_i(p_i - 1) - P_v(p_v - 1)\right] \qquad [13]$$

where β is the reciprocal of the product of the Boltzmann constant and the absolute temperature. P_j ($j = i, v$ for interstitials and vacancies, respectively) is related to the point-defect saddle-point relaxatidn volume and p_j is related to the anisotropy of the corresponding point-defect configuration. The values of P_j and p_j can be obtained from[17] for copper and a-iron (16 for copper and 39 for a-iron at 400°C). Following a previous paper,[8] a value of $\Delta\psi$ = 28 was used for the present calculation.

Results and Discussions

The theory presented in the foregoing sections is applied to consider the in-reactor deformation of pressurized stainless-steel tubes. The results are then compared with the experimental measurements in both the low and high steady-state swelling rate regimes. The input data are listed in Table 1. Here the ratio of the dislocation line sink strength to the total sink strength is estimated based on calculated steady-state number densities of intracascade point-defect clusters.[18]

Table 1: Input parameters for the calculation

Intracascade Recombination fraction (a)	0.90
lntracascade Interstitial Clustering Fraction (ε_i)	0.45
Intracascade Vacancy Clustering Fraction (ε_v)	0.50
Ratio of Dislocation Line Sink Strength/Total Sink Strength	0.50

at 400°C (with a steady-state swelling rate of ~0.1 %/dpa) has a value of about 3, as shown in table 2 This agrees very well with the theoretical value, e.g. as shown in fig. 1.

TABLE 2. RATIO OF DIAMETRAL STRAIN RATES OF STRESSED VS. UNSTRESSED TUBES

Alloy	Condition	Reactor	Stress Level	$\frac{3\dot{d}}{D\dot{S}}$	Reference
304L	Annealed	EBR-II	188 MPa	3.24	Porter et al. [17]
316	20% CW	EBR-II	343 MPa	3.30	Garner and Porter [18]
316	20% CW	EBR-II	206 MPa	2.82[b]	Garner and Porter [18]
D9[a]	20% CW	FFTF	200 MPa	2.28[c]	Toloczko et al. [19]
PCA[a]	20% CW	FFTF	200 MPa	3.33	Toloczko et al. [19] and Garner and Puigh [20]

(a) D9 and PCA are Ti-modified type 316 steels.
(b) After temperature changes from 550 to 400°C.
(c) This value represents an underestimate due to failure of the stressed tube following its measurement at the previous discharge.

It is interesting to note from fig.1 that the relative difference between the diametral strain rates of the stressed and the unstressed tubes represented by this ratio decreases with increasing swelling rate. At the swelling rate increases beyond 0.2%/dpa, the relative difference becomes insignificant, and at a swelling rate of 1%/dpa, the difference is only about 10%. There is no substantial difference of this behavior for different stress levels, except for swelling rates considerably smaller than 0.1%/dpa. Thus, as the swelling rate increases, there is a general tendency for the applied stress to become relatively less effective in causing deformation (i.e., in increasing the diametral strain rate). Experimentally, the reduction of the effect of stress on the diametral strain rate, at high swelling rate, is a well established observation, and has been interpreted as creep cessation at high swelling.[1] More recent results[2,19] also showed that relative to the swelling rate, the creep rate is very large at the onset of swelling when the swelling rate is low, but diminishes as the swelling rate increases.

To understand the mechanism responsible for this relative reduction of the creep rate at the high swelling rate, we plot in Figs. (2-5) the values of D, B_o, f, and the total creep rate, as functions of the swelling rate. It is immediately obvious that, of the two terms contributing to the deviatoric strain rate, it is the term associated with D, i.e., the one caused by SIG, that is responsible for reduction of creep relative to swelling, at high swelling rate. For a swelling rate lower than ~0.1%/dpa, the calculated value of D is $\sim 0.5\times10^{-2}$ MPa^{-1}, compared with an experimental value of $\sim 0.6\times10^{-2}$ MPa^{-1}.[3,20-22] The corresponding dislocation structure shows maximum anisotropy ($f_1 = 0$, $f_2 = 2/3$, $f_3 = 1/3$, which is the source of the significant strain rate due to SIG. Note that having attained the maximum anisotropy (because $f < 2/3$, see eqn.3) is the reason for the dislocation structure, and hence D and B_o, to become independent of the swelling rate at small swelling rate. At a high swelling rate, the calculated values of D diminishes rapidly. The drop is responsible for the reduction of the effect of stress on the diametral strain rate. The dislocation structure, according the Fig.(4), becomes almost isotropic at high swelling rates ($f_1 \cong f_2 \cong f_3 \cong 1/3$), and this is the reason for the low SIG creep rate in this situation. We note that the decrease of D as a function of the swelling rate has also been observed experimentally.[1] Compared to the value of D, the value of B_o is relatively constant as the swelling rate changes. In Fig.(3) the value of B_o only varies between 1.5 and 2.5×10^{-5} MPa^{-1} dpa^{-1} for the whole range of swelling rates considered. This agrees very well with the experimental values.[9,21]

It is interesting to note (Fig.5) that the absolute value of the creep rate does not decrease much at high swelling rate. However, as the swelling rate increases, the creep rate constitutes a less significant portion of the total strain rate. From the foregoing discussion, it is clear that in the presence of void swelling, SIG is a major factor in determining the total deformation of an irradiated specimen under stress. At low swelling rates (such as at temperatures below the high-swelling regime, or at the onset of swelling), void swelling accelerates the creep rate, mainly as a result of dislocation anisotropy developing. However, at high swelling rates, the stress-induced anisotropy of the dislocation structure decreases, thus reducing the SIG rate ($=D\dot{S}$) to values negligible compared with that of the swelling component. The reduction of the anisotropy of dislocation structure at high fluence, where swelling rate is high, has been reported by Garner and Gelles.[1]

The relation between the anisotropy of dislocation structure and the swelling rate can be understood by referring to Eqn.(2). Here the dislocation line generation rate (proportion to the dislocation climb rate) is made up of two terms. The first term depends on the direction of the particular Burger's vector under consideration while the second term does not. Remembering that it is the difference in the dislocation line generation rate that creates the dislocation anisotropy, a large swelling rate means a dominant second

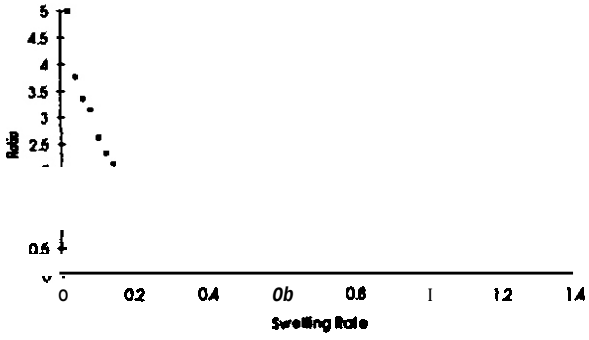

Figure **1:** The calculated ratio of the diametral strain rate of a stressed tube to a stress-free tube as a function of the swelling rate (%/dpa).

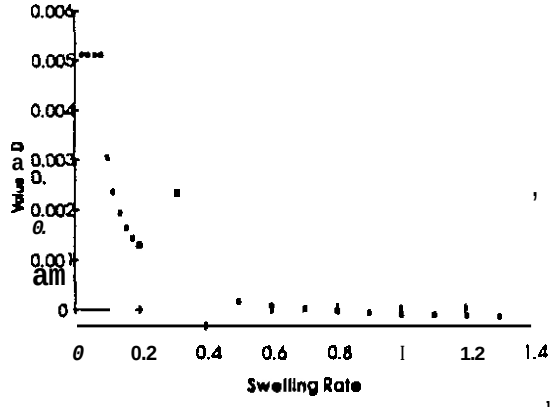

Figure *2:* The calculated value of $D(MPa^{-1})$ function of the swelling rate (%/dpa).

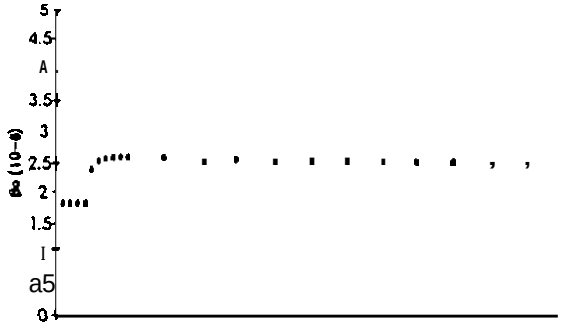

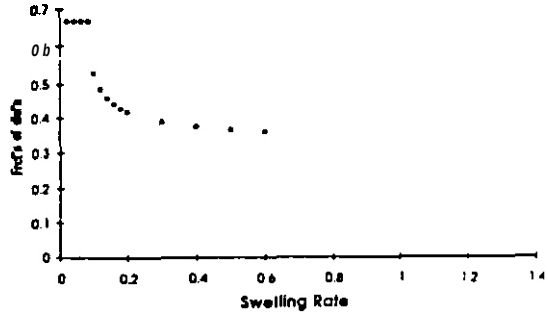

Figure 4: The fraction of dislocations aligned with the hoop stress, i.e. f_{θ} vs swelling rate (%/dpa).

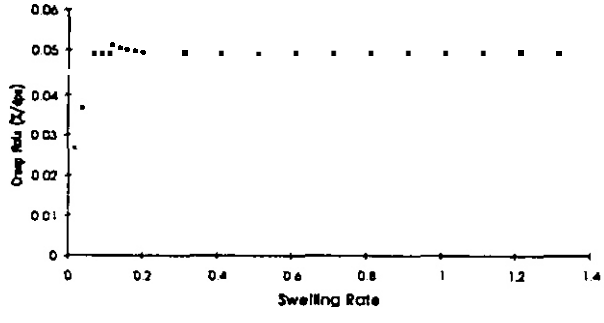

Figure *5:* The total creep rate (%/dpa) vs swelling rate (%/dpa).

term and thus an isotropic dislocation structure is the result. On the other hand, a small swelling rate would mean a generation rate which strongly depends on the class of dislocation, resulting in an anisotropic dislocation structure.

From this point of view, it is evident that in those cases where the stress is already present at the onset of swelling (e.g. the irradiated pressurized tubes) the proportion of the creep contribution is larger than in those cases where the stress grows with the swelling and becomes significant only when the swelling (and hence the swelling rate) is large. Differences observed between the measured fuel pin deformation and the predicted deformation based on the pressurized tube data[4] shows that the prediction of the present,theory is indeed correct.

It should be noted that the present model is for the steady-state case. However, in the foregoing discussion, we have used results to analyze experiments that are conducted under transient conditions where the swelling rate increases with time. This is a good approximation as long as it is realized the dislocation structure at a higher swelling rate is actually more characteristic of that of an earlier but lower swelling rate, because it takes time for the dislocation structure to evolve.

CONCLUSIONS

The deviatoric strain rate caused by SIPA and the associated SIG can be written as observed in eqn.(10). B_o is relatively independent of the swelling rate and has a value of about 1 to 2×10^{-6} dpa^{-1} MPa^{-1}. D is relatively constant (with a value of $\sim0.5\times10^{-2}$ MPa^{-1}) at low swelling rates (~0.1%/dpa), where its contribution is several times that of the direct SIPA contribution. At high swelling rates, D reduces to almost zero.

The experimentally observed deviatoric strain rates for irradiated pressurized tubes agree well with the present theoretical predictions. The onset *of* swelling (when swelling rates are low) is correctly predicted to accelerate the creep rate (fig.5). At high swelling rates the creep rate is limited, so that the total deformation rate under stress does not significantly exceed the stress-free case (fig.1).

The present theory predicts that the dislocation anisotropy is only significant at low swelling rate, and is much reduced at high swelling rates. This is also consistent with experimental observations.

It *is* also predicted that the creep equations for irradiated stressed tubes, in which the stress already exists at the onset of swelling (low swelling rate), always overpredicts creep in fuel pins, in which the stress develops slowly, becoming significant only at some high fluence at which the swelling has already begun.

ACKNOWLEDGMENT

The authors C.H.W and R.A.G would like to thank the CANDU Owners Group for financial support. F.A.G's participation was funded by the U.S. Department of Energy under contract DE-AC06-76RLO 1830.

FUTURE WORK

This effort will continue, analyzing new data as it becomes available

REFERENCES

1. F. A. Garner and D. S. Gelles, J. Nucl. Mater. 159(1988) 286

2. F. A. Garner and M. B. Toloczko, Fusion Reactor Materials Semiannual Progress Report, DOE/ER-0313/12, 1992, pp. 145-147.

3. F. A. Garner and D. L. Porter, J. Nucl. Mater. 155-157 (1988) 1006.

4. F. A. Garner, O. L. Porter and B. J. Makenas, J. Nucl. Mater. 148(1987)279.

5. C. H. Woo, Philos. Mag.42 (1980) 551.

6. C. H. Woo and B. N. Singh, Philos. Mag 65 (1992)889.

7. C. H. Woo and B. N. Singh and F. A. Garner, J. Nucl. Mater. 1992 (in press).

8. C. H. Woo and F. A. Garner, J. Nucl. Mater. 1992 (in press).

9. C. H. Woo and A. A. Semenov, 1992 (submitted for publication).

10. C. H. Woo, 1992, unpublished results.

11. B. B. Glasgow and W. G. Wolfer, ASTM STP 870, eds. F. A. Garner and J. S. Perrin, 1985, p.98.

12. H. R. Brager, F. A. Garner and G. L. Guthrie, J. Nucl. Mater, 66 (1977) 301.

13. F. A. Garner, W. G. Wolfer and H. R. Brager, ASTM STP 683, eds. J. A. Sprague and D. Kramer, 1979, p.160.

14. O. S. Gelles, F. A. Garner and H. R. Brager, ASTM STP 725, eds. D. Kramer, H. R. Brager and J. S. Perrin, 1981, p.680.

15. F. A. Garner, J. Nucl. Mater. 122 & 123 (1984) 459.

16. C. H. Woo, J. Nucl. Mater. 120 (1984) 55.

17. H. R. Schober, J. Phys. F7 (1977), 1127.

18. C. H. Woo and A. A. Semenov, unpublished results

19. F. A. Garner, M. B. Toloczko and R. J. Puigh, Fusion Reactor Materials Semiannual Progress Report, DOE/ER-0313/12, 1992, pp. 148-162.

20. D. L. Porter, F. A. Garner, and G. D. Hudman, J. Nucl. Mater. 179 (1991) 581.

21. M. B. Toloczko, F. A. Garner and C. R. Eiholzer, Fusion Reactor Materials Semiannual Progress Report, DOE/ER-0313/9, pp. 160-171.

22. F. A. Garner and R. J. Puigh, J. Nucl. Mater. 179 (1991) 577.

SIMULATING HIGH ENERGY CASCADES IN METALS - H. L. Heinisch, (Pacific Northwest Laboratory)[a]

OBJECTIVE

The objective of this work is to determine the spectral dependence of defect production and microstructure evolution for the development of fission-fusion correlations.

SUMMARY

The processes of radiation damage, from initial defect production to microstructure evolution, occur over a wide spectrum of time and size scales. An understanding of the fundamental aspects of these processes requires a spectrum of theoretical models, each applicable in its own time and distance scales. As elements of this multi-model approach, molecular dynamics and binary collision simulations play complementary roles in the characterization of the primary damage state of high energy collision cascades. Molecular dynamics is needed to describe the individual point defects in the primary damage state with the requisite physical reality. The binary collision approximation is needed to model the gross structure of statistically significant numbers of high energy cascades. Information provided by both models is needed for connecting the defect production in the primary damage state with the appropriate models of defect diffusion and interaction describing the microstructure evolution. Results of binary collision simulations of high energy cascade morphology are reviewed. The energy dependence of freely migrating defect fractions calculated in recent molecular dynamics simulations are compared to results obtained much earlier with a binary collision/annealing simulation approach. The favorable agreement demonstrates the viability of the multi-model approach to defect production in high energy cascades.

PROGRESS AND STATUS

Introduction

Irradiation of crystalline solids with energetic neutrons, ions or protons produces atomic displacement damage in the form of collision cascades. A cascade occurs when the projectile or a recoiling primary knock-on atom (PKA) loses its energy in a sequence of displacive collisions with other atoms, which in turn displace more atoms, resulting in a discrete region of high defect concentration. For the high energy PKAs typical of those produced by d-t fusion neutrons, on the order of 300 keV in steels and copper alloys, the distance between high energy secondary collisions in some materials is great enough that multiple, well-separated damage regions, commonly referred to as subcascades, are formed. The primary damage state of a cascade consists of the lattice defects -- immobile clusters, dislocation loops, small mobile clusters and isolated point defects -- remaining after the cascade energy has dissipated.

The spatial distribution of the lattice defects when they are first produced profoundly affects their survival and subsequent disposition. Thus, to understand the irradiation-induced changes in the microstructure of a material under cascade-producing irradiation, it is important to know the temporal and spatial disposition of lattice defects in the primary damage state of cascades. The processes of radiation damage, from initial defect production to changes in the microstructure, occur over a wide spectrum of time and size scales. Figure 1 schematically illustrates the stages of evolution of collision cascades and their link to changes in the microstructure.

Once initiated by the creation of the PKA, the collisional stage lasts approximately until no atom has enough energy to permanently displace another atom, about 10^{-13} s. During the quenching stage, about 10^{-11} s, the cascade energy is shared among a larger number of the atoms in the cascade region through many-body interactions, forming "molten" zones, which then dissipate their heat to the rest of the material. Significant rearrangement of the defects produced in the collisional stage occurs in the molten zones. During the short-term annealing stage, the defects surviving the quench interact through normal, thermally-activated diffusion within the cascade region, resulting in immobile and mobile defects that cause changes in the microstructure.

Experimental information on defect production in cascades is largely confined to observing spatially- and temporally-averaged characteristics of the defect population or features of the changes in microstructure observable by transmission electron microscopy (TEM). Presently, the only means of obtaining detailed information on the spatial arrangement of individual point defects in the primary damage state is by computer simulation with models at the atomic scale. A multi-model approach (MMA), consisting of a series of different models, each valid over a specific range of time, space and energy, is required to describe all the stages of cascade development.

'Pacific Northwest Laboratory is operated for the U.S. Department of Energy by Battelle Memorial Institute under Contract DE-AC06-76RLO 1830.

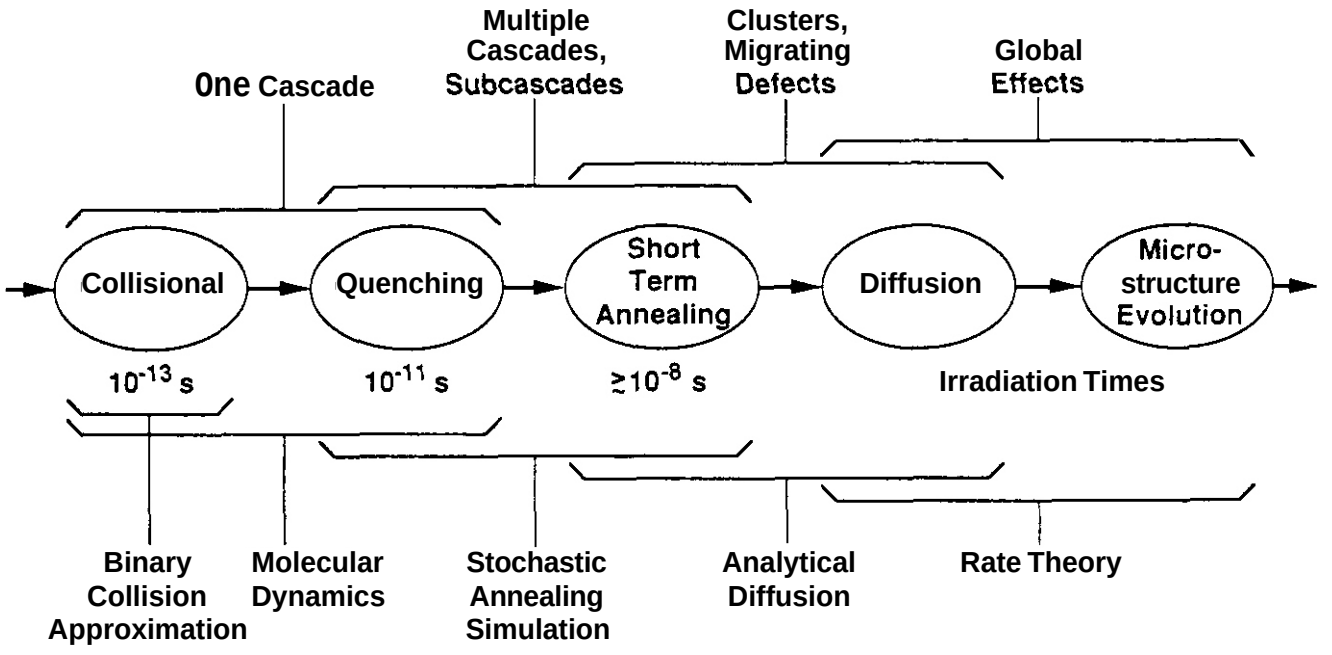

Fig. 1 The Stages of Cascade Development, indicating the microstructural features, the time frame involved and the type of model used to describe each stage.model approach (MMA), consisting of a series of different models, each valid over a specific range of time, space and energy, is required to describe all the stages of cascade development.

The Multi-model Approach

In principle, molecular dynamics (MD) computer simulations provide the most realistic description of the primary damage state. Today's MD codes, utilizing the Embedded Atom Method and optimized for vectorization on a supercomputer, can simulate cascades through the quenching stage at energies near the threshold of subcascade formation, [2] about 30 keV in copper. However, in practice, MD is limited to simulating only small numbers of cascades with energies in the subcascade threshold range. Since the cascade process is stochastic in nature, one cascade, or even several, may not be representative of the average cascade behavior. The spatial distribution of subcascades in high energy cascades is highly irregular, so statistical treatments are necessary.

In practice, MD is limited to simulating times on the order of picoseconds for the highest energy cascades it can treat. Thus, it is effective for simulating only through the quenching stage. Following this stage there may be considerable interaction of migrating defects both within an individual subcascade and among nearby subcascades. Since this aspect of subcascade interactions cannot be modeled by MD, diffusion-based models of cascade and subcascade interactions must be used. In the absence of complete information on the position of each lattice defect in the high energy events, it is important to at least quantify the spacing and density of subcascades to serve as starting conditions for the diffusion-based models.

The binary collision approximation (BCA) applied to collision cascades in crystalline materials is the best way td realistically model the collisional phase of high energy cascades in statistically significant numbers. Since many-body interactions are ignored in the BCA, it is valid only at relatively high energies (strictly, well above the displacement threshold energy). The BCA can be used to model only the collisional phase of a cascade; however, the high energy collisions determine the spatial distribution of subcascades. The BCA provides a realistic description of the gross features of the defect distribution, but, because the BCA simulation cannot treat the dissipation of energy to the rest of the crystal, it cannot correctly describe the ultimate positions of the point defects within each subcascade. Modeling the details of recombination, clustering, and the dissipation of the thermal energy requires the more physically rigorous approach of MD.

BCA modeling is useful for investigating the tendency to form visible microstructural features. Certainly the formation of molten zones in cascade cores or the formation of loops or clusters depends on low energy, many-body atomic interactions that can be realistically addressed only in molecular dynamics simulations. However, the tendency to form these features also depends on the initial spatial deposition of energy. If the major collisions occur very far apart, there may not be sufficient energy density to drive clustering, produce molten zones or form loops. BCA modeling of the collisional phase can provide sufficient information on the deposited energy density to identify such cases even if it cannot predict the actual atomic configurations that result.

The MMA utilizes the BCA, MD, and a model for defect rearrangement by diffusional processes. The BCA describes the arrangement of cascades and subcascades at high energies. MD can describe the defect distribution at the

end of the quenching phase for representative lower energy cascades. Stochastic, atomistic annealing simulations can describe the short-term annealing phase,[3] while a diffusional approach appears feasible[4] for describing short-term annealing as well as aspects of cascade interactions and global diffusion. The annealing and diffusion simulations require input on the cascade morphology obtainable from MD (for the spatial distribution of point defects within individual subcascades after the quenching stage) and the BCA (for the spatial distribution of subcascades).

Dramatic progress has been made in MD cascade simulations in the past few years. Two 25 keV cascades in copper have been generated and analyzed by Diaz de la Rubia and Guinan[2], and significant numbers of cascades in copper at energies below 10 keV have been generated by Foreman, Phythian and English[5]. Thus, a data base of cascade behavior through the quenching stage is being generated for low energy cascades in copper. Recently, BCA simulatigns have also been used to investigate the characteristics of subcascade production in high energy cascades. Some of the results of the BCA simulations will be discussed in the following section.

BCA Simulations of Cascade and Subcascade Prooerties

Binary collision computer simulations have vividly portrayed the highly irregular configurations of high energy cascades and subcascades from high energy recoils. Recently, a systematic characterization of subcascade production in monatomic fcc, bcc and hcp metals as a function of primary recoil energy, atomic charge and mass, and crystal structure has been done[6] with the BCA code MARLOWE'. Moliere potentials were used, local inelastic energy losses were subtracted, and thermal displacements representing room temperature were applied. MARLOWE parameter values and other details of the calculations are in Ref. 6. The threshold energies for subcascade formation and the average number and spacing of subcascades were determined as a function of cascade energy. The average density of defects produced in the collisional phase of cascades, which is related to the deposited energy density, was also investigated. The cascade features were compared on the basis of Lindhard's reduced energy[8],

$$\frac{a}{2 Z^2 e^2} T_{dam},$$

where Z is the atomic number, e is the electronic charge, a is the screening radius and T_{dam} is the recoil damage energy.

The threshold energy for the production of subcascades, the "break-up" energy," was determined by analysis of the average density of vacancies in MARLOWE-generated cascades. The density of vacancies was determined for each cascade, the cascade volume being defined as the volume of the enclosing rectangular parallelepiped oriented along the cubic crystal axes (and along the orthogonal axes defined in MARLOWE for the hcp metals). The vacancy densities were averaged over the set of cascades at each energy, and the average densities were plotted as a function of cascade damage energy on log-log plots. On a log-log plot of the data for a metal, a straight line can be drawn through the points at the lower energies. The energy at which the data deviate from this straight-line behavior is identified as the cascade break-up energy[6]. Below the break-up energy the data exhibit the fractal behavior of a typical branching configuration. Above the break-up energy the production of widely-spaced subcascades results in even more rapidly increasing cascade volume and rapidly decreasing defect density with increasing energy -- also possibly fractally, but scaled by the inter-subcascade spacing rather than inter-defect spacing. Figure 2 shows the trends of the data for fcc metals in log-log plots as a function of reduced damage energy. The break-up energy has a reduced energy value of about 0.06 for all the fcc metals.

The break-up energies in the fcc, bcc and hcp metals, normalized on the basis of reduced damage energy are compared in Fig. 3. The values for the metals of each crystal structure occur in separate ranges, respectively, differing overall by about a factor of four. Within the same crystal structure, values differ by only about 50%. The geometrical reason for the differences is not readily apparent. The atomic volumes, in units of nearest neighbor distance, differ by less than 10%. However, they differ in the same sequence as the break-up energies, i.e., fcc < hcp < bcc.

The method used to identify the break-up energy clearly indicates the onset of widely-separated damage regions. The density of the cascade varies with energy differently when the recoils have energies above the maximum spike energy. This method will not recognize as separate subcascades those that form adjacent to each other. However, during the quenching stage, immediately adjacent subcascades will interact with each other strongly, behaving as a single damage area. This has been observed in the molecular dynamics simulations of Diaz de la Rubia and Guinan[2]. The widely-separated subcascades will also interact during quenching, but each will react individually to the share of the defect flux and thermal energy being dissipated by the others that it sees.

The volumes of the rectangular parallelepipeds enclosing the vacancy distributions of individual cascades of the same energy vary over an order of magnitude or more. Figure 4 shows the distributions of cascade volumes for sets of cascades at 20, 30, and 50 keV in copper. The onset of subcascade production with increasing energy is illustrated by the contrast of the more sharply peaked distribution at 20 keV, just below the break-up energy, to the nearly flat distribution spread over more than an order of magnitude at 50 keV, which is above the break-up energy. When compared at the same damage energy, the average volume increases with decreasing Z. When compared on the basis of reduced energy, the average cascade volumes in the different metals display approximately the same reduced energy dependence. The actual (rectangular) volumes of material

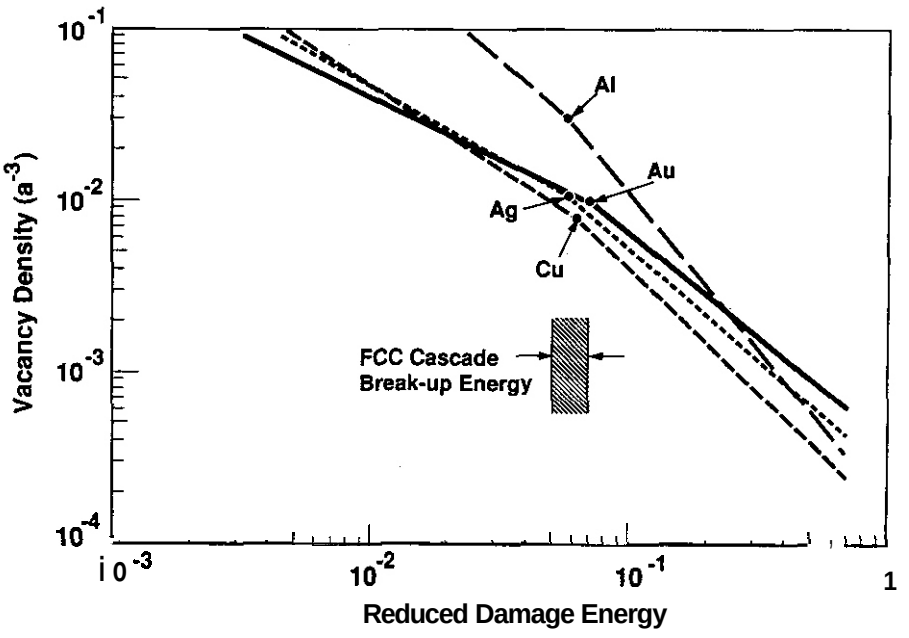

Fig. 2. The average density of vacancies in the rectangular parallelepipeds enclosing cascades in fcc metals as a function of reduced recoil damage energy. The lines are those fitted to the MARLOWE simulations of the collisional phase. The change in slope identifies the threshold energy for the production of subcascades (the "break-up energy").

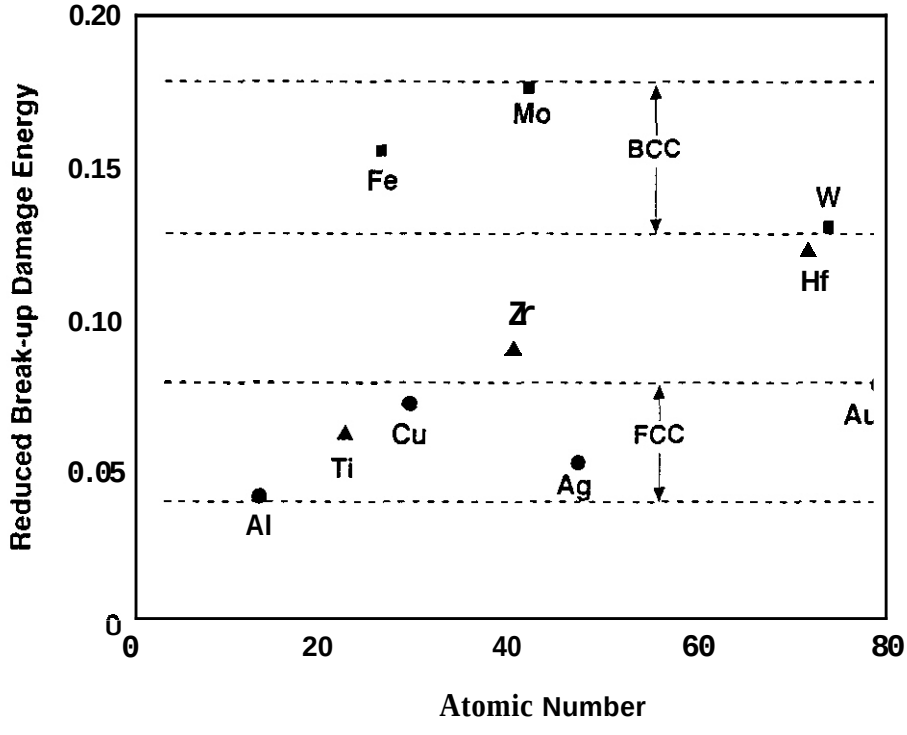

Fig. 3. The reduced break-up damage energies as a function of atomic number, Z, in fcc, hcp and bcc metals. The values for each crystal structure lie in the indicated ranges.

disturbed by the occurrences of the cascades should be somewhat greater than these values, since these volumes do not include the displaced atoms, nor do they account for all the atoms involved during the development and quenching of the molten zone.

To determine the subcascade configuration (the number and spacing of subcascades) in the BCA simulations, it was necessary to determine whether or not a group of defects should be identified as a subcascade. For this analysis a subcascade was defined as a damage region of approximately the maximum spike energy, i.e. the break-up energy, that is well-separated from other damage regions. The subcascade analysis was done entirely by computation using a subcascade identification algorithm based on the local density of vacancies. See Ref. 6 for details. Some comparisons with graphical depictions of cascades were made as a means of checking its effectiveness. The results show that the average number of subcascades increases linearly with damage energy in all the metals (except for Al, for which subcascades could not be defined). The number of subcascades as a function of reduced recoil damage energy is about the same in all metals.

The center-to-center separations of nearest neighboring subcascades at the same energy in a given metal have a wide distribution of values. The distributions look much the same at all energies where at least two subcascades are produced. The average value of subcascade separations is constant with energy to within about 20% in each metal. The values lie within 40-60 atomic diameters. with no discernable dependence on atomic number or crystal structure.

Discussion

It is assumed that the regions of high defect density in the collisional phase are associated with high initial energy density, and that following quenching, these regions will continue to define distinct cascade features such as subcascades. A comparison of the BCA simulations of high energy cascades with the experimental results of Kiritani, Yoshiie, Kojima and Satoh[10] is described in Ref. 6. They analyzed TEM micrographs of 14 MeV neutron-irradiated fcc metals and extracted the recoil energy dependence of many features of the visible defect distributions. Comparison of the BCA simulations of the collisional phase subcascade distributions with the TEM results shows that in Cu, on the average, one visible defect cluster is associated with each

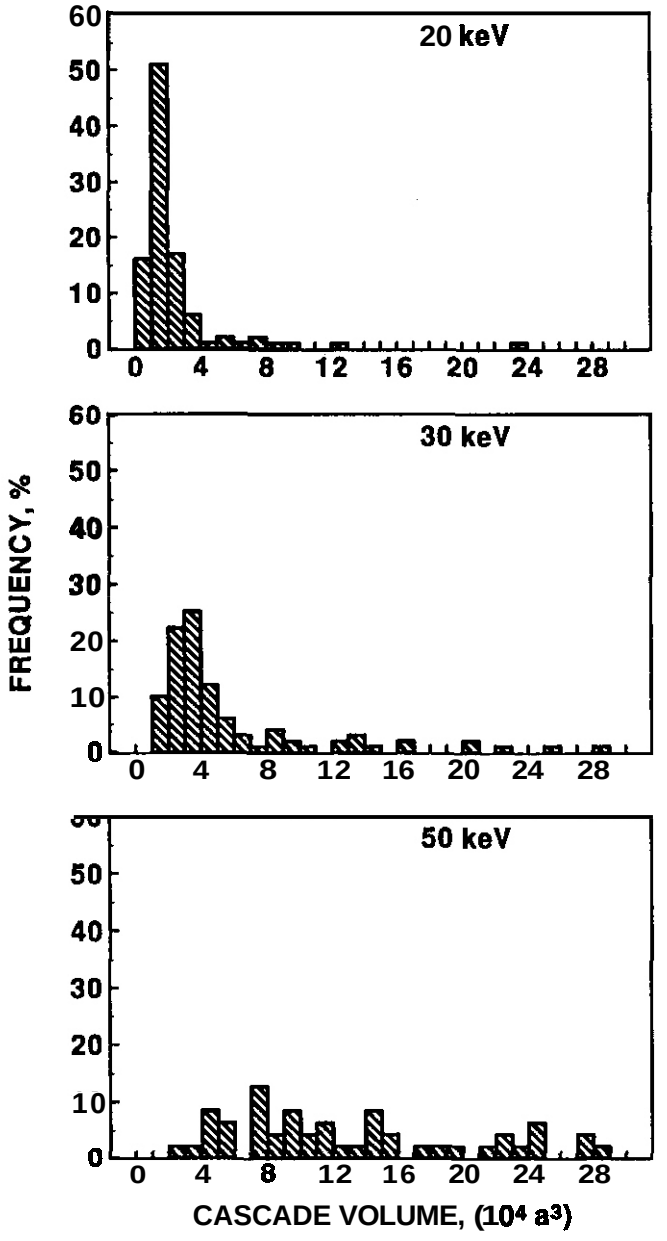

Fig. 4. The distribution of cascade volumes for sets of MARLOWE-generated cascades of 20, 30 and 50 keV in copper. The cascade volumes are the volumes of the rectangular parallelepipeds enclosing the vacancy distributions.

subcascade. The simulations also show that in 14 MeV neutron irradiation of the higher Z materials Ag and Au, few cascades should occur with energies above the threshold energy for subcascades. Thus, in Ag, and especially in Au, the multiple visible clusters observed by Kiritani et al. to form in groups of closely spaced clusters must be formed within a single subcascade. The size and spacing of these clusters will be governed by the kinetics within the cooling spike rather than by the physics of high energy atomic interactions. The consequences of this fundamental difference with respect to defect production and its effect on the evolution of the microstructure could be substantial and must be thoroughly understood. This same consideration also applies to the cascades of higher energy density produced by ions (or molecules) of much higher mass than the target atoms.

The BCA simulations show that the vacancy densities of the set of 20 keV cascades in copper (representative of individual subcascades) have a distribution of values with a standard deviation of about 100% of the mean value. The deposited energy densities are expected to have a similar distribution. This has implications with respect to the production of TEM-visible defect clusters or loops. A recent comparison[9] of collapse efficiencies in ion irradiated foils with results of MARLOWE simulations of the foil irradiations demonstrates that only those cascades or subcascades with energy density above a critical value collapse to form a TEM-visible defect.

A recent study by Alurralde, Caro and Victoria,[11] analyzed BCA cascades by relating the deposited energy density in a cascade to thermal energy and identifying potential molten zones as subcascades. The numbers of subcascades as a function of recoil energy that they determined from a fairly small sample of cascades compare favorably with the results in Ref. 6. A complete understanding of the correlation between collisional-phase defect density, deposited energy density and visible clusters must be obtained through detailed comparisons of BCA and MD results

Further encouragement of the possibility of a successful MMA is realized with the recent results of Foreman, Phythian and English,[5] who reported the numbers of mobile interstitial defects surviving the quenching stage in their MD cascades (up to 10 keV in Cu). In Fig. 5 their results are compared with the energy deoendence of the efficiencv of producing freely migrating interstitials that-was determined using a semi-empirical, BCA/annealing simulation approach employing MARLOWE and the ALSOME annealing code[12]. The good agreement of the MO and BCA-annealing results indicates that the partitioning of the defects into clustered and migrating defects in the primary damage state may not be very sensitive to some of the details that only MD can properly treat.

In summary, defect production in the primary damage state of high energy, subcascade-producing cascades cannot practically be described realistically by a single model. Aspects of both MD and BCA models are required, as well as a model for diffusion during short-term annealing. Favorable direct comparisons of BCA results with experimental observations, thermal analysis and low energy MO cascades are encouraging signs that this MMA will be successful.

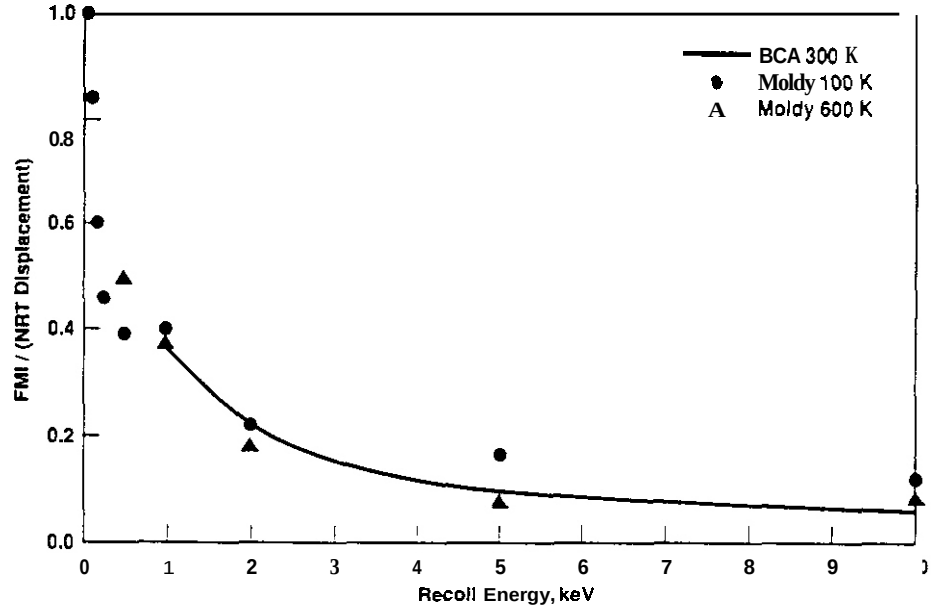

Fig. 5. The fraction of freely migrating interstitial defects relative to the calculated number of displacements per cascade as a function of recoil energy for MD and BCA cascades in copper. The points are for MD cascades at 100 K and 600 K[5]. The line represents a function fitted to results from BCA cascades at 1 keV and above".

REFERENCES

1. T. Oiaz de la Rubia, R. S. Averback, R. Benedek and W. E. King, Phvs. Rev. Lett. **59,** 1930 (1987).

2. T. Diaz de la Rubia and M. W. Guinan, Phvs. Rev Lett. **66,** 2766 (1991).

3. H. L. Heinisch, J. Nucl. Mater. **117,** 46 (1983)

4. C. H. Woo, B. N. Singh and H. L. Heinisch, J. Nucl. Mater. **174,** 190 (1991).

5. A. J. E. Foreman, W. J. Phythian and C. A. English, 1992, Phil. Mag. in press (1992).

6. H. L. Heinisch and B. N. Singh, Phil. Mas., in press (1992).

7. M. T. Robinson and I. M. Torrens, Phvs. Rev. B 9, 5008 (1974).

8. J. Lindhard, V. Nielsen and M. Scharff, Mat. Fvs. Medd. Dan. Vid. Selsk. 36 (1968).

9. K. Morishita, H. L. Heinisch and S. Ishino, Fusion Reactor Materials Semiannual Progress Reoort for Period Ending Sept. 30, 1992, DOE/ER-0313/13 (1992).

10. M. Kiritani, T. Yoshiie, S. Kojima and Y. Satoh, Rad. Eff. and Def. in Sol. **113,** 75 (1990).

11. M. Alurralde, A. Caro and M. Victoria, J. Nucl. Mater. 183, 33 (1991).

12. H. L. Heinisch and F. M. Mann, J. Nucl. Mater. **122&123,** 1023 (1984).

PUBLICATIONS

This report was presented at the International Conference on Computer Simulations of Radiation Effects in Solids, August 23-28, 1992, Berlin, Germany. It has been submitted for inclusion in the conference proceedings, to be published in Radiation Effects and Defects in Solids.

Swelling of Pure Nickel Observed in the Second Discharge of the AA-14 Experiment - F. A. Garner (Pacific Northwest Laboratory)[a]

OBJECTIVE

The objective of this effort is to determine the factors which influence the microstructural evolution of neutron-irradiated metals.

SUMMARY

The swelling of neutron-irradiated pure nickel is strongly dependent on its tendency toward saturation. The factors which induce saturation also lead to a strong dependence on irradiation temperature for nickel in the annealed condition. When irradiated in the cold-worked condition, however, the temperature dependence of swelling is strongly reduced but the tendency toward saturation persists.

PROGRESS AND STATUS

Introduction

In an earlier report, it was shown that the microstructural evolution of pure nickel, a metal often selected in fission-fusion correlation studies, is dominated by its tendency toward saturation in void swelling (1). This tendency was cited to explain the strong dependence of swelling on irradiation temperature for the annealed condition and also to explain the role of both cold-work and aging in reducing the temperature dependence. This behavior is shown in Figure 1.

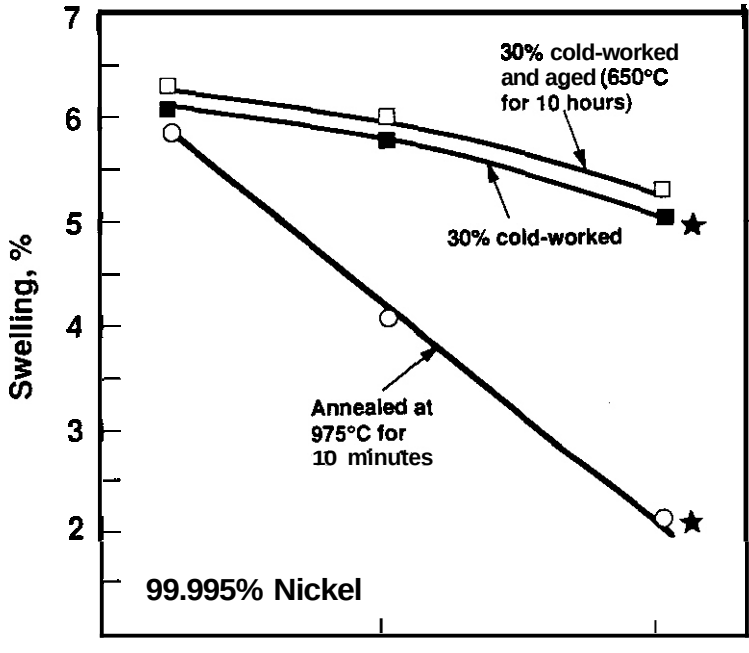

Fig. 1. Swelling of pure nickel observed after 12-14 dpa in EBR-II as a function of irradiation temperature and starting condition. All data taken at 14 dpa except for two data at 12 dpa, each marked with a star.

These data were derived from the first discharge of the AA-14 experiment at 12 to 14 dpa (2). The second and final discharge of this experiment also contained some of these nickel specimens, although the aged condition was not included and one of the cold-worked conditions was not available.

Results and Discussion

The swelling was measured using an immersion density technique described earlier (2). Figure 2 shows the swelling behavior derived from both the first and second discharges of the experiment. The swelling at 425°C was increased by cold-work at 32 dpa, with 9.1% compared to 7.5% for the annealed condition. The tendency toward saturation was observed not only at 425°C and 500' in the annealed condition, but also at 425 and 600°C in the cold-worked condition.

Cold-working exerts a greater degree of influence as the irradiation temperature is increased. The net effect of cold-working is

dependence-has been observed in other studies; an example is shown in Figure 3. Note that boron doping to produce helium (and lithium) did not alter the temperature dependence, indicating that void nucleation is not the controlling factor. Collapse of the dislocation population was earlier shown to lead to the saturation behavior (2).

---

[a]Pacific Northwest Laboratory is operated for the U.S. Department of Energy by Battelle Memorial lnstitute under Contract DE-AC06-76RLO 1830.

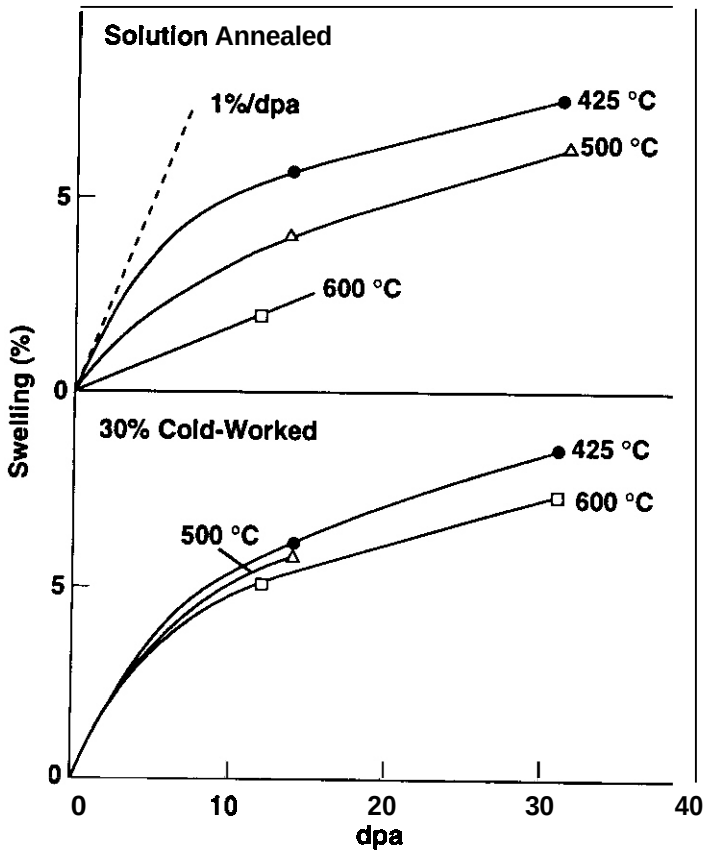

Fig. 2. The dose dependence of swelling for pure nickel in the annealed and 30% cold-worked conditions.

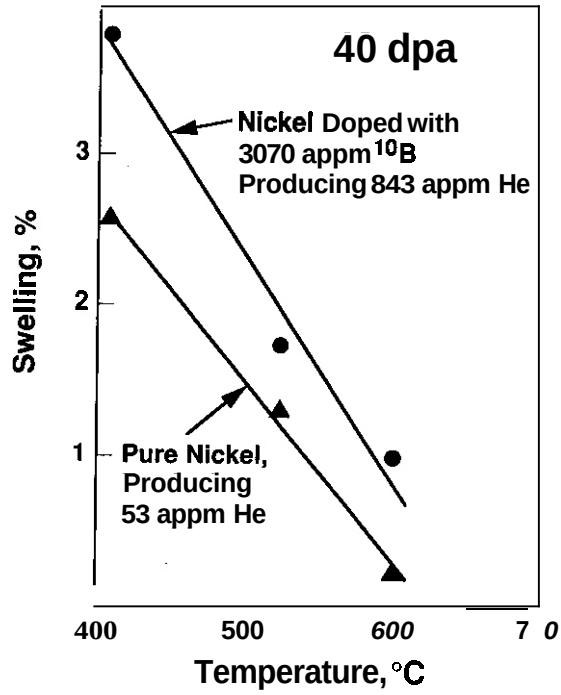

Fig. 3. Swelling of pure nickel and boron-doped nickel, both in the annealed condition after irradiation to 40 dpa in FFTF-MOTA.

FUTURE WORK

This study is complete.

REFERENCES

1. F. A. Garner, Fusion Reactor Materials Semiannual Progress Report DOE/ER-0313/8 (1990) p. 125.

2. J. F. Stubbins and F. A. Garner, J. Nucl. Mater. 191-194 (1992) in press.

3. T. Muroga, Annual Progress Report for Fusion Year 1990, FFTF-MOTA Japan-USA Collaboration, p. 95.

Completion of the ORR/MFE-4 Experiment Involving High Rates of Helium Generation in Fe-Cr-Ni Alloys · N. Sekimura, (University of Tokyo) and F. A. Garner, (Pacific Northwest Laboratory)[3]

OBJECTIVE

The objective of this effort is to determine the relative influence of helium and other important variables on neutron-induced microstructural evolution.

SUMMARY

Completion of the microscopy examination of the ORR/MFE-4 experiment confirms the conclusions reached earlier in this study. Helium generated at very high levels (~30 to 60 appm/dpa) does indeed strongly influence the microstructural evolution of Fe-Cr-Ni austenitic alloys, especially when the temperature history involves a large number of low temperature excursions. Under these conditions the effect of composition and starting condition are relatively unimportant.

PROGRESS AND STATUS

Introduction

In an earlier report it was shown that two nominally similar irradiation experiments conducted in ORR and EBR-II involving simple ternary Fe-Cr-Ni alloys yielded vastly different responses in mechanical behavior[1]. Microscopy analysis on a subset of the alloys from this experiment have been reported earlier[2] and demonstrated that a significant and unprecedented refinement of cavity microstructure had occurred during irradiation in the ORR. This refinement caused an atypically large strengthening of the various alloys. The cavity microstructure also was only weakly dependent on the nickel content of the alloys, a result that was inconsistent with the behavior usually exhibited in Fe-Cr-Ni alloys irradiated in other reactors. It was shown, however, that the usual behavior observed in the ORR/MFE-4 experiment reflected primarily the action of large reductions in temperature on an almost daily basis.[2,3]

Whereas the microscopy results were presented earlier for Fe-15Cr-XNi (X=20, 25, 30, 35, 45 wt.%) in the annealed condition at 330, 400 and 500°C, the other conditions examined in this experiment have now been completed. These are (1), the annealed Fe-15Cr-XNi series at 600°C, (2) 20% cold worked Fe-15Cr-25Ni and Fe-15Cr-35Ni at both 500 and 600°C, and (3), the annealed Fe-YCr-35Ni (Y=7.5, 15, 22, wt.%) alloys at both 500 and 600°C.

Results

Figures 1 and 2 present comparisons of the cavity densities and sizes observed in the annealed Fe-15Cr-XNi series from the ORR experiment with the densities observed in comparable experiments conducted in EBR-II. The densities at 330°C in ORR are higher than those observed at 400°C but cannot be easily measured. Except at 20Ni the sizes at 330°C are comparable to those at 400°C. While the densities observed in EBR-II usually fall with nickel content at relatively low temperatures and sometimes exhibit a minimum with nickel content at higher temperatures, the cavity densities in ORR tend to increase slowly with nickel content at all temperatures studied.

Whereas it was shown earlier that the cavities at 330 and 400°C were clearly helium bubbles,' at higher temperature the behavior is a little more complex. Note in Figure 3 that at 500°C a transition from void- to bubble-dominated microstructure occurs with increasing nickel. Figure 4 shows that bubble-dominated behavior has probably returned at 600°C.

As shown in Figure 5, cold working seems to exert very little influence on cavity size or density for each of the four alloy/temperature combinations examined. In general, cold working decreases swelling, except for the 35Ni alloy at 600°C (Figure 6). A comparison of the cavity size distributions for the annealed and cold worked alloys at 500°C (Figure 7) shows that cold working leads to a suppression of the larger void sizes only. These larger voids are probably those that nucleated early in the irradiation, before large amounts of helium were generated. These voids appear to be the ones most likely to be suppressed by cold working. At 600°C the void size distributions mirror the swelling behavior (Figure 8), with cold working decreasing the higher void sizes at 25Ni but increasing them at 35Ni.

Chromium generally increases swelling in Fe-Cr-Ni alloys[4] and this clearly happens at 500°C as shown in Figure 9a, but the influence of chromium is not as pronounced as observed in EBR-II irradiations. At 600°C this situation is less clear and may reflect the known tendency of these alloys to densify prior to swelling in response to a radiation-induced spinodal-like decomposition. The cavity sizes and densities are shown in Figures 9a, 9b and 10.

'Pacific Northwest Laboratory is operated for the U.S. Department of Energy by Battelle Memorial Institute under Contract DE-AC06-76RLO 1830.

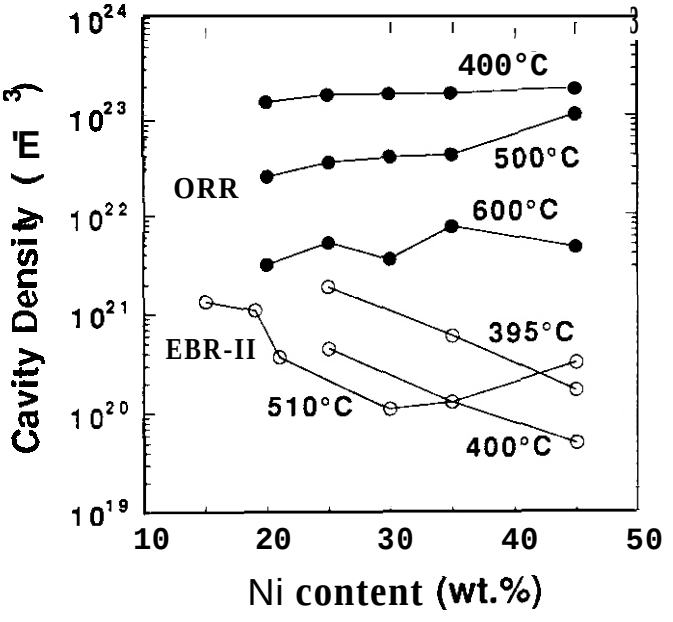

Fig. 1. Comparison of cavity densities observed in annealed Fe-15Cr-XNi alloys after irradiation in ORR and EBR-II. The EBR-II data are drawn from references 2 and 5.

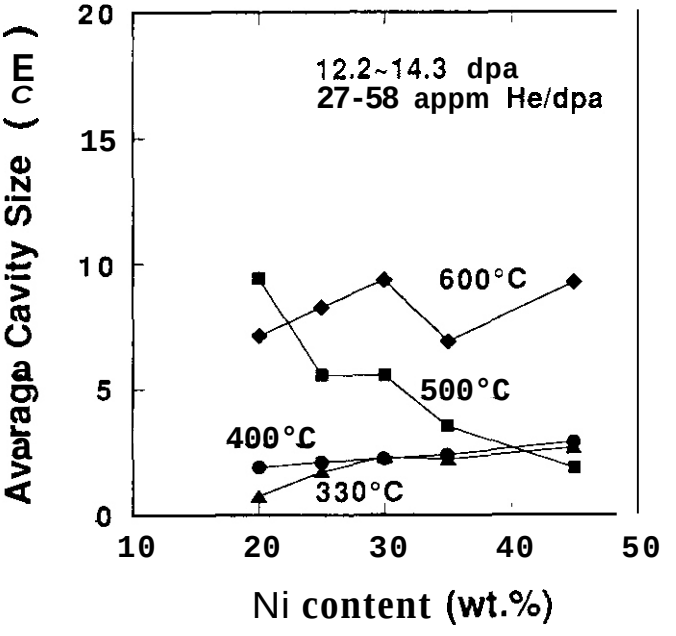

Fig. 2. Average cavity sizes observed in annealed Fe-15Cr-XNi alloys in the ORR experiment.

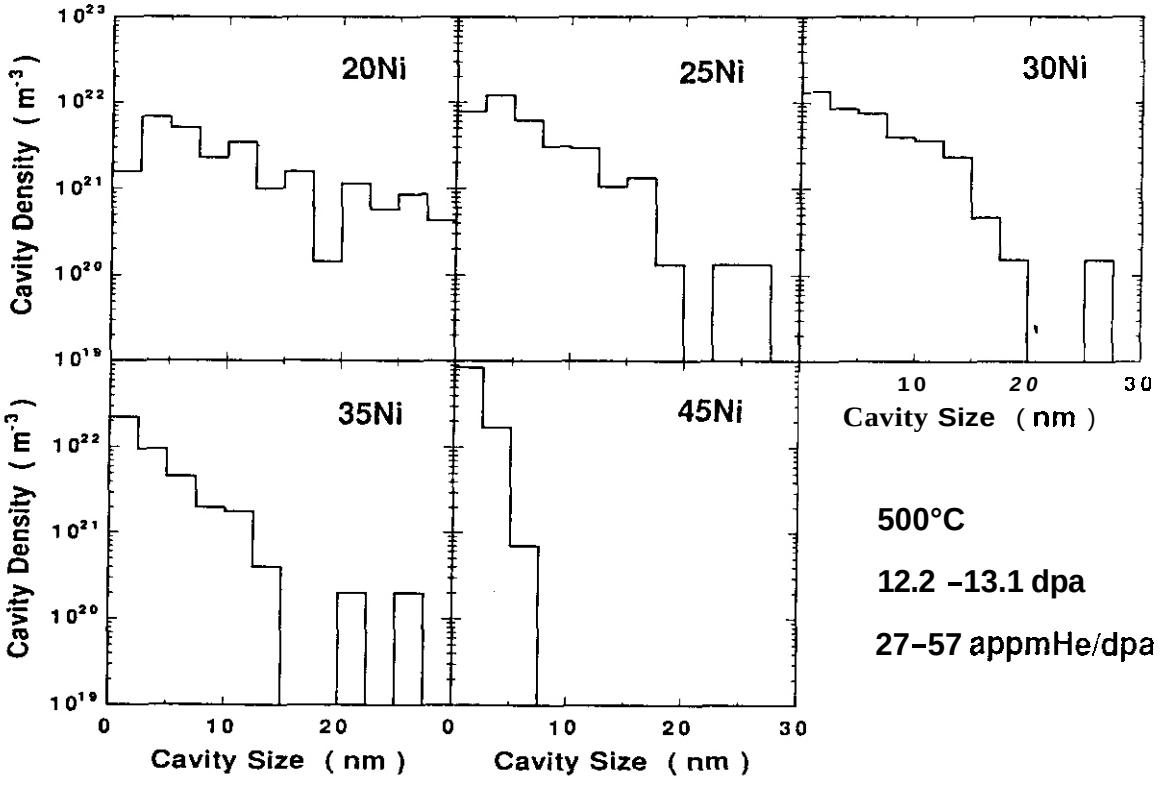

Fig. 3. Cavity size distribution observed in annealed Fe-15Cr-XNi alloys irradiated in ORR at 500°C

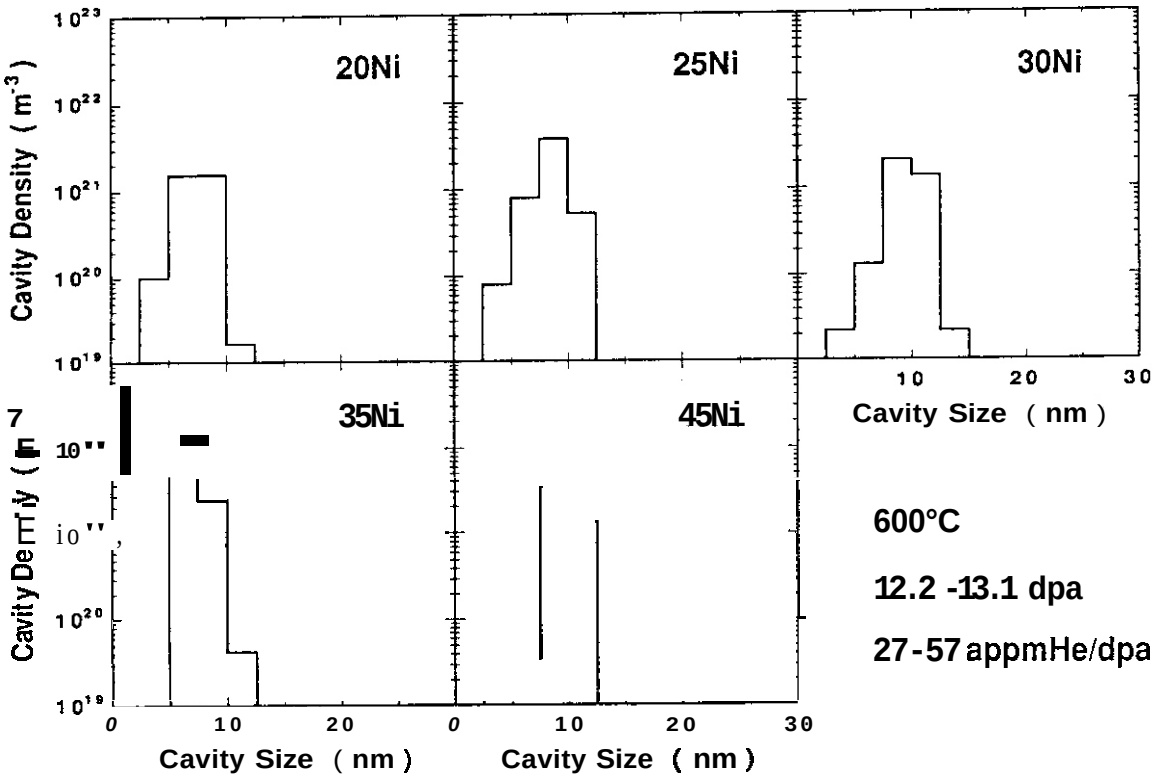

Fig. 4. Cavity size distributions observed in annealed Fe-15Cr-XNi alloys irradiated in ORR at 600°C.

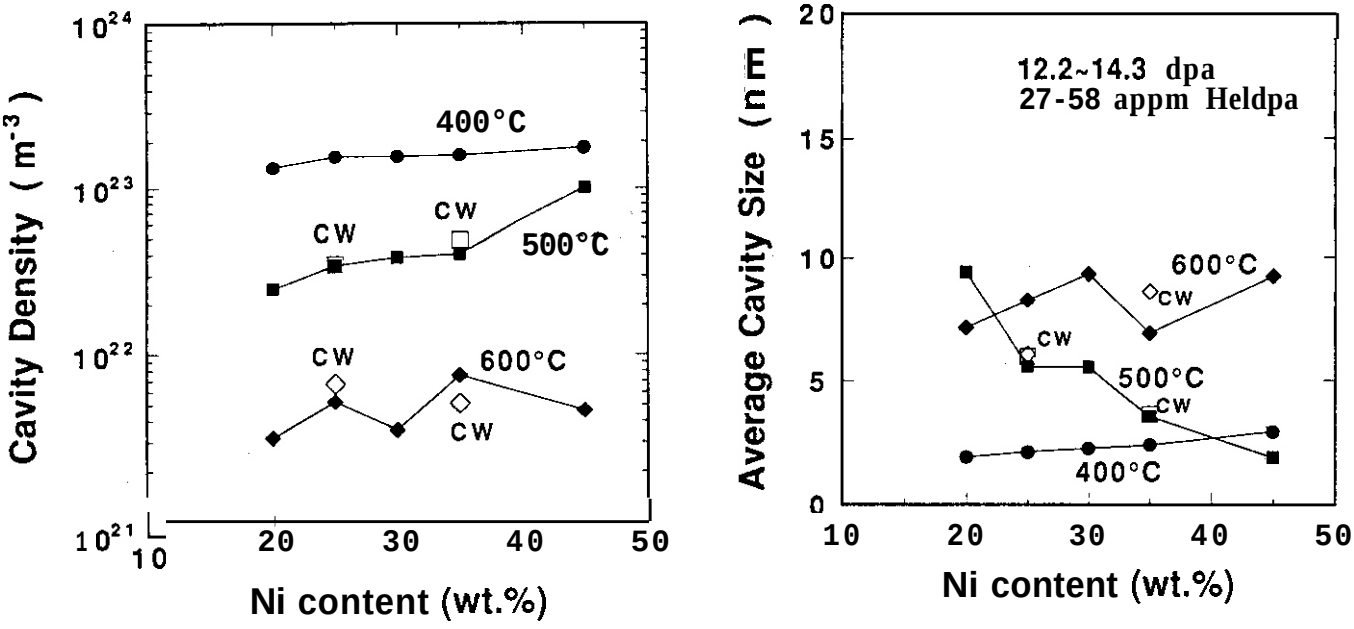

Fig. 5.Effect of cold work on cavity sizes and densities.

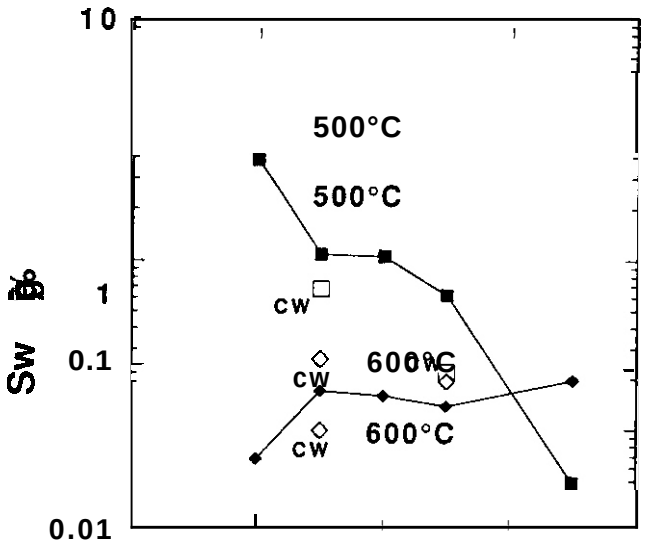

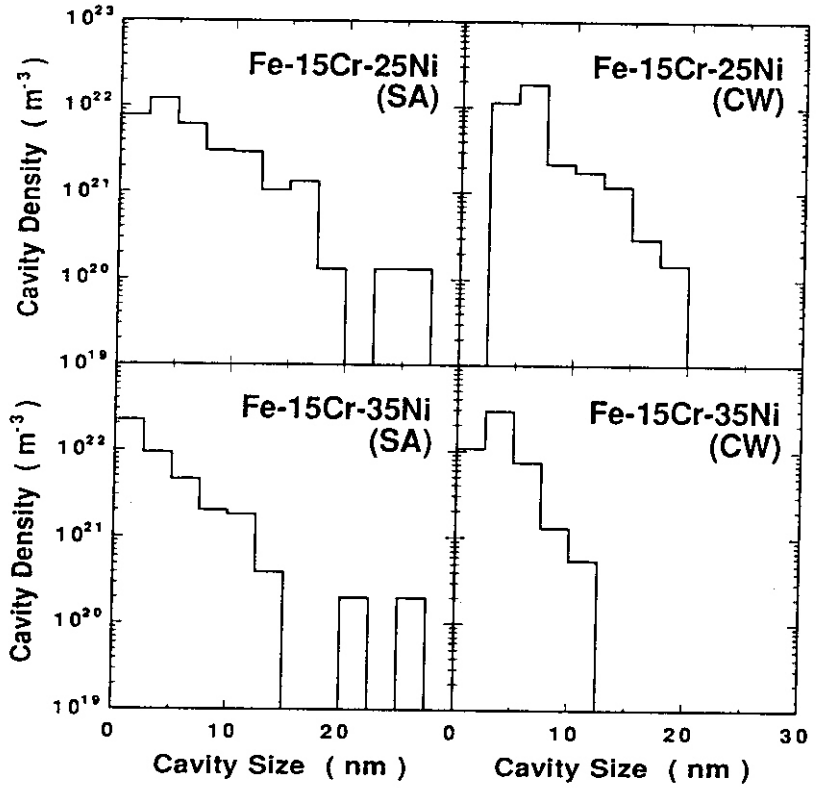

Fig. 7. Effect of cold work on cavity size distribution at 500°C.

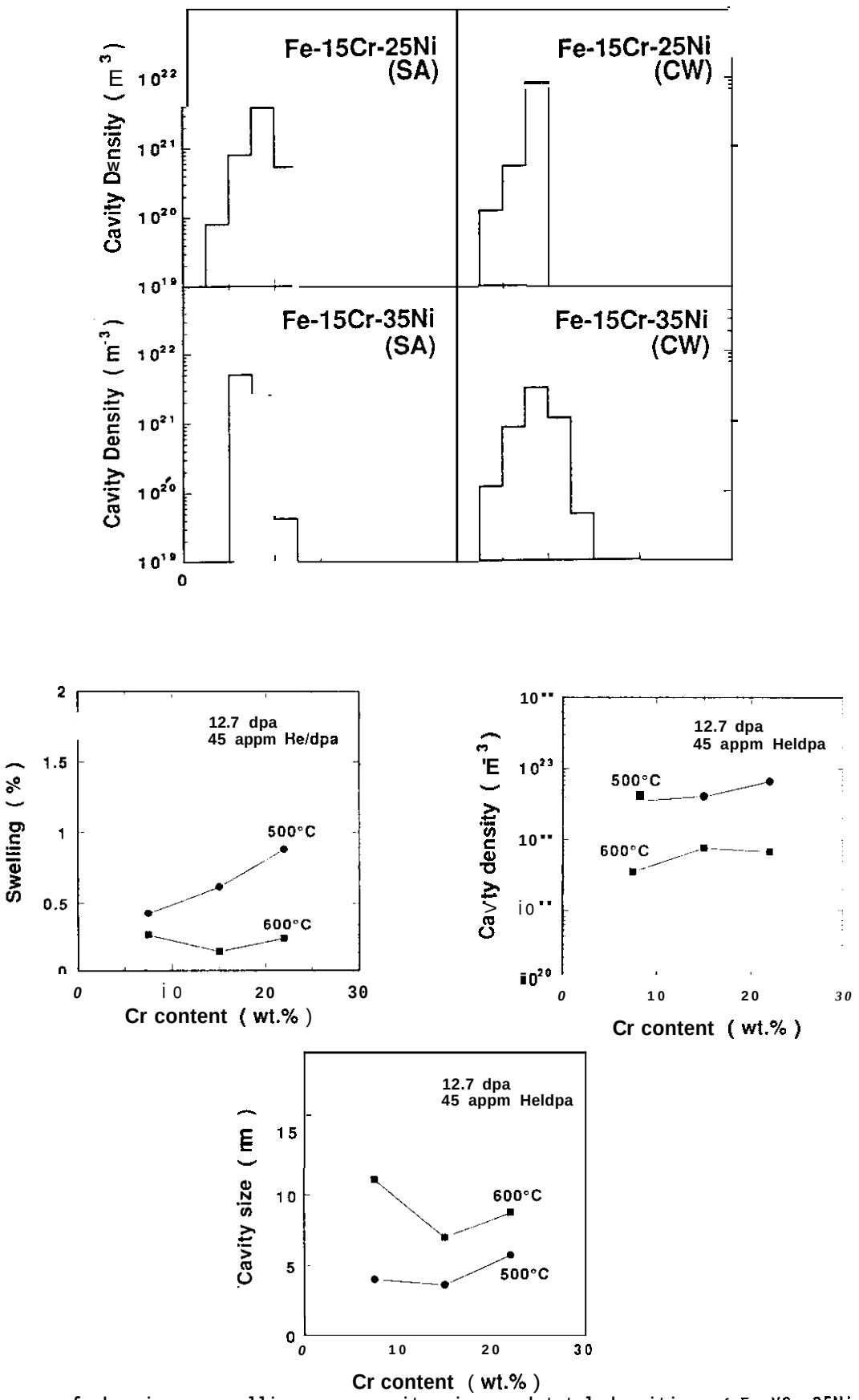

Fig. 9. Influence of chromium on swelling, mean cavity sizes and total densities of Fe-YCr-35Ni alloys in ORR.

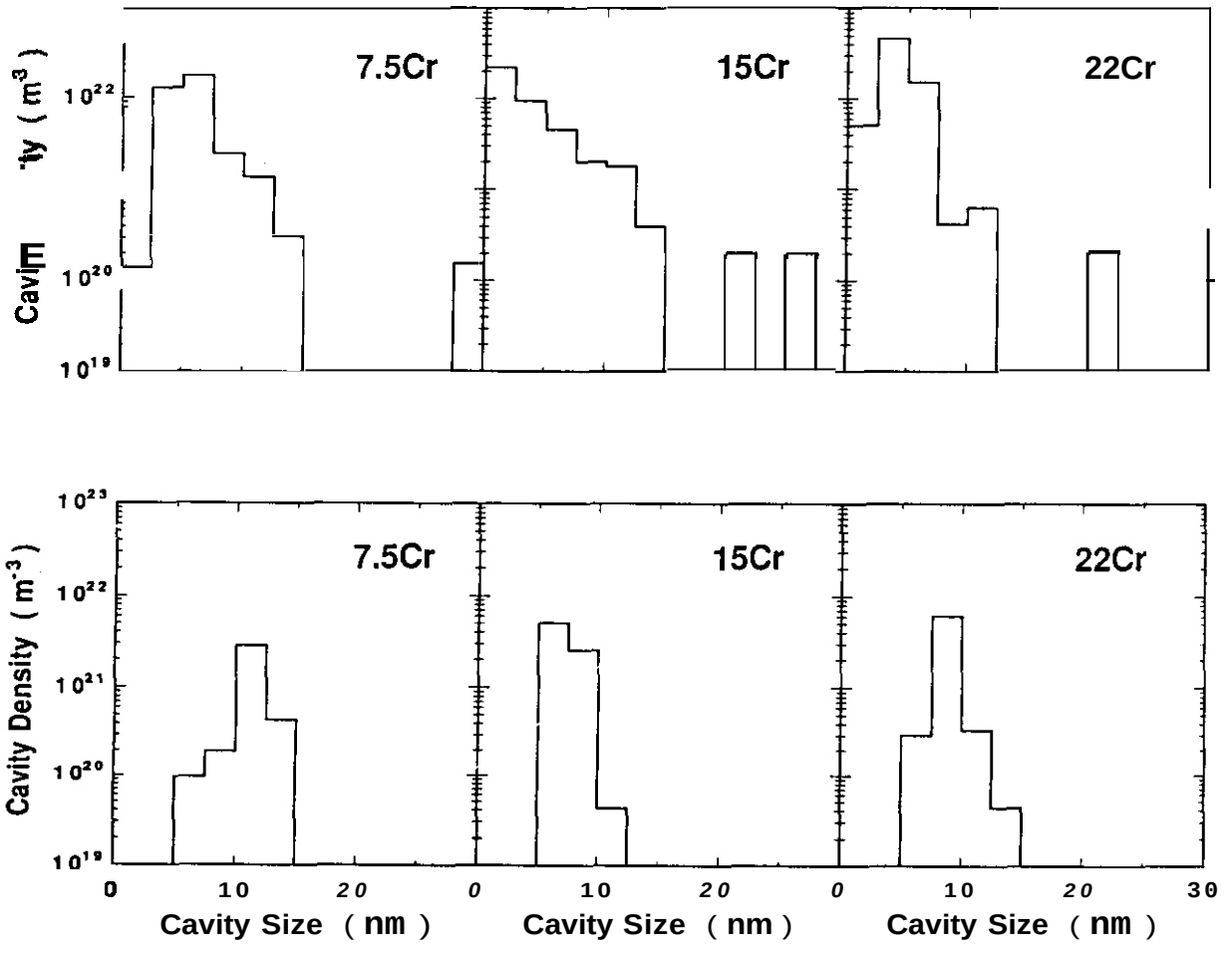

Fig. 10. Effect of chromium level on the details of void size distributions of Fe-YCr-35Ni alloys at 500°C (top) and 600°C (bottom).

Discussion

It appears that the most important variable in this experiment is not the nickel content directly, but is the indirect effect of nickel in determining the helium generation rate. The latter is compounded, however, by the temperature history of this experiment, whereby frequent (~600) setbacks in temperature lead to constant and profuse nucleation of low temperature microstructural components, primarily small dislocation loops. Nucleation of helium bubbles on these loops is thought to be the origin of the unprecedented high density of cavities.

FUTURE WORK

Analysis of these data will continue.

REFERENCES

1. M. L. Hamilton, A. Okada and F. A. Garner, J. Nucl. Mater. 179-181 (1991) 558.

2. N. Sekimura, F. A. Garner and R. D. Griffin, J. Nucl. Mater. 191-194 (1992) in press.

3. F. A. Garner et al., The Influence of Details of Reactor History on Microstructural Development During Neutron Irradiation, in this semiannual report.

4. F. A. Garner and A. S. Kumar, ASTM STP 955, p. 289 (1987).

5. T. Muroga, F. A. Garner and S. Ohnuki, J. Nucl. Mater. 179-181 (1991) 546

^{59}Ni Isotopic Tailoring Experiment: Results of Tensile Tests on MOTA-1G Specimens

M. L. Hamilton and F. A. Garner, (Pacific Northwest Laboratory)[a]

OBJECTIVE

The objective of this study is to provide insight into the influence of helium on radiation-induced microstructural evolution and the subsequent change in mechanical properties of austenitic alloys.

SUMMARY

Tensile tests have been conducted on the last two groups of isotopic tailoring specimens discharged from MOTA-1G. The results agree with those reported earlier, showing a very small impact of fusion-relevant helium/dpa levels on neutron-induced changes in tensile properties of three model austenitic alloys.

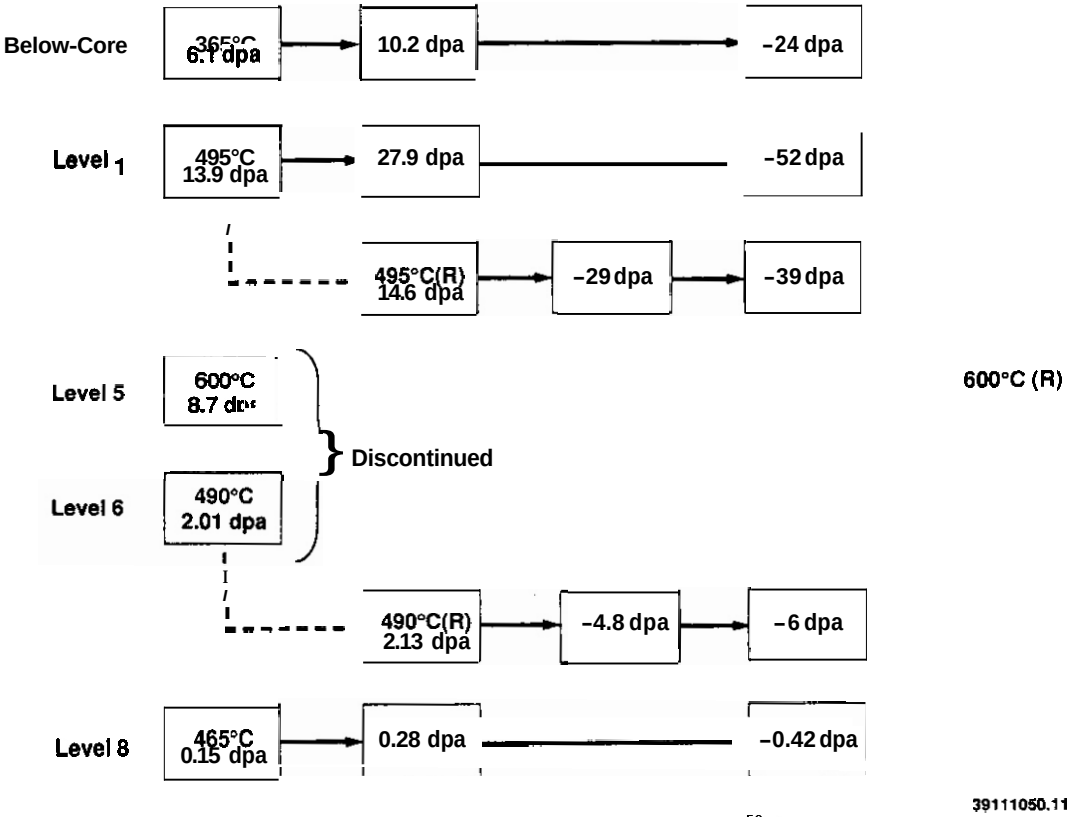

Fig. 1. Schematic representation of irradiation sequences for the ^{59}Ni isotopic tailoring experiment. "495°C(R)," "490°C(R)" and 600°C(R) refer to the replacement sequences substituted for the original compromised sequences at these temperatures. Damage levels shown represent cumulative totals. The dpa level for 600°C(R) is undefined at present.

[a]Pacific Northwest Laboratory is operated for the U.S. Department of Energy by Battelle Memorial Institute under Contract DE-AC06-76RLO 1830.

The last two sets of tensile tests have now been conducted at room temperature. These are the (490°C, 6 dpa) and (465°C, 0.42 dpa) groups of specimens. These sequences were run at (0.3 and 20 appm He/dpa) and (0.3 and 62 appm He/dpa), respectively. Note that the original 490°C sequence was discontinued after an overtemperature/undertemperature event compromised the experiment. The replacement sequence, 490°C(R), was conducted in a completely isothermal manner.

Results

The yield strength and total elongation data for the full series of irradiations at 490 and 465°C are shown in Figures 2 and 3. At 490°C the yield strengths of the cold-worked and annealed specimens are converging in each of the three alloys studied, although the gap in strength is closing rather slowly. The elongation data exhibit a similar convergence. While the yield strengths of both the annealed and cold-worked alloys exhibit essentially no dependence on helium/dpa level, there is a small effect of helium on the elongation, but only for the annealed Fe-15Cr-25Ni-0.04P alloy. The cold-worked alloys do not exhibit a significant influence of helium on elongation. The impact of the non-isothermal temperature history appears to be significant only for the Fe-15Cr-25Ni alloy (hoth starting conditions).

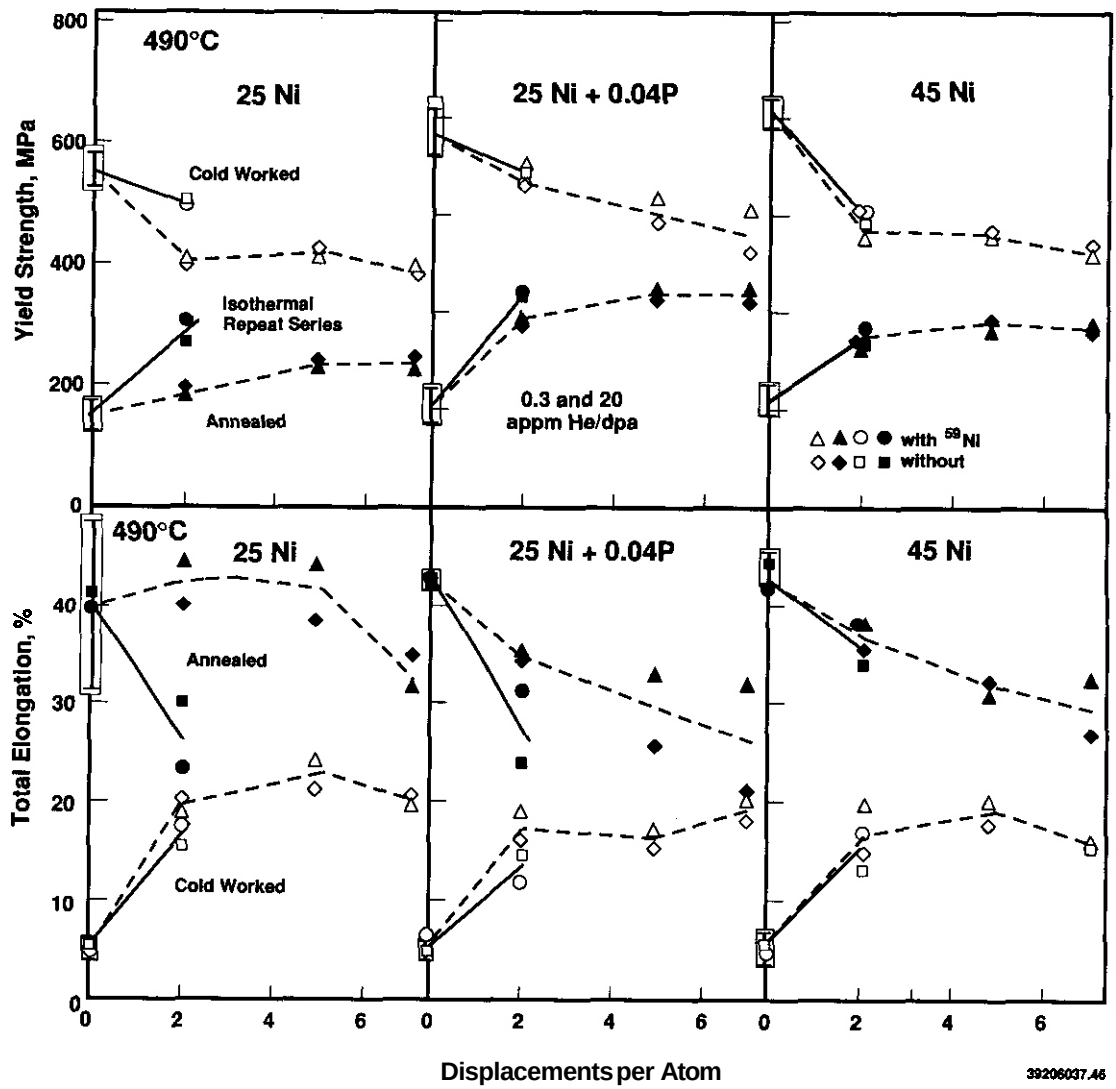

Fig. 2. Influence of thermomechanical starting state, isotopic doping and temperature history on yield strength and elongation following irradiation just above the core at 490°C. The dotted lines correspond to the isothermal repeat sequence.

Convergence also appears to be occurring in the 465°C sequence with very little influence of helium on the yield strength. Approximately 25 appm have accumulated in the doped specimens at an exposure of 0.4 dpa in this low dose rate experiment. There may be some increasing influence of helium on the elongation of the cold-worked Fe-15Cr-25Ni+0.04P alloy with increasing dpa level. This possibility will be examined further using microscopy.

Future Studies

Microscopy on the 465 and 490°C series is in progress at the University of Illinois (J. F. Stubbins) and the University of Tokyo (H. Kawanishi), respectively. When complete, the microstructural data will be used to make predictions of yield strength for comparisons with the measured values.

A repeat sequence at 600°C has completed irradiation in MOTA-26. After discharge from the reactor, tensile tests and microstructural examination will be conducted. This will complete the final stage of the ^{59}Ni isotopic tailoring experiment.

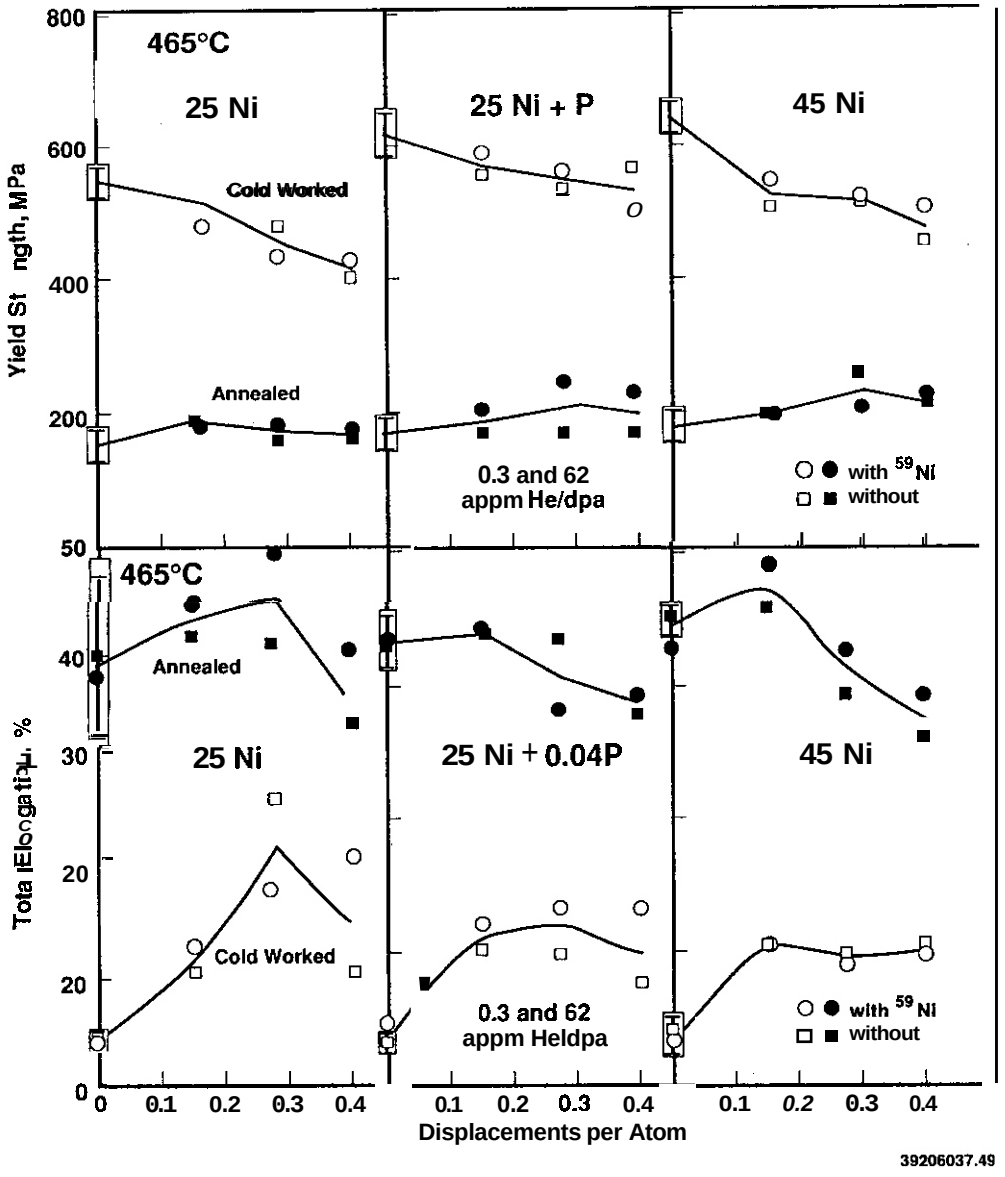

Fig. 3. Influence of thermomechanical starting state and isotopic doping on yield strength and elongation following irradiation high above the core at 465°C.

REFERENCES

1. R. L. Simons, H. R. Brager and W. Y. Matsumoto, Journal of Nuclear Materials 141-143 (1986) 1057-1060.

2. M. L. Hamilton and F. A. Garner, in Fusion Reactor Materials Semiannual Progress Report DOE/ER-0313/11 (1992) 63-71.

MICROSTRUCTURAL EVOLUTION IN IRRADIATED Fe-Cr-M ALLOYS: SOLUTE EFFECTS - D. S. Gelles, (Pacific Northwest Laboratory)[a]

OBJECTIVE

The objective of this effort is to improve understanding of the effect of fast neutron irradiation on microstructural evolution in ferritic alloys.

SUMMARY

A series of alloys based on Fe-10Cr with solute additions of silicon, vanadium, manganese, tungsten, tantalum, and zirconium at 0.1 and 1.0% levels, has been examined by transmission electron microscopy following fast neutron irradiation. Marked differences in dislocation evolution and void shape following neutron irradiation were found as a function of alloying. The present study extends previous examinations by investigating microstructural response following irradiation at a lower temperature (365°C) to 30 dpa and to a higher dose, 100 dpa, at 410°C. Swelling level, void shape, and dislocation configuration continued to vary as a function of the various solutes present in the same manner as seen previously. However, two additional observations were made. Irradiation at the lower temperature promotes precipitation of chromium rich a' phase and reduces microstructural evolution. Also, irradiation to higher dose, reduces the effect each solute exerts by lessening the wide variation in void shape and dislocation evolution that were found at lower dose.

PROGRESS AND STATUS

Introduction

Effects of radiation induced segregation in ferritic alloys are generally difficult to demonstrate.[1-11] The scale of the segregation is small, often on the order of 1-2 nm, neutron irradiation drives many solute additions away from point defect sinks,[8-11] and precipitation rapidly removes solute from solution. Microchemical analysis procedures based on analytical electron microscopy are more difficult than for example for austenitic alloys, due to the added complication of inherent specimen magnetism. However, a series of alloys based on Fe-10Cr with solute additions of silicon, vanadium, manganese, tungsten, tantalum, and zirconium at 0.1 and 1.0% levels, has shown marked differences in dislocation evolution and void shape following neutron irradiation at 426°C to 30 dpa.[12] This has been interpreted as a direct demonstration of segregation effects.[12] The present study extends previous examinations by investigating microstructural response following irradiation in the Fast Flux Test Facility/Materials Open Test Assembly (FFTF/MOTA) at a lower temperature (365°C) to 30 dpa and to a higher dose, 100 dpa, at 410°C.

Experimental Procedure

A series of ternary substitutional solid solution alloys was prepared using standard laboratory arc melting practices as previously described.[11] The series was based on Fe-10Cr (all compositions given in weight percent) with solute additions of Si, Mn, V, W, Ta and Zr at levels of 0.1 and 1.0%. Disk specimens for transmission electron microscopy (TEM) in a fully heat treated condition (1040°C/1 h/air cool (AC) + 760°C/2 h/AC) were irradiated in FFTF/MOTA in weeper positions in-core and below-core for three successive runs, MOTA 1C-1E, in-core in positions 2C-4, 2C-2 and 2C-2 and below core in positions 8D-1, BD-1 and BD-4, respectively. Positional differences resulted in differences in irradiation flux as well as temperature, so that although irradiqtion times were identical, the resulting temperatures and doses were 411±12°C to 92.6 dpa (2.05×10^{23} n/cm , E > 0.1 MeV) and 365°C to 25.9 dpa (7.15×10^{22} n/cm^2, E > 0.1 MeV), respectively. These doses are rounded to 100 and 30 dpa, respectively, in the remainder of this paper. In comqarison, the irradiation of these specimens as previously reported,[12] resulted in a dose of 32.7 dpa ($\times 10^2$ n/cm^2, E > 0.1 MeV) at 426°C.

Following irradiation, densities were determined by the immersion density technique, and then specimens were prepared for TEM examination using standard procedures. Examinations were performed on a JEOL JEM-1200 EX scanning transmission electron microscope (STEM) using a double tilting side-entry goniometer stage. Images were generally taken near (011) using $\vec{g}$ = 200 and 011 dislocation contrast and using void contrast, but on occasion, images could not be stigmated near (011) and orientations near (001) had to be used.

Results

Density measurements

The results of density measurements are given in Table 1. Followin irradiation at 365°C, swelling levels were below 1% and generally about ±0.2%. The highest swelling was found in alloys containing silicon, 0.44 and 0.60% for 0.1 and 1.0% Si, respectively. Alloys containing manganese showed densification, indicating that phase instability had occurred.

---

[a]Pacific Northwest Laboratory is operated for the U.S. Department of Energy by Battelle Memorial Institute under Contract DE-AC06-76RLO 1830.

Table 1. Results of density measurements on solute containing Fe-10Cr alloys irradiated at 365°C to 30 dpa and 410°C to 100 dpa.

Alloy	Heat No.	Code	Unirrad Density (gm/cm^3)	365°C Irrad. Density (gm/cm^3) Code KZ	Swelling (%)	410°C Irrad. Density (gm/cm^3) Code K3	Swelling (%)
-10Cr-0.1Si	R117	R9	7.8069	7.7665	0.44	7.5817	2.88
-10Cr-1Si	R118	AH	7.7194	7.6734	0.60	7.6104	1.41
-10Cr-0.1Mn	R119	AU	7.7402	7.7688	-0.37	7.6134	1.64
-10Cr-1Mn	R120	AX	7.7550	7.7554	-0.01	7.4469	3.97
-10Cr-0.1V	R121	AZ	7.7641	7.7526	0.15	7.6959	0.88
-10Cr-1V	R122	A1	7.7601	7.7455	0.19	7.7167	0.56
-10Cr-0.1W	R123	A3	7.8248	7.8113	0.17	7.5935	2.96
-10Cr-1W	R124	A4	7.8316	7.8344	0.04	7.5942	3.11
-10Cr-0.1Ta	R125	A5	7.7730	7.7660	0.09	7.7665	0.08
-10Cr-1Ta	R126	A6	7.8060	7.7962	0.13	7.5468	3.32
-10Cr-0.1Zr	R127	A7	7.7824	7.7705	0.15	7.6792	1.33
-10Cr-1Zr	R128	A9	7.7687	7.7419	0.27	7.6280	1.81

Following irradiation at 410°C, swelling levels were much higher, generally in the range from 1 to 4%. The highest swelling was found in the 1.0% Mn alloy, and the lowest in the vanadium alloys and the alloy containing 0.1% Ta.

The results are shown plotted in Figure 1 along with previous swelling measurements based on TEM for the alloys containing 1% solute following irradiation at 410°C to lower dose.[12] The solutes have been arranged on the abscissa in approximate order of increasing atomic size misfit such that Zr *is* the largest atom under consideration. From Figure 1, it can be shown that swelling following irradiation at 410°C is

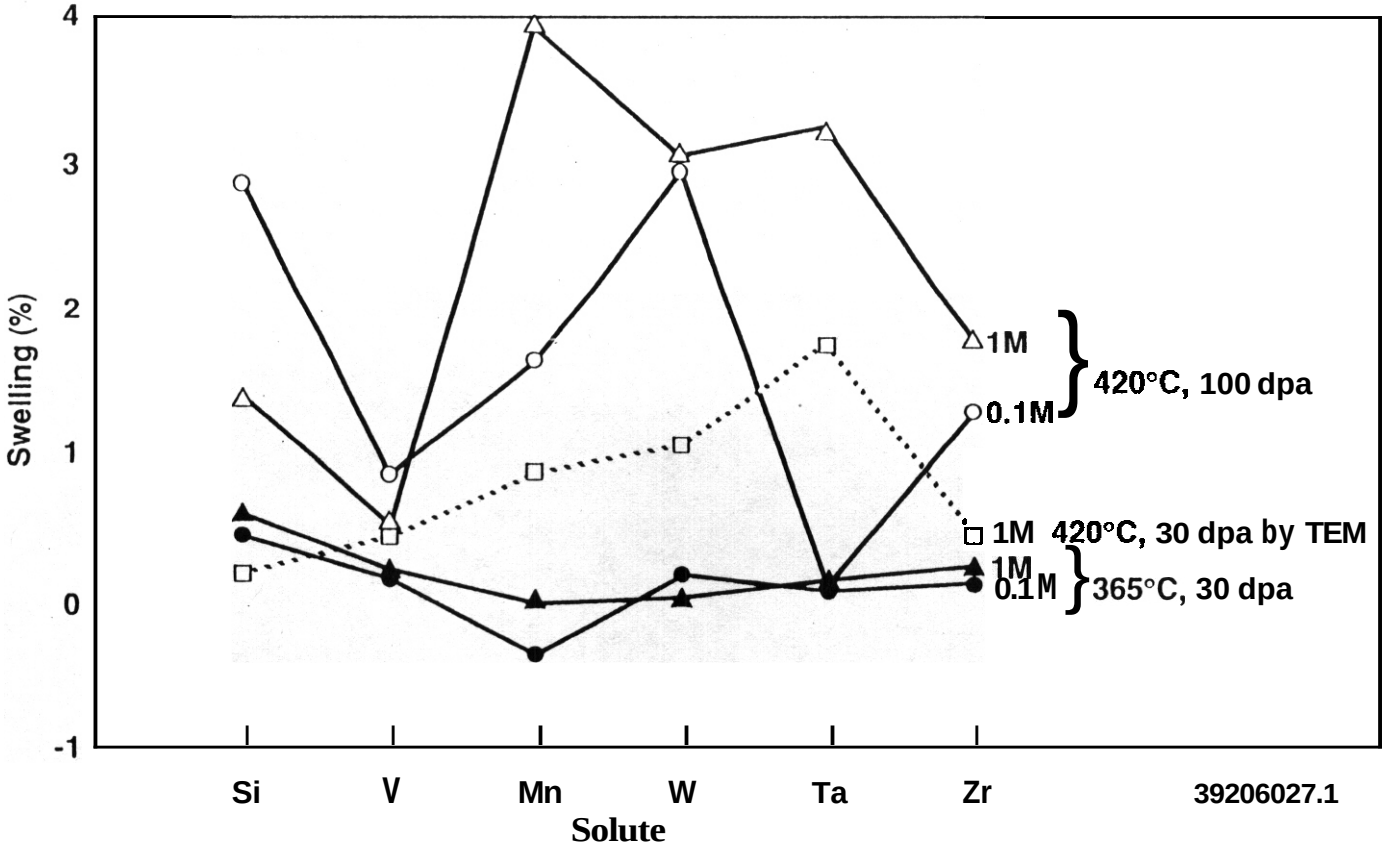

Fig. 1. Swelling as measured by density change in Fe-10Cr-M alloys following irradiation at 365°C to 30 dpa and at 410°C to 100 dpa in comparison with swelling measured by electron microscopy following irradiation at 426°C to 30 dpa. Solute elements are arranged in order of increasing atomic size mismatch.

highest for alloys containing Mn, Ta and W, followed by alloys containing Si and Zr, and with the lowest swelling in alloys containing V. This trend is based on the average swelling for the two solute levels. The trend is insensitive to solute level, with only somewhat higher swelling in alloys with 1% solute, except for the cases of Si, V, Mn, and Ta, where swelling is higher for alloys with 0.1% Si or V and swelling is much lower in the alloys containing 0.1% Mn and Ta.

Swelling in specimens irradiated at 365°C is shown to be much lower. Only additions of Si and Mn produce significantly different behavior. Silicon additions produced the highest levels of swelling following irradiation at 365°C and manganese caused densification. Otherwise, swelling levels were limited to the range 0-0.2%.

When comparing these results with TEM results on alloys with 1.0% solute irradiated at 426°C to 30 dpa, similar but not identical response is found. The 426°C lower dose irradiation had appeared to indicate that Ta additions produced the greatest swelling and Si additions produced the lowest swelling, whereas neither trend was found following irradiation to higher dose. Also, irradiation at the lower temperature of 365°C to similar neutron dose shifted highest swelling response from Mn, W, and Ta to Si, and significantly reduced the amount of swelling. Swelling is higher following irradiation at the higher temperature for all cases except Si. Therefore, Si appears to represent the interesting case where solute additions can shift the peak swelling temperature to lower temperatures.

Microstructural Examination

Microstructural examination revealed that swelling as indicated by density change was due to void formation. Examples of the microstructures at low magnification are given in Figures 2 through 5. Figures 2 and 3 show void distributions following irradiation at 365°C for 0.1% and 1% solute levels, respectively, and Figures 4 and 5 provide similar information at lower magnification for specimens irradiated at 410°C. Voids can be identified in each micrograph, but densities are low and void sizes small following irradiation at 365°C, whereas after irradiation at 410°C, void distributions are more uniform and voids sizes are larger with the largest void sizes corresponding to specimen conditions with the largest density change. The low density change response in the vanadium containing alloys following irradiation at 410°C can be attributed to limited void growth, but for the alloy containing 0.1% Ta low swelling appears to be due to delayed void nucleation.

Many of these micrographs show a mottled background contrast due to phase instability. Phase instability is most apparent in specimens irradiated at 365°C; all micrographs in Figures 2 and 3 show background mottling typical of a' phase separation. Phase instability is less apparent in specimens irradiated at 410°C as indicated by a lower density of second phase particles. In fact, for alloys containing Mn and Ta, precipitation is very difficult to recognize, indicating the Mn and Ta additions tend to discourage a' formation.

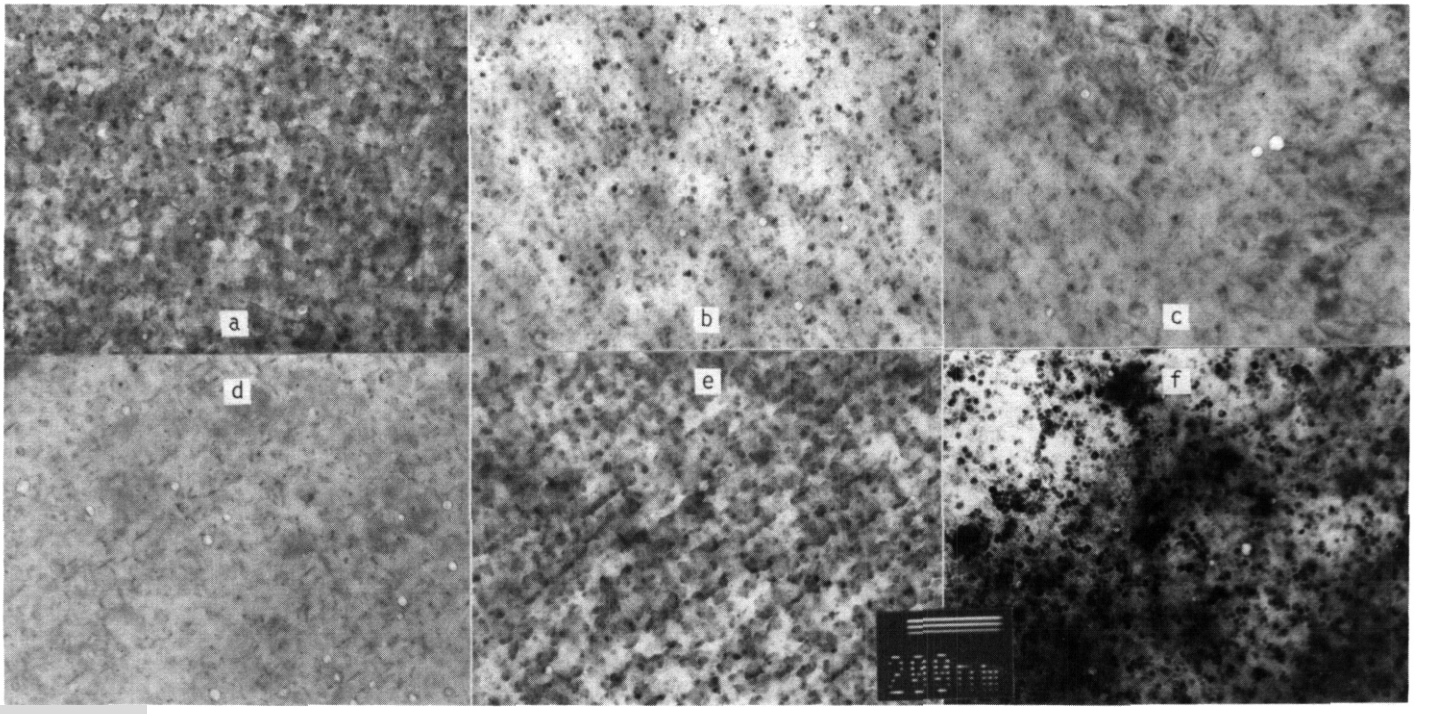

Fig. 2. Swelling microstructures in Fe-10Cr-0.1M alloys following irradiation at 365°C to 30 dpa for a) Si, b) V, c) Mn, d) W, e) Ta and f) Zr.

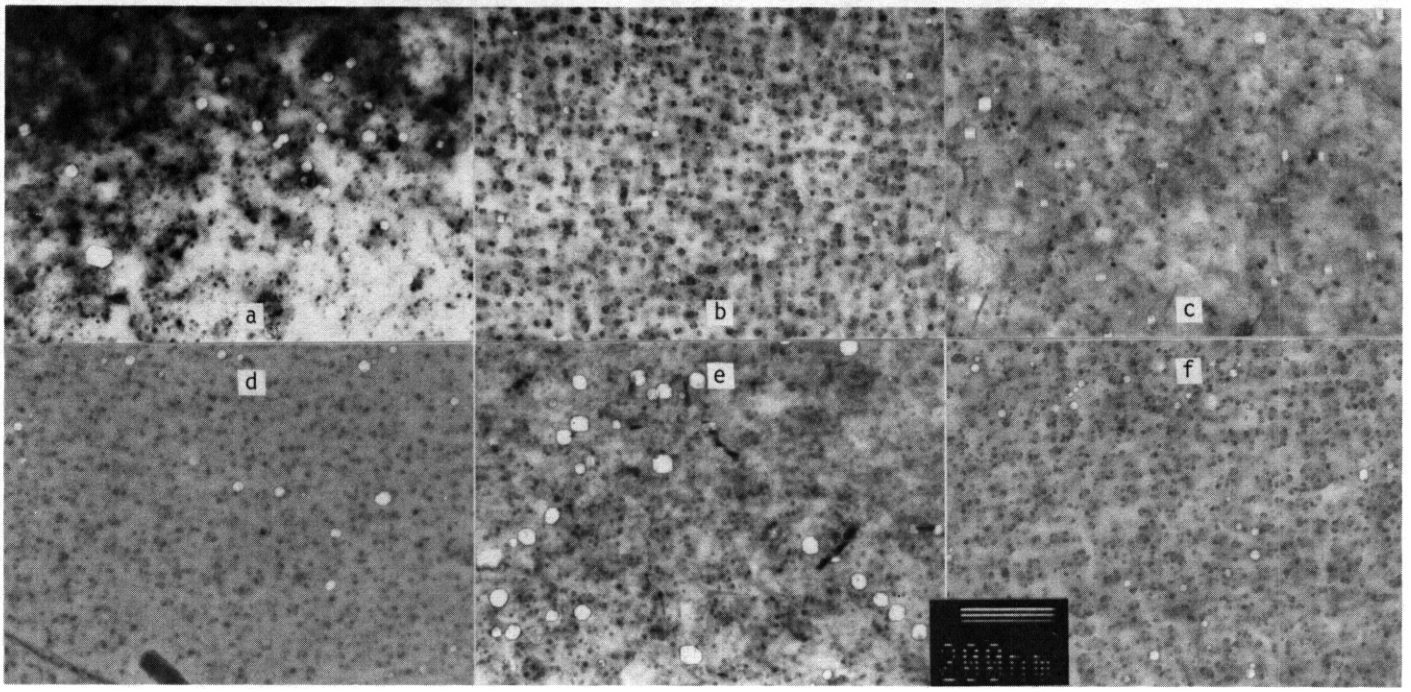

Fig. 3. Swelling microstructures in Fe-10Cr-1M alloys following irradiation at 365°C to 30 dpa for a) Si, b) V, c) Mn, d) W, e) Ta and f) Zr.

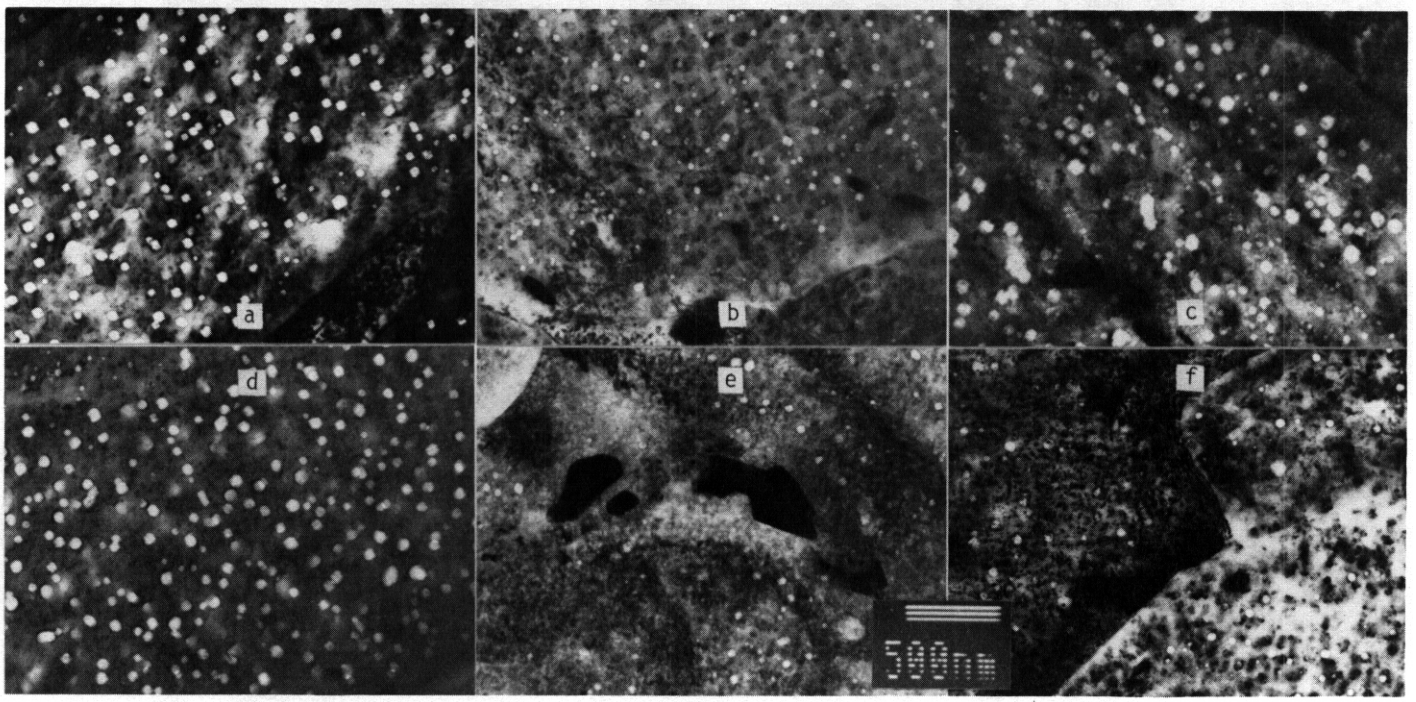

Fig. 4. Swelling microstructures in Fe-10Cr-0.1M alloys following irradiation at 410°C to 100 dpa for a) Si, b) V, c) Mn, d) W, e) Ta and f) Zr.

Microstructural evolution is shown in greater detail for specimens irradiated at 410°C to 100 dpa in Figures 6 through 17. In each case, the same area is shown using three imaging conditions. Where possible, for a foil orientation near (011), dislocation contrast using g = 011 is given in part a), dislocation contrast using g = 200 is given in part b) and void contrast is provided in part c). Exceptions occur in Figures 8 and 9 for V containing specimens and Figure 14 for 0.1% Ta where it was not possible to obtain acceptable imaging conditions for a foil orientation near (011) and so part a) uses $\vec{g}$ = 110 and part b) uses g = 200 for a foil orientation near (001).

To interpret these micrographs, the following may be noted. Comparison of $\vec{g} = 01\bar{1}$ and 200 images shows all a<100> and $\frac{a}{2}$<111> dislocations present. In g = 200 contrast, a[100] dislocations are in strong contrast and all $\frac{a}{2}$<1$\bar{1}$1> dislocations are in weaker contrast. In g = 011 contrast, the remaining a[010] and a[001] dislocations and half the $\frac{a}{2}$<111> dislocations are in contrast. Therefore, the shape and distribution of

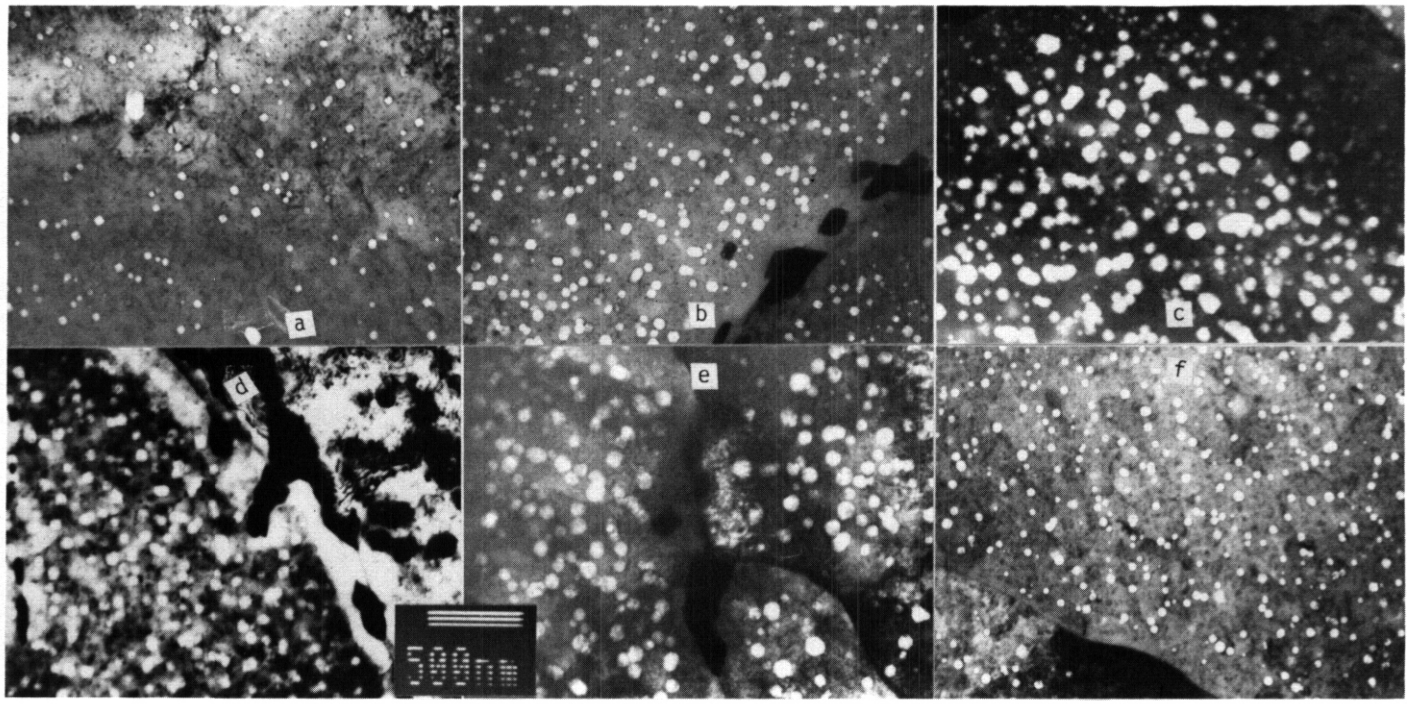

Fig. 5. Swelling microstructures in Fe-10Cr-1M alloys following irradiation at 410°C to 100 dpa for a) Si, b) V, c) Mn, d) W, e) Ta and f) Zr.

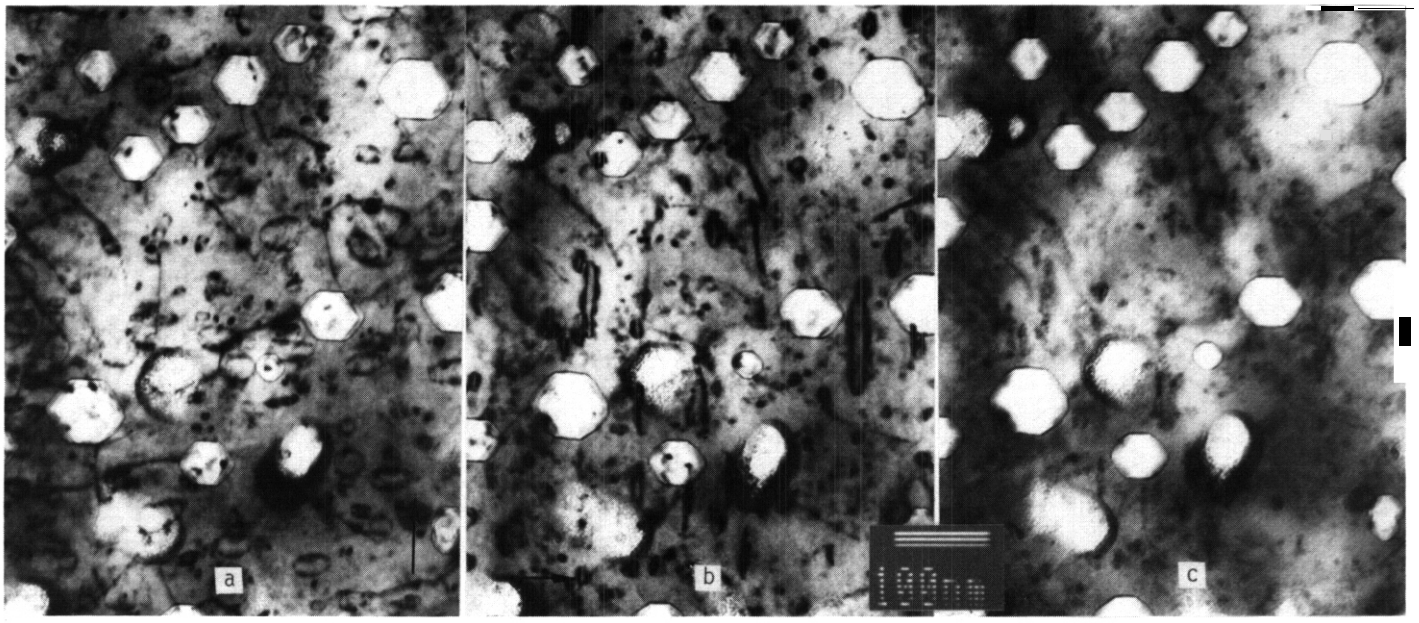

Fig. 6. Microstructure of Fe-10Cr-0.1Si following irradiation at 410°C to 100 dpa in dislocation contrast using $\vec{g}$ = 011 in a), dislocation contrast using $\vec{g}$ = 200 in b) and void contrast in c) for a foil orientation near (011).

all a<100> and $\frac{a}{2}$<111> dislocations can be determined. Figure 18 is provided to simplify void shape determination, following, for a foil in (011) orientation, void shapes from cubes to octahedra with intermediate truncation in part a), and void shapes from cubes to dodecahedra with intermediate truncation in part b).[13]

For example, Figure 6 of Fe-10Cr-0.1Si shows strong vertical dislocation images in $\vec{g}$ = 200 contrast corresponding to a<100> loops and smaller equiaxed loops in weaker contrast corresponding to $\frac{a}{2}$<111> loops. Voids are found to be dodecahedral with slight (100) truncation based on comparison with Figure 18. In like manner, Figure 7 of Fe-10Cr-1Si also contains large a<100> loops, but $\frac{a}{2}$<111> dislocations are long and winding, connected in a network, and larger voids are truncated octahedra (slightly tilted from a perfect (011) orientation.) However, smaller voids are a different shape, with greater (100) truncation approaching cubes. At lower dose, it was found that small cube shaped voids formed in Fe-10Cr-1Si but

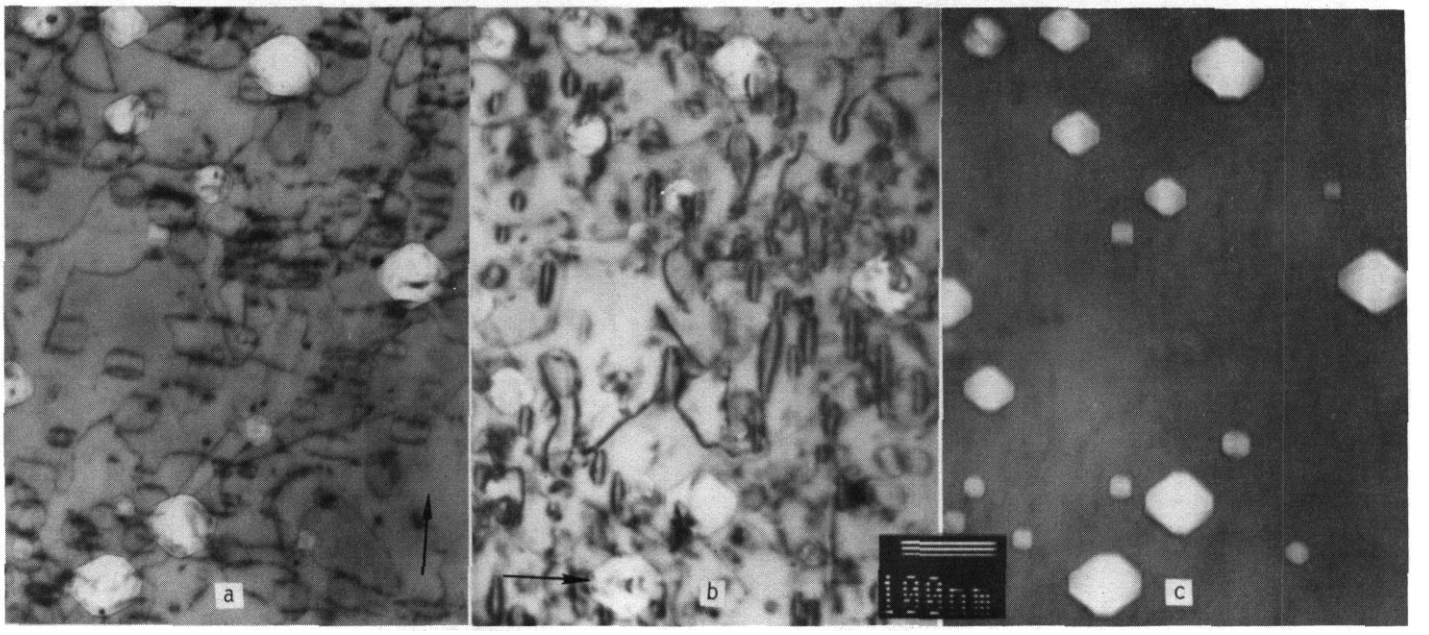

Fig. 7. Microstructure of Fe-10Cr-1Si following irradiation at 410°C to 100 dpa in dislocation contrast using $\vec{g}$ = 011 in a), dislocation contrast using $\vec{g}$ = 200 in b) and void contrast in c) for a foil orientation near (011).

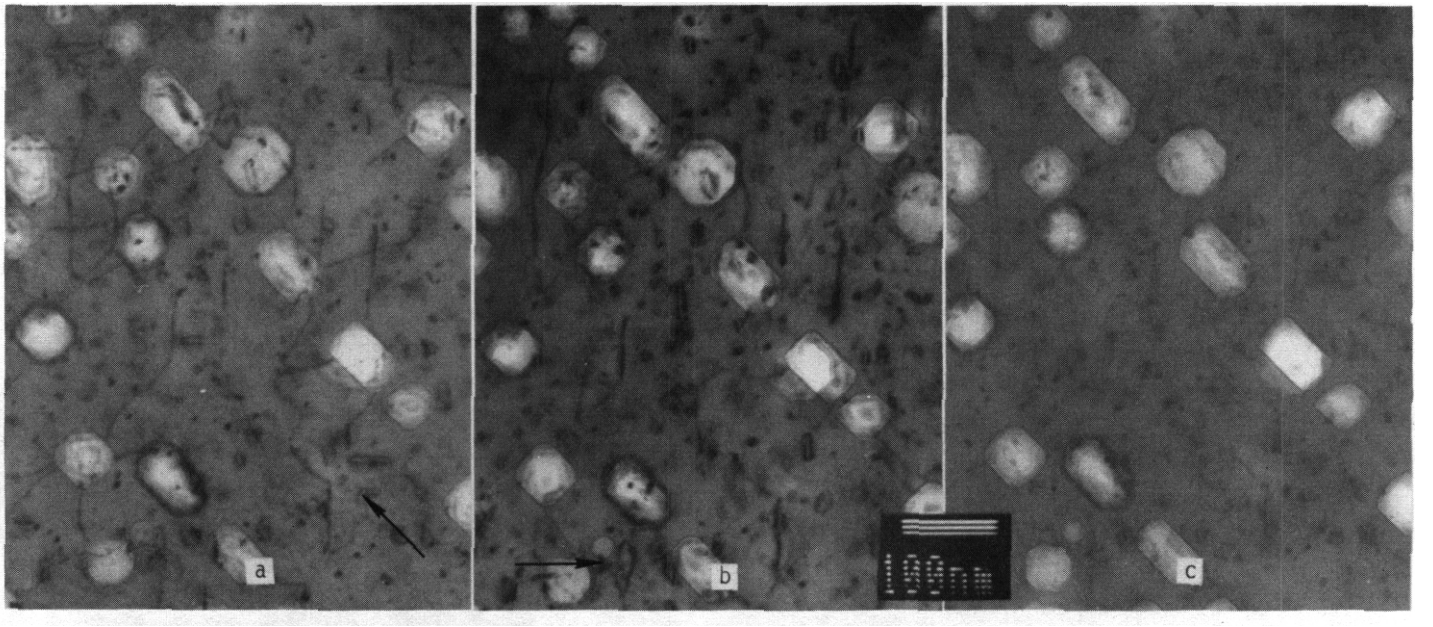

Fig. 8. Microstructure of Fe-10Cr-0.1V following irradiation at 410°C to 100 dpa in dislocation contrast using g = 110 in a), dislocation contrast using g = 200 in b) and void contrast in c) for a foil orientation near (001).

small dodecahedral voids formed in Fe-10Cr-0.1Si[12] and therefore, as cubic voids grow, with 1% Si present, a different void shape results.

Because foil orientations are near (001), interpretations from Figures 8 and 9 for alloys containing V are more difficult. Figure 8 for Fe-10Cr-0.1V shows a dislocation structure with a<100> loops and a network of both a<100> and $\frac{a}{2}$<111> dislocations and voids of dodecahedral shape with varying degrees of (100) truncation. The void shape is distinguishable from the fringe structure in Figure 8 b) indicating (110) truncation rather than (111) truncation. Figure 9 for Fe-10Cr-1V shows a dislocation structure with large a<100> loops, smaller $\frac{a}{2}$<111> loops and a network of $\frac{a}{2}$<111> dislocations. Voids can be either cuboidal with (110) truncations or dodecahedral with (100) truncations. However, void shape is not directly related to void size, so void growth does not appear to result in a change in void shape.

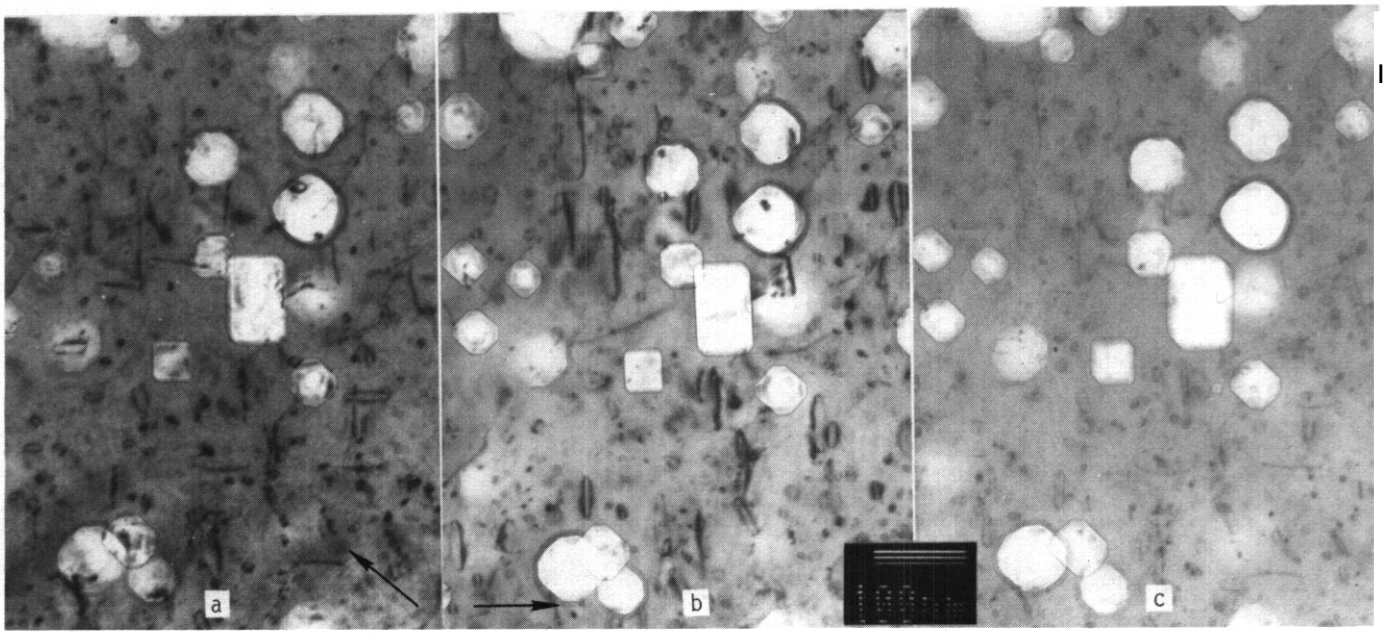

Fig. 9 Microstructure of Fe-10Cr-1V following irradiation at 410°C to 100 dpa in dislocation contrast using g = 110 in a), dislocation contrast using g = 200 in b) and void contrast in c) for a foil orientation near (001).

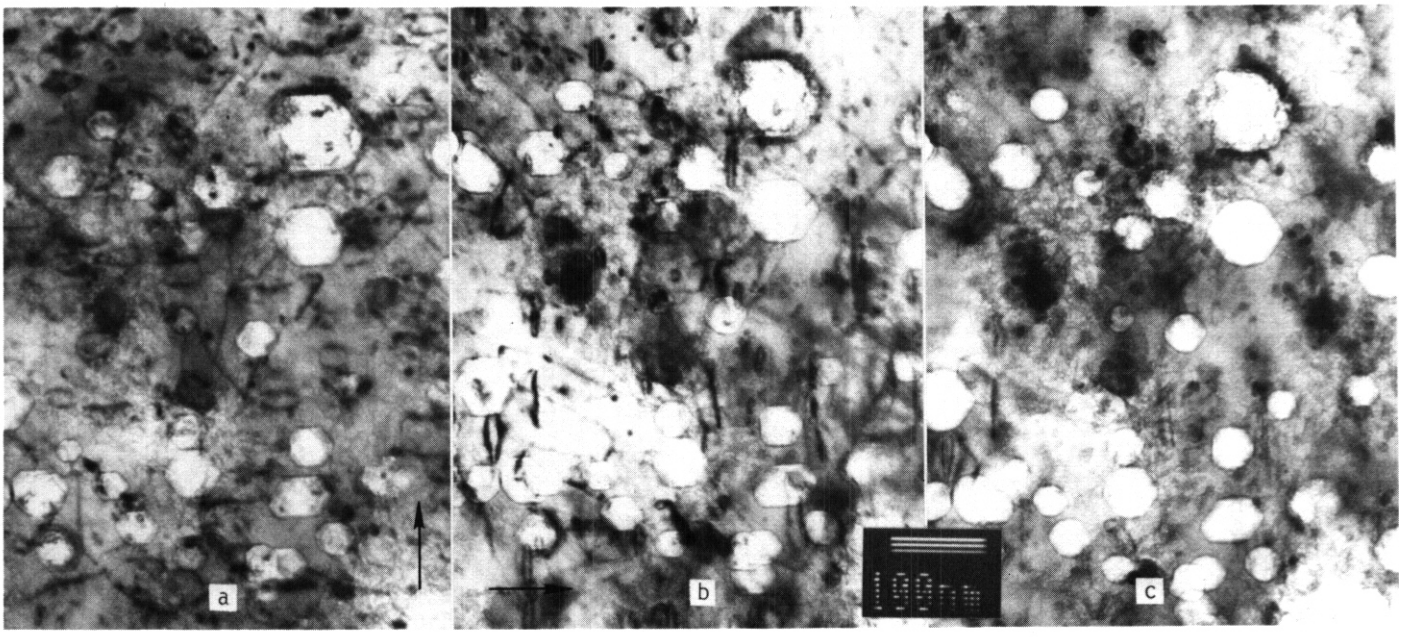

Fig. 10. Microstructure of Fe-10Cr-0.1Mn following irradiation at 410°C to 100 dpa in dislocation contrast using $\vec{g}$ = 011 in a), dislocation contrast using $\vec{g}$ = 200 in b) and void contrast in c) for a foil orientation near (011).

Microstructural development following irradiation at 410°C to 100 dpa in alloys with Mn additions gave similar but not identical response. Figures 10 indicates that for Fe-10Cr-0.1Mn, the dislocation structure consists of a<100> loops and a network of $\frac{a}{2}$<111> dislocations and voids are dodecahedral with (110) truncations. Figure 11, for Fe-10Cr-1Mn shows similar dislocation structure but voids are cuboidal with (110) truncations. Some of the largests voids were found to have large (110) truncations.

With alloys containing W additions, the level of W did not significantly change response. Figures 12 and 13 appear similar. Dislocation structures contain a<100> loops and a network of $\frac{a}{2}$<111> dislocations. This may account for the similarity in swelling response, as shown in Table I.

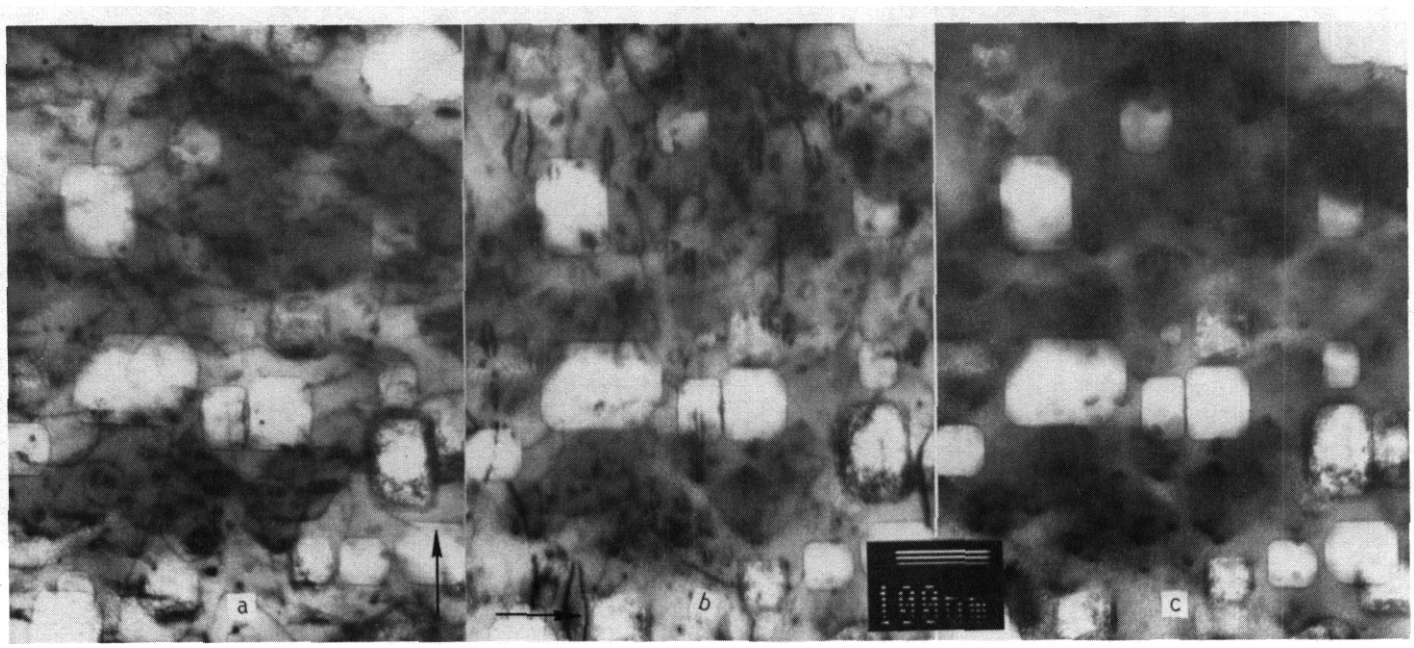

Fig. 11. Microstructure of Fe-10Cr-1Mn following-irradiation at 410°C to 100 dpa in dislocation contrast using $\vec{g}$ = 011 in a), dislocation contrast using g = 200 in b) and void contrast in c) for a foil orientation near (011).

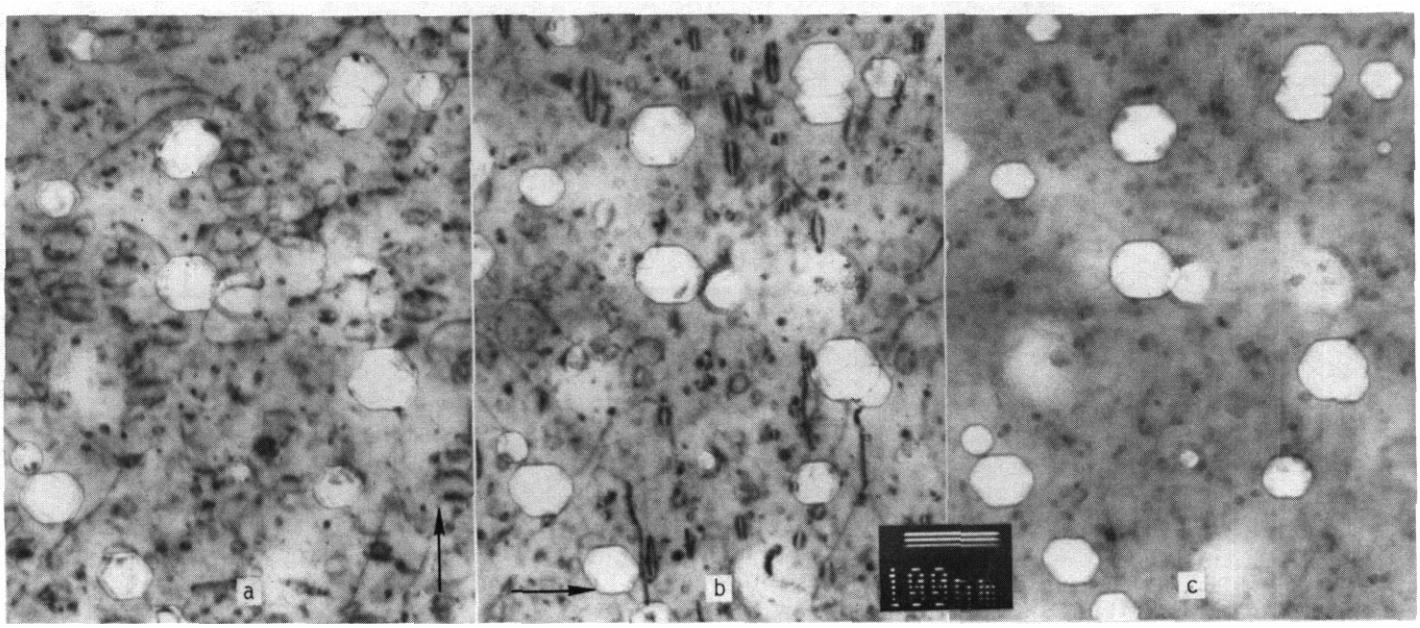

Fig. 12. Microstructure of Fe-10Cr-0.1W following irradiation at 410°C to 100 dpa in dislocation contrast using $\vec{g}$ = 011 in a), dislocation contrast using $\vec{g}$ = 200 in b) and void contrast in c) for a foil orientation near (011).

Figure 14, showing the microstructure of Fe-10Cr-0.1Ta is again for a foil near (001) orientation. Interpretation is difficult, but the dislocation structure consists of a<100> loops and a network of $\frac{a}{2}$<111> dislocations. Figure 15 shows the only grain found with a (011) orientation in a specimen of Fe-10Cr-1Ta. The dislocation structure contains a<100> loops and a network of $\frac{a}{2}$<111> dislocations, possibly including a<100> segments. Of particular note is that the void shape is different, corresponding to a shape midway between a cube and a dodecahedron.

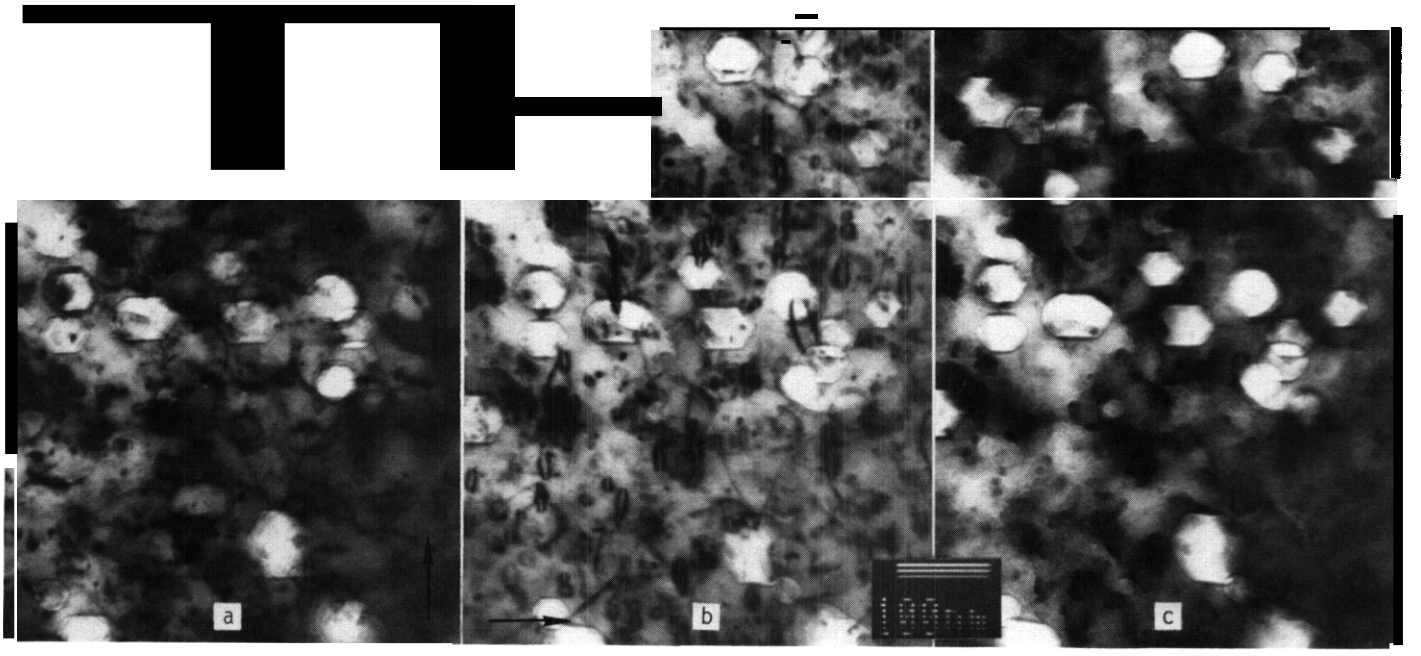

Fig. 13. Microstructure of Fe-10Cr-1W following irradiation at 410°C to 100 dpa in dislocation contrast using $\vec{g}$ = 011 in a), dislocation contrast using g = 200 in b) and void contrast in c) for a foil orientation near (011).

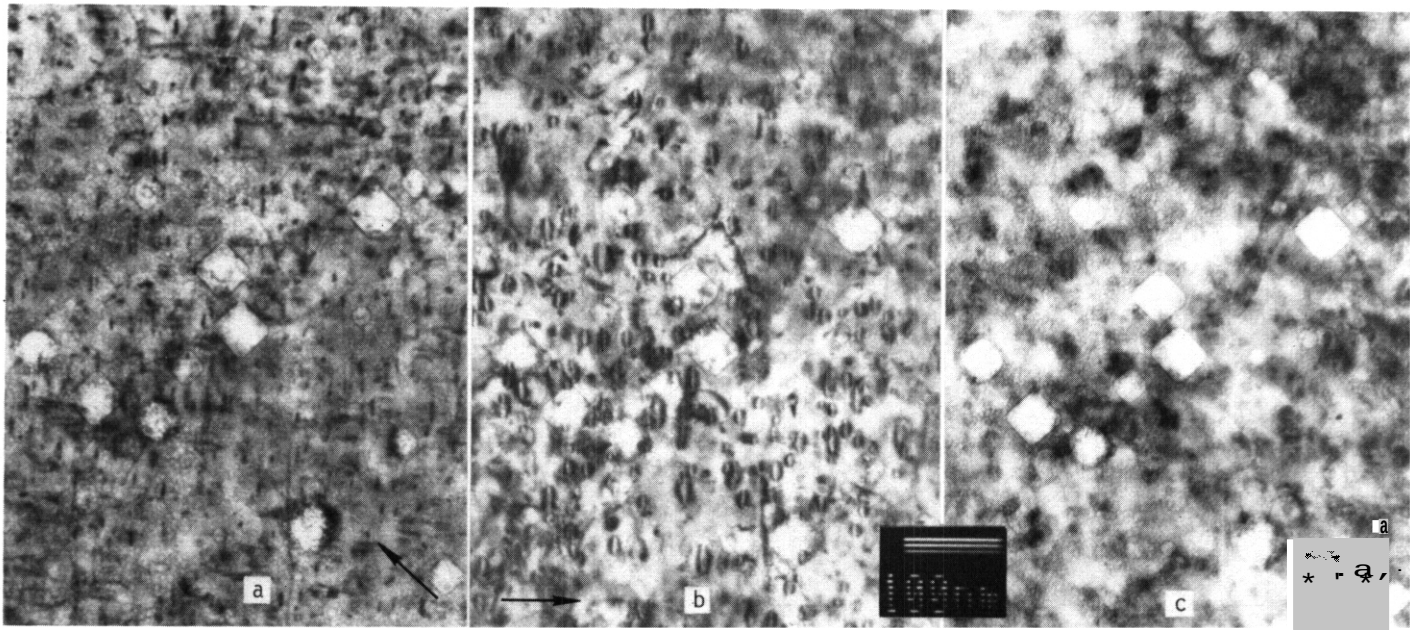

Fig. 14. Microstructure of Fe-10Cr-0.1Ta following irradiation at 410°C to 100 dpa in dislocation contrast using $\vec{g}$ = 011 in a), dislocation contrast using $\vec{g}$ = 200 in b) and void contrast in c) for a foil orientation near (011).

The microstructure of Fe-10Cr-0.1Zr shown in Figure 16 is similar to that of Fe-10Cr-1Ta. The dislocation structure contains a<100> loops and a network of $\frac{a}{2}$<111> dislocations, and voids are midway in shape between cubes and dodecahedra. However, as shown in Figure 17, Fe-10Cr-1Zr develops a different dislocation structure, consisting mainly of small $\frac{a}{2}$<111> loops but with some a<100> loops. Void shapes remain midway between cubes and dodecahedra.

In comparison, microstructures created by irradiation at 365 to 30 dpa contained a more dense dislocation loop structure and void swelling was less developed. Interpretation of the dislocation loop structure was complicated by the presence of precipitation, believed to be α'. However, in general, behavior was not very different from response at 410 to 100 dpa and therefore in order to simlify reporting, the

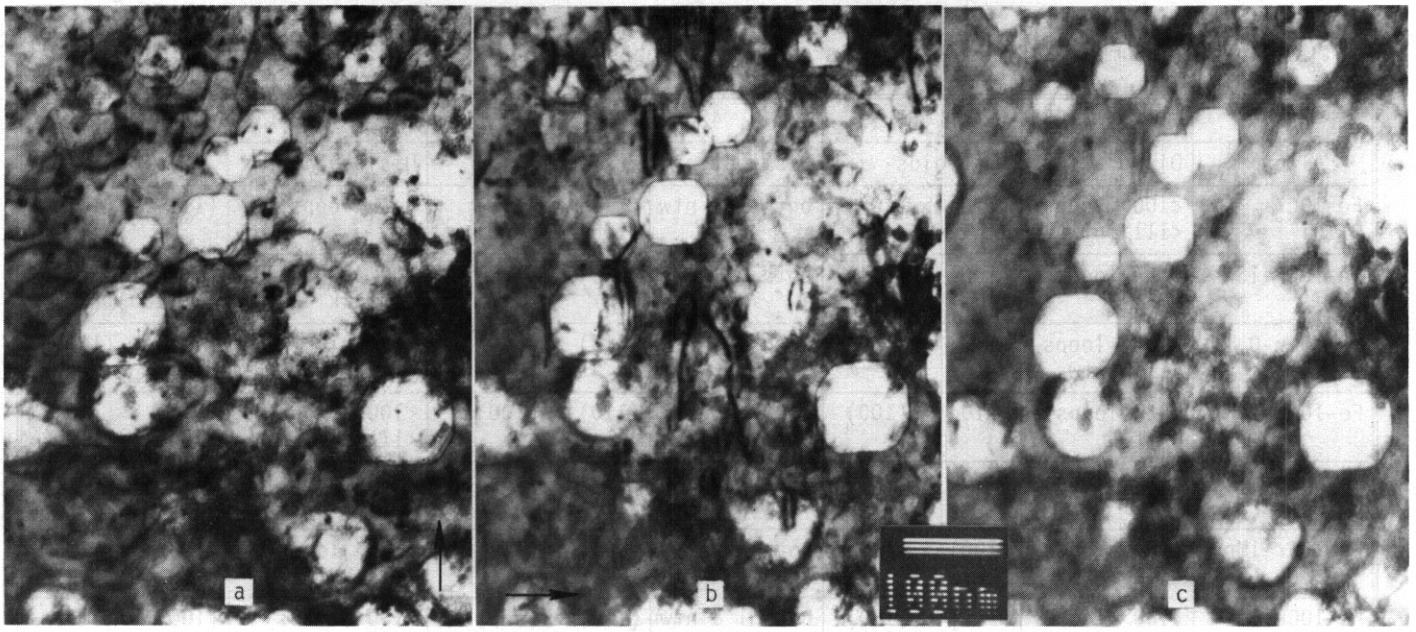

Fig. 15. Microstructure of Fe-10Cr-1Ta following irradiation at 410°C to 100 dpa in dislocation contrast using $\vec{g} = 01\bar{1}$ in a), dislocation contrast using $\vec{g} = 200$ in b) and void contrast in c) for a foil orientation near (011).

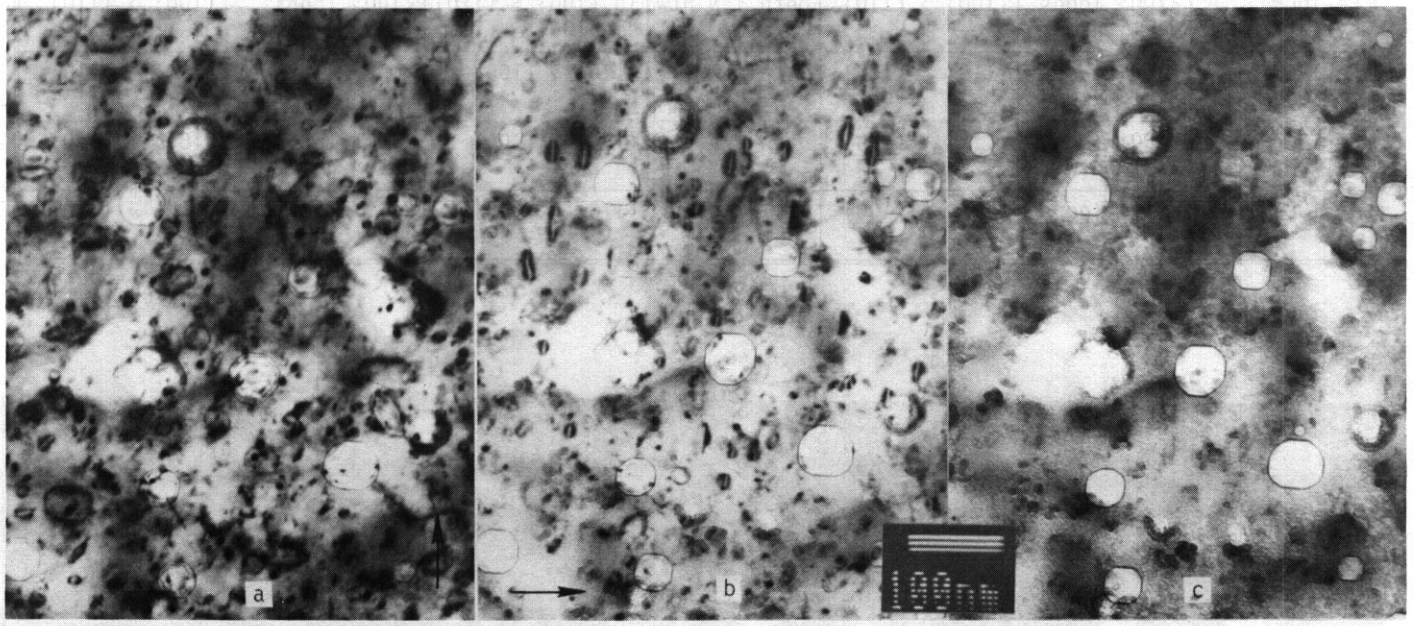

Fig. 16. Microstructure of Fe-10Cr-0.1Zr following irradiation at 410°C to 100 dpa in dislocation contrast using $\vec{g} = 01\bar{1}$ in a), dislocation contrast using $\vec{g} = 200$ in b) and void contrast in c) for a foil orientation near (011).

microstructures will not be shown. Instead, the observations are only described below and tabulated in Table 2 along with results irradiation at 410°C to 30 and 100 dpa.

In Fe-10Cr-1Si irradiated at 365°C to 30 dpa, the dislocation structure was difficult to interpret. The a<100> loops were present, and it is likely that $\frac{a}{2}$<111> loops were also present. Voids were dodecahedral with slight (100) truncations. In comparison, Fe-10Cr-1Si contained larger a<100> loops and a network of $\frac{a}{2}$<111> dislocations, indicating greater dislocation evolution in accordance with higher swelling. However, voids in the alloy containing 1% Si were cuboidal with (111) truncations, one of the few examples of (111) truncation in this series of alloys.

In Fe-10Cr-0.1V following irradiation at 365°C, the dislocation structure contained a<100> loops and $\frac{a}{2}$<111> network dislocations, and voids were dodecahedra with (100) truncations. Dislocation evolution was significantly reduced in the Fe-10Cr-1V, consisting of small loops, probably of both a<100> and $\frac{a}{2}$<111> type. Voids in the 1% V alloy were also dodecahedra with (100) truncations.

Table 2. Summary of results of microstructural observations on irradiated Fe-Cr-M alloys

	365°C to 30 dpa		426°C to 30 dpa		410°C to 100 dpa	
Alloy	Dislocations	Voids	Dislocations	Voids	Dislocations	Voids
Fe-10Cr-0.1Si	<100> loops <111> ntw	{110} > {100}	both l & ntw	{110} > {100} {100} > {110}	both loops	{110} > {100}
Fe-10Cr-1Si	both loops	{100} > {111}	both ntw	{100} > {110}	100 loops 111 network	lg {111}>{100} sm {100}>{111}
Fe-10Cr-0.1V	<100> loops <111> ntw	{110} > {100}	both l & ntw	{110} > {100}	<100> l & ntw <111> ntw	{110} > {100}
Fe-10Cr-1V	both loops	{110} > {100}	<100> loops	{110} > {100}	<100> loops <111> l & nt	{110} > {100} {100} > {110}
Fe-10Cr-0.1Mn	<100> loops <111> ntw	{110} > {100}	both l & ntw	{110} > {100}	<100> loops <111> ntw	{110} > {100}
Fe-10Cr-1Mn	<100> loops <111> ntw	{100} > {110}	both ntw	{100} > {110}	<100> loops <111> ntw	{100} > {110}
Fe-10Cr-0.1W	<100> loops <111> ntw	{110} = {100}	both l & ntw	{110} > {100}	<100> loops <111> ntw	{100} = {110}
Fe-10Cr-1W	both loops	{110} > {100}	both ntw	{110} > {100}	<100> loops <111> ntw	{110} > {100}
Fe-10Cr-0.1Ta	<100> loops <111> ntw	{100} > {110}	both l & ntw	lg {100} = {110} sm {100} = {110}	<100> loops <111> ntw	{100} > {110}
Fe-10Cr-1Ta	<100> loops <111> ntw	{110} ≈ {100}	both ntw	{110} > {100}	<100> loops <111> ntw	{100} = {110}
Fe-10Cr-0.1Zr	<100> loops <111> ntw	{110} > {100}	both l & ntw	{110} > {100}	<100> loops <111> ntw	{100} = {110}
Fe-10Cr-1Zr	<111> loops	{110} = {100}	<111> loops	{110} > {100}	<111> loops <100> loops	{100} = {110}

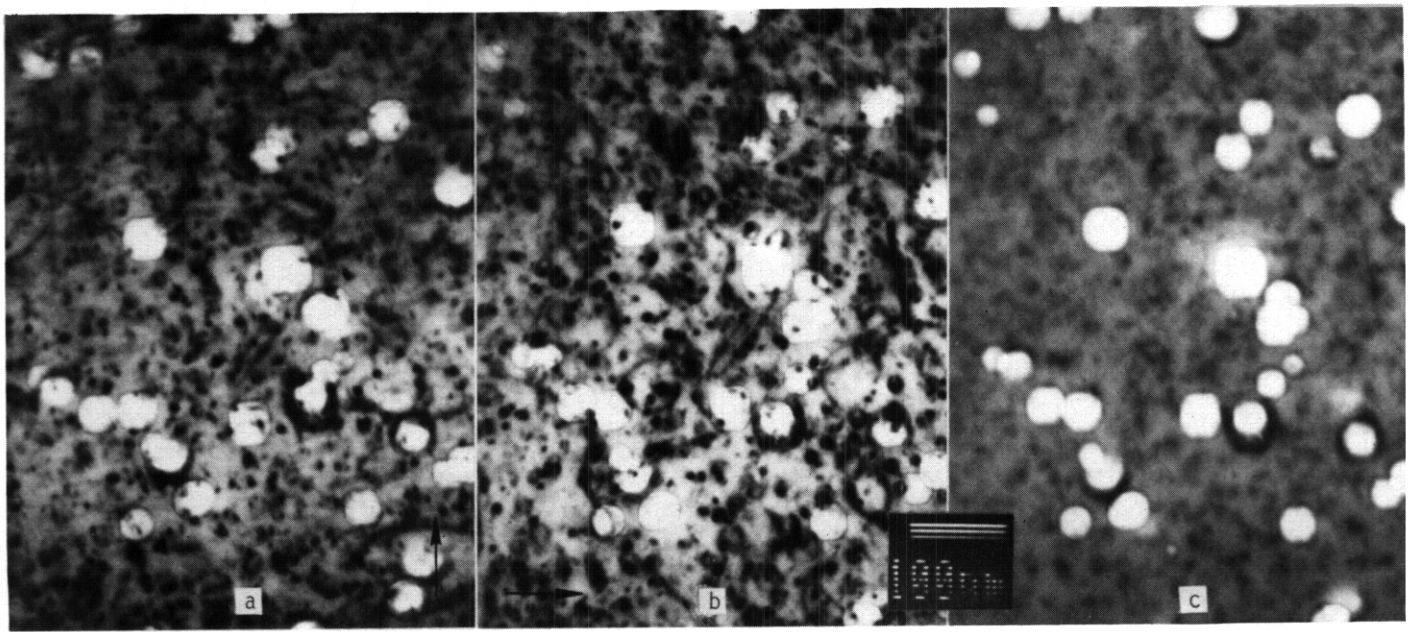

Fig. 17. Microstructure of Fe-10Cr-1Zr following-irradiation at 410°C to 100 dpa in dislocation contrast using $\vec{g}$ = 011 in a), dislocation contrast using g = 200 in b) and void contrast in c) for a foil orientation near (011).

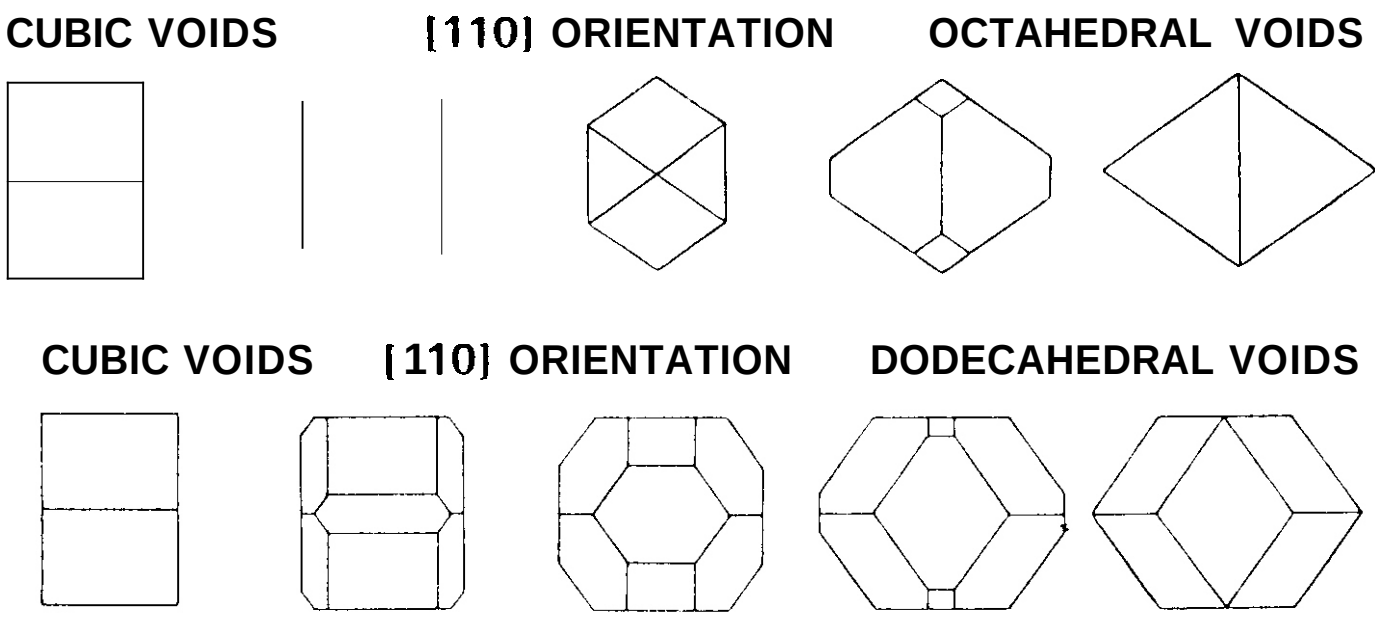

Fig. 18. Void shapes for a foil in (011) orientation, from cubes to octahedra with intermediate truncation in a), and from cubes to dodecahedra with intermediate truncation in b).

The dislocation structures in alloys containing Mn following irradiation at 365°C both contained a<100> loops and a network of $\frac{a}{2}$<111> dislocations. However, void shapes were found to be different, with voids in the 0.1% Mn alloy of dodecahedral shape with (100) truncations, whereas in the 1%alloy, voids were cubic with only small (110) truncation.

Following irradiation at 365, alloys containing W again behaved similarly. Dislocation structures consisted of a<100> loops and $\frac{a}{2}$<111> network dislocations, but in the alloy containing 1%W, some large $\frac{a}{2}$<111> loops were also found. In both alloys, voids were between cubic and dodecahedral shapes with several examples found of truncated cubes and dodecahedra in the same field of view. Similar results were found for alloys containing Ta. Dislocation structrures contained a<100> loops and $\frac{a}{2}$<111> network dislocations. Voids were cuboidal with (110) truncations in the case of 0.1% Ta, an8 varied between truncated cubes and dodecahedra in the case of 1%Ta.

In Fe-10Cr-0.1Zr following irradiation at 365°C, the dislocation structure contained a<100> loops and $\frac{a}{2}$<111> network dislocations. Voids were probably dodecahedra with (100) truncations. The alloy containing 1% Zr had a dislocation structure that was quite different, and more characteristic of other irradiation conditions for specimens containing Lr. It was probably dominated by $\frac{a}{2}$<111> loops, (but the images were not sufficiently clear for absolute identification.) In this case, voids were midway between cubes and dodecahedra.

Discussion

The purpose of this experiment was to investigate effects of solute additions on microstructural development under fast neutron irradiation. The first set of results based on irradiation at 410°C to 30 dpa indicated that large changes in swelling response and microstructural evolution did arise from differences in solute addition. The present results provide confirmation that these difference can be maintained to higher dose, and similar behavior occurs at a lower irradiation temperature as well. The purpose of this discussion section will be to provide comparison of the behavior as a function of compositon, temperature and dose.

It can first be noted that additions of solute, either at the 0.1% or 1% level, do appear to lead to reductions in swelling in comparison with the simple binary alloys. Fe-9Cr and -12Cr binary alloys have been irradiated in the Experimental Breeder reactor to 95 dpa resulting in 4.2 and 4.7% swelling, respectively.[12] As neutron spectra are similar in FFTF and EBR-II, it appears reasonable to conclude that swelling levels of less that 4.0%, as found in the present study, represent examples of reduced swelling due to solute additions even for the case of Fe-10Cr-1Mn, and certainly for all other alloy conditions.

As noted for the case of alloys containing Si irradiated at 365°C, solute additions can also result in shifts in the peak swelling temperature. This is obviously the case both in comparison to other alloying additions and to the base binary alloy composition, where peak swelling is generally found to be about 425°C.

Comparisons of the effects of the various solute additions on microstructural development are difficult to make due to the large number of observations provided by the present study. Table 2 has been organized in order to simplify such comparison procedures. Table 2 provides summaries of dislocation and void information for each of the alloys studied following irradiation at 365°C to 30 dpa and following irradiation at 410°C to 30 and 100 dpa. To simplify the table, several notational abbreviations have been used. Dislocation notation <100> and <111> refers to a<100> and $\frac{a}{2}$<111>, l to loops, ntw to network, lg and sm to large and small, and void shape is denoted by the most stable plane present, so that (110) > (100) means that voids are dodecahedral with (100) truncations.

From Table 2 it can be shown that void shape is invariant for a given alloy except when voids grow large after irradiation at 410°C to 100 dpa. At high dose, differences arise in alloys containing Zr, 0.1% W and 1% Ta where void shape shifts midway between cubes and dodecahedra, and in alloys containing 1%Si where large voids become octahedral. Similar invariance is found with dislocation structures except that at 410°C and high dose, all conditions show a<100> loops whereas evidence for network evolution was indicated at lower dose. An explanation for this behavior is not straightforward. It may indicate a<100> loops only grow to a finite size as a result of solute segregation, and that network evolution is not as straightforward as expected.

CONCLUSIONS

Marked differences in dislocation evolution and void shape following neutron irradiation were found as a function of alloying in a series of Fe-10Cr alloys with solute additions of Si, V, Mn, W, Ta, and Zr. Swelling level, void shape, and dislocation configuration vary as a function of the various solutes present in the same manner as seen previously at lower dose. However, two additional observations were made. Irradiation at the lower temperature promotes precipitation of chromium rich α' phase and reduces microstructural evolution. Also, irradiation to higher dose reduces the effect each solute has by reducing the wide variation in void shape and dislocation evolution that were found at lower dose.

FUTURE WORK

Quantitative void swelling measurements remain to be performed to complete this work.

REFERENCES

1. M. K. Miller and M. G. Burke, in Effects of Radiation on Materials, 15th International Symposium, (ASTM, Philadelphia, 1992) to be published.

2. W. J. Phythian, A. J. E. Foreman, C. A. English, J. Buswell, M. Hetherington and K. Roberts, IBID.

3. J. L. Brimhall, D. R. Baer and R. H. Jones, J. Nucl. Mater., 117, (1983) 1415-1419.

4. E. A. Little, T. S. Morgan and R. G. Faulkner, Materials Science Forums, 97-99 (1992) 323-328

5. S. Ohnuki, H. Takahashi and T. Takeyama, J. Nucl. Mater., 103-104 (1981) 1121-1126.

6. R. E. Clausing, L. Heatherly, R. G. Faulkner, A. F. Rowcliffe and K. Farrell, J. Nucl. Mater., 141-143 (1986) 978-981.

7. H. Takahashi, H. Kinoshita, S. Ohnuki, R. Nagasaki, F. A. Garner and D. S. Gelles, J. Nucl. Mater., 155-157 (1988) 908-911.

8. H. Takahashi, S. Ohnuki and T. Takeyama, IBID, 1415-1419.

9. S. Ohnuki, H. Takahashi and R. Nagasaki, J. Electron Microsc., 35 (1986) 415-421

10. J. Kameda and A. Bevolo, Scripta Met., 21 (1987) 1499-1503.

11. H. Takahashi, K. Shiba, S. Nakahigashi, S. Ohnuki, H. Kinoshita and F. A. Garner, in Reduced Activation Materials for Fusion Reactors, ASTM STP 1047, R. L. Klueh, D. S. Gelles, M. Okada and N. H. Packan, Eds., (ASTM, Philadelphia, 1990) 93-102.

12. D. S. Gelles, in Effects of Radiation on Materials, 14th International Symposium, V. 1, ASTM STP 1046, N. H. Packan, R. E. Stoller and A. S. Kumar, Eds., (ASTM, Philadelphia, 1989) pp. 73-97 or DOE/ER-0313/1 rev. 1, 150.

13. D. S. Gelles, R. M. Claudson and L. E. Thomas, in Electron Microscopy 1990, V. 4, (San Francisco Press, Inc., San Francisco, 1990) 844-845.

Postirradiation Deformation Behavior in Ferritic Fe-Cr Alloys - M. L. Hamilton and D. S. Gelles, (Pacific Northwest Laboratory)[a] and P. L. Gardner, (University of Missouri-Rolla)

OBJECTIVE

The objective of this effort is to provide an understanding of postirradiation deformation behavior in martensitic stainless steels by studying behavior in simple alloys.

SUMMARY

It has been demonstrated that fast neutron irradiation produces significant hardening in simple Fe-(3-18)Cr binary alloys irradiated to about 35 dpa in the temperature range 365 to 420°C, whereas irradiation at 574°C produces hardening only for 15% or more chromium. The irradiation-induced changes in tensile properties are discussed in terms of changes in the power law work hardening exponent. The work hardening exponent of the lower chromium alloys decreased significantly after low temperature irradiation (≤ 420°C) but increased after irradiation at 574°C. The higher chromium alloys failed either in cleavage or in a mixed ductile/brittle fashion. Deformation microstructures are presented to support the tensile behavior.

PROGRESS AND STATUS

Introduction

Ferritic/martensitic steels continue to be considered for application as structural materials in proposed fusion irradiation devices. Since it is not possible to duplicate for testing purposes the irradiation conditions anticipated in a fusion device, significant effort is devoted to understanding the fundamental irradiation response of ferritic materials to facilitate extrapolation to a fusion environment from the response in the available fission environment. Experiments on simple alloys have therefore been included in the fusion materials program to allow comparison with the behavior of more complex alloys.

Miniature tensile specimens of six binary Fe-(3-18)Cr alloys were previously irradiated in the Fast Flux Test Facility (FFTF) and tested at room temperature.[1] Neutron exposures ranged from ~7 dpa at 365°C to ~35 dpa at 403 and 574°C. Significant hardening was observed in alloys irradiated at 365 and 403°C, whereas irradiation at 574°C produced hardening only for chromium levels of 15% or more. Several unusual types of yield behavior were also observed that raised questions about the deformation response of the alloys. The work hardening behavior of the alloys was therefore determined to provide an improved understanding of post-irradiation deformation response in simple ferritic alloys. Deformed microstructures were also examined using transmission electron microscopy.

ExDerimental Procedure

The load and displacement data obtained in reference 1 were digitized manually between the 0.2% offset yield point and the maximum load, and converted to true stress and true strain according to $\sigma = s(e+1)$ and $\epsilon = \ln(e+1)$, where σ and ϵ are true stress and strain, respectively, and s and e are engineering stress and strain, respectively. The data were fit by linear regression to the power law definition of strain hardening, $\sigma = K\epsilon^n$, where K is a constant. The strain hardening coefficient n was determined as the slope of $\log \sigma$ versus $\log \varepsilon$ for as many tests as possible. The value of r^2 for the regressions was generally on the order of 0.9 or higher, except where brittle failure precluded the reasonable application of the work hardening concept.

Transmission electron microscopy disks were successfully prepared from the gauge sections of two tested tensile specimens. The thinned area being examined was therefore located about 1.5 mm from the actual fracture surface, theoretically well within the uniformly deformed region of the gauge. Microscopy was performed on a 1200EX electron microscope operating at 120 keV.

Results

Previous Tensile Data

The original tensile data are summarized in Figure 1. Only yield strength and total elongation are shown since the ultimate tensile strength and uniform elongation behaved similarly. Significant hardening and loss of ductility were observed at all chromium levels after irradiation at 365 and 403°C (to ~7 and ~35 dpa, respectively). Similar irradiation-induced changes in behavior after irradiation at 574°C were only observed for chromium levels of 15% or more.

[a]Pacific Northwest Laboratory is operated for the U.S. Department of Energy by Battelle Memorial Institute under Contract DE-AC06-76RLO 1830.

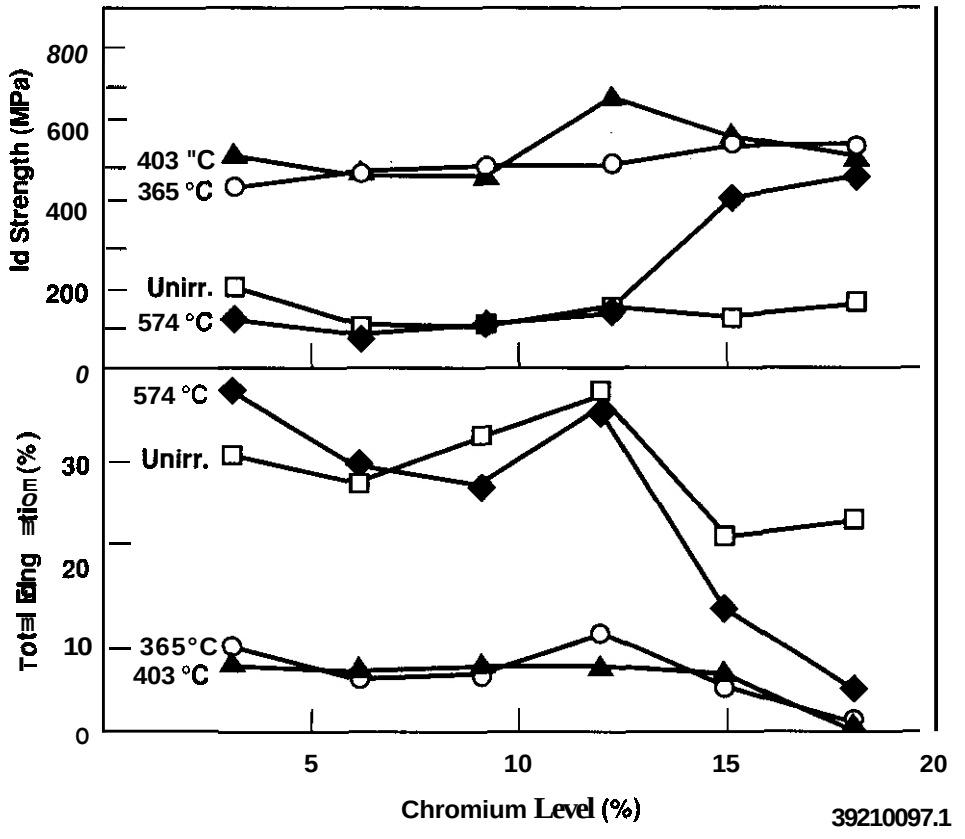

Fig. 1. Room temperature tensile data on Fe-(3-18)Cr binary ferritic alloys irradiated in FFTF to ~7 dpa (365°C) and ~35 dpa (403 and 574°C).

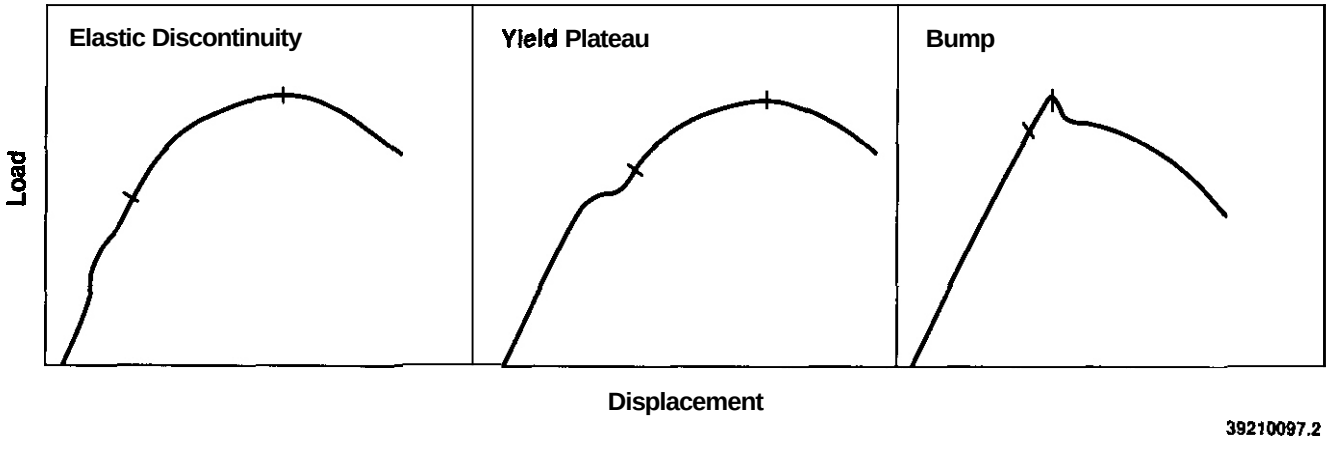

Fig. 2. Schematic representations of unusual yield phenomena observed in room temperature tensile tests on binary ferritic alloys.

Schematic examples of the unusual yield responses that were observed are shown in Figure 2. The hatch marks on each type of curve delineate the data used for the determination of the work hardening coefficient. The "bump" occurs as a short, gradual decrease in load from the maximum load, very shortly after the 0.2% offset yield point. A yield plateau was sometimes observed, although it was not preceded by the upper yield point that is typical of ferritic alloys, nor did it exhibit the irregularities typically associated with the propagation of Lüder's bands. The third type of unusual response could be characterized as a slight "wow" in the elastic portion of the data, where the data immediately preceding and succeeding the "wow" are collinear.

The possibility that equipment-related problems could be the source of any of these unusual behaviors was eliminated by repeated checks on the machine operation. All three of these types of behavior were reproducible when duplicate specimens were available and allowed multiple tests of the same alloy condition. Both the "bump" and the yield plateau phenomena have also been observed in tensile data

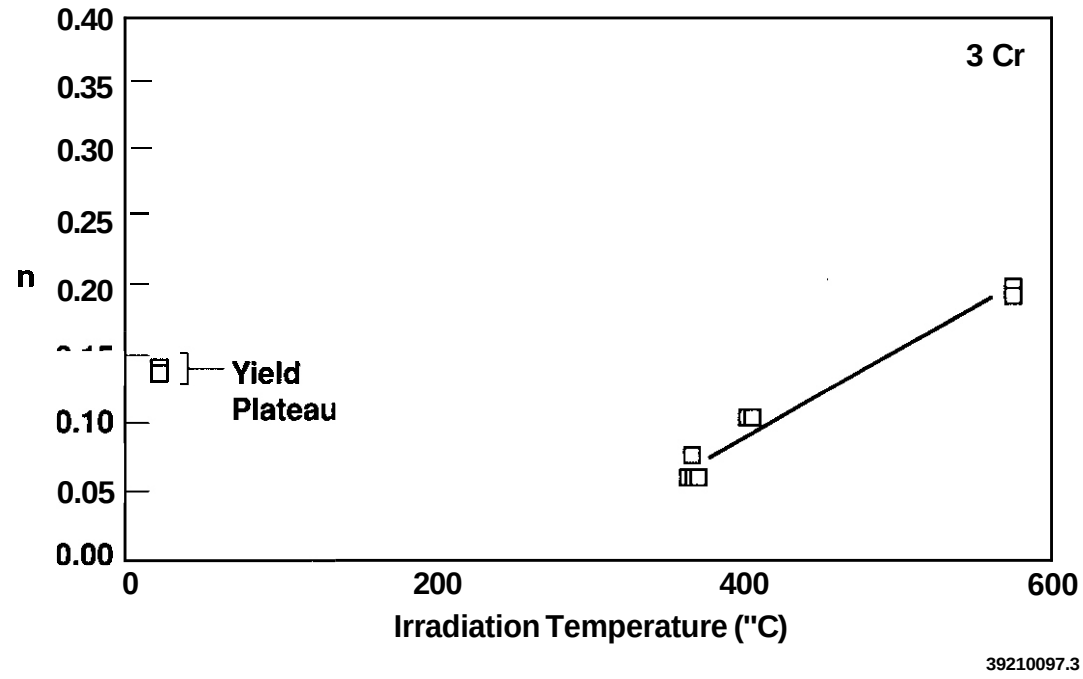

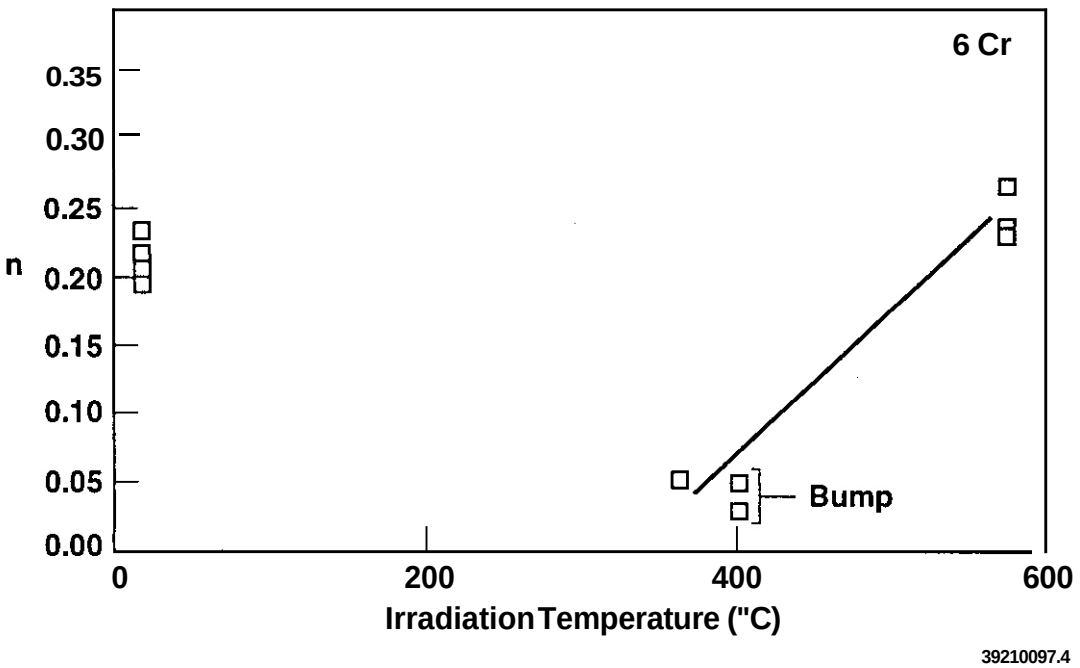

Fig. 4. Values of work hardening coefficient determined for 6Cr specimens.

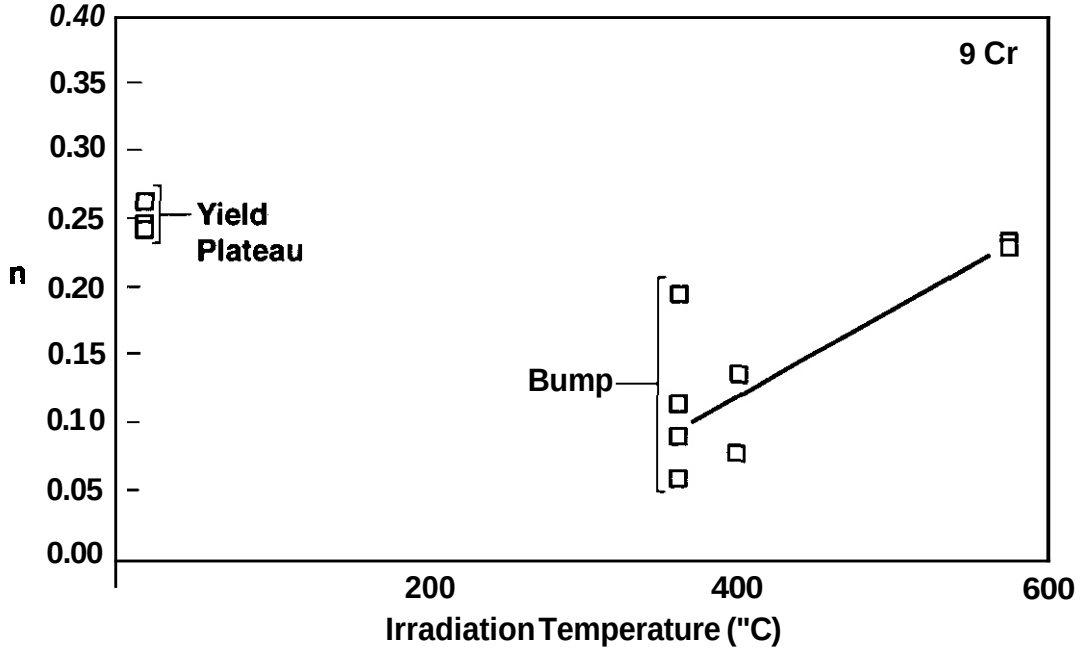

Fig. 5. Values of work hardening coefficient determined for 9Cr specimens.

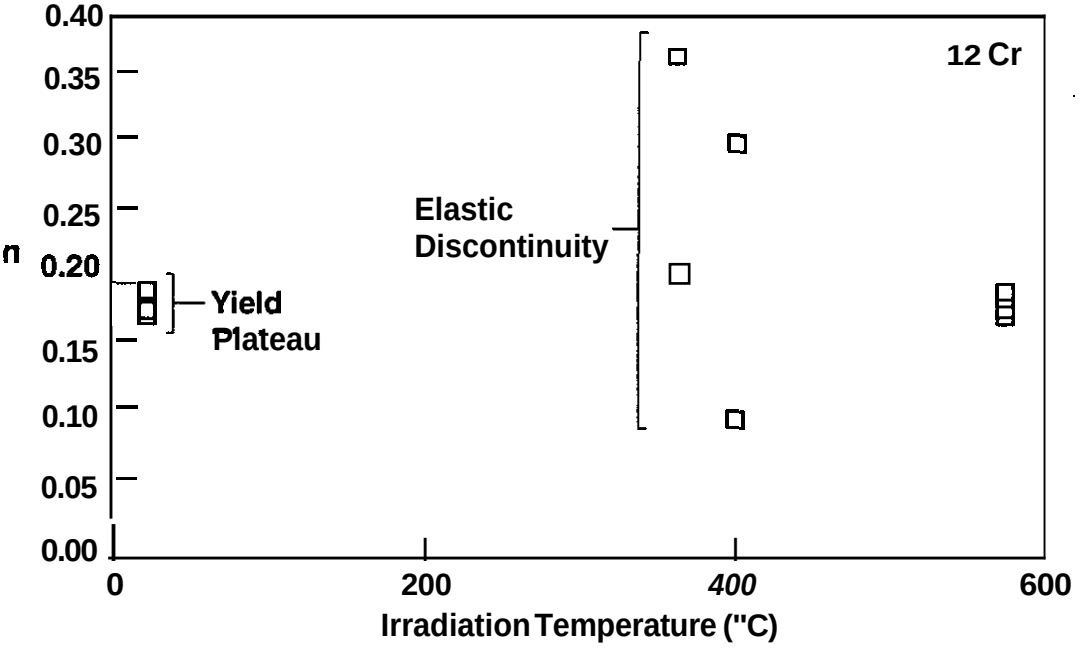

Fig. 6. Values of work hardening coefficient determined for 12Cr specimens.

The 12Cr specimens exhibited virtually identical values of n in the unirradiated condition and following irradiation at 574°C, but exhibited highly variable values at the lower irradiation temoeratures. where the "wow" appeared in the load-displacement curves. The 12Cr specimens also exhibited a yield plateau in the unirradiated condition similar to that shown by the 3 and 9Cr alloys.

The 15Cr specimens exhibited a large amount of variability in the values of n obtained for the unirradiated condition, consistent with the variability in the tensile data itself.' Most of the specimens irradiated at the lower temperatures failed by cleavage. Those 15Cr specimens for which valid n values were determined exhibited almost classic elastic-perfectly plastic load-displacement traces, hence the very low values of n.

The work hardening coefficient data are summarized in Figure 8. It is evident that the lower Cr alloys are reduced to very low n values at low irradiation temperatures, which then increase with increased irradiation temperature. The low values of n appear to be associated with load-displacement traces exhibiting "bumps". Yield plateaus appear to be associated with unirradiated material only, and the

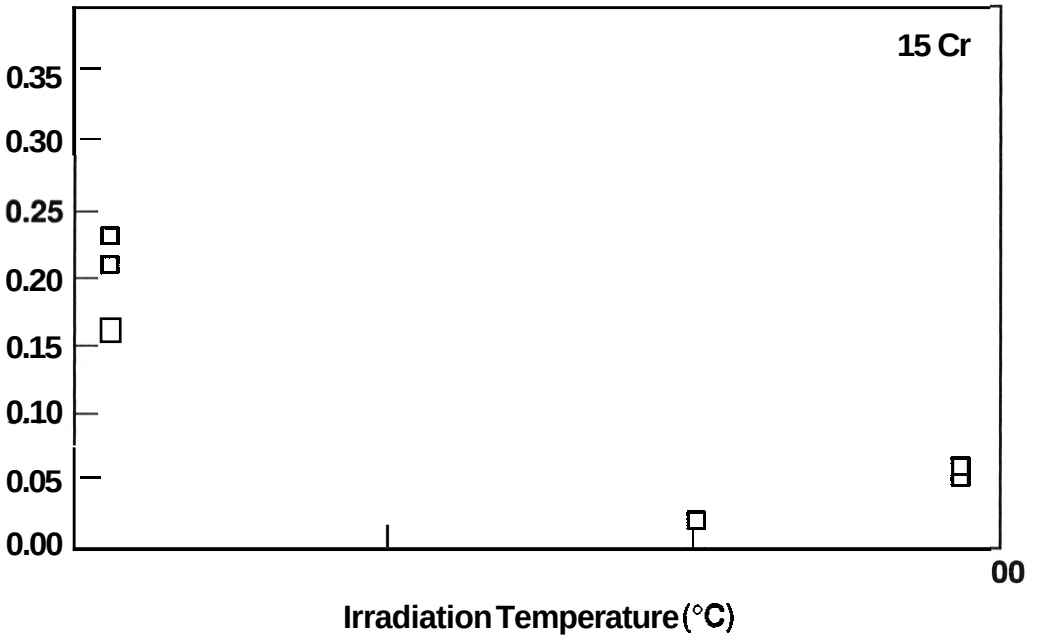

Fig. 7. Values of work hardening coefficient determined for 15Cr specimens.

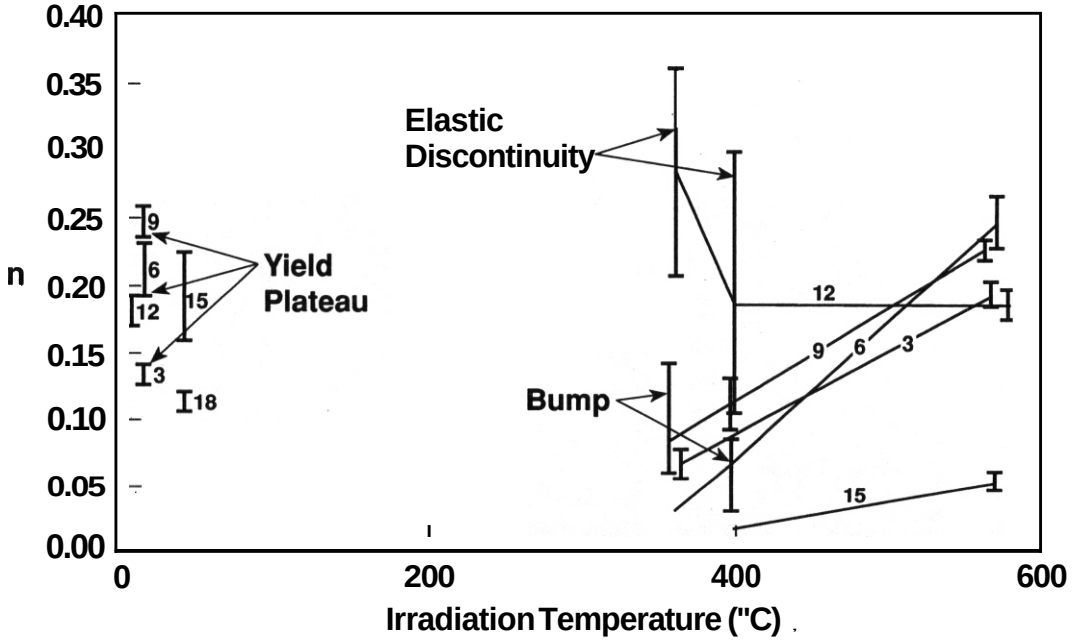

Fig. 8. Summary of work hardening coefficients for 3-15Cr alloys.

variability evident in the values of n for the 12Cr alloy at the lower irradiation temperatures appears to be associated with load-displacement traces exhibiting a "wow".

Electron Microscopy

Two specimens were prepared for transmission electron microscopy, one each of the 6 and 12Cr alloys, from the gauge sections of miniature tensile specimens that had been irradiated at 403°C and then tensile tested at room temperature. Uniform elongations were on the order of 0.6% for both tensile tests. The purpose of the microscopy examinations was to determine the consequences of postirradiation deformation on the dislocation structure.

The dislocation structures contained a<100> loops and $\frac{a}{2}$<111> dislocation line segments similar to those found in Fe-6Cr and Fe-12Cr specimens irradiated at 403°C to 15 dpa.[2] Examples are given in Figures 9 and 10 for Fe-6Cr and Fe-12Cr, respectively. The dislocation structure was imaged in each case using both $\vec{g}$=011 and 200 for a grain tilted near <011> and then with either $\vec{g}$=110 or 101 after further tilting. The 200 contrast image shows one set of a{100} loops in strong contrast elongated vertically and all of the

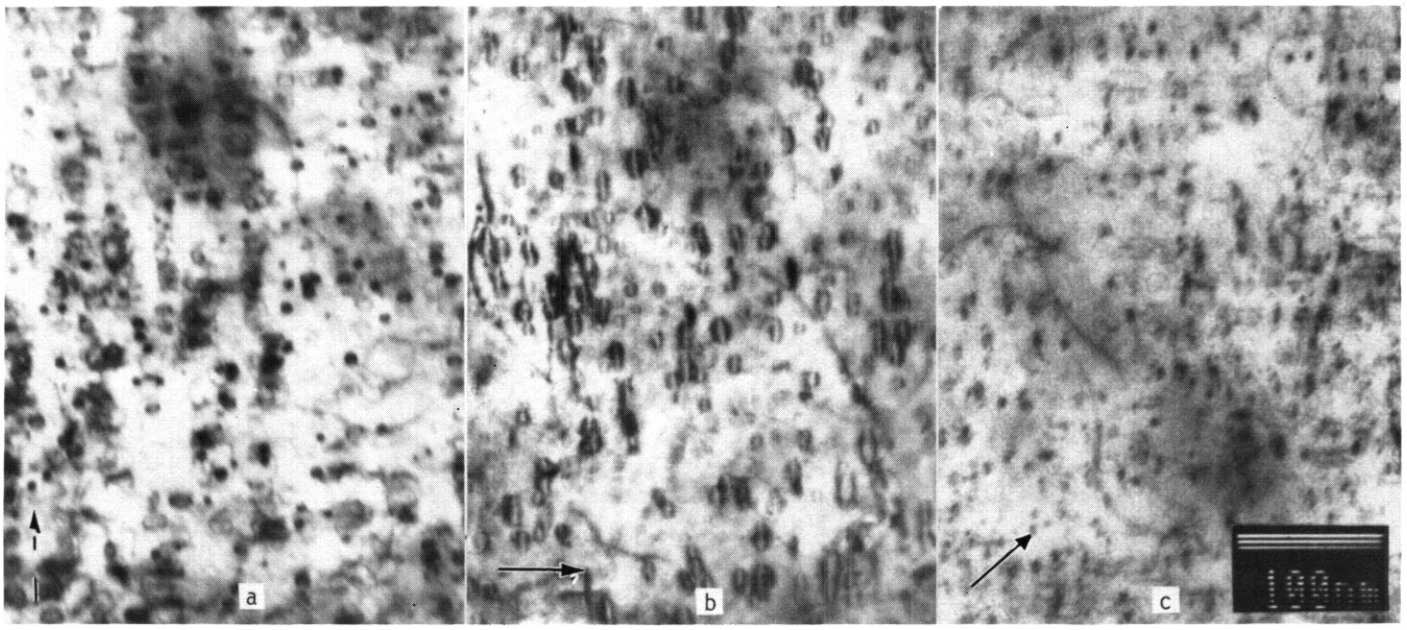

Fig. 9. Dislocation structures in an area of the gauge section of a specimen of Fe-6Cr irradiated at 403°C to 37.3 dpa using (a) $01\bar{1}$, (b) 200 and (c) $\bar{1}10$ contrast.

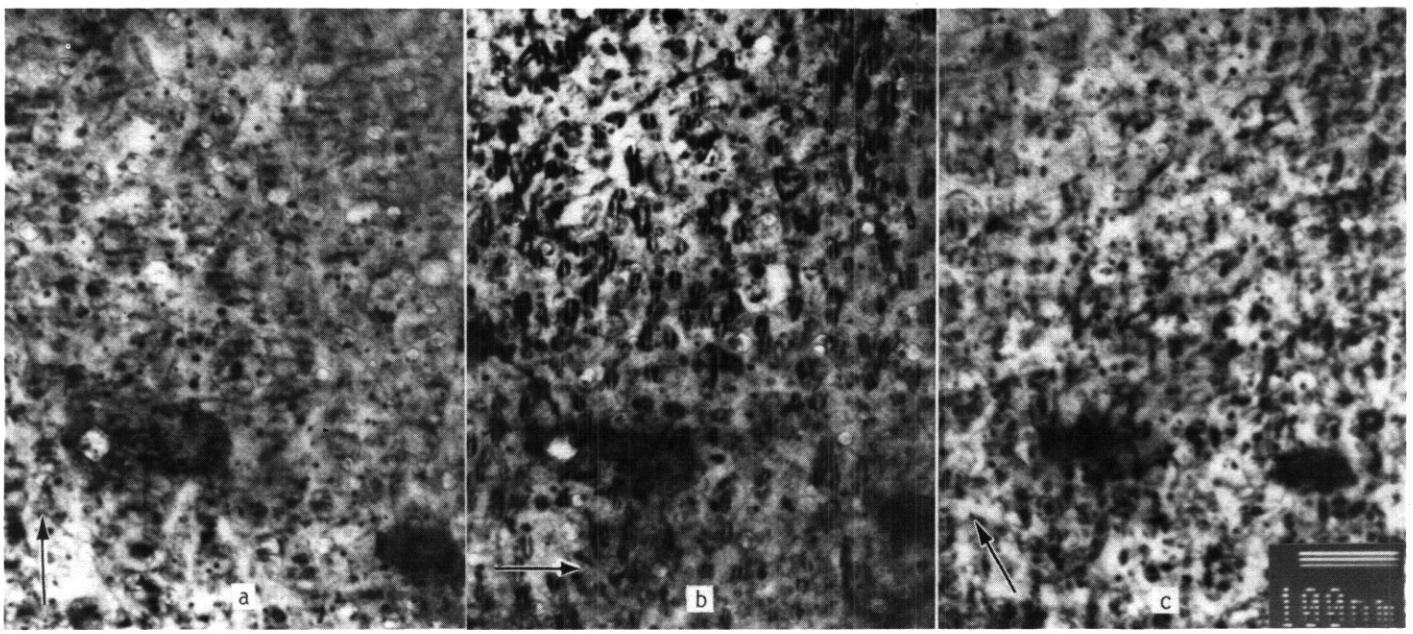

Fig. 10. Dislocation structures in an area of the gauge section of a specimen of Fe-12Cr irradiated at 403°C to 37.3 dpa using (a) $01\bar{1}$, (b) 200 and (c) $\bar{1}01$ contrast.

$\frac{a}{2}$<111> dislocation segments in weaker contrast. In comparison, the $01\bar{1}$ contrast shows the other sets of a<100> loops and only half of the $\frac{a}{2}$<111> dislocation line segments.

No interactions are apparent between the $\frac{a}{2}$<111> line segments and the a<100> loops in Figures 8 and 9. Nor are there indications of distorted a<100> loop shapes. Stereoscopic examination of stereo pair micrographs confirmed that there was no interaction between the $\frac{a}{2}$<111> dislocation line segments and a<100> loops, as well as the absence of any irregularities in the size or shape of a<100> loops. Deformation does not appear to have occurred in either of the regions examined despite their proximity to the fracture, and the local strain in these regions is therefore effectively zero rather than the 0.6% indicated by the uniform elongation data.

Discussion

This work was initiated to provide further understanding of the consequences of the complex dislocation structures encountered in irradiated ferritic alloys. Such dislocation structures generally included both $\frac{a}{2}$<111> and a<100> Burgers vectors, the former common in unirradiated ferritic alloys, but the latter generally occurring only as a result of radiation damage. Furthermore, it has been suggested that channel deformation may occur in ferritic alloys following irradiation,[2] although it was not observed in this study. Further investigation of deformation in ferritics was therefore warranted.

This work has demonstrated that the ability of a material to work harden is decreased when radiation significantly increases dislocation densities, but after irradiation at higher temperatures, the work hardening capability can increase. It remains to be seen whether a high pre-irradiation dislocation density, such as that conferred by cold work, could exhibit similar decreases in work hardening capability with the creation of $\frac{a}{2}$<111> and a<100> dislocations during irradiation. Such a study could be considered in the future, but similar reductions in work hardening coefficient are unlikely due to inherent limitations in the hardenability of a material.

The observation that no interaction could be found between mobile $\frac{a}{2}$<111> dislocations and a<100> loops in a region approximately 1.5 mm from the fracture surface and in the gauge section characterized by 0.6% uniform elongation appears to verify the potential for channel deformation in irradiated ferritic alloys. Further efforts appear to be warranted to determine the possible existence of channel deformation and its mechanism.

CONCLUSIONS

The work hardening capability determined for Fe-(3-9)Cr following irradiation was significantly reduced for low irradiation temperatures (365-403°C) but was effectively unchanged at 574°C. The response in Fe-12Cr was different, with unusual yield behavior in the elastic regime and wide scatter in the work hardening coefficients for low temperature irradiation.

Microstructural examination of irradiated and deformed Fe-6Cr and Fe-12Cr specimens with nominally 0.6% uniform deformation showed no interaction between $\frac{a}{2}$<111> network dislocations and a<100> loops. Localized rather than uniform yielding is indicated.

FUTURE WORK

This effort is comoleted

REFERENCES

1. Hamilton, M. L. and Gelles, D. S., "Postirradiation Strength and Deformation of Ferritic Fe-Cr Binary Alloys," Effects of Radiation on Materials: 15th International-Symposium, ASTM *STP* 1125, R. E. Stoller, A. S. Kumar and D. S. Gelles, Eds., ASTM, Philadelphia, 1992, to be published.

2. Gelles, D. S., in Effects of Radiation on Materials: 14th International Symposium, Volume 1, ASTM STP 1046, N. H. Packan, R. E. Stoller and A. S. Kumar, Eds., ASTM, Philadelphia, 1989, pp. 73-97.

6.0 DEVELOPMENT OF STRUCTURAL ALLOYS

6.1 Ferritic Stainless Steels

CHARPY IMPACT TOUGHNESS OF MARTENSITIC STEELS IRRADIATED IN FFTF **EFFECT** OF HEAT TREATMENT - R. L. Klueh and D. J. Alexander (Oak Ridge National Laboratory)

OBJECTIVE

The goal of this study is **to** evaluate the impact behavior of irradiated ferritic steels and relate the change in properties to the heat treatment of the steel.

SUMMARY

Plates of 9Cr-1MoVNb and 12Cr-1MoVW steels were normalized and then tempered at two different tempering conditions. One-third-size Charpy specimens from each steel were irradiated to 7.4-8x10^{26} n/m^2 (about ≈35 dpa) at 420 °C in the Materials Open Test Assembly (MOTA) of the Fast Flux Test Facility. Specimens were also thermally aged to 20,000 h at 400 °C to compare the effect of aging and irradiation. Previous work on the steels irradiated to 4-5 dpa at 365 °C in MOTA were reexamined in light of the new results. The tests indicated that prior-austenite grain size, which was varied by different normalizing treatments, had an effect on impact behavior of the 9Cr-1MoVNb hut not on the 12Cr-1MoVW. Tempering treatment had relatively little effect on the shift in DBTT for both steels. Conclusions are presented on how heat treatment can he used to optimize properties.

PROGRESS AND STATUS

Introduction

The effect of irradiation on the toughness of ferritic/martensitic steels is a prime concern when these steels are considered as structural materials for magnetic fusion reactors. At temperatures up to ≈450 °C, neutron irradiation causes large increases in the ductile-brittle transition temperature (DB'IT) and decreases in the upper-shelf energy (USE), as determined in a Charpy impact test. For these steels to he used successfully, it is necessary to understand this irradiation effect and develop steels in which the effect is minimal.

Heat treatment variations affect the kind of microstructure (e.g., prior austenite grain size, dislocation structure, and the character of the precipitates) developed in Cr-Mo steels, and microstructure determines the mechanical properties, such as the impact behavior. Thermal aging can also affect microstructure, and thus, mechanical properties. This paper examines how heat treatment, thermal aging, and irradiation affect Charpy impact behavior of the 9Cr-1MoVNb and 12Cr-1MoVW steels that are prime candidate alloys for fusion reactor applications. Irradiations were at **365** and **420-C.** The **365 °C** results were presented previously in limited detail [1]. They will be presented here again **,** along with Charpy curves, and they will be discussed in light of the 420 °C tests and the thermal aging results.

Emerimental Procedure

The 9Cr-1MoVNb (modified 9Cr-1Mo) steel was taken from an argon-oxygen decarburized (AOD) and electroslag-remelted (ESR) heat (Heat 30176) processed by Carpenter Technology into 25.4-mm-thick plate. The 12Cr-1MoVW steel (Sandvik HT9 composition) **was** from an AOD/ESR melt that was processed into hot-rolled plate (National Fusion Heat 9607-R2) by Universal Cyclops. Compositions for the steels are given in Table **1.**

Sections of 25.4-mm plate were rolled to 9.5-mm plate for heat treatment to obtain the Charpy specimens. Plates 88.9 by 152 by 9.5 mm were normalized and tempered. Two plates of 9Cr-1MoVNb and **two** plates of 12Cr-1MoVW were austenitized 1h at 1040 °C and air cooled; two plates of each steel were also austenitized 1 h **at** 1100 °C and air cooled. Then one plate with each normalization treatment was tempered 1h at 760 °C or ***2.5*** h at 780 °C.

Subsize Charpy specimens essentially one-third the standard size measuring 3.3 by 3.3 by 25.4 mm with a 0.51-mm-deep 30' V-notch with a **0.05-to** 0.08-mm-root radius were taken from the center of the normalized-and-tempered plates along the rolling direction with the notch running transverse to the rolling direction (L T orientation). Specimens were irradiated in the Fast Flux Test Facility (FFTF) in the Materials Open Test Assembly (MOTA) in the MOTA 1E experiment.

For the 420' C irradiations, specimens austenitized at 1040 • C and tempered at 760 and 780 • C were used. Six Charpy specimens from each heat-treated condition were irradiated. The 9Cr-1MoVNb steel tempered at 760 and 780 • C was irradiated to fluences of 7.8 and 8.0×10^{26} n/m^2 (≈36 and 37 dpa), respectively; the 12Cr-1MoVW steel tempered at 760 and 780 • C was irradiated to fluences of 7.4 and 7.8×10^{26} n/m2≈34 and 36 dpa), respectively. Less than 5 appm He formed in the specimens during irradiation.

The results from the 420 • C irradiations are to he compared with results from the 365°C irradiations [1]. In that experiment, six Charpy specimens from each heat and each heat treatment (1040 and 1100 • C austenitization treatments and 760 and 780 • C tempering treatments for each austenitization treatment) were irradiated in the below-core region of MOTA in a sodium "weeper" at ≈365 • C, which is slightly above the coolant ambient temperature. All of the 9Cr-1MoVNb steel specimens were irradiated to a fluence of about 1.3 x 1026 n/m^2 (>0.1 MeV), which produced ≈5 dpa. The 12Cr-1MoVW steels were in a different position in the below-core region and received about 1.1×10^{26} n/m^2, ≈4 dpa, at 365 • C. Less than 1 appm He formed in these specimens during irradiation.

In addition to the unirradiated normalized-and-tempered specimens and the irradiated specimens, a series of thermally aged 1/3-size Charpy specimens was also tested. Specimens for both steels were thermally aged in all four normalized-and-tempered conditions; aging was at 400 • C for 5000, 10000, and 20000 h.

Details on the test equipment and procedure for testing the subsize Charpy specimens have been published [2]. Individual Charpy data sets were fitted with a hyperbolic-tangent function to obtain the transition temperatures and upper-shelf energies. Transition temperatures were determined at half the upper-shelf energy.

Results

Tempered martensite microstructures were observed after the steels were normalized and tempered. One objective was to determine the effect of grain size. Grain size was varied by austenitizing at 1040 and 1100 • C. The difference in grain size for the different austenitization treatments is shown in Figs. 1 and 2; grain sizes are given in Table 1. The different austenitizing treatments resulted in a small difference in average grain diameter for the 9Cr-1MoVNb steel (Fig. 1): 20 and 30 μm for the 1040 and 1100 • C, respectively. A larger difference occurred for 12Cr-1MoVW steel (Fig. 2): 32 and 105 mm for 1040 and 1100• C, respectively.

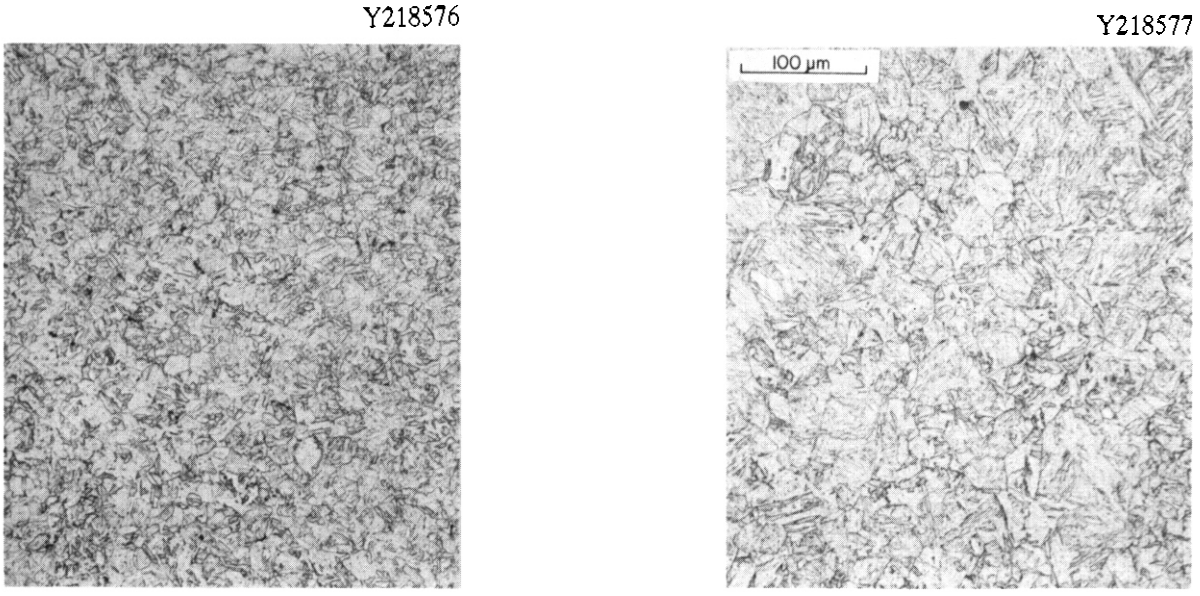

Fig. 1. Microstructures of 9Cr-1MoVNb normalized by annealing 1 h at (a) 1040 • C and (h) 1100 • C followed by an air cool.

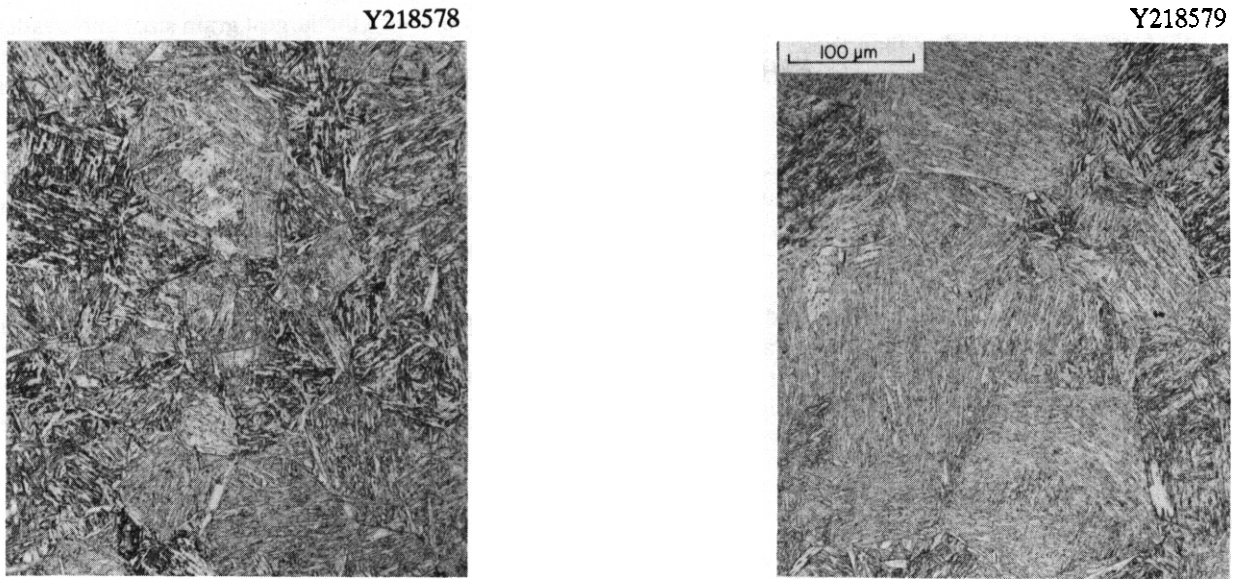

Fig. 2 Microstructures of 12Cr-1MoVW normalized by annealing 1 h at (a) 1040°C and (b) 1100°C followed by an air cool.

Table 1. Chemical composition of steels tested

	C	Si	Mn	P	S	Cr	Mo	Ni	Nb	N
9Cr-1MoVNb	0.092	0.15	0.48	0.012	0.004	8.32	0.86	0.09	0.06	**0.054**
12Cr-1MoVW	0.20	0.17	0.57	0.016	0.003	12.1	1.04	0.51		0.027

The effect of the normalizing-and-tempering heat treatment (no irradiation or thermal aging) on the Charpy impact behavior can be seen in Table 3. For the 9Cr-1MoVNb steel austenitized at 1040 and 1100°C and given a common tempering treatment (either 760 or 780°C), the steel austenitized at 1040°C had the lowest DB'IT. There was little difference in the USE. The only effect of austenitizing temperature for the 12Cr-1MoVW steel is the slightly lower DBTT for the steel tempered at 780°C after austenitizing at 1100°C, although the difference was small. The USE of the 12Cr-1MoVW given the 1100°C austenitization treatment (for a common tempering treatment) had a slightly lower value than that given the 1040°C treatment.

Tempering (for a given austenitization temperature) affected the 9Cr-1MoVNb steel: tempering at 780°C lowered the DBTT relative to the 760°C temper. The USE was not affected. Much less effect of tempering occurred for the 12Cr-1MoVW steel. No change in DBTT was observed for the specimens austenitized at 1040°C, but after austenitizing at 1100°C, the DBTT for specimens tempered at 780°C showed a decrease relative to that for specimens tempered at 760°C. The USE of the 12Cr-1MoVW steel increased slightly with increasing tempering temperature for both austenitizing temperatures.

Thermal aging for up to 20000 h at 400°C had little effect on the Charpy behavior of the 9Cr-1MoVNb and 12Cr-1MoVW steels (Table 3). The largest effect was for 9Cr-1MoVNb normalized at 1100°C and tempered at 760°C, which showed a lowering of the DBTT with aging time. The USE for this heat treatment increased slightly.

Table 4 gives the unirradiated and irradiated DBTT and USE values along with the increase in DBTT (ΔDBTT) and decrease in USE (ΔUSE). Figures 3 to 6 show Charpy curves for the irradiated specimens along with curves for the unirradiated specimens. Irradiation caused an increase in DBTT and a decrease in USE for all conditions. For all conditions, the shift in DB'IT for the 12Cr-1MoVW steel was over twice that for 9Cr-1MoVNb.

The ΔDBTT for the 9Cr-1MoVNb specimens austenitized at 1100 °C (the ones with the largest grain size) and irradiated to ≈5 dpa at 365 °C were ≈10 °C higher than those austenitized at 1040 °C (Fig. 3). However, tempering had no effect on ΔDBTT. The ΔUSE was also fairly constant, although the change in USE was slightly less after the 780 °C temper (for a given austenitization temperature).

Irradiation of the 12Cr-1MoVW steel at 365 °C, resulted in little difference in the DBTT for the four different heat treatments (Fig. 4). The USE values for all four conditions also appeared similar after irradiation. The only noticeable difference was in the USE values after austenitizing at 1100 °C, where the steel tempered at 780 °C had a significantly higher USE than that tempered at 760 °C.

When the 9Cr-1MoVNb was irradiated to 36 dpa at 420 °C (Fig 5), the specimens austenitized at 1040 °C and given the two different tempering treatments developed similar ΔDBTTs (39 and 45 °C). Thus, the heat treatment with the lowest DBTT and highest USE before irradiation maintained that relative position after irradiation. There was a somewhat larger difference for the 12Cr-1MoVW steel irradiated at 420 °C (Fig. 6), where the specimens tempered 2.5 h at 780-C developed a slightly larger ΔDBTT and ΔUSE.

Discussion

The change in grain size. (Table 2) caused by different austenitization temperatures was considerably greater for the 12Cr-1MoVW (32 and 105 μm for 1040 and 1100 °C, respectively) than for the 9Cr-1MoVNb (20 and 30 μm for 1040 and 1100 °C, respectively). The smaller change for the 9Cr-1MoVNb is attributed to the niobium in this steel; niobium inhibits grain growth.

The prior austenite grain size effect on Charpy behavior can be discerned by comparing the behavior of steels given the 1040 and 1100 °C austenitizing treatment and then given a common tempering treatment. For the 9Cr-1MoVNb steel prior austenite grain size had a slight effect on DBTT (Table 3), because for both the 760 and 780 °C tempers, the steel austenitized at 1040 °C had the lower DBTT. As expected, the 780 °C temper has the greatest effect on lowering the DBTT of the 9Cr-1MoVNb for both austenitizing treatments. Tempering the steel austenitized at 1100 °C at 780 °C has a relatively larger effect than it does for the 1040 °C austenitization temperature. The USE of the 9Cr-1MoVNb steel appears to be unaffected by the normalizing-and-tempering treatment.

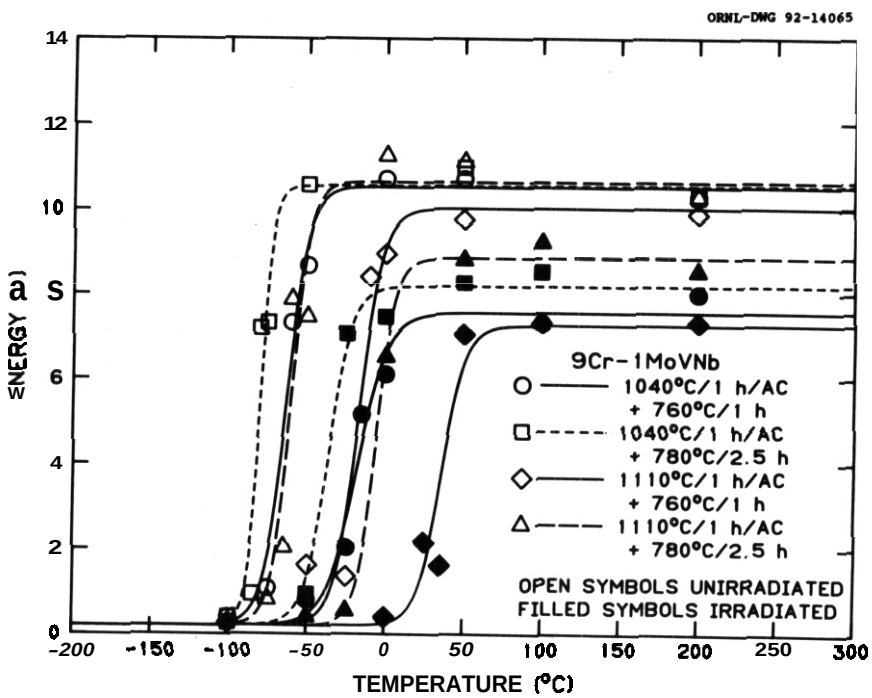

Fig. 3. Charpy impact curves for 9Cr-1MoVNb steel given four different heat treatments and tested as heat treated and after irradiation to 5 dpa at 365 °C.

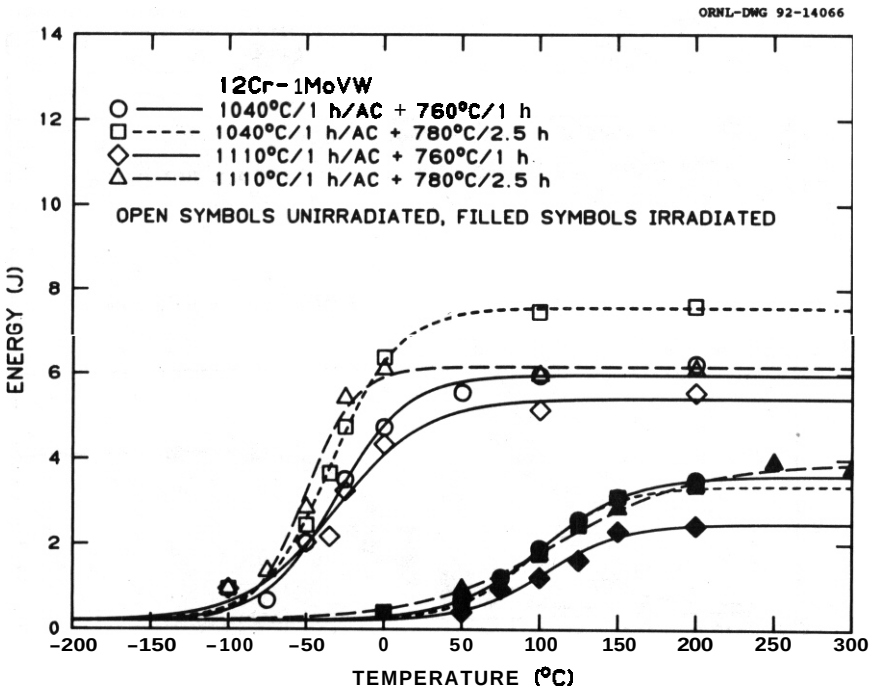

Fig. 4. Charpy impact curves for 12Cr-1MoVW steel given four different heat treatments and tested as heat treated and after irradiation to 4 dpa at 365° C.

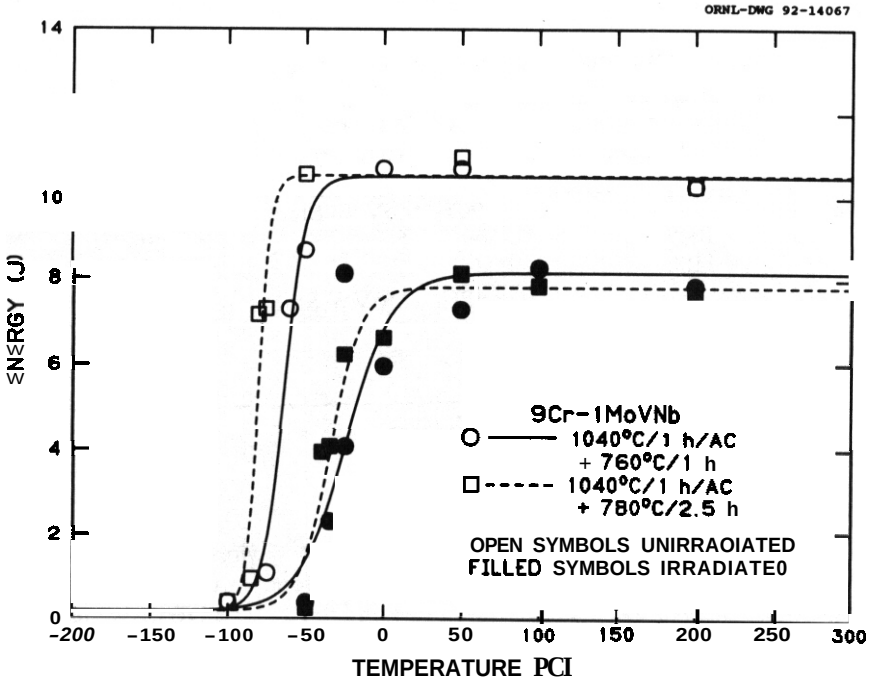

Fig. 5. Charpy impact curves for 9Cr-1MoVNb steel normalized at 1040◦ C and then given two different tempering treatments and tested as heat treated and after irradiation to 36 dpa at 420° C.

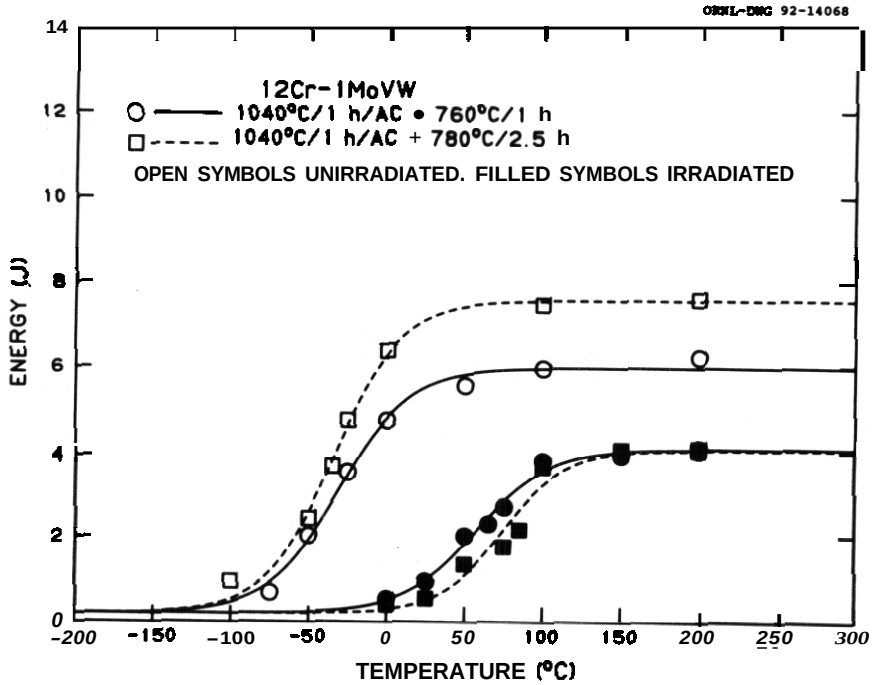

Fig. 6. Charpy impact curves for 12Cr-1MoVW steel normalized at 1040°C and then given two different tempering treatments and tested as heat treated and after irradiation to 35 dpa at 420°C.

Table 2 Estimated grain sizes of steels tested

Austenitization Temperature, °C	ASTM Grain Size Number*	Average Grain Diameter, mm
	9Cr-1MoVNb Steel	
1040	8	20
1100	7	32
	12Cr-1MoVW Steel	
1040	7	32
1100	3-4	153

* Estimated with grain size eyepiece.

The normalized-and-tempered 12Cr-1MoVW steel showed a different behavior from the 9Cr-1MoVNb steel (Table 3). Although a change in austenitization temperature produced a larger difference in prior-austenite grain size than for 9Cr-1MoVNb, there was no apparent effect of prior austenite grain size on DBTT. The DBTT values were the same for the 12Cr-1MoVW given the two different austenitizing treatments and then tempered at 760°C. There was a difference when tempered at 780°C, but the difference was opposite to that expected for a grain-size effect. The specimen austenitized at 1040°C and tempered at 780°C had a DBTT similar to that of the two steels tempered at 760°C, but the steel austenitized at 1100°C and tempered at 780°C had a lower DBTT (16°C lower). A larger prior austenite grain size would be expected to give a higher DBTT. Therefore, if this difference is significant, it must be due to the higher tempering temperature and not the difference in grain size. The USE of the 12Cr-1MoVW in the normalized-and-tempered condition appears to be affected slightly by tempering (Table 3). In each case, the steel tempered at 780°C had a higher USE than that tempered at 760°C.

Table 3. Impact properties of aged steels

Heat Treatment	Aging Time (h)	DBTT (°C)	USE (J)
	9Cr-1MoVNb Steel		
1040/1h/AC;760/1h	0	-64	10.5
	5000	-58	9.4
	10000	-56	11.1
	20000	-54	11.6
1040/1h/AC;780/2.5h	0	-80	10.6
	5000	-77	11.6
	10000	-78	12.2
	20000	-80	12.4
1100/1h/AC;760/1h	0	-17	10.0
	5000	-28	11.1
	10000	-41	11.8
	20000	-39	11.8
1100/1h/AC;780/2.5h	0	-61	10.6
	5000	-60	11.3
	10000	-54	11.6
	20000	-56	12.5
	12Cr-1MoVW		
1040/1h/AC;760/1h	0	-32	6.0
	5000	-28	6.1
	10000	-25	6.3
	20000	-23	5.7
1040/1h/AC;780/2.5h	0	-35	7.6
	5000	-38	7.1
	10000	-31	7.2
	20000	-27	8.0
1100/1h/AC;760/1h	0	-34	5.4
	5000	-30	5.2
	10000	-22	5.3
	20000	-24	5.2
1100/1h/AC;780/2.5h	0	-51	6.2
	5000	-44	6.2
	10000	-47	6.8
	20000	-48	6.7

The lack of a prior-austenite grain size effect in 12Cr-1MoVW steel compared to the 9Cr-1MoVNb steel may indicate that the precipitate in the microstructure of the 12Cr-1MoVW controls the fracture behavior [1]. The 12Cr-1MoVW contains twice as much carbon as the 9Cr-1MoVNb steel, and in the normalized-and-tempered condition, the 12Cr-1MoVW contains over twice as much precipitate (3.8 wt% precipitate in the 12Cr-1MoVW compared to 1.5 wt% in 9Cr-1MoVNb) [3]. This difference in precipitation can be seen in Fig. 7, where carbide extraction replicas of the 9Cr-1MoVNb and 12Cr-1MoVW steels are shown after similar normalizing-and-temperingtreatments. (The majority of the precipitate in both steels was shown to be $M_{23}C_6$, with a small amount of MC [3].) These photomicrographs [3] show the large amount of precipitate in 12Cr-1MoVW steel, which could affect the fracture process. Furthermore, the precipitate in the 12Cr-1MoVW is uniformly distributed within the prior austenite grains and therefore may minimize the role of the grain boundaries, while for the 9Cr-1MoVNb, precipitate is along prior austenite grain boundaries, which could enhance the role grain boundaries play in the fracture process.

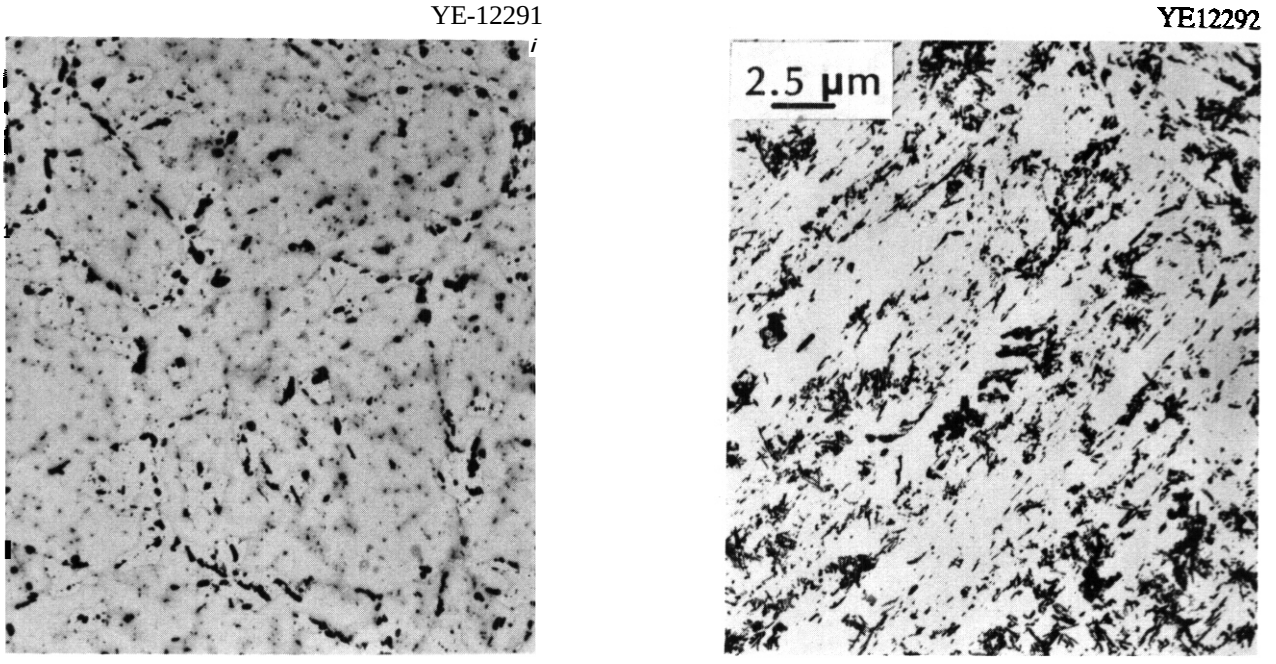

Fig. 7. Extraction replicas of normalized-and-tempered (1040°C/0.5h/AC + 780°C/2.5h/AC) (a) 9Cr-1MoVNb and (b) 12Cr-1MoVW steels.

This interpretation can be rationalized with results obtained by Little et al. [4], who studied three steels: 12Cr-0.1C (steel 1), 12Cr-0.1Mo-0.3V-0.14C (steel 2), and 12Cr-0.6Mo-0.15V-0.25Nb (steel 3) (all three steels contained ≈0.5Ni). A strong effect of prior-austenite grain size on DBTT was found for steel 2, which appears similar to 12Cr-1MoVW. The differences in steel 2 and 12Cr-1MoVW involve the carbon and molybdenum content (steel 2 also did not contain tungsten). Based on the microstructural studies described by Little et al., it is concluded that the difference is probably due to the lower carbon content, which caused less precipitate to form in steel 2. This implies that the DB'IT of the 12Cr-1MoVW could be affected significantly by lowering the carbon content. Little et al. also noted an increase in USE with increasing tempering temperature and time, similar to the observations of the present investigation.

The presence of niobium in steel 3 of Little et al. makes it somewhat similar to the 9Cr-1MoVNb steel, although there was considerably more niobium present in steel 3. Those investigators found that the niobium stabilized the prior austenite grain size, similar to the observations of the present work. Because of the larger amount of niobium in steel 3, it was not possible to change the prior-austenite grain size for the austenitizing treatments used by Little, et al.

No degradation of properties was observed after thermal aging at 400°C (Table 3). The most significant changes appeared to be decreases in DBTT and increases in USE for the 9Cr-1MoVNb steel austenitized at 1100°C and tempered at 760°C. The observed changes are the opposite of effects observed during irradiation. Thus, any properties degradation observed during irradiation cannot be attributed to thermal aging that occurred simultaneously with irradiation.

The irradiation results at 365°C indicated that there may be a slight effect of grain size on ΔDBTT for the 9Cr-1MoVNb (compare different austenitization temperatures for a common tempering temperature in Table 4). There was no apparent effect of tempering on ΔDBTT, but there did appear to be an effect of tempering on USE tempering at 780°C resulted in a higher USE (lower ΔUSE) after irradiation than tempering at 760°C.

After irradiating the 9Cr-1MoVNb at 420°C to a much higher fluence, the results confirm the observation of the 365°C tests that there is no effect of tempering on DBTT. The effect of tempering on USE noted for the 365°C tests is not present in these tests.

TABLE 4. Impact properties of irradiated steels

Heat Treatment	DBTT, °C Unirrad	DBTT, °C Irrad	USE, J Unirrad	USE, J Irrad	ΔDBTT °C	ΔUSE J (%)
		9Cr-1MoVNb Steel				
5 dpa at 365°C						
1040/1h/AC;760/1h	-64	-19	10.5	7.6	45	2.9 (38)
1040/1h/AC;780/2.5h	-80	-37	10.6	8.2	43	2.4 (29)
1100/1h/AC;760/1h	-17	36	10.0	7.3	53	2.7 (37)
1100/1h/AC;780/2.5h	-61	-6	10.6	8.9	55	1.7 (19)
36 dpa at 420°C						
1040/1h/AC;760/1h	-64	-25	10.5	8.2	39	2.3 (22)
1040/1h/AC;780/2.5h	-80	-35	10.6	7.8	45	2.8 (26)
		12Cr-1MoVW Steel				
4 dpa at 365°C						
1040/1h/AC;760/1h	-32	97	6.0	3.6	129	2.4 (40)
1040/1h/AC;780/2.5h	-35	95	7.6	3.4	130	4.2 (55)
1100/1h/AC;760/1h	-34	100	5.4	2.5	134	2.9 (54)
1100/1h/AC;780/2.5h	-51	107	6.2	3.9	158	2.3 (37)
35 dpa at 420°C						
1040/1h/AC;760/1h	-32	55	6.0	4.1	87	1.9 (32)
1040/1h/AC;780/2.5h	-35	72	7.6	4.1	107	3.5 (46)

Because austenitization at 1100°C resulted in only a 10°C larger ΔDBTT for the 9Cr-1MoVNb irradiated at 365°C and there was no effect of tempering on DBTT or USE after 36 dpa at 420°C, it is concluded that heat treatment has a minor effect on the irradiated properties. These results lead to the conclusion that decreasing the grain size would be the preferred way to produce the lowest possible DBTT before irradiation in order to maintain the DBTT as low a possible after irradiation, Increased tempering temperatures or times would not be preferred, because these processes cause a reduction in strength.

No grain size effect could be detected for the 12Cr-1MoVW steel in the unirradiated condition or after irradiation at 365°C. Here, the steel with the lowest DBTT before irradiation had the highest ΔDBTT after irradiation, although all steels had quite similar DBTTs after irradiation. The USE, which appeared to be affected by tempering before irradiation, was essentially the same for all four conditions after irradiation. After irradiation to 35 dpa at 420°C, the specimens given the 780°C temper had a larger ΔDBTT and ΔUSE than after the 760°C temper. From these results, it is concluded that there is an incentive to use a lower tempering temperature than the 780°C often used for this steel, since a lower tempering temperature would give a better strength without any penalty in ΔDBTT.

Qualitatively, the results are in agreement with previous tests of these steels irradiated in fast reactors [5,6]. Hu and Gelles [5] irradiated 9Cr-1MoVNb and 12Cr-1MoVW steels at 390°C in EBR-II to 13 and 26 dpa and found that the ΔDBTT had saturated by 13 dpa. Saturation occurred at a ΔDBTT of about 54 and 144 dpa for the 9Cr-1MoVNb and 12Cr-1MoVW, respectively. The saturation ΔDBTT for 12Cr-1MoVW steel at ≈400°C in a fast reactor has been shown to be similar for different heats of the steel irradiated and tested by different investigators. Several investigators have shown that ΔDBTT decreases with increasing irradiation temperature in a fast reactor [5-6]. Therefore, the ΔDBTTs observed after irradiation at 420°C have the expected magnitude (slightly lower than the EBR-II results at 390°C). The fact that the values at 365°C are not larger than those observed at 390°C indicates that saturation did not occur in 4-5 dpa. Previous observation on the same heat of 12Cr-1MoVW steel irradiated to 10 and 17 dpa at 365°C in MOTA indicated that saturation occurred by 10 dpa at a ΔDBTT of ≈160°C [6]. Specimens are in the reactor at both 365 and 420°C to determine whether the observations on heat treatment continue to apply at higher fluences.

Wassilew and Ehrlich examined the effect of tempering on the Charpy behavior of miniature specimens of the MANET steel (Fe-12Cr-0.5Mo-0.3V-0.25Nb-0.7Ni-0.5Si-0.1C) that was developed for fusion reactor applications [7]. Three tempering treatments were used 2 h at 600°C, 2 h at 750°C, and 2 h at 780°C. The DBTT and USE before irradiation varied with the tempering treatment: the higher the tempering temperature, the lower the DBTT and the higher the USE. The DBTT varied

from -45 to 25 °C when the steel was tempered at 780 and 600 °C, respectively. No DBTT was given for the steel tempered at 750 °C, but the curves shown indicated it was slightly above that obtained after tempering at 780 °C. The USE values were respectively 6.75, 6.1, and 5.25 J for the 780, 750, and 600 °C tempering temperatures. After irradiation to 5 dpa at 300 °C in the HFR (High Flux Reactor in Petten, The Netherlands), the ΔDBTT showed a dependence on tempering: 210 and 310 °C for the steels tempered at 780 and 600 °C, respectively. The ΔDBTT for the 750 °C temper was not given, but the curve fell between the other two, and was closest to the curve for the 780 °C temper.

1MoVW steel. Tempering treatment also had only a slight effect. The shift in DBTT was relatively independent of heat treatment, but the shifts for the 12Cr-1MoVW steel were over twice those for 9Cr-1MoVNb steel. Therefore, it does not appear possible to use heat treatment to reduce the effect of irradiation on the DB'IT of 12Cr-1MoVW. Because of the lack of a heat treatment effect on DBTT, however, it may be possible to use this steel without tempering to the low strength levels at which the steel is usually used.

References

[1] Klueh, R. L. and Alexander, D. J., "Heat Treatment Effects on Toughness of 9Cr-1MoVNb and 12Cr-1MoVW Steels Irradiated at 365 °C," Journal of Nuclear Materials. Vol. 191-194, 1992.

[2] Alexander, D. J., Nanstad, R. K., Corwin, W. R., and Hutton, J. T., "A Semiautomated Computer-Interactive Dynamic Impact Testing System," Applications of Automation Technolow to Fatigue and Fracture Testing, ASTM STP 1092, A. A. Braun, N. E. Ashbaugh, and F. M. Smith, Eds., American Society for Testing and Materials, Philadelphia, 1990 pp. 83-.

[3] Vitek, J. M. and Klueh, R. L., "Precipitation Reactions During the Heat Treatment of Ferritic Steels," Metallurgical Transactions A, Vol. 14.4, 1983 pp. 1047-1055.

[4] Little, E. A., Hames, D. R., Pickering, F. B., and Keown, S. R., "Effectsof Heat Treatment on Structure and Properties of 12% Cr Steels," Metals Technology, Vol. 4, 1977, pp. 205-217.

[5] Hu, W. L. and Gelles, D. S., 'The Ductile-to-Brittle Transition Behavior of Martensitic Steels Neutron Irradiated to 26 dpa," Influence of Radiation on Material Properties: 13th International Symoosium (Part II), ASTM STP 956, F. A. Gamer, C. H. Henager, Jr., and N. Igata, Eds., American Society for Testing Materials, Philadelphia, 1987, pp. 83-97.

[6] Klueh, R. L. and Alexander, D. J., "Irradiation Effects on Impact Behavior of 12Cr-1MoVW and 2 1/4Cr-1Mo Steels," Effects of Radiation on Materials: 15th International Symposium, ASTM STP 1125, R. E. Stoller, A. S. Kumar, and D. S. Gelles, Eds., American Society for Testing and Materials, Philadelphia, 1992, to he published.

[7] Wassilew, C. and Ehrlich, K., "Effect of Neutron Irradiation on the Dynamic Fracture Toughness Behaviour of the 12% Cr Steel MANET-I Investigated using Subsize V-Notch Specimens," Journal of Nuclear Materials, Vol. 191-194, 1992.

RELATIONSHIP OF BAINITIC MICROSTRUCTURE TO IMPACT TOUGHNESS IN Cr-Mo AND Cr-W STEELS

R. L. Klueh and D. J. Alexander (Oak Ridge National Laboratory)

OBJECTIVE

The task under which this work was carried out has the objective of developing ferritic steels for fusion reactor applications. The work reported here seeks to develop an understanding of the relationship between microstructure and properties of ferritic steels, which should aid the development of steels for fusion.

SUMMARY

Non-classical bainite microstructures can develop during continuous cooling of low-carbon alloy steels. These differ from classical upper and lower bainite developed by isothermal transformation. Two non-classical bainite microstructures were produced in a 3Cr-1.5Mo-0.25V-0.1C steel using different cooling rates after austenitizing—water quenching and air cooling. The carbide-free acicular bainite formed in the quenched steel had a lower ductile-brittle transition temperature (DBTT) than the granular bainite formed in the air-cooled steel. With increasing tempering parameter, the DBTT of both decreased and approached a common value, although the final value occurred at a much lower tempering parameter for the quenched steel than for the air-cooled steel. The upper-shelf energy was similarly affected by microstructure. These observations along with similar observations in two Cr-W steels indicate that control of the bainite microstructure can be used to optimize strength and toughness.

PROGRESS AND STATUS

Introduction

Ferritic steels that are of interest for fusion reactor applications include the martensitic 9Cr-1MoVNb (modified 9Cr-1Mo) and 12Cr-1MoVW (Sandvik HT9) steels and the bainitic 2 1/4Cr-1Mo steel. In addition to these conventional ferritic steels, reduced-activation ferritic steels are being developed [1]. These are hainitic and martensitic steels that are patterned after the conventional ferritic steels. It is felt that an understanding of the relationship of the microstructure to properties of these steels would aid in the successful development of reduced-activation ferritic steels and/or an improvement of Cr-Mo steels for fusion reactors.

Previous work demonstrated that the type of bainite microstructure developed in a 3Cr-1.5MoV steel during continuous cooling from the austenitization temperature affected the impact toughness [2]. Since the toughness of femtic steels and the effect of irradiation on toughness is one of the main concerns for ferritic steels in fusion reactors, it is of interest to understand how this heat treatment affects the properties. The 3Cr-1.5MoV steel is considered as a possible replacement for 2 1/4Cr-1Mo in fossil-fired power plants and could also be used for fusion applications. Therefore, an understanding of the effect of heat treatment on the microstructures and properties of these steels could aid in the development of steels for fusion applications—both Cr-Mo steels and reduced-activation steels.

In this paper, an extension of the previous work on the 3Cr-1.5MoV is discussed along with similar observations on reduced-activation Cr-W steels.

Emerimental Procedure

Details on the chemical composition of the argon-oxygen-decarburized (AOD) heat of 3Cr-1.5MoV steel (3Cr-1.5Mo-0.1V-0.1C, compositions in wt. %) used for this study have been published [1]. The ingot was processed to 100-mm-thick plate, and plates measuring 0.1 x 1.6 x 1.4 m were heat treated. One plate was air cooled (normalized) and one was water quenched after annealing 2 h at 955°C; both were stress relieved 2 h at 565°C. Despite the stress relief, these materials will be referred to as normalized and quenched, respectively (there was little indication of precipitation after the stress relief [1]). Impact properties were measured with standard Charpy V-notch specimens (10mm x 10mm x 55mm) taken from the 1/4- and 3/4-thickness depths in the plates. Cooling rates at these thicknesses were approximately 0.12 and 1.67°C/s (7 and 100°C/min) for the normalizing and quenching heat treatment, respectively. The plates were tempered at 663 to 704°C and from 1 to 30 h. Tempering conditions were expressed as a tempering parameter, $TP = T(20 + \log t) \times 10^{-3}$, where T is temperature in Kelvin and t is time in hours.

The Cr-W steels were experimental heats with the following nominal compositions (in wt %): 2.25Cr-2W-0.1C (designated 2 1/4Cr-2W) and 2 1/4Cr-2W-0.25V-0.1C (designated 2 1/4Cr-2WV). Details on composition, microstructure, and processing have been published [1]. To demonstrate the effect of cooling rate on the steels, 10-mm square and 3.3-mm square bars were normalized by first austenitizing in a helium atmosphere in a tube furnace and then cooling by pulling into the cold zone. To austenitize, the 2 1/4Cr-2W steel was annealed 1 h at 900 °C, and the 2 1/4Cr-2WV was annealed 1 h at 1050 °C. The higher temperature was used for the latter steel to assure that any vanadium carbide present dissolved during austenitization.

Miniature Charpy specimens of the Cr-W steels were machined from 15.9-mm-thick plate. Specimens were essentially one-third the standard size and measured 3.3 x 3.3 x 25.4 mm and contained a 0.51-mm deep 30° V-notch with a 0.05 to 0.08-mm-root radius. Specimens were machined from 15.9-mm plate in the longitudinal orientation with a transverse crack (LT). To determine the effect of heat treatment, specimens taken directly from 15.9-mm heat-treated plate were tested. Tests were also carried out on specimens that were normalized directly. The normalizing treatments were the same as those used for the bars. Tempering conditions were 1 h at 700 °C and 1 h at 750 °C.

Results

Microstructures

Transmission electron microscopy (TEM) of the quenched and the normalized 3Cr-1.5MoV steel plates is shown in Fig. 1. Based on optical microscopy, TEM, and the continuous-cooling transformation diagram [3], both the quenched and the air-cooled microstructures were entirely bainite, although neither microstructure was typical of classical upper or lower bainite.

The quenched steel had a lath structure that contained a high density of dislocations. Figure 1(a) is typical of most of he specimen, although a few isolated areas contained laths that were not as developed and were similar to the more equiaxed microstructure of the normalized steel, although there were no indications of the dark islands that appeared in the normalized steel [Fig. 1(b)].

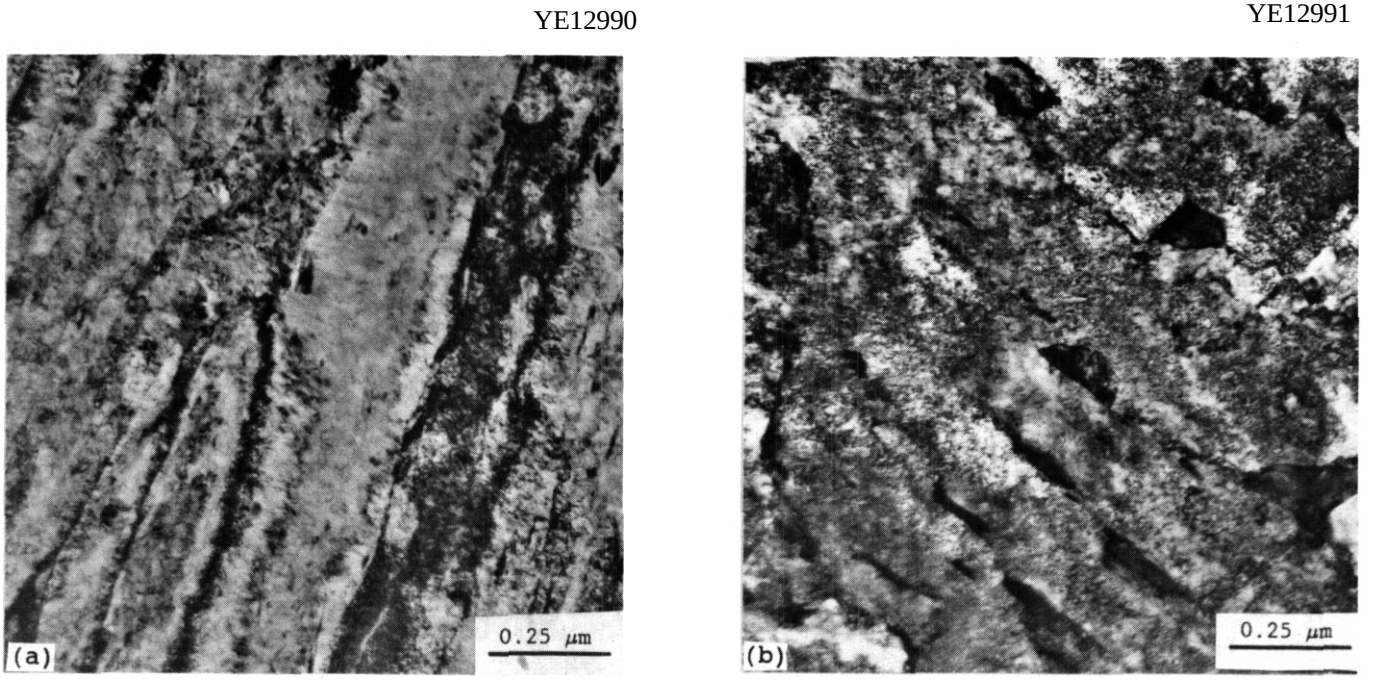

Fig. 1. Transmission electron micrographs of (a) quenched and (b) normalized 3Cr-1.5MoV steel

The normalized steel microstructure consisted mainly of regions containing a high dislocation density in which dark regions or "islands" were scattered throughout [Fig. 1(b)]. The subgrain structure was equiaxed, rather than the lath-type morphology of the quenched steel. A few scattered regions contained indistinct laths, indicating a tendency toward elongated subgrains. The lath structure was not as developed as it was during quenching and it contained islands, which were often elongated.

Before tempering, there was little indication of any precipitate present in either the quenched or the normalized steel [2]. After tempering, TEM and carbide extraction replicas indicated that the quenched steel developed carbides on the lath boundaries with smaller needle-like precipitates within the matrix. The normalized steel also developed two types of precipitate morphologies: regions containing an agglomeration of globular carbides surrounded by a high density of finer needle-like precipitates. The agglomeration of globular carbides was associated with the islands in Fig. 1(b) [2].

The 2 1/4Cr-2W and 2 1/4Cr-2WV steels were examined after cooling at two different rates (different sized specimens were cooled). Optical metallography indicated both steels were 100% bainite after both the fast and slow cool, although there were differences in appearance (Fig. 2). The specimen given the fast cool appeared more acicular. When microstructures were examined by TEM, the results were similar to those for the 3Cr-1.5MoV steel. The fast-cooled steel had a lath structure [Fig. 3(a)], and the slow-cooled steel had an equiaxed structure with dark islands [Fig. 3(b)].

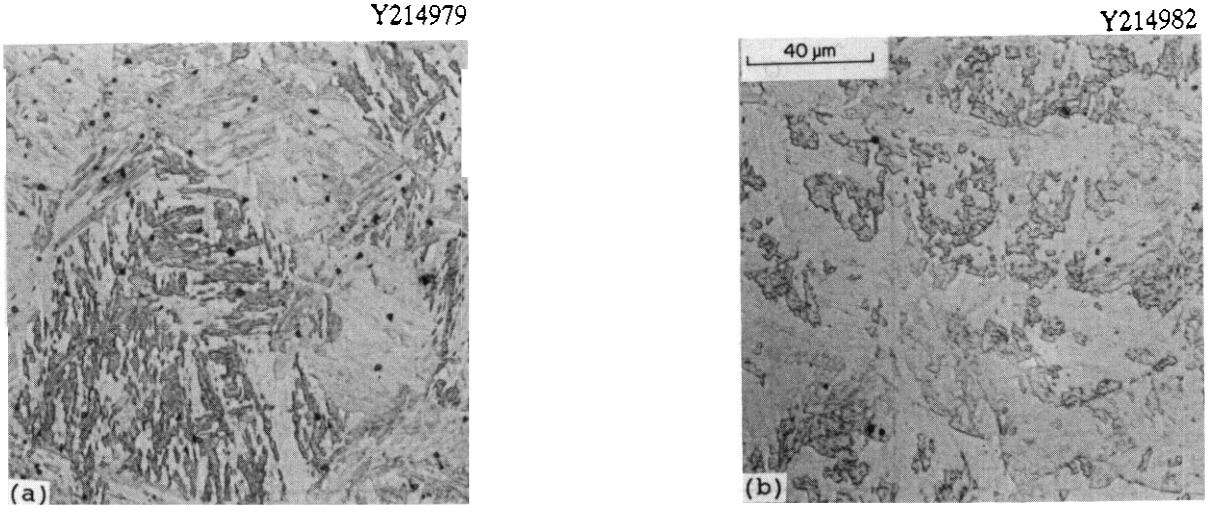

Fig. 2. Optical microstructure of 2 1/4Cr-2WV steel after (a) fast coo1 and (b) slow cool.

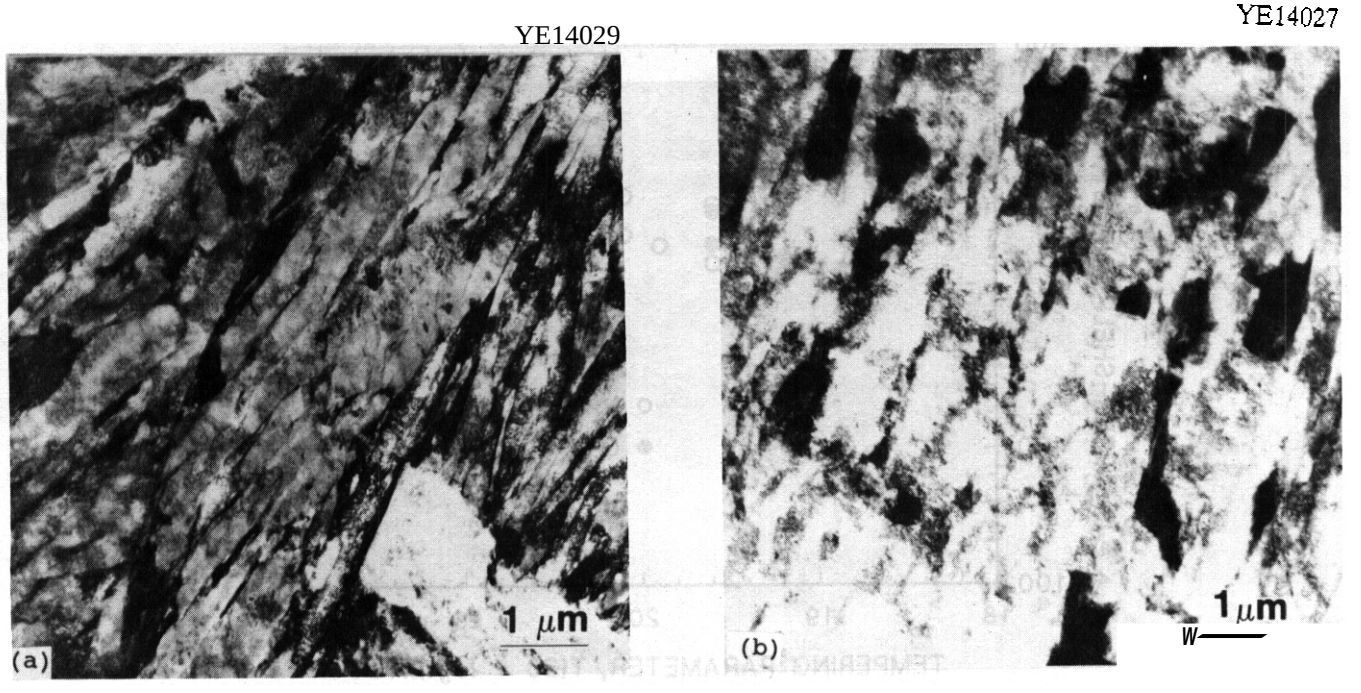

Fig. 3. Transmission electron micrographs of 2 1/4Cr-2W steel after (a) fast-cool and (b) slow-cool.

Impact Toughness

Charpy impact tests were conducted on the quenched and the normalized plates of 3Cr-1.5MoV steel after various tempering treatments (different tempering parameters) (Fig. 4). Tempering had a larger immediate effect on the ductile-brittle transition temperature (DBTT) of the quenched plate than the normalized plate [Fig. 4(a)]. A tempering parameter of 18.7 x lo) (1 h at 663°C) lowered the DBTT of the quenched plate from 67 to -48°C, whereas the same tempering treatment for the normalized steel lowered it from 98 to 60°C. With continued tempering, the DBTT of both the quenched and the normalized plates decreased, with the decrease more pronounced for the normalized plate. Only after the highest tempering parameter used (20.7 x lo), 16 h at 701°C), however, did the DBTT of the normalized steel approach that for the quenched steel. The relative effect on the upper-shelf energy (USE) was somewhat similar [Fig. 4(b)]. The lowest tempering parameter produced a high USE for the quenched plate relative to that for the normalized plate. However, for higher tempering parameters, the USE of the quenched and the normalized plates had similar values.

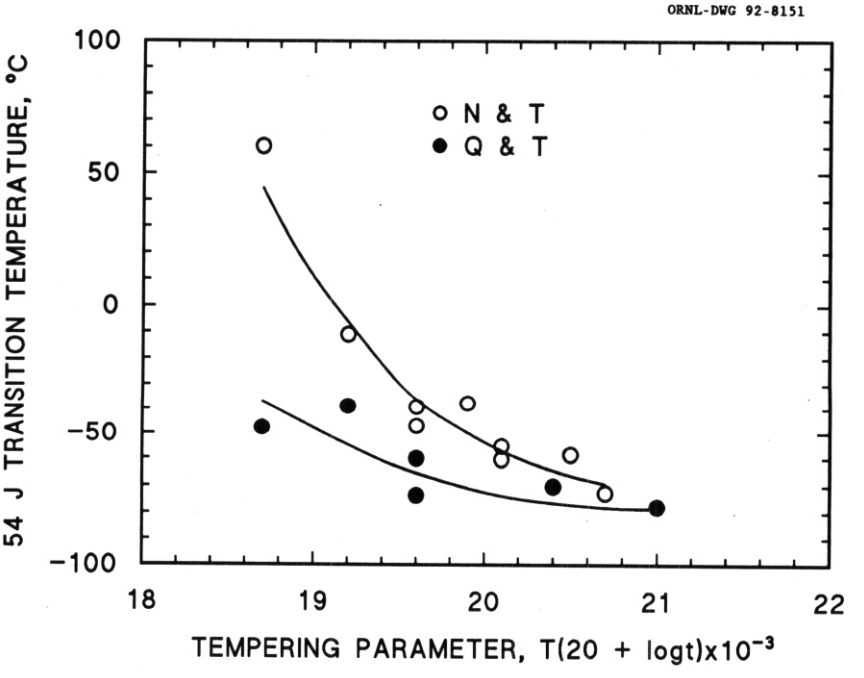

(a)

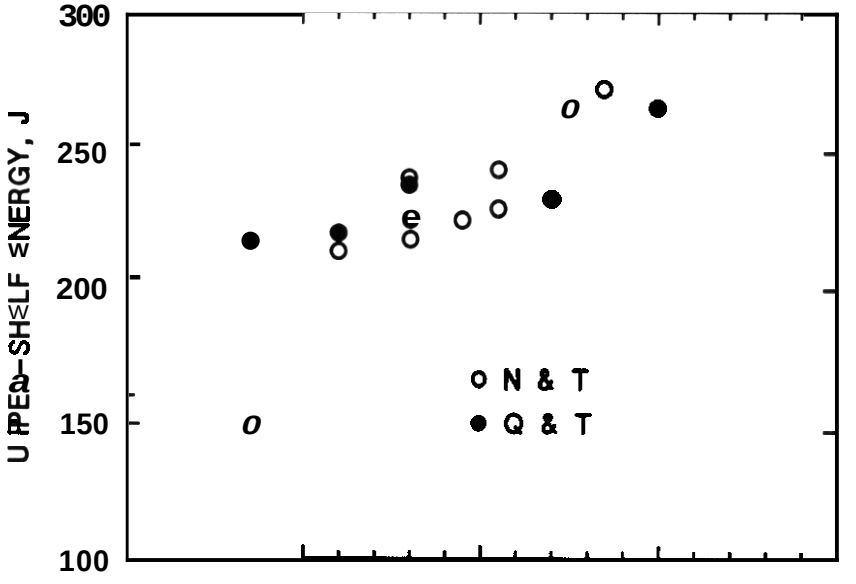

When the two Cr-W steels were heat treated in the 113-size Charpy specimen geometry (3.3-mm square cross section), they were 100% bainite. Table 1 shows the Charpy impact test results when the steels were heat treated as 1/3-size Charpy specimens and tempered at 700 and 750' C, respectively. *Also* given are results when heat treated **as** 15.9-mm plate (the 2 1/4Cr-2W **was** tempered at 700 °C, and the 2 1/4Cr-2WV at 750 °C). For the latter tempering treatment, 2 1/4Cr-2W was 100% bainite, and 2 1/4Cr-2WV contained 80% bainite and 20% polygonal ferrite. The DBTT in Table 1 was determined where the impact energy was one-half of the USE.

Table 1. Charpy Impact Properties of Reduced-Activation Steels

Alloy	Heat Treatment Geometry					
	1/3-Size Specimen				15.9-mm Plate[1]	
	1 h at 700°C		1 h at 750°C			
	DBTT (°C)	USE (J)	DBTT (°C)	USE (J)	DBTT (°C)	USE (J)
2¼Cr-2W	-56	11.5	-77	10.1	-48	9.6
2¼Cr-2WV	-9	7.0	-52	11.0	0	9.7

[1]2¼Cr-2W was tempered 1 h 700°C; 2¼Cr-2WV was tempered 1 h 750°C.

The microstructure, as reflected in the size of the specimen heat treated, had a large effect on the properties of 2 1/4Cr-2WV, with much less effect on the 2 1/4Cr-2W (Table 1). Whereas tempering the 1/3-size specimen of 2 1/4Cr-2WV at 750 °C significantly lowered the DBTT and raised the USE relative to values obtained when tempered at 700 °C, the effect of this tempering treatment had much less effect for the 2 1/4Cr-2W. In fact, for the 2 1/4Cr-2W, there was little difference when heat treated as 15.9 mm plate (and tempered at 700 °C) or as a 113-size Charpy specimen (and tempered at 700 or 750 °C). This contrasts with the 2 1/4Cr-2WV steel with a high DBTT for the bainite plus polygonal ferrite microstructure of the 15.9-mm plate, the slightly lower DBTT when the 1/3-size Charpy specimen was normalized and tempered at 700 °C, and then the **still** lower value for the 113-size Charpy specimen normalized and tempered at 750 °C.

DISCUSSION

Bainite develops in steels when transformation from austenite occurs between the temperatures where ferrite and pearlite form, at high temperatures, and martensite forms, at low temperatures. It was originally thought to consist of two easily distinguishable morphological variations, upper and lower bainite, defined according to the temperature of formation. Habraken [3] demonstrated there were microstructural variations on these classical bainite microstructures that formed in the bainite transformation temperature regime. Such "nonclassical" bainite formed more easily during continuous cooling than during isothermal transformation [3,4], where upper and lower bainite formed.

Habraken and Economopoulos [4] contrasted classical and nonclassical bainite using the isothermal transformation (IT) and continuous-cooling transformation (CCT) diagrams. The bainite transformation region of an IT diagram can be divided into two temperature regimes by a horizontal line. Transformation above this line results in upper bainite and below it in lower bainite. For nonclassical bainite, Habraken and Economopoulos [4] showed that a CCT diagram could be divided into three vertical regions. Three different microstructures form when cooling rates are such as to pass through these different zones. A steel cooled rapidly enough to pass through zone I produces a "carbide-free acicular" structure, which consists of side-by-side plates or laths of ferrite containing a high-dislocation density [4]. For an intermediate cooling rate through zone II, a carbide-free "massive" or "granular" structure results, which is generally referred to as granular bainite [4]. Granular bainite has a ferrite matrix consisting of equiaxed subgrains of ferrite with a high dislocation density coexisting with dark "islands" [4]. These islands are enriched in carbon during the bainitic transformation and have been shown to be high-carbon retained austenite, part of which can transform to martensite when cooled below M_s, the martensite start temperature. These regions are referred to as martensite-austenite (or M-A) islands [4]. Since the microstructures developed by slow cooling through zone III were not observed in this study, they will not be discussed.

Microstructures observed by TEM on the quenched and on the normalized (Fig 1)3Cr-1.5MoV steel and on the different-sized specimens of normalized 2 1/4Cr-2W and 2 1/4Cr-2WV (Fig. 3) are indicative of the differences between acicular and granular bainite. Micrographs of the specimens cooled rapidly [Figs. 1(a) and 3(a)] are characteristic of carbide-free acicular bainite [3,4]. The dark areas in the more slowly cooled specimens of Figs. 1(b) and 3(b) are the M-A islands. When granular bainite is tempered, large globular carbides form in the high-carbon M-A islands, whereas elongated carbides form on the lath boundaries of acicular bainite. These are just the morphologies observed when the 3Cr-1.5MoV steel [2] and the 15.9mm plates of 2 1/4Cr-2W and 2 1/4Cr-2WV steel [1] were tempered.

The impact studies indicated that carbide-free acicular bainite had a high impact toughness (low DBTT and high USE) after tempering at a lower temperature or for a shorter time (constant temperature) than for granular bainite (Fig. 4 and Table 1) [1]. Once these toughness properties were reached at a low TP for the acicular bainite, further tempering had little additional rffect. Although the quenched and the normalized steels had similar tensile properties in the as-heat-treated conditions and after similar tempering treatments [2], the observations on toughness mean that a steel consisting of acicular bainite can be optimized for strength and toughness, because it will not be necessary to temper to a low strength to achieve acceptable toughness. This optimization is being applied to develop the Cr-W steels for fusion reactor applications. A low DBTT is important for this application, since the DBTT will increase during neutron irradiation in a fusion reactor.

ACKNOWLEDGEMENT

We wish to thank the following people who helped in this work T. N. Jones carried out the Charpy tests, R. W. Swindeman and R. K. Nanstad reviewed the manuscript, and Frances Scarboro prepared the manuscript.

REFERENCES

1. Klueh, R. L. and Maziasz, P. J.: Met. Trans. A, 1989, 20A, 373.
2. Klueh, R. L. and Nasreldin, A. M.: Met. Trans. A, 1987, 18A, 1279.
3. Habraken, L. J.: Proc. 4th Intern. Conf. Electron Microscopy, Vol 1, (Springer-Verleg, Berlin), 1966, p. 621.
4. Habraken, L. J. and Economopoulos, M.: Transformation and Hardenability in Steels, (Climax Molybdenum Co., Ann Arbor, MI), 1961, p. 69.

REDUCED ACTIVATION FERRITIC ALLOYS FOR FUSION - D. S. Gelles, (Pacific Northwest Laboratory)'

OBJECTIVE

The objective of this work is to provide a summary of reduced activation ferritic alloy development efforts in support of the ITER design activity.

SUMMARY

Reduced activation martensitic alloys can now be developed with properties similar to commercial counterparts, and oxide dispersion strengthened alloys are under consideration. However, low chromium Bainitic alloys with vanadium additions undergo severe irradiation hardening at low irradiation temperatures and excessive softening at high temperatures, resulting in a very restricted application window. Manganese additions result in excessive embrittlement, as demonstrated by post-irradiation Charpy impact testing. The best composition range for martensitic alloys appears to be 7 to 9 Cr and 2 W, with swelling of minor concern and low temperature irradiation embrittlement perhaps eliminated. Therefore, reduced activation martensitic steels in the 7 to 9 Cr range should be considered leading contenders for structural materials applications in power-producing fusion machines.

PROGRESS AND STATUS

Introduction

It has been four years since the last review of effects of irradiation on reduced activation ferritic/martensitic alloys.' To provide input for an upcoming IEA Workshop on Ferritic Steels and to provide a data base for the International Thermonuclear Experimental Reactor (ITER) design, the original review will be updated.

Development of reactor structural materials with low levels of long-term residual radioactivity has been accepted as a goal of the U.S. Fusion Materials Program.[2] For ferrous alloys, this effectively requires that radioactivity levels be negligible 500 years after reactor decommissioning. Such a criterion for reduced activation necessitates that certain deleterious elemental additions be carefully controlled; namely, Cu, Ni, Mo, Nb, and N, with Nb representing the most severe constraint. Within the restrictions of such a reduced activation guideline, ferritic steels can be designed for fusion applications. The design criterion requires for example, that Ni be replaced by C or Mn, and that substitutes be found for Mo and Nb, such as W, V, Ta and Ti.

Allovs under consideration

The alloy compositions being considered for reduced activation ferritic steels are based on two commercially important alloy classes: 2¼ Cr steels and the super 9 to 12 Cr steels. The former is a Bainitic class and the latter a martensitic class. Both of these steels contain Mo at levels of about 1%. Also, reduced activation oxide dispersion strengthened (ODS) ferritic alloys can be based on MA957, a 14Cr-1Ti-0.25Y O, mechanically alloyed product from IncoMAP, Huntington, WV, USA containing Mo at a level of 0.25%. Therefore, design of reduced activation alternatives to these commercial alloys requires substitution for Mo; W and V are leading candidates. In cases where NbC is used effectively in the commercial composition, Ta or Ti can be substituted for Nb. Where Ni additions are needed, for example, to obtain a fully martensitic 12 Cr steel, other austenite stabilizing additions must be included. Mn and C have thus far been considered. Therefore, four classes of reduced activation ferritic/martensitic alloys are possible: low chromium Bainitic alloys, 5 to 9 Cr martensitic alloys (the range being expanded to lower Cr levels), 12 Cr stabilized martensitic alloys, and 14 Cr mechanically alloyed ODS ferritic alloys.

The alloy compositions which have been considered are given in Table 1. The alloys have been grouped by increasing Cr composition in order to emphasize the similarities between the approaches taken in designing reduced activation steels by different experimenters. The 5 to 9 Cr alloy class and the 12 Cr alloy class are about equal in size, and the smallest groups comprise the 2 Cr range and ODS alloys. In each steel class, each of the alloying approaches has been tried: W substituted for Mo, V substituted for Mo, small additions of Ta substituted for Nb, and in a few cases, Ti substituted for Nb. However, in many cases, the higher Cr steels were found to be duplex martensitic/delta ferritic and therefore further changes in composition specification were needed. The ODS option has received the least attention by far. One group of alloys specified is, in fact, a reduced activation composition being considered for liquid metal fast breeder reactor structural applications."

'Pacific Northwest Laboratory is operated for the U.S. Department of Energy by Battelle Memorial Institute under Contract DE-AC06-76RLO 1830.

Table 1. Compositions of reduced activation ferritic/martensitic alloys.

Alloy Designation	Composition in weight percent												Ref.
	Cr	W	V	C	Si	Mn	Ta	B	N	P	S	Other	
2Cr-2W	2.06	1.96	--	0.10	0.29	0.50			.001	<.00	.004		[3]
JLF-4	2.25	2.0	0.2	0.1	0.05	0.5	0.07		0.05				[4]
2¼CrV	2.36	--	0.25	0.11	0.17	0.40							[5]
2¼Cr-1WV	2.30	0.93	0.25	0.10	0.13	0.34							
2¼Cr-2W	2.48	1.99	0.01	0.11	0.15	0.39							
2¼Cr-2WV	2.42	1.98	0.24	0.11	0.20	0.42							
AS-3	3.0	2.0	0.4	0.12									
AS-4	3.0	2.5	0.2	0.12	--				.004			0.01Ti	
L1	2.32	<.01	0.50	0.09	0.08	<.01			.004	<.005	.003		[5]
L2	2.82	<.01	1.01	0.09	0.08	<.01			.003		.002		
L3	2.46	--	1.50	0.11	0.30	0.30			.015	<.005	.015		
5Cr-2W	4.84	1.98	--	0.10	0.30	0.50			.002	<.002	.004		[3]
5Cr-2WV	5.00	2.07	0.25	0.13	0.25	0.47							[5]
F-82	7.52	2.2	0.19	0.10	10.17	10.49	--	.0035	.002	.003	.002		[6]
F-82H	7.65	2.0	0.18	0.09	0.09	0.49	0.04	.0034	.002	.005	.001		
9Cr-2W	8.92	1.92	--	0.10	0.28	0.48			.002	<.002	.003		[3]
9Cr	8.96	--	--	0.10	0.30	0.49			.001		.003		
9Cr-1W	9.01	0.99	--	0.10	0.29	0.48			.002		.004		
9Cr-2W	8.92	1.92	--	0.10	0.28	0.48			.002		.003		
9Cr-4W	9.09	3.93	--	0.10	0.29	0.50			.002		.002		
9Cr-.25V	8.82	--	0.26	0.13	0.30	0.46			.019		.002		
9Cr-.5V	8.86	--	0.53	0.11	0.29	0.48			,020		,003		
9Cr-1V	8.72	--	1.08	0.12	0.31	0.51			.018		,003		
Mod.9Cr-1W	9.24	1.06	0.18	0.13	--	--	0.10	.005	.003	--	--		[7]
Mod.9Cr-3W	9.16	3.08	0.16	0.17	--	--	0.10	.007	.003	--	--		
9Cr-2WV	8.73	2.09	0.24	0.12	0.25	0.51							[5]
9CR-2WVTa	8.72	2.09	0.23	0.10	0.23	0.43	0.07						
3A3X nom.	9	2.5	0.3	0.15	--	--					--		[5]
melt	7.5	1.95	0.02	0.17		.002					.005		
3A3X	9.00	2.0	3.30	0.15	0.06	0.04			.002	.001	.001		[8]
3A5X	8.92	2.1	3.30	0.15	0.05	0.04					,002		
A12	9.1	3.68	3.24	0.16									[9]
A13	9.2	2.90	3.25	0.17									
A13	9.22	2.90	1.25	0.17	0.42	0.74	--		.059				[10]
A13Ta	3.0	2.96	1.25	0.18	0.04	0.70	0.11		.045				
A12	3.1	1.68	1.24	0.16	0.37	0.79	--		.06				
A12Ta	3.8	1.85	1.27	0.16	0.03	0.80	0.10		.042				
A12TaLN	3.1	1.77	1.25	0.17	0.02	0.74	0.10		,004				
A12LC	3.0	1.76	1.38	0.09	0.03	1.01			.033				
A12TaLC	3.9	1.76	1.39	1.09	0.03	1.01	0.09		.019				
.4	9.13	1.01	1.52	0.10	0.09	0.02			.003	.005	003		[5]
.6	3.14	1.02	1.23	0.20	0.09	1.08			.003		003		
.5	3.02	1.01	0.51	0.10	0.09	2.68			,003		003		
7	3.82	1.89	0.27	0.10	0.10	2.44			,002		004		
JLF-3	1.00	2.0	0.2	0.1	0.05	0.5	0.07		.05				[4]
JLF-1	3.00	2.0	0.2	0.1	0.05	0.5	0.07		.05				
JLF-2	3.00	2.0	0.2	0.1	0.05	0.5	0.07		.05			0.02Ti	
	9.5	1.80	1.60	0.16	0.06	1.22	0.29	.008	.016	.008	005	0.02Ti	[11]
	9.6	1.81	1.59	0.18	0.07	1.35	0.48	.008	.015	.008	004	0.04Ti	
1	9.8	1.72	1.50	0.23	0.08	0.87	0.14	.008	.020	.003	008	<0.005Ti	
	9.8	1.90	1.50	0.18	0.58	0.89	0.42	.009	,022	.003	.010	0.0087i	

lable 1. Cont.

Alloy Designation	Cr	W	V	C	Si	Mn	Ta	B	N	P	S	Other	Ref.
						mpo	ion in weigh		perc				
.A2	11.4	<.02	*0.26*	3.16									[9]
.A3	11.5	0.24	0.25	**3.16**									
_A4	10.9	0.65	*0.25*	3.17									
.A5	10.9	1.12	0.24	3.16									
.A6	11.7	1.95	0.24	3.15									
.A7	11.2	3.04	**0.23**	3.17									
.A8	11.1	**0.66**	0.46	0.16									
.A9	11.7	0.77	0.80	0.15									
LA10	11.4	0.70	0.25	0.16				0.0083					
LA11	11.2	0.69	0.25	0.16					.103				
LA14	11.4	2.94	0.25	0.17			1.19		.04				
LA7	11.3	2.94	0.25	0.17	1.26	).7(	--		1.59				[10]
LA7Ta	11.4	2.90	0.25	0.15	1.07	).7(	1.12		).73				
LA7TaLN	11.1	2.95	0.24	0.18	3.04	).7(	1.10		005				
L8	12.19	<.01	1.05	0.09	).10	i.41			003	.005	.005		[5]
L9	11.81	0.89	0.28	0.10	3.11	i.41			003		.005		
12Cr1WVTa	11.96	0.82	0.23	0.09	).10	).5(	1.14		,008	.005	.004		[12]
12Cr1WVTa'	11.95	0.80	0.25	0.10	).09	).4!	1.20		,003	.005	.006		
12Cr1VWTa	11.80	0.22	0.97	0.10	).10	'.8(	1.23		005	,005	.006		
12Cr-2WV	11.49	2.12	0.23	0.10	3.24	).4(							[16]
12Cr2WV3Mn	11.23	1.79	0.21	0.08	3.23	).7(							
12Cr2WV6Mn	10.86	1.97	0.21	0.08	0.20	).5'							
1Cr2WV	11.52	1.83	*0.22*	0.17	0.20	).4(							
GA4X nom.	11	*2.5*	0.3	0.15									[5]
melt	10.2	1.1	0.2	0.01	--	,011					<.003		
GA4X	11.0	2.0	0.30	0.14	0.05	1.01			.002	.001	.001		[8]
GA6X	11.1	2.1	0.30	0.15	0.07	).0(					.002	0.01Ti	
JLF-5	12.00	*2.0*	0.2	0.1	0.05	0.5	3.07		).05				[4]
JLF-6	12.00	2.0	0.2	0.1	0.05	*0.5*	3.07		3.05			.0.2Ti	
12Cr-2W	11.56	1.96	--	0.10	0.32	).4!			.001	:.002	.003		[3]
15Cr-2W	14.72	1.94	--	0.11	0.3(				.001		.003		
12Cr-¼Y_2O_3	12.14	--	--	*0.02*	0.05	).0(			.014			.11Y_2O_3	[15]
12Cr-½Y_2O_3	12.11	--	--	0.02	0.03	1.0'			.013			.46Y_2O_3	
12Cr-¼Y_2O_3-.8Ti	12.14	--	--	0.06	*0.01*	).0(			.063			.20Y_2O_3	
12Cr-¼Y_2O_3-.5V	12.19	--	**0.46**	0.04	0.06	).0!			.010			.27Y_2O_3	
12Cr-¼Y_2O_3-1V	12.12	--	0.92	*0.02*	0.05	).0(			.014			.28Y_2O_3	
10Cr-½Y_2O_3-2.7W	10.07	2.72	--	0.14	0.08	).0(			.029			.56Y_2O_3-.49Ti	
10Cr-¼Y_2O_3-.5Ti	10.37	--	--	0.16	0.06				.047			.50Y_2O_3-.40Ti	
9Cr-2W	9.10	2.01	0.30	0.10								.23Y_2O_3	[13]
14Cr-1Ti-.5W	13.8	0.73	--	0.05								.23Y_2O_3-.62Ti	
9Cr-W	9.58	0.80	--	0.04								.21Y_2O_3-.80Ti	[14]
14Cr-1Ti-.5W	12.96	0.76	--	0.05								.23Y_2O_3-.73Ti	

nom. - nominal composition
melt - actual melt composition

The effect of fast neutron irradiation on microstructure and properties has been examined on some alloys for each class of steel, but irradiation experiments are not yet organized for reduced activation ODS alloys. Experiments include irradiation creep, postirradiation tensile strength and Charpy impact measurements. This paper summarizes the similarities and differences in alloy response to neutron irradiation in order to predict the optimum reduced activation ferritic alloy composition for fusion reactor applications.

Summary of Results

Mechanical properties

Studies of the effect of irradiation on reduced activation ferritic alloys have included irradiation creep to fluences as high as 45 dpa covering the temperature range 390 to 600°C,[17] uniaxial tensile tests

following irradiation to fluences as high as 45 dpa,[18-20] Charpy impact tests following irradiation at 365°C to 15 dpa[23-25] and microstructural examinations following irradiation to 115 dpa.[1,18,19,26-28]

Irradiation creep has been studied for all classes of reduced activation ferritic steels: $(2\frac{1}{4}$-3)Cr-(1-2)W, F82H, and (7-12)Cr-(1-2)W.[17] Pressurized tube specimens were irradiated in the Fast Flux Test Facility in the Materials Open Test Assembly (FFTF/MOTA) covering the temperature range 390 to 600°C to doses as high as 9.7 x 10^{22} n/cm or 48.5 dpa. Response was comparable to that of the commercial martensitic alloys, with lowest creep rates found at the lowest and highest chromium contents. The highest creep rates were found at 410°C, corresponding to the peak swelling temperature. Therefore, reduced activation ferritic steels can be expected to perform adequately under irradiation creep conditions, with the worst performance corresponding to conditions promoting void swelling.

Postirradiation uniaxial tensile testing results have also been compiled for all classes of reduced activation ferritic steels. Irradiation conditions included irradiation in the Japanese Materials Testing Reactor (JMTR), in the temperature range 265 to 300°C to low doses up to 3 x 10^{20} n/cm^2 or about 0.1 dpa,[20] and irradiation in the FFTF/MOTA in the temperature range 365 to 585°C to moderate doses up to 46 dpa.[18,19] Specimen geometry included miniature and subminiature sizes, and testing was performed at room temperature, at the irradiation temperature, or over a range of temperatures from room temperature to 600°C. These results are therefore for irradiation conditions that do not match the neutron energy spectrum or helium to dpa ratio of a fusion reactor. Nonetheless, they provide a reasonable prediction of expected hardening due to phase stability and swelling response in reduced activation ferritic/martensitic steels in fusion applications.

The effect of irradiation on tensile properties as a function of dose at 365, 420, and 585°C are tabulated in Table 2 and summarized in Figure 1. Test temperature for the conditions listed was room temperature except for specimens irradiated at 365°C, where the test temperature was the irradiation temperature. Table 1 includes yield strength, ultimate tensile strength, and total elongation values for unirradiated and irradiated specimen conditions, as well as a measure of the change in property as a ratio of the irradiated value compared to the control value. Large deviations from 1.0 in the change in property indicate that significant changes arise from irradiation.

The alloy groups with smallest changes in properties are the 5 to 12Cr alloys. As an example, Figure 1 shows ultimate tensile strength as a function of irradiation dose in FFTF for the three alloy classes. Considering first the case for irradiation at 365 or 420°C, the low chromium Bainitic alloys exhibited large increases in yield strength (and corresponding decreases in elongation) following irradiation to 10 dpa. Irradiation to higher dose produced moderate further increases in strength, except that one alloy became brittle and failed at low stress. In comparison, the 5 to 9 and 12 Cr steels showed only minor changes in strength and elongation as a function of dose. However, the 12 Cr steels provided higher inherent strength following irradiation. In comparison, after irradiation at 585°C all alloys became weaker and gave increased elongation, except for the 9Cr-2WMnVTaTi alloys where response was only slightly affected by irradiation temperature. However, the 2 Cr steels all showed the lowest strength, with saturation in properties by 13 dpa. The 9 Cr steels exhibited intermediate yield strength values.

The evidence of minor increases in strength in 9 Cr alloys following the decreases observed at 13 dpa probably indicates sluggish precipitation reactions that continue beyond 20 dpa. The 12 Cr steel was the strongest but underwent decreases in strength similar to the 9 Cr response. Therefore, 9 Cr steels can be designed to provide high-temperature strength similar to those of 12 Cr steels, but 12 Cr steels appear to have the best tensile properties.

Postirradiation Charpy impact tests on reduced activation steels are based on tests using miniature Charpy specimens, mostly on one third sized specimens irradiated in FFTF at 365°C to about 7 dpa[23,24] but also on specimens with a 1.5 mm square cross section geometry irradiated in JMTR at 300°C to about 0.01 dpa.[25] The one third sized specimens included precracked[23] and unprecracked[24] conditions. Therefore, the most meaningful comparison for these differences in crack tip geometry is change in ductile to brittle transition temperature (DBTT) due to irradiation.

The effect of irradiation on DBTT is summarized in Table 3 and Figure 2. DBTT measurements, based on the temperature at half the difference between lower and upper shelf Charpy impact energies, are for one third size unprecracked miniature Charpy specimens before and after irradiation at 365°C to about 7 dpa, one third sized precracked miniature Charpy specimens before and after irradiation at 420 to about 12 dpa, and 1.5 mm specimens before and after irradiation at 300°C to approximately 0.01 dpa. Table 3 includes control and irradiated specimen results for DBTT and upper shelf energy (USE), shift in DBTT, and decrease in USE. The lowest values for irradiated DBTT and shift in DBTT are found for the 7 to 9 Cr alloys.

An example of the Charpy data is shown in Figure 2, where DBTT is plotted as a function of dose and arranged according to Cr content. The 2 Cr steels are shown in Figure 2a, the 5 to 9 Cr steels in Figure 2b, and the 12 Cr steels in Figure 2c. Open symbols are used to denote unirradiated response at 365 and 427°C and closed symbols to denote behavior following irradiation at 300°C. From Figure 2, it is apparent that the 5 to 9 Cr steels have better resistance to irradiation than the 2 or 12 Cr steels. The shift in DBTT due to irradiation was much smaller and, as can be shown from Table 3, the initial USE were similar. The shifts in DBTT for the $2\frac{1}{4}$ Cr and 12 Cr stabilized steels were much larger, and for the 2 Cr steel in

Table 2. Summary of tensile properties in low activation ferritic alloys following irradiation (from references 18, 19, 20 and 28).

Alloy	ode	Control σ_y (MPa)	Control UTS (MPa)	Control Elong. (%)	Postirradiation Cond. (°C/dpa)	Postirradiation σ_y (MPa)	Postirradiation UTS (MPa)	Postirradiation Elong. (%)	Change* σ_y	Change* UTS (fraction)	Change* Elong.
2Cr-0.5V	L1	785	901	13.9	420/8	1248	1279	8.3	1.59	1.42	0.60
				"	420/44	992	1014	7.6	1.26	1.13	0.55
				"	585/39	204	319	>32.5	0.26	0.35	>2.34
2Cr-1.0V	L2	312	555	26.7	420/12	1055	1086	8.1	3.38	1.96	0.30
				"	420/43	1110	1121	8.0	3.56	2.02	0.30
				"	585/14	146	351	38.9	0.47	0.63	1.46
				"	585/39	204	319	>32.5	0.65	0.57	>1.22
2Cr-1.5V	L3	297	477	24.4	420/8	706	755	6.1	2.38	1.58	0.25
				"	420/44	Failed @179 MPa, 0.17% Strain				0.37	0.00
				"	585/14	180	367	25.7	0.61	0.77	1.05
				"	585/37	199	346	16.4	0.67	0.73	0.67
2¼CrV		649	723	12.0	365/7	950	980	6.2	1.46	1.36	0.52
2¼Cr-1WV		643	733	12.3	365/7	924	960	7.5	1.43	1.31	0.61
2¼Cr-2W		509	618	13.7	365/7	773	798	8.8	1.52	1.29	0.64
2¼Cr-2WV		606	693	12.7	365/7	789	811	7.8	1.30	1.17	0.61
5Cr-2WV		537	645	13.0	365/7	730	771	9.1	1.36	1.20	0.70
8Cr-2WVTaB	82H	679	811	5.0	365/7	697	780	6.9	1.03	0.96	1.38
				"	405/36	671	764	7.8	0.99	0.94	1.56
				"	550/37	470	717	9.5	0.69	0.88	1.90
				"	670/28	253	442	24.8	0.37	0.54	4.96
				"	750/37	213	355	28.3	0.31	0.44	5.66
9CrV	L4	566	665	15.7	420/12	660	698	12.0	1.17	1.05	0.76
				"	420/46	550	626	16.1	0.97	0.94	1.03
				"	585/14	310	460	22.7	0.55	0.69	1.45
				"	585/37	348	491	23.9	0.61	0.73	1.52
9Cr-2MnV	L5	582	675	15.8	420/10	599	677	16.9	1.06	1.02	1.08
				"	420/46	544	652	18.6	0.93	0.97	1.18
				"	585/14	343	419	33.5	0.59	0.62	2.12
				"	585/35	348	542	32.2	0.60	0.80	2.05
9Cr-1Mn-1V	L6	566	722	15	420/12	622	730	15.9	1.10	1.01	1.06
				"	420/43	581	718	18.6	1.03	0.99	1.24
				"	585/14	367	562	30.2	0.65	0.78	2.01
				"	585/35	362	597	28.9	0.64	0.83	1.93
9Cr-1W	L7	716	587	15.8	420/10	608	714	15.8	1.04	1.00	1.00
				"	420/43	564	693	19.1	0.96	0.97	1.21
				"	585/39	463	626	25.9	0.79	0.87	1.64
9Cr-2WV		659	549	12.3	365/7	710	764	10.2	1.29	1.16	0.83
9Cr-2WVTa		652	544	12.3	365/7	669	732	10.8	1.23	1.12	0.88
9Cr-1WVTa		503	634		265/.1	583	679		1.16	1.07	
9Cr-3WVTa		483	666	16.2	265/.1	588	705	13.1	1.22	1.06	0.80
9Cr-1V		440	580	18.5	300/.004	560	640	14.0	1.27	1.10	0.76
9Cr-2WMnVTaTi*		510	611	18.8	420/33	538	708	15.0	1.05	1.16	0.85
				"	520/35	481	722	18.9	0.94	1.18	1.01
				"	600/35	565	715	15.2	1.11	1.17	0.91
9Cr-2WMnVTaTiB*		505	602	17.2	420/33	525	729	15.6	1.04	1.21	0.91
				"	520/35	483	690	15.4	0.96	1.15	0.90
				"	600/35	460	733	17.8	0.91	1.22	1.03
12Cr-6Mn-1W	L9	1002	10.1	822	420/8	848	942	14.7	1.03	0.94	1.46
				"	420/44	684	853	16.1	0.83	0.85	1.59
				"	585/14	531	749	19.4	0.65	0.75	1.92
				"	585/37	449	744	21.2	0.55	0.74	2.10
12Cr-2WV		657	13.0	522	365/7	857	885	8.0	1.64	1.35	0.62

irradiated prop y) / (control propert
From Dr. Hiroak urishita, Oarai Branc , Tohoku University, Oarai, Japan

one case, the DBTT following irradiation was above the capability of the test apparatus. The tabulation of results in Table 3 demonstrates that the 7 to 9 Cr steels exhibited shifts in DBTT due to irradiation of 4 to 68°C (and for the 5 Cr steel, it was 103°C), whereas the 2 Cr steels and 12 Cr stabilized steels developed shifts on the order of 200°C. In all cases where results were obtained, the USE was at reasonable levels. Therefore, based on DBTT response, the 7 to 9 Cr alloy class is superior.

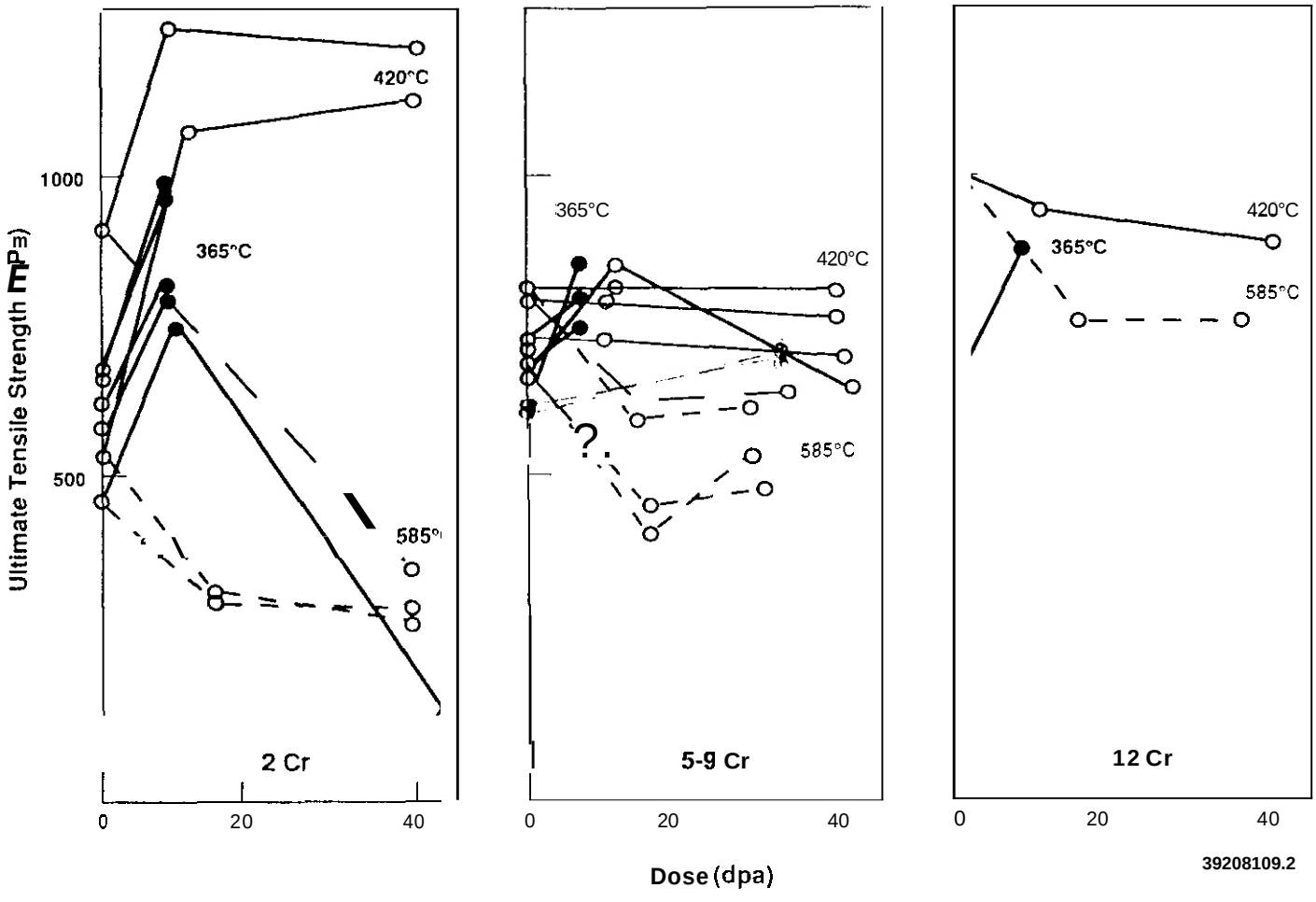

Fig. 1. Ultimate tensile strength as a function of dose for (a) 2Cr, (b) 5 to 9 Cr, and (c) 12 Cr reduced activation steels.

Fractography

Fractographic examinations have been performed on several of the specimens for which results are shown in figure 2.[23] The examinations revealed that in several cases, the brittle fracture mode changed from transgranular cleavage to intergranular fracture as a result of irradiation. However, ductile failure remained transgranular. For the 7 Cr alloy, brittle fracture in irradiated specimens remained transgranular, whereas in the 9 Cr alloys, containing manganese, the fracture mode changed from predominantly brittle transgranular cleavage in unirradiated specimens to predominantly intergranular fracture following irradiation. Therefore, although the Charpy response in these alloys was little affected by irradiation, a change in fracture mode did occur, an indication that irradiation weakened grain boundary cohesion in comparison with the grain interiors. For 12Cr-Mn-1V and 12Cr-6Mn-1WV steels, brittle failure was by transgranular cleavage irradiated specimens, but following irradiation, brittle failure was due to failure at grain boundaries. There, grain boundary decohesion was responsible for degradation of the DBTT. However, the observation that no change in fracture mode occurred for the 7Cr-2W alloy (with the highest tungsten content) indicates that excess tungsten is probably not responsible for the change in the 12 Cr alloys. A more likely explanation is that manganese additions are responsible, as has been shown in a similar alloy series.[29]

Microstructure

Microstructural examinations have been performed on reduced activation ferritic alloys following irradiation at temperatures from 365 to 600°C to doses as high as 115 dpa. The specimen matrix consisted of alloys L1 to L9 irradiated at ~420°C to 9.8, 43.3 and 114.2 dpa, at 520°C to 14.4 dpa and at 600°C to 33.8 dpa[7,18,19]; alloys GA3X and GA4X following irradiation at 365°C to 11.3 and 34 dpa, at 426°C to 33.5 and 103 dpa, at 520°C to 33.8 dpa, and at 600°C to 33.8 dpa[26,27]; and alloy F82H irradiated at 365°C to 6.7 dpa and 405, 550, 670, and 750°C to about 35 dpa.[28] Examinations have shown that reduced activation ferritic alloys are affected by radiation over the full range of temperatures examined. Following irradiation at 365 and 420°C, dislocation evolution and precipitate development were found, and several examples of irradiation-induced void swelling were identified. Following irradiation at 520°C, effects of irradiation were not as apparent, but examples of void swelling and precipitate coarsening could be identified.

Table 3. Summary of DBTT behavior in low activation ferritic allow following irradiation at 365°C to ~10 dpa (from references *23*, 24, and *25*).

Alloy	Code	Condition (°C/dpa)	Control DBTT (°C)	Irrad. DBTT (°C)	Shift in DBTT (°C)	Control USE (J/cm²)	Irrad. USE (J/cm²)	% Decrease in USE (J/cm²)
2Cr-1.5V	L3	365/11.3	(60)	>250	na	308	na	na
2¼CrV		365/7	14	*250*	*236*	10*	4.2*	58
2¼Cr-1WV		365/7	-*28*	192	*220*	11.8*	5.6*	53
2¼Cr-2W		365/7	-19	140	159	9.2*	4.6*	50
2¼Cr-2WV		365/7	4	111	107	9.1*	5.2*	43
2¼Cr-2WV	JLF-4	300/.01	-53	-52	1	.93*	.88*	5
5Cr-2WV		365/7	-70	33	103	9.2*	6.5*	29
7Cr-2WV	JLF-3	300/.01	-103	-61	42	.92*	.94*	-*2*
7.5Cr-2W	GA3X	365/10.5	-24	0	24	405	345	15
9Cr-1V	L5	365/12	-44	18	*62*	*280*	239	15
9Cr-1W	L7	365/12	12	44	*32*	370	330	11
9Cr-2WV		365/7	-60	8	***68***	8.4*	6.4*	24
9Cr-2WVTa		365/7	-88	-84	4	11.2*	8.6*	23
9Cr-2WVTa	JLF-1	300/.01	-106	-84	*22*	.97*	.92*	5
9Cr-2WVTaTi	JLF-2	300/.01	-67	-37	30	.93*	.89*	4
12Cr-6Mn-1V	L8	365/12	10	200	190	201	201	0
12Cr-6Mn-1W	L9	365/12	-*52*	165	217	219	219	0
12Cr-2WV		367/7	-18	156	174	8.3*	5.9*	29
12Cr-2WVTa	JLF-5	300/.01	-**66**	-38	28	.85*	.84*	1
12Cr-2WVTaTi	JLF-6	300/.01	-59	4	63	.79*	.68*	14

na : not available
* : not required to cm^{-2} boundaries

Finally, following irradiation at 600°C and above, coarsening of both precipitate and Martensite lath structures was found.

Results at 365 to 420°C

Microstructural development at 365 and 420°C varied as a function of composition. Most notable was fine M_7C_3 precipitate development and void formation in 2Cr-V alloys; void formation in 7 to 9 Cr alloys; and α' precipitate development, intermetallic precipitation,. and carbide coarsening in 12 Cr alloys.

Examination of 2Cr-V alloys following irradiation at 420°C showed extensive precipitation of rod shaped particles on the order of 25 nm long and 3 nm in diameter, and a<100> perfect dislocation loop formation [approximately 40 nm in diameter) even at doses as low as 10 dpa.[18] The precipitate contained equal proportions of V and Cr and modest amounts of Fe.[19] These microstructural changes were undoubtedly responsible for the large increases in strength observed in the alloy class following irradiation at 420°C. Swelling response is very sensitive to the amount of V present; for levels of 0.5 and 1.0 V, negligible swelling was found but, for 1.5 V, extensive swelling developed. Void formation was noted at fluences as low as 10 dpa in the 1.5 V alloy.[18] Therefore, void swelling resistance is imparted by additions of 0.5 to 1.0 V, probably due to precipitation, but when the additions are too high, swelling resistance may break down.

In comparison, 7 to 9 Cr alloys were more resistant to precipitation but less resistant to void swelling. Examples of behavior in 9Cr-1V (alloy L6) and 9Cr-1WV (alloy L7) following irradiation at 420°C are shown as a function of dose in Figures 3a through f. Voids were not found in the 9Cr-1WV alloy following irradiation to *10* dpa (Figure 3d) but can be seen under all other conditions. With continuing irradiation, the dislocation structures evolve from loop dominated structures to network structures, to structures consisting of dislocation line segments connected to voids. Increasing the level of W to *2* percent does not change microstructural response significantly and, in the 7.5Cr-2W [alloy GA3X), behavior at 365°C is similar to that at 420°C but on a finer scale. Examples are provided in Figures 3g and h, which show void swelling in 7.5Cr-2W [alloy GA3X) following irradiation at 420°C to 33.5 and 103 dpa. Figure 3g and h can be compared with figure 3e and f to show that additions of W at levels of 1 or *2* percent do not significantly alter swelling incubation. The differences that are evident can be ascribed to differences in dose. figures 3i and j give microstructural examples for F82H irradiated at 365°C to 6.7 dpa and at 405°C to 35.8 dpa, respectively. Swelling is higher following irradiation at 405°C to higher dose. Most evident from Figure 3 is the similarity in response for these 7 to 9 Cr reduced activation ferritic steels.

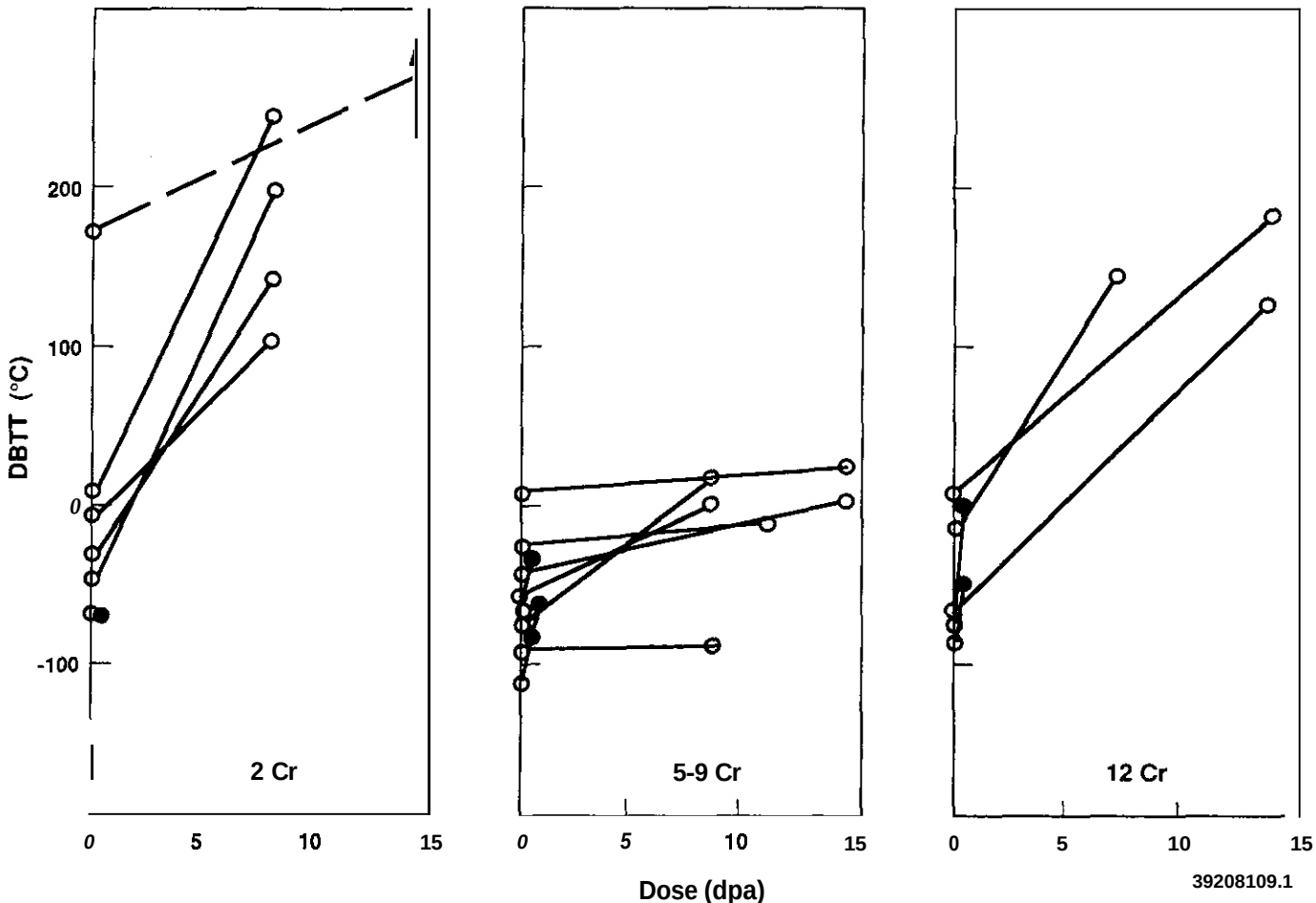

Fig. 2. Ductile to brittle transition temperature as a function of dose for (a) 2Cr, (b) 5 to 9 Cr, and (c) 12 Cr reduced activation steels.

The 12 Cr alloys were found to represent an intermediate case. Void swelling was found to develop after 40 dpa; after 115 dpa, swelling was extensive in the 12Cr-1V (alloy L8) but still in the incubation stage in the 12Cr-1WV (alloy L9). The precipitate structure included a fine distribution of equiaxed particles on the order of 10 nm in diameter, which were nonuniformly distributed from one Martensite lath to the next. The precipitate was present after 15 dpa and remained stable with only minor coarsening to higher dose. It has been identified as Cr rich a' based on dark field imaging characteristics and similarities to behavior in other 12 Cr steels.[30]

Results at 520°C

Following irradiation at 520°C, the alloys were found to be relatively unaffected by irradiation. No void swelling was observed in Bainite or Martensite, and only a few examples of irradiation-induced dislocation loops were found. The exception, a 10Cr-1W alloy (GA4X) with negligible carbon and therefore containing mainly delta ferrite, where void and dislocation evolution was found near grain boundaries and where voids were generally elongated and associated with precipitate particles. In general, the carbide structure present prior to irradiation was retained.

However, compositional analysis of extracted particles revealed unexpected phases and carbide compositions. The 2Cr-0.5V alloy developed a dominant precipitate phase equally rich in Fe and Cr with minor additions of V. Also, 9 and 12 Cr alloys containing W developed $M_{23}C_6$ precipitates with W levels in the range from 10 to 20 percent. The observation of void formation in 10Cr-1W may indicate that W additions can enhance void-swelling behavior at higher temperatures such as 520°C.

Results at 600°C

All alloy microstructures were altered considerably due to irradiation at 600°C. The major effect was rearrangement of Martensite lath boundaries into more equiaxed subgrain structures with concurrent carbide and subgrain coarsening. This coarsening was undoubtedly responsible for observed losses in strength. However, alloys containing high Mn had developed fault structures, often in regions containing carbides. These structures were more prevalent in 12Cr-1WV. The faults are believed to be stacking faults *in* austenite, and therefore austenite is believed to form during irradiation at 600°C. This explanation

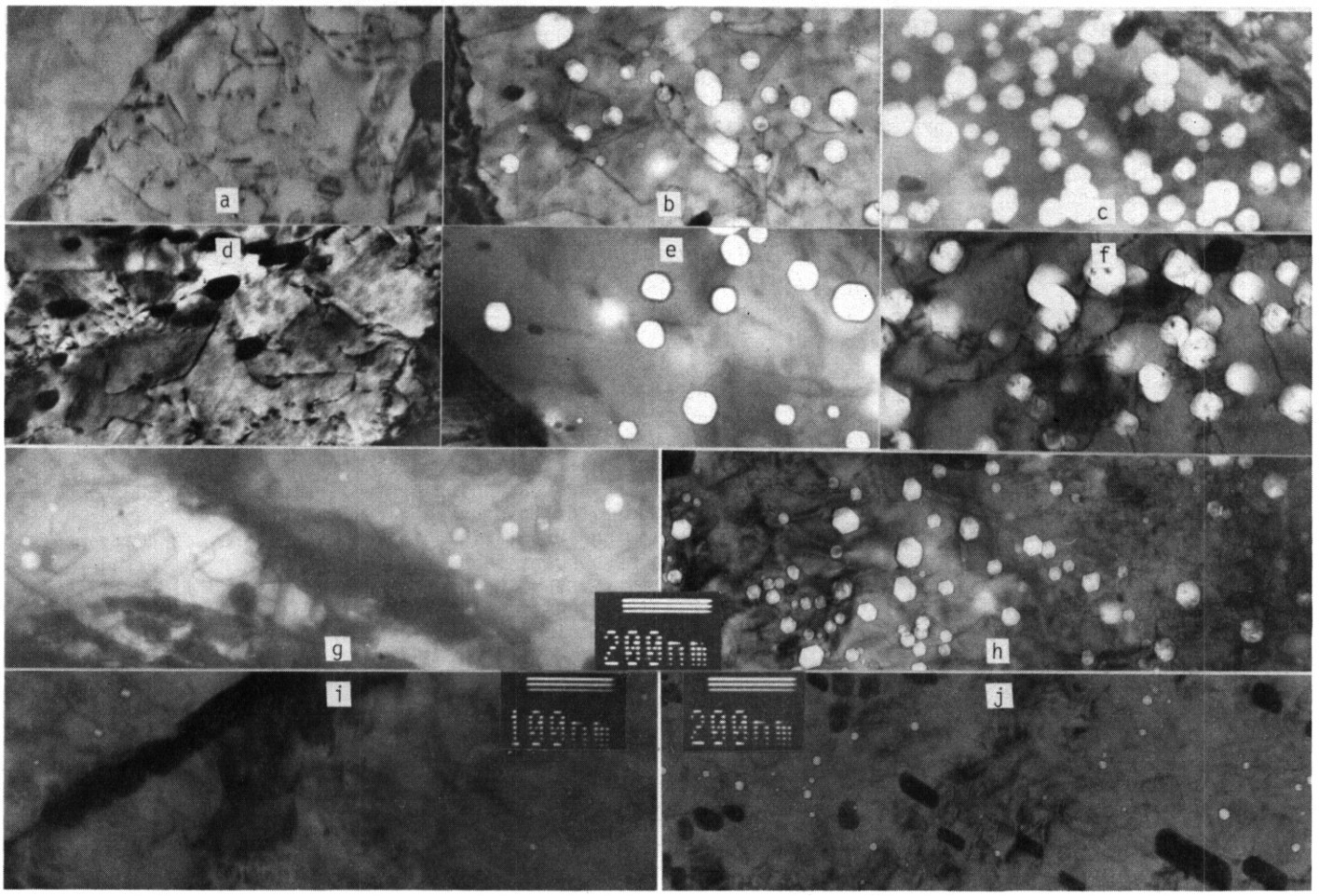

Fig. 3. Examples of void swelling in irradiated 7 to 9 Cr reduced activation ferritic alloys: 9Cr-1V irradiated at 420°C to (a) 9.8, (b) 43.3, and (c) 114.2 dpa; 9Cr-1WV irradiated at 420°C to (d) 9.8, (e) 43.3, and (f) 114.2 dpa; GA3X irradiated at 420°C to (g) 33.5 and (h) 103 dpa; and F82H irradiated (i) at 365° to 7 dpa and (j) at 405°C to 35.8 dpa.

indicates that Mn additions on the order of 6 percent have the added disadvantage of lowering the Ac, temperature (the temperature at which austenite forms on heating) to below 600°C.

Discussion

Although only a small fraction of the alloy compositions listed in Table 1 have been tested or examined following fast neutron irradiation, sufficient information has been obtained to provide reasonable prediction of performance for each of the alloy classes. The important results obtained can be summarized as follows. The 2Cr-1V alloy class is inherently susceptible to precipitation hardening following irradiation at 420°C and to excessive softening following irradiation at 585°C. Similar difficulties are indicated for 2Cr-W alloys based on data for irradiation hardening and DBTT shift, but microstructural verification is not yet available. However, creep properties for 2Cr-W alloys are encouraging and may indicate better high temperature stability and therefore a larger application window.

The 12 Cr alloys that are stabilized with additions of Mn can also be eliminated as potential reduced activation fusion alloys. Although tensile properties are generally better than those in lower Cr alloys, impact properties are sufficiently degraded following irradiation to cause concern. Also, formation of austenite and intermetallic chi phase in such alloys, and reduced weldability,[31] indicate that Mn additions to 12 Cr steels do not offer a viable composition range for reduced activation steels.

Insufficient information is available to provide prediction of behavior for 12 Cr alloys stabilized with carbon. Carbon levels on the order of 0.2 percent are possible, giving good tensile and high temperature properties. Impact properties following irradiation are of most concern. Tests are being initiated on an improved heat of GA4X, 11Cr-2.5WV with 0.15C, but it will still be a year or two before results are available.

The 7 to 9 Cr alloys appear most promising for reduced activation fusion reactor applications. The alloys have good tensile and impact properties, both prior to and following irradiation, good resistance to phase instability during irradiation, and sufficient high temperature strength. The example of 9Cr-2W alloys

with similar postirradiation ultimate tensile strengths irrespective of irradiation temperature from 420 to 600°C is very encouraging. This alloy class is expected to be sufficiently corrosion resistant. The major detriment to its use is void swelling and the resultant degradation in irradiation creep resistance. However, dimensional changes due to irradiation-induced swelling in ferritic alloys are expected to remain small because swelling rates are so low,[32] and therefore swelling resistance is not expected to be a major consideration for these alloys. Irradiation creep response with accompanying swelling is also acceptable. Comparisons between V and W alloying additions indicate that higher W levels are superior. In fact, results to date indicate that W levels on the order of 2 percent are very effective. Concerns about phase instability, such as Fe-Cr-W chi phase formation, have proven to be groundless up to doses on the order of 100 dpa.[26] Therefore, the most promising composition developed to date appears to be 7 to 9 Cr-2WV.

CONCLUSIONS

A broad range of reduced activation ferritic alloys is possible. Reduced activation Bainitic alloys in the Fe-2Cr composition range, martensitic alloys in the Fe-7 to 9Cr range, and stabilized martensitic alloys in the Fe-12Cr range have been successfully fabricated and are undergoing international testing. However, irradiation significantly degrades the properties of Bainitic and stabilized martensitic alloys. Bainitic alloys containing vanadium develop severe hardening due to irradiation-induced precipitation at temperatures below 450°C and extreme softening due to carbide coarsening at temperatures above 500°C. Stabilized martensitic alloys that rely on manganese additions to provide a fully martensitic microstructure are embrittled at grain boundaries following irradiation, leading to severe degradation of impact properties. The most promising composition regime appears to be the Fe-7 to 9 Cr range with tungsten additions in the 2 percent range, where high temperature mechanical properties and microstructural stability are retained and impact properties are relatively unaffected by irradiation. The higher void-swelling behavior observed in these alloys and the resultant increase in irradiation creep response are not expected to be major problems.

FUTURE WORK

This work is a continuing effort.

ACKNOWLEDGEMENTS

The opportunity to release recent postirradiation tensile data not yet published from Dr. Hiroaki Kurishita is greatfully acknowledged.

REFERENCES

1. D. S. Gelles, in Reduced Activation Materials for Fusion Reactors, ASTM STP 1047, R. L. Klueh, D. S. Gelles, M. Okada, and N. H. Packan, Eds. (ASTM, Philadelphia, PA 1990) 113.

2. Report of the DOE Panel on Low Activation Materials for Fusion Applications, R.W. Conn, Panel Chairman, UCLA/PPG-728, June 1983.

3. T. Noda, F. Abe, H. Araki, and M. Okada, J. Nucl. Mater., 141-143 (1986) 1102-1106.

4. H. Kayano, H. Kurishita, A. Kimura, M. Narui, M. Yamazaki, and Y. Suzuki, J. Nucl. Mater., 179-181 (1991) 425.

5. R. L. Klueh, D. S. Gelles, and T. A. Lechtenberg, J. Nucl. Mater., 141-143 (1986) 1081-1087.

6. M. Tamura, H. Hayakawa, M. Tanimura, A. Hishinuma, and T. Kondo, J. Nucl. Mater., 141-143 (1986) 1067-1073.

7. F. Abe, T. Noda, H. Araki, and S. Nakazawa, J. Nucl. Mater., 179-181 (1991) 663

8. Letter; C-Y. Hsu to D. S. Gelles, September 29, 1987 providing compositions of alloys manufactured by Mitsubishi Corporation, Japan.

9. D. Dulieu, K. W. Tupholme, and G. J. Butterworth, J. Nucl. Mater., 141-143 (1986) 1097-1101

10. K. W. Tupholme, D. Dulieu, and G. J. Butterworth, J. Nucl. Mater., 179-181 (1991) 684.

11. E. Dequidt, J. Arroyo, and M. Schirra, J. Nucl. Mater., 179-181 (1991) 659.

12. M. L. Hamilton and D. S. Gelles, unpublished alloy compositions.

13. A. N. Niemi, M. G. McKimpson, and D. S. Gelles, in Fusion Reactor Materials Semiannual Progress Report for Period Ending March 31, 1989, DOE/ER-0313/6, 187.

14. A. N. Niemi, M. G. McKimpson, and D. S. Gelles, in Fusion Reactor Materials Semiannual Progress Report for Period Ending March 31, 1990, DOE/ER-0313/8, 177.

15. S. Nomura, T. Okuda, S. Shikakura, M. Fujiwara, and K. Asabe, in Solid State Powder Processing, A. H. Clauer and J. J. deBarbadillo, Eds. (TMS, Warrendale, PA, 1990) 203.

16. R. L. Klueh, in Allov Development for Irradiation Performance Semiannual Progress Report for the Period Ending September 30, 1985, DOE/ER-0045/15, 117.

17. A. Kohyama, K. Asakura, Y. Kohno, C. R. Eiholzer, and R. J. Puigh, "Irradiation Creep Behavior of Low Activation Steels in FFTF/MOTA," presented at the 16th ASTM Symposium on the Effects of Radiation on Materials, Denver, CO, June 23-25, 1992.

18. D. S. Gelles and M. L. Hamilton, J. Nucl. Mater., 148 (1987) 272-278; for an expanded version see Alloy Development for Irradiation Performance Semiannual Progress Report for the Period Ending September 30, 1984, DOE/ER-0045/13, 128.

19. D. S. Gelles and M. L. Hamilton, in Allov Development for Irradiation Performance Semiannual Progress Report for the Period Ending March 31, 1986, DOE/ER-0045/16, 131.

20. R. L. Klueh, J. Nucl. Mater., 179-181 (1991) 728.

21. F. Abe, T. Noda, H. Araki, M. Narui, and H. Kayano, J. Nucl. Mater., 166 (1989) 265.

22. F. Abe, T. Noda, H. Araki, M. Narui and H. Kayano, to be published as part of the proceeding of the International Conference on Fusion Reactor Materials-5 in J. Nucl. Mater.

23. N. S. Cannon, and D. S. Gelles, J. Nucl. Mater., 186 (1991) 68; also in Fusion Reactor Materials Semiannual Progress Report for the Period Ending March 31, 1987, DOE/ER-0313/2, 119.

24. R. L. Klueh, D. J. Alexander, and P. J. Maziasz, J. Nucl. Mater., 186 (1992) 185.

25. H. Kayano, H. Kurishita, A. Kimura, M. Narui, M. Yamazaki, and Y. Suzuki, J. Nucl. Mater., 179-181 (1991) 425.

26. D. S. Gelles, C-Y. Hsu, and T. A. Lechtenberg, J. Nucl. Mater., ICFRM-3 Conference Proceedings, to be published; for an expanded version see in Fusion Reactor Materials Semiannual Progress Report for the Period Ending September 30, 1987, DOE/ER-0313/3, 150.

27. D. S. Gelles and C-Y. Hsu, in Fusion Reactor Materials Semiannual Progress Report for the Period Ending September 30, 1989, DOE/ER-0313/7, 105.

28. Y. Kohno, D. S. Gelles, A. Kohyama, M. Tamura, and M. L. Hamilton, in Fusion Reactor Materials Semiannual Progress Report for the Period Ending March 31, 1991, DOE/ER-0313/10, 78.

29. D. S. Gelles and W. L. Hu, in Fusion Reactor Materials Semiannual Progress Report for the Period Ending September 30, 1986, DOE/ER-0313/1, 251.

30. D. S. Gelles and L. E. Thomas, in Topical Conference on Ferritic Allovs for Use in Nuclear Energy Technologies, J. W. Davis and D. J. Michel, Eds. (AIME, Warrendale, PA., 1984) 559.

31. H. T. Lin and B. A. Chin, in Fusion Reactor Materials Semiannual Progress Report for the Period Ending March 31, 1987, DOE/ER-0313/2, 135.

32. D. S. Gelles and R. L.Ermi, in Allov Development for Irradiation Performance Semiannual Progress report for the Period ending September 30, 1983, DOE/ER-0045/11, 103.

MECHANICAL PROPERTIES OF MARTENSITIC ALLOY AISI 422 - M. L. Hamilton, (Pacific Northwest Laboratory)[a], F. H. Huang, and W. Hu (Westinghouse Hanford Company)

OBJECTIVE

The objective of this study is to provide insight on the factors controlling radiation-induced embrittlement of ferritic steels.

SUMMARY

HT9 is a martensitic stainless steel that has been considered for structural applications in liquid metal reactors (LMRs) as well as in fusion reactors. AISI 422 is a commercially available martensitic stainless steel that closely resembles HT9, and was studied briefly under the auspices of the U.S. LMR program. Previously unpublished tensile, fracture toughness and charpy impact data on AISI 422 were reexamined for potential insights into the consequences of the compositional differences between the two alloys, particularly with respect to current questions concerning the origin of the radiation-induced embrittlement observed in HT9.

PROGRESS & STATUS

Introduction

HT9 is a martensitic stainless steel that has been considered for structural applications in liquid metal reactors (LMRs) and is currently under consideration for similar applications in fusion reactors. The U.S. LMR program was interested in establishing the properties and irradiation-induced changes in behavior of an American alloy that closely resembles HT9, referred to as AISI 422. Only a fraction of the work originally proposed under the U.S. LMR program was completed prior to the termination of the program. Due to the similarities in composition between HT9 and 422, however, and the fact that HT9 exhibits irradiation-induced embrittlement the source of which is not completely understood, it appeared that reexamination of the AISI 422 database established under the LMR program might provide some useful insights into the post-irradiation embrittlement of this class of alloy.

Backsround

AISI 422 is also referred to as Carpenter 636, AISI 616 and Unitemp 1420 WM. It is a hardenable steel that was designed for service at temperatures up to 650°C. It is a modification of AISI 420, with additions of nickel, molybdenum, tungsten and vanadium to improve the elevated temperature strength and resistance to stress corrosion cracking.[1,2] The composition of the LMR heat of AISI 422 is compared to that of a typical LMR heat of HT9 in Table 1. Note that relative to HT9, AISI 422 contains 60% more manganese, 30% more silicon and nickel, and more than double the amounts of phosphorus and tungsten.

It is well known that martensitic stainless steels such as HT9 can exhibit significant embrittlement following irradiation, particularly at temperatures on the order of 350 to 385°C, where a pronounced

Table 1. Compositions of AISI 422 (heat 20818) and HT9 (heat 91353).

ALLOY	C	Mn	Si	P	Cr	Ni	Mo	V	W
HT9	0.21	0.49	0.22	0.008	11.97	0.57	1.03	0.33	0.52
422	0.22	0.80	0.29	0.018	11.79	0.80	1.05	0.29	1.16

increase in strength occurs. It is not well understood, however, whether the embrittlement arises primarily from the helium-induced cavities or the precipitation that develops during irradiation. Both factors are related to the level of nickel present in the alloy, and as such are very difficult to separate clearly. The purpose of this work was therefore to use the slight compositional variation between HT9 and AISI 422 to glean some insight into the behavior of HT9 following irradiation.

---

[a]Pacific Northwest Laboratory is operated for the U.S. Department of Energy by Battelle Memorial Institute under Contract DE-AC06-76RLO 1830.

Experimental Procedure

A 9½-inch (241.3 mm) long piece of 5¼-inch (533.35 mm) diameter AISI 422 bar stock was purchased in a normalized and tempered condition. The original ingot, produced by AlTech Specialty Steel, was melted in an electric furnace and refined by argon-oxygen decarburization (AOD). A f-round piece of the bar was rolled to two thicknesses (¼ and 1/8 inch [6.35 and 3.18 mm]) with intermediate heat treatments similar to those used for processing HT9. The final heat treatment for both thicknesses comprised austenitizing at 1038°C for 5 minutes and tempering at 760°C for 30 minutes. Both treatments were followed by an air cool. The final tempered martensite structure had an ASTM grain size of about 8 and a Vickers hardness of about 298 DPH (500 g load). No delta ferrite was present in the heat treated AISI 422 microstructure, whereas HT9 generally contains about 1% delta ferrite at prior austenite grain boundaries.

Miniature (½-size) charpy specimens were machined from the thicker sheet stock, while miniature tensile and compact tension specimens were machined from the thinner sheet stock according to the drawings given in Figure 1 and in the orientations given in Figure 2. Tensile specimens were tested in the unirradiated condition only at temperatures ranging from 25 to 540°C and a nominal strain rate of 1.5×10^{-4} s^{-1}. Compact tension specimens were irradiated in the Fast Flux Test Facility at ~400 and ~540°C but were tested only in the unirradiated condition, at temperatures ranging from 25 to 427°C, using a single specimen electropotential technique. Charpy specimens were irradiated at ~400°C in a precracked condition to a fluence of ~4 x 10^{22} n/cm^2 ($E > 0.1$ MeV), or about 17 dpa. Impact tests were performed on both irradiated and unirradiated specimens in an instrumented drop tower. The fracture energy was normalized against the area of the fracture surface. The ductile-brittle transition temperature (DBTT) is determined as the midpoint between the upper shelf (USE) and the lower shelf. More details on each of the test techniques, demonstrating their validity as applied to miniature specimens, are given in references 3-5.

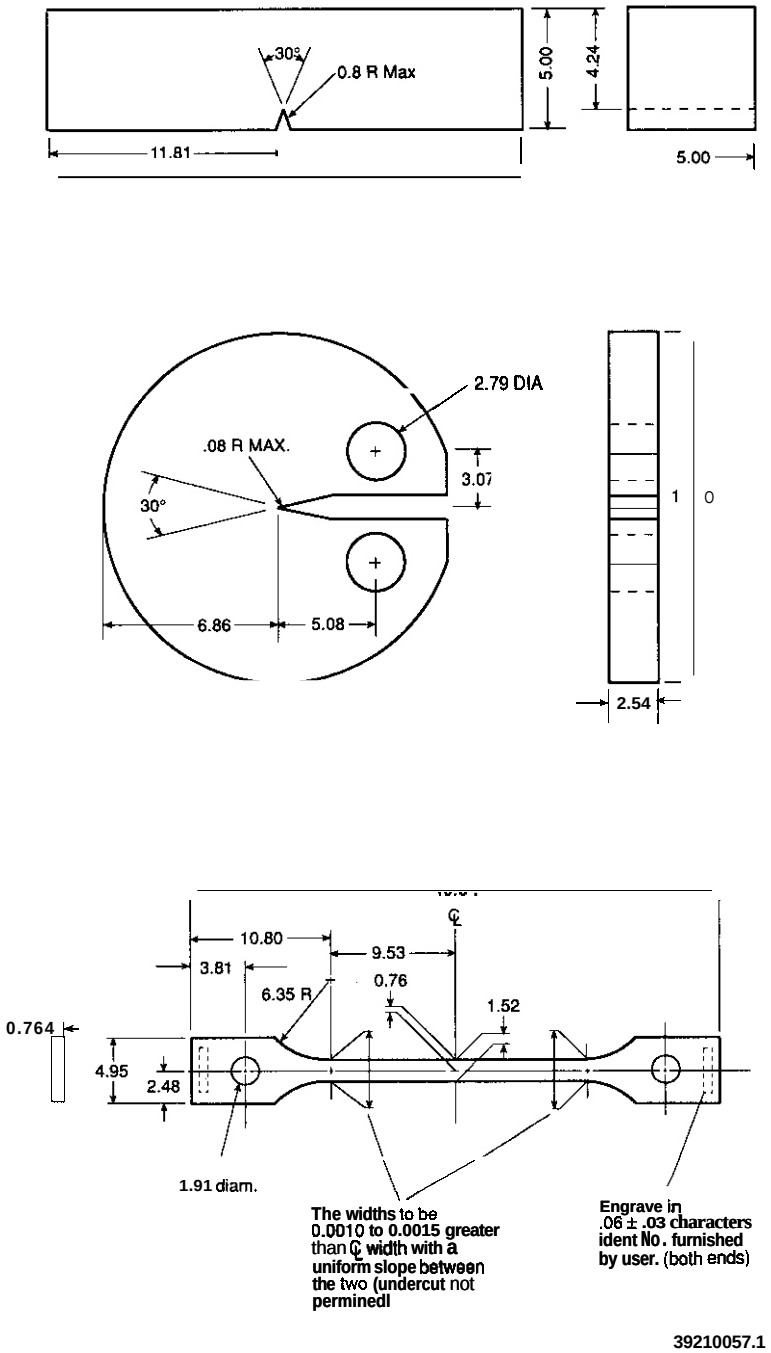

39210057.1

Fig. 1. Dimensions of miniature AISI 422 specimens. (top) Charpy impact specimen, (middle) Compact tension specimen, and (bottom) Tensile specimen. All dimensions are given in mm.

Results and Discussion

The tensile data obtained on AISI 422 are shown in Figure 3 in comparison with similar data on HT9. It is evident that AISI 422 is slightly stronger and somewhat more ductile than HT9 in the unirradiated condition.

The fracture toughness data obtained from the compact tension specimens of unirradiated AISI 422 are shown in Figure 4 in comparison with similar HT9 data. The toughness of AISI 422 is higher than that of HT9, although it should be noted that the tearing modulus is 20 to 40 percent lower in AISI 422, depending on the test temperature, ranging from 95 at 70°C to 81 at 427°C.

The impact behavior of unirradiated AISI 422 is compared to that of HT9 in Figure 5. While the two data sets appear to be very similar at first glance, it should be noted that the orientations and heat treatments of the two types of specimens are different. While the AISI 422 specimens were fabricated from rolled sheet in the TL orientation, the HT9 specimens were fabricated from forged bar in the CR

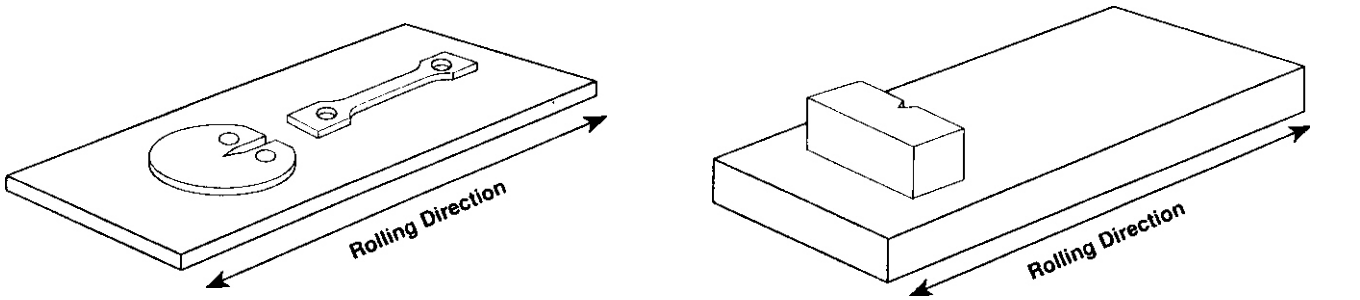

Fig. 2. Orientation of miniature AISI 422 specimens relative to the rolling direction. The tensile specimen axis was parallel to the rolling direction. Compact tension and charpy impact specimens were fabricated in the TL orientation.

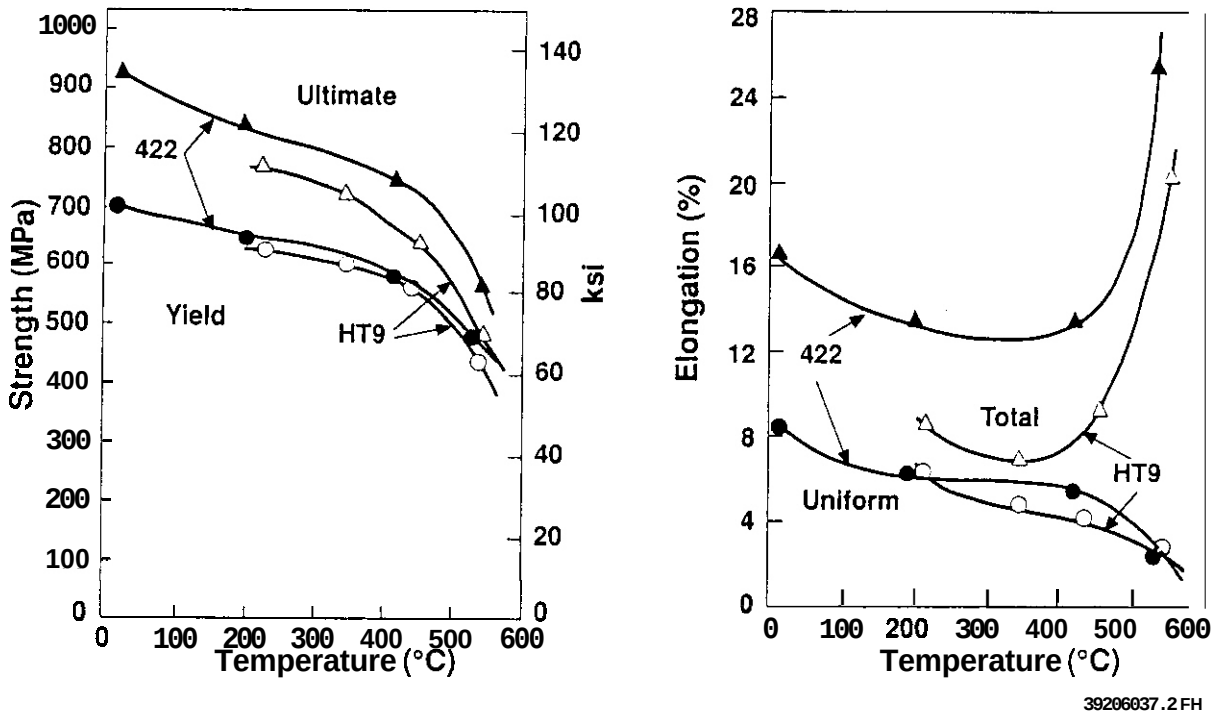

Fig. 3. Tensile data on unirradiated AISI 422 compared with similar HT9 data. (a) Strength and (b) Ductility.

orientation. The difference between these two orientations is shown in Figure 6. The orientation of the crack front and the direction of crack propagation are parallel to the rolling direction in the TL AISI 422 specimens, while they are perpendicular to the working direction in the CR HT9 specimens. In addition, the HT9 bar from which the specimens were machined was in a slightly different condition than that of the AISI 422 sheet, a mill annealed condition that comprises normalization at 1150°C for more than one hour followed by hot working and tempering at 750°C for 1 hour.

The similarity between the HT9 and AISI 422 impact data in the unirradiated condition is somewhat surprising in light of the differences in delta ferrite level and the fact that the AISI 422 is stronger as well as tougher. The orientation difference is the only factor than could account for the similarity, since the difference in heat treatment is relatively minor. The CR orientation could be considered as approximating a crack arrest geometry, particularly in the presence of delta ferrite stringers in HT9, whereas the TL orientation could be considered as approximating a crack divide geometry, where the crack might be divided along prior austenite grain boundaries.

The similarity between HT9 and AISI 422 is maintained when both are irradiated at similar temperatures to approximately the same neutron exposure, as shown in Figure 7. The HT9 specimens were actually irradiated at ~390°C,[7] but the difference between 390 and 400°C is minimal relative to the uncertainties in

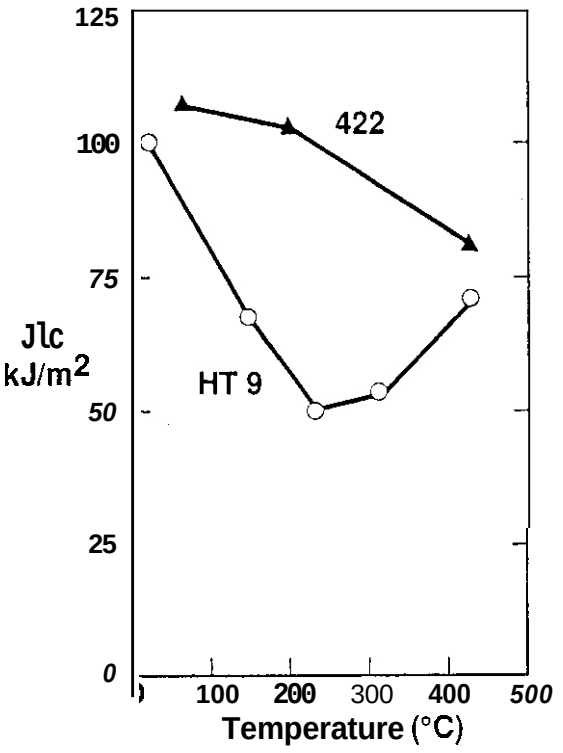

Fig. 4. Fracture toughness data on unirradiated AISI 422 compared with similar HT9 data.

irradiation temperature. The HT9 specimens were irradiated only to ~3 x 10^{22} n/cm^2, but since it has been demonstrated that the shift in DBTT saturates at about fast fluences of 2-3 x 10^{22} n/cm^2 in this temperature range,[6] the HT9 and AISI 422 data are considered comparable.

The data in Figure 7 indicate that the two alloys exhibit the same shifts in DBTT and USE independent of the orientation differences. The data also imply that a small amount of delta ferrite has no effect on the irradiation-induced shifts in DBTT and USE.

Other data are available, however, on HT9 specimens in the TL orientation.[8] These data are shown in Figure 8, and indicate that, while the shift in DBTT and USE are slightly worse in the CR than in the TL orientation, the difference between orientations is small relative to the effect of irradiation itself. Since the data suggest that there is no orientation dependence in the irradiation-induced shifts in DBTT and USE, and since both HT9 (CR) and AISI 422 (TL) exhibit similar shifts in DBTT and USE, one can surmise that the difference between HT9 (TL) and AISI 422 (TL) in the irradiated condition reflects a difference in the original condition of the materials rather than an effect of radiation, i.e., $DBTT_{HT9(TL)} < DBTT_{422(TL)}$ for unirradiated material.

CONCLUSIONS

AISI 422 appears to be as good an alloy as HT9 on the basis of its strength and fracture toughness properties, but the impact behavior of AISI 422 does not appear to be as good as that of HT9 when orientation differences are taken into account. In addition, the impact behavior of AISI 422 (TL) is worse than

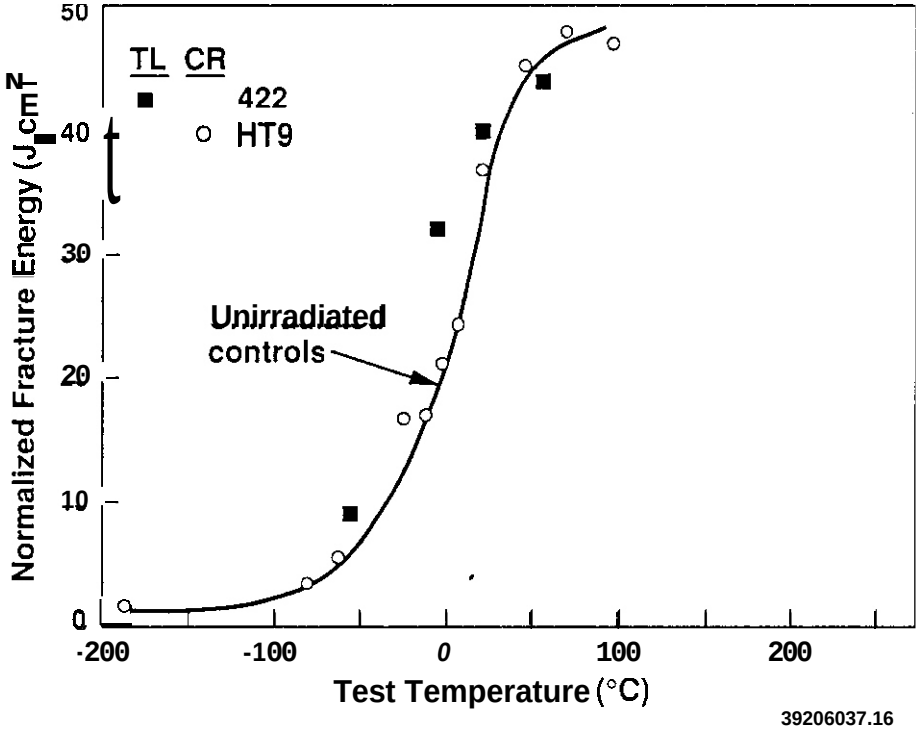

Fig. 5. Impact data on unirradiated AISI 422 (TL) compared with HT9 (CR) data

that of HT9 (TL) following irradiation to a saturation fluence. With the mixture of positive and negative results, it is not really possible to draw firm conclusions concerning the effect of composition on irradiation-induced changes in behavior, and no real insights can be obtained concerning the origin of the irradiation-induced embrittlement observed in HT9. It is possible, however, to specify that the effect of

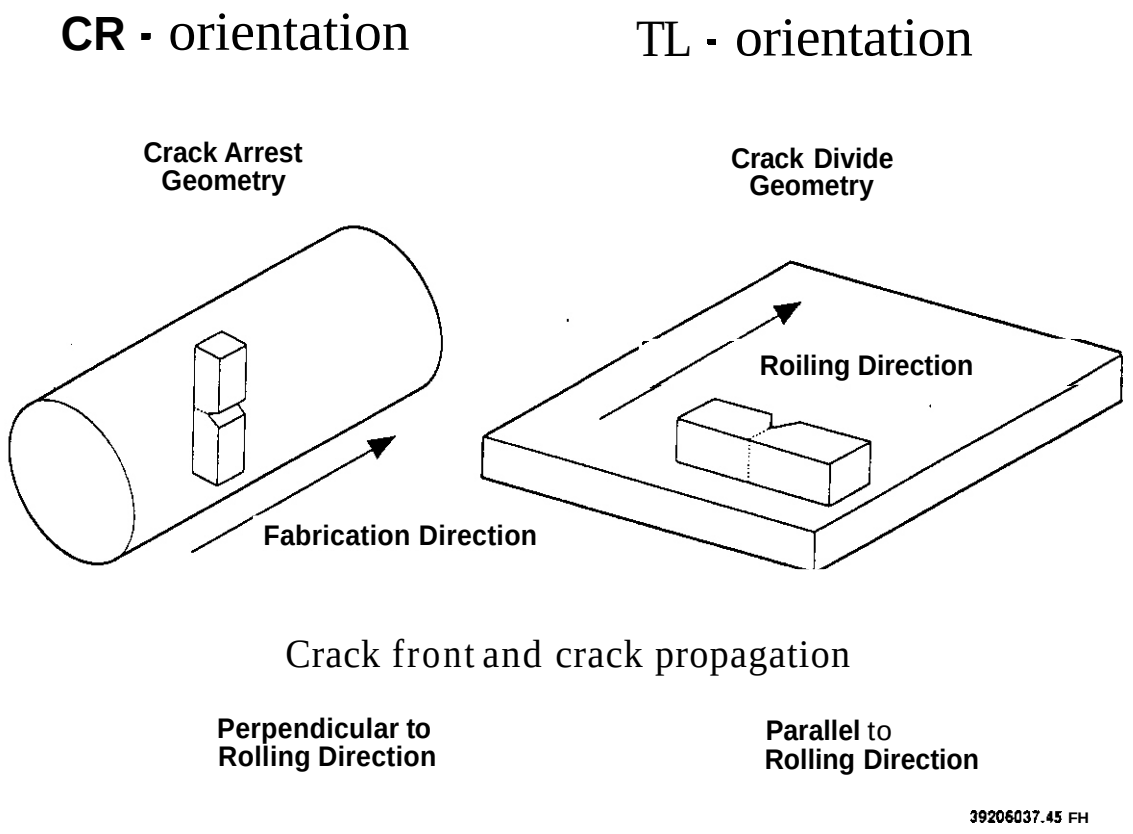

Fig. 6. Orientation differences between charpy specimens of AISI 422 (TL) and HT9 (CR).

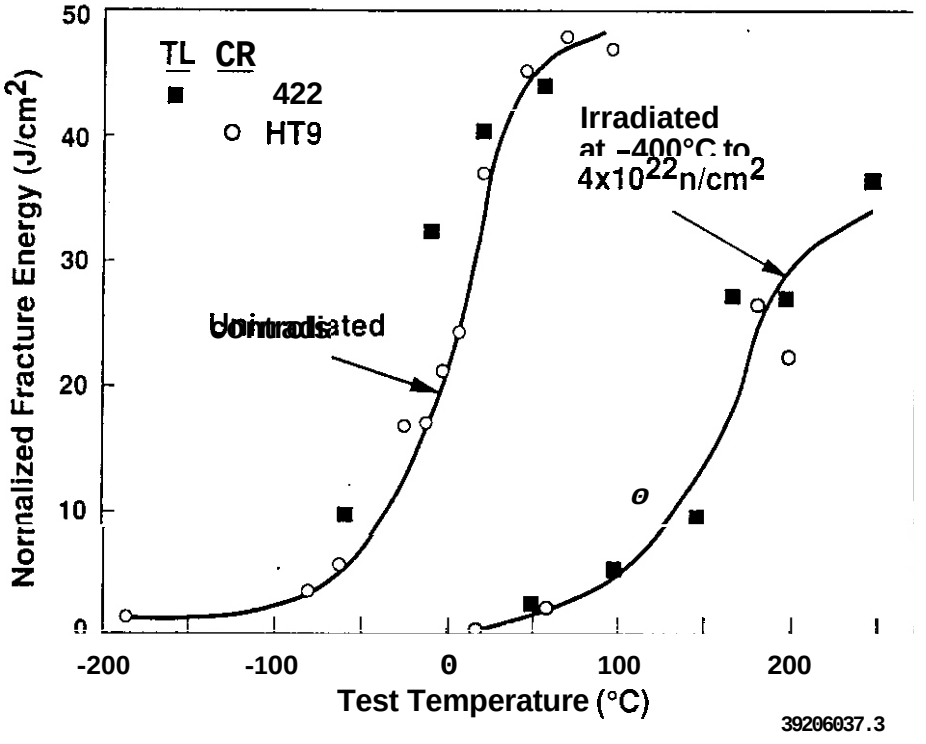

Fig. 7. Impact data on AISI 422 (TL) irradiated to ~4 x 10^{22} n/cm^2 at ~400°C, compared to HT9 data (CR).

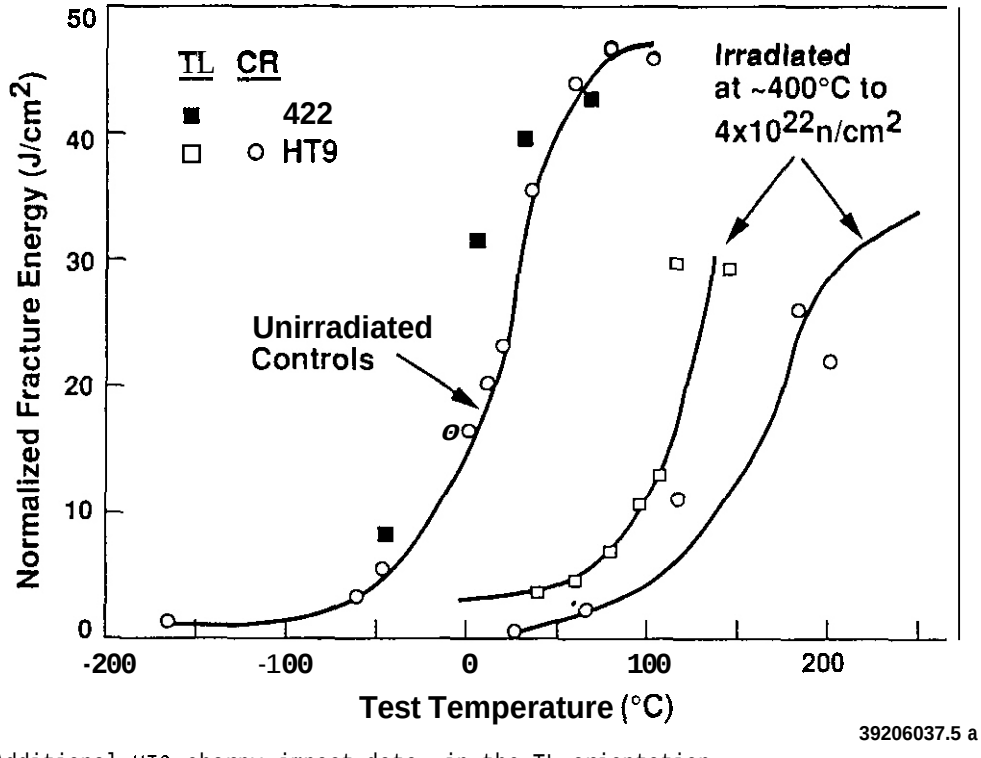

Fig. 8. Additional HT9 charpy impact data, in the TL orientation.

radiation on this class of steel is a general phenomenon, albeit one that is influenced by the details of processing procedures and irradiation environment.

FUTURE WORK

This effort is complete.

REFERENCES

1. Aerospace Structural Metals Handbook, Code 1403, Belfour Stulen, Inc., 1972.

2. Alloy Digest, Carpenter 636 Alloy, Filing Code 22-294, Engineering Alloys Digest, Inc., New Jersey, 1974.

3. Brager, H. R., Garner, F. A., and Hamilton, M. L., Journal of Nuclear Materials, 133 & 134, 1985, pp. 594-598.

4. Hu, W. L., and Gelles, D. S., "Miniature Charpy Impact Test Results for the Irradiated Ferritic Alloys HT9 and 9Cr-1Mo," Proceedings of AIME Tooical Conference on Ferritic Alloys for Use in Nuclear Energy Technologies, June 1983, pp. 631-646.

5. Huang, F. H., and Hamilton, M. L., Journal of Nuclear Materials, 187, 1992, pp. 278-293.

6. Hu, W. L., and Gelles, D. S., "The Ductile-to-Brittle Transition Behavior of Martensitic Steels Neutron Irradiated to 26 dpa," Influence of Radiation on Material Properties: 13th International Symposium (Part II), ASTM STP 956, Frank A. Garner, Charles H. Henager, Jr., and Naohiro lgata, Eds., American Society for Testing and Materials, Philadelphia, 1987.

7. Hu, W. L., "Alloy Development for Irradiation Performance" Semiannual Progress Report for Period Ending September 30, 1982, DOE/ER-0045/9, pp. 255-271.

8. Hu, W. L., Alloy Development for Irradiation Performance Semiannual Progress Report for Period Ending September 30, 1984, DOE/ER-0045/13, pp. 106-119.

6.2 Austenitic Stainless Steels

(no contributions)

6.3 Refractory Metal Alloys

STATUS OF THE DYNAMIC HELIUM CHARGING EXPERIMENT (DHCE)* - 6.

A. Loomis and D. L. Smith (Argonne National Laboratory). H. Matsui (Tohoku University), M. L. Hamilton (Pacific Northwest Laboratory), K. L. Pearce (Westinghouse Hanford Company), J. P. Kopasz and C. E. Johnson (Argonne National Laboratory), R. G. Clemmer and L. R. Greenwood (Pacific Northwest Laboratory).

OBJECTIVE

The objective of this experiment is to provide baseline irradiation data on the effects of concurrent helium production and neutron irradiation on the physical and mechanical properties of vanadium alloys. Effects of helium production and irradiation on the alloy microstructures will also be characterized.

SUMMARY

This report summarizes the status of the DHCE in FFTF-MOTA, the preparations for retrieval of specimens from the irradiation capsules, and experimental results on procedures for the removal of tritium from the irradiated specimens.

PROGRESS AND STATUS

Introduction

The DHCE experiment is designed to enhance helium production in vanadium alloys during irradiation in the FFTF-MOTA to simulate the simultaneous production of helium and irradiation damage (dpa) that is anticipated in a fusion device. Irradiation of vanadium-base alloys in the FFTF reactor results in the production of helium at a very low rate (≈0.02 appm per dpa) by fast neutron (n, α) reactions. However, the ratio of helium production to irradiation damage (dpa) in fusion reactors will be ≈5 appm per dpa due to the presence of 14 MeV neutrons. Since helium may influence the evolution of the irradiation-damage microstructure in alloys and. therefore, exacerbate swelling and irradiation hardening of vanadium alloys, simulations in the absence of a 14 MeV neutron source are necessary to assess the effects of concurrent helium production and irradiation damage on physical and mechanical properties of the alloys. In the DHCE experiment, helium is produced by the decay of tritium, which is dissolved uniformly in vanadium alloy specimens during irradiation. A detailed description of the DHCE experiment is presented in Ref. 1, and initial tritium loading, lithium isotopic ratio, and helium pressure data are presented in Ref. 2. The alloy compositions and types of specimens irradiated in this initial experiment (DHCE-i) in MOTA-26 are listed in Ref. 3.

In this report, we present the status of the DHCE-I irradiation in MOTA-26 and preparations for retrieval of specimens from the irradiation capsules. Also, experimental results are presented on procedures for removal of tritium from the irradiated specimens.

Irradiation Status

The irradiation of DHCE-I (in MOTA-26) commenced on May 27, 1991 and was concluded on March 19, 1992 with operation of the FFTF for 203.3 effective full power days (EFPD) at a nominal power level of 291 MW. The reactor operation schedule during this period (5/27/91 to 3/19/92) is shown in Table 1. This schedule of reactor operation resulted in ≈25 dpa of irradiation damage. The current FFTF schedule indicates that MOTA-26 and the DHCE-I specimens will remain in the FFTF until September, 1992, even though the reactor is in "standby" mode of operation. The temperature of MOTA-26 is 210-215°C in this FFTF "standby" mode. In order to minimize the production of helium in the V alloy specimens after conclusion of irradiation, it is important to retrieve the specimens as soon as possible because of tritium decay to helium. Based on the current FFTF schedule, processing and removal of the irradiation capsules in MOTA-26 is not expected to commence until October, 1992. Therefore, specimens will not be available for experiments until January, 1993. If this schedule for processing and removal of specimens is realized, the ratio of helium concentration to irradiation damage will increase to > 12 appm per dpa.[4]

Retrieval of Specimens from Capsules

The irradiated DHCE-I capsules (7) will contain 20-100 Ci of tritium. It is expected that the tritium will be appor-

*Work supported by the Office of Fusion Energy, U.S. Department of Energy, under Contract W-31-109-Eng-38.

Table 1. FFTF operation (291 MW) for DHCE-I.

Cycle No.	Operation Period	EFPD
12A-1	5/27/91 - 7/20/91	52.8
12A-2	7/30/91 - 9/21/91	48.6
128-1	11/21/91 - 1/15/92	50.3
128-2	1/26/92 - 3/19/93'	51.6
Total		203.3

tioned between the vanadium alloy specimens (≈30%) and the lithium (~70%).The capsules will be opened for retrieval of specimens in the Low-Level Irradiated Materials Laboratory in Bldg. 212 at Argonne National Laboratory. Standard procedures for opening of TZM irradiation capsules and retrieval of specimens (i.e., dissolution of lithium in liquid NH_3) will be modified to include a secondary containment of the capsules during opening and lithium dissolution so that the tritium can be collected and/or released at a rate in accordance with DOE and ANL guidelines.

Tritium Removal from Irradiated Specimens

The dependence of evolution of hydrogen from V-10Ti and V-5Cr-5Ti alloys on annealing temperature and on annealing time at 375-400°C in vacuum (≈10^{-7} torr) is shown in Figs. 1 and 2, respectively. The hydrogen concentration in the specimens was determined from the partial pressure of hydrogen that was evolved on heating a specimen at the rate of 15°C/min from 25°C to 1000°C (Ref. 5 contains additional information on this procedure). The evolution of hydrogen from these specimens was most pronounced at 300-550°C. The anneal of the V-10Ti alloy at 375°C for 1 h reduced the hydrogen concentration to 1295 appm, whereas the anneal of the V-5Cr-5Ti alloy at 400°C for 1 h reduced the hydrogen concentration to 180 appm.

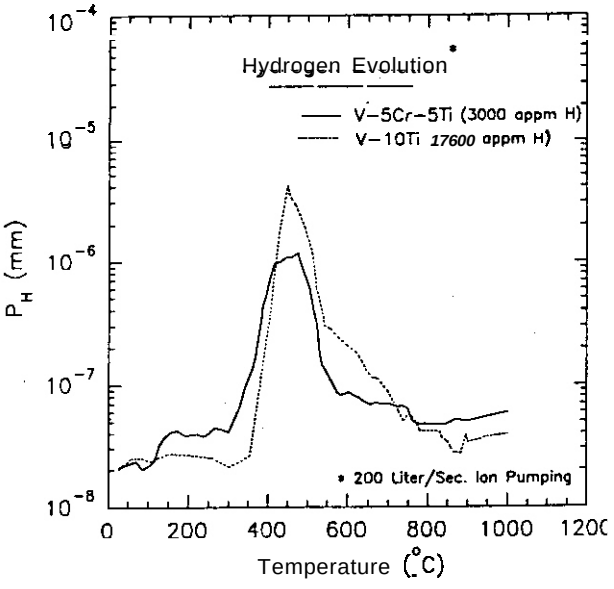

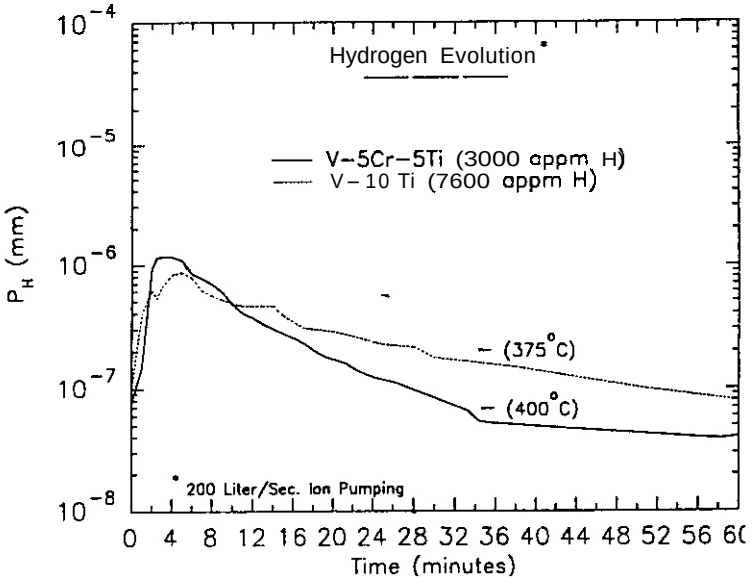

The TEM and tensile specimens retrieved from the DHCE-I capsules are expected to contain 1400-6600 appm tritium depending on the tritium distribution coefficient (k_w) for the capsule contents? The data shown in Figs. 1 and 2 suggest that the tritium concentration in the irradiated specimens can be reduced to <100 appm by annealing at 375-400°C for ≈2 h in vacuum. This post-irradiation anneal for tritium removal is expected to have an insignificant effect on the irradiation-produced microstructure, swelling, and mechanical properties of the alloy specimens?

FUTURE EFFORT

A document that presents detailed procedures for the removal of specimens from the capsules and the removal of tritium from the specimens as well as precautionary procedures against the inadvertent release of tritium will be prepared for approval by cognizant groups.

REFERENCES

1. D. L. Smith, H. Matsui. L. R. Greenwood, and B. Loomis, "Experimental Method for Investigating Helium Effects in Irradiated Vanadium." J. Nucl. Mater. 155-157 (1988) 1359-1363.

2. L. R. Greenwood, "Revised Calculations for the Dynamic Helium Charging Experiment in FFTF/MOTA 2B," in:

Fusion Reactor Materials, Semiannual Progress Report for Period Ending March 31, 1991, DOE/ER-0313/10, U.S. Department of Energy, Office of Fusion Energy, July 1991, pp. 156-158.

3. D. L. Smith, B. A. Loomis, H. Matsui. M. L. Hamilton, K. L. Pearce, J. P. Kopasz, C. E. Johnson, R. G. Klemmer. and L. R. Greenwood, "Status of the Dynamic Helium Charging Experiment (DHCE) in FFTF/MOTA," in: Fusion Reactor Materials, Semiannual Progress Report for Period Ending March 31, 1991, DOVER-0313/10, US. Department of Energy, Office of Fusion Energy, July 1991, pp. 159-163.

4. Memo: L. R. Greenwood to **M.** L. Hamilton, "Revised Calculations for the DHCE Experiment in MOTA-2B," Battelle Pacific Northwest Laboratories, April 28, 1992.

5. B. A. Loomis, A. B. Hull. **O.** K. Chopra, and D. L. Smith, "Hydrogen Concentration in Vanadium-Base Alloys after Surface Preparation and Exposure to Liquid Lithium," in: Fusion Reactor Materials, Semiannual Progress Report for Period Ending March 31, 1988, DOE/ER-0313/4, **U.S.** Department of Energy, Office of Fusion Energy, August 1988, pp. 160-167.

6. H. Takahashi. ***S.*** Ohnuki and T. Takeyama, "The Effect of Irradiation and Post-irradiation Annealing on the Yield Stress and Microstructure of Vanadium-Carbon Alloys," J. Nucl. Mater. 96 (1981) 233-242.

HYDROGEN EMBRITTLEMENT OF NIOBIUM-BASE ALLOYS FOR APPLICATION IN THE ITER DIVERTOR

– D. T. Peterson (Iowa State University). and A. B. Hull. B. A. Loomis (Argonne National Laboratory)

OBJECTIVE

The objective of this task is to obtain information on baseline mechanical properties, chemical compatibility, and radiation damage of selected niobium (Nb) alloys under conditions of interest for fusion reactors. Embrittlement and hydride formation in Nb alloys from long-term exposure to high-purity water in a refreshed stainless steel autoclave is being evaluated.

SUMMARY

The corrosion rate of Nb alloys in high-purity water was demonstrated to be quite low at 300°C and only a fraction of the hydrogen (H) produced by corrosion was absorbed. The calculated H concentrations in an ITER divertor plate are below levels expected to cause embrittlement.

Corrosion, H absorption, and resistance to embrittlement of Nb can be significantly improved by alloying. Alloying of **Nb** can increase the terminal solid solubility of H in Nb-V alloys. Consequently. alloying **Nb** with V reduces the embrittlement caused by H. Hence, there appear to be good prospects for increasing the solubility of the hydride phase and of increasing the tolerance for H by developing appropriate **Nb** alloys. Thermotransport of H may perturb H concentration and thus needs further evaluation.

PROGRESS AND STATUS

Introduction and Background

Niobium-base alloys have attractive properties for the ITER divertor structure.' but the use of these alloys requires resolution of concerns about H in the materials. Hydrogen could arise from corrosion of **Nb** alloys in the water coolant, by injection or solution of H, deuterium (D), and tritium (T) from the plasma, and by nuclear transmutation reactions, e.g., the (n,p) reaction. Hydrogen in a **Nb** alloy could accumulate as hydride precipitates, migrate to the coolant and undergo electrochemical or chemical oxidation reactions, or be evolved into the vacuum space of the plasma chamber. These potential sources and sinks for H isotopes must be investigated and characterized individually to understand the H inventory in the divertor structure.

The level of corrosion resistance of **Nb** in water and many acidic solutions is high[2] because of a passivating Nb_2O_5 layer. If this layer is not stable, Nb metal will corrode and may be embrittled by absorbed H. The overall corrosion reaction with water can be written as

$$2Nb + 5H_2O \rightarrow Nb_2O_5 + 5H_2$$

Hydrogen generated by this reaction may be evolved as H gas. oxidized by molecular oxygen (O) or other oxidants in the coolant, or absorbed by the Nb metal or alloy. The latter course could lead to H embrittlement if the extent of corrosion and H uptake were significant.

Experimental Procedures

The H concentrations of Nb and several **Nb** alloy specimens that had been corrosion tested[3] were measured by a vacuum-extraction method. The Nb alloy specimens were heated under vacuum to 800°C. the evolved gas was pumped into a calibrated volume by a mercury diffusion pump, and the pressure measured with a McLeod gauge. The specimens were not cleaned to remove the Nb oxide layer produced by corrosion. This layer might contain a small amount of occluded water but for a specimen that contained 153 ppm H. only 10 ppm was evolved below 500°C, which may have been due to occluded

water. As a result, the evolved gas was considered to be all H. The requirement of a higher temperature for hydrogen evolution suggests that the oxide corrosion layer functions as a hydrogen permeability barrier. Only one analysis was performed on each specimen due to limited mass.

Results and Analysis

Table 1 shows H concentrations measured in a series of Nb alloys after 30 days of corrosion testing. The values vary by more than a factor of 10 and the percentage of H absorbed varies by a similar amount. The brittleness index for the alloys correlates with the H concentration. It appears that alloying elements can substantially change the corrosion rate and degree of H uptake: consequently, the alloys are resistant to H embrittlement.

Table 1. Hydrogen and Brittleness Properties of Corroded Nb Alloys

Alloy[a] (a%)	Hydrogen Characteristics		Brittleness Index[c]
	Concentration (ppm)	Captured[b] (%)	
Nb	730	16	5
Nb-2.5Zr	85	7	1
Nb-2.5V	269	35	5
Nb-2.5Hf	120	8	2
Nb-2.5Ta-2.5Ti	63	5	2
Nb-2.5Mo	207	16	5

[a] Duration of exposure to Ngl-purity water environment[3] was 30 days at 300°C.

[b] Percent H captured is the amount absorbed, compared to the stoichiometric possiblllty. as determined by weight gain and Eq. 1

[c] Fracture susceptibility was defined[3] by the mechanical response following a bend test: a brittleness Index of 5 lndlcated fracture following a 90" bend a brittleness index of 2 lndlcated ductility such that no fracture occurred even on the unbending of a fold; a brittleness Index of 1 Indlcated that there was nelther fracturing nor surface cracking of the corrosion layer.

Hydrogen analyses of the Nb-2.5% Mo alloys after corrosion testing are shown in Table 2. The concentration of H in the specimens was compared with the stoichiometric amount of H that could have been generated by the corrosion reaction. To calculate the H concentrations, the corrosion weight gain was taken to be entirely due to oxidation of Nb according to Eq. 1. All the specimens had absorbed only a fraction of the available H.

Table 2. Hydrogen and Brittleness of Corroded Nb-2.5Mo

Time[a] (days)	Hydrogen Characteristics		Brittleness Index[c]
	Concentration (ppm)	Captured[b] (%)	
30	207	16	5
60	308	17	5
90	942	40	5
120	386	15	2

[a] Duration of exposure to high-purity water environment[3] at 300°C.

[b] Percent H captured is the amount absorbed. compared to the stoichiometric possibility, as determined by welght gain and Eq. 1.

[c] Fracture susceptibility was defined[3] by the mechanical response following a bend test: a brittleness Index of 5 indicated fracture following a 90" bend.

The high result at 90 days was due to absorption of a larger fraction of the H being absorbed rather than to more extensive corrosion of the specimen. The concentrations were all above 120 ppm, concentrations at which H was found to reduce ductility at room temperature.4 The ductility of the alloys was evaluated by a room-temperature bend test,[3] and **all** the alloys were deemed to be brittle.

The corrosion specimens exhibit higher H concentrations than would be present in a divertor component because of the larger surface-to-mass ratio of the specimens, which were 0.127 mm thick and corroded on both sides. A proposed Nb divertor plate5 would be 2.0 mm thick and exposed to water corrosion on only one side. This difference would be expected to lower the H concentration by a factor of 0.0318 and lower the concentration in pure Nb from 730 (Table 2) to **23** ppm. The slow rate of corrosion, coupled with the rapid diffusion of H in **Nb.** would ensure that the concentration would be uniform across a 2.0-mm-thick section. The time required for saturation of a 2.0-mm section from one side, based on the diffusion coefficient for H in Nb[6] is only 22 minutes, which **is** very short compared to the corrosion times. Additionally, in a divertor scenario, much of the Nb-base alloy will be at a low temperature (<100°C) relative to the conditions of these aqueous corrosion tests. Temperatures at the water interface at the peak heat flux regions will be ~ 300°C.

Discussion

Thermotransport of Hydrogen and Its Isotooes: The temperature difference between the plasma side and water-cooled sides of the ITER divertor will be large at the peak flux regions.[5] The temperature gradient can produce a H concentration gradient due to thermotransport of H and its isotopes. The concentration gradient is related to the thermal gradient at steady state, i.e.,

$$\ln C_1/C_2 = Q^*/R\,(1/T_1 - 1/T_2) \qquad (2)$$

where C_1 and C_2 are the H concentrations, and T_1 and T_2 are the temperatures (in K) at two points. Q^* is the heat of transport, and R is the gas constant. Values for the heat of transport, Q^*, for H and D in Nb are reported by Peterson and Smith in Refs. 7 and 8, respectively. Heat **of** transport values for tritium in Nb are reported in Ref. 9. These values are shown in Table 3, along with the concentration ratios that would be produced by temperatures of 1250 and 700 **K.** as postulated for an ITER plate.[5]

Table 3. Thermotransport Parameters in Nb Alloys

System	Resultant Characteristics[a]	
	Heat of Transport Q^* (kJ)	Concentration Gradient (C_1/C_2)
H in **Nb**	9.4	0.49
D in **Nb**	16.3	0.29
T in Nb	18.8	0.24
H in Nb-10V	15.8	0.30
D in Nb-10V	20.4	0.21

[a] Derived **from** Eq. 2, where thermal gradient is based on T_1 = 1250 K and T_2 = 700 K.

The concentration profile for D in a 2.0-mm-thick Nb-10V for such a temperature difference is shown in Fig. 1. The thermotransport effect on the concentration distribution becomes even larger at lower temperatures, e.g., temperatures of 370 and 300 **K** would produce the same concentration ratios as given in Table 3. The influence of thermotransport on H fluxes in a fusion reactor has been discussed by Sugisaki and Furuya.[10] The times required to reach the thermotransport steady state depend on the diffusion coefficient. but generally range from a few minutes to a few hours. These times are short enough ***so*** that the effect of thermotransport may need to be considered in fusion reactors.

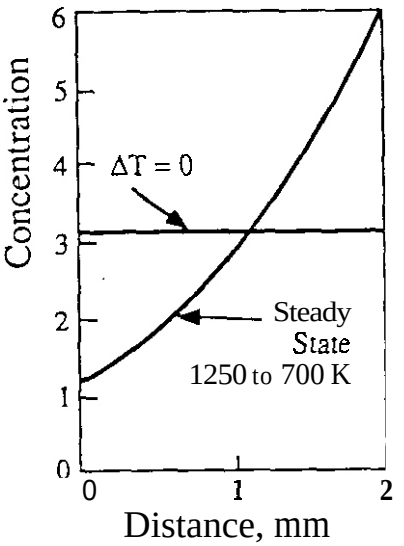

Fig. 1. Deuterium concentration (atomic %) in Nb-10V alloy section with and without a temperature gradient from 1250 to 700 K, representative of plasma side (left) and water side (right) of 2.0-mm thick divertor plate

Hydrogen Embrittlement of Niobium: The introduction of H into Nb produces significant changes in its mechanical properties. particularly in the reduction of area at fracture. If the concentration of H exceeds the terminal solid solubility limit. a hydride phase forms. which is always weak in tension and fractures easily if the stress is above the yield strength. Even when the concentration is below the solubility limit, hydride phases can form in the triaxially stressed area at a crack tip and assist the crack growth. which leads to fracture with very little reduction in area. Hydride embrittlement results in a ductile-brittle transition during tensile or impact tests even when there was no transition in the metal without H.[4] Alloying of Nb can produce a beneficial increase in the terminal solid solubility of H in Nb-V alloys[6] and embrittlement caused by H decreases at all temperatures.[11] In the case of V alloys. the addition of Ti reduced the embrittling effect of H, whereas the addition of Cr substantially increased H embrittlement. The prospects for increasing the solubility of the hydride phase and the tolerance for H embrittlement of Nb alloys appears to he good.

CONCLUSIONS

A preliminary corrosion and H embrittlement study of various Nb-base alloys in high-temperature deoxygenated water indicates that alloying Nb with V reduces H-induced embrittlement. Addition of Zr and Ti tends to reduce both the H pickup during aqueous corrosion and the embrittling effects of H.

FUTURE WORK

Additional niobium alloys will he screened on the basis of: hydrogen diffusion and permeability. aqueous corrosion, characterization and optimization of oxide film. and radiation embrittlement. With screening studies, the highest priority will be placed on the relationship between oxidation behavior and tritium inventory. It appears that by optimizing the aqueous-corrosion induced oxidation layer, the tritium inventory can be suppressed.

REFERENCES

1. T. Kuroda et al.. ITER Plasma Facing Components, ITER Documentation Series, No. 30. International Atomic Energy Agency, Vienna (1991).

2. D. Lupton. F. Aldinger. and K. Schulze, in: Niobium. Proceedings of the International Symposium, The Metallurgical Society of AIME, Warrendale, PA (1981) p. 533.

3. A. B. Hull. B. A. Loomis. and L. J. Nowicki, Preliminary Assessment *of Aqueous* Corrosion of Niobium Alloys for Structural Applications in the ITER Diuertor, Fusion Reactor Materials Semiannual Report for Period Ending March 31. 1991, DOE/ER-0313/10, *Oak* Ridge National Laboratory, p. 248.

4. T. ***G.*** Oakwood and R. ***G.*** Daniels. Trans. TMS-AIME. **242,** 1327 (1968).

5. R. F. Mattas. ITER Diuertor Plate Performance and *Lifetime* Considerations, ANL/FPP/TM-246, Argonne National Laboratory (March 1990).

6. D. T. Peterson and H. M. Herro, Metall. Trans. **17A.** 645 (1986).

7. D. T. Peterson and M. F. Smith. Metall. Trans. **13A**, 821 (1982).

8. D. T. Peterson and M. F. Smith, Metall. Trans. **14A.** 871 (1983).

9. M. Sugisaki. S. Mukai, K. Idemitsu and H. Furuya. J. Nucl. Mater. **116.** 91 (1983).

10. M. Sugisaki. H. Furuya. J. Nucl. Mater. **128 & 129.** 734 (1984).

11. C. V. Owen. D-S. Cheong, O. Buck. and T. E. Scott, Metall. Trans. **15A.** 147 (1984).

TENSILE **PROPERTIES OF** VANADIUM-BASE ALLOYS WITH A TUNGSTEN/INERT-GAS WELD ZONE* - B. A. Loomis, C. F. Konicek. L. J. Nowicki. and D. L. Smith (Argonne National Laboratory).

OBJECTIVE

The objective of this research is to determine the composition of a vanadium-base alloy with the optimal combination of mechanical properties, irradiation-damage resistance, corrosion resistance, fabricability, and weldability for use as a structural material in the environment of a magnetic fusion reactor.

SUMMARY

The tensile properties of V-(0-20)Ti and V-(0-15)Cr-5Ti alloys after butt-joining by tungsten/inert-gas (TIG) welding were determined from tests *at* 25°C. Tensile tests were conducted on both annealed and cold-worked materials with a TIG weld zone. The tensile properties of these materials were strongly influenced by the microstructure in the heat-affected zone adjacent to the weld zone and by the intrinsic fracture toughness of the alloys. TIG weld zones in these vanadium-base alloys had tensile properties comparable to those of recrystallized alloys without a weld zone. Least affected by the TIG welding were tensile properties of the V-5Ti and V-5Cr-5Ti alloys. Although the tensile properties of the V-5Ti and V-5Cr-5Ti alloys with a TIG weld zone were acceptable for structural material, these properties would be improved by optimization of the welding parameters for minimum grain size in the heat-affected zone.

PROGRESS AND STATUS

Introduction

The tensile properties of V-(0-20)Ti and V-(0-15)Cr-5Ti alloys in the annealed and recrystallized condition were previously reported by Loomis et al[1] for test temperatures of 25-700°C. In this report, the tensile properties of these alloys at 25°C are presented for **50%** cold-worked and cold-worked-annealed conditions with a butt-joint obtained by TIG welding.

Materials and Procedures

Unalloyed vanadium and vanadium-base alloys with the nominal compositions listed in Table 1 were obtained in sheet form with a 50% thickness reduction, i.e., cold-work, and thicknesses of 0.6-1.1 mm. Coupons (19 x 38 mm) of an alloy were clamped with additional "run-on" and "run-off" stock in a copper fixture for butt-joining by a TIG weld. The copper fixture and alloy coupons were placed in a weld chamber that was then evacuated to ≈2 mm pressure. The evacuated weld chamber was returned to atmospheric pressure with a 70% helium-30% argon gas mixture (99.995% purity). The TIG welds in the flowing gas mixture (0.16 m^3/s) were made with a Centaur welder (Model 7008) and

Table 1. Compositions of vanadium and vanadium-base alloys.

Nominal Composition	ANL I.D.	Concentration (wt.%)		Concentration" (ppm)			
		Cr	Ti	O	N	C	Si
V	BL 51			570	49	**56**	370
V-1Ti	BL **50**	-	1.0	230	130	235	1050
V-3Ti-1Si	BL 45	-	2.5	345	125	90	9900
V-5Ti	BL 46	-	4.6	300	53	85	160
V-10Ti	BL 12	-	9.8	1670	390	450	245
V-20Ti	BL 15	-	17.7	830	160	380	480
V-5Cr-5Ti	BL 47	4.1	4.3	350	220	200	870
V-7Cr-5Ti	BL 49	7.9	5.7	400	150	127	360
V-10Cr-5Ti	BL 43	9.2	4.9	230	31	100	340
V-12Cr-5Ti	BL 40	10.9	**5.0**	470	80	90	270
V-15Cr-5Ti	BL 41	14.5	**5.0**	330	96	120	400

'Hydrogen concentration < 30 appm.

*Work supported by the Office of Fusion Energy, U.S. Department of Energy, under Contract W-31-109-Eng-38.

power supply (Model 7001), a 2% thoriated tungsten electrode (1 mm dia.), and a 0.64 mm gap between stock and electrode. The thickness of the alloy coupons, and the TIG weld current for the alloy coupons, are listed in Table 2.

Table 2. Thickness of alloy coupons and TIG weld current.

Nominal Composition	Thickness (mm)	Weld Current (A)
V	1.09	48
V-1Ti	0.97	47
V-5Ti	0.89	41
V-10Ti	0.86	40
V-20Ti	0.86	35
V-5Cr-5Ti	1.09	50
V-7Cr-5Ti	1.07	50
V-10Cr-5Ti	0.86	38
V-12Cr-5Ti	0.61	22
V-15Cr-5Ti	0.91	41

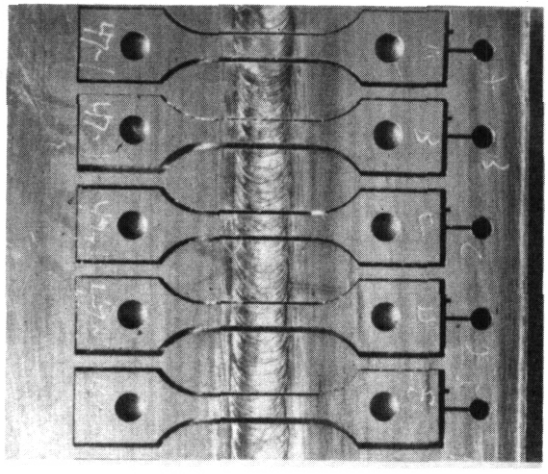

Fig. 1. TIG weld and tensile specimens.

Tensile specimens with 7.62 mm gauge length and 1.52 mm uniform-gauge width were obtained from the welded coupons by electrical discharge machining (EDM). The center of the weld zone (≈2.5 mm width) was positioned at the center of the uniform-gauge length. The typical appearance of the TIG weld and tensile specimens after EDM is shown in Fig. 1.

In this report, data are presented from tensile tests at 25°C on (1) recrystallized. unalloyed vanadium and vanadium-base alloy specimens without a weld zone (data from Ref. 1); (2) specimens (with a weld zone) mechanically ground, polished to a surface finish of ≈0.3 μm, and annealed at 950°C (to ensure absence of hydrogen); (3) specimens (with a weld zone) mechanically ground, polished to a surface finish of ≈0.3 μm, and annealed at 950°C with the gauge length and width of the specimens in the weld zone reduced to ≈2.5 mm and 1.1 mm. respectively (to ensure rupture in the weld zone); and (4) as-fabricated, cold-worked specimens with a weld zone. The anneal at 950°C was ≈100°C below the typical annealing temperature for recrystallized specimens. The tensile tests were conducted at a tensile strain rate of $0.0011\ s^{-1}$ with a machine crosshead speed of 0.008 mm · s.

The microstructures in the weld and heat-affected zones were revealed after electropolishing in a solution of 20% HNO_3, 20% HF, and 60% glycerine at 24 V and etching in a solution of 20% HNO_3, 20% HF, and 60% lactic acid.

ExDerimental Results

1. Yield strength and ultimate tensile strength

The yield strength (YS) and uiitimate tensile strenath (UTS) for V-(0-20)Ti and V-(0-15)Cr-5Ti alloys with a TIG weld zone are shown in Fig. 2. The YS and UTS for the alloys in the recrystallized condition without a weld zone are also shown in Fig. 2. With the exception of V and V-1Ti, the YS and UTS of the TIG weld zone in these alloys were comparable to the YS and UTS for the recrystallized alloys without a weld zone. The YS and UTS of the V-(5-20)Ti and V-(0-15)Cr-5Ti alloys in the annealed condition were decreased (2-17%) by the TIG weld zone from the values of the recrystallized alloys without a weld zone, but in the cold-worked condition were increased (2-20%) by the TIG weld zone. Tensile specimens with a uniform gauge width (i.e., "annealed + weld and "cold work + weld" in figure symbol legends) ruptured without exception in the heat-affected zone adjacent to the weld zone. In the case of specimens with a reduced gauge width in the weld zone (i.e., "weld zone" in figure symbol legends), rupture occurred in the weld zone.

2. Unform elongation and total elongation

Uniform elongation (UE) and total elongation (TE) for the V-(0-20)Ti and V-(0-15)Cr-5Ti alloys with a TIG weld zone are shown in Fig. 3. The UE and TE of the weld zone in unalloyed V and V-Cr-Ti alloy specimens were generally comparable or higher than the UE and TE for recrystallized specimens without a weld zone. The UE and TE for the V-Ti and V-Cr-5Ti alloy specimens in the annealed or cold-worked condition were substantially reduced (>25% relative to recrystallized material) by the presence of a TIG weld zone. The reduction of UE and TE by a TIG weld zone was particularly significant for the V-Cr-5Ti specimens in the cold-worked condition with >5 wt.% Cr. The reduction of uniform and total elongation in the alloys with a TIG weld zone (Fig. 3) may be a specious effect because deformation was mainly confined to the heat-affected zone (≈0.6 mm width) on either side of the weld zone.

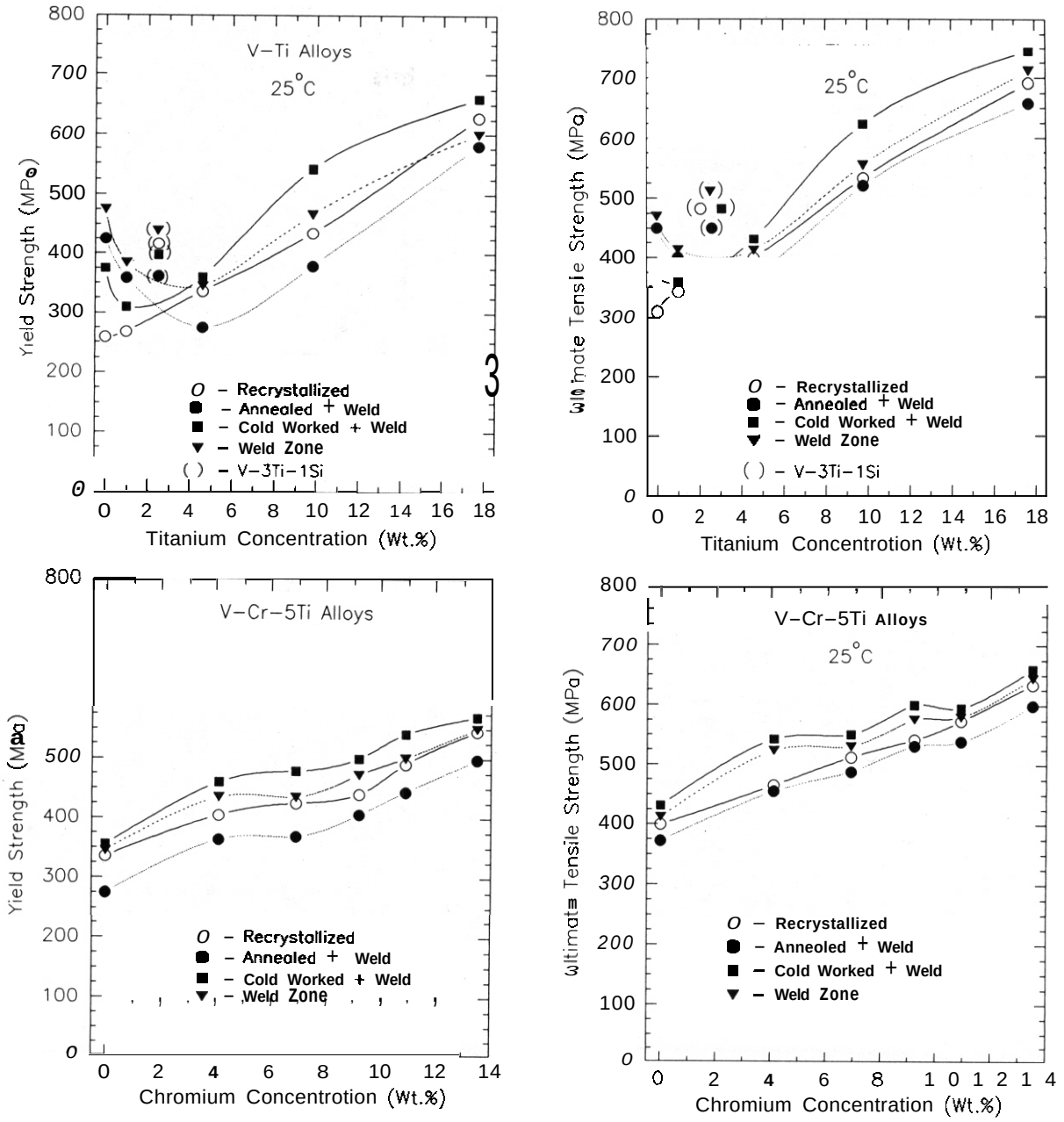

Fig. 2. Yield strength and ultimate tensile strength of V-(0-20)Ti and V-(0-15)Cr-5Ti alloys with and without TIG weld zone,

3. Reduction in cross-sectional area

Fig. 4 shows reduction in cross-sectional area (RA) of V-(0-20)Ti and V-(0-15)Cr-5Ti alloys in the recrystallized (without weld zone) and cold-worked (with weld zone) conditions after tensile deformation to rupture in the heat-affected zone. The RA for the recrystallized alloy specimens was >75% on testing at 25°C, while that for V-5Ti and V-5Cr-5Ti alloys was not affected by a TIG weld zone. However, substantial reduction of RA occurred for V-Ti alloys with >5% Ti and especially for V-Cr-5Ti alloys with >5% Cr. Fracture of the V-(0-15)Cr-5Ti alloys with >5% Cr was dominated by intergranular cracking, as shown in Fig. 5.

4. Microstructures

Microstructures of heat-affected and weld zones in V-5Ti, V-10Ti, V-5Cr-5Ti, and V-12Cr-5Ti alloy specimens are shown in Figs. 6 and 7. Weld zones in all of the alloys contained a high number-density of precipitates with a high

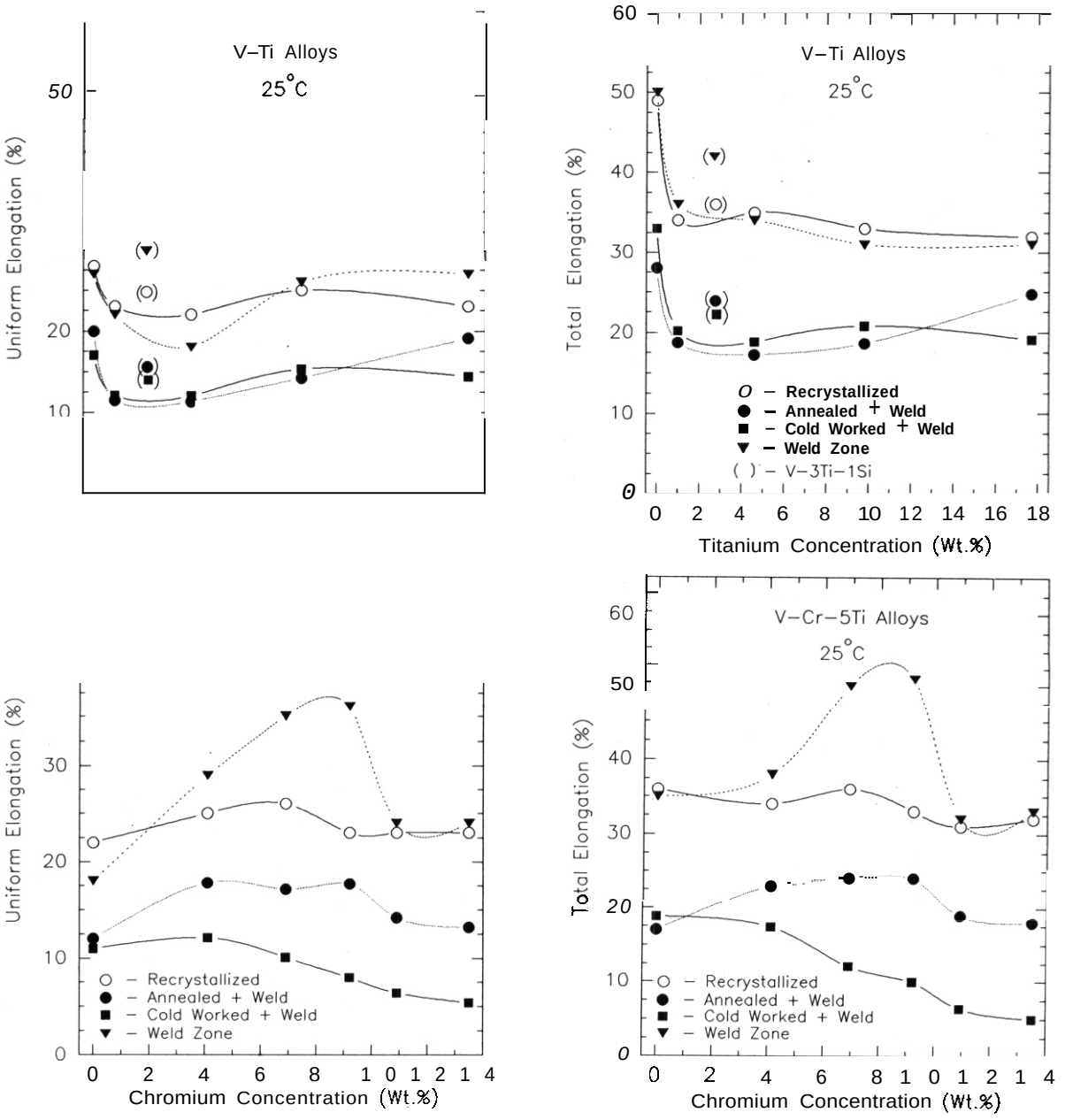

Fig. 3. Uniform elongation and total elongation of V-(0-10)Ti and V-(0-15)Cr-5Ti alloys with and without TIG weld zone.

degree of alignment. The number-density of precipitates in the weld zones was higher (10X) than the numberdensity of precipitates observed in recrystallized material without a weld zone (e.g., see Figs. 1 and 2 in Ref. 2). Moreover, aligned precipitates were not observed in recrystallized material. Conversely, the microstructures of the heat-affected zones contained substantially fewer precipitates than were observed in recrystallized material without a weld zone. Grain size in the heat-affected zone adjacent to the weld zone was substantially larger (6-8X) than the grain size (50.020 mm) in recrystallized material that was annealed typically at 1050-1150°C for one h.

Macroscopic cavities were observed only in weld zones in the V-7Cr-5Ti alloy specimens. We speculate that these cavities (≈1 mm dia.) were caused by macroscopic compositional inhomogeneities observed in this alloy. Microscopic cavities (<<1 mm dia.) were not observed in the microstructures of the alloy specimens with a weld zone.

DISCUSSION OF RESULTS

The tensile properties of a series of V-(0-20)Ti and V-(0-15)Cr-5Ti alloys with a TIG weld zone were determined at

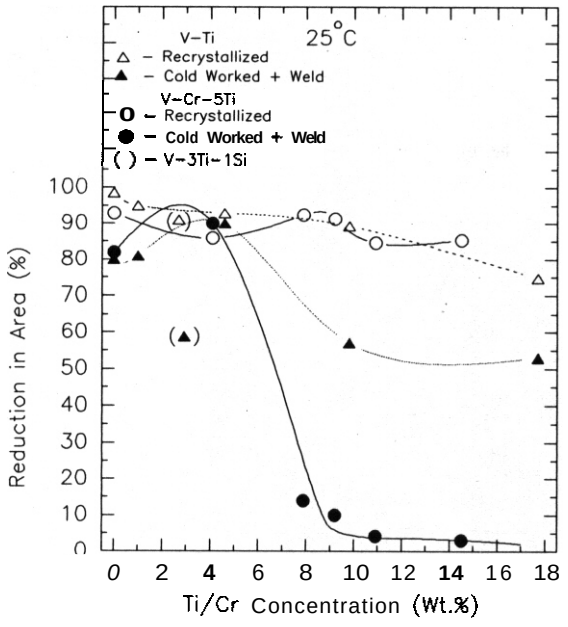

Fig. 4. Reduction-in-area of V-(0-20)Ti and V-(0-15)Cr-5Ti alloys with and without TIG weld zone.

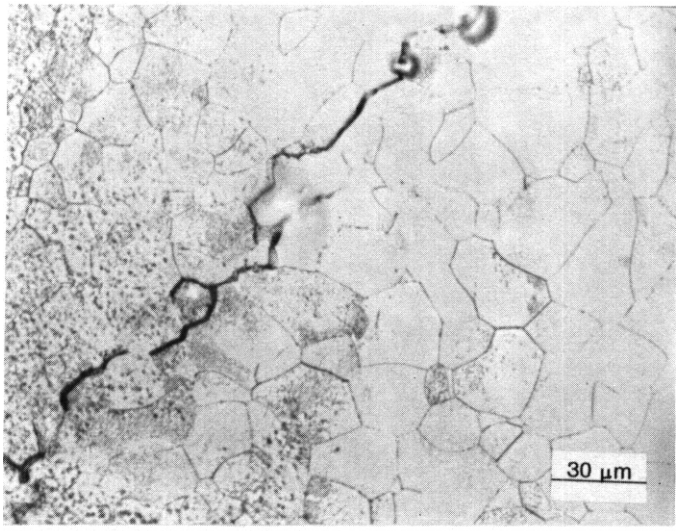

Fig. 5. Intergranular cracking in heat-affected zone of V-12Cr-5Ti alloy with TIG weld.

25°C. These results showed that the weld zones in these alloy specimens have tensile properties comparable to those of recrystallized alloys without a weld zone, even though the weld zones in these specimens contained a substantially higher number-density of aligned precipitates. Tensile specimens with uniform-gauge width in a gauge length of 7.62 mm ruptured without exception in the heat-affected zone. It would be expected that the heat-affected zones would have the lowest strength because of the exceptionally large grain size and paucity of precipitates in these zones. However, there does not appear to be a correlation between grain size and precipitate number-density and the embrittlement of the V-(0-15)Cr-5Ti alloy specimens for Cr concentrations >5 wt.% (Figs. 4 and 5). The embrittlement (i.e., low fracture toughness) of the V-(0-15)Cr-5Ti specimens for >5 wt.% Cr shown by the reduction-in-area data from these tensile tests confirms the low fracture toughness of these alloys deduced previously from the temperature dependence of energy absorption in Charpy-impact testing?

CONCLUSIONS

1. Tensile properties of TIG weld zones in V-(0-20)Ti and V-(0-15)Cr-5Ti alloys are comparable to tensile properties of recrystallized alloys without a weld zone.
2. The low fracture toughness of V-(0-15)Cr-5Ti alloys for Cr concentrations >5 wt.% deduced from reduction-in-area data on tensile testing confirms the low fracture toughness of these alloys deduced previously from Charpy-impact tests.
3. The rupture (fracture) of vanadium-base alloy structures with TIG welds will most likely occur in the heat-affected zone rather than in the weld zone.

FUTURE WORK

1. The O, N, and C concentration in the weld and heat-affected zones will be determined by secondary ion mass spectroscopy analyses.
2. The TIG weld parameters for the V-5Cr-5Ti alloy will be optimized for minimum grain size in the heat-affected zone adjacent to the weld zone.
3. The effect of the TIG weld on the tensile properties of 6.35-mm-thickness V-5Cr-5Ti alloy plate will be determined.
4. The effect of the TIG weld zone on the tensile properties of V-5Cr-5Ti alloy irradiated to a8 dpa at 360°C will be determined.
5. The effect of O, N, and C concentration on the tensile properties of V-5Cr-5Ti and V-5Cr-3Ti alloys will be determined by alteration of either O, N, or CH, concentration in the inert gas during TIG welding.

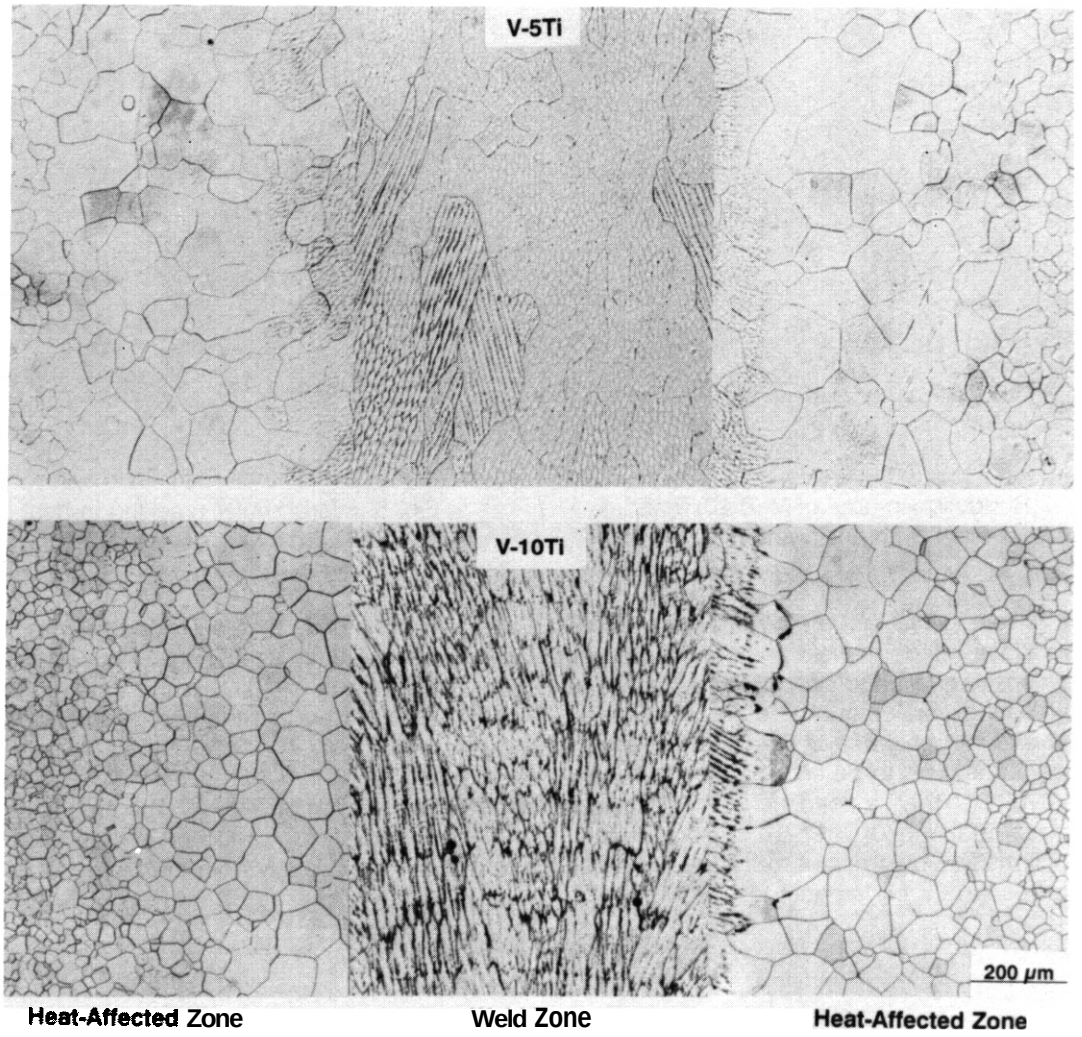

Fig. 6. Microstructures in heat-affectedand TIG weld zones in V-5Ti and V-10Ti alloys.

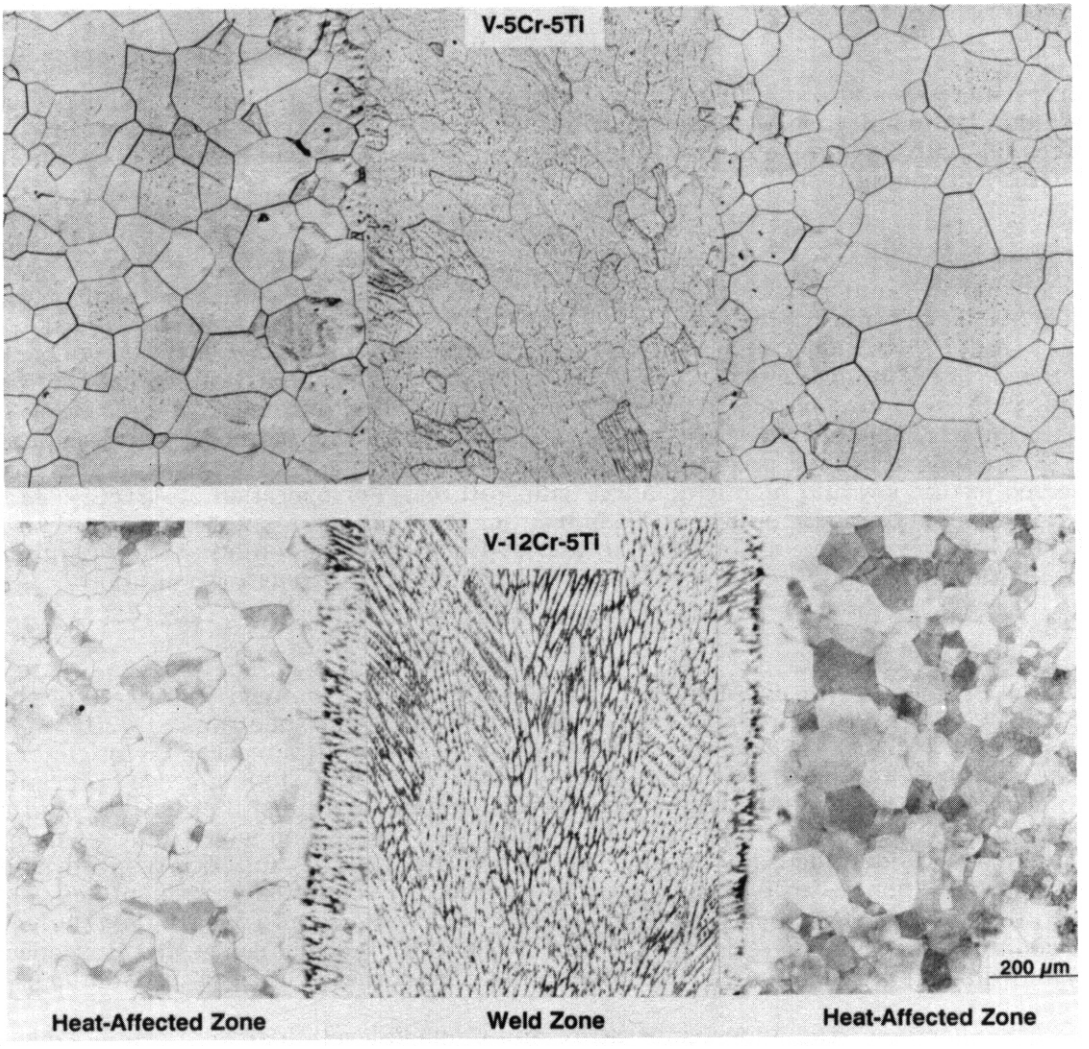

Fig. 7. Microstructures in heat-affected and TIG weld zones in V-5Cr-5Ti and V-12Cr-5Ti alloys.

REFERENCES

1. B. A. Loomis, L. J. Nowicki, and D. L. Smith, 'Tensile Properties of Vanadium and Vanadium-Base Alloys." in: Fusion Reactor Materials, Semiannual Progress Report for Period Ending March 31, 1991, DOE/ER-0313/10, U.S. Department of Energy, Office of Fusion Energy, July 1991, pp. 145-155.

2. B. A. Loomis, R. H. Lee, and D. L. Smith, "Effect of Heat Treatment and Impurity Concentration on the Tensile Deformation of Unirradiated and Irradiated Vanadium Alloys." in: Fusion Reactor Materials, Semiannual Progress Report for Period Ending March 31, 1987, DOE/ER-0313/2, U.S. Department of Energy, Office of Fusion Energy, September 1987, pp. 250-258.

3. B. A. Loomis, B. J. Kestel, B. D. Edwards, and D. L. Smith, 'Temperature Dependence of the Fracture Behavior and the DBTT for Dehydrogenated and Hydrogenated Vanadium-Base Alloys." in: Fusion Reactor Materials, Semiannual Progress Report for Period Ending September 30, 1988, DOE/ER-0313/5, U.S. Department of Energy, Office of Fusion Energy, April 1989, pp. 242-255.

EFFECTS OF IRRADIATION-INDUCED PRECIPITATION ON PROPERTIES OF VANADIUM ALLOYS, H. M. Chung (Argonne National Laboratory)

OBJECTIVE

The microstructures and properties of vanadium-base alloys are profoundly modified during neutron irradiation. The objective of this work is to characterize irradiation-induced precipitation and correlate the results with swelling and mechanical properties of several candidate V alloys after neutron irradiation, thereby providing insight for development of an optimal alloy.

SUMMARY

Two major and two minor types of irradiation-induced precipitates were identified in V-Ti, V-Cr-Ti. and V-Ti-Si alloys after neutron irradiation in the Fast Flux Test Facility (FFTF)at 420 and 600°C to fluences up to 114 dpa. The major precipitates are Ti_5Si_3 and Ti_2O phases. Effects of irradiation temperature and dose on the two major types of precipitation were examined after irradiation at 420. 600. and 600°C plus an excursion to 850°C for 50 min. Precipitation of the very fine Ti_5Si_3 particles at 420°C increases monotonically with increasing dose. whereas at 600°C the maximum precipitation occurs at ≈20-40 dpa. The characteristic precipitation kinetics were consistent with swelling and elongation behavior observed for the low and high irradiation temperatures. For operation at 420°C. it is important to optimize the Si level and ensure sufficient Ti "in solution" (i.e., Ti solutes not bound to thermal precipitates), and thereby optimizing the precipitation of Ti_5Si_3. For operation at 600°C, minimizing the O content, in addition to Si and Ti control, is important in minimizing Ti_2O precipitation.

INTRODUCTION

The swelling behavior,[1-4] mechanical properties,[5-9] and microstructural characteristics[10-14] of vanadium-base alloys (V-Ti, V-Cr. V-Cr-Ti, and V-Ti-Si) irradiated by fast neutrons at 420. 520. and 600°C in the Fast Flux Test Facility (FFTF),were reported earlier. In some of the earlier investigations, it was suggested that swelling[13] and mechanical properties[10,13] are profoundly influenced by recipitation reactions that occur during irradiation. Subsequent investigations identified thermal[12,14] and irradiation-induced precipitation[14] in Ti-containing alloys. In as-fabricated alloys, one major and two minor types of thermal precipitates were identified. i.e., blocky Ti(O,N,C) phase and TiP and TiS, respectively.[12,14] In neutron-irradiated specimens, two types of irradiation-induced precipitates were identified: Ti_2O and $Ti_5(Si,P)_3$.[14] In the study, it was suggested that copious precipitation of the very fine spherical $Ti_5(Si,P)_3$ particles was conducive to superior resistance to void swelling. It was also suggested that specimen ductility is significantly reduced when the precipitation of Ti_2O and $Ti_5(Si,P)_3$ is pronounced.

In this work. effects of irradiation temperature and damage level (dpa) were examined to provide a better understanding of the precipitation characteristics and alloy performance in long-term irradiation. Specimens irradiated up to 120 dpa at three temperatures were examined, i.e., 420, 600, and 600°C plus a temperature excursion to 850°C for approximately 50 min. The results were correlated to the effects of damage level on swelling and total elongation of the alloys. From previous studies,[1-4] uniaxial total elongation of most of the alloys has been reported to reach an asymptotic minimum after irradiation to ≥40 dpa. However, V-Ti alloys containing 18 to 20 wt.% Ti exhibited a peculiar behavior during irradiation at 600°C; ductility reached a minimum at ~20 dpa and increased subsequently at higher dose. While swelling during irradiation at 600°C generally increases monotonically with increasing damage level,[1-3] swelling of several alloys at 420°C has been reported to exhibit a peculiar maximum at ~30 to 70 dpa and to decrease subsequently at higher doses.[4] These peculiarities in ductility and swelling can be explained on the basis of irradiation-induced precipitation in the alloys.

MATERIALS AND PROCEDURES

Preparation of alloy specimens in this investigation was described in earlier reports.[13,14] Chemical compositions of as-fabricated alloys are given in Table 1. The alloys were irradiated in the FFTF Materials Open Test Assembly (MOTA) at 420 and 600°C to neutron fluences (E > 0.1 MeV ranging from 3×10^{22} n·cm^{-2} (17 dpa) to 1.9×10^{23} n·cm^{-2} (114 dpa). Some of the specimens irradiated at 600°C were exposed to unplanned temperature excursions up to 850°C for approximately 50 min. The specimens were sealed inside Li^7-filled TZM/Mo capsules during irradiation to prevent contamination by O, N, and C impurities dissolved in the Na coolant of the FFTF.

Table 1. Composition of Vanadium Alloys Irradiated In FFTF/MOTA

ANL ID	Nominal Composition (wt.%)	Concentration (wt. ppm) O	N	C	Si
BL-19	V	1101	161	360	....
BL-20	V	570	110	120	325
BL-36	V	810	86	250	<50
BL-51	V	570	49	56	370
BL-35	V-9.5Cr	340	45	120	<50
BL-4	V-10.0Cr	530	76	240	<50
BL-5	V-14.1Cr	330	69	200	<50
BL-50	V-1.0Ti	230	130	235	1050
BL-52	V-3.1Ti	210	310	300	500
BL-11	V-4.9Ti	1820	530	470	220
BL-46	V-4.6Ti	305	53	85	160
BL-34	V-8.6Ti	990	180	420	290
BL-12	V-9.8Ti	1670	390	450	245
BL-13	V-14.4Ti	1580	370	440	205
BL-15	V-17.7Ti	830	160	380	480
BL-16	V-20.4Ti	390	530	210	480
BL-10	V-7.2Cr-14.5Ti	1110	250	400	400
BL-21	V-13.7Cr-4.8Ti	340	510	180	1150
BL-22	V-13.4Cr-5.1Ti	300	52	150	56
BL-23	V-12.9Cr-5.9Ti	400	490	280	1230
BL-25	V-14.4Cr-0.3Ti	390	64	120	<50
BL-26	V-14.1Cr-1.0Ti	560	86	140	<50
BL-24	V-13.5Cr-5.2Ti	1190	360	500	390
BL-40	V-10.9Cr-5.0Ti	470	80	90	270
BL-41	V-14.5Cr-5.0Ti	450	120	93	390
BL-43	V-9.2Cr-4.9Ti	230	31	100	340
BL-44	V-9.9Cr-9.2Ti	300	87	150	270
BL-47	V-4.1Cr-4.3Ti	350	220	200	870
BL-49	V-7.9Cr-5.7Ti	400	150	127	360
BL-42	V-3.1Ti-0.5Si	580	190	140	5400
BL-27	V-3.1Ti-0.3Si	210	310	310	2500
BL-45	V-2.5Ti-1.0Si	345	125	90	9900

RESULTS AND DISCUSSION

Effect of Irradiation Temperature

Ti_5Si_3 was the only irradiation-induced precipitate observed upon irradiation at 420°C. At this temperature, the Ti_5Si_3 precipitates were extremely small (i.e, ~3 to 15 nm); see Fig. 1(A). Neither Ti_2O nor other minor irradiation-induced precipitates were observed at 420°C.

Ti_5Si_3 precipitates that formed during irradiation at 600°C were somewhat larger, i.e., ~15-30 nm; see Fig. 1(B). For irradiation at 600°C with the temperature excursion to 850°C for 50 min. the size was still larger (i.e., ≈30-50 nm wide and ~40-60 nm long), and many of the precipitates aligned themselves on dislocations: see Fig. 1(C). Morphology such as that in Fig. 1(C) could be mistaken for Ti_2O, and it was necessary to verify identification of the precipitates by matching the dark-field images with corresponding Ti_5Si_3 reflections in indexed diffraction patterns. Ti_5Si_3 precipitates were absent in the alloy of Fig. 1(C) (i.e., BL-27. V-3Ti-0.3Si) when irradiated at 420 and 600°C up to 114 dpa.[14] Despite the high Si content, Ti_5Si_3 precipitation in the alloy occurred only at the higher temperature (600°C plus excursion to 850°C) at high doses.

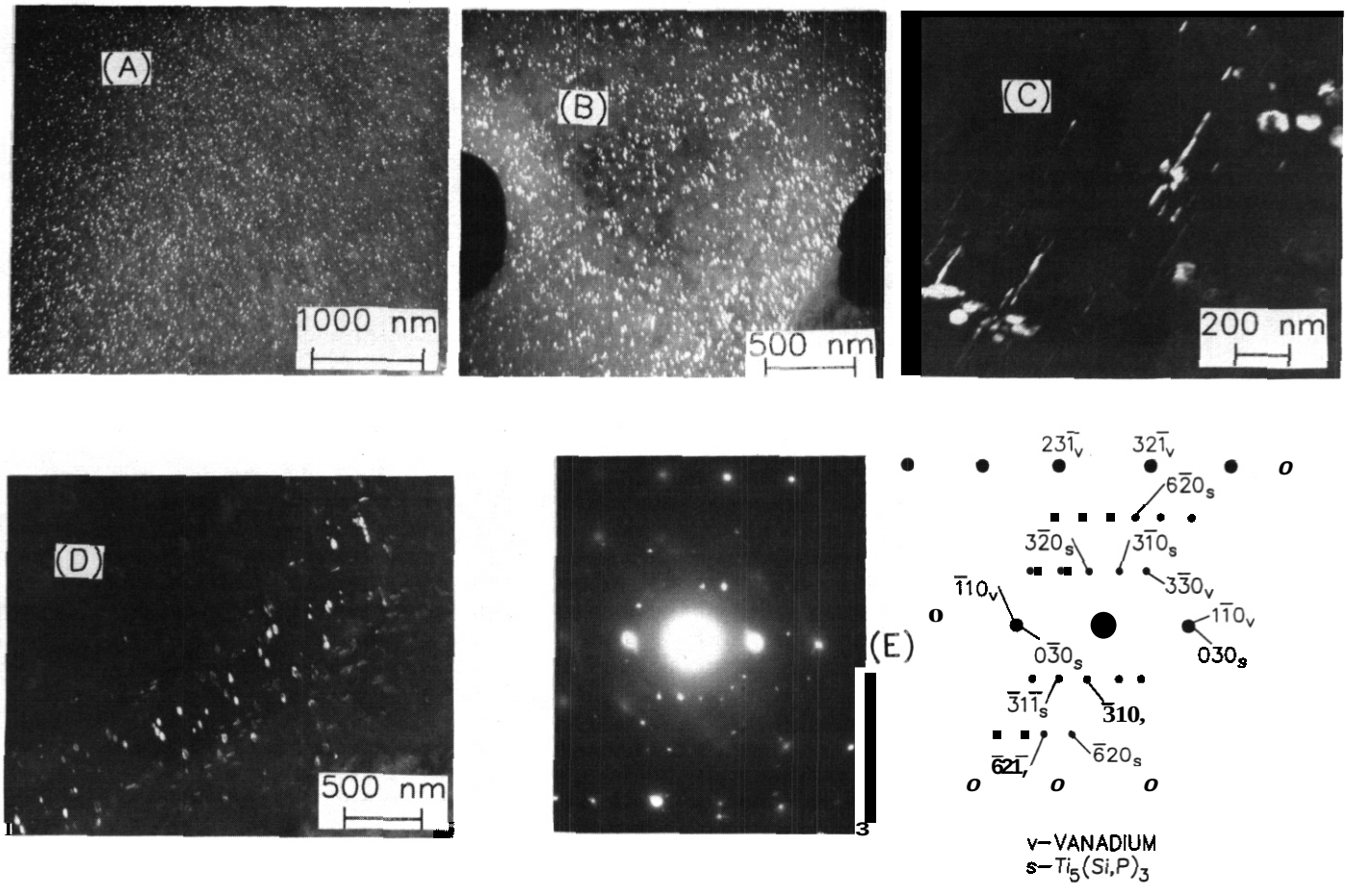

Fig. 1. Effect of irradiation temperature on size and morphology of Ti_5Si_3 precipitates: *(A)* V-*20Ti (BL-16)* irradiated at *420°C* to *114* dpa: *(B) V-15Cr-5Ti (BL-24)* irradiated at *600°C* to *17* dpa: *(C)* and *(D) V-3Ti-0.3Si (BL-27)* irradiated at *600°C* to *77* dpa with a temperature excursion to 850°C for 50 min: and *(E)* selected-area *diffraction* pattern of *(D).*

hecipitation of the short needlelike Ti_2O phase was observed at 600°C in some specimens containing relatively high levels of Ti and O, e.g., BL-15[14] (V-18Ti, 830 wt.ppm O), BL-12[11] (V-10Ti, *1670* ppm O),and BL-23 and BL-24[10] (V-15Cr-5Ti, 400-1190 ppm O). Ti_2O was also observed upon irradiation at temperatures exceeding 600°C, i.e., irradiation with the temperature excursion to *850°C.*

For irradiation at ***600°C*** and higher, another type of minor precipitate was observed near grain boundaries. Examples of selected-area diffraction patterns and dark-field images of this type of precipitate ***are*** shown in Fig. ***2.*** The morphology resembles long needles aligned mostly parallel to grain boundaries. Diffraction characteristics of the phase were identical to those of the isostructural phases of Ti_5Si_3 or Ti_5P_3,[14] except that extra reflections (believed to be superlattice reflections of the phase) were present. Titanium phosphides are usually observed on or near grain boundaries in as-fabricated12 or irradiated14 specimens. which indicates that P atoms tend to segregate thermally to grain boundaries. Therefore, regions near grain boundaries are believed to be relatively rich in P atoms, and the long-needlelike phase near the grain boundary of Fig. 2(B) is thus believed to be rich in P this phase has been tentatively identified as an ordered variation of $Ti_5(P, Si_{1-x})_3$ type. The dark-field image of Fig. 2(*B*) was produced from $(3\bar{1}1)$ reflection of the ordered variation (d-spacing 0.221 nm) and $(1\bar{1}1)$ reflection of Ti_2O (d-spacing ***0.226*** nm), which were nearly superposed. As a result of the superposition, weak images of the short Ti_2O are also visible away from the grain boundary and nearly perpendicular to the long needlelike precipitates in the figure.

For irradiation at **600°C.** one more type of minor precipitate was observed but could not be identified. Examples of spherical dark-field morphologies of the unidentified phase, observed in V-15Cr-5Ti and V-3Ti-0.3Si alloys after irradiation at **600°C** to **84** dpa, are shown in Fig. **3.** Although they are not shown in the figure, selected-area diffraction patterns of the spherical precipitates were not compatible with those of $Ti_5(Si,P)_3$. **A** summary of the temperature dependence of the precipitation **of** Ti_5Si_3, the ordered variation of $Ti_5(P,Si_{1-x})_3$, and Ti_2O is given in Fig. **4.**

The two types **of** precipitates shown in Figs. 2 and 3 were observed only in minor proportions, and their influences on swelling and mechanical properties are believed to be secondary. It was concluded that the major precipitations in the Ti-containing alloys are (1) thermal precipitation of Ti(O,N,C), (2) irradiation-induced precipitation of $Ti_5(Si,P)_3$ at **420°C** and higher, and (3) irradiatipn-induced precipitation of Ti20 at **600°C** and higher. Characteristic behavior of the three major precipitations is illustrated schematically in Fig. 5.

Effect of Dose

Effects of increased irradiation damage (dpa) on precipitation behavior of Ti_5Si_3 were examined in several alloys irradiated at **420** and 600°C. Number densities of Ti_5Si_3 precipitates in V-20Ti alloys *(BL-15* and *-16)* were determined from dark-field images after irradiation at 420°C to **46** and **114** dpa. The number density **for 114** dpa [Fig. 1(A)] was slightly higher or comparable to that for **46** dpa [Fig. 4(D),

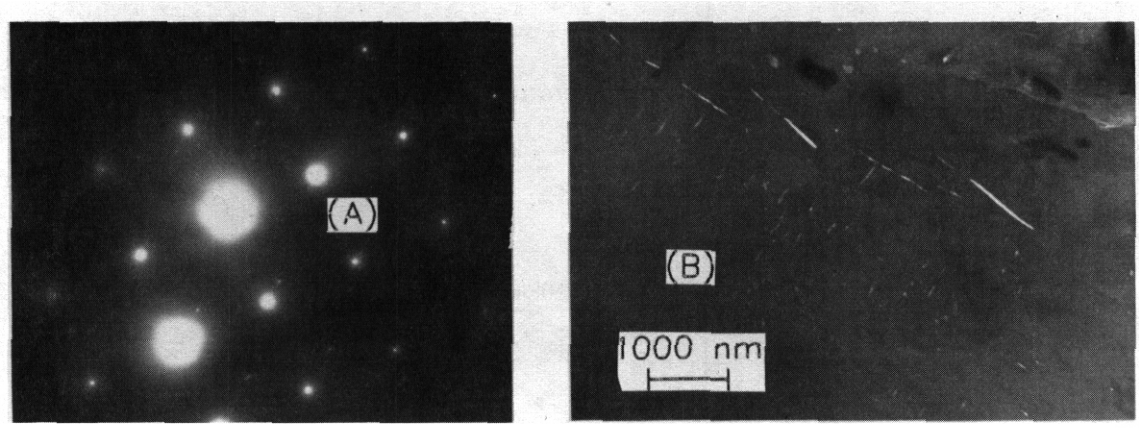

Fig. 2. Selected-area *diffraction* pattern *(A)* showing *(100)* of V parallel ***to*** *(411) of* P-rich long needlelike precipitates near grain boundary and believed ***to*** be ***an*** ordered *variation* of $Ti_5(P,Si_{1-x})_3$. *Dark-field* image of the precipitates is shown in *(B).*

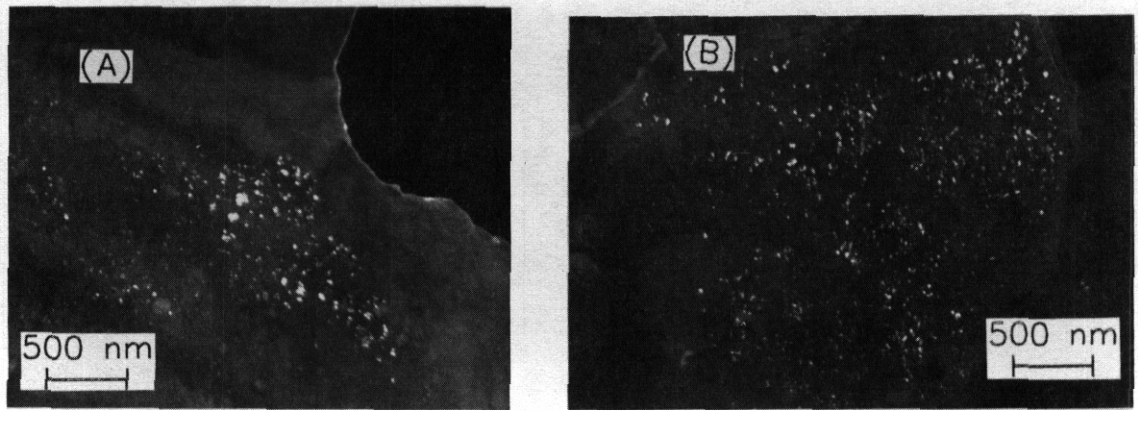

Fig. **3.** *Dark-field* morphologies ***of*** two types *of* unidentified minor precipitates observed in *(A) V-15Cr-5Ti* **(EL-241** irradiated at *600°C* to ***84*** *dpa.* and *(B) V-3Ti-0.3Si (BL-27)* irradiated ***at*** 600°C ***to 84*** dpa.

SUMMARY OF IRRADIATION-INDUCED PRECIPITATION

Irradiation temp. (°C)	$Ti_5(Si, P_{1-x})_3$	Ordered $Ti_5(P,Si_{1-x})_3$*	Ti20
420	■	no	no
	3-15 nm dia.		
600	●	▬	▬
	15-30 nm dia.	10-20 nm thick 500-1000 nm long	10-20 nm thick 20-200 nm long
600 plus temp. excursion	●	▬	▬
	30-50 nm wide 40-60 nm long	20-50 nm thick 100-300 nm long	10-20 nm thick 20-200 nm long

'Tentative identification.

Fig. 4. Summary of effects of irradiation temperature on size and **morphology** *of irradiation-induced precipitates.*

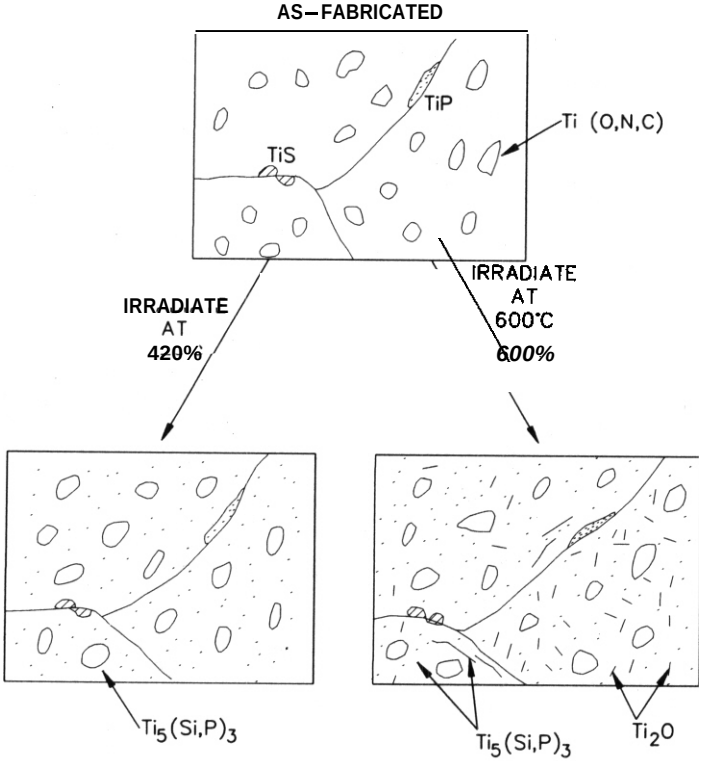

Fig. 5. Schematic illustration of irradiation-induced precipitation in Ti-containing V-base alloys.

Ref. 141, indicating that the density reached a saturation. This behavior of damage-level dependence for 420°C irradiation is illustrated schematically in Fig. 6(A). Precipitation kinetics at this temperature seem to exhibit an incubation dose, which is characteristic of each alloy. and then reach a saturation level at higher doses.

Effect of dose for irradiation at 600°C was examined for V-20Ti (BL-15 and BL-16) and V-15Cr-5Ti (BL-24) alloys after irradiation to 17. 77, and 84 dpa. For the latter alloy, the density of Ti_5Si_3 precipitates was very high after irradiation to only 17 dpa: see Fig. 1(B). However. for specimens irradiated to 84 dpa at the same temperature, the volume fraction of Ti_5Si_3 precipitates was negligible. and it was difficult to obtain dark-field images because reflections from precipitates were absent or extremely weak. Only limited unidentified precipitates, shown in Fig. 3, were observed in localized regions in the specimens. Therefore, it is believed that the number density of Ti_5Si_3 precipitates reached a maximum in V-15Cr-5Ti after irradiation to a relatively low dose (e.g., 20-30 dpa) and decreased subsequently at higher doses. This behavior, which is in contrast to that after irradiation at 420°C. is shown schematically in Fig. 6(B).

In an attempt to explain the good correlation between the high number density of Ti_5Si_3 precipitates and superior resistance to void swelling, it was suggested in a previous study that the large surface areas generated between the matrix and high-density Ti_5Si_3 Precipitates act as efficient sinks for vacancies to be annihilated.[14] According to this model, swelling dependence on damage level is expected be significantly different for the two situations in which contrasting kinetics of Ti_5Si_3 precipitation have been depicted (Fig. 6). For irradiation at 420°C, swelling is expected to exhibit a maximum after an incubation period and diminish subsequently at higher damage levels. For irradiation at 600°C. such a maximum is not expected. and void swelling will increase monotonically as damage level increases. These two contrasting swelling kinetics, schematically illustrated in Figs. 6(A) and 6(B), respectively. were consistent with observed swelling behavior reported earlier.4

The V-20Ti alloys exhibited a peculiar tensile behavior at 600°C in comparison with other alloys. namely, ductility of the alloy exhibited a minimum at 20 to 30 dpa before increasing to a higher level at higher doses.[5,15] It seems that this behavior is also consistent with the damage-level dcpcndcnce of the density of Ti_5Si_3 precipitates in the alloy (Fig. 7). When the density is very high (e.g., in the specimen irradiated to 17 dpa), deformation by dislocation movcment. and hence total elongation, arc expcctcd to be low. As dose level increases and the number density of Ti_5Si_3 precipitates dccrcascs. a relativcly easier plastic deformation and a higher ductility seem to occur. The mechanism that leads to lower precipitation of Ti_5Si_3 at higher doses in this alloy during irradiation at 600°C is not understood at

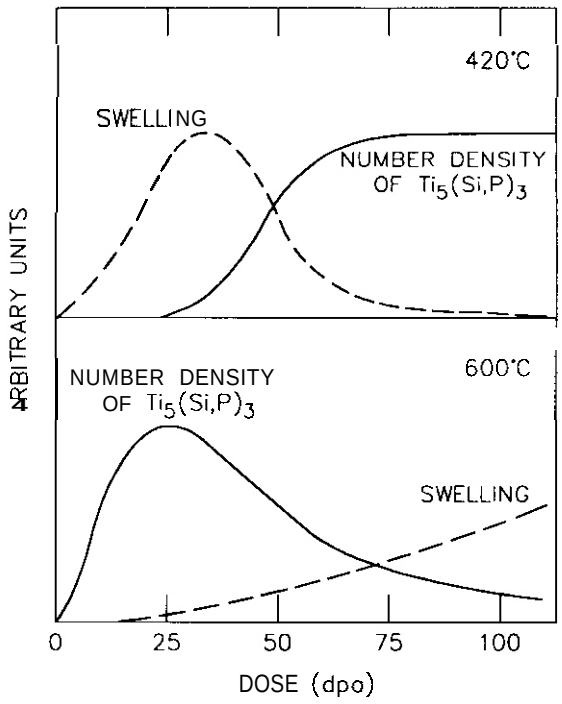

Fig. 6. Schematic illustration of observed number density of Ti_5Si_3 precipitates and expected swelling as *a function of dose for* irradiation at 420 and 600%.

present. For irradiation at 420°C, Ti_5Si_3 precipitation in the alloy was high for dose levels up to 114 dpa [Fig. 1(A)], swelling was low. and ductility decreased monotonically with increasing dose until it reached an asymptotic minimum.[15]

These observations on the kinetics (i.e., the effects of temperature and damage level) of Ti_5Si_3 precipitation, swelling. and uniaxial total elongation indicate that irradiation-induced precipitation of Ti_5Si_3 is a primary process that influences ductility and resistance to swelling of Ti-containing alloys for irradiation at 420 to 600°C. For irradiation at 600°C and higher, irradiation-induced precipitation of the Ti_2O phase is also believed to influence mechanical properties significantly. Therefore, it is desirable to minimize Ti_2O precipitation while maintaining an optimal level of Ti_5Si_3 precipitation for a given operational condition in a fusion reactor. This means that for operation at ≈420°C, for example. the key factors involve optimizing the Si level and ensuring a sufficient level of Ti "in solution." i.e., Ti solutes not bound to thermal precipitates of Ti(O,N,C) and. to a lesser extent, TiP and TiS. For operation at ≈600°C, minimizing **O** content in addition to Si and Ti control would be important.

CONCLUSIONS

1. Two primary and two secondary types of precipitates that form via irradiation-induced processes have been identified in V-base alloys containing Ti. The primary precipitates are Ti_5Si_3 for irradiation at ≥420°C and Ti_5Si_3 and Ti_2O for irradiation at 2600°C. Contrasting effects of dose on the precipitation behavior of Ti_5Si_3 have been observed for irradiation at 420 and 600°C for V-20Ti, V-15Cr-5Ti, and V-3Ti-0.3Si. Damage dependences **of** swelling and uniaxial total elongation in these alloys were consistent with the characteristic behavior of Ti_5Si_3 precipitation.

2. Precipitation of Ti_5Si_3 is a primary process that influence ductility as well as resistance to swelling of Ti-containing alloys upon irradiation at ≥420°C. At ≥600°C, irradiation-induced precipitation of the Ti_2O phase is **also** believed to degrade mechanical properties significantly. Therefore, it **is** desirable to minimize Ti_2O precipitation while maintaining an optimal level of Ti_5Si_3 precipitation for a given operational condition in a fusion reactor. This means that **for** operation at –420°C. for example. it is important to optimize the Si level and at the same time ensure a sufficient level of Ti "in solution," i.e., Ti solutes not bound to thermal precipitates of Ti(O,N,C) and, to a lesser extent. TiP and TiS. For operation at ≈600°C, minimizing the **O** level in the alloy in addition to Si and Ti control would be important.

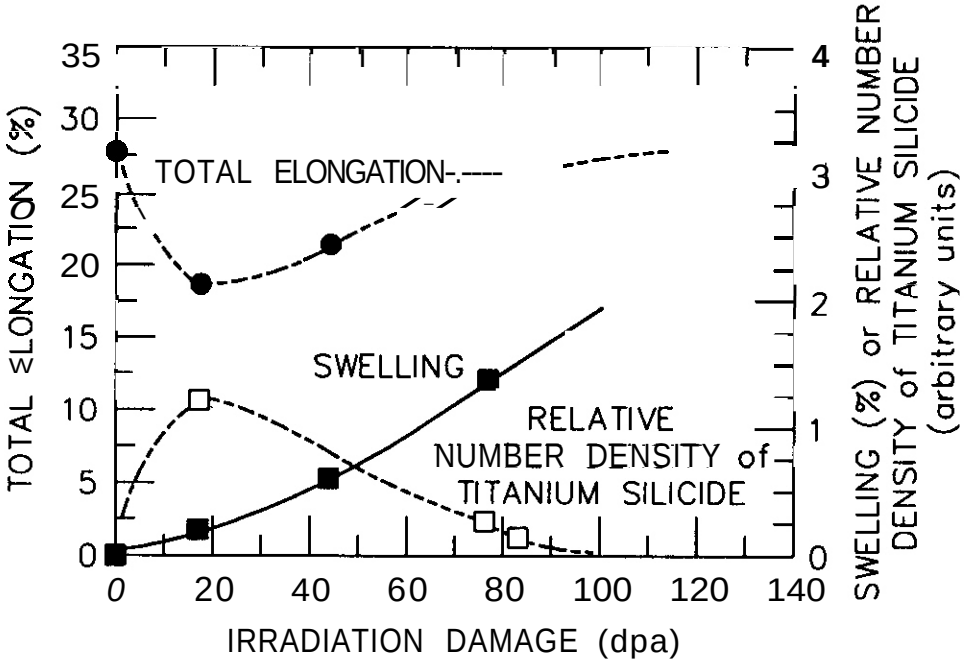

Fig. 7. Total elongation. swelling, and relatiue number density of Ti_5Si_3 precipitates versus dose measured for V-20Ti (BL-15 and -16) irradiated at 600°C.

FUTURE WORK

The ratio of Ti depletion from the matrix through thermal precipitation processes will be determined in order to predict the level of Ti "in solution" from a given bulk composition, and thereby, determine optimum levels of Si and Ti in V-Ti and V-Cr-Ti alloys. The role of Cr in the evolution of microstructure and mechanical properties during irradiation will be investigated to determine optimum level of Cr. Microstructures of specimens irradiated in the Dynamic Helium Charging Experiments will be characterized to determine the effects of dynamic helium charging and neutron irradiation.

ACKNOWLEDGMENTS

The author is grateful to B. A. Loomis and D. L. Smith for helpful discussions and to L. J. Nowicki for his contribution to experimental efforts.

REFERENCES

1. B. A. Loomis and D. L. Smith, "Swelling of Neutron-Irradiated Vanadium Alloys," Fusion Reactor Materials Semiannual Progress Report for Period Ending March 31. 1989, DOE/ER-0313/6, Oak Ridge National Laboratory, Oak Ridge. TN, August 1989, pp. 339-345.

2. B. A. Loomis and D. L. Smith. "Relationship of Microstructure and Tensile Properties for Neutron-Irradiated Vanadium Alloys." Fusion Reactor Materials Semiannual Progress Report for Period Ending March 31, 1990, DOE/ER-0313/8, Oak Ridge National Laboratory, Oak Ridge. TN, August 1990, pp. 225-235.

3. B. A. Loomis, D. L. Smith, and F. A. Garner. "Swelling of Neutron-Irradiated Vanadium Alloys." J. Nucl. Mater. 179-181 (1991) 771.

4. B. A. Loomis, K. Abe. L. J. Nowicki, H. Chung, and D. L. Smith, "Swelling Dependence of Neutron-Irradiated Vanadium Alloys on Temperature. Neutron Fluence, and Thermomechanical Treatment," Fusion Reactor Materials Semiannual Progress Report for Period Ending September 30, 1990, DOE/ER-0313/9, Oak Ridge National Laboratory, Oak Ridge, TN. p. 172.

5. B. A. Loomis and D. L. Smith, "Tensile Properties for Neutron-Irradiated Vanadium Alloys." Fusion Reactor Materials Semiannual Progress Report for Period Ending September 30. 1989. DOE/ER-0313/7, Oak Ridge National Laboratory. Oak Ridge, TN, pp. 203-209.

6. B. A. Loomis and D. L. Smith. "Relationship of Microstructure and Tensile Properties for Neutron-Irradiated Vanadium Alloys." Proc. 15th Intl. Symp. on the Effects of Radiation on Materials, Nashville, TN, June 17-21, 1990, in press.

7. B. A. Loomis, L. J. Nowicki. and D. L. Smith, "Tensile Properties of Vanadium and Vanadium-Base Alloys." Fusion Reactor Materials Semiannual Progress Report for Period Ending March 31. 1991, DOE/ER-0313/10, Oak Ridge National Laboratory. Oak Ridge, TN. July 1991, pp. 145-155.

8. M. L. Hamilton and B. A. Loomis. "Impact Behavior of Irradiated V-15Cr-5Ti Following Hydrogen Removal." Fusion Reactor Materials Semiannual Progress Report for Period Ending September 30, 1990. DOE/ER-0313/7, Oak Ridge National Laboratory. Oak Ridge, TN, pp. 190-192.

9. N. S. Cannon, M. L. Hamilton, A. M. Ermi. D. S. Gelles, and W. L. Hu,"Influence of Neutron Irradiation on the Charpy Impact Properties of V-15Cr-5Ti," J. Nucl. Mater. 155-157, 1988. pp. 987-991.

10. D. S. Gelles. S. Ohnuki, B. A. Loomis. H. Takahashi. and F. A. Garner. "Microstructural Explanation for Irradiation Embrittlement for V-15Cr-5Ti," Fusion Keactor Materials Semiannual Progress Report for Period Ending September 30. 1989. DOE/ER-0313/7, Oak Ridge National Laboratory. Oak Ridge, TN, pp. 193-202.

11. S. Ohnuki. D. S. Gelles. B. A. Loomis. F. A. Gamer, and H. Takahashi. "Microstructural Examination of Simple Vanadium Alloys Irradiated in the FFTF/MOTA," Fusion Reactor Materials Semiannual Progress Report for Period Ending September 30. 1989. DOE/ER-0313/7, Oak Ridge National Laboratory, Oak Ridge, TN, pp. 177-189.

12 T. Schober and D. N. Braski. "The Microstructure of Selected Annealed Vanadium-Base Alloys." Met. Trans. A 20, 1989. pp. 1927-1932.

13. H. M. Chung. B. A. Loomis, and K. Abe, "Correlation of Microstructure and Swelling Behavior of Vanadium Alloys Irradiated in FFTF/MOTA at 420°C." Fusion Reactor Materials Semiannual Progress Report for the Period Ending March 31. 1991, DOE/ER-0313/10, Oak Ridge National Laboratory. Oak Ridge, TN. pp. 135-144.

14. H. M. Chung, L. **J.** Nowicki, and D. L. Smith "Irradiation-Induced Precipitates in Vanadium Alloys Containing Titanium." Fusion Reactor Materials Semiannual Progress Report for the Period Ending September 30. 1991, DOE/ER-0313/11, Oak Ridge National Laboratory, **Oak** Ridge. TN. in press.

15. B. A. Loomis and D. L. Smith, 'Vanadium Alloys **for** Structural Applications in Fusion Systems: **A** Review of Mechanical and Physical Properties." in Proc. 5th Intl. Conf. on Fusion Reactor Materials. November 18-22. 1991, Clearwater, Florida.

PRELIMINARY ASSESSMENT OF CANDIDATE NIOBIUM ALLOYS FOR DIVERTOR STRUCTURES*

J. A. Todd (Illinois Institute of Technology) and I. M. Purdy (Argonne National Laboratory)

INTRODUCTION

The corrosion resistance of binary niobium alloys that contain additions of 2.5 at.% Ti, Zr, Hf, V, Ta. Mo. W, Fe, and Ni, and of ternary niobium alloys with additions of 2.5Ta-2.5Ti, 2.5Ti-2.5Mo, and 2.5Hf-2.5Mo has been assessed after exposure to high-purity (HP) water (<30 ppb dissolved oxygen) at 1300 psi and 300°C for times up to 120 days.[1-4] Preliminary results for the binary alloys indicated that Nb-2.5V showed the lowest weight gain and that Nb-2.5Ti and Nb-2.5Hf exhibited the best mechanical properties. Low weight gains were observed for the Nb-Hf-Mo and Nb-Ti-Mo ternary alloys: all three ternary alloys appeared to have promising mechanical properties. This report presents further analyses of the oxidation kinetics, along with microstructural studies of cross sections and surfaces of selected samples exposed to high-temperature water.

SUMMARY

Corrosion rates of several Nb-base alloys that contain ≈2.5 at.% Zr. V. Hf, Ti. Ta, Mo, or W were determined in HP deoxygenated water at 300°C. Microstructural characteristics of the corrosion-product layers were examined by optical and scanning electron microscopy (SEM). Although the weight-gain corrosion rates were not excessive and only a fraction (<20%) of the hydrogen liberated by the overall corrosion reaction was absorbed by the alloys, most of the alloys were deemed to be brittle, i.e., fracture occurred during a 90° bend test. The microstructural evaluations revealed numerous cracks and spalling of the oxide layers: this is characteristic of nonprotective film formation. Some of the crack surfaces in the alloys were covered by corrosion product, indicating that the cracks formed during exposure to high-temperature water. The present results suggest that Nb alloys with higher concentrations of alloying elements are required to improve the protective nature of the corrosion-product layers and to decrease hydrogen uptake and embrittlement. Procurement of candidate alloys is in progress and corrosion/H_2-embrittlement tests will be conducted at lower temperatures to determine material operating conditions that will lead to adequate performance of alloys as structural materials in the ITER divertor.

PROGRESS AND STATUS

Oxidation Kinetics

The oxidation kinetics for binary and ternary alloys Nb-base alloys[1] are shown in Fig. 1. The weight-gain vs. time data for the Zr, Hf, Mo, and Fe binary alloys and the Ti-Ta ternary alloy exhibit a $t^{0.52}$ relationship: V, Ti-Mo, and Hf-Mo alloys exhibited $t^{0.25}$ kinetics. The Ni, Ta. and Fe binary alloys lost weight after exposure times of 736, 2189, and 2906 h, respectively. The pure Nb reference specimen and the Fe-2.5W alloy were completely fragmented after 1453 h. Insufficient data were available for the oxidation kinetics of the Nb-2.5Ti alloy.

Microstructural Observations

Exposed Surfaces of *Nb-2.5Zr*

Scanning-electron micrographs of the surfaces of Nb-2.5Zr specimens following exposure to HP water at 300°C are presented in Figs. 2a-2d. The macroscopic appearance of the corrosion product changed significantly for exposure times between 30 and 60 days, with only slight differences after 60-, 90-, and 120-day exposures. Figures 2a-2b and 2c-2d compare the surfaces after 30 and 120 days,

*Work supported by the Office of Fusion Energy, U. S. Department of Energy, under Contract W-31-109-Eng-38.

respectively. All specimens exhibited "rosettes" that contain large (>10 μm) oxide particles, as shown in the center of Fig. 2a for the 30–day specimen. Similarly, all surfaces contained 3–μm particles and finer oxide particles, which had a filamentary appearance when the particles were viewed edge-on. The sample exposed for 30 days (Figs 2a and 2b) exhibited a higher fraction of the filamentary oxides than those exposed for 60, 90, or 120 days.

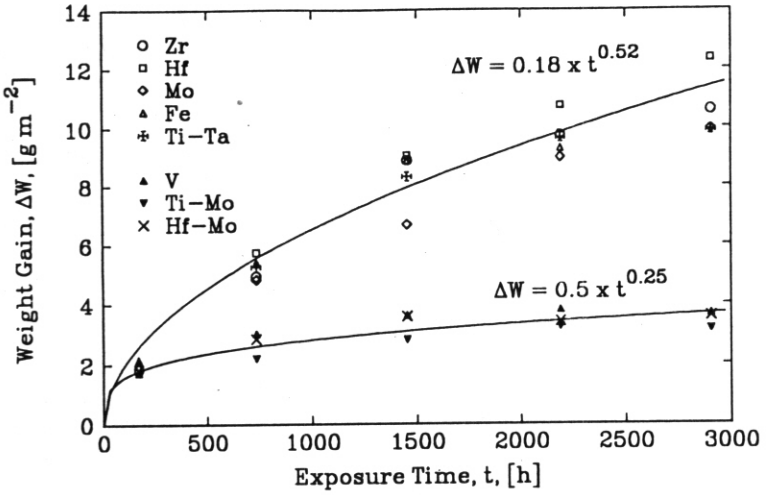

Figure 1. Weight gain vs. exposure time for Nb–base alloys in deoxygenated water at 300°C

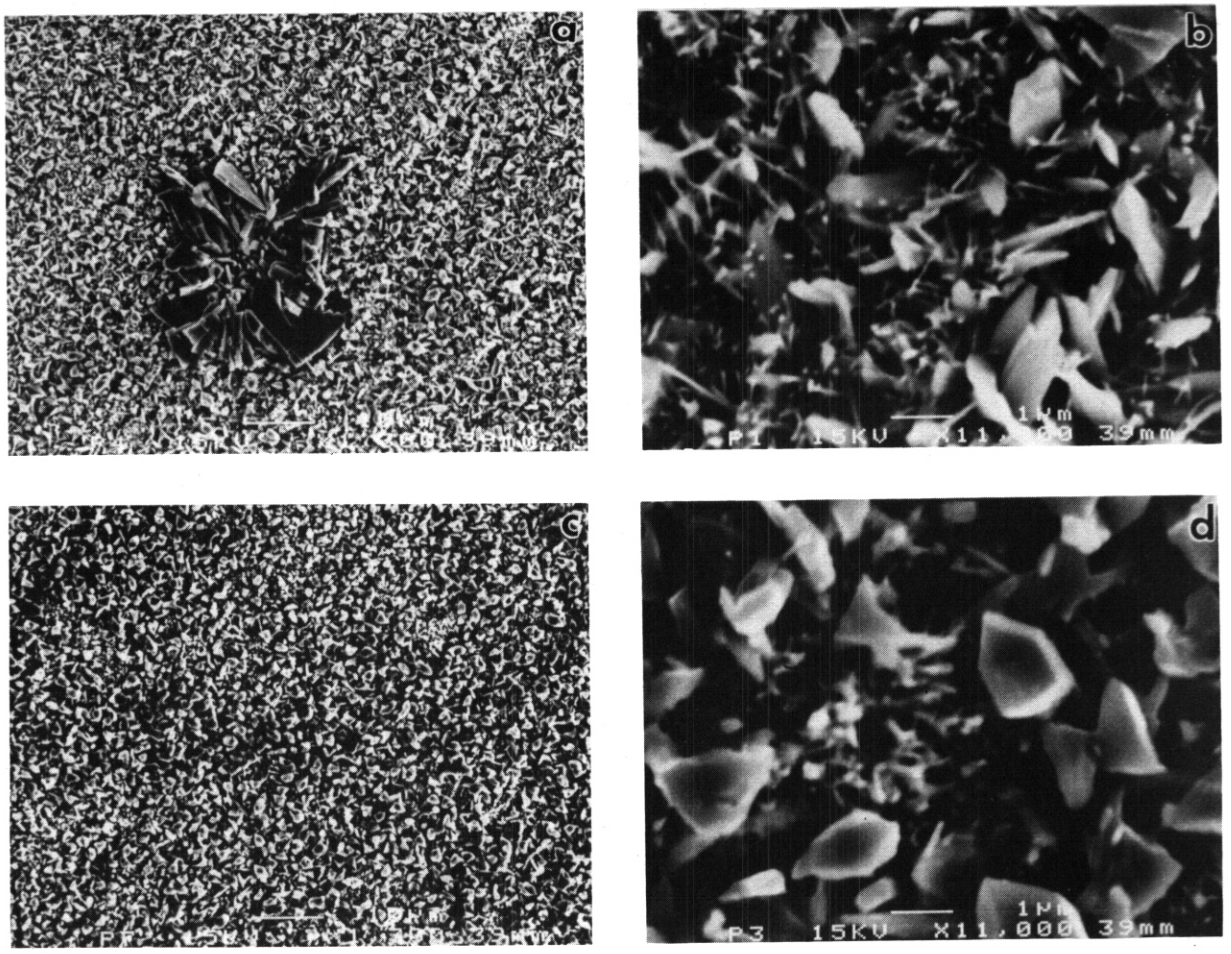

Figure 2. Oxidized surfaces of Nb-2.5Zr specimens at low and high magnification after exposure to HP deoxygenated water for (a and b) 30 days) and (c and d) 120 days at 300°C

Cross Sections of Nb, *Nb-2.5Zr*, and *Nb-2.5V* Alloy Specimens

Metallographic cross sections were prepared from the **Nb.** Nb-2.5Zr, and Nb-2.5V alloys to investigate the degree of oxide penetration as a function of exposure time. Specimens were prepared by cutting a small strip, mounting in epoxy, grinding through 600 grit, and vibratory polishing with 9, 3, and 0.5 μm alumina slurries. Samples were examined in a **JEOL** scanning electron microscope equipped with a NORAN energy-dispersive X-ray system.

Pure Nb

The pure Nb specimen was examined after a 30-day exposure: specimens completely disintegrated after 60 days. Figure 3a shows that a uniform oxide layer (≈10 μm thick) developed at the surface. The oxide film is mechanically unstable, and Fig. 3b shows cracks that initiated in the oxide and propagated into the metal. The absence of oxide within these cracks suggests that they developed either during the postexposure mechanical-property evaluation or when the Nb fragment was cut and mechanically polished. The Nb sample was very brittle after the 30-day exposure and cracked when bent to a 90" angle.

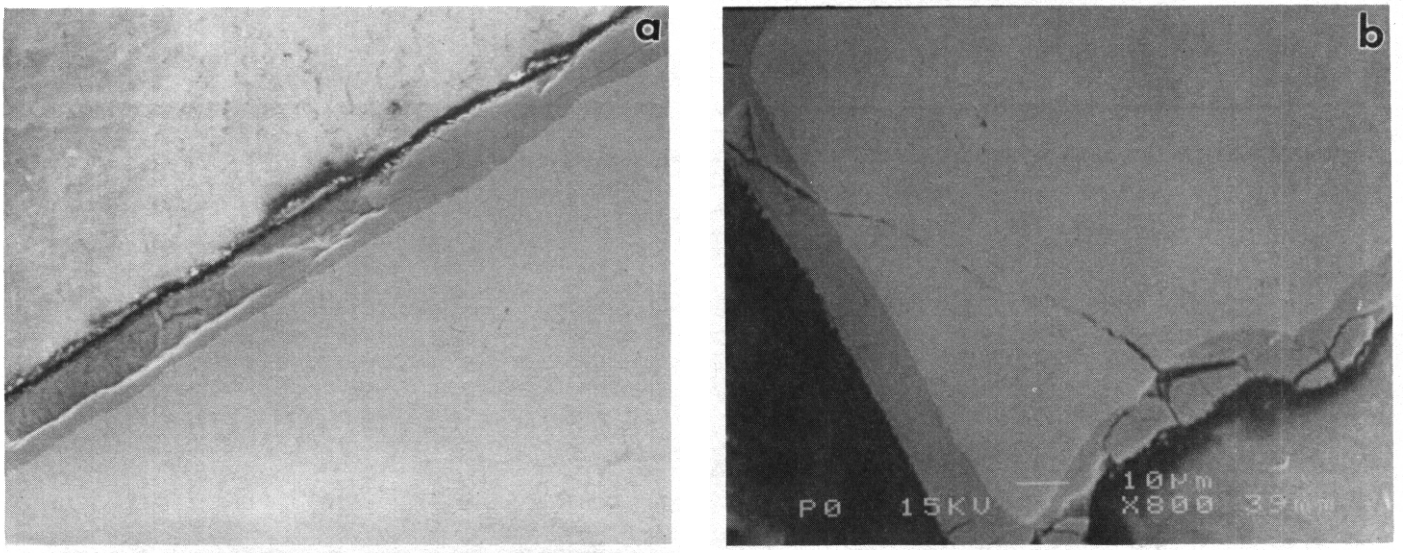

Figure 3. Scanning electron micrographs showing cross sections of a pure *Nb* specimen **after** exposure to HP deoxygenated water for 30 days at 300°C: *(a) uniform* oxide layer and *(b)* cracks originating in **oxide** layer

Nb-2.5Zr

After 30 days, the Nb-2.5Zr alloy exhibited a uniform oxide film ≈6 μm thick (Figs. 4a and 4b). Again, the brittle nature of the oxide layer is evident in Fig. 4b but no cracks were found in the metal. The oxide film thickness increased to ≈10 μm after 60 days (Figs. 5a-5c) and some porosity developed at the outer surface. Small cracks can also be seen adjacent to the metal/oxide interface in Fig. 5c. A double-layer oxide structure can be seen after 90 days in Fig. 6a and 6b, and a crack in the base metal is seen in Fig. 6c. It was not possible to estimate the thickness of the oxide layer because much of the surface oxide appeared to. have been removed during polishing. Extensive oxide penetration along cracks can be seen in Fig. 7a for the 120-day exposure. Two major cracks are shown on the right side of the specimen where the oxide thickness decreases following the progress of the crack. At the bottom left, a small oxide-filled crack is evident, and above, the oxide just begins to penetrate the metal. A higher-magnification view of the oxides within the crack is shown in Fig. 7b. where the porous nature

of the oxide surface can be observed. Figures 7c–7e show cracks that developed after exposure to water. Note that Nb-2.5Zr was assigned fracture and crack indices of 3 (corresponding to fracture after unbending a fold and moderate cracking of the surface layer) by Hull et al.[1] after a 120-day exposure.

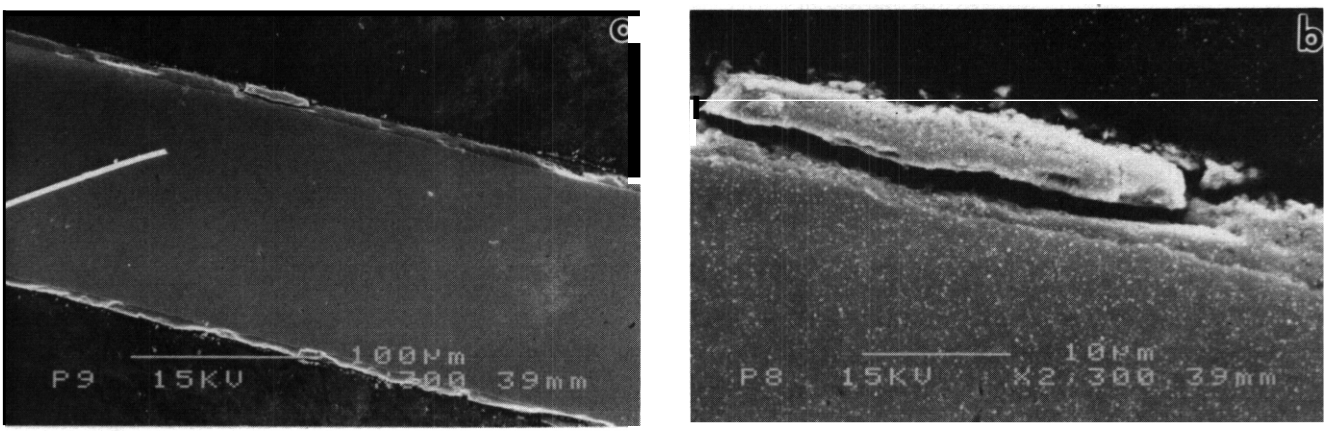

Figure 4. Scanning electron micrograph showing cross-sections of a Nb-2.5Zr specimen after exposure to HP water at 300°C for 30 day: (a) uniform oxide layer (≈6 µm thick) and (b) cracks in oxide layer

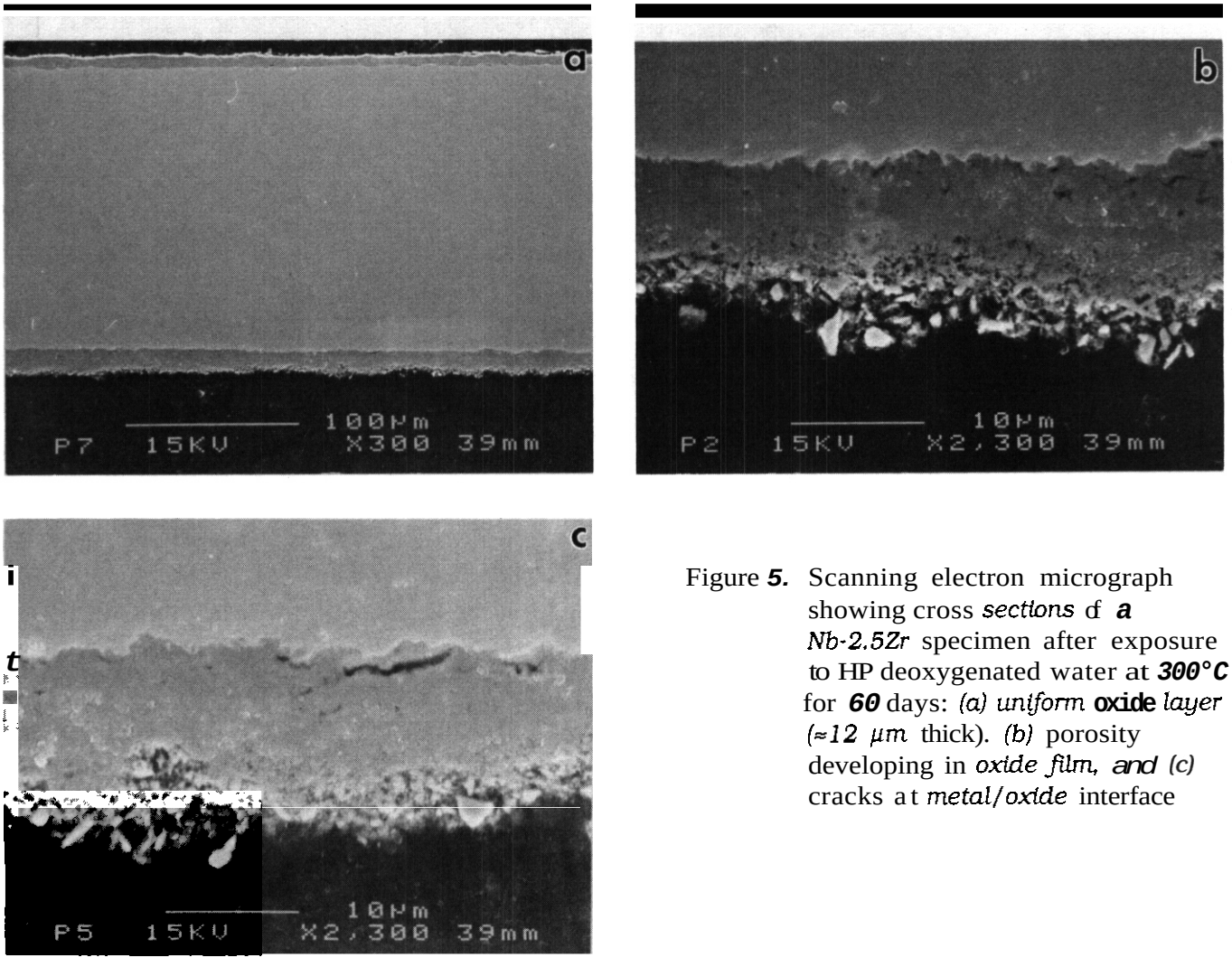

Figure 5. Scanning electron micrograph showing cross sections of a Nb-2.5Zr specimen after exposure to HP deoxygenated water at 300°C for 60 days: (a) uniform oxide layer (≈12 µm thick). (b) porosity developing in oxide film, and (c) cracks at metal/oxide interface

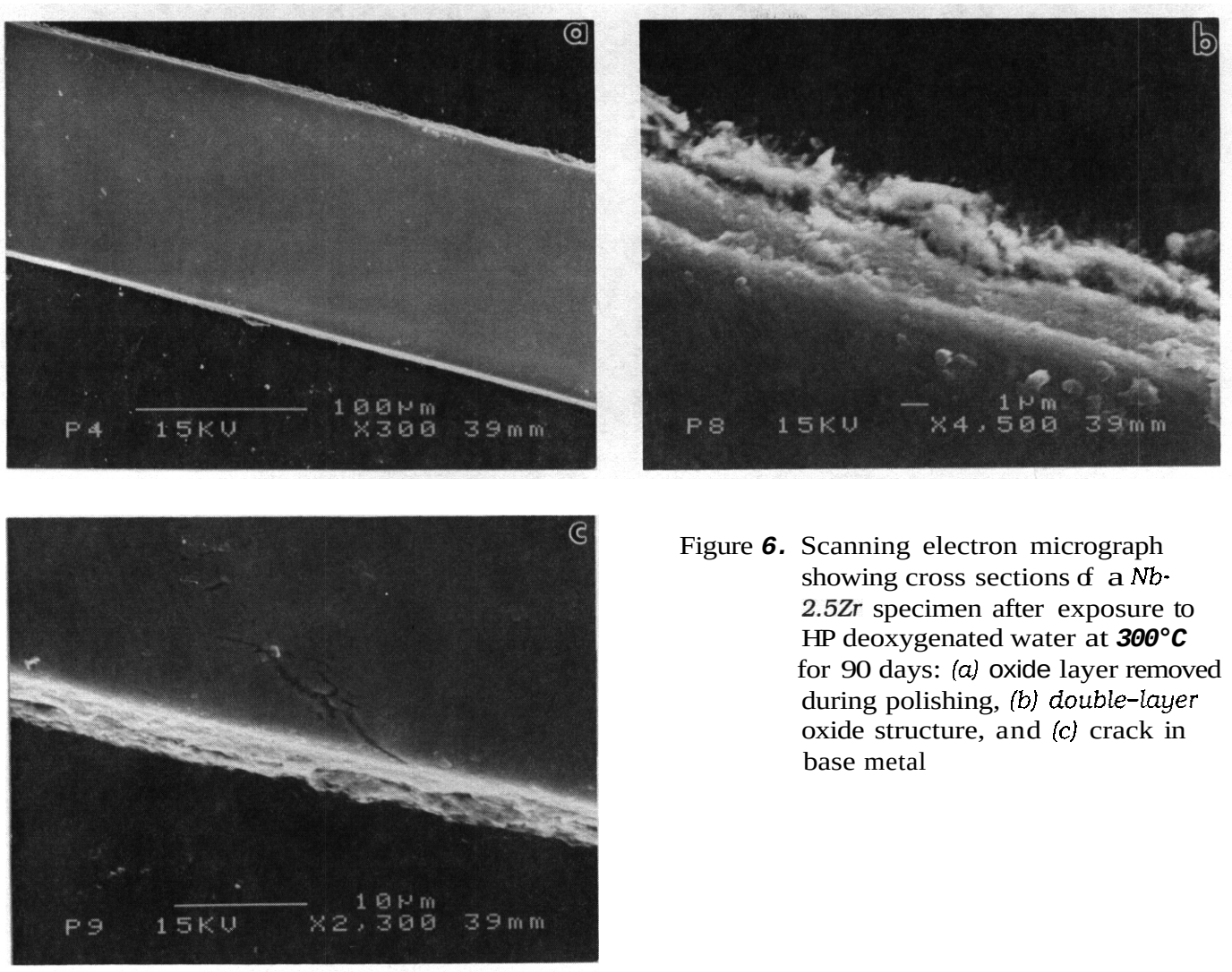

Figure 6. Scanning electron micrograph showing cross sections of a *Nb-2.5Zr* specimen after exposure to HP deoxygenated water at **300°C** for 90 days: *(a)* oxide layer removed during polishing, *(b) double-layer* oxide structure, and *(c)* crack in base metal

Nb-2.5V

The oxide films on the **Nb-V** alloy appeared to be more weakly bonded than those on the Nb–Zr alloy because considerable amounts of oxide were removed during either polishing or ultrasonic cleaning. Oxide film thickness was estimated to be ≈2–4 µm after 30– and 60–day exposures (Figs. **8** and 9), respectively. Extensive cracking was observed in specimens exposed for 90 days (Fig. 10a and 10b) and 120 days (Fig. 11a and 11b), which confirms a fracture index of 5 (fracture during a 90" bend) assigned by Hull et al.[1] Figures 10a and 10c indicate that there is a nonporous layer (≈2 µm thick) adjacent to the metal surface, covered by a 2-3 µm porous layer. An oxidized crack can be seen in Fig. 10d. The sample (exposed for 120 days) became dislodged from its holder during mounting, and hence, an inclined section through the oxide layer is observed in Figs. 11a–11d. Figures 11c and 11d also show that the metal is covered with a ≈2-3 µm nonporous layer and an outer porous region. The large oxidized region shown in Figs. 11c and 11d is probably a section through one of the "rosettes" shown in the SEM micrograph of the Nb-2.5Zr alloy.

Energy–dispersive X-ray analyses of the oxide layers were obtained but it was not possible to determine the oxidation state of the layers (e.g., NbO vs. NbO_2 vs. Nb_2O_5. However. both Fe and Mn were observed in the outer layers of the deposits for the longer exposure times.

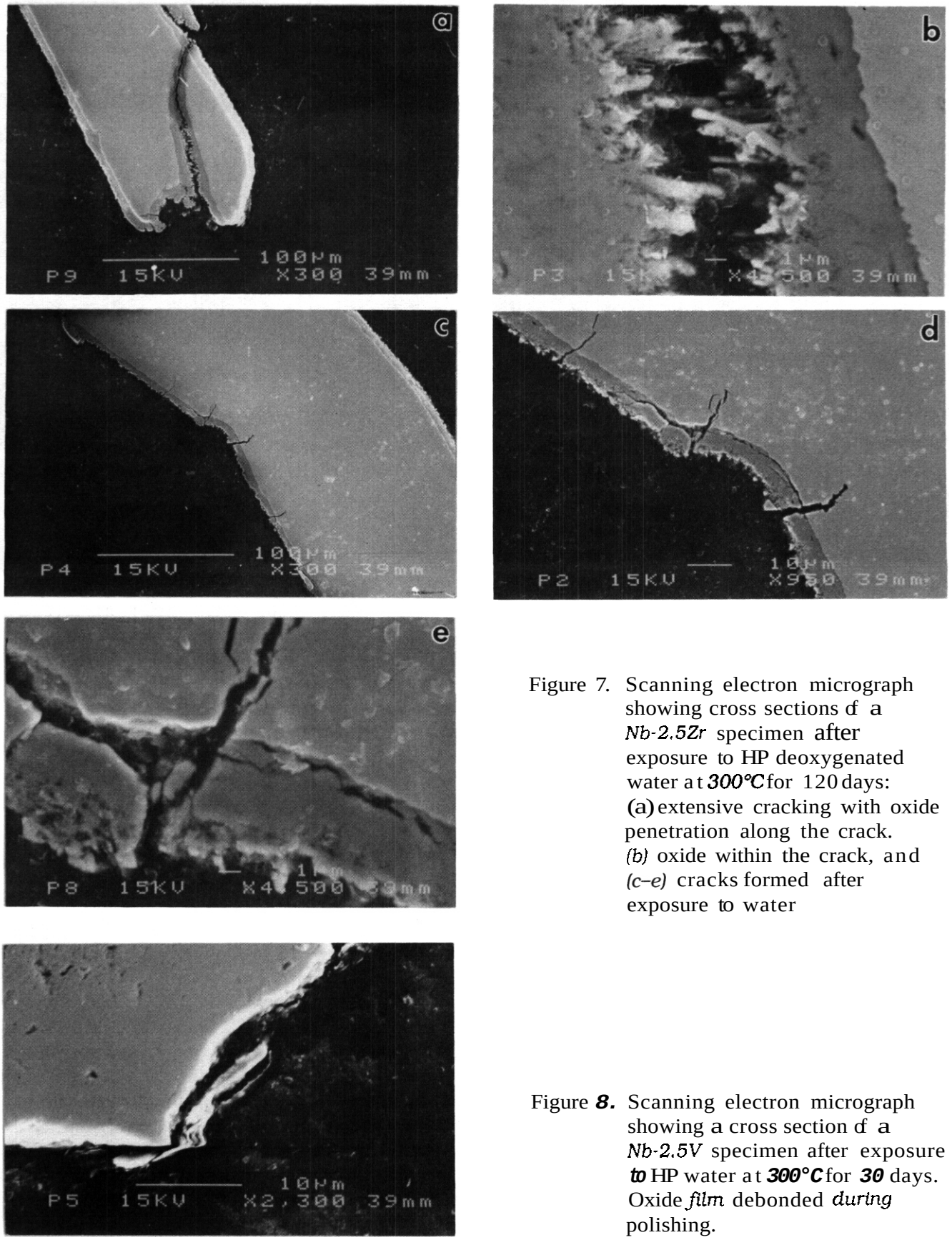

Figure 7. Scanning electron micrograph showing cross sections of a *Nb-2.5Zr* specimen after exposure to HP deoxygenated water at *300°C* for 120 days: (a) extensive cracking with oxide penetration along the crack. *(b)* oxide within the crack, and *(c–e)* cracks formed after exposure to water

Figure *8.* Scanning electron micrograph showing a cross section of a *Nb-2.5V* specimen after exposure *to* HP water at *300°C* for *30* days. Oxide *film* debonded *during* polishing.

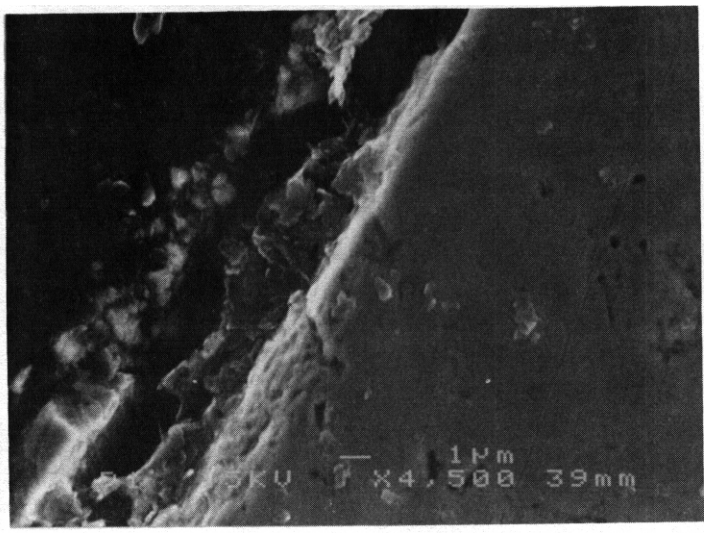

Figure 9. Scanning electron micrograph showing a cross section of a Nb-2.5V specimen after exposure to HP water at 300°C for 60 days

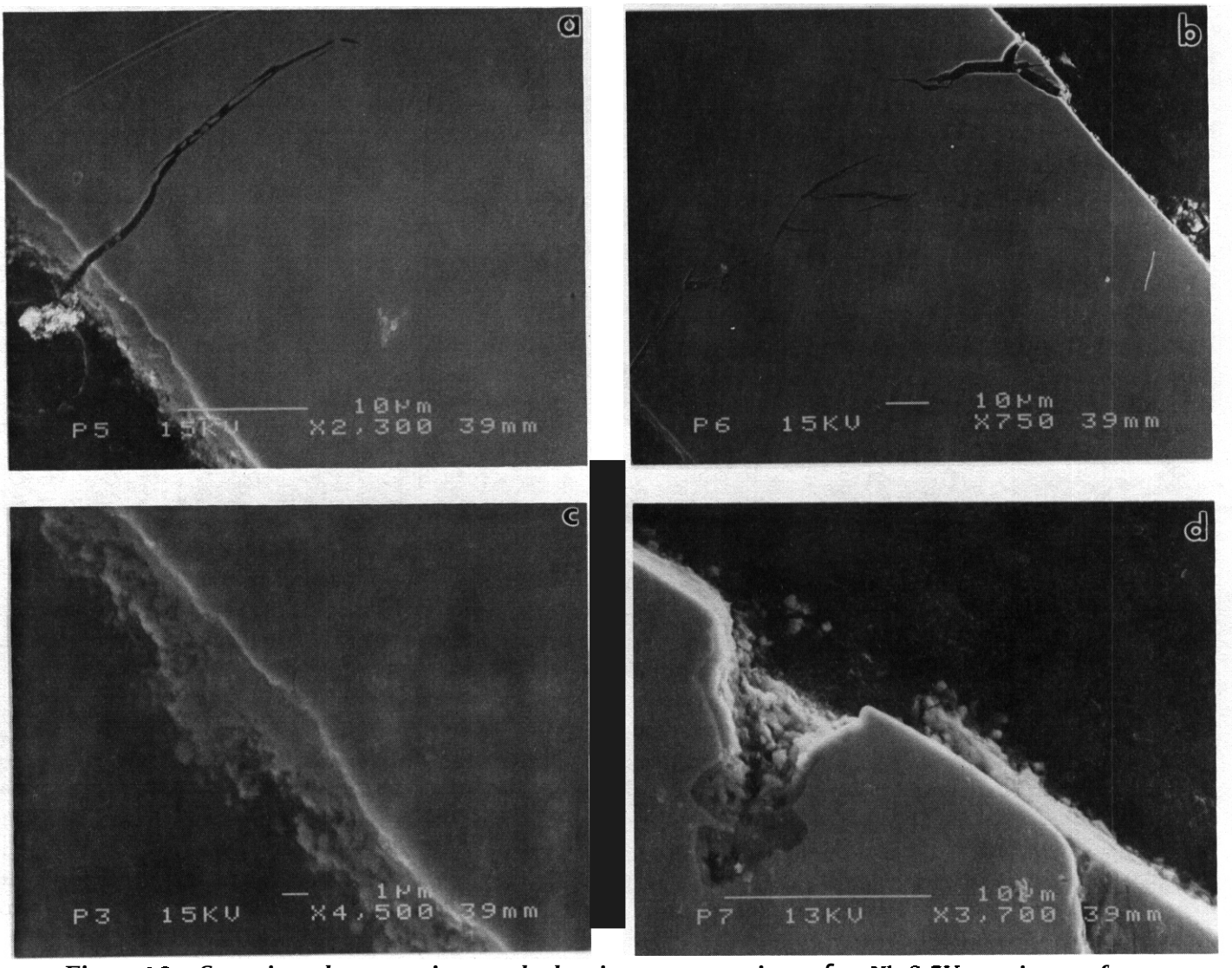

Figure 10. Scanning electron micrograph showing cross sections of a Nb-2.5V specimen after exposure to HP water at 300°C for 90 days: (a and b) extensive postexposure cracking of base metal and (c and d) oxide-filled cracks that formed during exposure

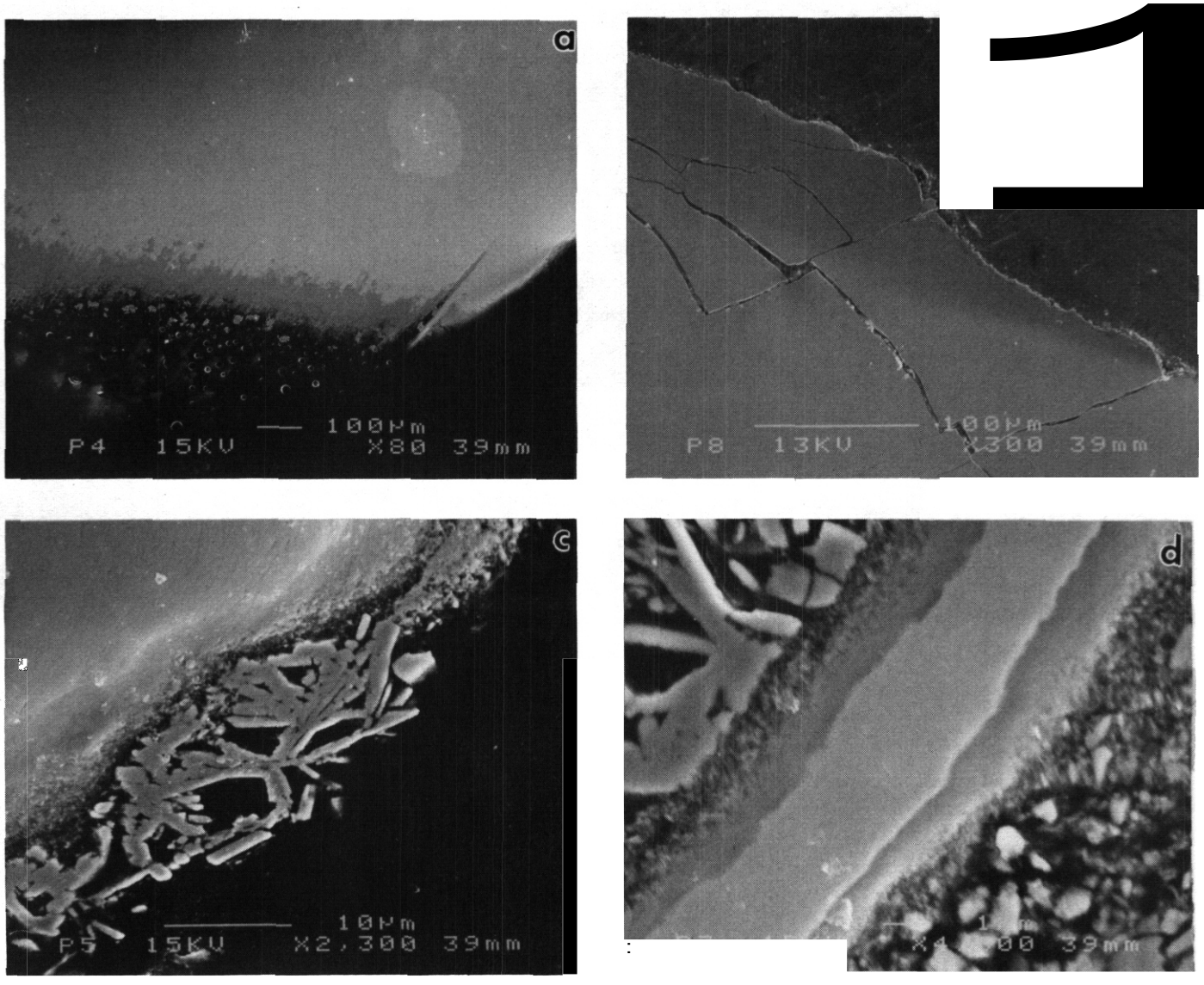

Figure 11. Scanning electron micrographs showing cross sections of a Nb-2.5V specimen after exposure to HP water at 300°C for 120 days. Extensive postexposure cracking of base metal is seen in (b), section through a surface rosette is shown In (c) and (d).

DISCUSSION

Gulbransen and Andrew[5,6] and Hurlen et al.[7] studied the low-temperature oxidation of Nb and showed that initial film formation is governed by a parabolic rate law. followed by a transition to a linear oxidation rate when the protective film breaks down. Blackburn and Gulbransen[8] found that the reaction of Nb with water vapor followed a cubic rate law at 200-223°C and 400-750°C. but a parabolic rate law at 250-350°C. Ivanov and Grigorovich[9] showed that Zr additions (≤40-50 at.%) improve the corrosion resistance of Nb in 300°C water, but that the maximum oxidation resistance at 400°C in air occurred at 10 at.% Zr.

Klopp et al.[10] found that binary additions of Ti, Zr, V. Mo. Cr. and W improved the high-temperature oxidation resistance of Nb. Klopp, Berry, and Maykuth[11] subsequently investigated the hot

water corrosion resistance of commercial–purity (CP) and HP Nb and of binary and ternary alloys in 315 and 360°C HP water (<1 $\mu S \cdot cm^{-1}$) and in 399°C steam at a pressure of 1500 psi. At 360°C, CP Nb exhibited an initial weight gain but lost weight rapidly after 3 to 7 days; HP Nb lost weight only after 56 days. The average weight gain of the HP samples was related to the exposure time, t, through the relationship $W = 41\ t^{0.26}$. The high weight losses observed in CP samples were partially caused by oxide penetration into the metal, and by expansion associated with oxide formation that leads to spalling of large pieces of partially oxidized metal. However, the HP samples exhibited similar spalling in the absence of subsurface oxide penetration. Hydrogen embrittlement at the metal surface was also considered a contributing factor. The oxide phase was identified as Nb_2O_5.

Analyses of both CP and HP Nb revealed that hydrogen levels increased with exposure temperature and corrosion rate. However, at 360°C. additions of V (4–24.2 at.%). Zr (10.5–45.7 at.%), Ti (9.4 at.%) and Mo (7.4 at.%) decreased the hydrogen levels from 590 ppm [observed for the CP alloy after 28 days) to <65 ppm in the binary alloys (for times up to 224 days).

Corrosion resistance of the binary alloys at 680°C was significantly improved by additions of V (<24 at.%). Zr [a minimum corrosion rate at 30 at.%). Ti (<35 at.%). and to a lesser extent. by Mo (<7 at.%). At 399°C. a minimum corrosion rate was observed at 3 at.% Mo. A trace of NbO was observed in the Nb-10.7 at.% V alloy tested for 196 days at 360°C. and $Nb_2O_5 \cdot 6ZrO_2$ was identified in the Nb-45.7 at.% Zr alloy tested for 42 days at 360°C. With the exception of the Nb-Ti-Cr alloys. ternary alloying did not further improve corrosion resistance over that of the best binary alloys. Optimum Nb–Ti-Cr alloy compositions were tentatively proposed as Ti >20 at.% and Cr >5 at.%. Resistance to contamination hardening was evaluated by microhardness measurements, and contamination coefficients were calculated as a function of alloy composition for the binary Zr, Ti. V. Mo, and W alloys.[10] At 360°C. the results indicated that Zr and Ti were most effective in reducing contamination, hut suggest that ≥10 at.% (significantly >2.5 at.% in this study) may be required to produce a significant improvement over the alloys that contain V.

Corrosion mechanisms are influenced by valence, ionic size, and stability of the oxides. As in the work of Klopp. Berry, and Maykuth,[11] where V was found to be more effective than Ti or Zr in improving corrosion resistance at alloying levels of ≈10–15 at.%, the present study also found the Nb-2.5V alloy to have lower oxidation kinetics than Nb-2.5Ti and Nb-2.5Zr. However, the low melting temperature of V_2O_5 makes alloys that contain V less attractive than those with Zr for fusion reactor applications.

Fisch. Douglas. and Dearing[12] found that the corrosion kinetics of Nb-V alloys (<8.9 at.% V) in high–temperature steam fit a cubic rate law over the temperature range 360–482°C [steam was produced from HP deionized water). Alloys that contain <1.2 at.% V formed Nb_2O_5, those with 1.2–3.6 at.% V formed a duplex scale of Nb_2O_5 and NbO_2, and alloys with 8.9 at.% V formed only NbO_2, giving rise to superior corrosion resistance. The protective nature of NbO_2 is thought to he related to its rutile structure. Consequently. alloying elements that promote the rutile structure. (e.g., Ti, Zr. V) should improve the corrosion resistance of Nb alloys. **An** interesting question arises in the present research, i.e., whether the development of an NbO_2 film on the surface of the Nb alloy prior to exposure may provide additional corrosion protection and also act as an initial barrier that decreases H pickup by the alloy during exposure to high–temperature water. It is clear from the above microstructural observations and discussion that alloying elements at the ≈2.5 at.% level are too dilute to provide adequate oxidation resistance and an effective harrier to hydrogen permeation.

FUTURE RESEARCH

In the next phase of the research, the corrosion, H uptake, and toughess properties of alloys with higher alloy concentrations will be evaluated. Of the commercial alloys listed in Table 1, experience has shown that alloys with high W (≈10 wt.%) and Mo (≈5 wt.%) contents are difficult to fabricate and weld. and that a high Ta content reduces the irradiation resistance of the material. Because our results have shown that (a) V additions lower the corrosion rate and (b) Hf and Zr additions lower both the H con-

centrations and the percentage of corrosion–product H that is absorbed by Nb–base alloys (compared to Nt–V alloys], the Cb-753 alloy (5 wt.% V-1.25 wt.% Zr) and either C-129Y (10 wt.% Hf-0.1 wt.% Y) or C-103 (10 wt.% Hf-1 wt.% Ti-0.7 wt.% Zr) are being considered for the next series of corrosion tests. Because the thermal–neutron cross section of Hf is much greater than that of the other proposed alloy additions, Hf may be less desirable. Noncommercial Nb-base alloys that contain ≥10 at.% Zr, V, or Ti (or combinations of these elements) may provide superior resistance to H permeability and corrosion. Small quantities of these alloys will he sought for screening tests.

Table 1. Nominal Compositions of Commercial Nh Alloys (wt.%)

Alloy	Source	W	Mo	Ta	V	Hf	Ti	Zr	Y	Al	C
				1960s Alloys							
Nb–1Zr	Wah Chang							1.00			
SCb–291	Fansteel Inc.			10.0							
C–103	Wah Chang					10.0	1.0	0.70			
C–129Y	Wah Chang	10.0				10.0			0.1		
FS–85	Fansteel Inc.			28.0				1.00			
Cb–753	Haynes				5.0			1.25			
				1950s Alloys							
8–33	Westinghouse				5.0						
B–66	Westinghouse		5.0		5.0			1.0			
C–129	Wah Chang	10.0				10.0					
Cb–22	Haynes				3.0					3.0	
Cb–24	Haynes				3.0		7.0			3.0	
Cb–65	Haynes						7.0	0.8			
Cb–67	Haynes				3.0		7.0	1.0		3.0	
Cb–752	Haynes	10.0						2.5			
D–12	Du Pont						5.0				
D–14	Du Pont							5.0			
D–31	Du Pont		10.0				10.0				0.1
D–36	Du Pont						10.0	5.0			
D–43	Du Pont	10.0						1.0			0.1
FS–82	Fansteel Inc.			33.0				1.0			
NC–155	Westinghouse		5.0					1.0			
NC–181	Westinghouse		5.0		5.0						

REFERENCES

1. A. B. Hull. B. A. Loomis. and L. J. Nowicki. Preliminary Assessment of Aqueous Corrosion of Niobium Alloys for Structural Applications in the ITER Diuertor. Fusion Reactor Materials Semiannual Report for Period ending March 31. 1991. DOE/ER-0313/10, Oak Ridge National Laboratory. pp. 248–255.

2. A. B. Hull and D. L. Smith. Aqueous Corrosion of Niobium in Proc. ITER PFC Meeting, May 9, 1990, MDAC. St. Louis, MO.

3. D. T. Peterson. A. B. Hull, and B. A. Loomis. Hydrogen Embrittlement of Niobium-base Alloys for Application in the ITER Diuertor, Addendum to Fusion Reactor Materials Semiannual Report for Period ending March 31. 1992, DOE/ER-0313/12, Oak Ridge National Laboratory, in press.

4. A. B. Hull. B. A. Loomis. and I. M. Purdy, Assessment of Niobium-Base-Alloy Chemical Compatibility for Structural Applications in the ITER Diuertor, presented at 5th Int. Conf. on Fusion Reactor Materials. November 18-22. 1991, Clearwater. FL.

5. E. A. Gulbransen and K. F. Andrew, Kinetics of the Reactions of Columbium and Tantalum with O_2, N_2, and H_2, Trans. AIME 188, p. 586. 1950.

6. E. A. Gulbransen and K. F. Andrew, Oxidation of Niobium between 375°C and 700°C, J. Electrochem. Soc. 105, p. 4, 1958.

7. T. Hurlen. H. Kjollesdal. J. Markali and N. Norman. Oxidation of Niobium. Tech. (Scientific) Note No. 1, Contract No. AF 61 (052)-90, April 1959.

8. P. E. Blackburn and E. A. Gulbransen, in Deuelopment of Niobium-Base Alloys, ed. R. T. Begley. WADC Tech. Report, 57-344, Part II, December 1958.

9. O. S. Ivanov and V. K. Grigorovich. Structure and Properties of Zirconium Alloys. Proc. of 2nd United Nations Int. Conf. on Peaceful Uses of Atomic Energy. A/CONF, 15/P/2046, August 1958.

10. W. D. Klopp. C. T. Sims. and R. I. Jaffee, Kinetics of Oxidation of Niobium Alloys. Proc. 2nd United Nations Int. Conf. on Peaceful Uses of Atomic Energy, Vol. 6, 1958, p. 293.

11. W. D. Klopp, W. E. Berry, and D. J. Maykuth, The Hot Water Corrosion Resistance of Columbium and Columbium Alloys, in Columbium Metallurgy, eds. D. L. Douglass and F. W. Kunz. Proc. TMS Symp., Bolton Landing, NY. June 9-10. 1960. pp. 685-718.

12. H. A. Fisch. D. L. Douglass, and B. E. Dearing. The High Temperature Steam Corrosion of Columbium-Vanadium Alloys, in Columbium Metallurgy, eds. D. L. Douglass and F. W. Kunz. Proc. TMS Symp.. Bolton Landing, NY, June 9-10, 1960, pp. 597-613.

CREEP OF V-5Cr-5Ti AND V-10Cr-5Ti ALLOYS AT 600°C* - B. A. Loomis, L. J. Nowicki, and D. L. Smith (Argonne National Laboratory).

OBJECTIVE

The objective of this research is to determine the composition of **a** vanadium base alloy with the optimal combination of mechanical properties, corrosion resistance, fabricability, and weldability for use as a structural material in the environment of a magnetic fusion reactor (MFR).

SUMMARY

Creep tests were conducted on V-5Cr-5Ti and V-10Cr-5Ti alloys at 600°C. The results of these tests show that the V-10Cr-5Ti alloy has significantly higher creep strength than the V-5Cr-5Ti alloy.

PROGRESS AND STATUS

Introduction

Vanadium-base alloys are considered candidate structural materials for MFRs because the mechanical, corrosion, and irradiation performance of these alloys is generally attractive.' By performing Cbarpy-impact tests on unirradiated and irradiated V-base alloys that contain Cr and/or Ti and Si alloying additions and are intended for use as a structural material in an MFR, Loomis et al.[1] have shown that these alloys should contain 3-9 wt.% total alloying addition for maximum resistance to H- andlor irradiation-induced embrittlement. However, the long-term creep properties of alloys containing 3-9 wt.% alloying addition have not been investigated for confirmation of the conclusions drawn from the Charpy-impact results. In this report, we present the results **of** initial investigations on the creep **of** V-5Cr-5Ti and V-10Cr-5Ti alloys at 600°C.

Materials and Procedures

Vanadium alloys with nominal compositions of V-5Cr-5Ti and V-10Cr-5Ti were obtained in the form of ≈50% cold-worked sheets approximately 0.9 mm thick. The elemental compositions of these materials are presented in Table 1. Tensile-shaped specimens with 7.62 mm gauge length and 1.52 mm gauge width were machined from the 50% cold-worked sheets. The surfaces **of** the specimens were mechanically ground and polished to a surface finish of ≈0.3 μm. The polished specimens were recrystallized by annealing at 1125°C for 1 h in a vacuum of 2 x 10^{-5} Pa.

Material	ANL No.	Cr (wt.%)	Ti (wt.%)	O (wt.ppm)	N (wt.ppm)	C (wt.ppm)	Si (wt.ppm)
V-5Cr-5Ti	BL 47	4.1	4.3	350	220	200	870
V-10Cr-5Ti	BL 43	9.2	4.9	230	31	100	340

* Analysis of the materials was performed by the Analytical Department of the Teledyne Wah Chang Albany Company.

The creep tests were conducted in a metal-quartz glass, ion-pumped system that could be evacuated to 7 x 10^{-6} Pa pressure. The creep specimen was heated by an infrared furnace, and the temperature of the specimen was controlled to ±1°C by use of a chromel-alumel thermocouple attached to the midpoint of the specimen gauge length. A calibrated load was applied to the specimen through a bellows seal. Elongation of a specimen during the test was determined with a linear variable differential transformer (LVDT) with digitized output.

The effect of a change in the concentration of interstitial impurities (i.e., O, N, and C) on the creep of a specimen was investigated by conducting creep tests with and without a 0.04-pm-thick Ti or Ta foil wrap on the specimens and by determining the microhardness of the specimens before and after a test. The microhardness of a specimen was determined with a Leitz Durimet Hardness Tester equipped with a Vickers indenter. The Vickers hardness number (VHN) was obtained from the indentation made on the specimen by applying a 50-g load to the indenter for 20 s. The VHNs for the recrystallized alloys are presented in Ref. 2.

*Work supported by the Office of Fusion Energy, U.S. Department of Energy, under Contract W-31-109-Eng-38

Exuerimental Results

The salient data obtained from the creep tests on the V-5Cr-5Ti and V-10Cr-5Ti alloys at 600°C are presented in Table 2, and the elongation versus time-to-rupture of these specimens is shown in Fig. **1.** These results show that the creep strength of the V-10Cr-5Ti alloy is significantly higher (≈100 MPa) than that of the V-5Cr-5Ti alloy, a finding that might be expected from the higher (≈75 MPa) ultimate tensile strength (UTS) determined for these alloys in a tensile test. Also, these results show the beneficial effect of a Ti or Ta wrap on the specimens in reducing the increase of VHN (i.e., A V '' in Table 2) and in the probable reduction of the increase of **O,** N, and C concentration during long-term creep tests. However, the post-test ΔVHNs (Table **2)** are not consistent with the ΔVHNs obtained upon annealing alloy specimens with and without a Ta wrap at 600°C for 100 h in a vacuum of $I \times 10^{-6}$ Pa; under these conditions, annealing showed no significant change in VHN for Ta-wrapped specimens. Moreover, **all** of the creep tests were terminated by reduction of the specimen cross-section to a knife edge, i.e., ductile failure. Changes in the concentration of **O,** N, and C in the specimens after the creep tests are currently being determined, and will be presented in **a** future report.

Table 2. Creep-test data for V-5Cr-5Ti and V-10Cr-5Ti alloys at 600°C.*

Material	ANL I.D.	Stress (MPa)	Time-to-Rupture (h)	Wrap	ΔVHN
V-5Cr-5Ti	BL 47E	371	541	Ta	75
V-5Cr-5Ti	BL 47C	401	1	Ta	15
V-10Cr-5Ti	BL 43B	507	162	Ti	82
V-10Cr-5Ti	BL 43A	512	243	None	211

*UTS for V-5Cr-5Ti is **434** MPa; for V-10Cr-5Ti, it is 512 MPa.[3]

The data on stress-rupture time obtained at 600°C in this investigation, together with the UTS for the alloys at 600°C,[3] were used to construct the tentative creep stress-rupture time curves shown in Fig. **2** for the V-5Cr-5Ti and V-10Cr-5Ti alloys. The creep-stress vs. rupture-time curves for unalloyed V and other V-base alloys in Fig. 2 were obtained from a recent review of these data by Loomis, et al.[4] It was not unexpected that the creep-stress vs. rupture-time curves for the alloys at 600°C would not decrease as significantly as the curves for the alloys at 650°C for $>10^3$ h, because the tensile properties for these alloys decrease significantly at temperatures >600°C.[3]

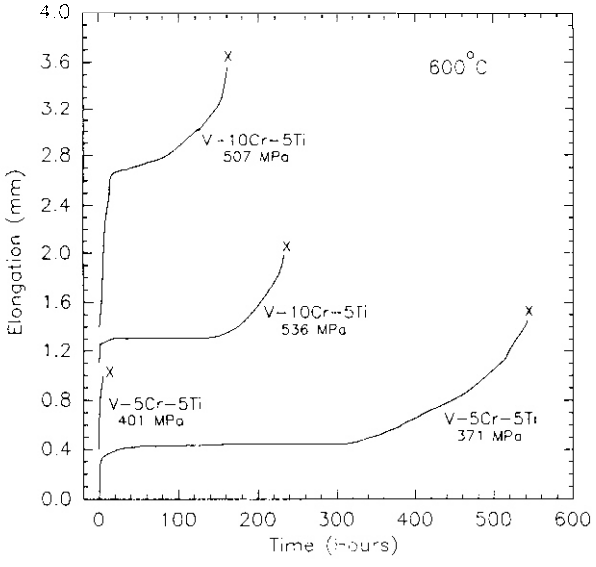

Fig. 1. Elongation of V-5Cr-5Ti and V-10Cr-5Ti alloys during creep tests at 600°C.

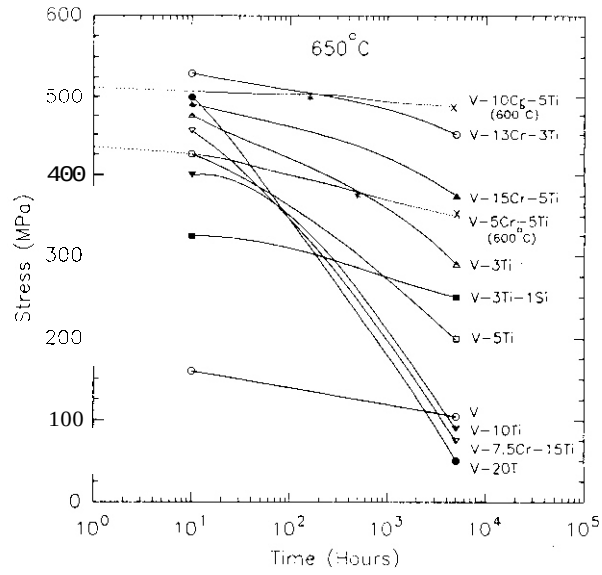

Fig. 2. Creep stress-rupture time of V and V alloys (V-5Cr-5Ti and V-10Cr-5Ti alloys at 600°C).

DISCUSSION OF RESULTS

The creep-test results on V-5Cr-5Ti and V-10Cr-5Ti alloys presented in this report should be regarded as preliminary because we are uncertain about the significance of the increase in VHN andlor the impact of a possible increase in O, N, and C concentration in the specimens during the tests. Nevertheless, these results show that the V-10Cr-5Ti alloy has significantly higher creep strength than the V-5Cr-5Ti alloy. If the high creep strength of the V-10Cr-5Ti alloy is considered to be of paramount importance for a structural material in an MFR, even though the ductile-brittle transition temperature of the V-5Cr-5Ti is significantly lower (≈200°C),[1,5] the creep properties of a V-7Cr-5Ti alloy may be an acceptable compromise.

CONCLUSIONS

1. The creep strength of the V-10Cr-5Ti alloy at 600°C is significantly higher (≈100 MPa) than that of the V-5Cr-5Ti alloy.
2. The use of Ta or Ti wrap on specimens significantly reduces the increase in VHN during long-term creep testing.

FUTURE WORK

1. Creep tests will be conducted on V-3Ti, V-3Ti-1Si, V-7Cr-5Ti, and V-5Cr-3Ti alloys at 600°C.
2. The change in VHN of the alloy specimens after creep tests will be correlated with changes in concentration of O, N, and C in the specimens.
3. An effort will be made to decrease the AVHN incurred during long-term creep tests by use of a Ti sublimation pump andlor an ion pump with greater pumping speed.

REFERENCES

1. B. A. Loomis, A. B. Hull, and D. L. Smith, "Evaluation of Low-Activation Vanadium Alloys for Use as Structural Material in Fusion Reactors," J. Nucl. Mater., 179-181(1991), 148-154.

2. B. A. Loomis, J. Gazda, L. J. Nowicki, and D. L. Smith, "Relationship of Hardness and Tensile Strength of Vanadium and Vanadium-base Alloys," in Fusion Reactor Materials, Semiannual Progress Report for Period Ending September 30, 1992, Report No. DOE/ER-0313/13 (in press).

3. B. A. Loomis, L. J. Nowicki, and D. L. Smith, "Tensile Properties of Vanadium and Vanadium-Base Alloys," in Fusion Reactor Materials, Semiannual Progress Report for Period Ending March 31, 1991, DOE/ER-0313/10, U.S. Department of Energy, Office of Fusion Energy, July 1991, pp. 145-155.

4. B. A. Loomis and D. L. Smith, "Vanadium Alloys for Structural Applications in Fusion Systems: A Review of Mechanical and Physical Properties," in Proceedings of the Fifth International Conference on Fusion Reactor Materials, November 18-22, 1991, Clearwater, Florida (in press).

5. B. A. Loomis, L. J. Nowicki, and D. L. Smith, "The Effect of Hydrogen, Chromium, Titanium, and Silicon on the Ductile-Brittle Transition Temperature of Vanadium and Vanadium-base Alloys," in Fusion Reactor Materials, Semiannual Progress Report for Period Ending September 30, 1991, Report No. DOE/ER-0313/11, US. Department of Energy, Office of Fusion Energy, April 1992, pp. 227-232.

RELATIONSHIP OF HARDNESS AND TENSILE STRENGTH OF VANADIUM AND VANADIUM-BASE ALLOYS*

- B. A. Loomis, J. Gazda, L. J. Nowicki, and D. L. Smith (Argonne National Laboratory).

OBJECTIVE

The objective of this research is to determine the composition of a vanadium-base alloy with the optimal combination of mechanical properties, corrosion resistance, fabricability, and weldability for use as a structural material in the environment of a magnetic fusion reactor (MFR).

SUMMARY

The Vickers hardness numbers (VHNs) of annealed and reclystallized vanadium and V-(0-15)Cr-(0-5)Ti-(0-1)Si alloys were determined at 25°C. The relationship between the VHN and the tensile strength of these materials previously reported by Loomis et al.[1] are presented in this report. These results show that the VHN, yield strength (YS), and ultimate tensile strength (UTS) of V-(0-15)Cr-5Ti alloys at 25°C have a similar dependence on Cr concentration and that the VHN, YS, and UTS of V-(0-20)Ti alloys at 25°C have a similar dependence on Ti concentration. On the basis of these results and the small size of the test specimen, it is recommended that the Vickers hardness test he utilized in the vanadium alloy development program to determine the effects of thermal-mechanical treatment, impurities (i.e., O, N, C, H, and Si), and irradiation on tensile properties of vanadium-base alloys.

PROGRESS AND STATUS

Introduction

Vanadium-base alloys are considered candidate structural material for a MFR.[2] Loomis et al. have shown from Charpy-impact tests on unirradiated and irradiated vanadium alloys that a vanadium-base alloy containing Cr andlor Ti and Si alloying additions and intended for use as a structural material in a MFR should contain 3-9 wt.% total alloying addition for maximum resistance to hydrogen- andlor irradiation-induced embrittlement.[3] However, the effects of thermal-mechanical treatment and impurities (i.e., O, N, C, H, and Si) on the mechanical properties of these alloys have not been sufficiently investigated to select an alloy composition with the optimal mechanical properties. Because of the small size (e.g., 3 mm diameter) of a hardness-test specimen, the hardness test could be useful in the initial evaluations of the effects of thermal-mechanical treatment and impurities on mechanical proprties of candidate alloys. In addition, the hardness test could be useful for evaluations of the effects of irradiation on mechanical properties of candidate alloys, since space in irradiation capsules is extremely limited. In this report, we present the relationship between the VHN and the YS and UTS for vanadium and several V-Cr-Ti-Si alloys at 25°C, and we also present the dependence of the VHN, YS, and UTS fur these materials on concentration of alloying addition.

Materials and Procedures

Unalloyed vanadium and vanadium-base alloys with the nominal compositions listed in Table 1 were obtained in sheet form with a 50% thickness reduction, i.e., cold work, resulting in a nominal thickness of 0.25 mm. Specimens (3 mm diameter) of these materials were mechanically polished (3 μm finish) and then annealed at 1050-1125°C for 1 h in a vacuum of 2×10^{-5} Pa. The annealing conditions for the cold-worked materials resulted in average recrystallized grain diameters in the range of 0.02-0.04 mm.

Microhardness measurements were conducted on the annealed and recrystallized specimens at 25°C using a Leitz Durimet Hardness Tester equipped with a Vickers indenter. The VKN was obtained from the indentation resulting from application of a 50 g load to the indenter for 20 s on the specimen.

Experimental Results

The VHN, YS, and UTS for unalloyed vanadium and V-(0-15)Cr-(0-5)Ti-(0-1)Si alloys are listed in Table 2. The YS and UTS data for these materials at 25°C were previously reported by Loomis et al.[1]

The dependence of the VHN, YS, and UTS for V-(0-20)Ti alloys on Ti concentration is shown in Fig. 1. These results show that the VHN, YS, and UTS of V-(0-20)Ti alloys have a similar linear dependence on Ti concentration. It can he noted in Table 2 and Fig. 1 that V-3Ti-(0.3-1)Si alloys have significantly higher VHN, YS, and UTS than the V-3Ti alloy.

*Work supported by the Office of Fusion Energy, U.S. Department of Energy, under Contract W-31-109-Eng-38

Table 1. Compositions of Vanadium and Vanadium-base Alloys.[*,**]

Material	ANL No.	Cr	Ti	Other	O	N	C	Si
V	BL 19	-			1101	161	360	-
V	BL 51	-	-	-	570	49	56	-
V-1Ti	BL 50	<100	1.0%	-	230	130	235	1050
V-3Ti	BL 62	<100	3.1%	0.07% Al	310	86	109	660
V-3Ti-0.3Si	BL 27	<50	3.1%	-	210	310	310	0.25%
V-3Ti-0.5Si	BL 42	<50	3.1%	-	580	190	140	0.54%
V-3Ti-1Si	BL 45	-	2.5%	-	345	125	90	0.99%
V-5Ti	BL 46	<100	4.6%	-	270	52	100	150
V-5Ti	BL 11	<100	4.9%	0.78% Fe	1820	530	470	220
V-10Ti	BL 12	<100	9.8%	0.63% Fe	1670	450	390	245
V-20Ti	BL 15	150	17.7%	-	830	160	380	480
V-20Ti	BL 16	-	20.4%	-	580	243	305	-
V-5Cr-5Ti	BL 47	4.1%	4.3%	-	350	220	200	870
V-7Cr-5Ti	BL 49	7.9%	5.7%	-	400	150	127	360
V-10Cr-5Ti	BL 43	9.2%	4.9%	-	230	31	100	340
V-12Cr-5Ti	BL 40	10.9%	5.0%	-	470	80	90	270
V-15Cr	BL 5	14.1	<50	0.27% Al	330	69	200	<50
V-15Cr-0.3Ti	BL 25	14.4	0.3%	0.33% Al	390	64	120	<50
V-15Cr-1Ti	BL 26	14.1	1.0%	0.31% Al	560	86	140	<50
V-15Cr-5Ti	BL 21	13.7%	4.8%	-	340	510	180	1150
V-15Cr-5Ti	BL 22	13.4%	5.1%	-	300	52	150	56
V-15Cr-5Ti	BL 23	12.9%	5.9%	-	400	490	280	1230
V-15Cr-5Ti	BL 24	13.5%	5.2%	-	1190	360	500	390
V-15Cr-5Ti	BL 41	14.5%	5.0%	-	330	96	120	400

*All concentrations in wt. ppm or wt. percent (%)
**Hydrogen concentration <30 appm.

The dependence of the VHN, YS, and UTS for V-(0-15)Cr-5Ti alloys on Cr concentration is shown in Fig. 2. These results show that VHN, YS, and UTS have a similar dependence on Cr concentration. However, in contrast to V-(0-20)Ti alloys, the dependence of the VHN, YS, and UTS for V-(0-15)Cr-5Ti alloys on Cr concentration is linear for Cr concentrations of < ≈10%.

The dependence of the VHN for V-15Cr-(0-5)Ti alloys on Ti concentration is shown in Fig. 3. The limited data on the YS and UTS for these materials suggest that the VHN, YS, and UTS have a similar linear dependence on Ti concentration.

DISCUSSION OF RESULTS

The experimental results show that the VHN, YS, and UTS of unalloyed vanadium and V-(0-15)Cr-(0-5)Ti-(0-1)Si alloys at 25°C have a similar dependence on the concentration of alloying addition. Since it can be expected that the mechanical properties of these materials will be significantly affected by thermal-mechanical treatment and concentration of

Material	ANL No.	VHN	YS (MPa)	UTS (MPa)
V				
V				
V-1Ti	BL 50	125	260	290
V-3Ti	BL 62	140	295	375
V-3Ti-0.3Si	BL 27	170	393	450
V-3Ti-0.5Si	BL 42	150	473	545
V-3Ti-1Si	BL 45	168	421	480
V-5Ti	BL 46	147	336	412
V-5Ti	BL 11	155	-	-
V-10Ti	BL 12	175	435	532
V-20Ti	BL 15	274	599	655
V-20Ti	BL 16	269	-	-
V-5Cr-5Ti	BL 47	171	387	454
V-7Cr-5Ti	BL 49	177	425	521
V-10Cr-5Ti	BL 43	192	440	541
V-12Cr-5Ti	BL 40	201	4Y1	573
V-15Cr	BL 5	177		
V-15Cr-0.3Ti	BL 25	175		
V-15Cr-1Ti	BL 26	190		
V-15Cr-5Ti	BL 21	225		
V-15Cr-5Ti	BL 22	232		
V-15Cr-5Ti	BL 23	234	533	555
V-15Cr-5Ti	BL 24	216	545	634
V-15Cr-5Ti	BL 41	221	570	674

interstitial (i.e., H, O, N, and C) impurities, the hardness test would be extremely useful for qualitative evaluation of these effects on mechanical properties because of the small size of specimen and non-destructive nature of the test. Moreover, the hardness test could be useful for qualitative evaluation of irradiation effects on mechanical properties of vanadium alloys. The vanadium alloy development program has a large inventory (500-600 specimens) of transmission electron microscopy (TEM) discs that have been irradiated at 420, 520, and 600°C to 20-114 atom displacements per atom (dpa). Hardness tests on these TEM discs would contribute significantly to the data base on the effects of irradiation temperature and damage (dpa) on mechanical properties of vanadium-base alloys.

CONCLUSIONS

1. The VHN, YS, and UTS of unalloyed vanadium, V-(0-20)Ti, V-(0-15)Cr-5Ti, and V-15Cr-(0-5)Ti alloys at 25°C have a similar dependence on concentration of alloying addition.

2. The hardness test can be useful for evaluation of effects of thermal-mechanical treatment, impurities, and irradiation on mechanical properties of vanadium-base alloys because of the small size of test specimen and the non-destructive nature of the test.

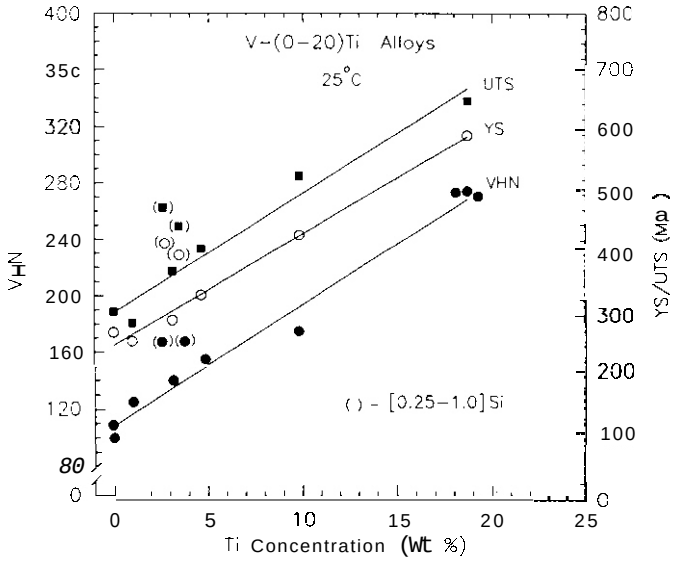

Fig. 1. Dependence of VHN, **YS,** and UTS for unalloyed vanadium and V-(0-20)Ti alloys at 25°C on Ti concentration.

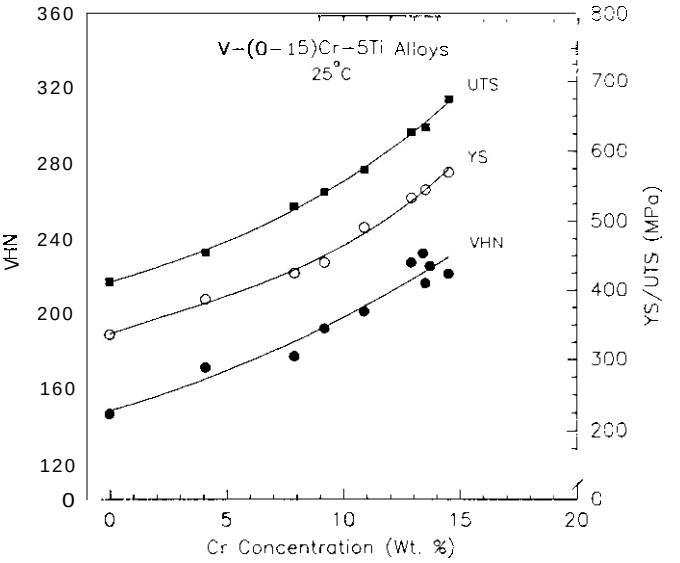

Fig. 2. Dependence of V▼, ▼ **YS,** and UTS for V-(0-15)Cr-5Ti alloys at 25°C on Cr concentration.

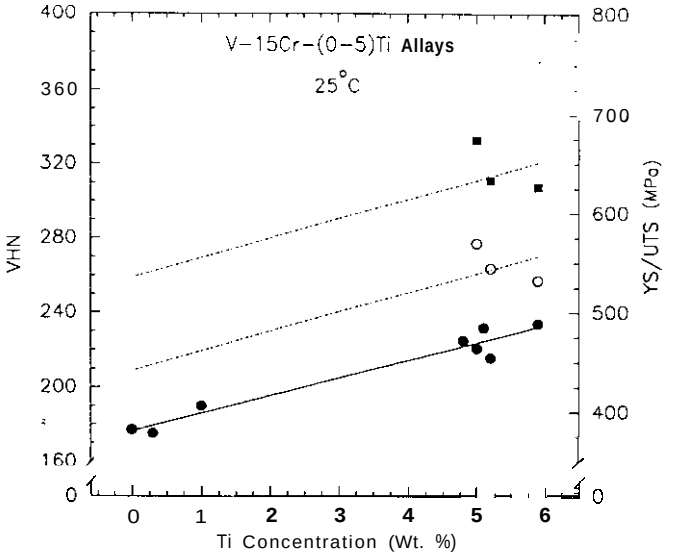

Fig. **3.** Dependence of VHN, **YS,** and UTS for V-15Cr-(0-5)Ti alloys at 25°C on Ti concentration.

FUTURE WORK

1. Determine the effect of **O,** N, ***C,*** and Si concentration on the VHN of vanadium-base alloys that are candidates for structural material in MFR.

2. Determine the effect of thermal-mechanical treatment on the VHN of vanadium-base alloys that are candidates for structural material in MFR.

3. Determine the VHN of vanadium-base alloys (TEM discs) irradiated at 420, 520, and 600°C to 20-114 dpa during Cycles **8-12** of the FFTF-MOTA.

REFERENCES

1. B. **A.** Loomis, L. J. Nowicki, and **D.** L. Smith, "Tensile Properties of Vanadium and Vanadium-Base Alloys," in: Fusion Reactor Materials, Semiannual Progress Report for Period Ending March 31, 1991, DOE/ER-0313/10, U.S. Department of Energy, Office of Fusion Energy, July 1991, pp.145-155.

2. D. L. Smith, B. A. Loomis, and **D.** R. Diercks, "Vanadium-Base **Alloys** for Fusion Reactor Applications- **A** Review," **J.** Nucl. Mater., 135 (1985), pp. 125-137.

3. B. **A.** Loomis and D. L. Smith, "Response of Unirradiated and Neutron-Irradiated Vanadium **Alloys** to Charpy-Impact Loading," J. Nucl. Mater., 179-181, Part A (1991), pp. 783-786.

CORRELATION OF MICROSTRUCTURE AND MECHANICAL PROPERTIES OF VANADIUM-BASE ALLOYS*

J. Gazda**†, S. Danyluk**, B. A. Loomis†, and D. L. Smith*

OBJECTIVE

The objective of this research is to determine relationships of mechanical properties to microstructure in vanadium and vanadium-titanium alloys.

SUMMARY

The mechanical properties and microstructure of V, V-3Ti-1Si, and V-5Ti alloys were investigated by microhardness testing, optical microscopy, and transmission electron microscopy (TEM). The microhardness data were related to tensile test data reported by Loomis et al. [1]. The microhardness and tensile strength of these materials were related to the number density of precipitates. The most common precipitates were identified as: V_6O_{13} and VS_4 for vanadium; Ti(C,N,O) and various forms of Ti-S for V-3Ti-1Si; Ti(C,N,O) and TiN for V-5Ti. The crystallographic lattice parameters for these alloys were determined by X-ray diffraction.

PROGRESS AND STATUS

Introduction

Vanadium-base alloys are being considered as possible structural material for a fusion reactor [2]. Some of their advantages are high strength, corrosion resistance, and irradiation performance. To optimize the physical and mechanical properties of vanadium-base alloys, it is necessary to understand the relationships between microstructure and mechanical properties.

The microstructures of V-15Cr-5Ti, V-3Ti-1Si, and V-20Ti alloys were investigated by T. Schober and D.N. Braski [3]. They found the most common precipitate to be $TiN_{1-x-y}C_xO_y$ with fcc NaCl-type structure. H.M. Chung et al. [4] have investigated the microstructure of irradiated vanadium-base alloys; they also found that Ti(N,C,O) precipitates were the most common thermally induced precipitates and also identified a set of radiation-induced precipitates.

The mechanical properties of vanadium and vanadium-base alloys were extensively investigated by Loomis et al. [1]. They determined an increase of yield and ultimate tensile strength of V on addition of 3-5 % wt. Ti. In the same range of titanium concentration, they reported an abrupt change in ductile-brittle transition temperature (DBTT) [5]. In this report, we present the results of microstructure investigations and relate the microstructure to the microhardness measurements and tensile properties of V, V-3Ti-1Si, and V-5Ti alloys.

Materials and Procedures

Specimens of unalloyed vanadium, V-3Ti-1Si, and V-5Ti were obtained from 0.25-mm-thick sheet fabricated by cold-work reduction to 50 % of original thickness. The compositions of these materials are listed in Table 1.

The TEM specimens were fabricated by punching 3-mm-diameter discs from the sheet. The discs were mechanically polished to 0.5 μm surface finish and then annealed in a ultrahigh-vacuum furnace for 1 h at 2×10^{-5} Pa. The annealing temperature was 1180°C for V and 1130°C for V-3Ti-1Si and V-5Ti.

For optical microscopy investigation of grain size, discs were electropolished for 30 to 60 s with a solution of 20 % vol. sulfuric acid in methyl alcohol with an open-circuit applied potential of 6 V. Swabbing the surface of the discs with a solution containing 40 mL HNO_3, 40 mL HF, and 120 mL lactic acid exposed the grain boundaries. These solutions were also used for preparation of carbon-extraction replicas.

Foils were prepared for TEM by electropolishing discs (using South Bay Technology single-jet electropolisher Model 550B) in a solution of 15% sulfuric acid, *12%* methanol, and 13% butyl cellosolve maintained at -35°C. TEM observations were conducted with a JEOL 100CX-II scanning-transmission electron microscope operating at 100 kV. Vanadium reflections were used as an internal standard in each selected-area- diffraction (SAD) pattern to calculate the precipitate lattice spacings.

---

* Work supported by the Office of Fusion Energy, U.S. Department of Energy, under Contract W-31-109-Eng-38

** University of Illinois at Chicago, CEMM Department, PO Box 4348. Chicago IL, 60680.

† Argonne National Laboratory.

Energy-dispersive X-ray spectroscopy (EDXS) was used as an aid in identifying precipitates. However, the relative concentrations of detected elements were not obtained because the computed k-factors were found to be unreliable. The EDXS attachment was unable to detect C, N, or O.

The microhardness measurements were conducted on the annealed specimens with a Leitz Durimet hardness tester fitted with a Vickers indenter. Stainless steel standards were used to ensure accuracy of the hardness measurement.

Table 1. Composition of V and V-base alloys

ID	Material	Ti	Si	N (ppm)	O (ppm)	C (ppm)
BL-51	V	130 ppm	370 ppm	49	570	56
BL27	V-3Ti-1Si	3.1 wt.%	0.25 wt.%	310	210	310
BL-46	V-5Ti	4.6 wt.%	150 ppm	52	270	100

Experimental Results

A summary of the mechanical properties and microstructure characteristics is presented in Table 2.

1. Vanadium (BL-51)

The grain size obtained by annealing at 1180°C was determined to be a115 μm. This was the largest grain size in the three investigated alloys. The Joint Committee on Powder Diffraction Standards (JCPDS) reports that the standard lattice parameter for vanadium is 0.30274 nm. SAD patterns obtained in this study indicated the same lattice cell size, within experimental error.

Optical microscopy was utilized for evaluation of the precipitate number density. The average precipitate number density in unalloyed vanadium was determined to be 0.4885 precipitates per μm^2. TEM observations at 10,000X and higher magnifications confirmed these observations.

Three types of precipitates were identified from the EDXS and TEM-SAD data. The most common was rectangular V_6O_{13} (PDF No. 27-013) with 100-900 nm length. The second most common type of precipitate was rectangular VS_4 (PDF No. 14-179) with $\approx$500 nm length. Oval-shaped particles of γ-Ti_3O_5 (PDF No. 40-806) with 200-300 nm diameter were also observed in the microstructure. None of these precipitates was coherent with the matrix. The precipitates are shown in Figure 1.

Microhardness measurements on unalloyed V gave an average Vickers hardness number (VHN) of 101 kg/mm^2. This measurement was performed on the alloy with large grain size, but specimens with grain size of $\approx$25 μm had a similar value. Loomis et al. [1] reported the yield strength (YS) and ultimate tensile strength (UTS) to be 259 and 309 MPa, respectively.

Table 2. Microstructure and mechanical property data for investigated alloys

	vanadium (BL-51)	V-3Ti-1Si (BL-27)	V-5Ti (BL-46)
Grain Size (pm)	114.9	24.8	27.9
Lattice Parameter (nm)	0.30274	0.30375	0.30390
Precipitate No. density $(\mu m^2)^{-1}$	0.48	1.79	0.81
Microhardness (kg/mm^2)	101	170	142
Yield Strength (MPa)	259	421	336
Ultimate Tensile Strength (MPa)	309	480	412

2. V-3Ti-1Si (BL-27)

The average grain size of the V-3Ti-1Si alloy was 25 μm. From precise lattice parameter measurements made with X-ray diffraction, the lattice parameter of the matrix in the sheet was determined to be 0.30375 nm. This value was used as a standard to determine camera length in the SAD patterns. During the X-ray measurements, Al was used as an internal standard.

From low-magnification optical micrographs, precipitate number density was found to be the highest of the three materials at 1.79 particles/μm^2. This corresponded to the average of 190 precipitates observed in the micrograph at 10,000X magnification. The most common type of particles identified from EDXS and SAD was rectangularly shaped Ti(N,C,O) with

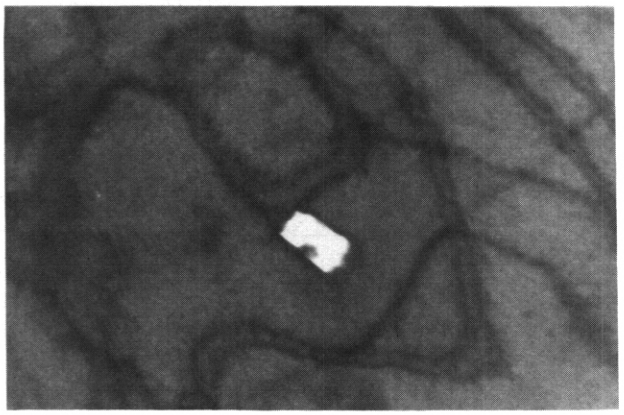

(a) ⟵⟶ 150 nm

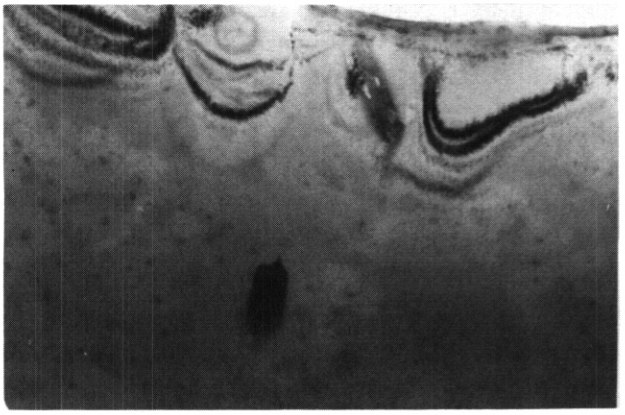

(b) ⟵⟶ 300 nm

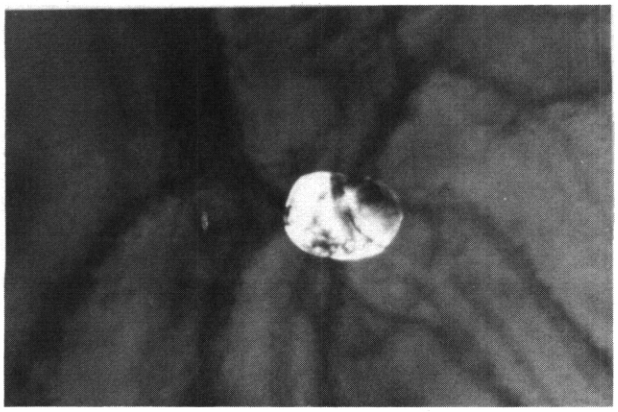

(c) ⟵⟶ 150 nm

Figure 1. Precipitates observed in vanadium: (a) Dark Field Image of V_6O_{13}; (b) Bright Field Image of VS_4; (c) Dark Field Image of γ-Ti_3O_5

fcc NaCl structure; size ranged from 200 to 300 nm. The same type of particles was reported by Schober and Braski [3], and by Chung [4]. They attributed its formation to the thermal processes during preparation of the alloy. EDXS study of the matrix and precipitate composition in the foils and in the carbon- extraction replicas showed no Si in any of the minor types of precipitates present in this alloy; Si was found only dissolved in the matrix. Less-common precipitates found in this alloy were TiP (PDF No. 33-1382) and $Ti_{17}P_{10}$ (PDF No. 22-945); these were found mostly on and in the immediate vicinity of the grain boundaries. A third type of particles was titanium sulfides. The EDXS and SAD data led to identification of Ti_8S_3 (PDF No. 27-909) and Ti_2S (PDF No. 21-1286). Two other sulfur-containing compounds were also observed but could not be identified. None of the above-mentioned particles was coherent with the matrix. Micrographs of some of the precipitates found in the V-3Ti-1Si alloy are shown in Fig. 2.

Microhardness measurements resulted in an average Vickers hardness number of 170 kg/mm^2. Loomis et al. [1] reported the YS and UTS to be 421 and 480 MPa, respectively. The increased number density of precipitates in this alloy may be the result of addition of Si and the tendency of Si to remain as a solute in the matrix.

3. V-5Ti (BL-46)

The average grain size resulting from annealing at 1130°C was found to be ≈28 μm. The precise lattice parameter measurements found the lattice constant to be 0.30390 nm. Al was used as an internal standard.

TEM observations showed the precipitate number density to be 0.815 particles/μm^2, significantly lower than the precipitate density in V-3Ti-1Si. As in the V-3Ti-1Si alloy, the most common precipitates were the rectangular fcc Ti(N,C,O) with lattice parameter ranging from 0.429 to 0.447 nm based on SAD; precipitate size was 200 to 750 nm. Three other types of precipitates were also found: $Ti_{17}P_{10}$ (PDF No. 22-945) on the grain boundaries and infrequently in the matrix, TiN (PDF No. 38-1420) in the matrix, and Ti_8S_3 (PDF No. 29-909) in the matrix. The $Ti_{17}P_{10}$ and Ti_8S_3 were reported by Schober and Braski [3] for the V-20Ti alloy. None of the precipitates in this material was coherent with the matrix. Vanadium-containing precipitates were not found in the V-3Ti-1Si and V-5Ti alloys. Microhardness measurements gave a Vickers hardness number of 142 kg/mm^2. Loomis et al. reported YS and UTS to be 336 and 412 MPa respectively [1]. Micrographs of some of the precipitates found in V-5Ti alloy are shown in Fig. 3.

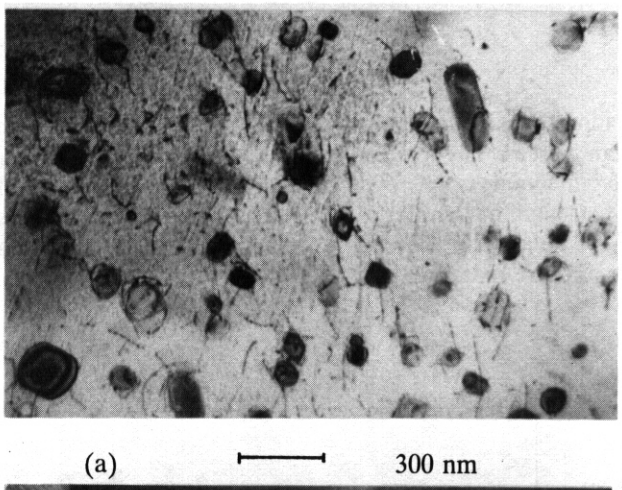

(a) 300 nm

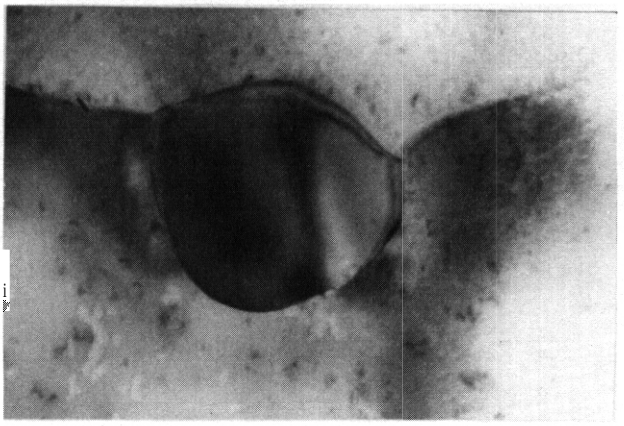

(b) 150 nm

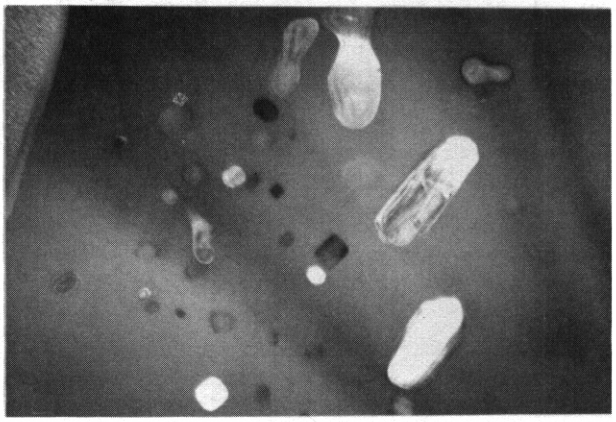

(c) 400 nm

Figure 2. Precipitates in V-3Ti-1Si: (a) Ti carbonitrides. This specimen was deformed to illustrate interaction of precipitates with dislocations; (b) Ti phosphite on a grain boundary; (c) Dark Field Image of Ti_8S_3 in matrix

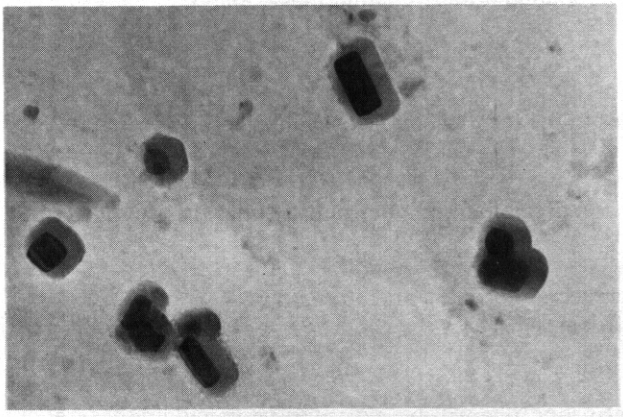

(a) 500 nm

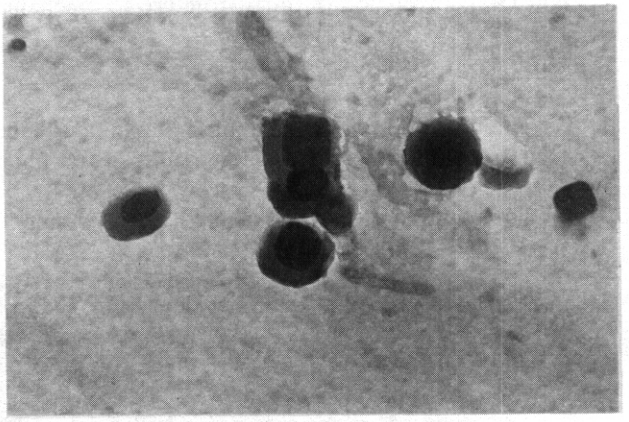

(b) 400 nm

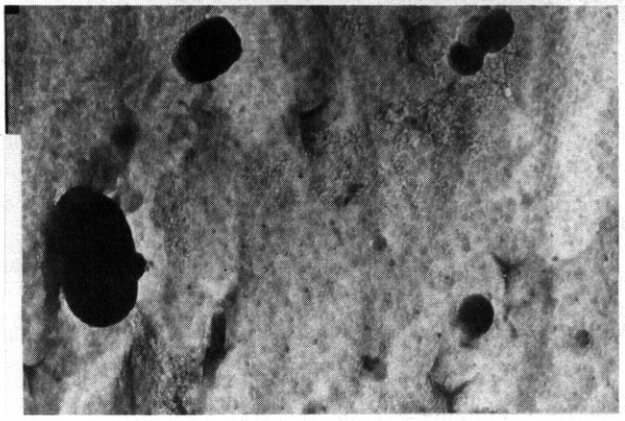

(c) 400 nm

Figure 3. Precipitates found in the carbon-extraction replica of V-5Ti: (a) Ti carbonitrides; (b) TiN; (c) Ti_8S_3

Discussion

The TEM observations indicate that addition of titanium to vanadium causes an increase in precipitate density. Titanium is useful for binding interstitial impurities, i.e. O, N, C, and Si, which can increase the brittleness of vanadium alloys [1]. Other impurities such as phosphorus and sulfur also react with titanium to form complex phosphides and sulfides. The presence of Si in the V-3Ti-1Si alloy increased the precipitate number density and strength of the alloy. The strength and microhardness data in Fig. 4 show that strength and hardness of V, V-3Ti-1Si, and V-5Ti alloys correlate with precipitate density. The data in Fig. 4 also show that microhardness is proportional to the strength of these materials.

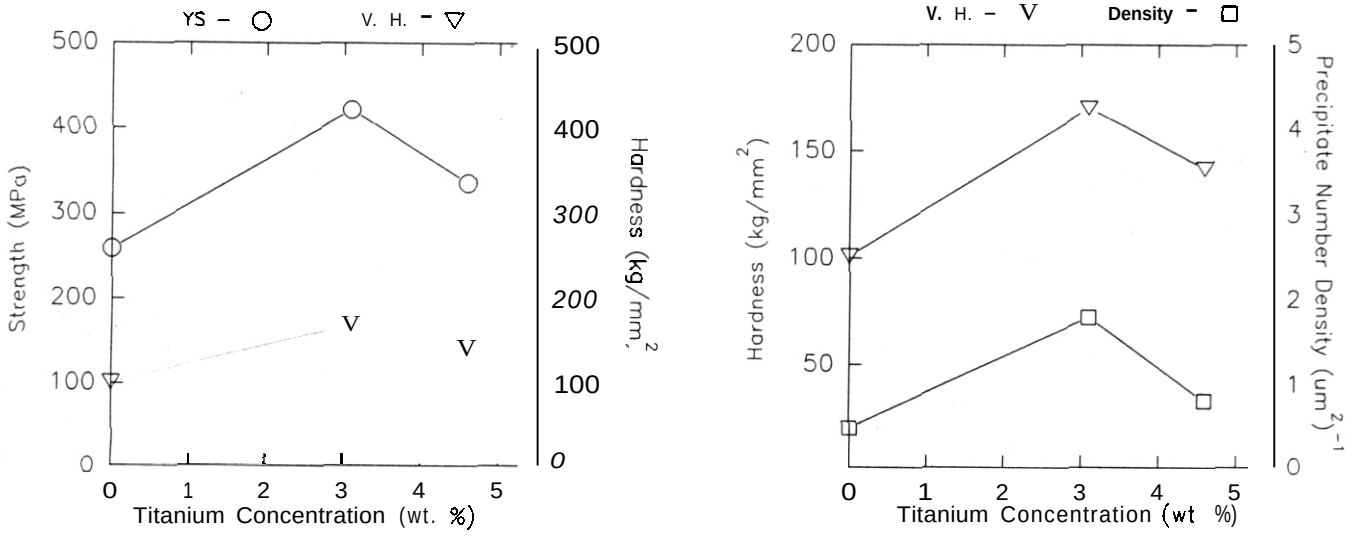

Figure 4. Correlation of microstructure to mechanical properties for vanadium and vanadium base alloys

Conclusions

1. Titanium addition helps to bind C, N, and O interstitial impurities in the form of simple carbonitrides, while S and P are bonded into complex titanium sulfides and phosphides.

2. The addition of alloying elements to vanadium results in increased precipitate number density, and the presence of Si has the most significant consequences.

3. Increased precipitate number density results in a significant increase in hardness and strength of V-Ti alloys.

FUTURE WORK

The study of microstructure and its relationship to mechanical properties will be extended to vanadium-base alloys containing up to 20 % wt. of titanium. Electron energy-loss spectroscopy (EELS), EDXS, and SAD will be used to further characterize the composition of the precipitates.

REFERENCES

1. B.L Loomis, LJ. Nowicki, and D.L. Smith, in: Fusion Reactor Materials, Semiannual Progress Report for Period Ending March 31, 1991, DOE/ER-0313/10, U.S. Department of Energy, Office of Fusion Energy, pp. 145-155.

2. D.L. Smith, B.A. Loomis, and D.R. Diercks, J. Nucl. Mater., 1985, Vol. 135, pp. 125-137.

3. T. Schober and D.N. Braski, Metal. Trans. A, Vol. 20A, Oct. 1989, pp. 1927-1932.

4. H.M. Chung, LJ. Nowicki, and D.L. Smith, in: Fusion Reactor Materials, Semiannual Progress Report for Period Ending September 30, 1991, DOE/ER-0313/11, pp. 215-226.

5. B.A. Loomis, LJ. Nowicki, and D.L. Smith, in: Fusion Reactor Materials, Semiannual Progress Report for Period Ending September 30, 1991, DOE/ER-0313/11, pp. 227-232.

EFFECTS OF IMPURITIES AND DOPING ELEMENTS ON PHASE STRUCTURE OF VANADIUM-BASE ALLOYS CONTAINING TITANIUM* -- M. Satou (Tohoku University) and H. M. Chung (Argonne National Laboratory)

OBJECTIVE

The objective of this study is to determine the effects of impurity elements O, N. and C and doping elements Si and Y on the phase structure of unirradiated and irradiated vanadium-base alloys that contain titanium.

SUMMARY

The thermal phase structure of vanadium-base alloys that contain Ti is strongly influenced by impurities. When the combined concentration of O, N, and C is >500 wt. ppm. Ti solutes form blocky Ti(O,N,C) precipitates during fabrication. When the O+N+C level is <400 wt. ppm. the Ti(O,N,C) phase is absent. With Si and Y in the alloy, Ti solutes form Ti_5Si_3 and $(Y,Si_{1-x})_2O_3$ precipitates. A low impurity concentration and Y doping promote preservation of Ti atoms in solution. Swelling of V-5Cr-5Ti specimens doped with Si, Y, and Al was low after irradiation at 406 and 600°C. The excellent resistance to swelling is attributed to dense distribution of ultrafine Ti_5Si_3 and Y_2O_3-like precipitates that are formed during irradiation and provide a large number of sinks for vacancies: and hence, they effectively suppress nucleation of voids during irradiation.

INTRODUCTION

It is well known that the addition of >4 wt.% Ti very effectively suppresses irradiation-induced swelling of V, V-Cr, and V-Si alloys under conditions relevant to a fusion-reactor first wall. In previous studies, the excellent resistance to swelling of vanadium-base alloys containing Ti has been attributed primarily to irradiation-induced formation of dense ultrafine Ti_5Si_3 precipitates, which act as efficient sinks for vacancies.[1,2] Irradiation-induced precipitation of Ti_5Si_3 and Ti_2O was also associated with degradation of mechanical properties.[1] In as-fabricated ingots, blocky Ti(O,N,C) is the primary type of precipitate that forms during the thermal process,[1,3] and as a consequence of their precipitation, the alloy matrix is depleted of Ti solute. This depletion subsequently influences irradiation-induced precipitation, and hence. swelling and mechanical properties. Therefore, it is important to understand the phase structure and behavior of Ti solute in the alloys. In this study, the effects of O, N. and C and doping elements Si and Y on the thermal–phase stability of several alloys containing Ti were investigated. A low-impurity V-5Cr-5Ti alloy doped with Si and Y exhibited a thermal–phase structure very different from those of alloys investigated previously that contained a relatively high level of impurities.[1] Microstructural evolution in the low-impurity alloys was characterized after irradiation in the Fast Flux Test Facility (FFTF) at 406 and 600°C. and the results were correlated with the swelling behavior of the alloy.

MATERIALS AND PROCEDURES

Procedures for preparation of alloy specimens in this investigation have been described in an earlier report.[1] The chemical composition of the as-fabricated alloys is given in Table 1. The low-impurity alloys doped with Si, Al. and Y were irradiated in the FFTF Material Open Test Assembly (FFTF/MOTA) at 406 and 600°C to 51 and 31 dpa. The specimens were sealed in Li^7-filled TZM/Mo capsules during irradiation to prevent contamination by O, N. and C impurities dissolved in the sodium coolant of the FFTF. Unirradiated and irradiated disk specimens were jet-thinned for transmission electron microscopy (TEM) in a solution of H_2SO_4-CH_3OH-butyl cellosolve (8:2:1 by volume) maintained at -35°C. Density change measurements and microstructural characterization of the irradiated V-5Cr-5Ti alloy

* Work supported by the Office of Fusion Energy, U. S. Department of Energy. under Contract W-31-109-Eng-38

doped with Si. Al, and Y were conducted on the same disk. TEM was conducted with a JEOL 100CX-II scanning–transmission electron microscope operating at 100 keV.

Table 1. Composition of Ti-Containing Vanadium Alloys and Type of Thermal Precipitates

	Nominal Composition	Concentration (wt. ppm)				Ti(O,N,C)	Other
Alloy ID	(wt.%)	O	N	C	si	Present	Precipitate
BL-34	V-8.6Ti	990	180	420	290	yes	
BL-12	V-9.8Ti	1670	390	450	245	yes	-
BL-15	V-17.7Ti	830	160	380	480	yes	-
BL-16	V-20.4Ti	390	530	210	480	yes	-
BL-10	V-7.2Cr-14.5Ti	1110	250	400	400	yes	-
BL-24	V-13.5Cr-5.2Ti	1190	360	500	390	yes	-
BL-43	V-9.2Cr-4.9Ti	230	31	100	340	no	-
BL-42	V-3.1Ti-0.5Si	580	190	140	5400	yes	-
BL-27	V-3.1Ti-0.25Si	2 10	310	310	2500	yes	-
	V-24.6Ti-13.5Cr-1Si[a]	250	75	187	9800	no	$Ti_5(Si,P_{1-x})_3$, $(YSi_{1-x})_2O_3$
	V-4.8Ti-4.0Cr-1Si[b]	140	54	126	8500	no	Ti_5Si_3, VP

[a]Contains 0.71 wt.46 Y and 0.54 wt.% Al.

[b]Contains 0.77 wt.% Y and 0.95 wt.% Al.

THERMAL PHASE STRUCTURE

Thermal precipitation of Ti(O,N,C) phase[1] was observed in all alloys containing >500 wt. ppm O+N+C (Table 1). As an example, dark-field (DF) morphology, selected-area diffraction (SAD). and energy-dispersive X-ray (EDAX) spectra, obtained from a V-3.1Ti-0.25Si (BL-27) specimen are shown in Fig. 1. The size of the Ti(O,N,C) precipitates in Fig. 1A is 100-600 nm.

In contrast to high-impurity alloys, thermally formed Ti(O,N,C) precipitates were absent in the three low-impurity alloys listed in Table 1, i.e., V-9.2Cr-4.9Ti (BL-43). V-24.6Ti-13.5Cr-1Si, and V-4.8Ti-4.0Cr-1Si. The absence or presence of thermal Ti(O,N,C) precipitates is summarized in Table 1 and is also plotted in Fig. 2 as a function of combined O+N+C concentration. The figure shows that Ti(O,N,C) precipitation is largely independent of Ti content (for Ti >3 wt.%) but is determined primarily by the O+N+C level. That is. for alloys with <500 wt. ppm O+N+C, the phase is not likely to precipitate, and vice versa.

In the cold-worked V-4.8Ti-4Cr-1Si alloy doped with 0.77 wt.% Y and 0.95 wt.% Al. the primary thermal precipitate was Ti_5Si_3. Bright-field (BF) morphology, an indexed SAD pattern. and an EDAX signal are shown in Fig. 3. The size of the thermally formed Ti_5Si_3 precipitates in Fig. 3A is ≈170 nm. In general, the size of the thermally formed Ti_5Si_3 precipitates was several times smaller than that of the blocky Ti(O,N,C) precipitates observed in high-impurity alloys. Secondary precipitates, observed only in limited quantity in this alloy, were vanadium phosphides (VP) [hcp, NiAs-type structure, a_o = 0.318 nm, c_o = 0.622 nm). Examples of DF morphology and SAD patterns of the VPs are shown in Fig. 4.

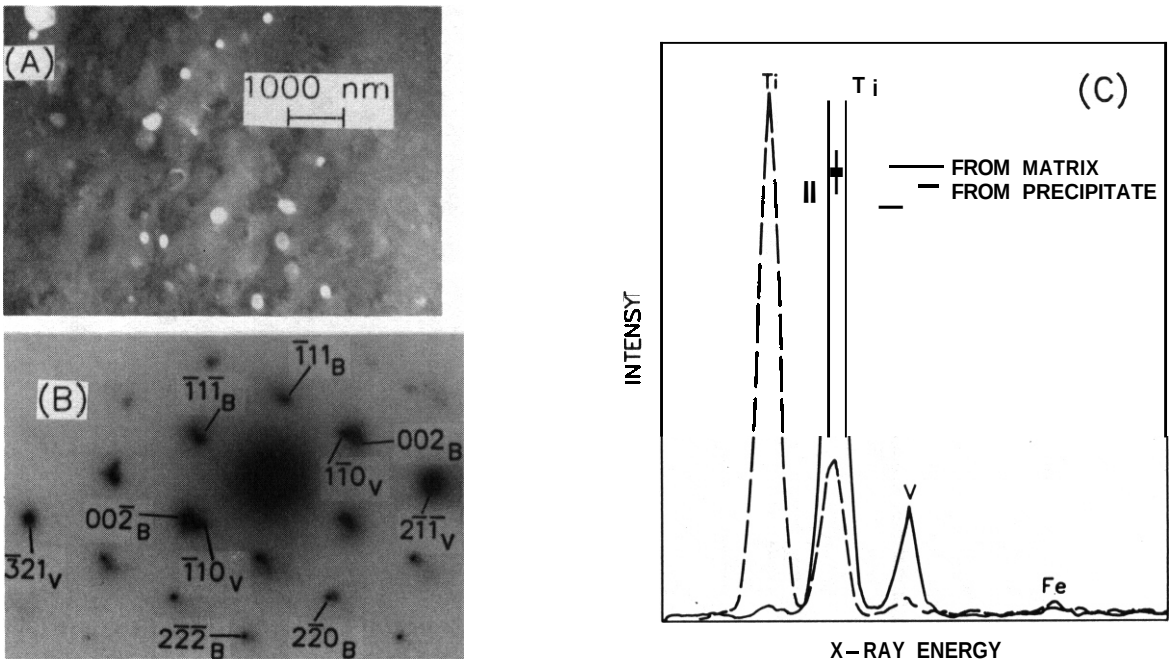

Figure 1. Dark-field (DF) image (A), SAD pattern (B), and EDAX signals (C), showing thermal precipitation of Ti(O,N,C) in V-3Tf *doped with 0.25 wt.% Si.* Subscripts *V and* B *in (B) denote V and Ti(O,N,C), respectively.*

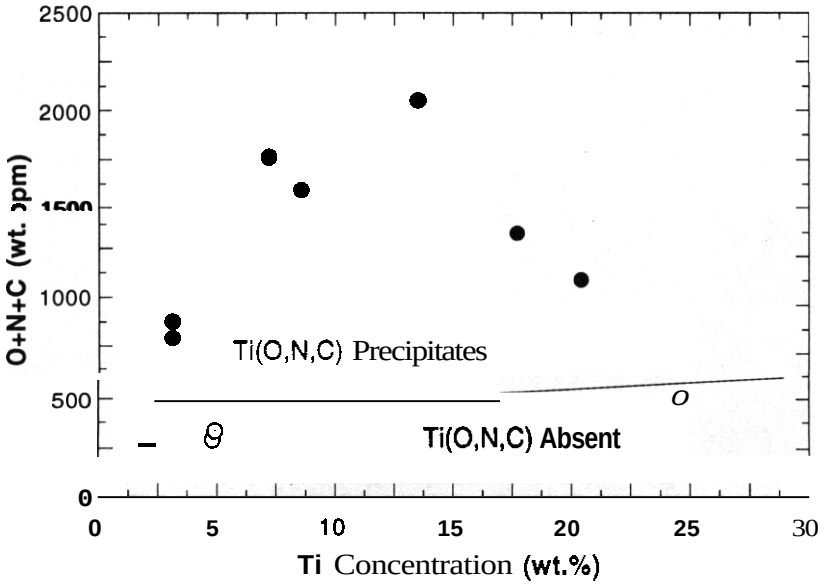

Figure 2. O+N+C us. Ti concentration, showing boundary of Ti(O,N,C) precipitation

In the annealed and recrystallized V-24.6Ti-13.5Cr-1Si alloy doped with 0.71 wt.% Y and 0.54 wt.% Al, the primary thermal precipitate was identified as $(Y,Si_{1-x})_2O_3$. Examples of BF morphology, a SAD pattern, and an EDAX signal of 150-250-nm precipitates are shown in Fig. 5. The *SAD* pattern in Fig. 5B could be indexed on the basis of the structure of Y_2O_3 (bcc, MnO_2-type structure, a_o = 1.06 nm). In this alloy. thermally formed ≈150-nm Ti_5Si_3 precipitates were also observed, in number density comparable to that of $(Y,Si_{1-x})_2O_3$. Both $(Y,Si_{1x})_2O_3$ and Ti_5Si_3 precipitates are visible in Fig. 5A. The two different types of precipitates could be discerned only from EDAX analysis or postexamination indexing of the corresponding *SAD* patterns.

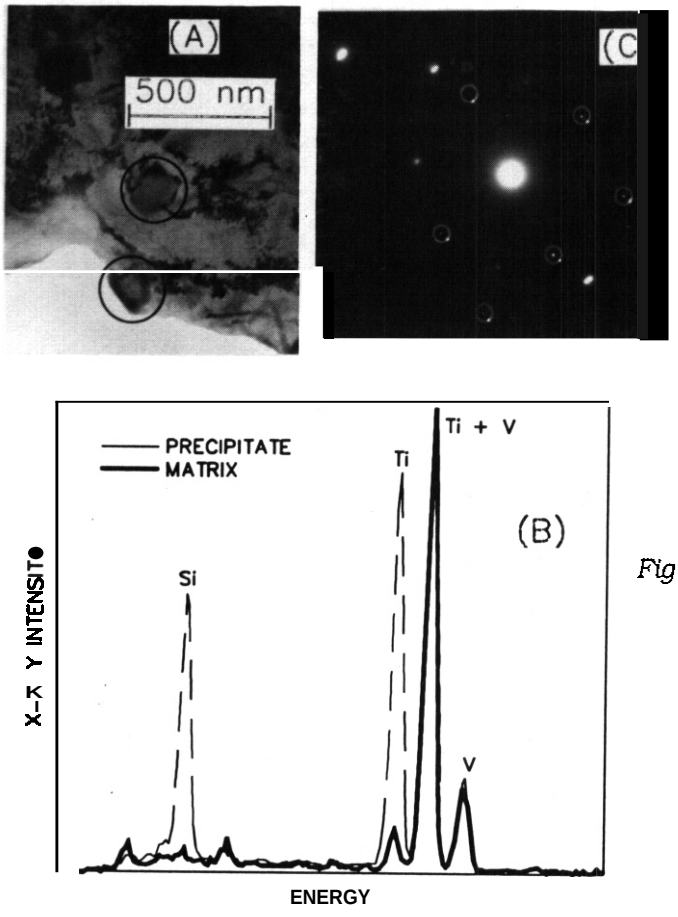

Figure **3.** *Bright-field (BF) image* (A), ***EDAX*** signals *(B),* and *SAD* pattern *(C), showing* thermal precipitation of Ti_5Si_3 in *V-5Ti-5Cr* doped with *1* wt.% **Si,** 0.77 wt.% ***Y*** and 0.95 wt.% *Al*

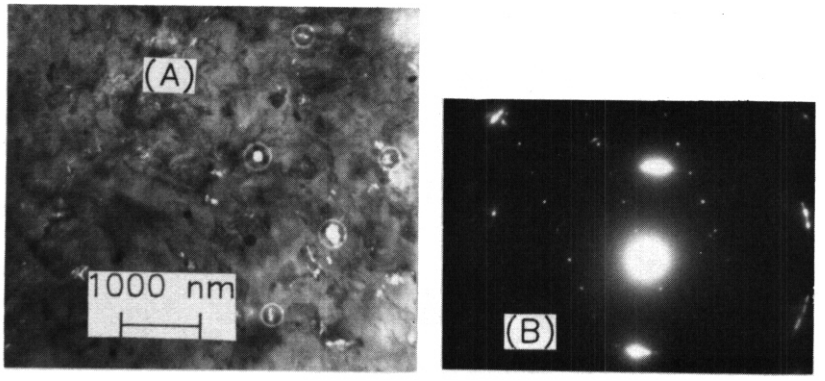

Figure *4.* DF image *(A)* and ***SAD*** pattern *(B),* showing thermal precipitation of *VP* in *V-5Ti-5Cr* doped with *1* wt.% Si 0.77 wt.% ***Y*** and ***0.95*** wt.% *Al*

It seems that when a sufficient level of O, N, and C (e.g., >800 **wt.** ppm. BL-27) is present. Ti solute tends to form Ti(O,N,C) precipitates during fabrication. When the O+N+C level is low (e.g., <400 **wt.** ppm) and the Si level is high. Ti solute tends to form only Ti_5Si_3. When ***Y*** is added as a doping element, **O** solute seems to be scavenged by Y rather than by Ti. This is probably because of the stronger affinity of **O** for **Y** than for Ti. Both factors. i.e., a lower level of O+N+C and ***Y*** doping, seem to promote preservation of Ti in solution. It should be possible to optimize the Si level (that is. lower Si in V-24.6Ti-13.5Cr-1Si alloy) to avoid thermal precipitation of Ti_5Si_3, and hence, to maximize Ti dissolved in solution.

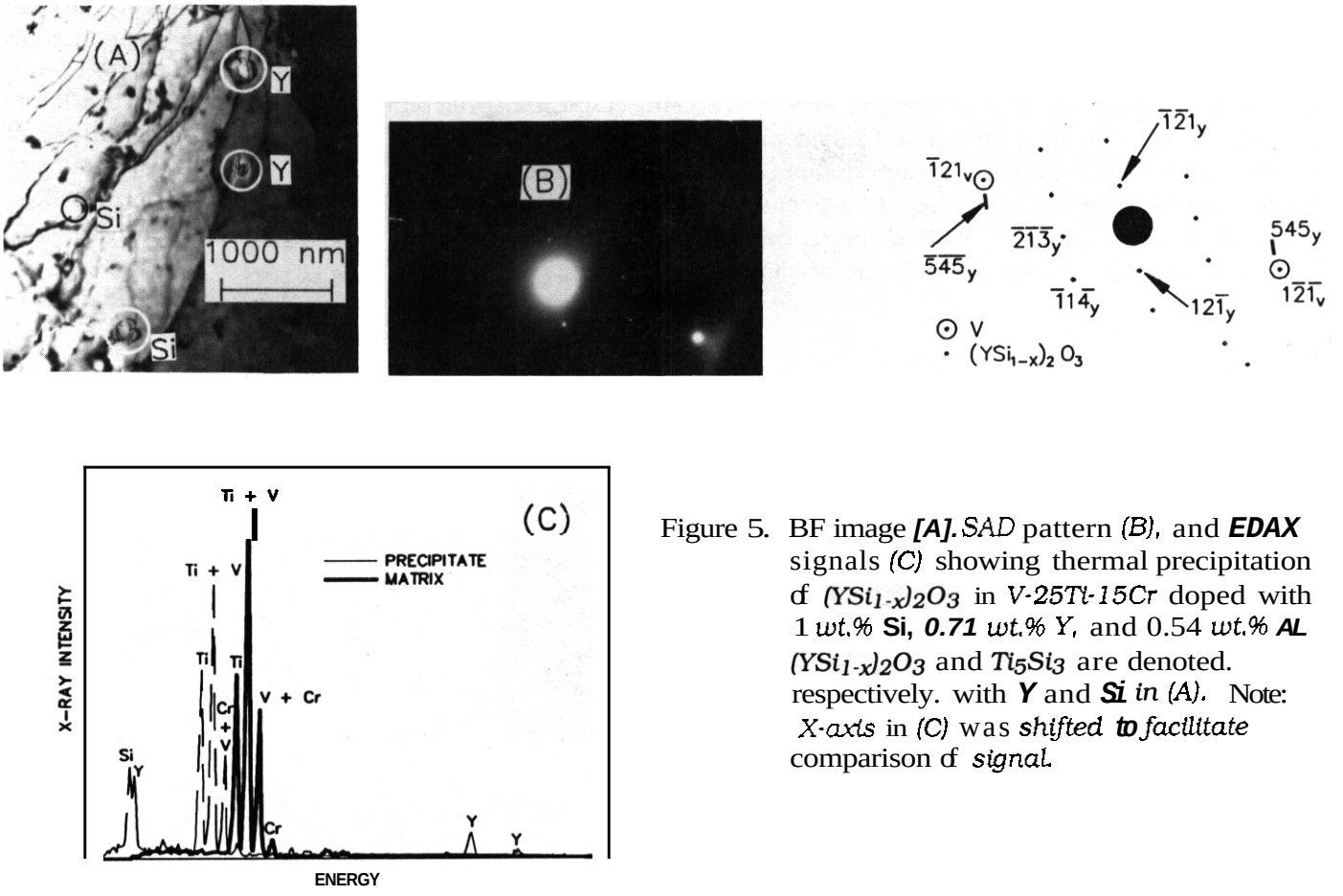

Figure 5. BF image *[A].* SAD pattern *(B),* and ***EDAX*** signals *(C)* showing thermal precipitation of $(YSi_{1-x})_2O_3$ in *V-25Ti-15Cr* doped with 1 *wt.%* **Si,** ***0.71*** *wt.% Y,* and 0.54 *wt.%* ***AL*** $(YSi_{1-x})_2O_3$ and Ti_5Si_3 are denoted. respectively. with ***Y*** and ***Si*** *in (A).* Note: *X-axis* in *(C)* was *shifted to facilitate* comparison of *signal.*

SWELLING AND MICROSTRUCTURE OF IRRADIATED V-5Cr-5Ti

The irradiation performance of V-5Cr-5Ti alloy is of particular interest, because the addition of 5 wt.% Cr and Ti seems to be close to the optimal level of alloying. The V-5Cr-5Ti alloy examined in this study **was.** however, more complex, because it was doped with 0.85 wt.% Si. ***0.77*** wt.% **Y.** and 0.95 wt.% Al. Some of the specimens were examined after irradiation at 406 and 600°C. The material state (i.e., recrystallized or stress-relieved), irradiation condition, density change,[4] and microstructural characteristics of the specimens are summarized in Table 2.

Table 2. Summary of Density Change and Microstructural Characteristics of Irradiated V-5Ti-5Cr-1Si[a]

Specimen ID No.	Material State before Irradiation	Irradiation Temperature (°C)	Damage Level (dpa)	Density Change (%)	Voids Present	Irradiation-Enhanced Precipitates and Size (nm)
F213	Recrystallized	406	51	0.274	negligible	negligible
F240	Stress-Relieved	406	51	0.138	negligible	Ti_5Si_3 <2, unidentified ***3-6***
F244	Stress-Relieved	406	51	0.281	negligible	Ti_5Si_3
F213	Recrystallized	600	31	0.452	no	Ti_5Si_3 15-100

[a]Contains *0.77* wt.% Y and 0.95 wt.% Al.

In a recrystallized specimen irradiated at 600°C to 31 dpa, no voids were observed (density change ≈0.45%). In this specimen, dense precipitation of Ti_5Si_3 was observed, as shown in Fig. 6. In the DF micrograph (Fig. 6A), two types of morphology of the Ti_5Si_3 precipitates are visible, i.e., ≈10-15-nm precipitates clustered on dislocations and 80-120-nm ellipsoidal precipitates. The identity of the latter type of Ti_5Si_3, probably thermally formed precipitates. was confirmed further from separate analyses of DF images and diffraction characteristics, as shown in Figs. 6C and 6D, respectively. The density of Ti_5Si_3 has been reported5 to be ≈4.32 g/cm^3, ≈1.4 times less than the estimated ≈6.1 density of V-5Cr-5Ti. Therefore, the 0.45 % density change observed in the void-free specimen is probably due to volume **expansion** associated with the precipitation of Ti_5Si_3.

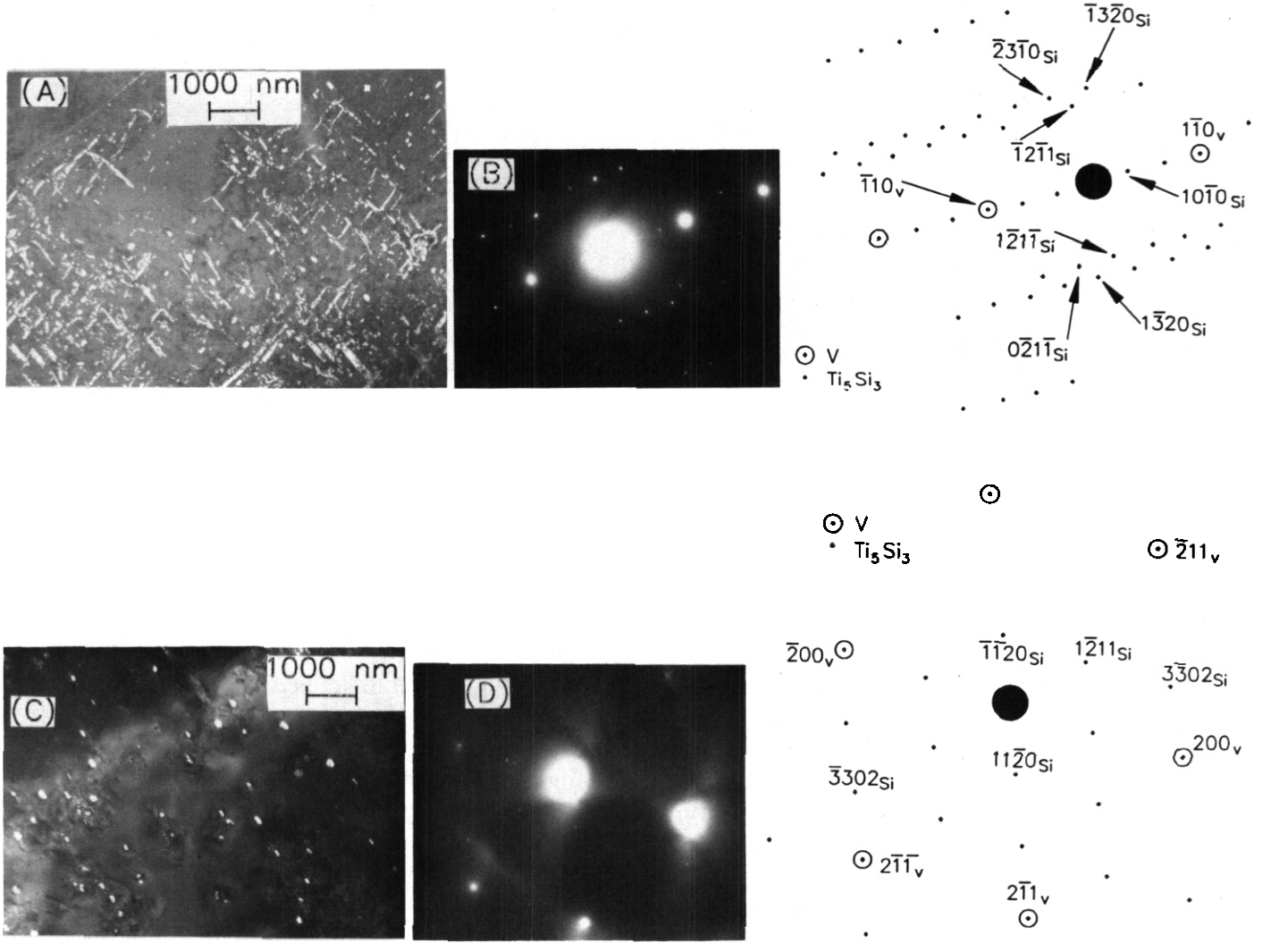

Figure 6. DF image *(A)* and *SAD* pattern *(B)* showing irradiation-enhanced precipitation of Ti_5Si_3 clustered on dislocations in *V-5Ti-5Cr* doped with *1 wt.% Si*, 0.77 *wt.% Y*, and 0.95 *wt.% Al*, and irradiated at *600°C* to 31 dpa *Similar* DF image *(C)* and *SAD* pattern *(D)* show different *morphology of* Ti_5Si_3.

Swelling in stress-relieved specimens irradiated at 406°C to 51 dpa was 0.14-0.28 %. In specimens irradiated at lower temperatures, the intensity of Ti_5Si_3 reflections was very weak, indicating a small volume fraction. However, DF imaging showed a dense population of ultrafine Ti_5Si_3 precipitates. The precipitate size was extremely small, <2 nm. i.e., near the limit of resolution of the **JEOL** 100CX-II transmission electron microscope. DF images of the ultrafine precipitates in original negatives (magnification of 30-50 thousand) were difficult to see without a magnifying glass. Because of the

ultrafine size, it was difficult to obtain good printed images. However, relatively larger 3-5-nm precipitates were observed on dislocations. An example of an indexed **SAD** pattern containing weak reflections from Ti_5Si_3 is given in Fig. **7A.**

The **SAD** pattern shown in Fig. **7A** also contains diffraction rings. The DF image produced from the first ring (Fig. **7B)** reveals dense 3-6-nm precipitates in the region. The four rings are consistent with the (222), (321). (521), and (541) reflections of Y_2O_3. However, the type of precipitate that gives rise to the characteristic ring patterns could not be identified convincingly at this time. These types of precipitate were observed in numerous local regions but were not distributed uniformly in the specimen. The characteristic ring pattern .indicates that the precipitates formed by mechanical fragmentation of larger precipitates by fast-neutron bombardment.

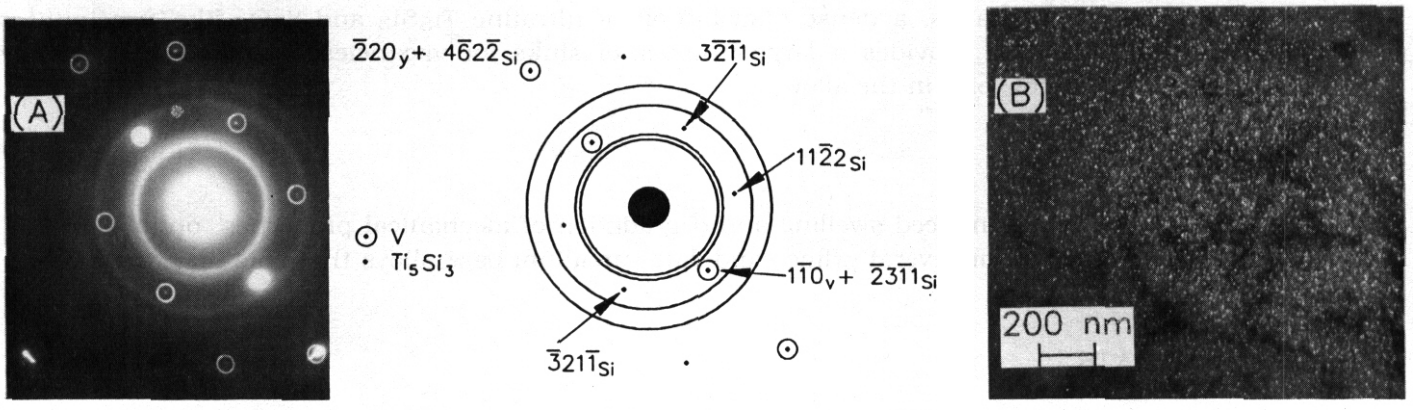

Figure 7. *SAD* ***pattern (A), showing reflections*** *of* Ti_5Si_3 ***and*** Y_2O_3***-like precipitates in stress-relieved V-5Ti-5Cr doped with 1 wt.% Si, 0.77 wt.% Y, and 0.95 wt.% Al and irradiated at 406°C to 51 dpa. DF image in (B), produced from the first ring of (A), shows the*** Y_2O_3***-like precipitates.***

From a preliminary examination, Ti_5Si_3 or the localized Y_2O_3-like precipitates could not be detected positively in a recrystallized specimen irradiated under the same condition, i.e., at 406°C to 51 dpa. Instead, the recrystallized specimen (F213, in Table **2)** was characterized by unusually dense dislocation loops, Fig. 8. Void density in the specimen was negligible.

The microstructural characteristics of the specimen irradiated at 600°C to 31 dpa and the stress-relieved specimens irradiated at ***406°C*** to **51** dpa seem to be consistent with the low swelling. That is. the dense distribution of ultrafine Ti_5Si_3 and Y_2O_3-like precipitates formed during irradiation provided a large number of sinks for vacancies, and hence, effectively suppressed nucleation of stable microvoids.

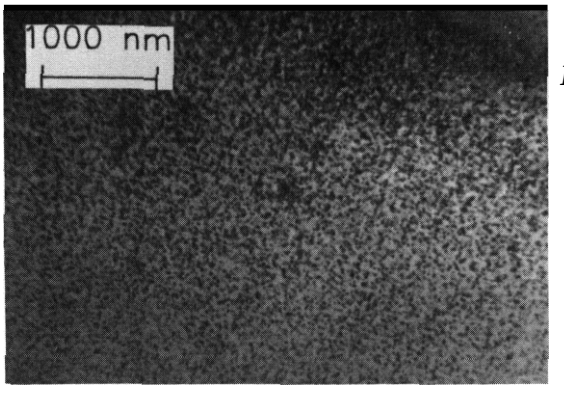

Figure 8. ***Dense dislocation loops in recrystallized V-5Ti-5Cr doped with 1 wt.% Si, 0.77 wt.% Y, and 0.95 wt.% Al, and irradiated at 406°C to 51 dpa***

CONCLUSIONS

1. The thermal phase structure of vanadium-base alloys containing Ti is strongly influenced by impurity level. When the combined concentration of O, N, and C is >500 wt. ppm, Ti solute forms blocky Ti(O,N,C) precipitates during fabrication. When the O+N+C level is <400 wt. ppm, the Ti(O,N,C) phase is absent. When the impurity level is low and alloys are doped with Si and Y, Ti solute tends to precipitate Ti_5Si_3 and $(Y,Si_{1-x})_2O_3$ instead of Ti(O,N,C) during fabrication. Thus, a low impurity levels and Y doping seem to promote preservation of Ti atoms in solution. It is desirable to optimize Si level to avoid thermal precipitation of Ti_5Si_3.

2. Swelling of V-5Cr-5Ti specimens doped with Si, Y, and Al was low after irradiation at 600°C to 31 dpa or at 406°C to 51 dpa. The microstructural characteristics are consistent with the excellent resistance to swelling, that is, a dense distribution of ultrafine Ti_5Si_3 and Y_2O_3-like precipitates formed during irradiation provides a large number of sinks for vacancies, and hence, effectively suppresses nucleation of voids in the alloy.

FUTURE WORK

To minimize irradiation-induced swelling and degradation of mechanical properties, optimal Si contents will be determined for several prime candidate vanadium-base alloys that contain practical impurity levels.

ACKNOWLEDGMENTS

The authors are grateful to B. A. Loomis and L. J. Nowicki for helpful discussions and for specimen preparation.

REFERENCES

1. H. M. Chung. L. J. Nowicki. and D. L. Smith, "Irradiation-Induced Precipitates in Vanadium Alloys Containing Titanium." Fusion Reactor Materials Semiannual Progress Report for Period Ending September 30. 1991, DOE/ER-0313/11, *Oak* Ridge National Laboratory. *Oak* Ridge, TN. pp. 215-226.

2. H. M. Chung. B. A. Loomis, and D. L. Smith, "Correlation of Microstructure and Tensile and Swelling Behavior of Neutron-Irradiated Vanadium Alloys." Proc. 5th Int. Conf. on Fusion Reactor Materials, November 18-22. 1991. Clearwater, FL (in press).

3. T. Schober and D. N. Braski, 'The Microstructure of Selected Annealed Vanadium-Base Alloys." Met. Trans. A *20.* 1927-1932 (1989).

4. M. Satou. K. Abe, H. Kayano. and H. Takahashi. "Low Swelling Behavior of V-Ti-Cr-Si Type Alloys." Proc. 5th Intl. Conf. on Fusion Reactor Materials, November 18-22. 1991. Clearwater. FL [in press).

5. G. Frommeyer. R. Rosenkranz, and C. Luedecke, *Z.* Metallkunde 81, 307-313 (1990).

INFLUENCE OF BORON-GENERATED HELIUM ON THE SWELLING OF NEUTRON-IRRADIATED PURE VANADIUM AND VANADIUM-5% CHROMIUM

N. Sekimura, [University of Tokyo) and F. A. Garner, [Pacific Northwest Laboratory)'

OBJECTIVE

The objective of this effort is to study the response of vanadium alloys to neutron irradiation, particularly the effect of helium produced by transmutation.

SUMMARY

In agreement with earlier reports, the addition of five weight percent chromium to pure vanadium leads to a Significant increase in neutron-induced void swelling at 600°C. Although the swelling of V-5Cr increases strongly with irradiation temperature, the influence of chromium is reversed at lower temperatures, with pure vanadium swelling more than V-5Cr. The use of boron additions to generate large amounts of helium in V and V-5Cr leads to a very complex swelling response, depending on boron level, chromium level and irradiation temperature. The most pronounced response occurs in V-5Cr at 600°C, where boron levels of 100 appm or greater cause a significant reduction in swelling. The complexity of swelling response is thought to result from the competition between helium effects and the separate chemical effects of boron and lithium, each of which may exhibit its own dependence on irradiation temperature.

PROGRESS AND STATUS

Introduction

It was recently shown by Matsui, Nakajima and their coworkers that V-5 at% Fe could reach very large levels of void swelling during irradiation in either the FFTF or JOYO fast reactors, especially at 600°C, the highest irradiation temperature studied.[1-3] The swelling was a strong monotonic function of irradiation temperature. Loomis, Smith and Garner found that V-Cr (Cr=9.5, 10.0, 14.1 wt %) binaries also exhibited at a strong temperature-dependent behavior with substantially enhanced swelling at 600°C.[4] A strong temperature dependence of swelling in V-5 wt % Cr was also reported by Garner and coworkers.[5] At 600°C ~26% swelling was reached by V-5Cr at 45 dpa.

Another factor thought to influence the swelling of vanadium is the helium generation rate, and a variety of experiments are in progress to study the effects of helium. One of these involves the introduction of boron to produce helium and lithium via an [n. α] reaction. Several earlier reports have compared the microstructural response of pure vanadium and V-1 at% ^{10}B irradiated in RTNS-II.[6,7]

Experimental Details

Boron-doped specimens were prepared and annealed at 900°C in a high vacuum, followed by rapid cooling to insure that most boron remained in solution. Pure vanadium and vanadium doped with 100, *500, 2500* appm natural boron as well as V-1 at% natural boron were irradiated side-by-side in FFTF MOTA-2A with V-5Cr (0, 100, 500, *2500* appm natural boron) at four sets of irradiation conditions described in Table *1*. The specimens were irradiated as TEM disks in sealed helium-filled stainless steel packets. After irradiation the neutron-induced density changes were determined using an immersion density technique known to be accurate to ±0.2% density change. An unirradiated specimen was not available for the V-1% B specimen, however. This measurement will be performed at a later time.

Temperature °C	Neutron Fluence n cm^{-2} (E>0.1MeV)	Displacement level, dpa
600	7.8 x 10^{22}	42.1
520	7.7 x 10^{22}	41.6
427	*8.6* x 10^{22}	46.4
411	2.9 x 10^{22}	15.1

"Pacific Northwest Laboratory is operated for the U.S. Department of Energy by Battelle Memorial Institute under Contract DE-AC06-76RLO 1830.

Results

The measured values of swelling are listed in Table 2. The largest swelling level observed in pure vanadium occurred at 427°C, while that in V-5Cr (without boron) occurred at 600°C. As shown in Figure 1, the temperature dependence of the average swelling rate of each of the two boron-free alloys is quite different and opposite. Of particular interest is the very strong temperature dependence of V-5Cr in the range 520-600°C. The swelling of V-5Cr alloys at 411°C at a much lower fluence is very small and lies below the accuracy of the measurement technique.

Table 2. Swelling ($\Delta V/V_0$,%) Measured in V-B and V-5Cr-B Alloys Irradiated in MOTA-2A

	Density of Unirradiated Alloy (g cm^{-3})	600°C 7.8 x 10^{22}*	520°C 7.7 x 10^{22}	427°C 8.6 x 10^{22}	411°C 2.9 x 10^{22}
V pure	6.130	0.50	0.85	2.33	1.44
V + 100 B	6.114	-0.26	1.09	0.61	0.72
V + 500 B	6.136	0.31	1.16	0.74	1.41
V + 2500 B	6.122	0.81	0.90	1.64	0.73
V + 1 at % B	not measured	(6.0491)**	(6.0586)**	(6.0754)**	(6.0520)**
V-5 Cr	6.195	15.4	0.40	0.97	0.11
V-5Cr + 100 B	6.173	10.1	0.50	0.04	-0.20
V-5Cr + 500 B	6.160	9.3	0.76	-0.20	0.22
V-5Cr + 2500 B	6.170	7.8	1.24	-0.03	0.09

* fluence given in n cm^{-2} (E > 0.1MeV)
** Measured density values in g cm^{-3}

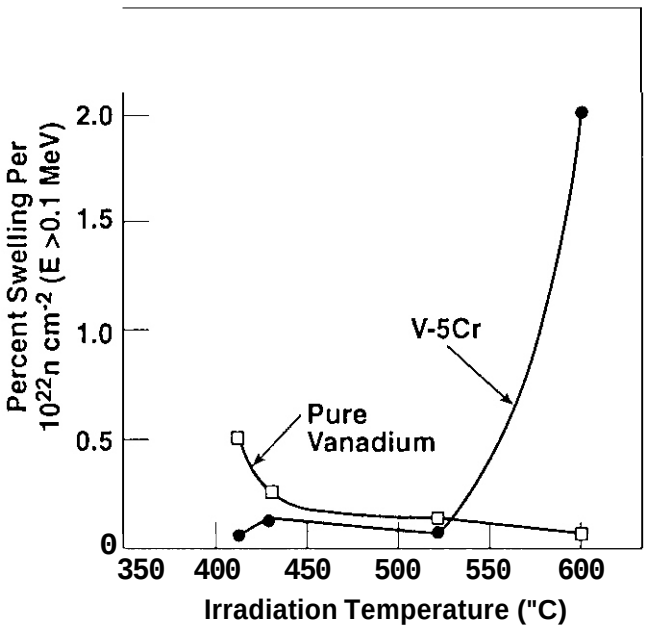

Fig. 1. Average swelling rates observed in this experiment. Note that the swelling at 411°C was accumulated at approximately one-third of the displacement rate compared to that at the other three temperatures.

Figure 2 shows that the action of boron on swelling of V-5Cr is rather complex. At 600°C relatively small levels of boron decrease swelling strongly, with the suppressant effect tending toward saturation at higher boron levels. A similar behavior is observed at 411 and 427°C, but boron additions increase swelling at 520°C. With the exception of the 520°C irradiation, as shown in Figure 3, the first small amount of boron decreases swelling in pure vanadium, with swelling increasing thereafter. It is probably not a coincidence that both pure V and V-5Cr exhibit a behavior at 520°C that is atypical of that at 427 and 600°C.

Discussion

The role of boron is obviously a complex function of irradiation temperature and concentration level. This probably reflects the separate and competitive influences of boron and lithium as chemical species and helium as a cavity-stabilizing gas. Lithium has been shown to accelerate swelling in stainless steels [8-10] and boron has been shown to exert both a chemical suppressant effect as well as a helium-stabilizing enhancement effect on swelling in pure nickel and Ni-2 wt% Si.[11]

The role of chromium on swelling has not yet been identified. Perhaps microstructural examination will provide some clues to the nature of its action. Another variable that may influence the swelling is the displacement rate. Note that the vanadium alloy without chromium developed swelling levels at 15 dpa that are comparable to or larger than those irradiated at higher flux to 42-46 dpa.

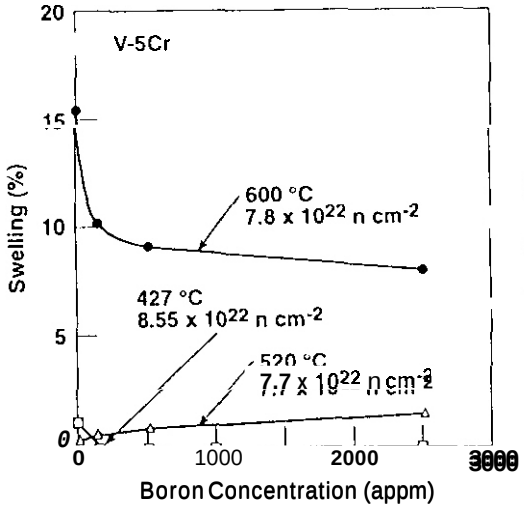

Fig. 2. Influence of boron on swelling of V-5Cr at ~42-46 dpa.

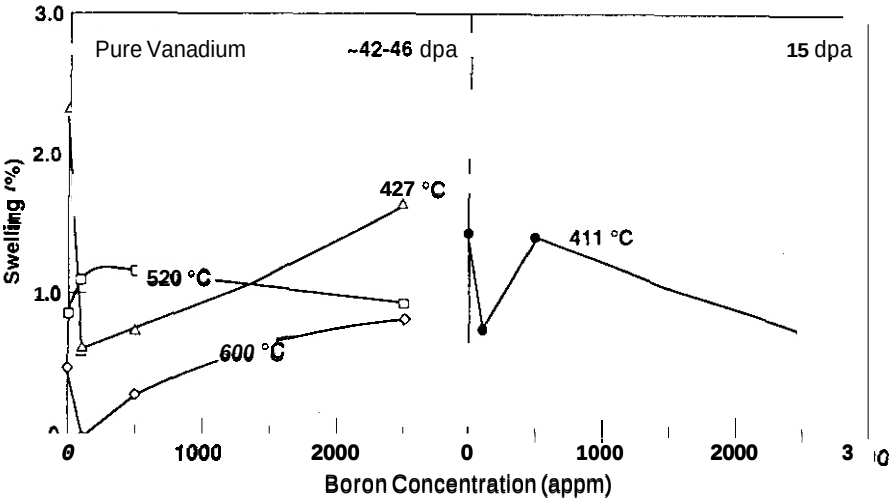

Fig. 3. Influence of boron on swelling of pure vanadium. The 411°C swelling curve is shown separately to remind the reader that it was produced approximately one-third of the dose and dose rate.

FUTURE WORK

Microscopy examination will proceed in the next calendar year. Measurement of the helium concentrations is scheduled soon.

REFERENCES

1. H. Matsui, D. S. Gelles and Y. Kohno, Proceedings 15th ASTM International Conference on Effects of Radiation in Materials, ASTM STP 1125, 1992, in press.

2. H. Nakajima, S. Yoshida and H. Matsui, Journal of Nuclear Materials 191-194(1992) in press

3. H. Matsui and H. Nakajima, ibid.

4. 8. A. Loomis, D. L. Smith and F. A. Garner, Journal of Nuclear Materials 179-181(1991)771

5. F. A. Garner, D. S. Gelles, H. Takahashi, S. Ohnuki, H. Kinoshita and B. A. Loomis, Journal of Nuclear Materials 191-194(1992) in press.

6. H. Kawanishi, S. Ishino and E. Kuramoto, Journal of Nuclear Materials 141-143(1986)899-902.

7. H. Kawanishi and S. Ishino, Journal of Nuclear Materials, 155-157(1988)940-944.

8. D. S. Gelles and F. A. Garner, Journal of Nuclear Materials 85-86(1979)689-693.

9. W. J. S. Yang, F. A. Garner and A. Kumar, Journal of Nuclear Materials 122-123(1984)659-663

10. A. S. Kumar and F. A. Garner, Radiation Effects 82(1984)61-72.

11. T. Muroga, Proceedings of 16th ASTM International Conference on Effects of Radiation on Materials, ASTM STP 1175, in press.

COMPATIBILITY OF VANADIUM ALLOYS WITH REACTOR-GRADE HELIUM FOR FUSION REACTOR APPLICATIONS - G. E. C. Bell and P. S. Bishop Oak Ridge National Laboratory (ORNL)

OBJECTIVE,

Tests were conducted to determine the compatiblity of vanadium alloys with reactor-grade helium and to define the helium gas chemistry requirements for fusion reactors.

SUMMARY

Miniature tensile specimens of V-5Cr-5Ti, V-10Cr-5Ti, and V-12.5Cr-5 Ti were exposed in a once-through system to helium with 70 vppm-H_2 (measured oxygen partial pressures of 10^{-12} atm) and bottle helium (measured oxygen partial pressures of 10^{-4} atm) between 500 and 700°C for up to 1008 h. The weight changes in the specimens were recorded. The helium-exposed specimens were tensile tested, and the effects of exposure on mechanical properties were assessed. Exposure between 500 and 700°C for 1008 h in He+70 vppm-H_2 resulted in complete embrittlement of all the alloys in room temperature tensile tests. The fracture mode was primarily cleavage, probably caused by a hydrogen-induced shift in the ductile to brittle transition temperature (DBTT). Weight gains increased with temperature and were largest for the V-5Cr-5Ti alloy. Specimens exposed for 531 h between 500 and 700°C in bottle He exhibited two distinct fracture morphologies on the fracture surfaces. Brittle cleavage around the edges of the specimens gave way to ductile dimpling in the center of the specimens. The brittle region around the periphery of the specimen is most likely the highest vanadium oxide, V_2O_5.

INTRODUCTION

Vanadium and vanadium alloys are attractive low-activation materials for application to the first wall/blanket structure of a fusion reactor due to their resistance to radiation damage, retention of strength, and excellent creep properties at elevated temperatures [1-6]. However, the chemical reactivity of vanadium-base alloys may result in unacceptable oxidation or embrittlement by oxygen, carbon, nitrogen, or hydrogen [7]. Fusion reactor designs, which utilize vanadium alloys as structural materials with helium as a coolant, with either liquid lithium or lithium-bearing solids as tritium-breeding materials, have been proposed [2]. Further, fusion reactor designs that utilize vanadium alloys and liquid lithium as both the coolant and breeder material will use helium as an "inert" atmosphere in order to minimize ambient oxidation. Thus, the long-term compatibility of vanadium and candidate vanadium alloys with "impure" or reactor-grade helium is of importance to all fusion reactor designs incorporating vanadium or vanadium-base alloys.

The oxidation of vanadium has been previously studied for nuclear applications [3-13]. The oxidation of pure vanadium at relatively high temperatures (700 to 1000°C) and high oxygen partial pressures (p_{O_2} >>0.01 MPa) for short periods of time (<1 h) was investigated by Price and co-workers [8 or 9]. At these relatively high oxygen pressures and temperatures, the heat released on oxygen uptake was sufficient to produce "burning" of the vanadium. The critical oxygen partial pressure ($p_{O_2}^{crit}$) for burning was found to increase with increasing temperature. For oxidations where $p_{O_2} < p_{O_2}^{crit}$, the weight gain of the specimen for a given time t decreased with increasing temperature and was

proportional to $\left(p_{O_2}\right)^{0.75}$ and $(t)^{0.70}$. It is important to note that the temperatures and partial pressures of oxygen in the experiments of Price and co-workers are far outside the range anticipated for most fusion reactor designs that incorporate vanadium-base alloys. Further, these exposures were at temperatures above the melting point of the highest stable oxide of vanadium (V_2O_5). Kohl [10] investigated the short-term (< 60 s) oxidation rate of vanadium at various helium pressures (p^{He}) at a constant oxygen partial pressure ($p_{O_2} = 10^{-4}$ MPa) between 600 and 900°C. A weight gain expression for the initial up-take of oxygen was derived from the data as:

$$v\left\{\frac{\text{mg-O}}{\text{cm}^2\text{-s}}\right\} = 5.14 \exp\left(\frac{2029}{T\{K\}}\right)\left[\frac{p_{O_2}\{torr\}}{\left(p_{He}\{torr\}\right)^{0.67}}\right]^{1} \quad (1)$$

where v is the rate of oxygen up-take, T is temperature, and the units of the parameter are shown in brackets. The initial oxidation rate decreases with increasing temperature (as was found in refs. 7 and 8) decreases with p^{He}, and increases with p_{O_2}. It is important to note that equation (1) is only applicable to the initial, transient oxidation rate, and the steady-state oxidation rate will be much lower than that calculated from equation (1) due to transport effects via the formation of oxide films on the surface of the vanadium. However, equation (1) is relevant in that it establishes an upper bound for long-term oxidation behavior of vanadium in helium at relatively low oxygen partial pressures. Noda et al. [11] investigated the corrosion of several refractory alloys, including a vanadium-25 weight percent (w/o) molybdenum (V-25Mo) alloy, in helium with 13 vppm oxygen for up to 250 h between 600 and 1000°C. Noda et al. found that weight gains decreased with increasing temperature for the V-25Mo, consistent with equation (1). It is not surprising that weight gains for vanadium alloys oxidized at temperatures above the melting point (675°C) of the V_2O_5 would decrease with increasing temperature due to competition between weight gain by oxide film formation near the metal and weight loss by flow or dripping of V_2O_5 from the surface of the specimens.

Loomis and Wiggins [12] investigated oxidation of vanadium-base alloys, primarily vanadium-chromium-titanium alloys, between 450 and 650°C (below the melting point of V_2O_5) in helium with 10 vppm water, and at 550°C in helium with 1 vppm hydrogen and 1 vppm water. The oxidation behavior of the vanadium-base alloys was compared, in terms of weight gains in the environment, with austenitic and ferritic steels. While alloys of vanadium with chromium and titanium exhibited larger weight gains as compared to the austenitic and ferritic steels, the addition of chromium and titanium to vanadium was beneficial in terms of significantly reducing weight gains, as compared to unalloyed vanadium. Weight gains were modeled according to a power law of the form:

$$w\left\{\frac{mg}{cm^2}\right\} = K\left[t\{h\}\right]^{n}, \quad (2)$$

where w is the weight gain of the specimen in time t, and the units of the parameters are shown in brackets. The value of n for vanadium-base alloys was between 0.4 and 0.5 in helium with 1 vppm hydrogen and 1 vppm water at 550°C. The values of K and n (thus, specimen weight gains) increased with temperature between 450 and 650°C in helium with 10 vppm water. Weight gains in both environments decreased with the addition of chromium and/or titanium to vanadium.

It has been observed that hydrogen introduced by mechanical polishing can cause shifts in the DBTT of vanadium alloys [13]. Hydrogen will be present in fusion helium streams to improve tritium recovery through isotopic exchange and to reduce the oxygen potential of the helium gas [14]. Currently, a vanadium-chromium-titanium alloy with 5 w/o chromium and 5 w/o titanium (V-5Cr-5Ti) has been identified as having the least sensitivity to hydrogen embrittlement and is considered the leading candidate for use in fusion reactor designs [3].

The above work has focused on the weight changes that occur due to oxidation in helium or the changes in mechanical properties due to hydrogen up-take from specimen preparation. In this work we have investigated the effect of exposure of a series of V-XCr-5Ti (X = 5, 10, and 12.5) to helium with high and low oxygen potentials on the room-temperature mechanical properties, fracture morphology, and weight changes between 500 and 700°C. The high oxygen potential (measured oxygen partial pressures of 10^{-5} atm) environment is representative of helium taken from large-batch industrial helium supplies. The low-oxygen potential (measured oxygen partial pressures of 10^{-12} atm) environment was produced by providing excess hydrogen on the order of 70 vppm.

EXPERIMENTAL APPARATUS AND METHODS

The once-through mixed-gas exposure system (OTMGES) is shown in Figure 1. The OTMGES permits the exposure of candidate materials in a gas of controlled purity. At the heart of the system are five 3-zone furnaces with independent temperature controllers capable of maintaining temperatures up to 1200°C. Each furnace can be fitted with alumina retorts up to 6.35 cm in dia. and 75 cm long. For these investigations, the furnaces were fitted with either 0.95-cm ID or 1.2-cm ID alumina tubes with a flow rate of 2 L/min through each tube at a pressure of 1.5 atm. Helium is supplied to the retorts from the gas purification and handling system. This system is supplied from two independent banks of six bottles of commercial welding-grade helium cylinders, which can be purified by flowing the gas through an activated charcoal trap at liquid nitrogen temperatures to remove nitrogen, methane, carbon monoxide, carbon dioxide, hydrogen, and water vapor, and through a heated copper-filled bed at 500°C to remove oxygen ($p_{O_2} < 10^{-8}$ atm). Further, in this system, it has been found that the efficiency of the oxygen removal in the copper bed furnace can be improved by adding ~70 to 100 vppm of hydrogen just prior to the copper bed resulting in ($p_{O_2} < 10^{-12}$ atm). After the helium is purified, low-level impurity species can be added, if desired, using micrometering valves to add back the desired impurities to simulate a particular helium coolant chemistry. The mixed gas flows into a common inlet header for the five retorts, past the specimens in the furnace, and out through individual outlet headers which vent to the laboratory atmosphere through oil-filled bubblers. The chemistry of the gas flowing in the common inlet header and the outlet for each retort can be monitored using either an Antek dual-column, dual-detector, or a Bendix dual column, single detector gas chromatograph (GC). Both GCs use helium ionization-type detectors. The partial pressure of oxygen can be monitored to a level of 10^{-20} atm using an Applied Electrochemistry, Inc., S-3A oxygen analyzer that utilizes a solid-oxide (stabilized zirconia) electrochemical detector. The moisture content of the helium is monitored at the common inlet and outlet headers using an Interatom HTMP-type hygrometer that works well at low partial pressures of water vapor (0.1 to 100 vppm-H_2O).

The first exposure was done with helium containing 70 vppm of hydrogen (designated He+70 vppm-H) for 1008 h at 500, 550, 600, 650, and 700°C with 0.2 vppm-H_2O and a measured p_{O_2} of approximately 10^{-12} atm. The results from this first long-term exposure suggested that a second, shorter exposure in the same environment would be of interest. The second exposure was also in He+70 vppm-H for only 73 h at 700°C with 0.3 vppm-H_2O and a measured p_{O_2} of approximately 10^{-12} atm. The third exposure of specimens was in welding-grade helium (designated bottle He) with no excess hydrogen added, with 0.5 vppm-H_2O and a measured p_{O_2} of 10^{-4} atm. Figure 2 shows the relationship between the measured oxygen partial pressure in these environments and the stability of the two highest oxides (V_2O_5 and VO_2) of vanadium as a function of temperature. For the bottle helium (ln p_{O_2} atm ~ -9.6), V_2O_5 should be stable and solid for all exposure temperatures except 700°C. For the He+70 vppm-H only VO_2 should be stable.

ORNL-DWG 92-15506

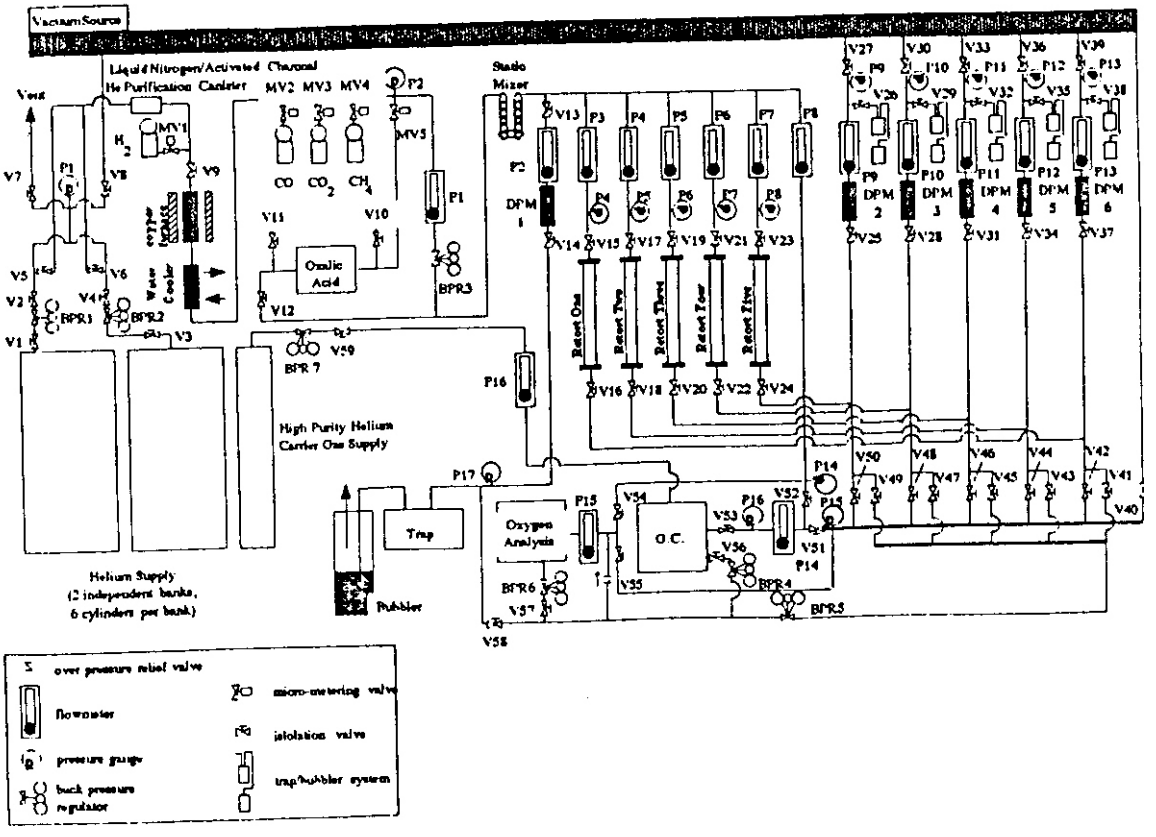

FIGURE 1 - Once-Through Mixed Gas Exposure System (OTMGES) schematic and flow diagram

ORNL-DWG 92-15507

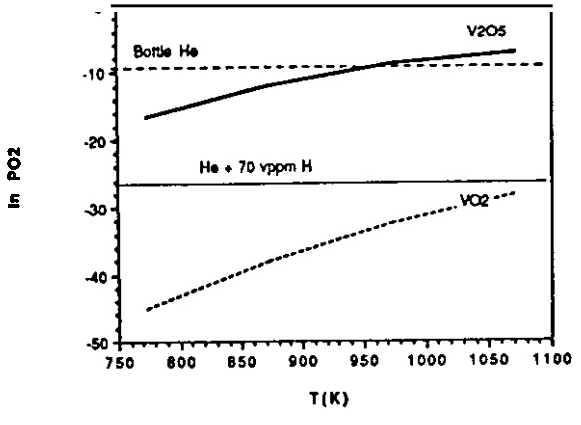

FIGURE 2 - Calculated oxide stability diagram as a function of temperature. Note: Oxygen potentials shown were measured in OTMGES, not calculated from H_2/H_2O equilibrium.

ORNL-DWG 84-14010R

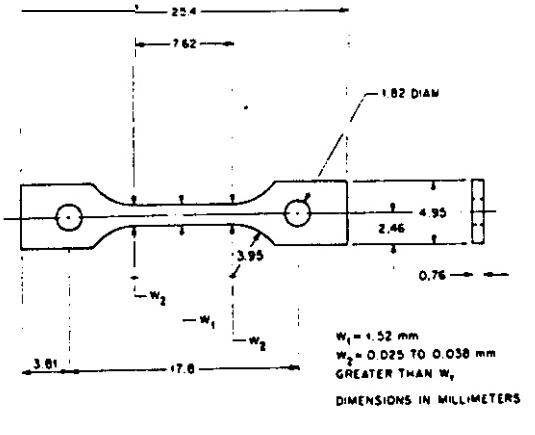

FIGURE 3 - SS-3 miniature tensile specimens used as corrosion specimens.

The specimens exposed in the OTMGES were in the form of miniature tensile specimens (so-called SS-3) shown in Figure 3. The specimens used in this study were fabricated from 0.762-mm-thick sheets of alloys that had nominal compositions of V-12.5Cr-5Ti, V-10Cr-5Ti, and V-5Cr-5Ti. The alloys were arc melted and drop cast to produce 350-g rectangular ingots (11 cm x 2.5 cm x 10 mm). The ingots were radiographed and then annealed at 1200°C in vacuum for 1 h before processing. The first step in processing consisted of warm-working the material (15% reduction in thickness per rolling pass) at 500°C from 10 to 6.8 mm followed by pickling (60% distilled water-30% HNO_3-10% HF) and annealing in vacuum at 1200°C. The above processing (warm-working followed by pickling and vacuum annealing) was repeated until the material was 2.54 mm thick. Then, the material was warm-worked at 500°C to its final thickness of 0.762 mm and pickled prior to machining of the specimens.

The specimens were degreased with acetone and weighed before exposure. After exposure in the helium environment, the specimens were weighed to determine the weight change during exposure and then tensile tested in air, at room temperature using an Instron 1350 load frame with specially designed grips for miniature specimens, and with a crosshead speed of 0.058 cm/min. The load displacement curves were recorded on a an X-Y recorder, and strength and ductility parameters were deduced manually from the chart recorded data. After tensile testing, the fracture surfaces of selected specimens were examined using Joel-35CF scanning electron microscope (SEM).

RESULTS AND DISCUSSION

The tensile test data for control specimens and post-exposure specimens in the three environments are shown in Tables 1 and 2. In general, exposure for 1008 h in He+70 vppm-H resulted in complete embrittlement of all the alloys when tested at room temperature. Ten of the 15 specimens broke in the elastic region of the load-displacement curves. Three of the 15 specimens broke during loading in the miniature specimen grip assembly. The two lowest temperature (500 and 550°C) specimens of V-5Cr-5Ti showed slight retention of ductility (<5%), but for the most part, all three alloys were severely embrittled by the He+70 vppm-H environment in 1008 h at all temperatures between 500 and 700°C. In general, weight gains increased with temperature and were largest for the V-5Cr-5Ti alloy and were consistent with weight gains on similar alloys reported by others [12]. Results from the second exposure for 73 h in He+70 vppm-H at 700°C showed only slight reductions in strength and ductility of the materials during this short exposure. However, significant changes in the morphology of fracture were beginning to occur even after only 73 h (see below). Exposure of specimens to bottle He at temperatures between 500 and 700°C for 531 h resulted, in general, in increases in yield strength and reductions in uniform and total elongations. At all temperatures and for all alloys, the load displacement curves were serrated (i.e., increases in load followed by sharp drops in load) in the region near the yield point. At temperatures above 600°C for the V-10Cr-5Ti alloy, the serrated behavior persisted throughout specimen loading, or failure occurred in the elastic region of the load-displacement curve. Only at 700°C did the V-12.5Cr-5Ti alloy exhibit serration throughout the loading.

The fracture surfaces for the V-5Cr-5Ti control and helium-exposed materials tensile tested in air at room temperature are shown in Figures 4 through 9. Fracture surfaces of the other alloys exhibited similar features. The control specimens exhibited completely ductile fracture surfaces characterized by the ductile dimpling of microvoid coalescence with large uniform and total elongation and reduction in area [Figures 4(*a*) and 4(*b*)]. Exposure of the alloys to the He+70 vppm-H for 1008 h between 500 and 700°C resulted in complete loss of ductility, and the fracture mode was primarily cleavage (Figures 5-7). Even after only 73 h at 700°C in He+70 vppm-H, changes in the fracture mode were evident (compare Figures 4, 5, and 8). Reduction-in-area decreased [compare Figures 4(*a*) and 8(*a*)], and the dimple structure of the fracture surface seemed to be moving toward cleavage [compare Figures 4(*b*), 5(*b*) and 8(*b*)]. This change in fracture morphology is most likely related to the shift in DBTT as reported in ref. 13 where hydrogen was introduced by mechanical polishing.

TABLE 1
SUMMARY OF RESULTS OF ROOM TEMPERATURES TENSILE TESTS OF CONTROL AND HE+70 VPPM-H FOR 1008 H EXPOSES V-XCRR-5TI ALLOYS

Environment	Specimen ID	V-XCr-5Ti Alloy (X = wt %)	Temperature (°C)	Yield or Maximum Stress (MPa)	Ultimate Tensile Stress (MPa)	Uniform Elongation (%)	Total Elongation to Failure (%)	Weight Gain $\left(\frac{\mu g}{cm^2}\right)$
Control	RP-35	5	N/A	430	514	21.2	34.1	N/A
	RP-30	5	N/A	441	544	22.1	35.0	N/A
	RO-36	10	N/A	499	599	22.1	33.3	N/A
	RO-40	10	N/A	594	645	25.0	39.1	N/A
	RN-04	12.5	N/A	591	679	22.5	35.8	N/A
	RN-23	12.5	N/A	560	656	22.5	34.1	N/A
He + 70 vppm-H $P_{O_2} = 10^{-12}$ atm 1008 h	RP-31	5	500	460-S	S	S	<5%	1724.3
	RP-54	5	550	269-S	S	S	<5%	3114.8
	RP-37	5	600	122-E	E	E	E	4519.2
	RP-44	5	650	L	L	L	L	5221.4
	RP-43	5	700	L	L	L	L	5888.9
	RO-37	10	500	576-E	E	E	E	5019.8
	RO-01	10	550	568-E	E	E	E	1411.4
	RO-45	10	600	L	L	L	L	1821.6
	RO-26	10	650	576-E	E	E	E	1543.5
	RO-49	10	700	526-E	E	E	E	3205.2
	RN-21	12.5	500	541-E	E	E	E	1147.2
	RN-40	12.5	550	595-E	E	E	E	862.1
	RN-09	12.5	600	457-E	E	E	E	2245.7
	RN-63	12.5	650	622-E	E	E	E	1133.3
	RN-51	12.5	700	557-E	E	E	E	1898.1

E = Specimen fracture occurred in elastic loading portion of load-displacement curve. Value given in table represents maximum stress at fracture.
L = Specimen fractured while being loaded into specimen grips.
S = Load-displacement curve was serrated and had no clearly defined yield or ultimate stress point.

TABLE 2
SUMMARY OF RESULTS OF ROOM TEMPERATURE TENSILE TESTS OF HE+70 VPPM-H FOR 73 H AND BOTTLE HE EXPOSED V-XCR-5TI ALLOYS

Environment	Specimen ID	V-XCr-5Ti Alloy (X = wt %)	Temperature (°C)	Yield or Maximum Stress (MPa)	Ultimate Tensile Stress (MPa)	Uniform Elongation (%)	Total Elongation to Failure (%)	Weight Gain $\left(\frac{\mu g}{cm^2}\right)$
He + 70 vppm-H $P_{O_2} = 10^{-12}$ atm 73 h	RP-38	5	700	499	603	20.8	27.5	N/A
	RO-20	10	700	503	599	21.0	27.5	N/A
	RN-34	12.5	700	606	702	18.3	20.8	N/A
Bottle He $P_{O_2} = 10^{-4}$ atm 531 h	RP-58	5	500	507-S	583	13.8	19.8	834.3
	RO-58	10	500	583-S	660	15.9	21.5	764.8
	RN-32	12.5	550	591-S	699	14.8	21.4	486.7
	RO-21	10	600	537-S	629	14.2	17.8	695.3
	RN-07	12.5	600	580	672	15.5	20.8	417.2
	RO-50	10	650	583-S	595-S	9.2	10.8	1182.0
	RN-39	12.5	650	594-S	683	12.5	14.7	699.3
	RO-18	10	700	691-E	E	E	E	1049.3
	RN-22	12.5	700	637-S	S	5.9-S	9.6-S	699.3

E = Specimen fracture occurred in elastic loading portion of load-displacement curve. Value given in table represents maximum stress at fracture.
S = Load-displacement curve was serrated and had no clearly defined yield or ultimate stress point.

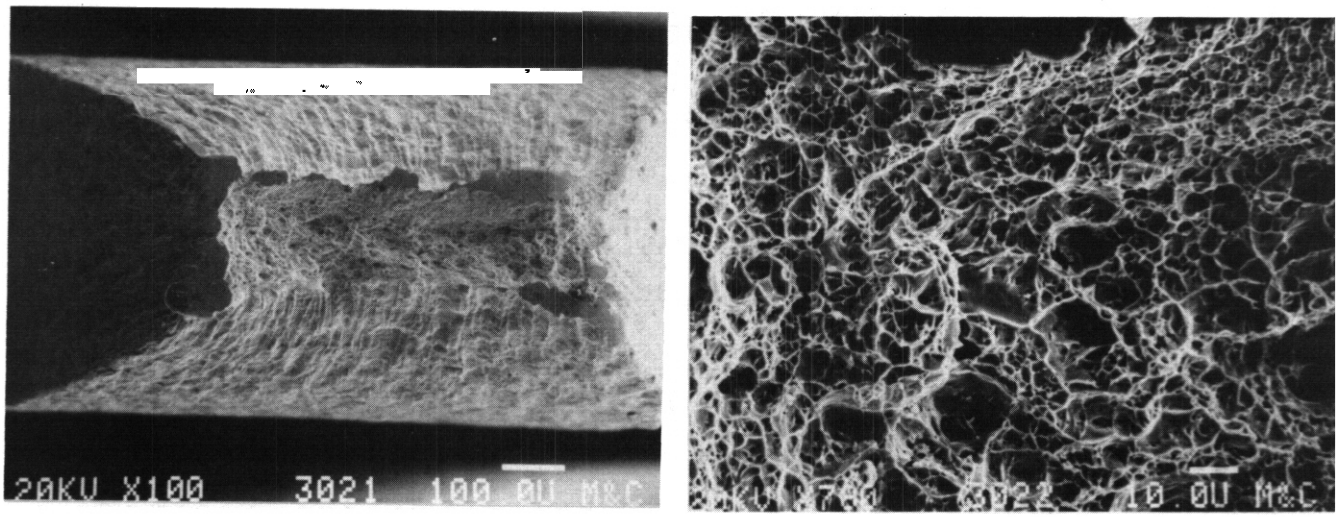

(a) (b)

FIGURE 4 - V-5Cr-5Ti unexposed control specimen:
(a) V-5Cr-5Ti control specimen, 100X (neg. 3021)
(b) V-5Cr-5Ti control specimen, center, 780X (neg. 3022)

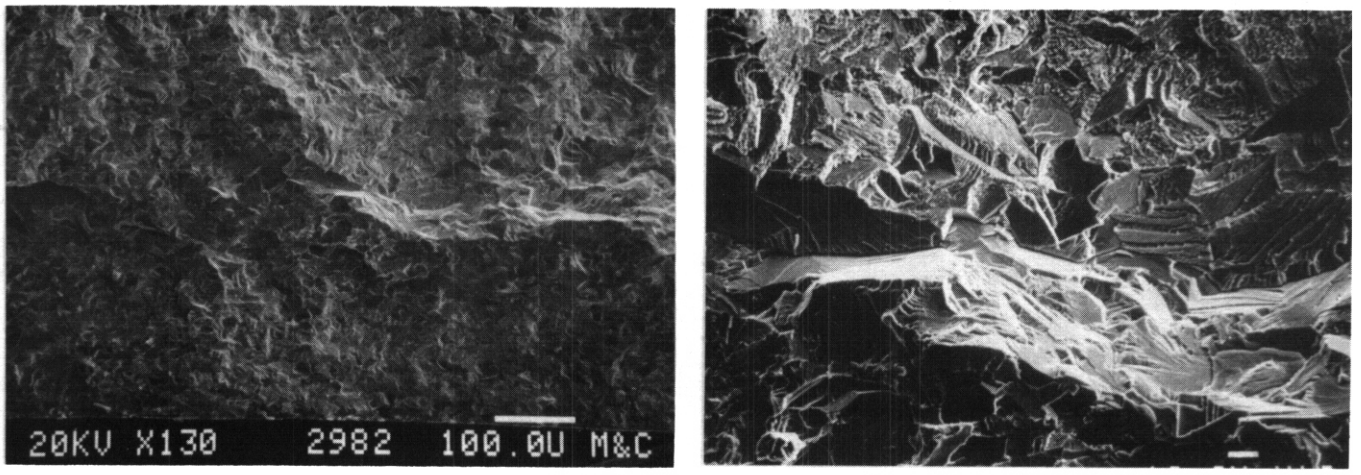

(a) (b)

FIGURE 5 - V-5Cr-5Ti 1008 h in He+70 vppm-H at 700°C:
(a) specimen RP-43, 130X (neg. 2982)
(b) specimen RP-43, center, 480X (neg. 2988)

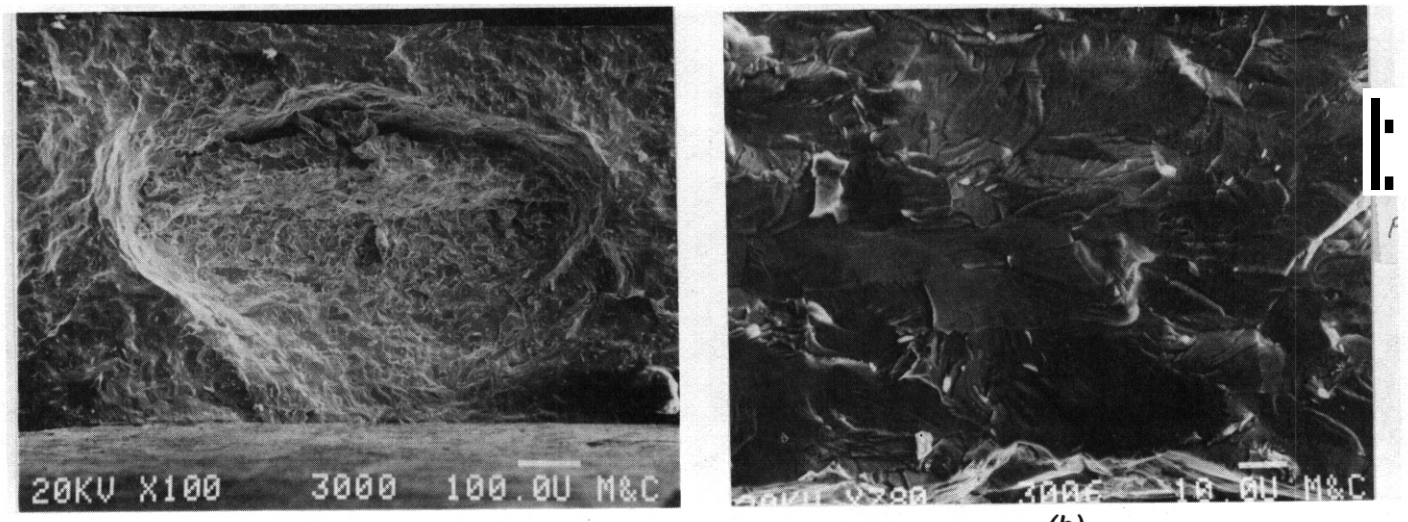

(a) *(b)*

FIGURE 6 - V-5Cr-5Ti 1008 h in He+70 vppm-H at 600°C:
(a) specimen RP-37, 100X (Neg. 3000)
(b) specimen RP-37, center, 780X (neg. 3006)

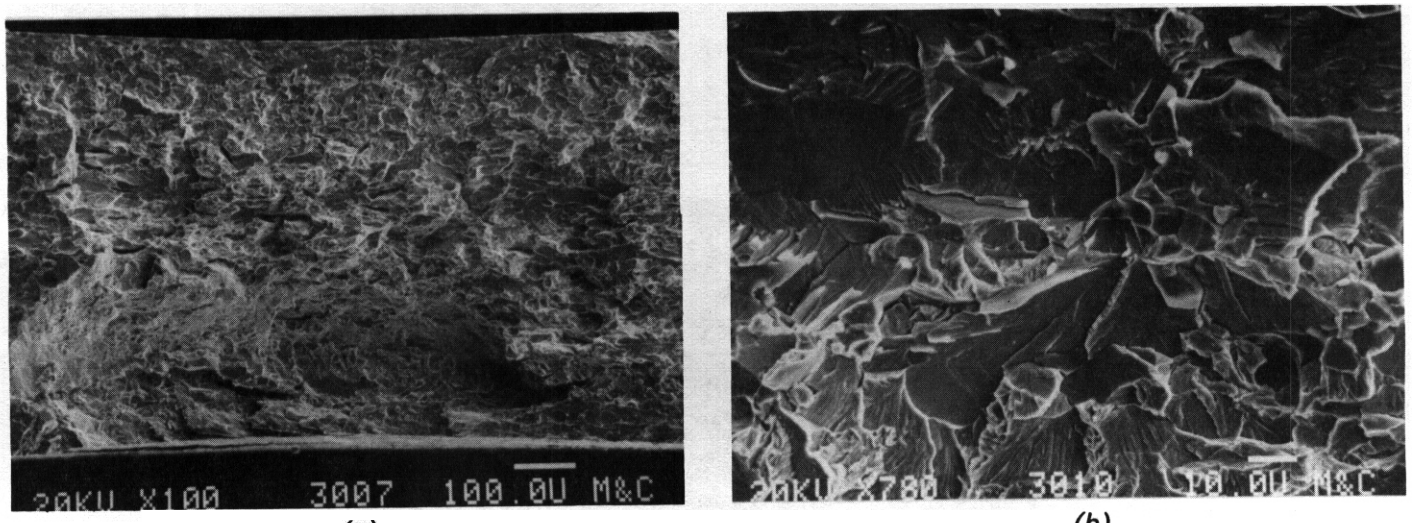

(a) *(b)*

FIGURE 7 - V-5Cr-5Ti 1008 h in He+70 vppm-H at 500°C:
(a) specimen RP-31, 100X (neg. 3007)
(b) specimen RP-31, center, 780X (neg. 3010)

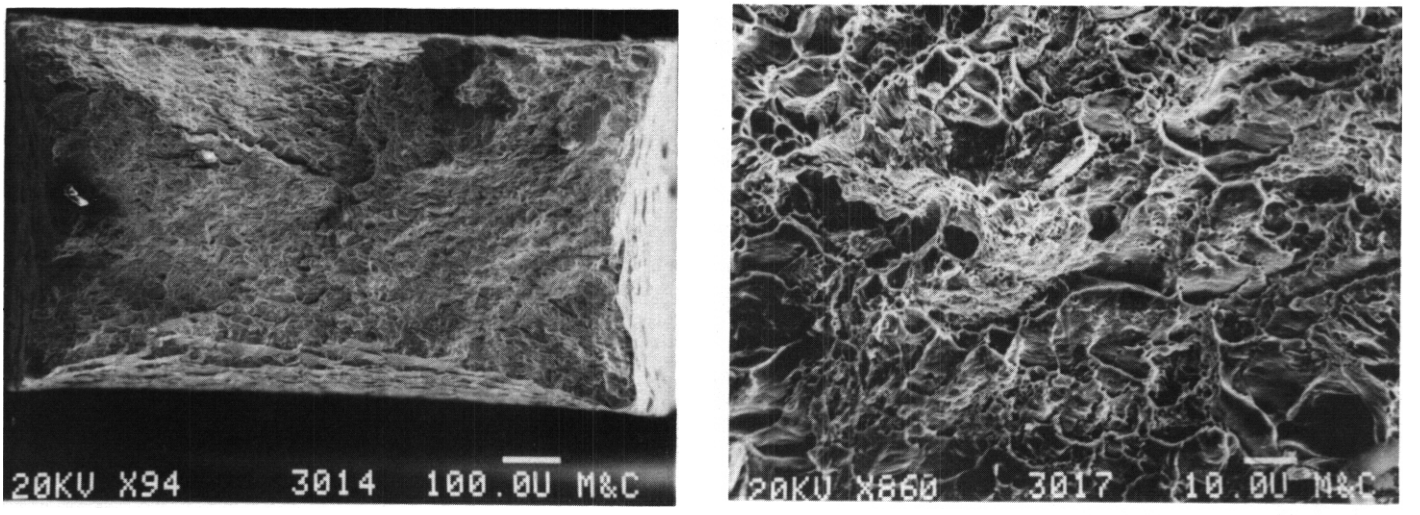

(a) (b)

FIGURE 8 - V-5Cr-5Ti 73 h in He+70 vppm-H at 700°C:
(a) specimen RP-38, 100X (neg. 3014)
(b) specimen RP-38, center, 780X (neg. 3017)

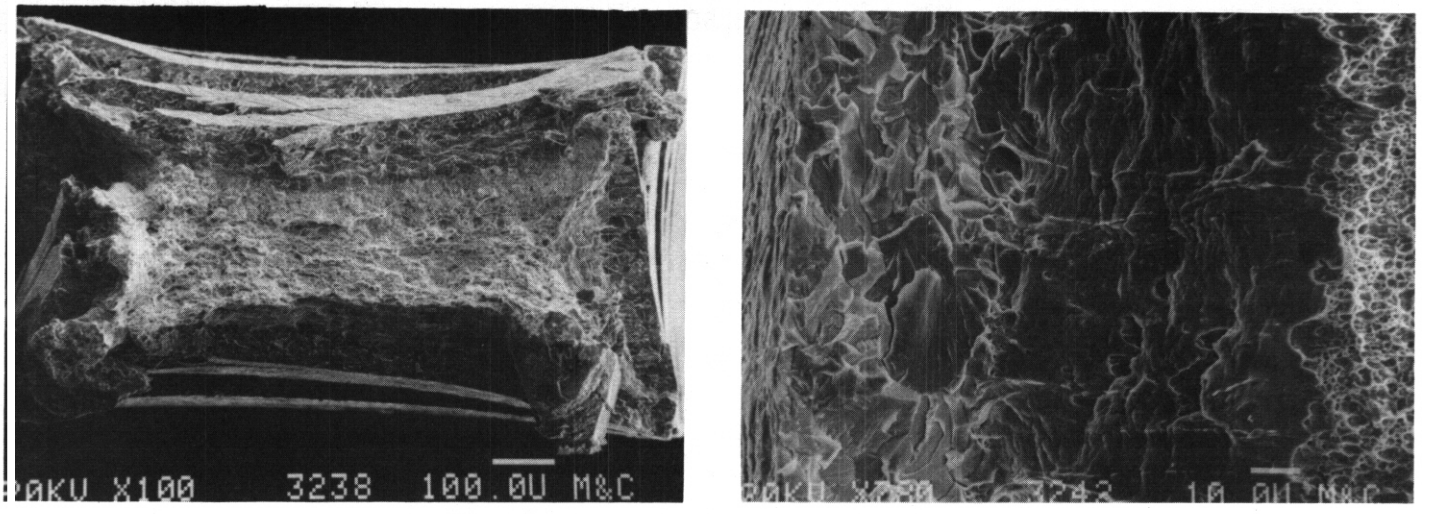

(a) (b)

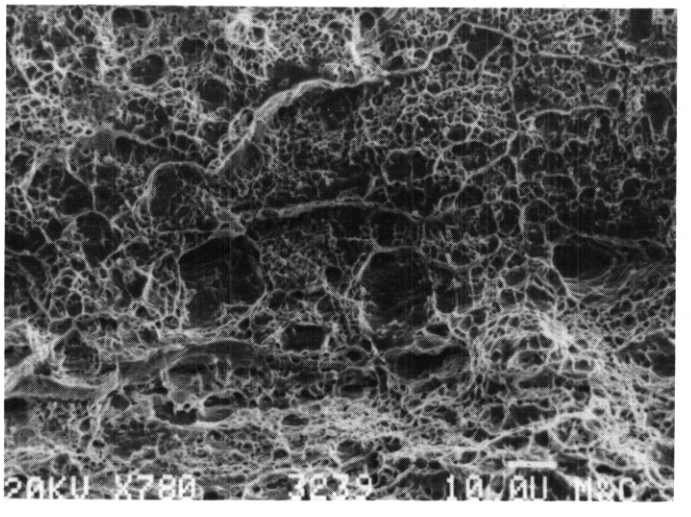

(c)

FIGURE 9 - V-5Cr-5Ti 531 h in Bottle He at 500°C:
(a) specimen RP-58, 100X (neg. 3238)
(b) specimen RP-58, near edge, 780X (neg. 3242)
(c) specimen RP-58, center of fracture, 780X (neg. 3239)

Figure 9(*a*) shows the overall fracture surface of specimen RP-58 V-5Cr-5Ti exposed for 531 h at 500°C in bottle He. There are two distinct fracture morphologies on the fracture surface - brittle cleavage around the edges of the specimens [Figure 9(*b*)] and ductile dimpling in the center of the specimen. The brittle region around the periphery of the specimen may be an oxide of vanadium or may be a solid solution of oxygen in the metal matrix (see Figure 3). The center of the specimen [Figure 9(*c*)] resembles the ductile dimpling observed on the control specimen surfaces [compare Figures 9(*c*) and 4(*b*)]. Table 2 shows that the specimen had a slightly higher yield stress, probably due to oxide strengthening in the bulk, and about two-thirds of the total elongation to failure compared with the control specimen data. Oxidation reactions do not produce the same sort of total embrittlement as oxidation observed in the hydrogen-containing environments,

Based on equilibrium considerations, to prevent oxide formation on vanadium in helium, requires that the oxygen potential in helium be below 10^{-42} atm at 25°C [3]. Experience from high-temperature gas-cooled reactors (HTGRs) [Fort St. Vrain, THTR, Peach Bottom, etc.] suggests that air-ingress, outgassing of materials, and pump and circulator leaks will certainly combine to produce oxygen potentials above this level [15]. While the oxidation is certainly an important consideration in the use of vanadium and vanadium alloys in helium environments, oxidation may not be the only limiting consideration in terms of loss of structural integrity. These results indicate that the presence of hydrogen even at the level of 70 vppm in the helium will lead to severe ambient embrittlement of the structural materials in a relatively short period of time. While it is true that the materials probably retain ductility at higher temperatures [13], fluctuations in reactor structure temperature to near room temperature during start-up, shut-down, and maintenance could result in catastrophic failure of the structure. If helium is to be seriously considered as a potential coolant or ambient atmosphere for vanadium alloys in fusion reactors, then methods for controlling the oxygen potential without introducing hydrogen will be needed. Further, if hydrogen is to be added to helium to improve tritium recovery via isotopic exchange [14] in the presence of vanadium alloys, then it will be necessary to determine the level of hydrogen below which embrittlement of the structure does not occur. In a more general sense, a definition of a reference helium gas chemistry, which takes advantage of the existing and extensive HTGR helium gas chemistry data base, is needed for near- and long-term fusion systems.

SUMMARY AND CONCLUSIONS

Miniature tensile specimens of V-5Cr-5Ti, V-10Cr-5Ti, and V-12.5Cr-5Ti were exposed to helium with 70 vppm-H (measured oxygen partial pressures of 10^{-12} atm) and bottle helium (measured oxygen partial pressures of 10^{-4} atm) between 500 and 700°C for up to 1008 h. The weight changes in the specimens were recorded, and the helium-exposed specimens were tensile tested and the effects of exposure on mechanical properties was assessed. The following conclusions can be drawn from the data presented:

1. Exposure between 500 and 700°C for 1008 h in He+70 vppm-H resulted in complete embrittlement *of* all the alloys in room-temperature tensile tests. The fracture mode was primarily cleavage, probably caused by a hydrogen-induced shift in the DBTT. Weight gains increased with temperature and were largest for the V-5Cr-5Ti alloy.

2. A short-term (73-h) exposure at 700°C in He+70 vppm-H did not significantly change the mechanical properties of the materials but was sufficient to begin to change the fracture mode of the alloys from microvoid coalescence to cleavage for all three alloys.

3. Specimens exposed for 531 h between 500 and 700°C in bottle He exhibited two distinct fracture morphologies on the fracture surfaces. Brittle cleavage around the edges of the specimens gives way to ductile dimpling in the center of the specimens. The brittle region around the periphery of the specimen is associated with oxygen pick-up and may be in part due to the formation of V_2O_5. The specimens had slightly higher yield stress, probably due to oxide strengthening in the bulk, and about two-thirds of the total elongation to failure compared with the control specimen data. Oxide film formation does not produce the same sort of total embrittlement as was observed in the hydrogen-containing environments.

4. While oxidation is certainly an important consideration in the use of vanadium and vanadium alloys in helium environments, it is not the only limiting consideration in terms of loss of structural integrity. Changes in reactor structure temperature to near room temperature during startup, shutdown, and maintenance could result in catastrophic failure of the structure if hydrogen is present in the helium. If helium is to be seriously considered as a potential coolant or ambient atmosphere for vanadium alloys in fusion reactors, then methods for purifying helium without introducing hydrogen will be needed. Further, if hydrogen is to be added to helium to improve tritium recovery via isotopic exchange in the presence of vanadium alloys, then it will be necessary to determine the level of hydrogen below which embrittlement of the structure will not occur. In a more general sense, a definition of a reference helium gas chemistry is needed for fusion systems.

ACKNOWLEDGMENTS

The authors thank J. H. DeVan and J. R. Keiser for carefully reviewing the manuscript. Further thanks to Mr. DeVan and for his assistance in understanding the nuances of thermodynamics and oxidation. Special thanks to C. S. Lee for preparation of the final manuscript, and K. Spence for editing the manuscript.

REFERENCES

1. D. L. Smith et al., Blanket Comparison and Selection Study-Final Report, Argonne National Laboratory, ANL/FPP-84-1 (1984).

2. M. A. Abdou et al., Blanket Comparison and Selection Study-Interim Report, Argonne National Laboratory, ANL/FPP-83-1 (1983).

3. J. Bethin and A. Tobin, "Application of Vanadium and Vanadium Alloys to a Fusion Reactor Blanket," Journal of Nuclear Materials, 122&123, p.864-68(1984).

4. B. A. Loomis and D. L. Smith, "Vanadium Alloys for Structural Applications in Fusion Systems: A Review of Mechanical and Physical Properties," proceedings of the Fifth International Conference on Fusion Reactor Materials, November 18-22, 1991, Clearwater, Florida, to be published in Journal of Nuclear Materials (1993).

5. B. A. Loomis. R. H. Lee. D. L. Smith, and J. R. Peterson. "Strength. Ductility. and Ductile-Brittle Transition Temperature for MFR Candidate Vanadium Alloys," journal of 'Nuclear Materials, 155-157, p. 631-38 (1988).

6. D. N. Braski, "The Effect of Neutron Irradiation on Vanadium Alloys," Journal of Nuclear Materials, 141-143, P. 1125-31 (1986).

7. D. R. Diercks and B. A. Loomis, "Alloying and Impurity Effects in Vanadium-base Alloys," Journal of Nuclear Materials, 141-143, 1117-1124 (1986).

8. W. R. Price and J. Stringer, "The Oxidation of Vanadium at High Temperatures." J. Less-Common Metals, 8, 165-85 (1965).

9. W. E. Price, S. J. Kennett, and J. Stringer, "The Oxidation of Vanadium in the Temperature Range of 700°-1000°C: The Non-Linear Rate Law," J. Less-Common Metals, 12, 318-25 (1967).

10. H. K. Kohl, "The Oxidation of Vanadium with Oxygen in Helium," Journal of Nuclear Materials, 41, 231-34 (1971).

11. T. Noda, M. Okada, and R. Watanabe, "The Compatibility of Candidate First Wall Metallic Materials with Impure Helium," Journal of Nuclear Materials, 85&86, 329-33 (1979).

12. B. A. Loomis and G. Wiggins, "Corrosion and Oxidation of Vanadium-base Alloys," Journal of Nuclear Materials, 122&123, 693-97 (1984).

13. B. A. Loomis, L. J. Nowicki, and D.L. Smith, "The Effect of Hydrogen, Chromium, Titanium, and Silicon on the Ductile-Brittle Transition Temperature of Vanadium and Vanadium-base Alloys," Fusion Reactor Materials Semiannual Progress Reoort for the Period Endina September 30. 1991, DOE/ER-0313/11, p. 227-32.

14. M. A. Abdou et al., FINESSE Phase I Reoort: Technical Issues and Reauirements of Experiments and Facilities for Fusion Nuclear Technology, University of California, Los Angeles, UCLA-ENG-85-29 (1985).

15. C. J. Sparks et al., characterization of Ft. St. Vrain Reactor Dust, Oak Ridge National Laboratory, ORNL/NPR-90/12 (1991).

6.4 Copper Alloys

Swelling of Copper Alloys Irradiated in MOTA 2A - F. A. Garner (Pacific Northwest Laboratory)[a], D. J. Edwards (University of Missouri - Rolla), B. N. Singh, (RISØ National Laboratory) and H. Watanabe (Kyushu University)

OBJECTIVE

The objective of this effort is to provide data on the response of copper alloys being considered for application in fusion reactors.

SUMMARY

Density measurements have been completed on copper alloys irradiated in MOTA 2A at (375°C, 12.7 dpa) and (423°C, 48.0 dpa). While most of the density changes observed are consistent with those of earlier studies, there were several surprises. The role of cold work on swelling of Cu-5Ni is relatively small and Cu-5Mn does not appear to swell at all.

PROGRESS AND STATUS

Introduction

In an earlier report (1) the status of on-going copper irradiation experiments was reviewed. One of the experiments discussed was a two-part irradiation sequence conducted in MOTA 2A and MOTA 2B at target temperatures of 373 and 418°C. Gamma heating raises the temperatures somewhat, raising the temperature to 375 and 423°C. The first segment of this irradiation sequence has now been completed and measurements made of the densities.

Results

Each part of the irradiation sequence consisted of two TEM packets. The first packet (OE01) operated at 375 ± 5°C and reached **2.61** x 10^{22} n cm^{-2} (E>0.1MeV) which is 12.7 dpa (1.333 x **9.5** dpa for stainless steel) for copper. The second packet (OE02) operated at 423 ± 5°C, reaching 8.53 x 10^{22} n/cm^2 (E>0.1MeV), which is 48.0 dpa for copper (**36.0** for stainless steel).

The swelling values calculated from the density changes observed in this experiment are listed in Table 1.

Table 1. Swelling of Copper Alloys from MOTA 2A

Alloy	Condition	Specimen Engraving Code	Swelling, %	
			375°C	423°C
Marz Cu	Annealed	1	4.7	21.6 (24.4)*
Cu-5Ni	Annealed	2	0.91	30.1
Cu-5Ni	40% CW	3	0.37	22.1
Cu-5Mn	Annealed	4	0.004	-0.04
Cu-5Mn	40% CW	5	-0.03	0.13
CuBe	Solutionized	6	(8.36293)+	(8.37641)+
CuBe	Solutionized and aged	7	0.66	-0.46
CuBeNi	Solutionized	8	0.06	0.38
CuBeNi	Solutionized and aged	9	-1.04	0.48
CuAl20	20% CW	10	0.29	-0.087
CuAl25	50% CW	11	-0.94	-0.099
CuAl20	Stress relieved	12	0.46	0.574
CuAl25	Stress relieved	13	-0.34	-0.223

* 3 specimens measured, one at **21.6%** and two at 24.4%.

\+ Unirradiated archive density is currently unavailable, so actual density is shown.

Discussion

The swelling of pure copper at 375°C is a little less (4.7 vs. **6.3%**) than expected from the ~0.5%/dpa

---

[a]Pacific Northwest Laboratory is operated for the U.S. Department of Energy by Battelle Memorial Institute under Contract DE-AC06-76RLO 1830.

swelling rate observed in earlier experiments conducted at ≥400°C. Whether this represents data scatter or a slight reduction in swelling rate below 400°C cannot be determined at this time. When data are generated from the MOTA 2B discharge it may be possible to answer this question.

There is a clear reduction of swelling by cold-work initially in Cu-5Ni, however, reading only 0.91% in the annealed condition and 0.37% in the 40% cold worked condition. At the higher dose level swelling of Cu-5Ni is increased relative to that of pure copper, reaching 30.1% for the annealed condition as compared to 24.4% for pure copper. There appears to be reduction in swelling from 30.1% to 22.1% by cold working.

Of most interest is the behavior of Cu-5Mn which did not appear to swell at all. The values shown in Table 1 are within the accuracy (±0.2%) of the measurement technique. Preliminary results of microscopy examination indicate that not only did these alloys resist swelling but that there was essentially no dislocation structure, even in the specimens which were initially in the cold worked condition.

The densities found in irradiated CuBe and CuBeNi are consistent with that observed in earlier studies (2,3) and imply that solute redistribution and precipitation is the controlling factor in determining the density changes. The behavior of the CuAl20 and CuAl25 alloys is also consistent with that observed earlier. CuAl20 swells a little and CuAl25 densifies.

FUTURE WORK

Microscopy on these alloys will proceed. The electrical conductivity will also be measured. Upon discharge of MOTA 28, examination of the second group of specimens will proceed.

REFERENCES

1. F. A. Garner, M. L. Hamilton, D. J. Edwards, B. N. Singh, J. F. Stubbins, T. Shikama, S. J. Zinkle and P. Samal, Fusion Reactor Materials Semiannual Progress Report DOE/ER-0313/10 (1991) pp. 186-191.

2. F. A. Garner, M. L. Hamilton, T. Shikama, D. J. Edwards and J. W. Newkirk, Fusion Reactor Materials Semiannual Progress Report DOE/ER-0313/12 (1992) pp. 198-204.

3. D. J. Edwards, A. S. Kumar, K. R. Anderson, J. F. Stubbins, F. A. Garner and M. L. Hamilton, Fusion Reactor Materials Semiannual Progress Report DOE/ER-0313/11 (1991) pp. 239-244.

COBRA-1A COPPER IRRADIATION EXPERIMENT IN EBR-II - F. A. Garner and M. L. Hamilton, (Pacific Northwest Laboratory)[a]

OBJECTIVE

The objective of this effort is to provide data on the radiation response of copper alloys selected as candidates for divertor service in ITER and other fusion devices.

SUMMARY

Specimen preparation for copper alloys to be irradiated in EBR-II Run 162 in the COBRA irradiation vehicle is complete. Specimens include TEM disks, miniature tensile and miniature fatigue specimens.

PROGRESS AND STATUS

Introduction

Pure copper and various dispersion-strengthened copper alloys have been proposed for use in the divertor plate assembly of ITER. Data are, therefore, required to define the response of these alloys to irradiation. Although several earlier experiments have been conducted [1-3], additional data are being sought using a cold B7A assembly, referred to as COBRA-IA in EBR-II, with the experiment scheduled to start in EBR-II run 162. Portions of each of the seven pins, designated A through G, will be used for irradiation of copper alloys.

Description of Specimens

TEM disks.: There are four sealed helium-filled TEM packets (0.8" long), each containing a variety of specimens, as listed in Table 1. Two of the packets will be irradiated at ~400°C in weeper capsules, one located in-core in capsule E and one below core in capsule B. The other two will be irradiated in gas-gapped capsules at ~500°C in capsule F, one in-core and another below-core. These packets are designated 76, 77, 79, and 9A respectively.

The TEM disks represent joint efforts with T. Shikama of Tohoku University, Japan (thermal conductivity measurements on irradiated Al_2O_3 -strengthened alloys), Y. Shimomura of Hiroshima University, Japan (oxygen effects on various copper alloys and pure metals), and B. N. Singh *of RISØ* Laboratory, Denmark (influence of nickel on behavior of copper). In addition to these various fundamentally-oriented studies, the experiment focuses on two Al_2O_3 dispersion-strengthened alloys, GlidCop CuAl25 from SCM Metal Products and a Japanese version of this alloy produced by another process. All specimens are separated by 0.001 inch thick molybdenum foils.

Miniature Tensile Specimens: There are four groups of twelve S-l tensile specimens each, two for irradiation at 400°C in capsules B and E, and two at 500°C in capsule F. One group of specimens at each temperature will be located in-core; the other will be below-core. Each group of twelve specimens (6 each of CuAl25 and the similar Japanese alloy) is bundled with molybdenum spacers and stainless steel wire, and sealed in a 0.37" diameter stainless steel container filled with helium. After irradiation these specimens will be tested in the MATRON tensile test facility at PNL under vacuum at three conditions (room temperature, irradiation temperature, and one intermediate temperature).

Miniature Fatigue Specimens

As discussed in another report [4], a joint RISØ/PNL/University of Illinois experiment is in progress in OR-3 and EBR-II to provide low-cycle fatigue data on pure copper and GlidCop CuAl25 (as-wrought) in both the unirradiated and irradiated conditions. This irradiation in EBR-II will be conducted below-core at ~400°C, comprising twelve helium-filled stainless steel subcapsules, each containing four identical specimens. Two subcapsules, containing eight specimens, comprise one set of specimens and will be tested at various strain ranges at the irradiation temperature.

As shown in Table 2, the four subcapsules in pins F and G (set A) will be removed from EBR-II after two reactor cycles. The other two sets (B and C) in pins A, B, C, and D will remain in-reactor to achieve higher, but as yet unspecified, exposures.

---

[a] Pacific Northwest Laboratory is operated for the U.S. Department of Energy by Battelle Memorial Institute under Contract DE-AC06-76RLO 1830.

Table 1. Copper Alloys Included in COBRA-1A as TEM Disks

Alloy	Source	Material Code[2]
OFHC Copper	RISØ	PA
Cu-0.17Ni (wt%)	RISØ	PE
Cu-1.0Ni	RISØ	PF
Cu-2.0Ni	RISØ	PH
Cu-5.0Ni	RISØ	PK
Cu-10.0Ni	RISØ	PL
Cu-0.5Be	RISØ	PM
CuAl25	RISØ	PR
CuAl25	PNL	XX
Cu-Al_2O_3	Tohoku	GT
JM Copper	Hiroshima	⊖
JM Copper (RM)[1]	Hiroshima	⊜
Dowa Copper	Hiroshima	⊝
Down Copper (RM)	Hiroshima	⊟
Cu-5Al	Hiroshima	⊛
Cu-SA1 (RM)	Hiroshima	⊜

[1] RM = remelted and vacuum degassed *to* remove oxygen and other gaseous impurities

[2] Some codes are laser engraved; others are score marks applied with a scalpel

Table 2. Fatigue Specimen Inventory in COBRA

Set	Subcapsule	Alloy	Specimen Codes	Number of Reactor Cycles
A	F02, G02	CuAl25	F21-F24, G21-G24	2
A	F01, G01	OFHC Copper	F11-F14, G11-G14	2
B	A02, B02	CuAl25	A21-A24, B21-B24	>2
B	A01, B01	CuAl25	All-A14, 811-814	>2
C	C02, 002	OFHC Copper	C21-C24, D21-D24	>2
C	C01, D01	OFHC Copper	C11-C14, 011-014	>2

REFERENCES

1. H. R. Brager, Journal of Nuclear Materials, 141-143 (1986) pp. 79-86, also 163-168.

2. F. A. Garner, M. L. Hamilton, K. R. Anderson, J. F. Stubbins, B. N. Singh, A. Horsewell and W. F Sommer, DOE/ER-0313/6 (1989) pp. 351-356.

3. F. A. Garner and M. L. Hamilton, DOE/ER-0313/10 (1991) pp. 186-191.

4. F. A. Garner, B. N. Singh and J. F. Stubbins, in this semiannual report

THE INFLUENCE OF TRANSMUTATION AND VOID SWELLING ON THE ELECTRICAL PROPERTIES OF COPPER AND SEVERAL COPPER ALLOYS

D. J. Edwards, (University of Missouri-Rolla), and F. A. Garner, (Pacific Northwest Laboratory)[a]

OBJECTIVE

The objective of this effort is to determine the irradiation-induced changes in the electrical and thermal conductivities of copper alloys selected for service in fusion reactors.

SUMMARY

A comparison of the predicted and measured electrical conductivities of MARZ copper and two copper alloys irradiated in FFTF shows that the calculated transmutation rates are ~15% higher than those required to produce the observed changes. It also appears that the contribution of transmutants and void swelling to conductivity changes are directly additive. Of the several models available, Euken's model has been found to best describe the contribution of void swelling.

PROGRESS AND STATUS

Introduction

Copper alloys have been proposed for service as high heat flux components in fusion reactors.[1-4] The electrical and thermal conductivities of these alloys will undergo changes, however, in response to the combined influence of radiation-induced solute redistribution, void swelling, and transmutation [5-9]. Since the transmutation process is very sensitive to neutron spectra, irradiation experiments currently being conducted in the Fast Flux Test Facility (FFTF) will produce levels of transmutants that are atypical of those anticipated from fusion spectra.

Some uncertainty still exists in our ability to predict the formation rates in FFTF of the important transmutants (Ni, Zn, Co), with the difficulties arising primarily from uncertainties in the neutron fluxes and spectra actually experienced by the irradiated specimens. Dosimetry measurements are not usually available at the exact location of the specimens within the core, so the predictions are based on extrapolations from calculations which assume idealized and homogenized loadings of the core and experiment. A drawback to this method is that in addition to calculational uncertainties, perturbations of the local flux and spectra due to structural and material inhomogeneities in the immediate area of the specimens cannot be estimated.

An estimate of the flux and spectral uncertainties could be made from direct measurement of the transmutants. The actual transmutation products are difficult to measure directly, however. The three major transmutant isotopes (^{64}Ni, ^{64}Zn, and ^{66}Zn) are not radioactive, thus eliminating the use of any radiation-based techniques such as activation analysis. The ^{60}Co isotope is radioactive, however, and although it is generated at small enough levels in FFTF that it does not influence the conductivity significantly, it does reach levels that discourage the use of wet chemistry techniques to measure the nickel and zinc concentrations.

Another approach in addressing this problem is to use the observed changes in electrical conductivity to assess the accuracy of the calculated transmutation rates. Even this approach involves some uncertainties, which arise from the lack of full knowledge of the role of various other contributions to conductivity changes. These uncertainties can be addressed, however, by comparing two types of alloys with different responses to irradiation.

This report presents an assessment of the contributions of void swelling and transmutation to radiation-induced conductivity changes in MARZ copper (99.999% pure) and two commercial copper products, the GlidCop CuAl20 and CuAl25 alloys manufactured by SCM Metal Products. These materials were irradiated in FFTF as part of a "second generation" copper irradiation experiment conducted at ~415-C to displacement levels ranging from 34 to 151 dpa.[7]

Assumptions Employed

This assessment assumes that the recently revised [10] transmutation rates calculated for FFTF using the REAC code [11] are essentially correct, but possibly perturbed locally to some minor extent. Since the cobalt transmutation rates are approximately three orders of magnitude smaller than those of nickel and zinc (see Table 1), it is further assumed in these calculations that only these latter two elements contribute significantly to the observed decrease in conductivity. Another assumption is that, to the first order, only void swelling and transmutation contribute to the conductivity decrease.

---

[a]Pacific Northwest Laboratory is operated for the U.S. Department of Energy by Battelle Memorial Institute under Contract DE-AC06-76RLO 1830.

Radiation-induced changes in the dislocation density introduced by mechanical deformation of the CuAl20 and CuAl25 or dislocation evolution in pure copper are assumed not to cause significant changes in conductivity, It is known for instance, that in pure copper a cold work level of 50% lowers the conductivity only by 3 to 4 %IACS (International Annealed Copper Standard).[12] Typical dislocation densities induced into pure copper during irradiation are much lower than that induced by cold-working (CW)[13]. In the CuAl20 (20% CW) and CuAl25 (50% CW) alloys, the starting dislocation density relaxes to some degree as the alloys recrystallize 100% and 40%, respectively, after irradiation to 50 dpa at ~415°C.[14]

It is further assumed that segregation of the nickel and zinc, if it occurs, does not alter the overall conductivity and also that the Al_2O_3 dispersoids in the CuAl20 and CuAl25 alloys remain undissolved. The latter assumption is important because aluminum and oxygen in solution each exert a strong influence on electrical conductivity. Both of these assumptions will be critiqued in the Discussion section.

Transmutation Elements	wt%/year[1]	Resistivity Change
Nickel	0.29	1.28 μohm-cm/wt% Ni[2]
Zinc	0.29	0.27 μohm-cm/wt% Zn[2]
Cobalt	0.0002	7.7 μohm-cm/wt% Co[3]

Table 2. Models Describing the Void* and Transmutation Contributions to Electrical Behavior

Modified Loeb's equation	$\rho^{eff} = (\rho_0 + \rho_{trans}) \left[\frac{1}{1 - \left(\frac{\Delta V}{V_f} \right)^{2/3}} \right]$
Modified Russell's equation	$\rho^{eff} = (\rho_o + \rho_{trans}) \left[\frac{1 + \frac{\Delta V}{V_f} - \left(\frac{\Delta V}{V_f} \right)^{2/3}}{(\quad)^{2/3}} \right]$
Modified Euken's equation	$\rho^{eff} = (\rho_o + \rho_{trans}) \left[1 + \frac{1}{2} \left(\frac{\Delta V}{\quad} \right) \right]$

* $\frac{\Delta V}{V_f}$ *is the void volume fraction.*

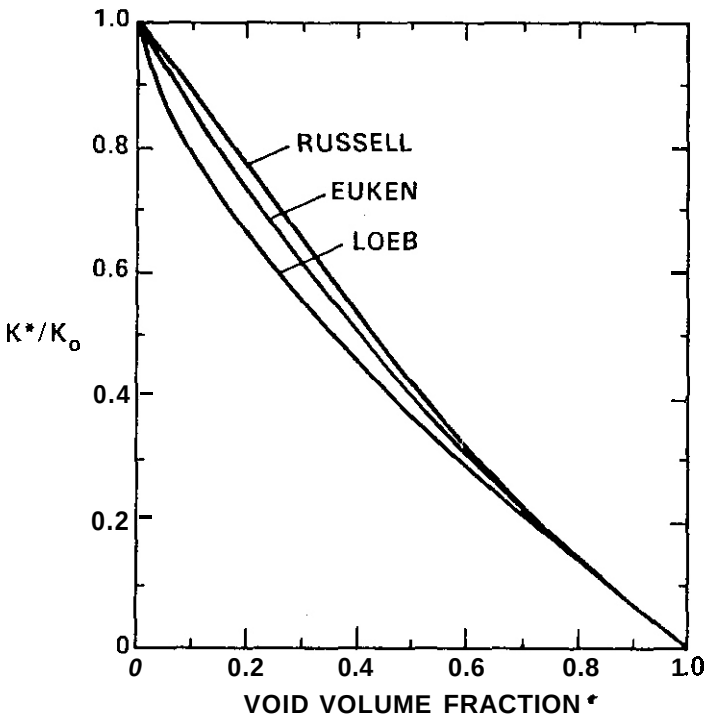

Fig. 1. Comparison of various models describing the contribution of voids to thermal conductivity change, as presented by Wolfer and Garner [ref. 17].

The Russell and Euken models were derived from Maxwell's relation for conductors and resistors. These two models allow the effective thermal conductivity of a porous solid to be calculated assuming a random distribution of either cubical or spherical cavities, respectively.[17] Loeb's model attempts to take into account more complex cavity shapes and orientations with respect to the flow path of the heat. Wolfer and Garner [20] chose Euken's model as the model having the best physical foundation. Each of the equations listed in Table 2 have been formulated by Wolfer and Garner in terms of the void volume fraction (and not swelling) for the special case of randomly oriented, spherical voids.

Unfortunately, however, it is very difficult to measure the thermal conductivity of highly radioactive specimens. It is much easier to measure the electrical conductivity. The thermal conductivity of metals is governed primarily by the conduction electrons, however, which allows the electrical conductivity, a, to be used to estimate the thermal conductivity, κ. This approach is based on the direct proportionality between the two conductivities at a given temperature, according to the Wiedemann-Franz law:

$$\sigma = \frac{\kappa}{LT}$$

where L is the Lorenz number and T is the absolute temperature. Based on this relationship the electrical conductivity was directly substituted for the thermal conductivitv. The equations were then formulated in terms of electrical resistivity, ρ, using the inverse relationship $\rho = 1/\sigma$. The swelling contribution in each model is assumed to operate on the transmutation-enhanced value of resistivity, represented by $(\rho_i + \rho_{trans})$.

The effective electrical resistivity ρ^{eff} was calculated using each of the three models. The electrical conductivity was calculated from the effective resistivity through use of the following equation:

$$\sigma = \frac{172.41}{\rho^{eff}} \quad (\%IACS) ,$$

since a copper wire with 100 %IACS conductivity has a corresponding resistivity of 1.7241 μohm-cm.[16]

Within the range of transmutation levels reached (< 1 wt% Ni or Zn) at 150 dpa, the resistivity of copper is assumed to increase linearly with nickel and zinc. Figure 2 shows that this assumption is valid for nickel and zinc in copper.[21]

Results

The swelling measured in CuAl20 to date is very small (<1% at 150 dpa) and somewhat variable. No swelling has yet been measured in CuAl25. Therefore these two materials were chosen to assess the validity of the recently revised REAC calculations of transmutation.[10] The predicted increase in resistivity for CuAl20 was found to be overpredicted using REAC-calculated rates. If the transmutation rates are reduced by 15%, however, the predicted and measured values for CuAl20 agree reasonably well (as shown in Figure 3) with the best fit arising from the use of either the Russell or Euken models. These two models yield essentially the same result at low values of swelling. A similar comparison for CuAl25 is shown in Figure 4, the data of which exhibited a somewhat larger degree of scatter. The transmutation rates were also reduced by 15% for this comparison.

The combined effect of transmutation and void swelling is illustrated in the conductivity behavior observed in MARZ copper, shown in figure 5. The effect of transmutation remains unchanged, but a swelling rate of ~0.5%/dpa causes the conductivity to fall rapidly throughout the irradiation sequence. Again, Euken's and Russell's models yield similar results; however, it appears that the use of Euken's model matches the data more clasely. It yields a good fit to the observed behavior if we once again assume a 15% reduction in the predicted transmutation rate.

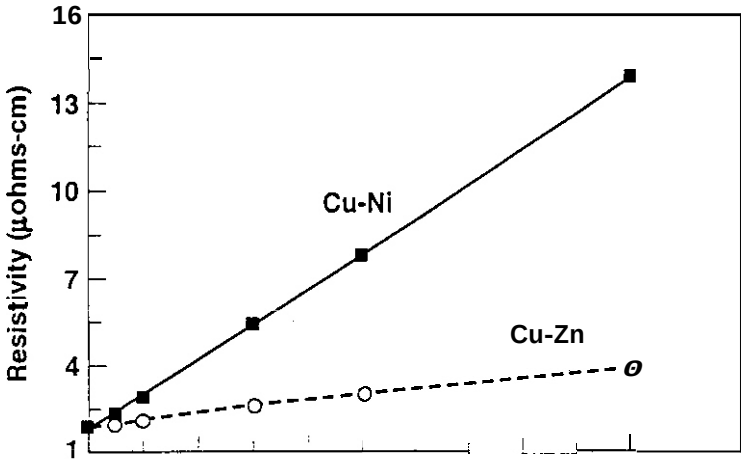

The scatter shown in the data arise not only from the variability of the swelling process but also from the difficulty of measuring the electrical conductivity of very radioactive specimens. This usually requires that the swelling is measured on the TEM disk while the conductivity is usually (but not always) measured on the gauge section of a minitensile specimen. Although these two types of specimens were irradiated together, it does not preclude the possibility of somewhat different responses caused by the natural

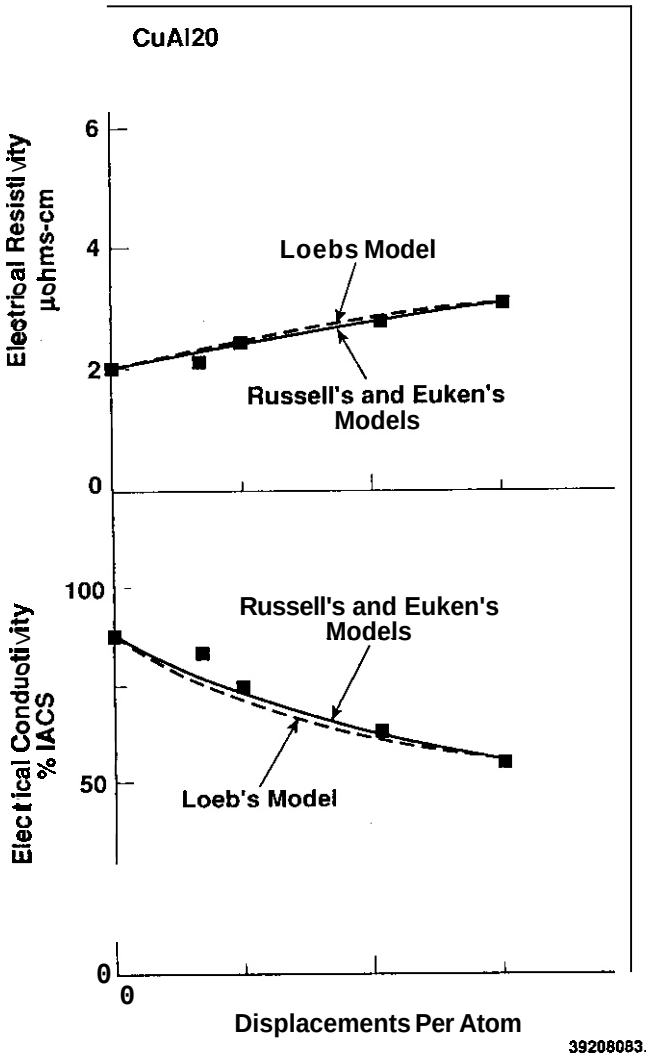

Fig. 3. Comparison of predicted and observed changes in the electrical behavior of CuAl20, assuming that the transmutation rates are 15% lower than calculated by the REAC code.

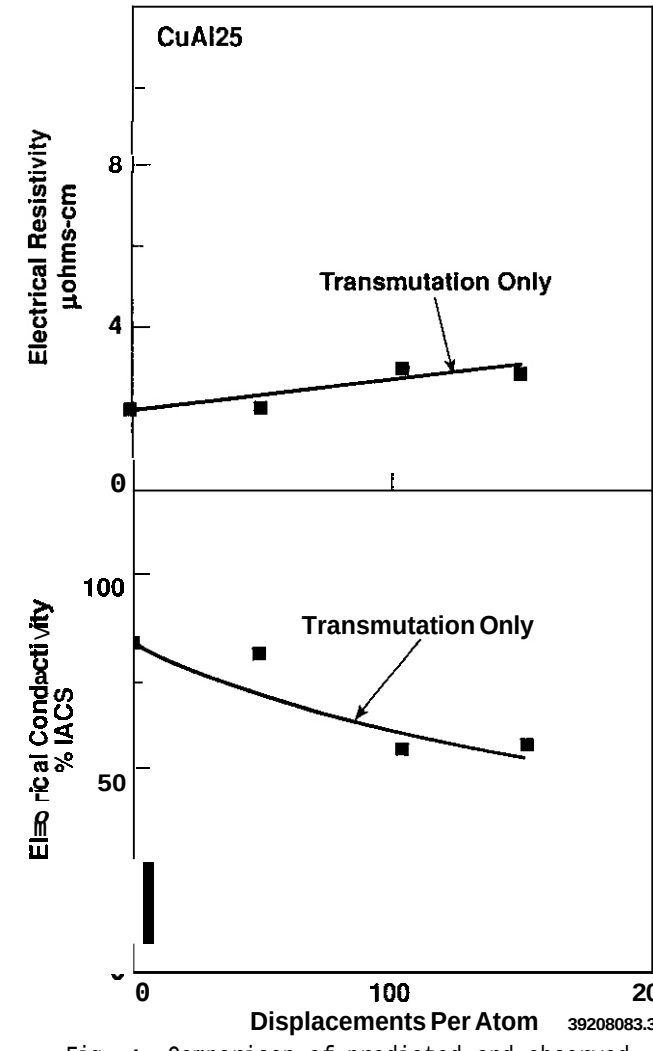

Fig. 4. Comparison of predicted and observed changes in the electrical behavior of CuAl25, assuming that the transmutation rates are 15% lower than calculated by the REAC code.

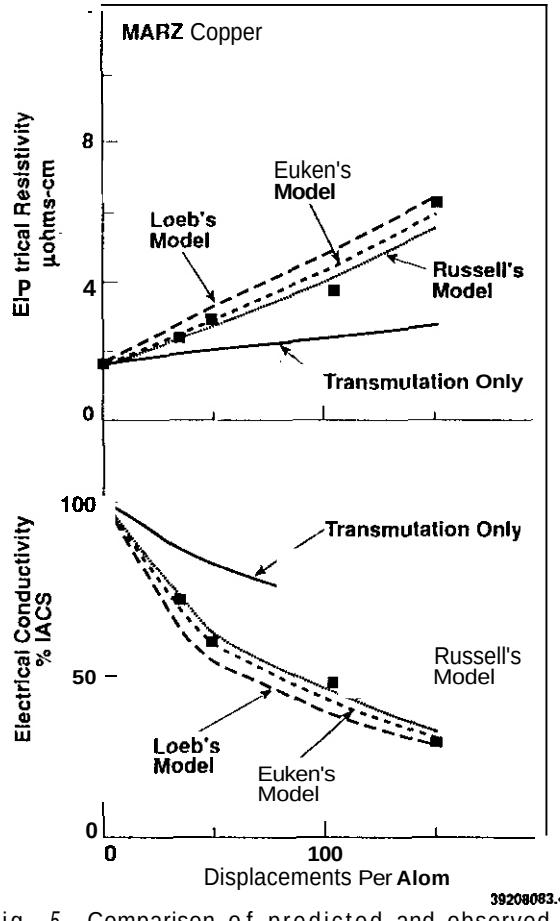

Fig. 5. Comparison of predicted and observed changes in the electrical behavior of MARZ copper, assuming that the transmutation rates are 15% lower than calculated by the REAC code.

If we ignore this variability it appears that the transmutation rates recently calculated for FFTF are only slightly larger (–15%) than those needed to reproduce the behavior observed in MARZ copper and the two GlidCop alloys. If the assumption that the Al_2O_3 particles do not dissolve during irradiation is incorrect, however, then the transmutation rates may need to be lowered even more. Edwards and coworkers [7] have calculated that the complete dissolution of the Al_2O_3 in CuAl25 would by itself yield a conductivity of ~68 %IACS. This is 7 %IACS lower than the observed conductivitv of the irradiated CuAl25 (with transmutants), indicating that very little of the aluminum and oxygen is in solution. In order to confirm this conclusion. the deuree of Al_2O_3 dissolution is now being measured in the-second generation series of copper irradiation experiments.

There are no Al_2O_3 particles in the MARZ copper, however, and the success in predicting the conductivity behavior using a 15% reduction in the predicted transmutation rates strongly suggests that the Al_2O_3 particles in the GlidCop alloys do not dissolve to any significant degree. According to Brager[8], Al_2O_3 dispersoids still exist in CuAl25 after irradiation at ~400°C to 63 dpa. Another possibility is that some fraction of the aluminum and oxygen are in fact in solution during the irradiation, but precipitate out of solution during the period following the end of the irradiation but before the specimens are removed from the reactor. This might allow the dissolved aluminum and oxygen sufficient time to reprecipitate. This in turn would appear to shift the size distribution to smaller sizes as observed by Zinkle and coworkers.[22] While the post-irradiation conductivity measurements would not be influenced by this redistribution, the reprecipitation will yield a higher conductivity than that existing during irradiation.

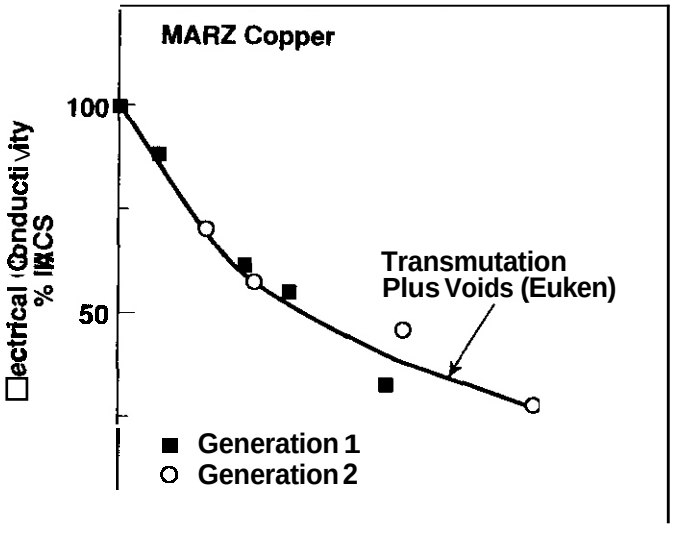

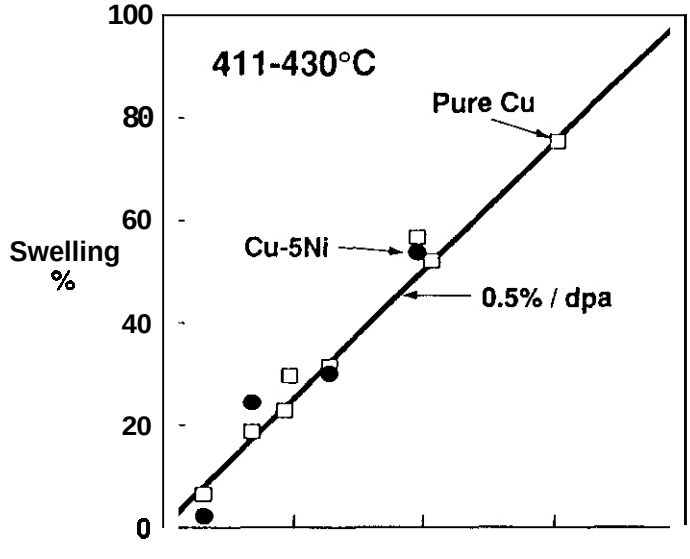

A 15% decrease in the transmutation rates does not necessarily require that the displacement rates must also he decreased by 15%. The required reductions may he smaller. While most displacements result from neutrons having relatively high energies, the nickel and zinc transmutants are produced primarily by lower energy neutrons.[10] The flux uncertainties at these lower energies are larger, due not only to calculational and measurement difficulties, but also to the presence of neighboring experiments which may contain materials such as europium oxide [23] that are strong absorbers of neutrons at lower energies. Since the ^{63}Cu and ^{65}Cu (n,γ) reactions exhibit a similar dependence on neutron energy, it is felt that reducing both the nickel and zinc transmutation levels by the same percentage is a realistic assumption.

The Euken model also appears to offer a marginally better prediction of the void contribution to changes in the electrical properties at higher swelling levels. Data scatter arising from the difficulty of measuring electrical resistivity on such highly radioactive specimens precludes a more confident comparison between the Russell and Euken models, but the Euken model was thought to be more physically realistic by Wolfer and Garner.[17]

Muroga and coworkers [24] have recently shown that during electron irradiation nickel segregates toward grain boundaries while zinc is depleted. No precipitation occurs as a consequence of this redistribution. The same type of redistribution probably develops at void surfaces also. It is felt by the authors, however, that averaged over the volume of the individual grains, the net effect of segregation (without precipitation) on the electrical properties is not significant, as long as the influence of each transmutant on conductivity is proportional to concentration (as shown in Figure 2).

CONCLUSIONS

The predicted levels of solid transmutants produced in MARZ copper and two copper alloys during irradiation in FFTF may be as much as 15% too high. This difference probably reflects uncertainties in neutron fluxes and spectra at the lower neutron energies. The major contributions to conductivity changes appear to be void swelling and the formation of solid transmutants. Dissolution of Al_2O_3 dispersoids and segregation of nickel and zinc transmutants do not appear to be major contributors.

REFERENCES

1. Conn, R.W., Chuyanov, V.A., Inoue, N., and Sweetman, D.R., Scientific American, April 1992, p. 103.

2. Vieider, G., Cardella, A., Akiba, M., Matera, R., and Watson, R., Fusion Eng. and Design, Vol. 16, 1991, pp. 23-34.

3. Zolti, E., Fusion Eng. and Design, Vol. 16, 1991, pp. 163-171.

4. Munz, D. and Diegele, E., Fusion Eng. and Design, Vol. 16, 1991, pp. 45-57

5. Garner, F.A., Hamilton, M.L., Edwards, D.J., Newkirk, J.W., Stubbins, J.F., and Mitchell, M.A., Proceedings of the 5th International Conference on Fusion Reactor Materials, Clearwater, Florida, 1991.

6. Garner, F.A. and Anderson, K.R., Fusion Reactor Materials Semiannual Progress Report DOE/ER-0313/7, 1989, p. 220.

7. Edwards, D.J., Newkirk, J.W., Garner, F.A., Hamilton, M.L., Nadkarny, A., and Samal, P., Proceedings of the 5th International Conference on Fusion Reactor Materials, Clearwater, Florida, 1991.

8. Brager, H. R., J. Nucl. Mater. 141-143, 1986, p. 79.

9. Garner, F.A., Brager, H.R., and Anderson, K.R., J. Nucl. Mater., Vol. 179-181, 1991, p. 250.

10. Garner, F.A., Greenwood, L.R., and Mann, F.M., in this semiannual report.

11. Mann, F.M., Transmutation of Alloys in MFE Facilities as Calculated by REAC, HEDL-TME 81-37, Hanford Engineering Development Laboratory, August, 1992.

12. Tyler, D.E., Metals Handbook, vol. 2, 10th ed., ASM International, 1990, p. 276.

13. Brager, H. R., J. Nucl. Mater. 141-143, 1986, p. 163.

14. Anderson, K.R., Garner, F.A., Hamilton, M.L., Stubbins, J.F., Proceedings of the 15th ASTM International Symposium on Effects of Radiation on Materials, June 1990, ASTM STP 1125 (in press).

15. Butterworth, G.J., J. Nucl. Mater., Vol. 135, 1985, p. 160

16. Gregory, P., Bangay, A.J., and Bird, T.L., Metallurgia, Vol. 71, 1965, p. 207.

17. Loeb, A.L., J. Amer. Cer. Soc., Vol. 18, 1954, p. 96.

18. Russell, J. Amer. Cer. Soc., Vol. 18, 1935, p. 1

19. Euken, A., Forsch. Geb. Ingenieurw., 83, Forschungsheft No. 353, 1932.

20. Wolfer, W.G. and Garner, F.A., Damage Analysis and Fundamental Studies Quarterly Progress Report, DOE/ER-0046/17, May 1984, p. 58.

21. Ho, C. Y., Ackerman, M. W., Wu, K. Y., Havill, T. N. Bogaard, R. H. Matula, R. A., Oh, S. G., and James, H. M., J. Phys. Chem. Ref. Data, Vol. 12, No. 2, 1983, p. 183.

22. S. J. Zinkle, A. Horsewell, B. N. Singh and W. F. Sommer, submitted to J. Nuclear Mater

23. Garner, F.A. and Hamilton, M.L., in this semiannual report.

24. Muroga, T., Ishimaru, E., and Yoshida, N., presented at the 16th International Symposium of Effects of Radiation on Materials, Denver, Co., 1992.

Status of Low Cycle Fatigue Studies on Irradiated Copper - F. A. Garner (Pacific Northwest Laboratory)[a], B. N. Singh (RISØ National Laboratory) and J. F. Stubbins (University of Illinois)

OBJECTIVE

The objective of this effort is to provide data on the response to radiation of copper alloys selected for service in the ITER divertor plate assembly.

SUMMARY

A joint irradiation program is being conducted by the RISØ National Laboratory, Pacific Northwest Laboratory and the University of Illinois to study the influence of neutron irradiation on the low cycle fatigue behavior of copper alloys. This program is directed toward both NET and ITER goals. Radiation is proceeding on miniature specimens in the OR-3 reactor in RISØ, and identical specimens have been prepared for the COBRA-IA experiment in EBR-II. A sire effect study on unirradiated specimens is in progress.

PROGRESS AND STATUS

Introduction

Pure copper and GlidCop CuAl25 are currently being considered as high heat flux structural components in the ITER divertor plate assembly. Data are required on the radiation performance of these materials and other studies are in progress to provide data on void swelling, tensile properties and electrical conductivity.

One of the most important properties for high heat flux applications, however, is the low cycle fatigue behavior, which is used to assess the mechanical strain contribution of thermal cycling on component lifetimes. A joint U.S./E.C. research program involving neutron irradiation of pure copper and GlidCop CuAl25 in the form of low cycle fatigue specimens is now in progress. The participants are the RISØ National Laboratory in Denmark, Pacific Northwest Laboratory and the University of Illinois. The program is directed toward serving the goals of both the ITER (International Thermonuclear Experimental Reactor) and NET (Next European Torus) programs.

Specimen Description

The specimens employed are not full-size tensile fatigue specimens as defined by ASTM standards but are typical of those employed in many fatigue studies. As shown in figure I the specimens are 6 mm in maximum diameter by 50 mm long, with the gauge section 7 mm in length and 3.1 mm in diameter. The pure copper specimens were cut from OFHC copper and then fully annealed, while the CuAl25 specimens were cut from the as-wrought condition as supplied to RISØ National Laboratory by SCM Metals Products. All specimens were prepared at RISØ to preserve uniformity between the various tests.

Irradiation Program in DR-3

The OR-3 mixed spectrum reactor at the RISØ National Laboratory is currently being used to provide data on the tensile and low cycle fatigue behavior of OFHC copper and CuAl25. Tensile specimens are also included for CuNiBe and CuCrZr, the latter being the E.C. version of MZC. This reactor has a neutron flux of 3.3 x 10^{13} n/cm^2 (E>1.0 MeV) and produces ~0.5 dpa in copper in 87 days. Irradiation is scheduled for room temperature, 100, 250, 350 and 450°C, with irradiation being conducted one temperature at a time.

There are ten identical specimens of each alloy at each temperature, each contained in an aluminum tube. The temperatures are controlled by a combination of gas mixture change and electrical heating. In subsequent irradiation sequences at temperatures above 100°C, the CuNiBe and CuCrZr may be deleted, and the program would then concentrate on the OFHC copper and CuAl25 specimens.

Irradiation Program in PIREX

An irradiation program similar to that in DR-3 has been conducted in the PIREX 600 MeV Proton Irradiation Facility at the Paul Scherrer Institute in Switzerland. The target exposure was 0.5-0.6 dpa and is expected to produce 50-60 appm He. The ~100 appm He/dpa produced in this irradiation is much larger than that expected in fusion-relevant neutron spectra but should provide a conservative indication of the possible effect of helium on fatigue behavior. In addition to the tensile fatigue specimens, sheet tensile specimens are also being irradiated in PIREX.

'Pacific Northwest Laboratory is operated for the U.S. Department of Energy by Battelle Memorial Institute under Contract DE-AC06-76RLO 1830.

Irradiation Program in EBR-II

Whereas the irradiations in DR-3 and PIREX are being conducted to ~0.5 dpa, the EBR-II program will produce displacement levels between 5 and 15 dpa. The EBR-II inlet temperature of ~360°C limits the irradiations to temperatures of ~375°C and above. A full description of this program is contained in a companion report[1]. All specimens have been prepared and placed in helium-filled subcapsules to await insertion into the COBRA-1A subassembly.

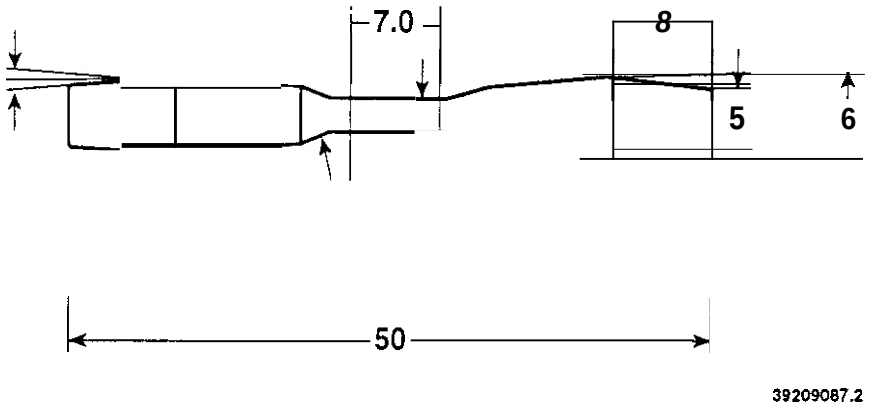

Fig. 1. Specimen dimensions of miniature tensile fatigue specimen. All dimensions are in mm.

Tests on Unirradiated Specimens

Room temperature fatigue tests are being conducted jointly by the University of Illinois and Pacific Northwest Laboratory, using both ASTM standard specimens and the miniature specimens described earlier. Comparison of the response of the two specimen sizes will be used to assess the impact of the reduced specimen size. Fatigue tests on unirradiated specimens at elevated temperatures will be conducted at RISØ with personnel assistance from Pacific Northwest Laboratory (D. J. Edwards). The test parameters are 10^5 cycles to failure (maximum), strain amplitude 0.01 to 1.0%, and $<10^{-5}$ torr vacuum.

All tests on neutron-irradiated specimens will be conducted at RISØ, while those from PIREX will be conducted at the Paul Scherrer Institute.

REFERENCES

1. F. A. Garner and M. L. Hamilton, COBRA-1A Copper Irradiation Experiment in EBR-11, this semiannual report.

6.5 Environmental Effects in Structural Materials

DEVELOPMENT OF ELECTRICAL INSULATOR COATINGS FOR LIQUID-METAL BLANKET APPLICATIONS

J.-H. Park, M. R. Fox, and G. Dragel (Argonne National Laboratory)

OBJECTIVE

Corrosion resistance of structural material and magnetohydrodynamic (MHD) force and its subsequent influence on thermal hydraulics and corrosion are major concerns in the design of liquid-metal blankets for magnetic fusion reactors (MFRs). The objective of this study is to develop stable ceramic coatings at the liquid-metal/structural-material interface. with emphasis on electrically insulating coatings that prevent adverse MHD-generated currents from passing through the structural walls.[1,2]

SUMMARY

Based on a preliminary survey of more than 15 oxides and nitrides, four ceramic materials (CaO, MgO, Y_2O_3, and BN) were identifled as candidates for insulator coating development.[3] These compounds were fabricated by various techniques and exposed to flowing Li at 400-410°C to assess chemical compatibility. Yttrium oxide exhibited excellent corrosion resistance in flowing liquid Li at 400°C; its corrosion rate was calculated to be 0.042 μm/yr.[4] Resistivity measurements by a standard four-probe method on Y_2O_3 in air at temperatures between ≈450 and 1000°C. before and after exposure to Li for 675 h at 410°C. indicated no deterioration in resistivity. The resistivity of in-situ-formed $(V,Ti)_xN$ reaction-product layers on V-20Ti and TIN on Ti was determined at room temperature and 80°C by a two-probe method. The resistivity of the film on the V-20Ti alloy was low (≈20 Ω·m) and the film on Ti exhibited metallic conduction.[5-7] Adhesion bonding between Y_2O_3 and Y, V, Ti, Y, V-20Ti, V-3Ti-1Si, and Types 304 and 316 stainless steel was investigated in reducing and oxidizing gaseous environments at 927°C. Except for the V-20Ti alloy. the V-base alloys, Ti, and Type 304 stainless steel were well bonded to Y_2O_3 in the reducing atmosphere. In the oxidizing atmosphere, bond regions of Types 304 and 316 stainless steel were better than in the reducing atmosphere because of reaction between the oxide scale on the steels (Cr_2O_3) and Y_2O_3 to form $YCrO_3$. Neither V. Ti, nor the V-alloys bonded with Y_2O_3. These results suggest that a low-melting eutectic layer forms between Y_2O_3 and the oxides layers present on V, Ti, and the V-alloys.

PROGRESS AND STATUS

Introduction and Background

MHD forces *and* their effects on corrosion, heat transfer, and pressure **drop are** a key concern with a V-alloy/Li system for first-wall applications in a magnetic fusion reactor (MFR). MHD effects could be reduced significantly by placing an electrical insulator coating at the V-alloy/Li interface.[2] For a material to work as an insulator coating in this environment, it must first meet two criteria: high corrosion resistance and electrical resistivity $>10^2$ Ω·m when exposed to Li and a radiation field. Corrosion tests have been conducted on candidate coating/substrate combinations in liquid Li.[4] The coating materials selected on the basis of chemical stability include BN, Y_2O_3, Cr_2O_3, MgO, CaO, Si_3N_4, V_2O_5, and in-situ coatings of calcium vanadate and a V-Ti-N reaction-product layer formed on V-20Ti in flowing Li. Electrical resistivity measurements have been made on some of the coating materials before and after exposure to Li.

Lithium compatibility studies indicated that failure resulted from one of three causes: (1) thermodynamic instability (Si_3N_4), (2) incomplete densification (CaO, MgO), or (3) impurities in the ceramic (BN). One of the most promising materials being considered for application **as** an electrical insulator coating in MFRs is Y_2O_3. Previous work has shown that Y_2O_3 has a low corrosion rate[3,8] and no gross loss of resistivity in static Li.[8]

Experimental Procedures and Results

1. Compatibility of Y_2O_3 with Liquid Lithium

Y_2O_3 was prepared by hot-pressing and sintering. as previously described by Wang et al.[3] The surface area was determined by micrometer, and weight was obtained with an Ohaus GA110 balance. The Y_2O_3 was then exposed in a facility for fatigue testing in Li[9] for 675 h at 405°C. Weight loss was measured and corrosion rate was determined. One specimen, with a surface area of 234 mm^2, showed no weight loss: another, with a surface area of 60.4 mm^2, had a weight loss of 100 μg and a corrosion rate of 0.042 μm/yr.

Y_2O_3 samples were examined by X-ray diffraction (XRD), electron energy dispersive spectroscopy (EDS), secondary ion mass spectroscopy (SIMS), and induction-coupled plasma spectroscopy (ICP) before and after exposure to Li to obtain more detailed information on compatibility and possible incorporation of Li into Y_2O_3. The XRD and EDS analyses did not reveal any differences in the as-received and Li-exposed specimens. The SIMS results in Fig. 1 indicate that Li diffused into the specimen and the $^6Li/^7Li$ ratio corresponded to the natural abundance of these isotopes. The ICP result for the concentration of Li in the Y_2O_3 specimen was 14 μg/g.

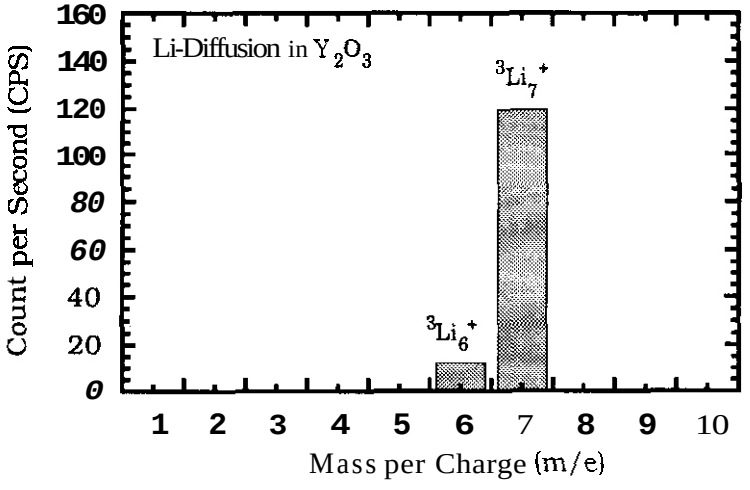

Figure 1. *SIMS* measurement of *Li in* Y_2O_3 after exposure at 410°C for 675 h.

2. Resistivity Measurements on Y_2O_3

Resistivity of Y_2O_3 was measured in air at temperatures between 400 and 1000°C. Two- and four-probe techniques[10] were used below and above 700°C. respectively. Exposed and unexposed samples were carefully sectioned, and four Pt electrodes were attached to notched specimens with Ag paint. A current I was passed through the outside two electrodes with a Keithley 263 Calibrator/Source, and the voltage drop V was measured across the two inside electrodes with a Data Precision 3500 voltmeter. Resistance R and resistivity ρ were calculated from Eqs. 1 and 2.

$$R = V/I \quad (1)$$

$$\rho = R(a*b)/c. \quad (2)$$

The data in Fig. 2 indicate that the resistivity of the Li-exposed sample is higher than that of the unexposed sample at temperatures <700°C. This suggests that Y_2O_3 at high O pressures (air) is a p-type electron-hole material. as was proposed previously.[11] When Li is incorporated into the lattice. electrons

are produced as a charge–compensating defect, and consequently, the concentration of mobile holes decreases by the process of hall-electron coupling. Because of equipment and sample size limitations, the highest resistivity that we could measure was 10^{12} Ω·m. Extrapolation of high–temperature data to lower temperatures is consistent with a resistivity of ≈10^{16} Ω·m for Y_2O_3 at room temperature."

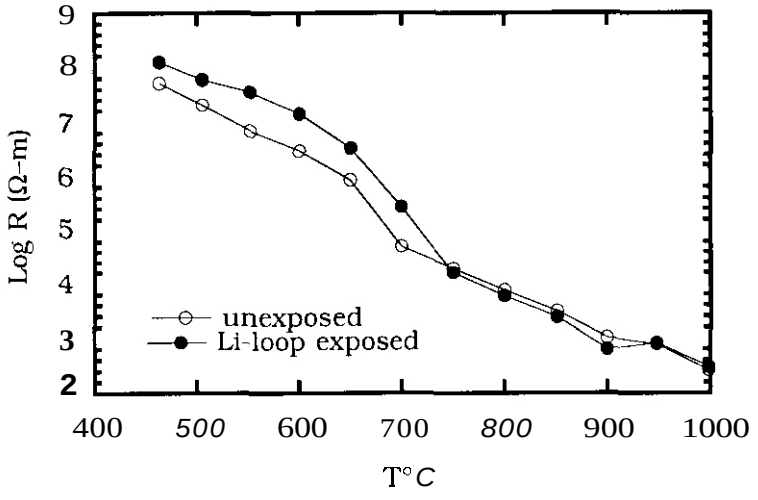

Figure 2. Electrical *resistivity of* Y_2O_3 in air *before* and after exposure to Li at 410°C for 675 h.

3. Resistivity Measurements on In-Situ–Formed $(Ti,V)_xN$

The electrical resistivity of the reaction–product film formed on V-20Ti during exposure to Li for 1384 h at 538°C was measured by the two–probe method. An XRD spectrum indicated that the film was V_2N, but this could not be confirmed by a powder diffraction pattern of material from the specimen surface. Electrical resistivity was 20 Ω·m at room temperature and increased by ≈30% at 80°C. In-situ formed films of TiN on Ti showed metallic conduction[12–14] and did not have a high enough resistivity for use as insulator coatings in MFR systems.

Although the extent of interdiffusion between N and the V-20Ti alloy was not evaluated. interdiffusion has been investigated in several metal/nitride systems. In general. most nitride ceramics are used either as hard coatings or oxidation–resistant coatings. Table 1 contains information from the literature on diffusivity in several materials.[15] An extrapolation of the high–temperature data to the 425–700°C range indicates a diffusion distance of <2 μm in one year.

4. Adhesion of Y_2O_3 Coatings to Alloy Substrates

Tests were conducted to determine the adhesion between Y_2O_3 and Y, V, Ti, V-20Ti, V-3Ti-1Si, and Types 304 and 316 stainless steel, Sintered discs of Y_2O_3 were obtained from Aldrich Chemical *Co.*. Inc. (10.3 mm in diameter x 4.0 mm thick). The discs were cut to a thickness of ≈2.0 mm and ground flat on Struers™ 4000 silicon carbide paper, The discs were then fired at 1000°C for 16 h in air. A thin disc of each metal was placed between two Y_2O_3 discs and the entire stack, with its cylindrical axis vertical, was placed in a furnace. By means of three springs, a compressive force was applied to the stack by an alumina rod. A detailed description of the apparatus is reported elsewhere.[16] The specimens were annealed at 987°C for 66 h in a flowing, reducing atmosphere of 3%H_2–N_2; a similar test was conducted in an oxidizing atmosphere (50 ppm O_2–N_2). The stack was sectioned in the vertical direction and Polished to examine the metal/Y_2O_3 interface regions.

Table 1. Interdiffusion in Metal/Ceramic Systems

Couple	Temp. (°C)	Do (cm^2 s^{-1})	Q (kcal/mole)	Composition of diffusion zone
V-Si_3N_4	1200-1500	1.7	74	V_3Si, V_5Si_3, VSi_2
Ti-Si_3N_4	1200-1400	4×10^{10}	145	Ti_5Si_3
Nb-Si_3N_4	1400-1600	10^7	141	Nb_5Si_3 + $NbSi_2$
Ta-Si_3N_4	1400-1650	401	104	Three Phases
V-AlN	1300-1550	0.3	67	-
Ti-AlN	1200-1400	0.07	63	T<1280°C
		4×10^{17}	192	T>1280°C
Nb-AlN	1400-1600	13	90	
Ta-AlN	1780	No diffusion detected after 70 h		

Source: Ref. 15

The overall results of the adhesion tests in the two environments are presented in Table 2, and SEM photomicrographs of the various alloy/Y_2O_3 interface regions after exposure to the reducing atmosphere are shown in Fig. 3. Except for the V-20Ti alloy, the V-alloys. Ti. and Type 304 stainless steel were well bonded to Y_2O_3 in the reducing atmosphere. In the oxidizing atmosphere, bond regions were better than in the reducing atmosphere for Types 304 and 316 stainless steel because of the reaction between the oxide scale (Cr_2O_3) and Y_2O_3 to form $YCrO_3$. Neither V, Ti, nor the V-alloys bonded with Y_2O_3. This finding suggests that a low-melting eutectic layer forms between Y_2O_3 and the oxide layers present on the V-alloys. V, and Ti. Oxygen diffusion in Y_2O_3 is too high[11] to protect the V. Ti, and V-alloy substrate from further oxidation.

Table 2. Results of Adhesion Tests between Y_2O_3 and Various Metals

Alloy	Bond test at 987°C for 66 h in a 3%H_2-N_2 environment		Bond test at 987°C for 66 h in a 50 ppm O_2-N_2 environment	
Y(I)	Good bond	Diffusion of O from Y_2O_3 to Y and Y diffusion from Y to Y_2O_3	No bond	Temperature too low for bonding between Y_2O_3 scale and Y_2O_3 disc
Y(II)	Good bond	[See Y(I); two samples tried]	No bond	[See Y(I)-two samples tried]
V	Good bond	Narrow diffusion	No bond	Interface weakness V-oxide/Y_2O_3 or formation of low melting phase
TI	Good bond	TI diffusion to Y_2O_3	No bond	Temperature too low
V-20Ti	No bond	Ti depletion from the alloy and Ti diffusionto Y_2O_3	No bond	Interface weakness V. Ti-oxide/Y_2O_3 or formation of low melting phase
V-3Ti-1Si	Partial bond	Vacancy coagulation at Interface	No bond	--
304 SS	Bond	Very narrow diffusion layer for bonding	Good bond	$YCrO_3$ formation at the interface Cr_2O_3-Y_2O_3
316 SS	Bond	Too narrow a diffusion layer for bonding	Good bond	$YCrO_3$ formation at the interface Cr_2O_3-Y_2O_3

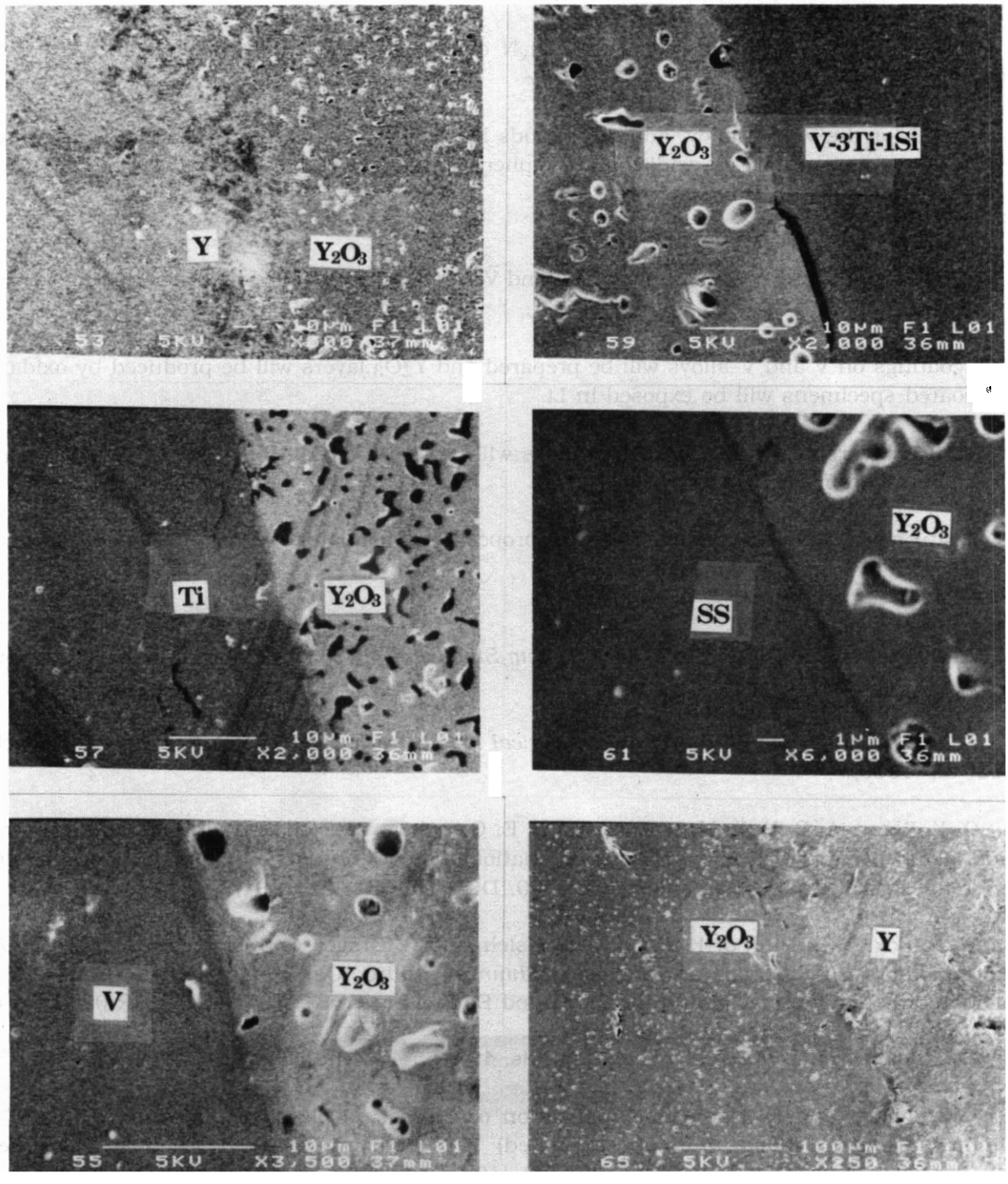

Figure 3. *SEM* photomicrographs *of* the *alloy/Y_2O_3* interface after exposure to a reducing atmosphere at *927°C* for 66 h

CONCLUSIONS

1. Ceramic electrical insulator coatings have great potential for **MFR** applications. Based on the chemical stability tests in Li thus far, Y_2O_3 appears to be a viable candidate for a ceramic insulator. Resistivity measurements by a standard four-probe method on Y_2O_3 in air at temperatures between ≈450 and 1000°C. before and after exposure to Li for *675* h at 410°C. indicated no deterioration in resistivity.

2. The resistivity of in-situ-formed $(V,Ti)_xN$ on V-20Ti was low (≈20 Ω·m) and TiN films on Ti exhibited metallic conduction.[5-7]

3. Except for the V-20Ti alloy, adhesion bonds between Y_2O_3 and Y. V. Ti, and V–3Ti–1Si were good in a reducing atmosphere. In an oxidizing atmosphere, neither V, Ti, nor the V–alloys bonded with Y_2O_3.

FUTURE WORK

1. In situ coatings of Ca, Si, Al, and Y on V and V–alloys will be studied by dissolution of Ca. Si, Al, and Y in Li.

2. Y coatings on V and V–alloys will be prepared and Y_2O_3 layers will be produced by oxidation. The coated specimens will be exposed in Li.

3. $(V,Ti)_xN$ layers on V–Cr-Ti and V-Ti alloys will be fabricated and exposed to Li to determine their chemical stability.

4. In situ methods for measuring electrical properties of insulator coatings in Li will be explored.

REFERENCES

1. C. C. Baker, et al., *Tokamak Power System Studies FY* **1985,** Argonne National Laboratory Report *ANL/FPP-85-2* (December 1985).

2. Y. Y. Liu and D. L. Smith, *Ceramic Electrical Insulators* **for** ***Liquid*** **Metal Blankets, J.** Nucl. Mater., **141-143**, 38 (1986).

3. D. Y. Wang, A. B. Hull, M. R. Fox, and C. E. Campbell, **Development** of **Ceramic Insulator Coatings** *for Liquid Metal Blanket Applications*, Oak Ridge National Laboratory Fusion Reactor Materials **Semiannual** Report for the Period Ending September 30, 1990, DOE/ER-0313/9 (1991).

4. M. R. Fox, A. B. Hull, J.–H. Park, J.–H. Hsieh, and G., Dragel. ***Corrosion*** and **Electrical** *Properties* of *Ceramic Insulators after Exposure to Flowing Lithium at 400°C,* Oak Ridge National Laboratory Fusion Reactor Materials Semiannual Report for the Period Ending March **31, 1991,** DOE/ER-0313/10 **(19911.**

5. **A** L. Ivanovsky, et al.: **J.** Phy. Chem. Solids, **49, 465-477** and **479-486** (1988).

6. **W.** Scharff and K. Hammer, 'Application of Optical, Mechanical resistant Coatings.' in ***High*** **Performance Ceramic** ***Films*** **and** ***Coatings,*** (ed) **P.** Vicenizini. Elsevier Science Publishers **B.V..** Amsterdam-Oxford-New York-Tokyo, pp. **695-711 (1991).**

7. M. R. **Fox, Fabrication** of **Ceramic Insulator Coatings for Liquid Metal Blanket Investigation.** Argonne National Laboratory Student Research Participation **Program** Report **(1992).**

8. J. E. Battles, **Materials for Advanced High Temperature Secondary Batteries.** Int. Mat. **Rev., 34.** 1 (1989).

9. O. K. Chopra and D. L. **Smith, Corrosion** of ***Ferrous Alloys*** **in** *a* **Flowing** ***Lithium*** Environment. J. Nucl. Mater., **133 & 134, 861 (1985).**

10 J.-H. Park and K. Natesan. **Electronic Transport** *in* **Thermally Grown** Cr_2O_3, Oxid. Met., **33, 31** (1990).

11. W. D. Kingery. et al., Introduction to Ceramics, 2nd. Edition, John Wiley and Sons, New York, p. 905 (1976).

12. H. Borgstedt. M. Grundrnann. J. Konys, and Z. Peric, A Vanadium Alloy for Application in a Liquid Metal Blanket of a Fusion Reactor. J. Nucl. Mater., 155-157. 690 (19881.

13. A. B. Hull, M. R. Fox. and J.-H. Hsieh. Vanadium-Base-Alloy Surface Modification for Liquid Metal Blankets and First-Wall in Magnetic Fusion Reactors. accepted for presentation at 5th Intl. Conf. on Fusion Reactor Materials, Nov. 17-22, 1991, Clearwater. FL.

14. G. Fenske and R. Erck. Ion Beams 'Nail' Thin Films. Ceramic Industry. March 25-28 (1991)

15. P. Lampaeter. S. Steeb, and A. Gukelberger. High-Temperature – High Pressures, 3, 727-740 (1971).

16. J.–H. Park and R. N. Blumenthal, Electronic Transport in 8 Mole Percent Y_2O_3–ZrO_2,, J. Electrochem. Soc., 136. 2867–2876 (1989).

AQUEOUS STRESS CORROSION OF CANDIDATE AUSTENITIC STEELS FOR ITER STRUCTURAL APPLICATIONS* - D. M. French, W. K. Soppet. and T. F. Kassner (Argonne National Laboratory)

OBJECTIVE

The corrosion resistance of the structural material to be used in an aqueous environment characteristic of candidate first-wall/blanket systems in the International Thermonuclear Experimental Reactor (ITER) has not been quantified. Information on the stress corrosion cracking (SCC) susceptibility of several candidate stainless steels under ITER-relwant conditions **will** help to identify an optimal combination of structural materials, coolant chemistry, and operational conditions for ongoing ITER design work. The objective of this task is to provide baseline information on SCC susceptibility of candidate stainless steels in high-purity oxygenated water that simulates many important parameters anticipated in ITER first-wall/blanket systems. SCC tests **will** also be conducted under off-normal water chemistry conditions and at higher temperatures to establish the performance limits of the materials.

SUMMARY

Susceptibility of Types 316NG and sensitized 304 stainless steels (SS) to SCC was investigated at temperatures of 60-289°C in slow-strain-rate-tensile (SSRT] tests in oxygenated water that simulates important parameters anticipated in first-wall/blanket systems. Several additional SSRT tests were performed on crevice specimens of Type 316NG SS in oxygenated water containing 100 ppb sulfate at temperatures between 150 and 289°C to establish the effect of temperature on SCC resistance. This steel exhibits good resistance to SCC under crevice and noncrevice conditions at temperatures <150°C in a nominal ITER coolant chemistry. In contrast, sensitized Type 304 SS exhibited intergranular stress corrosion cracking (IGSCC) at <100°C under crevice conditions. **SSRT** tests have been conducted on weldment specimens of Type 316L *SS* with matching filler metal under crevice conditions in oxygenated water containing 0.06-6.0 ppm chloride at 150-225°C. Most specimens fractured in the base metal, and several others fractured in the heat-affected zone (HAZ) of the weld, but none failed in the weld metal.

PROGRESS AND STATUS

Research and development needs[1] **of** the ITER with respect to aqueous corrosion include establishing a reliable data base on reference materials (viz., Types 316, 316L, and 316NG SS in the solution-annealed, cold-worked, and welded conditions). The nominal ITER water chemistry will most likely be high-purity water containing stable radiolysis/electrolysis products, e.g., dissolved O_2, H_2O_2, and H_2 at ppm levels, and ionic species at ppb levels, namely, soluble corrosion products and impurities in the makeup water and from release by ion-exchange resins in water purification systems. Higher concentrations of ionic impurities (e.g., Cl^-, SO_4^{2-}, H+. etc.) in the coolant may be present during off-normal operating and extended lay-up conditions of the system.

Although the nominal ITER coolant operating temperature is ≈60°C, periodic increases to 150°C and above might occur. Mechanical loads and temperature gradients across the first-wall structure will produce both static and cyclic stresses, which when coupled with residual tensile stresses associated with welds, can exceed the yield strength of the material. Tensile stresses above yield under cyclic operation (ITER =10^4 cycles) are conducive to crack propagation under corrosion fatigue conditions. Coolant-channel geometry and material microstructure in the heat-affected zone of weldments (both diffusion and fusion welds) can lead to crevice conditions that increase susceptibility of the materials to SCC.

Previous work[2,3] focused on developing criteria to define the simulated ITER water chemistry and establishing experimental methods for SSRT tests on noncrevice and crevice specimens. Results from

* **Work** supported **by** the Office of Fusion Energy, U.S. Department **of** Energy. under Contract W-31-109-Eng-38

experiments to evaluate SCC susceptibility from SSRT tests on Types 316NG, 316, and 304 SS have been reported previously.[4-8] No indication of SCC was observed in tests on noncrevice specimens of Type 316NG SS in oxygenated water containing 0.1-1.0 ppm SO_4^{2-} at temperatures of 95 and 150°C and a strain rate of 3×10^{-7} s^{-1}.[7] Crevice specimens were also resistant to SCC in oxygenated water containing 0.1 ppm SO_4^{2-} at temperatures ≤150°C.[8] Predominantly ductile fracture (a minor amount of transgranular cracking, TCSCC] was observed in crevice specimens of Type 316NG SS at higher temperatures. Intergranular failure occurred in Type 304 SS crevice specimens heat treated to yield sensitization values of 2 and 20 $C \cdot cm^{-2}$ by electrochemical potentiokinetic reactivation (EPR).[7,8] Results described in this report are from additional SSRT tests on crevice specimens of Type 316NG SS and tests on crevice weldment specimens of Type 316L SS in **air** and in water containing O_2, H_2O_2, and Cl^- at several temperatures between 150 and 225°C.

ExDerimental Procedures

Cylindrical tensile specimens with a 6.35-mm diameter and a 36.0-mm gage length were fabricated from Types 316NG and 316L SS. The chemical compositions of the materials used in these experiments are given in Table 1. The experimental methods have been described in previous papers.[5,7-9] Crevice specimens were created by drilling two small-diameter (≈0.8-0.9 mm) through holes in the gage section of the Type 316NG SS specimens and placing a corresponding austenitic SS pin in the top hole to form a tight crevice: the bottom hole was left open. In the case of the weldment SSRT specimens (Fig. 1), three holes were drilled in the gage section, i.e., in the base metal, the HAZ of the weld (edge of the hole =1–2 mm from the fusion line), and in the weld metal. The location of the hole in the HAZ was selected on the basis of experimental measurements and model predictions of variations in the degree of sensitization across this region in welds of 24-in.-diameter Type 304 and 316 SS pipe.[10] This location corresponds to maximum sensitization (i.e., chromium depletion and carbide precipitation at grain boundaries]. Although sensitization does not occur in low-carbon grades of Types 316L and 316NG SS, this location may be synonymous with other thermal segregation processes involving alloying elements and impurities in the steel. Austenitic SS pins were inserted into all holes to form tight crevices. The Type 316L SS weldment specimens were tested in the as-received condition without any heat treatment. Tests were carried to failure at strain rates of 1×10^{-5} s^{-1} in air and 3×10^{-7} s^{-1} in water in small-diameter autoclaves with a once-through water system.

Water chemistry was established by bubbling a 20% O_2-80% N_2 gas mixture through deoxygenated/deionized feedwater (conductivity <0.2 μS/cm) contained in a 130-L SS tank to produce a dissolved-02 concentration of ≈8.0 pprn. H_2O_2 (8.0 ppml and either H_2SO_4 (0.1 ppm) *or* NaCl (0.06 to 6.0 ppm Cl^-) were added to the feedwater before sparging with the gas mixture to ensure adequate mixing. *An* external 0.1 M KCl/AgCl/Ag reference electrode, a thermocouple, and Pt and Type 304 *SS* electrodes were located at the autoclave outlet to establish redox and open-circuit potential, respectively. The electrochemical potentials (ECPs) measured during the experiments were converted to the standard hydrogen electrode (SHE) scale by using thermocell and liquid junction potentials.[11]

Table 1. Composition of Austenitic Stainless Steels (wt.%)

Alloy	Heat No.	Cr	Ni	Mo	Mn	Si	Cu	N	C	P	S	Fe
316NG	P91576	16.42	10.95	2.14	1.63	0.42	0.20	0.068	0.015	0.020	0.010	Bal
316NG	467958	17.14	12.74	2.43	1.51	0.64	0.16	0.069	0.020	0.029	0.008	Bal
316NG	D442604	17.29	12.85	2.52	1.66	0.46	0.08	0.100	0.014	0.018	0.002	Bal
316NG	D440104	17.91	13.25	2.48	1.75	0.49	0.01	0.098	0.015	0.011	0.002	Bal
316L	16650	16.50	10.39	2.09	1.78	0.43	0.19	0.540	0.018	0.026	0.013	Bal
316L[a]	4H3367	18.69	12.29	[b]	1.98	0.63	0.25	[b]	0.018	0.023	0.018	Bal

[a]Type 316L *SS* filler metal **for** weld specimens.
[b]Not analyzed.

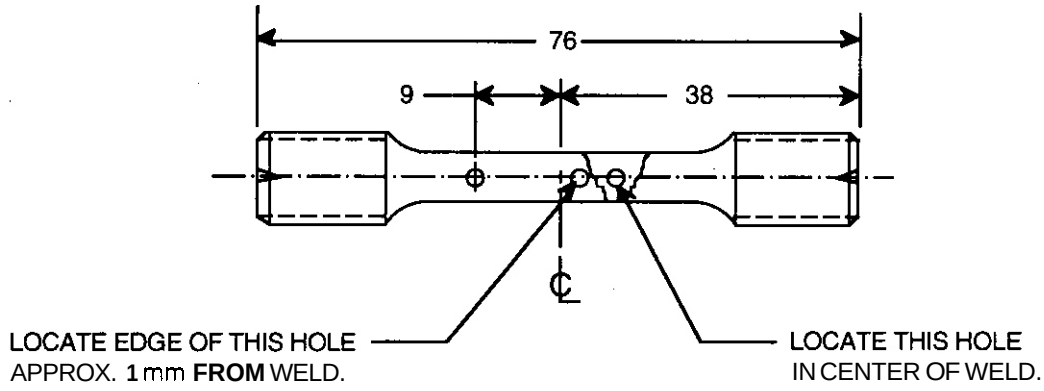

Figure 1. Weld specimen fabricated from gas-metal-arc welded plate of Type 316L SS with matching filler metal. Crevices were formed by inserting tight-fitting SS pins into the holes.

Tests provide information on time-to-failure. total strain, maximum stress, and fracture surface appearance. The load applied to each specimen was recorded continuously as a function of time. and an engineering-stress-versus-strain curve was produced for each specimen. Total elongation and reduction in area were determined from measurements on the fractured specimen. The fracture surfaces were examined by both optical microscopy and scanning electron microscopy (SEM) to determine the fractions of reduced cross-sectional areas with ductile, transgranular. and intergranular morphologies.[12]

Results and Analysis

Cracking susceptibility can be assessed from various parameters. Total elongation. reduction in area, and maximum stress are often used, as are fracture surface morphology and maximum crack length (either on the fracture surface or on the sectioned surface after test interruption). Because of the high SCC resistance of Type 316NG SS relative to that of sensitized Type 304 SS, it is difficult to quantify SCC behavior of Type 316NG SS in terms of crack growth rate[13] from SSRT results. An alternative. employed here, is evaluation of SCC susceptibility in terms of the ratio of the strain at failure ($\varepsilon_{env}/\varepsilon_{air}$) from companion tests on identical specimens in water and in air. Values of the strain ratio <1.0 indicate environmentally assisted cracking.

Results of SSRT tests at temperatures between 60 and 289°C on crevice and noncrevice specimens of Types 316NG and 304 SS were presented previously.[5,7,8] Additional work on SCC of Type 316NG SS under crevice conditions focused on temperatures between 150-289°C where the effect of temperature was not adequately defined. The SSRT results in Tables 2 and 3 and Fig. 2 were obtained from the engineering-stress (based on a cross-sectional area after subtracting the area associated with the hole) versus engineering-strain curves in air and water on identical specimens. Although the air tests were performed at a higher strain rate (e.g., 1×10^{-5} s^{-1}), the yield and ultimate strengths, total elongation. reduction in area, and fracture morphology can be compared in the two environments to assess SCC susceptibility. Because the tests were performed at two strain rates, time-to-failure is not a useful parameter. Compared with noncrevice specimens, crevice specimens exhibit lower total elongation values in both water and air. The lower values are caused by the diametral holes in the gage length. In contrast to elongation behavior, the small holes act as notches and fortuitously produce a degree of strengthening that offsets the reduced load-carrying capacity of the smaller cross-sectional area caused by the hole.[14] The apparent yield and tensile strengths of the crevice specimens in air (Table 4) are higher than those of noncrevice specimens (Table 2).

For Type 316NG SS. there is relatively little variation in SSRT parameters from air to oxygenated water containing 0.1 ppm SO_4^{2-} at temperatures ≤150°C, even under crevice conditions (Table 2). At higher temperatures, the strain ratio ($\varepsilon_{env}/\varepsilon_{air}$) at failure in Table 3 and Fig. 2 decreases from ≈1.0 to

0.5; this is indicative of environmentally assisted cracking in a relatively resistant material. In almost all tests on crevice specimens, fracture occurred in the hole that contained the pin, and we attribute this to the more aggressive water chemistry, although noncrevice specimens actually have lower S_T values, at least at lower temperatures.

Table 2. Influence of Temperature on SCC Susceptibility of Type 316NG SS Crevice Specimens Strained to Failure

								SSRT Parameters							
			Strain	Feedwater Chemistry[a]				Fail.	Yield	Max.	Total	Reduct.		Potentials	
Test No.	Heat No.	Temp. (°C)	Rate (s^{-1})	H_2O_2 (ppm)	O_2 (ppm)	Cond. ($\mu S \cdot cm^{-1}$)	pH at 25°C	Time (h)	Stress (MPa)	Stress (MPa)	Elong. (%)	in Area (%)	Fracture Morphology[b]	304 SS (mV[SHE])	Pt
55	P91576	60	3×10^{-7}	—— air test ——				285	197	532	31	*E6*	1.0 D	--	--
49	P91576	60	3×10^{-7}	0	7.4	0.91	5.67	287	187	520	31	64	0.9D.0.1T	433	483
6R	P91576	95	1×10^{-5}	—— air test ——				8.2	194	514	29	Ea	1.0 D	--	--
42	P91576	95	3×10^{-7}	7.0	7.1	0.81	5.76	281	172	496	30	70	1.0 D	413	473
7	467958	95	1×10^{-5}	—— air test ——				5.8	355	574	21	Ea	0.9 D, 0.1 T	--	--
3	467958	95	3×10^{-7}	0	7.2	0.97	5.68	267	318	547	21	70	0.8D.0.2T	*346*	*449*
56	D442604	95	2×10^{-7}	—— air test ——				417	193	518	31	69	1.0 D	--	--
57	D442604	95	2×10^{-7}	7.3	5.0	0.97	5.75	419	194	515	30	Ea	1.0 D	380	365
58	D440104	95	3×10^{-7}	—— air test ——				275	210	519	30	69	1.00	--	--
59	D440104	95	3×10^{-7}	7.3	5.3	0.89	5.69	295	190	517	32	*E6*	1.0 D	453	427
46	P91576	105	2×10^{-7}	—— air test ——				401	181	*505*	29	69	1.0 D	--	--
29	P91576	105	2×10^{-7}	6.1	7.9	0.90	5.72	400	194	509	29	69	1.0 D	489	392
69	467958	105	1×10^{-5}	—— air test ——				7.5	237	545	27	72	1.0 D		
30	467958	105	2×10^{-7}	5.3	7.6	0.94	5.73	358	235	555	26	71	0.9D, 0.1 T	499	414
19	P91576	150	1×10^{-5}	—— air test ——				7.2	192	478		71	1.0 D	--	--
13	P91576	150	3×10^{-7}	5.7	7.0	0.92	580	252	175	485	27	70	0.8D, 0.2 T	431	410
20	467958	150	1×10^{-5}	—— air test ——				7.0	*246*	528	25	72	1.0 D	--	--
14	467958	150	1×10^{-7}	7.0	6.9	0.92	5.71	661	218	534	24	73	0.8 D, 0.2 T	418	380
74	191576	190	1×10^{-5}	—— air test ——				7.4	162	467	*27*	75	1.0 D	--	--
75	P91576	190	3×10^{-7}	8.0	9.0	1.20	5.63	229	159	479	*24*	69	0.8 D, 0.2 T	304	305
76	P91576	225	1×10^{-5}	—— air test ——				7.2	170	466	26	75	1.0 D	--	--
77	P91576	225	3×10^{-7}	7.0	8.0	0.96	5.65	194	157	--	20	67	0.8 D. 0.2T	246	279
78	P91576	240	1×10^{-5}	—— air test ——				7.0	156	453	*26*	70	1.0 D	--	--
79	P91576	240	3×10^{-7}	8.0	8.0	1.10	5.66	156	148	382	16	62	0.9 D. 0.1T	249	268
50	P91576	289	2×10^{-7}	—— air test ——				403	142	466	*29*	64	0.9 D, 0.1 T	--	--
c	P91576	289	2×10^{-7}	0	0.25	0.90	5.70	203	--	314	15	43	--	21	--

[a] Conductivity and pH were adjusted by addition of 0.1 ppm H_2SO_4.

[b] Ductile (D) and transgranular (T) in terms of fraction of cross-sectional area. Characterization of fracture surface morphologies is in accordance with illustrations and definitions in Ref. 12.

It is well known that chloride concentration in oxygenated water has a significant effect on SCC and pitting of austenitic stainless steels.[15-21] Most available SCC data pertains to standard grades (e.g., Types 316 and 304 in the sensitized and solution-annealed conditions) under noncrevice conditions. As temperature and the chloride and/or dissolved-oxygen concentration in the water increase, these steels become susceptible to SCC, particularly in the sensitized condition. Types 316L and 316NG SS, both with low carbon contents and the latter with a controlled nitrogen content (0.06-0.10%), are expected to be more resistant to SCC in oxygenated water containing low levels of chloride. Results of initial SSRT tests on crevice weldment specimens of Type 316L SS with matching filler metal are shown in Tables 4 and 5 and Fig. 3. The present results indicate that low-carbon-content Type 316L SS steel is susceptible to transgranular SCC under crevice conditions in high-temperature oxygenated water. The curves in Fig. 3 indicate that as the temperature increases [from 150 to 225°C], the critical chloride concentration in the water for the onset of SCC (a strain ratio of <1.0) is <0.1 ppm. The actual values at temperatures >150°C can only be approximated from the results in Fig. 3. However, for chloride concentrations of >0.6 ppm in the bulk water, SCC is significant, as indicated by values of the strain ratio between ≈0.3 and 0.7.

Table 3. Influence of Temperature on *SCC* Susceptibility of Type 316NG *SS* Specimens in Oxygenated Water,[a] Based on Strain Ratio ($\varepsilon_{env}/\varepsilon_{air}$) at Failure

Crevice SSRTs				Noncrevice SSRTs			
Test Nos.	Heat NO.	Temp. (°C)	Straln Ratlo	Test Nos.	Heat No.	Temp. (°C)	Straln Ratlo
49/55	P91576	60	1.00	52/54	P91576	60	0.89
42/68	P91576	95	1.03	9/35	P91576	95	0.87
3/7	467958	95	1.00	10/35	P91576	95	0.91
57/56	D442604	95	0.97	8/4	467958	95	0.79
59/58	D440104	95	1.06	11/17	P91576	150	1.04
29/46	P91576	105	1.00	15/17	P91576	150	0.98
30/69	467958	105	0.96	12/16	467958	150	1.00
13/19	P91576	150	1.03	C/51	P91576	289	0.65
14/20	467958	150	0.96				
75/74	P91576	190	0.89				
77/76	P91576	225	0.77				
79/78	P91576	240	0.62				
C/50	P91576	289	0.52				

[a]Conductivity and pH were adjusted by addltlon of 0.1 ppm H_2SO_4.

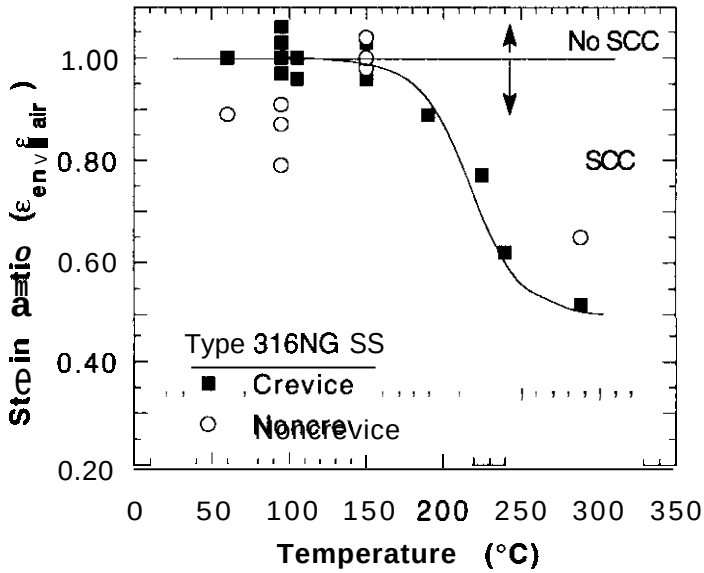

Figure 2. Strain ratio at *failure us.* temperature *for* creuice *and noncrevice SSRT* specimens *of Type 316NG SS*

As indicated in Table 4, most of the specimens failed in the base metal and two specimens failed in the HAZ of the weld, but no failures occurred in the weld metal. Fracture surfaces of the specimens have been examined by SEM to determine the mode of cracking and to establish whether the cracks initiated in the crevice as expected. Figure 4 shows fracture surfaces of several specimens. The region adjacent to the hole that contained the pin indicates that the transgranular crack initiated within the crevice and that the crack was uniform in depth across the diameter of the specimen. The micrographs

show that the extent of transgranular cracking increases with temperature at a constant chloride level in the water (namely, 0.6 ppm) and with chloride concentration at a constant temperature (i.e., 225°C). The region beyond this zone reveals ductile tearing, which occurred near the end of the tests.

Table 4. SCC Susceptibility of Type 316L SS Base Metal and Weld (Crevice and Noncrevice) Specimens[a] Strained to Failure

				Feedwater Chemistry					SSRT Parameters							Potentials	
Test No.	Heat No.	Temp. (°C)	Strain Rate (s^{-1})	H_2O_2 (ppm)	O_2 (ppm)	Cl^- (ppm)	Cond. (μS·cm⁻¹)	pH at 25°C	Fail. Time (h)	Yield Stress (MPa)	Max. Stress (MPa)	Total Elong. (%)	Reduct. in Area (%)	Failure Region[b]	Fracture Morphology	304 SS (mV[SHE])	Pt (mV[SHE])
61	16650	95	3×10^{-7}	0	5.9	[c]	0.96	5.79	573	165	468	62.0	84	B	1.0 D	237	237
60	Weld[d]	95	3×10^{-7}	0	6.3	[c]	1.1	5.69	350	256	489	38.0	82	B	1.0 D	401	508
53	Weld[e]	95	3×10^{-7}	0	6.6	[c]	0.77	5.73	165	229	506	18.0	66	B	1.0 D	253	255
en	Weld[e]	150	1×10^{-5}	———		air test	———		4.4	296	497	15.7	66	B	1.00	--	--
82	Weld[e]	150	3×10^{-7}			0.06	1.5	6.01	152	281	498	16.2	65	B	0.9 D, 0.1 T	359	331
67	Weld[e]	150	3×10^{-7}	7.0	8.0	0.6	3.4	6.06	97	280	439	10.6	61	B	0.8 D, 0.2 T	359	367
83	Weld[e]	150	3×10^{-7}	7.0	8.0	6.0	23.0	5.95	96	291	456	10.4	52	HAZ	0.8 D, 0.2 T		
84	Weld[e]	175	1×10^{-5}	———		air test	———		4.5	292	493	16.1	67	B	1.00	--	--
86	Weld[e]	175	3×10^{-7}	8.0	8.0	0.06	2.1	6.05	141	279	494	14.3	66	B	0.9 D, 0.1 T	333	349
85	Weld[d]	175	3×10^{-7}	6.0	8.0	0.6	3.6	5.80	89	281	434	9.2	52	B	0.8 D, 0.2 T	346	384
88	Weld[e]	200	1×10^{-5}	———		air test	———		4.4	279	485	16.1	65	B	1.0 D	--	--
90	Weld	200	3×10^{-7}	8.0	8.0	0.06	2.0	6.17	>80	276	>431	>6	f	f	--	246	246
89	Weld[e]	200	3×10^{-7}	7.0	8.0	0.6	3.6	5.60	m	275	402	7.5	53	B	0.8 D, 0.2 T	280	287
91	Weld[e]	200	3×10^{-7}	8.0	8.0	6.0	21.6	6.02	61	247	338	6.6	39	HAZ	0.9 D, 0.1 T		
92	Weld[e]	225	1×10^{-5}	———		air test	———		4.6	284	486	16.7	68	B	1.0 D	--	--
94	Weld[e]	225	3×10^{-7}	6.0	9.0	0.06	1.8	5.92	89	262	429	9.5	61	B	0.7 D, 0.3 T	284	307
93	Weld.	225	3×10^{-7}	8.0	8.0	0.6	4.0	5.86	58	270	388	5.9	54	B	0.6 D, 0.4 T	g	g

[a] SSRT spedmens from a gas-metal-arc weldment of Type 316L SS plate [Heat No. 16650) and filler metal (Heat No. 4H3367).

[b] Specimen failed in the base metal (B), in the heat affected wne (HAZ), or in the weld (W).

[c] Conductivity and pH were adjusted by addition of 0.1 ppm H_2SO_4.

[d] Noncrevice weld specimen.

[e] Crevice SSRT specimen that contained three small-diameter holes (In the base metal, the weld heat-affected wne. and in the weld metal) with Type 316 SS pins Inserted into them to produce Ught crevices.

[f] Specimen did not fracture: test was terminated because of an equlpment problem.

Table 5. Influence of Temperature on SCC Susceptibility of Type 316NG SS Crevice Weld Specimens[a] in Oxygenated Water Containing Several Chloride Concentrations. Based on Strain Ratio ($\varepsilon_{env}/\varepsilon_{air}$) at Failure

Test Nos.	Temp. (°C)	Cl^- (ppm)	Straln Ratlo	Test Nos.	Temp. (°C)	Cl^- (ppm)	Straln Ratio
82/80	150	0.06	1.03	90/88	200	0.06	>0.4
87/80	150	0.6	0.68	89/88	200	0.6	0.47
83/80	150	6.0	0.66	91/88	200	6.0	0.41
86/84	175	0.06	0.89	94/92	225	0.06	0.57
85/84	175	0.6	0.57	93/92	225	0.6	0.35

[a] Crevice SSRT specimens from a gas-metal-arc weldment of Type 316L SS plate (Heat No. 16650) and filler metal (Heat No. 4H3367).

Additional SSRT tests are being conducted on crevice weldment specimens of Type 316NG SS to define the critical chloride concentration in oxygenated water for the onset of SCC. These data, when coupled with the present results, will be used to establish the regime of temperature and chloride concentration for which these materials are resistant to SCC under crevice conditions. From the present results, it appears that the purity of bulk coolant water (e.g., Cl^- and SO_4^{2-} concentrations) will have to be maintained to a high standard to mitigate SCC of low-carbon grades of austenitic SSs, particularly at temperatures >150°C.

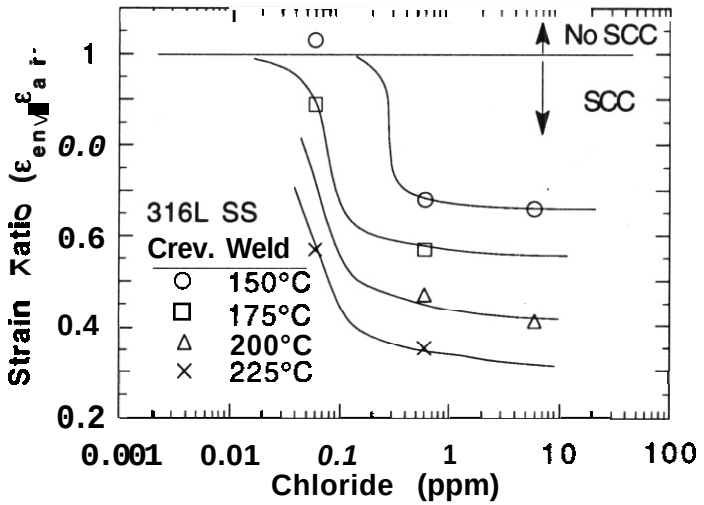

Figure 3. Strain ratio at failure for crevice SSRT weldment specimens of Type 316L SS us. chloride concentration in oxygenated water at seueral temperatures

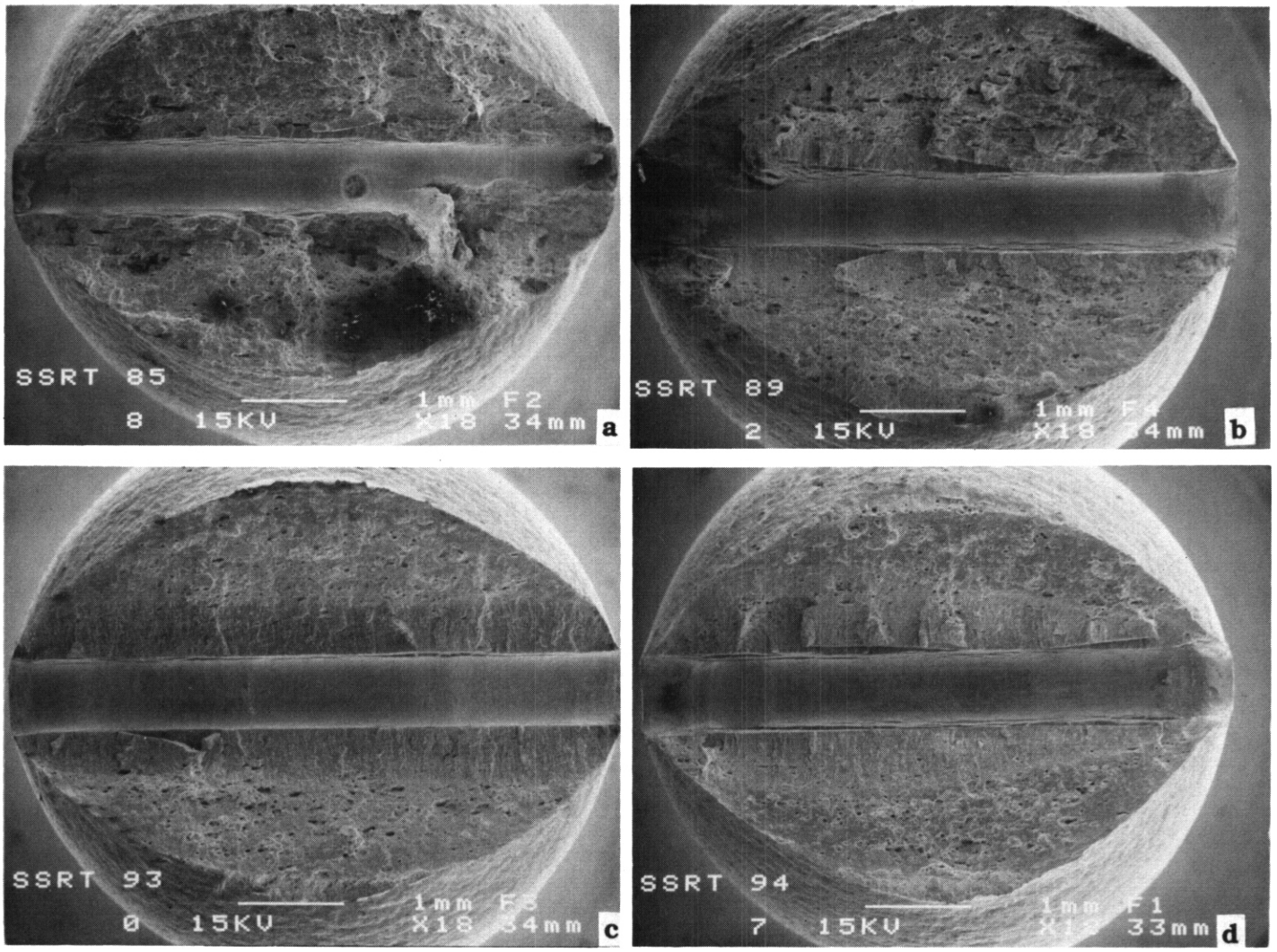

Figure 4. Fracture surfaces of creuice SSRT *specimens of Type 316L SS strained to failure at several temperatures in oxygenated water containing 0.6 ppm Cl^- at (a) 175°C, (b) 200°C, (c) 225°C, and (d) 0.06 ppm Cl^- at 225°C*

CONCLUSIONS

Types 316L and 316NG SS exhibit good resistance to SCC in SSRT tests under crevice and noncrevice conditions in oxygenated water containing 20.1 ppm Cl^- or SO_4^{2-} at temperatures 2150°C. This environment is representative of a nominal coolant chemistry for the ITER first wall/blanket system, except for short-lived radical species from radiolysis of water. Most of the Type 316L SS crevice-weldment specimens fractured in the base metal rather than in the heat-affected zone of the weld or in the weld metal. Present guidelines for the design and operation of water purification systems for light-water-cooled fission reactors can be employed to ensure that impurity levels in the ITER coolant are maintained at levels that will limit corrosion and SCC of system materials.

FUTURE WORK

Additional SSRT tests will be conducted on crevice weldment specimens of Type 316NG SS in water containing dissolved O_2, H_2O_2, and Cl^- to establish conditions for the onset of SCC and the margin of performance of the material under off-normal or poor lay-up water chemistry conditions at temperatures ≤150°C. Baseline tests will be performed in air to evaluate SCC susceptibility from the strain-ratio parameter. Crack-growth-rate tests on compact-tension specimens from several heats of Type 316NG SS will be conducted in simulated ITER water chemistries under cyclic loading conditions.

REFERENCES

1. D. L. Smith, *Aqueous* Corrosion *Task for* ITER *R&D,* **U.S.** Coordination Meeting, Argonne National Laboratory. August **6,** 1990.

2. H. G. Khalak. ***Computer Simulation of Water Coolant Chemistry in a Fusion Reactor,*** Proc. 3rd National Conference on Undergraduate Research, April 27-29, 1989, University of North Carolina. Asheville, p. 287.

3. H. **Khalak.** A. B. Hull. and T. F. Kassner. ***Aqueous Stress*** Corrosion *of Austenitic Steels,* 6th Fusion Reactor Materials Semiannual Progress Report for Period Ending March 31, 1989, DOE/ER-0313/6, **Oak** Ridge National Laboratory, p. 379.

4. **A.** Patel, A. B. Hull. and T. F. Kassner. ***Aqueous* Stress *Corrosion*** of ***Structural Materials.*** 7th Fusion Reactor Materials Semiannual Progress Report for Period Ending September 30, **1989.** DOE/ER-0313/7, Oak Ridge National **Laboratory.** p. ***250.***

5. A. B. Hull, M. R. Fox, **J.** W. Pascoe, and T. **F.** Kassner, ***Environmental* Effects** on ***Aqueous Stress Corrosion of Candidate Austenitic* Steels *for*** ITER Structural ***Applications.*** 9th Fusion Reactor Materials Semiannual Progress Report for Period Ending September 30, 1990, DOE/ER-0313/9, *Oak* Ridge National Laboratory, p. 228.

6. A. B. Hull and T. F. Kassner. ***Aqueous Stress*** Corrosion of ***Candidate Austenitic Steels for*** ITER ***Structural Applications,*** 10th Fusion Reactor Materials Semiannual Progress Report for Period Ending March 31. 1991. DOE/ER-0313/10, **Oak** Ridge National Laboratory, p. 241.

7. M. R Fox, A. B. Hull, and T. F. Kassner, ***Stress*** Corrosion ***Cracking of Candidate Structural Materials under Simulated First-Wall/Aqueous Coolant Environments.*** Fusion Technol., **19**, 1619-1628 (1991).

8. A. B. Hull. P. R. Luebbers, M. R Fox. W. K. Soppet. and T. F. Kassner, Aqueous ***Stress*** Corrosion ***of Candidate Austenitic Steels for*** ITER ***Structural Applications,*** 12th Fusion Reactor Materials Semiannual Progress Report for Period Ending March 31. 1992, DOE/ER-0313/12, *Oak* Ridge National Laboratory, p. 225.

9. P. S. Maiya. *Plastic Strain. Enuironmental and Crevice Effects on SCC Initiation and Propagation in Types 316NG and 304 Stainless Steel* Corrosion **45. 915-924 (1989).**

10. S. M. Bruemmer, L. A. Charlot, and D. G. Atteridge. *Sensitization Deueloprnent in Austenitic Stainless Steel—Measurement and Prediction of Thermomechanical History Effects.* Corrosion **44. 427-442 (1988).**

11. D. D. Macdonald, A. C. Scott, and P. Wentrcek. *External Reference Electrodes for Use in High Temperature Aqueous Systems.* J. Electrochem. Soc., **126, 908-911 (1979).**

12. H. **D.** Solomon, *Transgranular, Granulated, and Intergranular Stress Corrosion Cracking in AISI 304 SS,* Corrosion **40. 493-506 (1984).**

13. W. **E.** Ruther, W. K. Soppet. and T. F. Kassner. *Effect of Temperature and Ionic Impurities at Very Low Concentrations on Stress Corrosion Cracking of AISI 304 Stainless Steel,* Corrosion **44. 791-799** (1988).

14. R Hill. The *Mathematical Theory of Plasticity.* Oxford Press, UK, pp. **245-252 (1950).**

15. B. M. Gordon, *The Effect of Chloride and Oxygen on the Stress Corrosion Cracking of Stainless Steels: Review of Literature,* Materials Performance **IS (4) 29-37 (1980).**

16. P. L. Andresen and D. J. Duquette, The *Effects of Dissolved Oxygen, Chloride Ion, and Applied Potential on the SCC Behavior of Type 304 Stainless Steel in 290°C Water,* Corrosion **36, 409-415 (1980).**

17. J. Congleton. H. C. Shih. T. Shoji, and R. **N. Parkins,** The *Stress Corrosion Cracking of Type 316 Stainless Steel in Oxygenated and Chlorinated High Temperature Water,* Corrosion Science **25. 769-788 (1985).**

18. W. M. M. Huijbregts, *Oxygen* and *Corrosion Potential Effects on Chloride Stress Corrosion Cracking.* Corrosion **42, 456-462 (1986).**

19. J.–H. Wang, C. C. **Su.** and Z. Szklarska-Smialowska, *Effects of Cl^- Concentration and Temperature on Pitting of AISI 304 Stainless Steel,* Corrosion **44, 732-737 (1988).**

20. H. **K.** Juang and C. Altstetter. *Effect of pH and Chloride Contents on Stress Corrosion Cracking of Austenitic Stainless Steels at Room Temperature,* Corrosion **46, 881-887 (1990).**

21. H. M. **G.** Smets and W. F. L. Bogaerts, *SCC Analysis of Austenitic Stainless Steels in Chloride Bearing Water by Neural Network Techniques.* Corrosion **48, 618-623 (1992).**

DEVELOPMENT OF IN-SITU-FORMED ELECTRICAL INSULATOR COATINGS ON HIGH-TEMPERATURE ALLOYS IN LITHIUM*

J.-H. Park and G. Dragel (Argonne National Laboratory)

OBJECTIVE

The corrosion resistance of structural materials and the magnetohydrodynamic (MHD) force and its subsequent influence on thermal hydraulics and corrosion are major concerns in the design of liquid-metal blankets for magnetic fusion reactors (MFRs). The objective of this study is to develop in-situ stable ceramic coatings at the liquid-metal/structural-material interface, with emphasis on electrically insulating coatings that prevent adverse MHD-generated currents from passing through the structural walls.[1-3]

SUMMARY

Various intermetallic films were produced on vanadium, vanadium-base alloys. and Types 304 and 316 stainless steel (SS) by exposing the materials to liquid- and/or vapor-phase lithium containing dissolved elements (3-5 at.%) in sealed capsules at temperatures between 600 and 775°C. After each test, the capsules were opened and the samples were examined by optical and scanning electron microscopy: they were then analyzed by electron-energy-dispersive and X-ray diffraction techniques. The nature of the coatings, i.e., surface coverage, thickness, and composition, varied with exposure time and temperature. solute in lithium, and alloy composition. Solute elements that yielded adherent coatings on various substrates provide a means of developing in-situ electrical insulator coatings by oxidation of the reactive layers with dissolved oxygen and/or nitrogen in liquid lithium.

INTRODUCTION

Corrosion resistance of structural materials and magnetohydrodynamic (MHD) force and its subsequent influence on thermal hydraulics are major concerns in the design of liquid-metal cooling systems.[1-3] The objective of this study is to develop in-situ stable corrosion-resistant and electrically insulating coatings at the liquid-metal/structural-material interface. The electrically insulating coatings should be capable of forming on various shapes such as the inside of tubes or irregular shapes during operational conditions to prevent adverse MHD-generated currents from passing through the structural walls. The coatings could also improve general corrosion resistance and act as a diffusional barrier for deuterium or tritium.

EXPERIMENTAL PROCEDURE

Coatings on vanadium and vanadium-base alloys (V-Ti, V-Cr-Ti, V-Ti-Si) and Types 304 and 316 SS were produced by vapor- and/or liquid-phase reaction with liquid lithium containing various metals (Al, Mg, Si, Ca. Y-Pt, Cr) to form intermetallic layers. The tests were conducted in Type 304 SS capsules and in V-20Ti and V capsules that were placed in a stainless steel capsule to prevent oxidation of the vanadium at temperatures of 600-775°C. Figure 1 shows a capsule that was cut open above the lithium level to remove the samples. The capsule was placed in a beaker of water to dissolve the small volume of lithium. The samples were removed. cleaned ultrasonically in acetone and ethanol, and dried in air.

The samples were examined by optical and scanning electron microscopy (SEM) and by electron-energy-dispersive (EDS) and X-ray diffraction analysis. The coatings were characterized by EDS spectra at a beam energy of 10-15 KeV. The diffusion distance of the electron beam is confined to ≈1 μm of the surface in this energy range, although the depth varies with density and composition of the material and beam energy. If the coating layer is thicker than electron-beam diffusion range, the spectrum is characteristic of the coating, hut when the coating layer is thinner than the electron diffusion range, the EDS spectrum shows an additional signal from the substrate. Based on these considerations, the following criteria were used to evaluate the coatings: "none," "fair," and "good" denote no or <5 wt.%,

*Work supported by the Office of Fusion Energy, U.S. Department of Energy. under Contract W-31-109-Eng-38.

≈30 wt.%, and ≈50 wt.%, respectively, of the coating species present on the surface as measured by the relative peak heights. The specimens were sectioned and surface coverage and coating thicknesses were examined by SEM. These methods were deemed adequate to guide further development of insulator coatings.

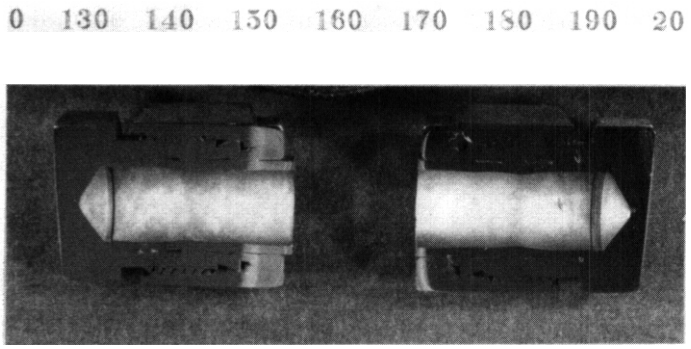

Figure 1. Cross section of V-20Ti capsule (inside) that was encapsulated in a stainless steel capsule (outside) after sectioning to remove the specimens

RESULTS

The test conditions, materials, and qualitative results from the metalliding experiments in liquid lithium containing various solutes are given in Tables 1–5. In these scoping tests, the effect of exposure time, temperature, environment above the Li (i.e., high-purity Ar or vacuum), and the capsule material (Type 304 SS or V-20Ti) was explored. In the various experiments, aluminides, silicides. chrominides. and Ca and Mg intermetallic layers formed on many but not all of the specimens. The degree of surface coverage and thickness of the layers varied considerably. depending on exposure conditions. solute in lithium, and alloy composition. Qualitative evaluations of the metallide coatings in Tables 1–5 provide some guidance as to their potential for conversion to electrically insulating oxides or oxynitrides in-situ in lithium or by oxidation in other controlled environments. For example, if the metallide coating is not uniform, too thin, or has too low a concentration of the reactive element (e.g., Al. Ca. Y. etc.). it could not be converted to a ceramic insulator.

Table 1. Formation of Metallides[a] on Vanadium, Vanadium-Base Alloys, and Stainless Steels during Exposure to Liquid Lithium Containing 3-4 at.% of Several Elements in Sealed Capsule Tests[b] at 700°C for 234 h

Solute Species	Alloy Substrate						
	V	V-5Ti	V-20Ti	V-5Cr-5Ti	V-15Cr-5Ti	304 SS	316 SS
Al	None	None	None	Fair	Fair	Good	Good
Ca	NA[c]	NA	NA	NA	NA	NA	NA
Si	Fair	Fair	Fair	Fair	NA	Good	Good
Mg	Fair	Fair	Fair	Fair	Fair	NA	NA
Cr	Fair	Fair	Fair	Fair	Fair	Good	Good
Al-BN	None	None	None	Fair	Fair	Good	Good
Y-Pt[d]	Pt	Pt	Pt	Pt	Pt	Pt	Pt

[a]Evaluation of coatings on specimen surfaces by electron-energy dispersive spectrum at a beam energy of 10–15 KeV; "none" Indicates no coating present. "fair" and "good" denote the extent of surface coverage and thickness of the coatings as measured by the relative peak heights.

[b]Tests conducted In Type 304 SS capsules under an argon (99.999%) atmosphere.

[c]Not analyzed yet.

[d]Platinum coatings were present on the surface of all materials; yttrium was not detected on any samples.

Table 2. Formation of Aluminidesa on Vanadium, Vanadium–Base Alloys, and Stainless Steels during Exposure to Liquid Lithium Containing 5 at.% of Aluminum in Sealed Capsule Testsb at 700 and 750°C for 247 h

Temp. °C	Alloy Substrate						
	V	V–5TI	V–20TI	V–5Cr–5Ti	V–15Cr–5Ti	304 SS	316 SS
700	Poor	Poor	Poor	Poor	Fair	Good	Good
750	Good	Good	Good	Good	Good	Good	Good

[a]Evaluation of coatings on specimen surfaces by electron–energy dispersive spectrum at a beam energy of 10–15 KeV; "poor" indicates a thin coating, "fair" and "good" denote a greater extent of surface coverage and thickness of the coatings as measured by the relative peak heights.

'Tests conducted In Type 304 SS capsules under an argon (99.999%) atmosphere.

Table 3. Formation of Aluminidesa on Various Metals and Alloys during Exposure to Liquid Lithium Containing 5 at.% of Aluminum in Sealed Capsule Testsb at 775°C for 31 h

Temp, °C	Alloy Substrate						
	V	V–20Ti	Nb	Ta	Mo	W	304 SS
775	Fair	Fair	Poor	None	Good	None	Good

[a]Evaluation of coatings on specimen surfaces by electron–energy dispersive spectrum at a beam energy of 10–15 KeV; "none" indicates no coating present, 'poor' indlcates a thin coating, "fair" and "good" denote a greater extent of surface coverage and thickness of the coatings as measured by the relative peak heights.

[b]Test conducted under vacuum in a Type 304 SS capsule.

Table 4. Formation of Aluminidesa on Vanadium, Vanadium–Base Alloys, and Stainless Steels during Exposure to Liquid Lithium Containing 5 at.% of Aluminum in Sealed Capsule Testsb at 650, 700. and 750°C for 247 h

Temp, °C	Alloy Substrate						
	V	V–5Ti	V–20Ti	V–5Cr–5Ti	V–15Cr–5Ti	304 SS	316 SS
650	Poor	Poor	Poor	Poor	Fair	Good	Good
700	Poor	Poor	Poor	Poor	Fair	Good	Good
750	Poor	Poor	Poor	Poor	Fair	Good	Good

[a]Evaluation of coatings on specimen surfaces by electron–energy dispersive spectrum at a beam energy of 1–15 KeV; "poor" indlcates a thin coating. "fair" and "good" denote a greater extent of surface coverage and thickness of the coatings as measured by the relative peak helghts.

[b]Tests conducted in V–20Ti capsules under an argon (99.999%) atmosphere. V-alloy capsules were sealed In a Type 316 SS capsule to prevent oxidation.

The layers on most of the specimens have been characterized: however, only a few typical examples are given below. Figure 2 shows an SEM micrograph and an *EDS* spectrum of an aluminide surface on a V–20Ti specimen after exposure to Li containing ~5 at.% Al for 87 h at 775°C. The surface characteristics and EDS spectrum are typical of those of other V–base alloys under these conditions (Table 5). Figure 3 shows the surface and cross section of a Type 304 SS specimen after exposure to lithium containing ≈5 at.% Al for 144 h at 700°C. The nonporous, tightly adherent aluminide layers in Fig. 3b are typical of those formed on Types of 304 and 316 SS specimens in other experiments.

Table 5. Formation of Aluminidesa on Vanadium–Base Alloys during Exposure to Liquid Lithium Containing 5 at.% of Aluminum in a Sealed Causule Testb at 775°C for 87 h

Alloy Substrate							
V-3Ti-0.5Si	V-3Ti-0.5Si	V-5Ti	V-5Cr-5Ti	V-10Cr-5Ti	V-12Cr-5Ti	V-12Cr-5Ti	V-20Ti
cAl:V:Ti=37:60:3	38602	36:60:4	35:62:3	34:62:4	33:60:7	34:61:5	37:49:14

[a]Evaluation of coatings on specimen surfaces by electron–energy dispersive spectrum at a beam energy of 10–15 KeV; Al in lithium interacted with the alloys by forming a solid solution.

[b]Tests conducted in V-20Ti capsules under an argon (99.999%) atmosphere. V-alloy capsules were sealed in a Type 316 SS capsule to prevent oxidation.

[c]Composition of the alloy surface in atomic percent ratio of Al:V:Ti.

Figure 4 shows cross sections of an aluminided Type 304 SS specimen after air oxidation at 1000°C for 65 h. A thin adherent outer layer of Al_2O_3 formed on the specimen (Fig. 4a). The outer layer is predominantly small-grain Al_2O_3 and the inner layer is composed of large-grain Fe_3O_4 (Fig. 4b). This oxidation experiment suggests that the concentration of aluminum on the alloy surface produced during exposure to liquid Li containing ~5 at.% Al is sufficient to form an electrical insulator coating layer during subsequent oxidation.

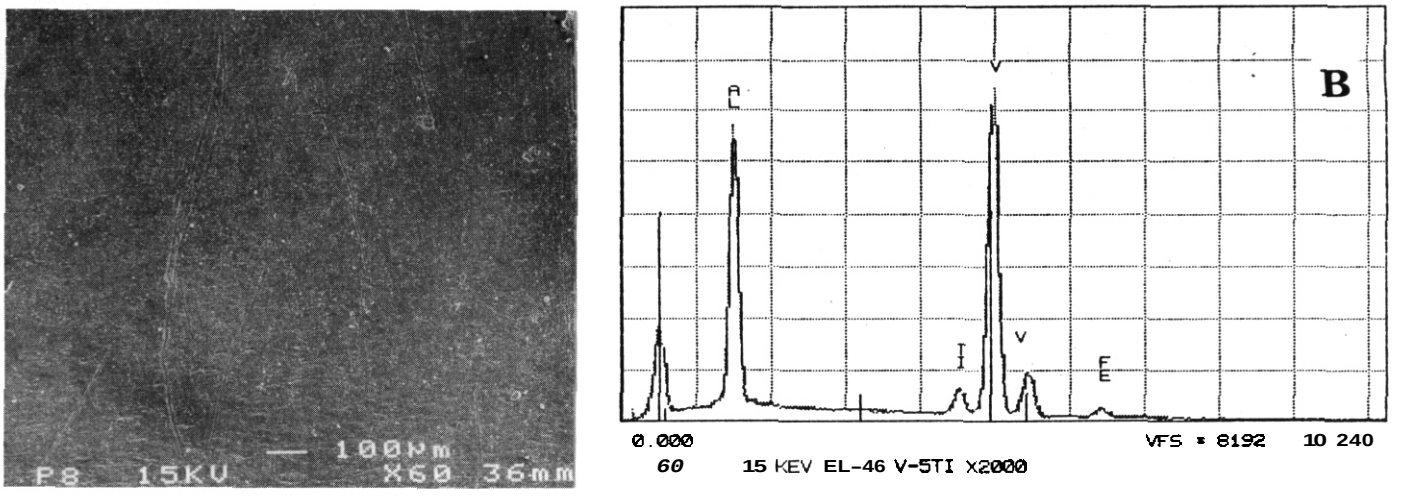

Figure 2. (a) surface and (b) EDS spectrum of aluminide surface on V–20Ti after exposure to liquid lithium containing ≈5 at.% Al for 87 h at 775°C

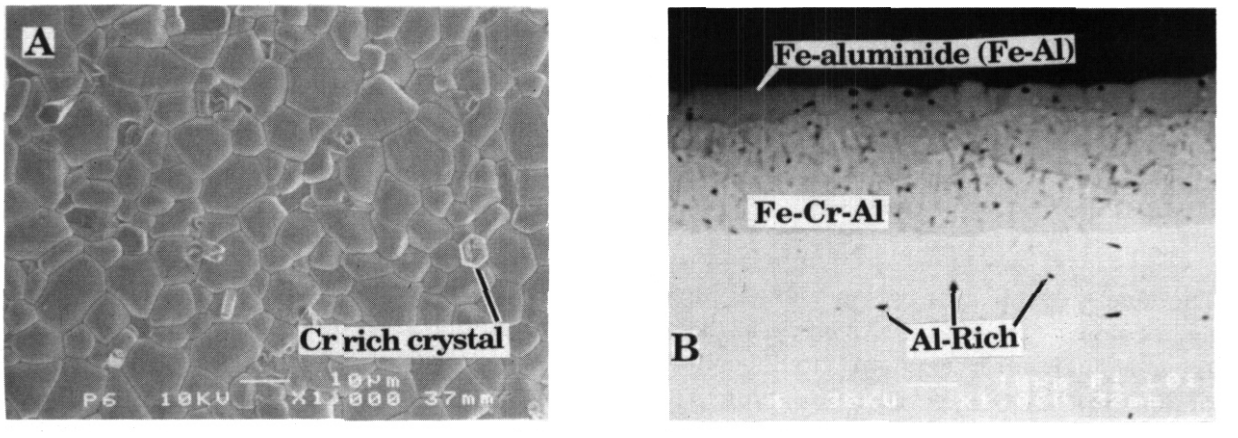

Figure 3. (a) surface and (b) cross-section of Type 304 SS specimen after exposure to liquid lithium containing ≈5 at.% Al for 14.4 h at 700°C. showing aluminide layers

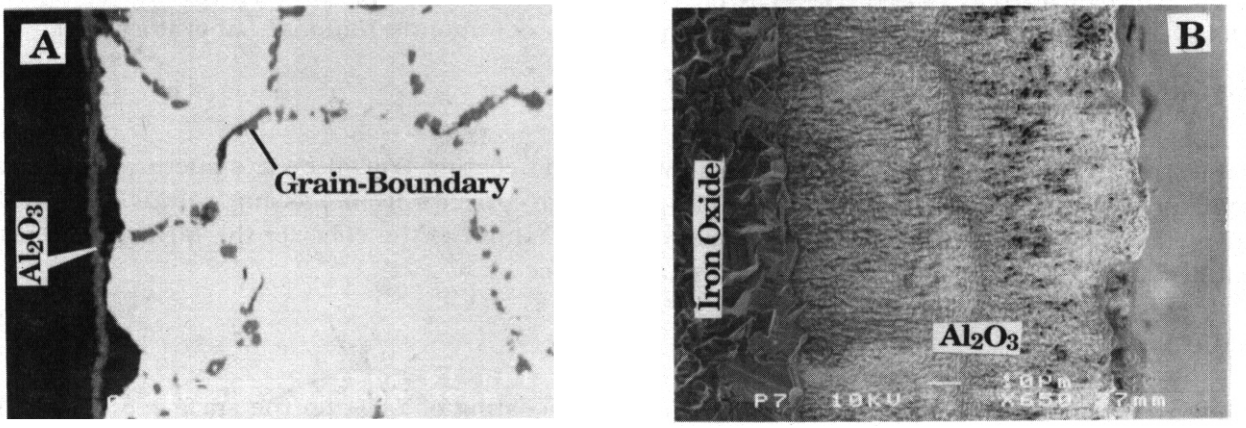

Figure 4. Cross-section of aluminided Type 304 SS specimen after oxidation in air for 65 h at 1000°C showing *(a)* thin alumina film, underlying iron oxide layer, and metal: and *(b)* alumina and iron oxide layers at higher magnification

CONCLUSIONS

Surface modification via high-temperature liquid-phase deposition (LPD) and vapor-phase deposition (VPD) can provide intermetallic coatings on various alloys. namely V, V-Ti, V-Ti-Si. V-Cr-Ti, and Types 304 and 316 SS. This process is facilitated in liquid lithium because surface contamination by oxygen or oxide films is virtually eliminated and the process to produce homogeneous coatings on various surface shapes can be controlled by exposure time and temperature, and by composition of the liquid metal. Coating integrity does not appear sensitive to defects (e.g., open pores, fissures. or microcracks) in the alloy substrate. A tightly adherent alumina film formed on an aluminized specimen of Type 304 SS that was oxidized in air. Consequently, conversion of the metallide layers to electrical insulator coatings may be more feasible than our initial expectations.

FUTURE STUDIES

The investigation of intermetallic film formation on V. V-Ti, V-Ti-Si. V-Cr-Ti. and Type 304 and 316 SS in liquid lithium will continue to further explore and optimize the conditions for specific alloys of interest as a structural material in a magnetic fusion reactor. The metallide coatings will be exposed to flowing lithium with controlled oxygen and nitrogen concentrations to investigate the corrosion behavior and the feasibility of producing in-situ an electrically insulating corrosion-product layer.

REFERENCES

1. C. C. Baker, et al.. *Tokamak* Power System *Studies FY* 1985, Argonne National Laboratory Report ANL/FPP-85-2 (December 1985).

2. Y. Y. Liu and D. L. Smith, *Ceramic Electrical Insulators* for Liquid Metal Blankets, J. Nucl. Mater., 141-143, 38 (1986).

3. T. Kammash. *Fusion* Reactor Physics, Chapter 15, Ann Arbor Science Pub. Inc., Ann Arbor, MI (1975), pp. 405-439.

ELECTRICAL INSULATOR COATINGS FOR LIQUID-METAL BLANKET APPLICATIONS-YTTRIA COATING ON VANADIUM*—M. R. Fox and J.-H. Park (Argonne National Laboratory)

OBJECTIVE

The objective of this study is to develop a stable ceramic coating (Y_2O_3) on a structural material (V) to prevent adverse magnetohydrodynamic (MHD)-generated currents from passing through the walls in a liquid-metal blanket of a magnetic fusion reactor and to minimize the effect of the MHD force on thermal hydraulics at the liquid-metal/structural-material interface.

SUMMARY

Research has been conducted to develop a diffusion coating of Y_2O_3 on the surface of V, which could help eliminate the MHD effect. The process involves yttriding. in which a diffusion coating of Y is formed on the surface of V by immersing the samples in a molten salt and applying a potential. The yttrium layer can then be oxidized to form the electrical insulator Y_2O_3. An yttrium coating up to 10 μm in thickness with a diffusion zone of ≈1 μm has been produced.

PROGRESS AND STATUS

Liquid lithium has been proposed as a coolant in current fusion reactor designs. However, a major drawback is the MHD force exerted on the liquid metal. Reactor designs must compensate for MHD effects by invoking higher pumping requirements, which result in higher coolant pressures and make the designs more difficult. One way to reduce the effect of MHD is to put an electrical insulator coating at the structural-material/liquid-metal coolant interface. The coating must exhibit three characteristics: (1) it must be a nonconductor, i.e., the resistance of 1 cm^2 of coating area must be >2.54 Ω to meet design criteria:' (2) the coating must be compatible with liquid Li (among various insulators. Y_2O_3 had the greatest stability[2,3]); and (3) the coating must adhere to the structural material, even under thermal cycling conditions. Initial studies indicate that Y_2O_3 is stable in contact with the V-base alloys being considered for structural materials. Furthermore, the thermal expansion coefficients of Y_2O_3 and V-base alloys are similar. Therefore, recent activities have concentrated on coating Y on V and oxidizing the Y coating to Y_2O_3.

An ideal coating would be one that forms in-situ by a diffusion process involving the structural material and nonmetallic impurity elements in the liquid Li, such that the coating could regenerate if any portion of the coating should crack or spall. Two processes that produce diffusion coatings are chemical vapor deposition (CVD) and metalliding. The research presented here is concerned with metalliding. which is the electrolytic deposition of a metal onto a conductive substrate immersed in a molten salt bath.[4] The process is similar to electrolysis, but the use of a molten salt allows coating of materials (such as Y) that could not be coated by electrolysis because of their reactivity with water. After the metalliding process, Y_2O_3 can be formed either by oxidation in a gas atmosphere or possibly in-situ in liquid lithium.

Exuerimental Methods

The electrolytic cell used in these experiments was similar in design to the cell used by Taxil and Mahenc.[6] Figure 1 is a diagram of the cell. The molten salt was contained in a 30-mL Ni crucible. The crucible was held in a 450-mm-long steel tube that was closed at the bottom and sealed at the top with O-rings. The lower portion was heated in a furnace while the top was cooled by a fan. A sheet of stainless steel was placed about halfway up in the cell to act as a heat and vapor shield. An Ar atmosphere was maintained over the salt. Before entering the furnace, high-purity Ar (99.999%)was passed through a molecular sieve and then through a Ti-chip getter at 400°C to remove any remaining water or O_2 impurities. A stainless steel tube supplied the Ar at a position 20 mm above the surface of the salt. A 0.25-in.-diameter 998 alumina rod with four small-diameter holes was used to guide the electrodes down to the salt. Various materials were used as the anode and reference electrode, and V was used as

*Work supported by the Office of Fusion Energy. U.S. Department of Energy, under Contract W-31-109-Eng-38.

the cathode. The electrodes were suspended by Ni wire. The four holes at the top of the rod were sealed with silicone adhesive. Temperature was measured with a K-type thermocouple. The thermocouple and the alumina rod were sealed at the top of the cell with Conax fittings.

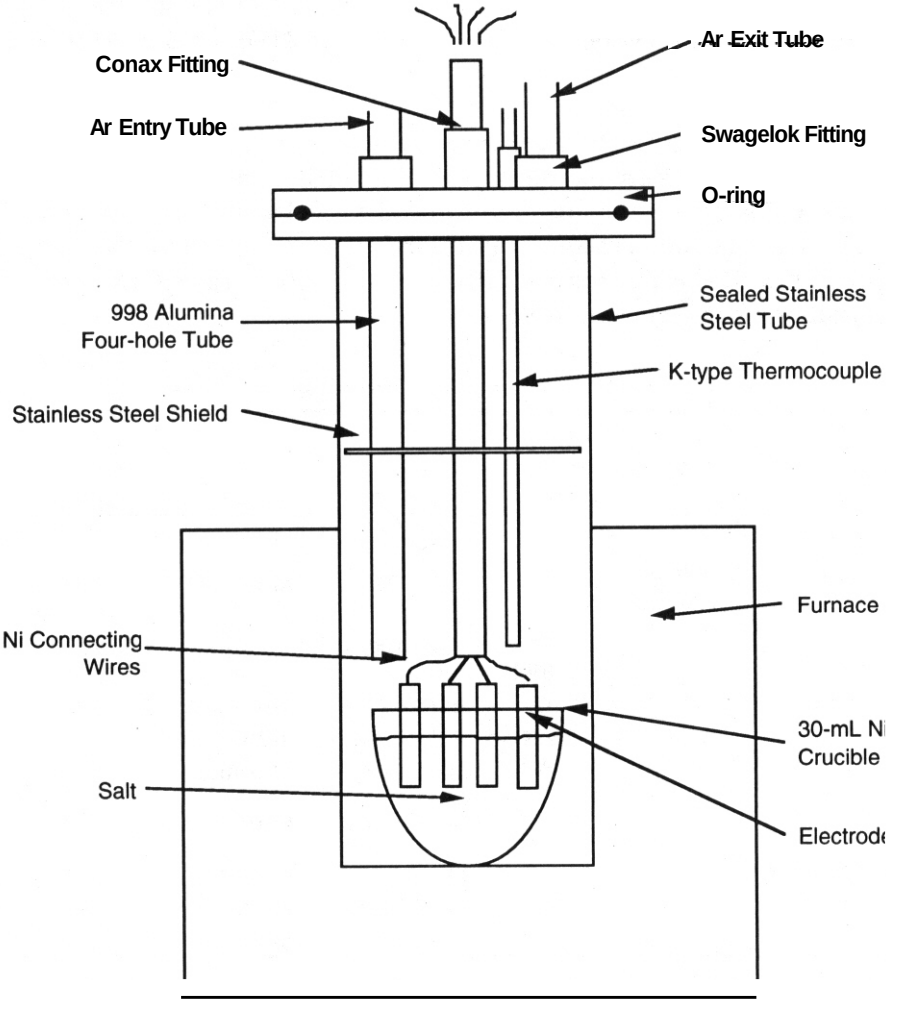

Ffgure 1. Schematic of electrochemical cell

Potential was applied with an EG&G Princeton Applied Research potentiostat/galvanostat. Potentiograms and ammograms were recorded with a Hewlett Packard X-Y recorder model #7045A. Current was monitored by measuring the potential across an Electro Scientific Industries 1-kΩ standard resistor connected in series with the electrochemical cell.

Because the dissolution rates of the anodes were much higher than expected, the electrodes and the salt were changed several times. Platinum was the first material that was eliminated as an electrode. It was unstable with both the liquid and vapor phases of the salt. Yttrium was the next material used as an anode and reference electrode. It had a higher-than-expected dissolution rate and was therefore required to be in the form of a large piece instead of a coupon. Nickel wire was also used as an anode and a reference electrode: it had a lower dissolution rate in the salt.

The composition of the salt was changed several times. Initially, LiF/NaF eutectic (LiF-39 mol% NaF) was used, but yttrium readily dissolved and V was severely embrittled in this salt. Replacing this salt by LiF/YF_3 eutectic resolved the V embrittlement problem, but even with **8.93** g of excess Y added, the Y electrodes still dissolved. Then, Ni wire was substituted for the Y foil because it exhibited a much lower dissolution rate. Corrosion by the liquid salt required other changes in the experimental design. The

original design used a four-hole mullite rod instead of a 998 alumina rod. The mullite tube was very unstable in the presence of the LiF/NaF salt vapor. After just one run. the rod had turned from white to black and the strength of the material was greatly reduced. Analysis revealed Si enrichment at the surface. Initially. the alumina spacer was used to prevent electrical contact between the samples because the Pt wire was too thin to hold its shape. Once the conversion to a thicker Ni wire was made, the spacer was no longer necessary.

The electrodes were attached to Ni wires and electrical contact was made simply by twisting the wires together. The distance between the electrodes was ~10-20 mm. The salt was dried by flowing Ar over the surface at 630°C for 16 h. During this time, the electrodes were suspended ~20 mm above the salt surface. After drying, the temperature was raised to 730°C to melt the salt. Then the electrodes were lowered into the salt and the desired potential was applied. Argon flow continued during each test. The experimental conditions are given in Table 1.

Table 1. Conditions for Yttriding Experiments, in Chronological Order

Test No.	Time (h)	Temperature (°C)	Applied Current (mA)	Applied Potential M	Salt (mol %)	Tube	Alumina Spacer	Electrodes	Wire
1	23	690	_a	_	LiF-39NaF	mullite	Yes	2Y, V, Pt	Pt
2	20.7	705	3.7h@0 17h@20	-	LiF-39NaF	alumina	Yes	2Y, V, Pt	Pt
3	27	708	_	1h@0 26h@1	LiF-39NaF	mullite	Yes	3Y.V	Ni+Pt
4	91	730	0	0	LiF-20YF_3	alumina	Yes	3Y, V	Ni
4a	_	727	_	-2 to +2	LiF-20YF_3	alumina	No	4Ni	Ni
5	24	726	0	0	LiF-20YF_3[b]	alumina	Yes	3Y. V	Ni
6	25.5	701-715	-	4h@0 21.5h@10	LiF-20YF_3[b]	alumina	No	3Ni, V	Ni
9&10	24	727-643	_	1.51-1.94	LiF-20YF_3[b]	alumina	No	2Ni, 2V	Ni
7&8	21.2	727		0-2	LiF-20YF_3[b]	alumina	No	2Ni, 2V	Ni
11&12	-	_	_	_	LiF-19YF_3	alumina	No	2Y. 2v	Ni

[a]Wiring was set up incorrectly for this run.

[b]An 8.9-g piece of pure Y was added to this salt

Results and Analysis

After several attempts, a layer of Y was successfully coated on V in Test 6. Backscatter X-ray analysis in the SEM revealed a layer of Y up to 10 μm thick (Fig. 2). Small amounts of F were also detected with Y. Lineal X-ray analysis in the SEM showed a 1-μm-thick diffusion zone between the Y and V (Fig. 3). The interdiffusion coefficient between Y and V was calculated from the equation $x = (Dt)^{-0.5}$, where x, D, and t are the diffusion distance, diffusion coefficient. and time, respectively. For Test 6, D was $\approx 10^{-13}$ cm^2 s^{-1}.

The molten fluoride salts presented some unusual corrosion problems. Previous work suggested the use of a Ni crucible to contain the salt. The stability of Ni in the presence of the molten salt was confirmed in these tests. One crucible lasted for 11 tests at ~730°C. each ~24 h. Vanadium was stable in the LiF/YF_3 salts, but it was severely embrittled in LiF/NaF. Mullite was not stable in the presence of the fluoride vapors. There seemed to be a reaction between Si in the mullite and F in the salt. More analysis is required to verify this. Degradation of Pt in the presence of the salt, and particularly in the presence of salt vapor, was not expected. Also. a large amount of vapor was deposited on the alumina spacers, and in some cases. a layer up to 2 mm thick formed. Even in the thickest deposition zones, Al was still detected by surface analysis in the SEM. In other areas on the spacer where deposition was less, egg-shaped particles of pure Al were found (Fig. 4). Across much of the surface of the spacer, oxide crystals with a ratio of 56 atoms of Al to 44 atoms of Y were found (Fig. 5).

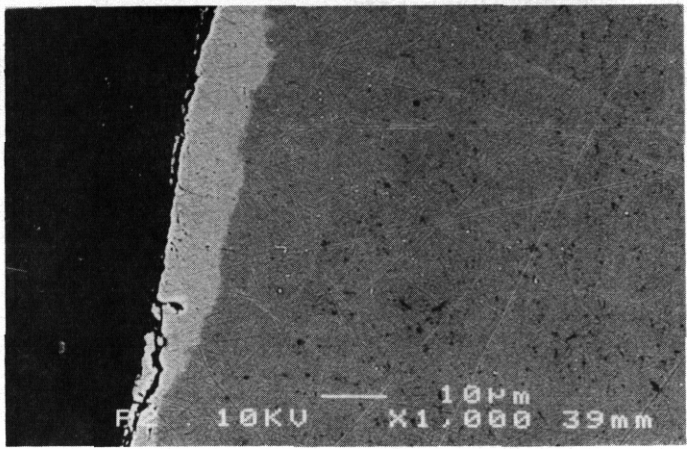

Figure 2. ***SEM*** photo using backscattered electrons of polished cross-section of sample from Test 6. Dark gray area is mounting material *light* gray is Y *coating,* and *medium* gray is V.

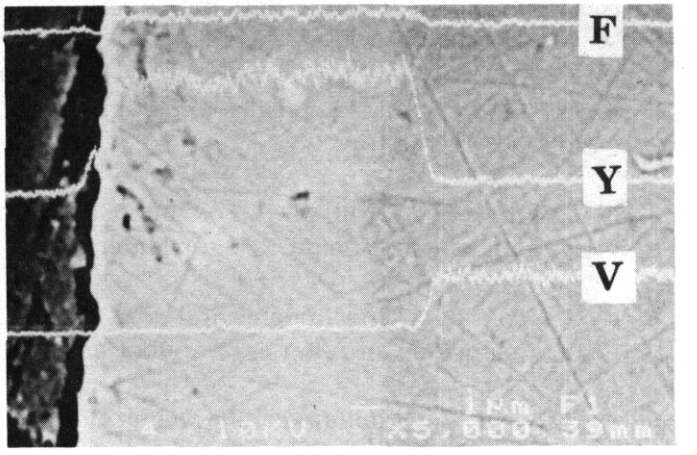

Figure **3.** ***SEM*** photo using backscattered electrons of polished cross-section from Test 6. Lineal x-ray *analysis shows* Y-V *diffusion* zone. Top, middle, ***and*** bottom analyses represent *F,* ***Y,*** and V concentrations, respectively

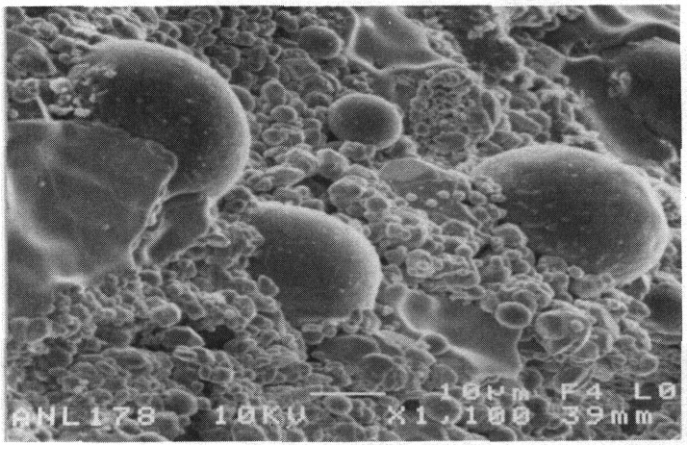

Figure 4. *Al* spheres on surface of alumina spacer in Test 5

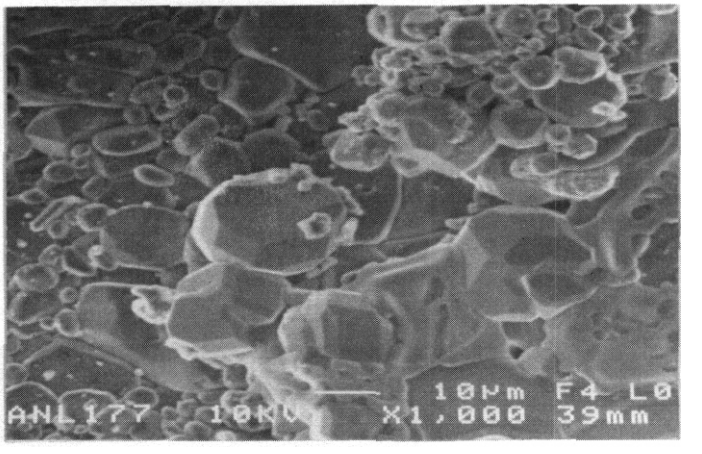

Figure 5. Oxide crystals with ***a*** ratio of 56 *atoms* ***Al*** **to** 44 atoms Y on surface of alumina spacer in Test ***5***

CONCLUSIONS

An electrolytic cell with a molten salt bath was constructed. Several discoveries were made during initial operation that led to changes in the original cell design. For example, the mullite tube was found to be unstable in the presence of LiF/NaF vapors and this led to the use of 998 alumina. Platinum could not be used as a connecting wire and as an electrode: however, Ni was a viable alternative. Because the thin Y electrodes rapidly dissolved in both salts, Ni and thicker Y electrodes were used. The goal of this research, formation of a diffusion coating of Y on V, was achieved. **A** coating of Y up to 10 μm thick with a 1-μm diffusion zone was formed on a V substrate. The interdiffusion coefficient was $\approx 10^{-13}$ cm^2 s^{-1}.

REFERENCES

1. B. F. Picologlou, Argonne National Laboratory, personal communication, 1991.

2. M. R. Fox, A. B. Hull, J.-H. Park, J.-H. Hseih, and G. Dragel, *Corrosion and Electrical Properties of Ceramic Insulators After Exposure to Lithium at 400°C*, Fusion Reactor Materials, DOE/ER-0313/9, Oak Ridge, TN (1990), p. 252.

3. D. Y. Wang, A. B. Hull, M. R. Fox, and C. E. Campbell, *Development of Ceramic Coatings for Liquid Metal Blanket Applications*, Fusion Reactor Materials, DOE/ER-0313/10, Oak Ridge, TN (1991), p. 330.

4. N. C. Cook, B. A. Foschnocht, and J. D. Evans, *Alloying of Metal Surfaces in Molten Fluorides*, Proc. 24th Int. Corrosion Conf. Series, National Association of Corrosion Engineers, Houston, TX (1968), p. 520.

5. R. S. Sethi, *Electroplating from Molten Salts*, J. App. Electrochem., **9** (1979), p. 411.

6. P. Taxil and J. Mahenc, *The Preparation of Corrosion-Resistant Layers by the Electrolytic Deposition of Tantalum on Nickel and Stainless Steel*, Corrosion Science, **21** (1981), p. 31.

7.0 SOLID BREEDING MATERIALS AND BERYLLIUM

TRITIUM RELEASE FROM CERAMIC BREEDER MATERIALS' - **J.** P. Kopasz, C. A. Seils, and C. E. Johnson (Argonne National Laboratory)

SUMMARY

Lithium aluminate is an attractive material (in terms of its chemical, mechanical, and irradiation properties) for breeding tritium in fusion reactors; however, its tritium release characteristics are not as good as those of other candidate materials. To investigate whether tritium release from lithium aluminate can be improved, we have studied tritium release from irradiated samples of lithium aluminate, lithium aluminate doped with magnesium, and lithium aluminate with a surface deposit of platinum. The release was studied using the Temperature Programmed Desorption (TPD) method. Both the platinum coating and magnesium doping were found to improve the tritium release characteristics as determined by TPD. Tritium release shifted to lower activation energies for the altered materials. In addition, information gained from the TPD experiments on the pure material were used to improve our tritium release model. The new model containing no adjustable parameters was used to successfully model in-pile tritium release from $LiAlO_2$.

OBJECTIVE

The objective of this work is to determine if tritium release from lithium aluminate can be improved by modifying the material and, in the process, to determine the mechanism for tritium release from lithium aluminate and obtain values for the rate constants involved

PROGRESS AND STATUS

Introduction

Tritium release from lithium aluminate is of interest due to the potential **use** of the aluminate as a tritium breeding material in a fusion device. Lithium aluminate compares favorably with the other candidate solid breeder materials in terms of its chemical, mechanical and irradiation properties; however, tritium release from lithium aluminate is slower than that from lithium oxide or lithium zirconate. We are investigating means of improving tritium release from the aluminate in hopes of gaining a more thorough understanding of the mechanisms involved in tritium release from this class of materials.

Our efforts to enhance the tritium release characteristics of $LiAlO_2$ have focused on changes in the bulk caused by doping with Mg. and changes on the surface caused by placing a Pt deposit on the surface. Unfortunately, changing the bulk often times also **causes** changes to the surface. This appears to have occurred in our case.

Experimental

Single crystals of pure and Mg doped $LiAlO_2$ were supplied by CEA. These crystals were grown using the Czochralski technique from a bath containing $LiAlO_2$ plus 3% by weight Li_2O (plus 0.5% Mg for the doped material).' Platinum was deposited onto the surface using a sputter chamber.' This deposition technique provided an incomplete Pt coating and left much of the surface unchanged. Two types of tritium release experiments were performed. The first type of experiment was a series of isothermal anneals performed on the same sample. The furnace was heated to temperature T1, and the sample moved into the heated portion of the apparatus. The tritium release was determined by a proportional counter and recorded as a function of time until a fixed time had elapsed or the release had reached the baseline value. The temperature was then raised to a new value T2 and the tritium release was observed as a function of time. In some cases, the temperature was increased to a third value after a specified period of time. Crystals for these

Contribution to: Fusion Reactor Materials Semiannual Progress Report for Period Ending March 31, 1992 - Report **No.** DOE/ER-0313/12.

'Work supported by the Office of Fusion Energy, U.S. Department of Energy, under Contract W-31-109-Eng-38.

experiments were irradiated at a flux of 0.4 x 10^{14} n/cm^2s for 10 hours in the OSIRIS reactor. Details of the annealing apparatus are given in reference 3. The second type of experiment is a Temperature Programmed Desorption. Crystals for this type experiment were irradiated at OSIRIS under the conditions above or in the Cadmium Lined Neutron Activation Tube at the University of Illinois, Champaign-Urbana, for 3 hours at a power level of 1500 kW. The cadmium lined facility was used to harden the spectrum and insure uniform tritium production throughout the single crystal. The TPD experiments were performed at CEA/Saclay and at Argonne. The experimental details are given in references 2 and 3.

Results and Discussion

Successive anneal experiments were performed on spherical single crystals (1 mm dia) of LiAlO, and LiAlO, doped with Mg. A typical example is illustrated in Fig. 1. The anneals are at 538, 777, and 950°C. The rapid initial release at 538°C followed by a return to the baseline seems to suggest that the majority of tritium has been released. However, when the temperature is increased to 777°C, a large tritium release peak is observed. Thus, the tritium that is released at 538°C is only a small fraction of the total tritium in the sample. This type of release is inconsistent with a simple diffusion controlled release mechanism or a simple desorption mechanism with one desorption site. The fraction of the total tritium released was analyzed as a function of time to determine the effective diffusion coefficient using the standard mathematics.[3] The effective diffusion coefficient was found to vary by up to an order of magnitude over the time of annealing at a single temperature, indicating the tritium release was not diffusion controlled at any of these temperatures (535, 750 and 950°C). Similar analyses of the fraction released indicated first-order desorption rate constants which are fairly constant over the time of the anneal. However, the values at the same temperature differ depending on the history of the anneal. These results suggest that tritium may be desorbed from several types of sites with discreet activation energies. To test this hypothesis, the tritium release curves from the isothermal anneal experiments were modeled as a combination of three first order processes. The rate constants were calculated from the individual anneals and then used to calculate activation energies and preexponential terms. These terms, plus a term describing the distribution of tritium between the three sites, were then used to calculate the tritium release for an experiment with successive anneals at 538, 777 and 950°C. The fit to the observed data was quite good and gave activation energies for desorption of 63, 133, and 142 kJ/mol.

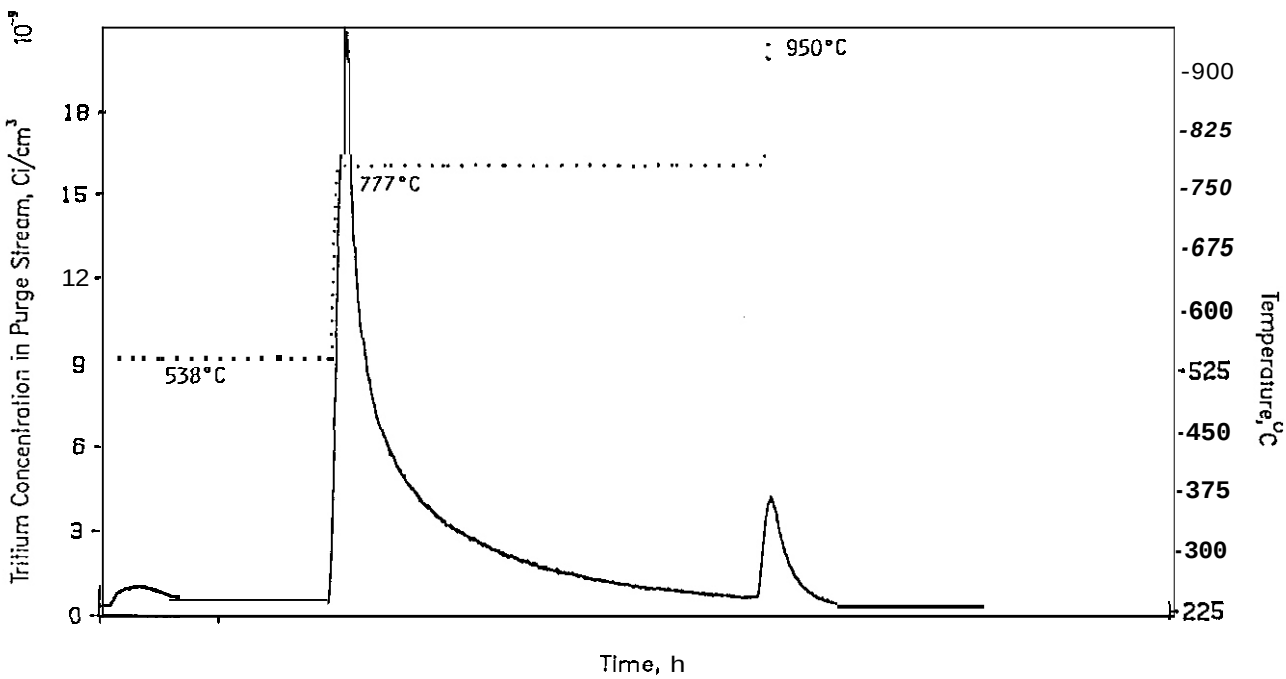

Fig. 1. Typical observed tritium release successive anneals at 538°C, 777°C, and 950°C

The TPD experiments are consistent with the hypothesis that the tritium is released from several types of sites and that tritium release from these single crystals does not follow a simple diffusion controlled release mechanism. Temperature programmed desorption measurements performed on single crystal (2 mm dia) $LiAlO_2$ show several overlapping peaks. If diffusion were rate limiting over this temperature range, only a single peak would have been observed. The TPD experiments were performed on single crystals of pure $LiAlO_2$, $LiAlO_2$ doped with Mg, and $LiAlO_2$ coated with Pt. Multiple peaks were observed in each case. Examples are shown in Figures 2 a-c. The resulting curves were fit to a sum of first-order desorption curves using a nonlinear least-squares optimization routine. The results for the pure material indicate five curves are present, with activation energies of 61, 99 129. 154, and 174 kJ/mol (Fig. 2a). These activation energies are in good agreement with those determined previously at CEA.[3] The energies of 61, 129 and 154 kJ/mol are also in good agreement with those used in the three site model to predict the release from the successive isothermal anneal experiment. The amount of tritium released from each state is proportional to the area under each of the first order desorption curves. The majority of the tritium in the pure $LiAlO_2$ (roughly 60%) was released from the state with the highest activation energy.

Doping the $LiAlO_2$ with Mg appears to have improved the low temperature tritium release. For the Mg doped material, the deconvolution indicated five peaks were present with activation energies of 47, 95, 113, 156 and 205 kJ/mol (Fig. 2b). The peaks at the low energies are shifted slightly from those in the pure material and are increased in intensity. The two lowest energy peaks account for roughly 25% of the tritium released from the doped material, while in the pure material the corresponding peaks account for only 13% of the detected tritium. In the doped material, 60% of the tritium is released with activation energies below 160 kJ/mol, while only 40% is released with activation energies below this value in the pure material. The activation energy of 95 kJ/mol is in excellent agreement with the energy for desorption of hydrogen from MgO (99.4 kJ/mol),[4] suggesting the doping altered the surface, creating low energy MgO sites from which the tritium can desorb.

The Pt coating also improved the tritium release. Four peaks with activation energies of 71, 99, 146, and 177 kJ/mol were determined in the TPD curves of the Pt coated samples (Fig. 2c). Approximately 40% of the tritium was released from peaks with activation energies below 150 kJ/mol, while for the pure material only 25% of the tritium was released from states with activation energies below this value. The activation energy of the low energy peak (71 kJ/mol) is shifted from that in the pure material (61 kJ/mol), and is in excellent agreement with the 68 kJ/mol determined for desorption of H_2 from platinum.[5] The activation energy of 146 kJ/mol is also in good agreement with that observed for desorption of H_2O from Pt.[6] One might suggest that since the platinum coating left the peaks with activation energies of 99 and 174 kJ/mol in the pure material relatively unchanged that these peaks are due to bulk processes. However, these peaks may be associated with surface processes since the platinum coating did not cover the whole surface and it is expected that tritium would bind to any portion of the surface uncovered by platinum with the same energies with which it was bound to the pure material.

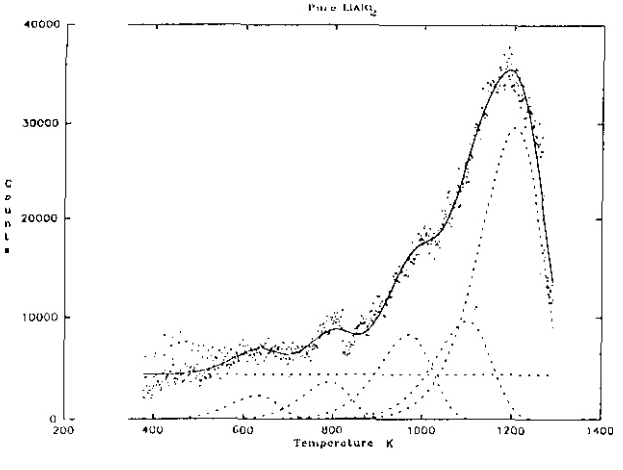

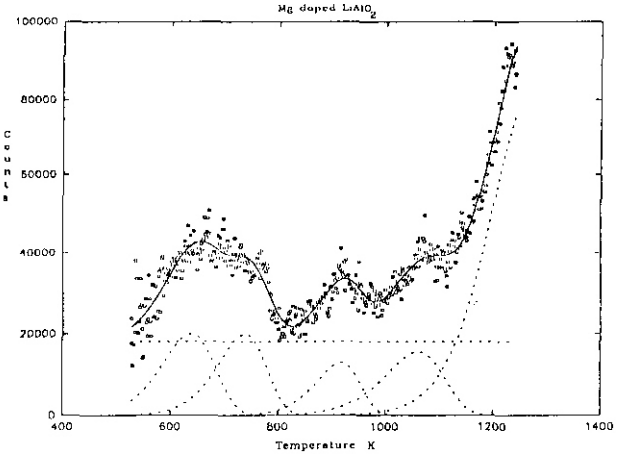

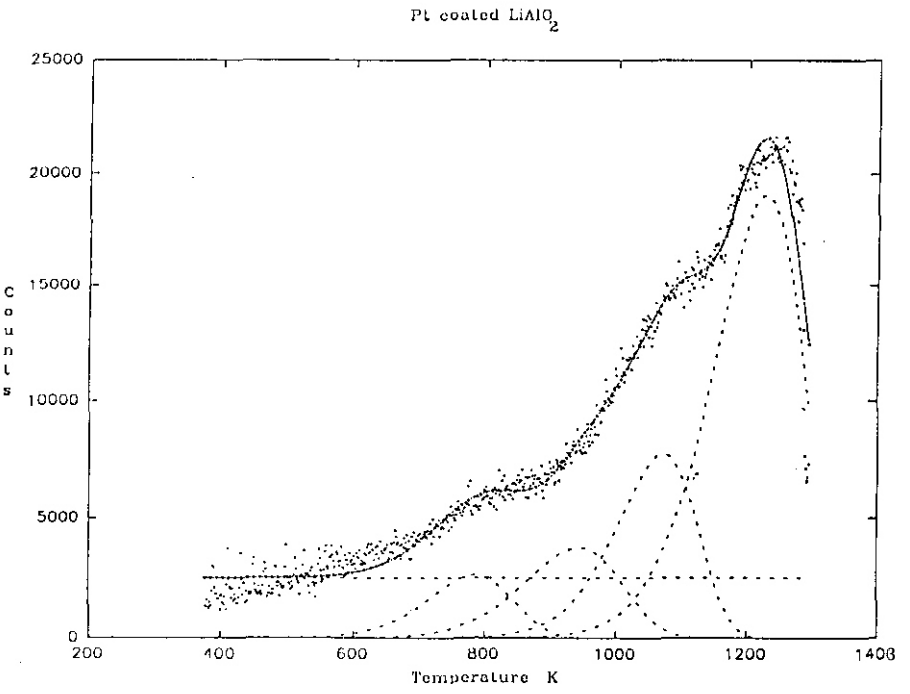

Figs. 2a-c. TPD curves for heating rates of 0.75°/man. Dashed curves indicate calculated values for individual peaks; solid curve represents total calculated curve; points represent observed for a) pure $LiAlO_2$, b) Mg doped LiAlO,. and c) Pt coated LiAlO,.

In order to test our interpretation of the TPD data and our current hypothesis for the mechanism of tritium release from LiAlO, (i.e., that the tritium is desorbed from several different sites), we have developed a tritium release model allowing for desorption from multiple sites. The model contains no adjustable parameters and uses data from our TPD experiments as well as experiments by Fischer[7] and Bruning et al.[8] This model was used to calculate the tritium release for temperature increases and decreases under conditions experienced in the MOZART in-pile tritium release experiment. The fit of the calculated tritium release to the experimental data is quite good. Examples are shown in Figs. 3a and 3b. Previously, this level of agreement has not been obtained without adjustment of some of the input parameters.

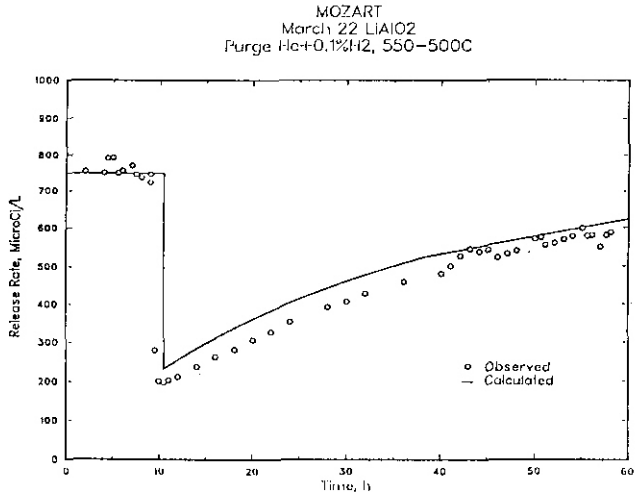

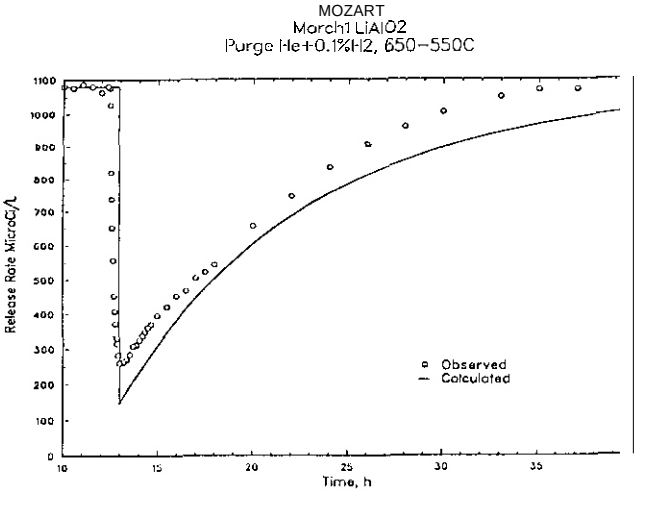

Figs. 3a-b. Calculated and observed tritium release from LiAlO, for in-pile temperature decreases a) from 650°C to 550 C° and b) from 550-C to 500°C.

CONCLUSION

Tritium release from $LiAlO_2$ occurs from several different sites. The good correlations between the activation energies for desorption of H_2 from MgO and Pt and H_2O from Pt with those found in the Mg doped and Pt coated samples suggest that some of these sites are located on the surface. This is supported further by the fact that the tritium release was improved by the platinum coating, which should have had no effect on the bulk, and the isothermal anneal experiments which could not be fit with a diffusion controlled release mechanism. Using a multiple desorption site model for tritium release, we were able to successfully model in-pile tritium release from lithium aluminate.

FUTURE WORK

Future work will be directed towards determining the relative contributions of desorption and diffusion to tritium release from $LiAlO_2$ at various temperatures by obtaining tritium profiles within the single crystals after isothermal anneals. The tritium distribution within the crystals will provide information on the tritium diffusivity and the effect of Mg doping on diffusivity, while the surface concentrations and tritium release curves will provide information on the desorption processes. With this information we will be able to answer more definitively what the rate controlling processes are under different conditions.

REFERENCES

1) N. Roux. CEA/Saclay, private communication (1990).
2) "Tritium Release from Irradiated Lithium Aluminate, Can it be Improved?" J. P. Kopasz, C. A. Seils, and C. E. Johnson, to be published in J. Nucl. Mat.
3) "Mechanism of Tritium Release from Lithium Ceramics Irradiated with Neutrons", F. Botter, J. Mougin, B. Rasneur, S. Tistchenko, and J. Kopasz, Proceedings of the 16th Symposium on Fusion Technology (North-Holland, New York, 1991) p. 924.
4) "Isotopic Study of Hydrogen Adsorption on Magnesium Oxide Powders", T. Ito, T. Murakami, and T. Tokuda. J. Chem. Soc. Faraday Trans. I, 79 (1983) 913.
5) P. R. Norton, J. A. Davies, and T. E. Jackman, Surface Science, 121 (1982) 103.
6) "Determination of the Activation Energy for OH Desorption in the $H_2 + O$ Reaction on Polycrystalline Pt", T. Wahnstrom, E. Fridell. S. Ljungstrom, B. Hellsing. B. Kasemo, and A. Rosen, Surface Science, 223 (1989) L905.
7) A. K. Fischer, to be published in Proc. of the International Conference on Fusion Reactor Materials-5, J. Nucl. Mater.
8) "The Diffusivity of Tritium in the System Li_2O-Al_2O_3", D. Bruning, D. Guggi, and H. R. Ihle. Proc. of the 12th International Symposium on Fusion Technology, (1982)543.

TRITIUM MODELING/BEATRIX-II DATA ANALYSIS - M.C. Billone, H. Attaya, C.E. Johnson, and J.P. Kopasz (Argonne National Laboratory)

SUMMARY

Models have been developed to describe the tritium transport in Li_2O. The mechanisms considered are bulk diffusion, surface desorption, surface adsorption, and solubility. These models have been incorporated into the TIARA steady-state inventory code and the DISPLZ steady-state and transient code. Preliminary validation efforts have focused on the inventory and tritium release rate data from in-reactor, purge-flow tests VOM-15H, EXOTIC-2, CRITIC-1, and MOZART. The models and validation effort are reported in detail in ANL/FPP/TM-260. Since the BEATRIX-II data were released officially in November 1991, validation efforts have been concentrated on the tritium release rate data from the "isothermal" thin-ring sample. In this report, results are presented for the comparison of predicted long-time inventory changes (in response to temperature and hydrogen purge pressure changes) to values determined from the tritium release data.

OBJECTIVE

The objective of this work is two-fold: to evaluate the BEATRIX-II data base to determine its adequacy for code validation and to use that part of the data base which is deemed to be physically reasonable for validation of the Li_2O tritium transport models in DISPL2.

PROGRESS and STATUS

BEATRIX-II data sets were made available to the modeling community at the Modelers/Code Developers Meeting in Clearwater, FL, on November 16, 1991. The data sets included temperatures, H_2 purge gas content, and tritium release rate histories for the thin-ring "isothermal" sample in response to changes in temperature and H_2 partial pressure for the standard flow rate condition of 0.1 L/min. Prior to the release of these data sets, models had been developed for diffusion, desorption, adsorption, and solubility of tritium in Li_2O. Model parameters were determined from well-controlled laboratory tests of samples either soaked with tritium or pre-irradiated at low temperature to generate the bulk tritium. The models were incorporated into the steady-state inventory code TIARA and the steady-state and transient DISPL2 code. Model/code validation focused on inventory data and tritium release-rate data from in-reactor, purge-flow tests VOM-ISH, EXOTIC-2, CRITIC-1, and MOZART. The model and code development efforts, as well as the validation effort, are documented in detail in Ref. 1.

Logically, the evaluation of BEATRIX-II data and the code validation would proceed as follows: 1) compare the end-of-test measured tritium inventory in the thin-ring sample to the calculated inventory; 2) evaluate the long-term inventory changes (obtained from integrating the tritium release-rate data) in response to changes in temperature and purge H_2 content to insure consistency with the measured end-of-life inventory; 3) compare calculated inventory changes to those implied inventory changes from the data base which exhibit consistency with end-of-test measurements; and 4) compare code predictions to the detailed tritium release-rate data. Unfortunately, the inventory measurements will not be conducted until late this summer, *so* steps 1 and *2* have to be deferred. The comparison of inventory changes calculated from models and calculated from tritium release-rate data is presented in the following.

Table 1 shows the generation rate, temperatures and H_2 purge content for the cases included in the BEATRIX-II data sets. Also included in the table are the model-calculated tritium inventory (I) for each set of conditions, the model-calculated tritium inventory change (ΔI) with each temperature and H_2 change and the inventory change deduced from the transient release rate data. The ΔI values deduced from data were calculated by the formula

$$\Delta I = \int_0^t (\dot{G} - \dot{R})\, dt \qquad (1)$$

where $\dot{R}$ is the measured release rate, $\dot{G}$ is the estimated generation rate and t is time. The major uncertainty in the ΔI deduced from data is the uncertainty in the generation rate and any changes in ion chamber baseline and calibration as temperature and H_2 partial pressure are changed. Small changes (on the order of a few percent) in the assumed generation rate cause large changes in the deduced ΔI. The uncertainty is much larger for the H_2 partial pressure changes than it is for the temperature changes. For the H_2 changes, it is not clear why the inventory changes appear *so* large and the uncertainty is *so* great. It could be due to changing baseline and calibration of the ion chambers, system effects which account for retained tritiated moisture (HTO) as the H_2 pressure is lowered or excessive retention in the Li_2O ceramic. The latter is unlikely based on previous experience with Li_2O under similar conditions.

The agreement between model-calculated ΔI and data-deduced ΔI is reasonable for the first large (e.g., 636 → 550 → 636°C) temperature change in 0.1% H_2. The model calculations remain essentially the same for the subsequent three large-temperature cycles, but the results deduced from data increase by about 70%. For the smaller temperature changes, the error is too large to allow a meaningful comparison. Also, for the H_2 purge partial pressure changes, the uncertainty band is orders of magnitude larger than the predicted value.

Table 1. Model predictions for inventory change in BEATRIX-II thin ring sample in response to temperature and H_2 purge partial pressure changes. Purge flow is 0.1 ℓ/min. A tritium generation rate of (50 ± 5) μCi/s = (4.31 ±0.43) x 10^{-4} wppm/s is assumed for all calculations.

Case	T, °C		P_{H_2}	I (model)		ΔI, mCi	
	Min	Max	Pa	wppm	mCi	Model	Data
1	598	638	150	0.0595	6.9		
	562	600	150	0.1173	13.6	+ 6.7	+28 ± 54
	513	550	150	0.3531	41.0	+27.4	+36 ± 27
	559	597	150	0.1248	14.5	-26.5	-24 ± 19
	596	636	150	0.0597	6.9	- 7.6	-1 ± 36
	513	550	150	0.3531	41.0	+34.1	+42 ± 10
	596	636	150	0.0597	6.9	-34.1	-55 ± 22
2	596	636	150	0.0597	6.9		
	596	636	-0	0.1412	16.4	+ 9.5	+(15±10) × 10^3
	596	636	15	0.1065	12.4	- 4.0	-(3±10) × 10^3
	596	636	150	0.0597	6.9	- 5.5	-(5±10) × 10^3
3	509	545	150	0.3939	45.7		
	509	545	-0	0.6855	79.5	+33.8	+(15±10) × 10^3
	509	545	15	0.6781	78.7	- 0.8	-(4±10) × 10^3
	509	545	150	0.3939	45.7	-33.0	-(7±10) × 10^3
4							
(80 EFPO)	599	639	150	0.0567	6.6		
	508	544	150	0.4036	46.8	+40.2	+75 ± 5
	598	638	150	0.0595	6.9	-39.9	-85 ± 15
(215 EFPD)	594	634	150	0.0620	7.2		
	511	547	150	0.3753	43.5	+36.3	+63 ± 13
	594	634	150	0.0620	7.2	-36.3	-88 ± 13
(290 EFPO)	602	642	150	0.0537			
	510	546	150	0.3845			+80 ± 10
	602	642	150	0.0537	6.2	-38.4	-100 ± 10

At this stage of data evaluation and model validation, it is difficult to determine how good the data are for model validation. Part of the problem is that the inventory and inventory changes in Li_2O may be too small to determine accurately from tritium release rate data. A second problem comes from not fully understanding how much of the recorded signal is due to system (e.g. long purge lines, condensing cells, molecular sieves, etc.) effects and how much is an accurate portrayal of the response from the breeder. The third problem has to do with possible baseline drift and changing calibration of the ion chambers. These problems exist in interpreting all in-reactor purge-flow tritium release rate data. However, the reason that they are emphasized with the BEATRIX-II data set is that it was a better-controlled test than the others and the experimenters were very scrupulous about addressing these problems. Some of the uncertainty in interpreting the BEATRIX-II temperature change data will be resolved once the end-of-test inventory is measured directly. The final BEATRIX-II run was conducted in 0.1% (150 Pa) H_2 at an average breeder temperature of 530°C. For example, in order for the data interpretation in Table 1 to be correct, the breeder must at least have on the order of 40-80 mCi of tritium in it in order for it to release that much with a temperature increase of 90-100°C.

FUTURE WORK

Future efforts will be directed toward obtaining a detailed temperature and reactor history of the last FFTF run, including reactor shutdown period (during which the FFTF power was decreased from 100% to 0%), for both the "isothermal" thin-ring sample and the temperature-gradient solid pellet sample. With the relatively long reactor shutdown ramp, tritium is generated as the breeder temperature decreases. The retained tritium during this period, especially for the thin-ring sample, may be greater than the tritium retained during full-power operation. It is important that inventory calculations he performed for this last run before the data are obtained in order to add credibility to the modeling and to aid in the interpretation of the data.

REFERENCES

1. M.C. Billone, H. Attaya, and J.P. Kopasz, "Modeling of Tritium Behavior in Li_2O," Argonne National Laboratory report ANL/FPP/TM-260, April 1992 (draft under review).

DESORPTION CHARACTERISTICS OF THE Li_2O SYSTEM' - A. K. Fischer and C. E. Johnson (Argonne National Laboratory)

OBJECTIVE

The objective of this activity is to investigate the energetics and kinetics of desorption of $D_2O(g)$, $HDO(g)$, $H_2O(g)$, HD, and D from the surface of Li_2O in the presence and absence of H_2, yielding data that facilitate predictions of the characteristics of tritium release.

SUMMARY

Preparations were completed for temperature programmed desorption (TPD) measurements of the kinetics of desorption from the D_2-H_2-HD-HDO-H_2O-Li_2O system. These preparations consisted of a series of blank and calibrating runs to determine the effects of the empty sample tube on the TPD spectra and to calibrate the mass spectrometer for the gaseous species of interest. Data from the blank tube runs revealed the importance of isotope exchange reactions in interpreting desorption data. A preliminary examination was made of the raw spectra of desorption from Li_2O that had been treated with Ar-D_2 (921 vppm) at temperatures of 473, 673, 873, and 1108 K (200, 400, 600, and 835°C). The TPD spectra appear to contain fewer peaks than were observed earlier for $LiAlO_2$.

PROGRESS AND STATUS

Introduction

Earlier reports in this series discussed the background for the temperature programmed desorption (TPD) technique for measuring the activation energy and pre-exponential terms for the desorption rate equation. Recently, measurements were reported for the H_2O-H_2-$LiAlO_2$ breeder system.' With interest in the ITER program centering on Li_2O as the first choice of breeder, the focus of the TPD measurements has been shifted to develop understanding of desorption from Li_2O. In particular. the quantitative determination of the effectiveness of H_2 in enhancing desorption processes is of interest. Part of the earlier work revealed the existence of tube effects which required stabilizing the tube in respect to desorption of H_2O. In the present situation, baseline data are needed for tube performance in respect to both desorption of H_2 and H_2O as well as exchange with deuterium-containing species.

Results and Discussion

Blank experiments with an empty sample tube were performed in order to have baseline data for the performance of the system. Such information is needed to allow corrections to be made on raw data and to interpret the TPD spectra.

Some of the blank experiments involved passing argon containing H_2 and D_2, both singly and as mixtures, through the empty sample tube at temperatures to be covered in the ensuing TPD measurements. In the case of the mixtures, it was found that the isotopic exchange reactions proceed to a significant degree. One of these reactions is $H_2 + D_2 \rightleftharpoons 2$ HD. Figure 1 shows smoothed data for the mass spectrometrically measured H_2, HD, and D_2 levels in the argon stream in which the H_2:D_2 ratio was changed in stepwise fashion. The important observation is that HD appears essentially immediately, indicating that the H_2-D_2 exchange occurs quickly. This process is rapid even at a temperature of 373 K (100°C), as well as 873 K (600°C).

Contribution to: Fusion Reactor Materials Semiannual Progress Report for Period Ending March 31, 1992 - Report No. DOE/ER-0313/12.

Work supported by the Office of Fusion Energy, U.S. Department of Energy, under Contract W-31-109-Eng-38.

The reaction quotient which relates the observed partial pressures represented by (H_2), (D_2), and (HD), and which is given by $(HD)^2/((H_2)(D_2))$, ranged from about 4.4 to 5.7. The equilibrium constant for this reaction, which has been studied thoroughly and reviewed,, ranges from 3.5 to 4.0 in the given temperature range. Considering 10 to 20% as the error bar for each measured species, the observed reaction quotient could be consistent with attainment of equilibrium in the gas phase exchange reaction.

In addition to exchange among the reduced species, exchange with the oxidized species also must be considered. This would involve exchange among all of the species, H_2, HD, D_2, H_2O, HDO, and D_2O. Residual H_2O adsorbed on the tube walls was available at low levels for the exchange processes. Figure 2 shows the traces for the species HD. D_2, H_2O, HDO, and D_2O. H_2 was not measured because our instrument accepts only 5 **selected** species. Again, H_2 and D_2 at several ratios in the input argon stream were used. Effects at 873 K (600°C) and 1073 K (800°C) were examined. The rapid appearance of HDO and D_2O again attests to rapid exchange. For the exchange reaction, $D_2 + H_2O \rightleftharpoons HDO + HD$, the reaction quotient is $(HDO)(HD)/((D_2)(H_2O))$. The observed value ranged from approximately 7 to 10.7. For equilibrium, the equilibrium constant is **4.5** to 4.8 at these temperatures. For exchange among only the oxidized species, $H_2O + D_2O \rightleftharpoons 2$ HDO, the observed reaction quotient was 1.2 to 3.3, to be compared with the equilibrium constant of 4. Overall, these results cannot, strictly speaking, be claimed to reflect reactions at equilibrium without further work. However, they do indicate substantial progress toward equilibrium. At high temperature, about 873 K (600°C), equilibrium was achieved in a relatively short reaction **zone,** about 10-20 cm long. At **lower** temperature, about 373 K (100°C), equilibrium was achieved in a longer path length, less than 1 m.

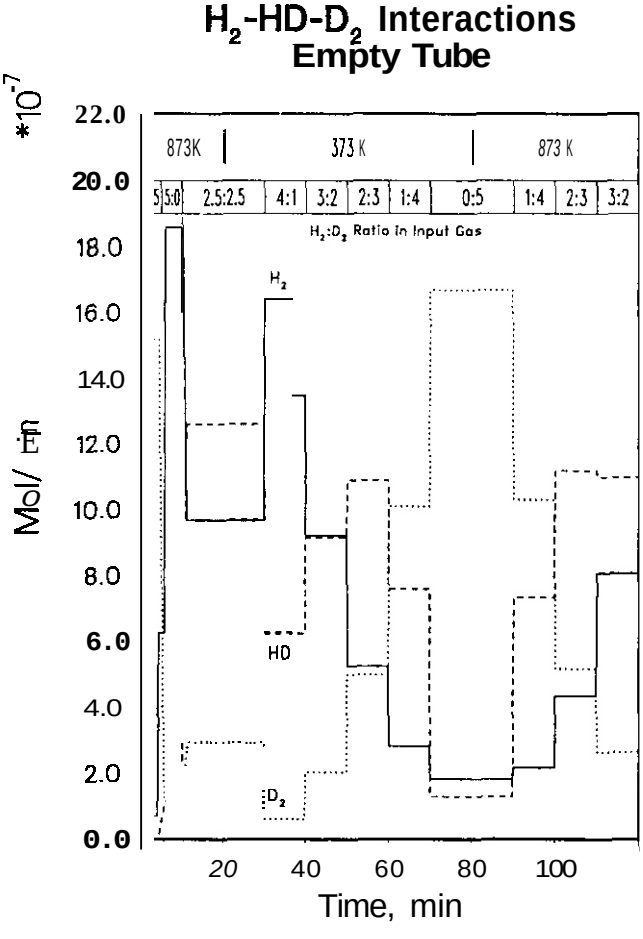

Fig. 1. H_2-HD-D_2 interactions in empty sample tube **at** 373 and 873 K.

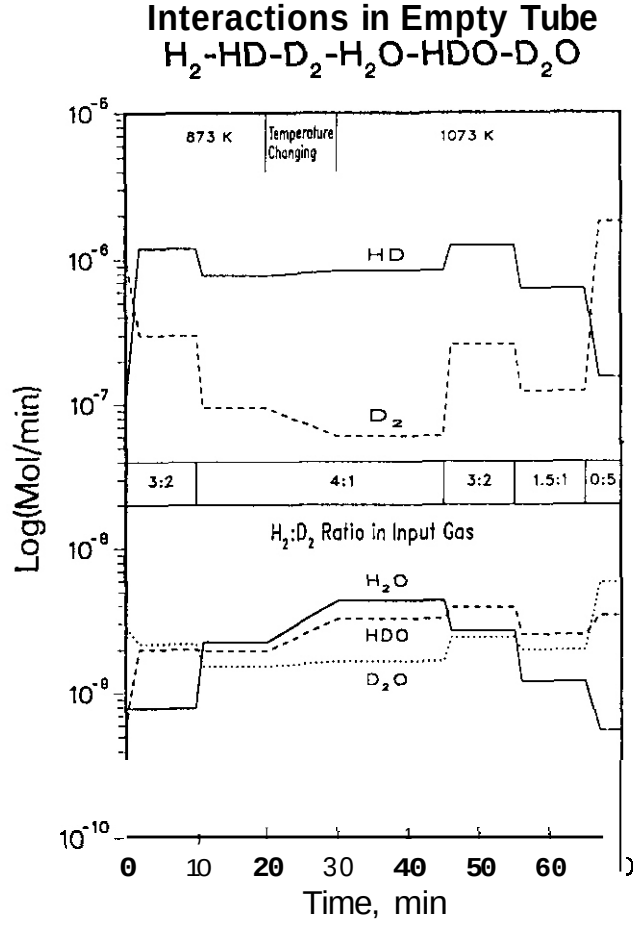

Fig. **2.** H_2-HD-D_2-H_2O-HDO-D_2O interactions in empty sample tube at 874 and 1073 K.

The rapid isotope exchange demonstrated by these empty tube experiments has important implications for the interpretation of in-reactor and out-of-reactor tritium release experiments. In such tests. lines are often much longer than 1 m and are often maintained at 373 K or somewhat higher temperature to minimize adsorption of aqueous species on the walls. Exchange must be expected. When H_2 is added to the sweep gas to facilitate release of tritium and is present in an amount that swamps the tritium, it follows that the gas that is analyzed downstream from the breeder may be expected to contain the tritium dominantly as HT, regardless of the form in which it was released. Therefore, statements in the literature claiming that tritium was released in various proportions of oxidized and reduced forms must be regarded skeptically unless there is evidence that the exchange question was addressed.

Further work on this question is needed to understand the roles of the surfaces of various tube materials and of the breeder itself as catalysts, both positive and negative, in promoting or inhibiting the exchange processes.

In the work with Li_2O, the sample was being loaded with deuterium by exposure to a stream of argon with 921 vppm D_2 at temperatures of 473,673,873, and 1108 K (200, 400,600, and 835°C). The soaking time was 18 h (overnight) or 66 h (over weekend). The TPD processes into a sweep gas of either argon or argon containing 1000, 500,250, or 100 vppm H_2 have been measured. This provides a close analog of the tritium release process in a reactor situation at least in respect to the reduced species. Data reduction remains to be completed before conclusions may be drawn. However, the raw data suggest that fewer peaks are involved than were found in the earlier work with $LiAlO_2$.

FUTURE WORK

Beyond the measurements on Li_2O and reduction and analysis of the data, analogous data will be needed for Li_2ZrO_3, the alternate ceramic breeder for ITER.

REFERENCES

1. A. K. Fischer and C. E. Johnson, "Desorption Characteristics of the $LiAlO_2$-H_2-H_2O(g) System." Fusion Reactor Materials Semiannual Progress Report for the period ending March 31, 1991, DOE/ER-0313/10, p. **284.**
2. I. Kirshenbaum, "Physical Properties and Analysis of Heavy Water," McGraw-Hill, 1951, Chapter 2.

TRITIUM TRANSPORT IN SINGLE CRYSTAL $LiAlO_2$* - J. P. Kopasz, C. A. Seils, and C. E. Johnson (Argonne National Laboratory)

OBJECTIVE

The objective of this study is to determine the tritium diffusion and tritium desorption rate constants for $LiAlO_2$, and to determine the effects of dopants on these rate constants.

SUMMARY

Tritium transport in $LiAlO_2$ has been studied by performing isothermal anneals followed by sectioning of the sample to determine the tritium concentration profiles within the sample. The anneals were performed over the 528 to 783°C temperature range under a He + 0.1% H_2 purge gas flow. The results indicate that: 1) tritium diffusion in $LiAlO_2$ is fast, and is not sensitive to impurities, and 2) tritium release for these samples is in the mixed diffusion-desorption regime. For samples with a grain size of 100 μm or less, the tritium release will be desorption controlled.

PROGRESS AND STATUS

Introduction

Tritium transport in lithium ceramics has received considerable attention, due to the potential of these ceramics to be selected as tritium breeding materials in fusion reactors. While tritium transport in lithium aluminate has been investigated by several authors,[1-7] the mechanism of tritium release from $LiAlO_2$ and the diffusion and desorption rate constants are still uncertain. Values for the tritium diffusivity over six orders of magnitude have been reported.[1-7] Further, the question as to whether diffusion or desorption is the rate limiting mechanism is still being debated.

Generally, the method for determining the diffusion and desorption rate constants has been to measure the tritium released from the lithium aluminate, analyzing the time dependence of the release process based upon a diffusion, desorption, or mixed diffusion-desorption model. Quanci[8] and Verrall[9] have put forward mathematical tests based upon plots of the natural log of the fraction of tritium released versus the natural log of the time to determine whether the release falls in the diffusion or desorption controlled regime. Frequently, the initial release behavior does not follow the prescribed mathematics due to mixing and time delays in the experimental apparatus. An alternative to overcome these difficulties would be to examine the tritium distribution within the solid rather than observing the tritium released from the solid.

In the solid, contributions from desorption are expected to be small and should be most Influential in the near-surface region. In the interior, the concentration gradient should be less sensitive to the desorption rate constant than the external tritium release, making it possible to obtain good diffusion values, even in the mixed diffusion-desorption regime.

Some of the observed spread in the reported tritium diffusivities may be due to the presence of impurities in the materials. Impurities can alter the diffusivity by creating vacancies, interstitials or other defects that have strong influences on transport behavior. In lithium aluminate, it has been postulated that tritium diffusion occurs via a lithium-vacancy tritium complex.[10] If this is the case, then impurities which affect the number of lithium vacancies should affect the tritium diffusivity. The sensitivity of the tritium diffusivity to these impurities will depend on the number of lithium vacancies due to the impurity relative to those present in the pure material.

In an attempt to determine the diffusivity of tritium in lithium aluminate, we have performed isothermal anneal tests on single crystal samples. In order to minimize the contributions to tritium release from desorption, we have employed large (2 mm dia.) single crystals and have sectioned the material to determine the tritium profile within the solid. The larger the crystal the closer one will be to the diffusion regime, however, the release may still be in the mixed diffusion-desorption regime which would make obtaining the rate constants from the time dependence of the tritium release difficult. Therefore, we have sectioned the samples and determined the tritium concentration profile within the sample. In an attempt to understand the effects of impurities on the tritium transport, we have studied the tritium profiles in pure and Mg doped (0.3%) $LiAlO_2$.

*Work supported by the Office of Fusion Energy, U.S. Department of Energy, under Contract W-31-109-Eng-38

Experimental

Single crystals of pure and Mg doped $LiAlO_2$ were supplied by CEA. The crystals were grown using the Czochralski technique and the Mg dopant level determined to be 0.3% by spark source spectrometry.[11] The samples were dried under vacuum at 800°C for 4 hours and then packaged in aluminum capsules which were cold welded in an inert He atmosphere glovebox. The capsules were irradiated in the Cadmium Lined Neutron Activation Tube at the University of Illinois, Urbana Champaign, for 3 hours at a power level of 1500 kW. The cadmium lined facility was employed to harden the spectrum and ensure that the tritium production within the single crystal was spatially uniform. The calculated amount of tritium produced is 1 μCi per single crystal.

In preparation for the isothermal anneal tests, the single crystals were transferred from the Al capsules to a sample holder in an inert atmosphere glovebox. The sample holder was designed with two compression fittings, which enabled isolation of the sample from the atmosphere while transferring it from the glovebox to the annealing apparatus. The annealing apparatus was preheated to the desired temperature, and a purge flow established. The sample was then introduced to the furnace by loosening the compression fittings and sliding the sample into the furnace. The fittings were tightened and the sample annealed for a specified time. The released tritium was reduced in a zinc bed, detected with a proportional counter, then oxidized over a CuO bed and trapped in ethylene glycol. After the anneal, the sample was quenched by loosening the compression fittings and sliding the sample out of the furnace into a cool zone in the apparatus. The temperature of the sample would drop 200°C in about 3-5 minutes.

After cooling, the sample diameter was measured using a spring loaded dial micrometer. The sample was then placed in a vial containing 1 ml of an HCl/HF acid solution (6 N HCl, 0.5 N HF) which was placed in a thermostated bath at 50°C. After approximately 30 minutes in the bath, the vial was removed and 2 ml of water added. A 1 ml aliquot of this solution was removed and placed in a scintillation vial along with 18 ml of scintillation cocktail. The remaining solution was pipetted out of the vial and discarded. The vial and crystal were washed 4 times with 1 ml of water. The crystal was then removed from the vial, blotted dry and its diameter measured again with a dial micrometer. The crystal was then placed in a vial with 1 ml of acid solution and the above steps repeated until the crystal size was too small too handle. At that point the crystal was left in the acid solution overnight, then 2 ml of water were added to the acid solution, and a 1 ml aliquot taken for scintillation counting.

Calculations

Tritium release from single crystal lithium aluminate can be represented using a diffusion model with desorption occurring at the surface. The differential equations governing the tritium transport are:

$$\frac{\partial C}{\partial t} = D\left(\frac{\partial^2 C}{\partial r^2} + \frac{2}{r}\frac{\partial C}{\partial r}\right)$$

for $0 \le r < a$;

$$\frac{\partial C}{\partial r} + \frac{K}{D}C = 0$$

for $r = a$.

The solution to these equations for the case of a constant initial concentration C_i is given below.[12]

$$C = \frac{2hC_i}{r}\sum e^{(-D\alpha_n^2 t)}\frac{a^2\alpha_n^2 + (ah-1)^2}{\alpha_n^2[a^2\alpha_n^2 + ah(ah-1)]}\sin(a\alpha_n)\sin(r\alpha_n)$$

From this equation, one can determine the diffusivity and desorption rate constant given the initial tritium concentration and the tritium concentration at the surface and at the center of the annealed crystal. In practice we found that it was better to fit the total observed tritium profile to the equation. This practice would minimize errors due to the difficulties in measuring the very small crystal size left near the end of the dissolution. Diffusivities were obtained by using the initial concentration and a minimization routine to fit the concentration data to the equation for tritium concentration as a function of radial distance.

RESULTS AND CONCLUSIONS

Data are presented in Figs. 1-4 as graphs of tritium concentration as a function of radial position. Representative plots showing the observed tritium profile and the fit to the data with the calculated diffusivity and desorption rate constant are shown. Results for the pure and Mg doped LiAlO, are illustrated in Fig. 5. The diffusivity was observed to follow a simple Arrhenius type temperature dependence. The measured diffusivities for the doped and undoped materials were the Same within experimental error. 'The calculated diffusivity is given by $\ln D = -2.246 - 1.519 \times 10^{4}/T$, yielding an activation energy of 30.1 kcal/mol. The desorption rate constants determined by this sectioning method exhibit some scatter. The scatter may be due to experimental difficulties in determining the concentration at the surface, or due to a more complex surface desorption process with different mechanisms contributing at different temperatures. If one looks at the data from the doped sample, it suggests there may be two desorption activation energies, however, more data are needed to provide conclusive information.

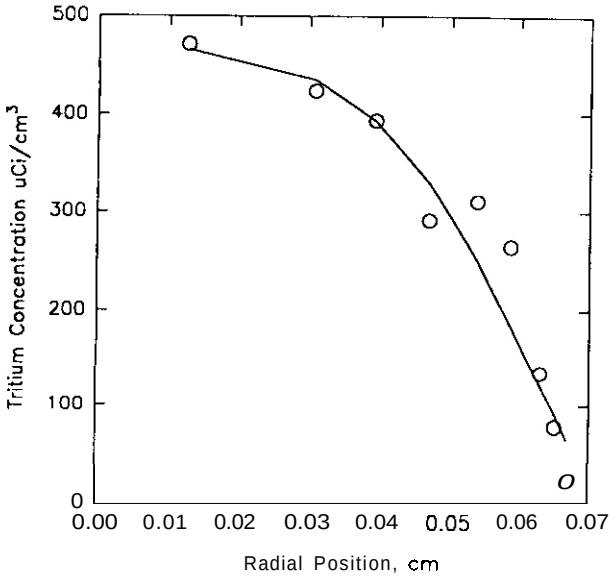

Fig. 1. Observed and calculated tritium profile for an anneal at 783°C for 4,500 seconds, curve calculated for $D=3.24\times10^{-8}$ cm^2/s and $K=9.0\times10^{-6}$ cm/s.

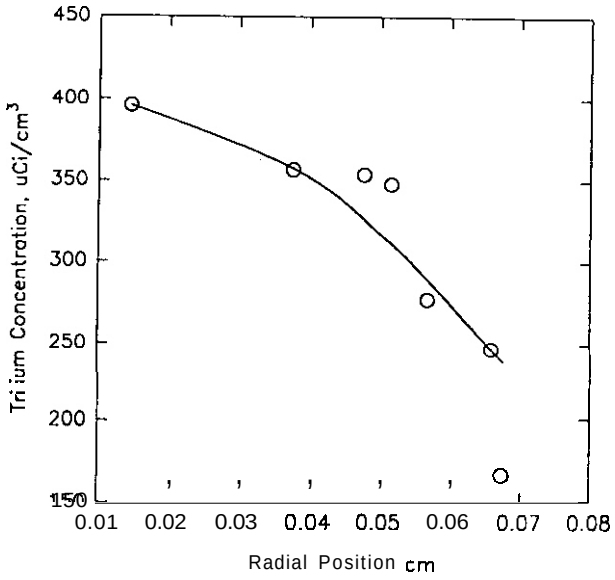

Fig. 2. Observed and calculated tritium profile for an anneal at 606°C for 64,500 seconds, curve calculated for $D=6.39\times10^{-9}$ cm^2/s and $K=1.37\times10^{-7}$ cm/s.

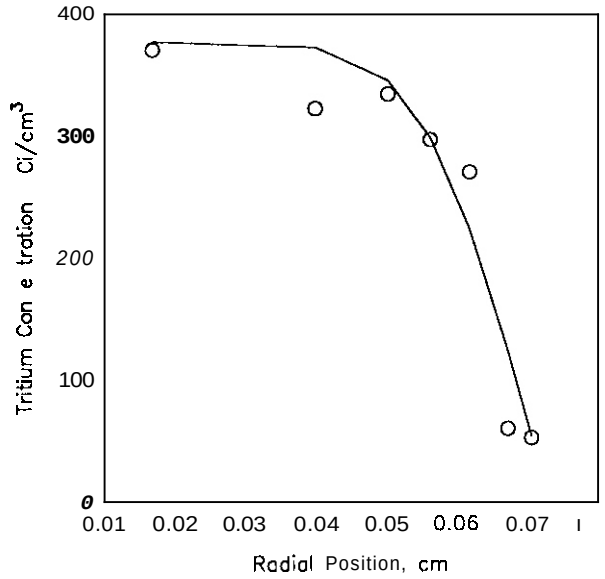

Fig. 3. Observed and calculated tritium profile for an anneal of a Mg doped sample at 572°C for 61,200 seconds, curve calculated for $D=1.2\times10^{-9}$ cm^2/s and $K=1.2\times10^{-7}$ cm/s.

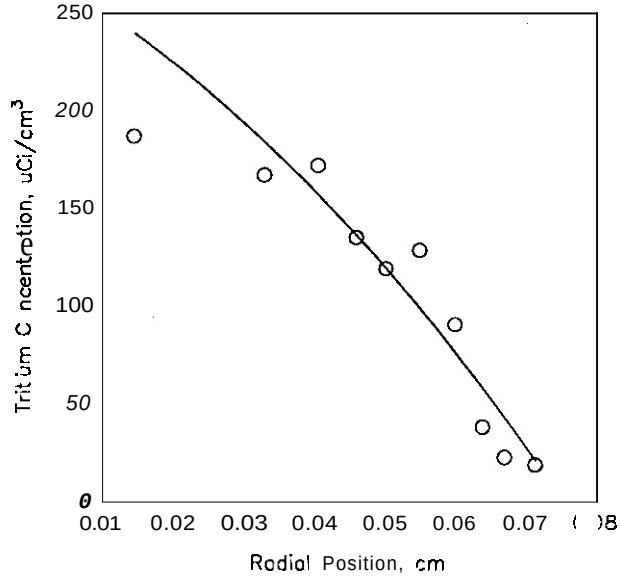

Fig. 4. Observed and calculated tritium profile for an anneal of a Mg doped sample at 750°C for 18,000 seconds, curve calculated for $D=3.9\times10^{-8}$ cm^2/s and $K=9.0\times10^{-6}$ cm/s.

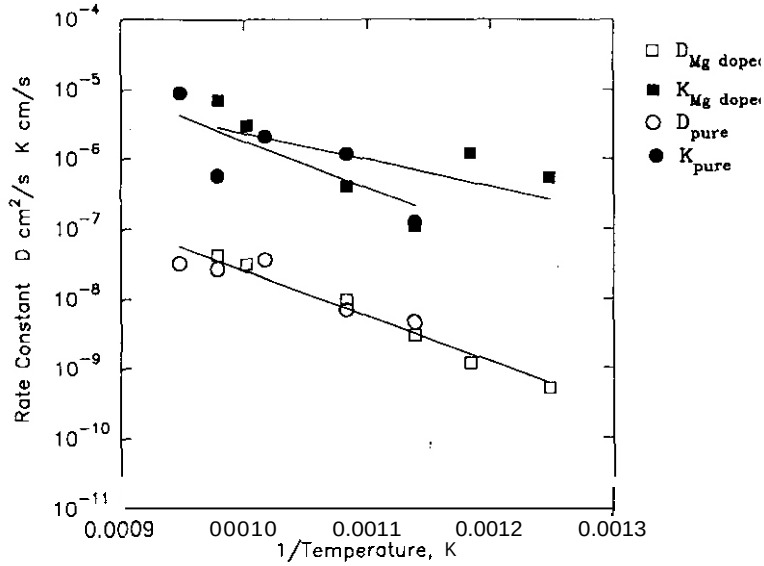

Fig. 5. Temperature dependence of rate constants for tritium transport in $LiAlO_2$.

The tritium diffusion coefficient determined in these samples is higher than most of the reported values, but is comparable to the single value reported by Botter,[3] and the value determined by Bruning et al.[1] These latter studies give tritium diffusivities which are several orders of magnitude above other literature values.

Using the values determined for D and K (desorption rate constant) in these large single crystals, and the rule that desorption will be rate controlling when the ratio aK/D is less than or equal to 1 (a=grain radius), we see that for grain sizes less than or equal to 200 μm, the tritium transport will be in the desorption controlled regime. Thus, for in-pile tests using small grain material, these results suggest tritium release should be desorption controlled.

FUTURE WORK

More data need to be collected to ensure greater precision in the values for the tritium diffusivity and isothermal anneals need to be performed on small single crystals with release in the desorption regime. The anneals on the small samples will allow us to obtain values for the desorption rate constants from the release curves, with little or no distortion due to diffusion contributions. We can then determine if the scatter observed in the desorption rate constants for the large single crystals is due to the experimental difficulty of determining the surface concentration or to the presence of more than one desorption mechanism.

ACKNOWLEDGMENTS

We would like to acknowledge CEA, France for supplying us with single crystals of pure and Mg doped $LiAlO_2$.

REFERENCES

1) D. Bruning. D. Guggi, and H. R. Ihle, Fusion Technology, 1 (1982), 543.
2) R. Clemmer et al., The TRIO Experiment.
3) F. Botter, Proceedings of the 14th SOFT, Avignon, France, Sept. 1986.
4) K. Okuno and H. Kudo, J. Nucl. Mater., 138 (1986).357.
5) T. Kurasawa, H. Watanabe, G. W. Hollenberg. Y. Ishii, A. Nishimura, H. Yoshida, Y. Naruse, M. Aizawa, H. Ohno, and S. Konishi, J. Nucl. Mater., 141-143 (1986), 265.
6) S. Tanaka, A. Kawamoto. M. Yamawaki. T. Terai, Y. Takahashi, H. Kawamura, and M. Saito. Fusion Eng. and Des., 8 (1989), 155.
7) J. P. Kopasz, C. A. Seils, and C. E. Johnson, Proceedings of International Conference on Fusion Reactor Materials -5, Clearwater, FL, Nov. 18-22, 1991.
8) J. F. Ouanci, Princeton University Dissertation. Department of Chemical Engineering, 1989.
9) R. Verrall, Proceedings of the International Workshop on Ceramic Breeder Blanket Interactions. Clearwater, FL, Nov. 22-23, 1991.
10) J. P. Kopasz, S. W. Tam, and C. E. Johnson, J. Nucl. Mater., 179-181 (1991), 816.
11) N. Roux, CEA, Personal communication, 1990.
12) H. S. Carsiaw and J. C. Jaeger, "Conduction of Heat in Solids", Clarendon Press, 1959.

NEUTRON IRRADIATION OF BERYLLIUM: RECENT RUSSIAN RESULTS - D. S. Gelles (Pacific Northwest Laboratory).

OBJECTIVE

The objective of this work is to disseminate in the US results recently obtained during the United States/Russian Federation (US/RF) Exchange Meeting on Fusion Reactor Materials.

SUMMARY

Results on postirradiation tensile and compression testing, swelling and bubble growth during annealing for various grades of beryllium are presented. It is shown that swelling at temperatures above 550°C is sensitive to material condition and response is correlated with oxygen content. Swelling on the order of 15% can be expected at 700°C for doses on the order of 10^{22} n/cm^2. Bubble growth response depends on irradiation fluence.

PROGRESS AND STATUS

Introduction

Neutron damage effects in beryllium are becoming issues of increasing interest. Beryllium has long been a leading candidate as a neutron multiplier for a solid tritium breeding blanket.[1] More recently, beryllium has also become a leading contender as a plasma interactive material for a first wall coating, based on performance in the Joint European Torus (JET) project where it was found that plasma disruptions were significantly reduced both in intensity and frequency.[2] Most recently, beryllium was specified as a possible divertor material in JET and is under serious consideration for the same application in the International Thermonuclear Experimental Reactor (ITER).[3] However, it is understood that beryllium is embrittled by neutron damage, and helium generation by transmutation leads to swelling arising from bubble growth.[4] Unfortunately, data defining these responses are limited. During the recent US/RF Exchange Meeting on Fusion Reactor Materials and the following Second International Conference on Effects of Irradiation on Materials far Fusion Reactors, held in St. Petersburg, Russia (September 16 - 25, 1992) three recent reports and a summary on neutron irradiation effects were obtained.[5-8] Much of the information contained in these works had formerly been classified as part of the Russian space program. The purpose of this report is to summarize the information that was obtained, to rapidly disseminate this information to the fusion reactor materials community in the US.

SUMMARY OF RESULTS

Mechanical Properties

In his summary report,[5] V. Barabash indicated that irradiation creep measurements have been made on hot pressed, cast, and single crystal specimens of beryllium, although details have not yet been provided. Barabash also reported that postirradiation deformation behavior has been investigated for reactor grade beryllium and hot pressed material. The results are reproduced in Figures 1 and 2. Figure 1 shows response for reactor grade beryllium in both tensile and compressive modes (Figure 1a) and hot pressed beryllium in tension (Figure 1b) as a function of dose. It may be noted that in Figure 1a, specimens tested parallel to the basal plane (•) appear to have been tested in compression, and specimens tested perpendicular to the basal plane (▲) appear to have been tested in tension. Specimens were irradiated "at low temperature" (possibly in the range 400 to 600°C) to a dose as high as 1.5 x 10^{22} n/cm^2 and tested at 20°C. Curves are shown for yield strength (σ_y), ultimate strength (σ_u), and elongation (6). Following irradiation at 650°C, data for ultimate compressive strength, yield strength, and elongation as a function of dose to doses as high as 6 x 10^{21} n/cm^2 are shown in Figure 2, comparing response for testing at 20°C (left hand axis) and 650°C (right hand axis). No details on the irradiation conditions or the test conditions were included.

Swelling

A series of three papers, one by Burmistrov and co-workers[6] and two by Sernyaev,[7,8] provides both high temperature neutron irradiation swelling response and low temperature neutron irradiation swelling response followed by high temperature annealing for beryllium.

Sernyaev[7] notes that at low temperature, swelling in beryllium can be determined by the expression:

$$\Delta V/V_o \sim 8.2 \times 10^{-25} \Phi t \qquad (1)$$

---

*Operated for the U.S. Department of Energy by Battelle Memorial Institute under Contract DE-AC06-76RLO 1830.

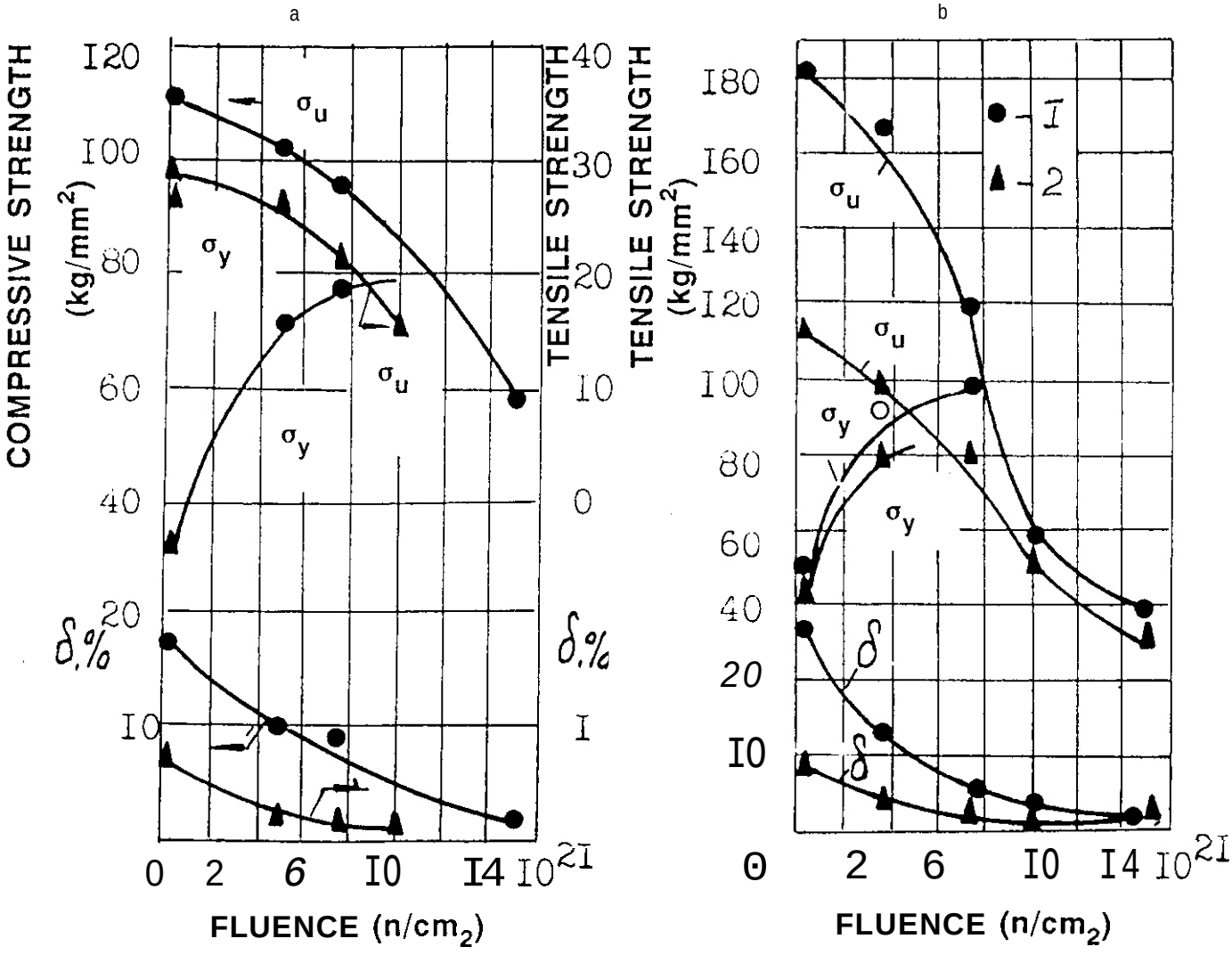

Fig. 1. Tensile and Compressive Strength and Elongation in Various Grades of Beryllium as a Function of Fluence. (a) is response for reactor grade beryllium, and (b) is response for hot pressed beryllium, (σ_y) is yield strength, (σ_u) is ultimate strength and (δ) is elongation (•) is for tests conducted parallel to the plate, and (▲) is for tests conducted perpendicular to the plate. Specimens were probably irradiated in the temperature range 400 to 600°C and were tested at 20°C.

where ϕt is fast fluence in n/cm^2, E > 0.85 MeV. This is based on irradiations at 60°C, but can be used over the range of temperatures where helium remains in supersaturated solid solution.

Irradiation of beryllium at higher temperatures, where point defect mobilities are sufficient to allow formation of fairly large gas bubbles, was performed in the SM-2 reactor at a flux of ≈3 x 10^{14} n/cm^2 to quantify swelling behavior. Variations in grain size were studied by using hot pressed powder materials with grain sizes varying from 56 to 600 μm and by using thermally extruded powder with a grain size of 400. μm. The results are reproduced in Figure 3, where swelling is a function of irradiation temperature. Also, equation (1) was assumed to apply for temperatures of 500°C and below, as marked by "x" symbols. In Figure 3, the curves are numbered to indicate the material type: curve I represents single crystal beryllium; curves 2, 6, and 7 represent hot pressed beryllium, grain size 56 μm; curves 3 and 5 represent hot pressed beryllium, grain size 600 μm; and point 4 represents thermally extruded beryllium, grain size 400 μm. These curves correspond to different fluence levels: curves I through 3 are at 6 x 10^{20}, curves 4 and 5 are at 5.7 x 10^{21}, curve 6 is at 8.9 x 10^{21} and curve 7 is at 1.02 x 10^{22} n/cm^2, E > 0.85 MeV.

Swelling at 500°C is predicted to be "tens of times" smaller than at higher temperatures, and maximum swelling occurred at about 700°C, which corresponded to maximum fluence. Also, swelling response is very sensitive to material condition such that the highest swelling occurs in material with the smallest grain size. This swelling response was analyzed according to the expression:

$$\Delta V/V_o = M \cdot T \cdot \exp(-2.1/4kT) \cdot (\phi t)^{3/2} \qquad (2)$$

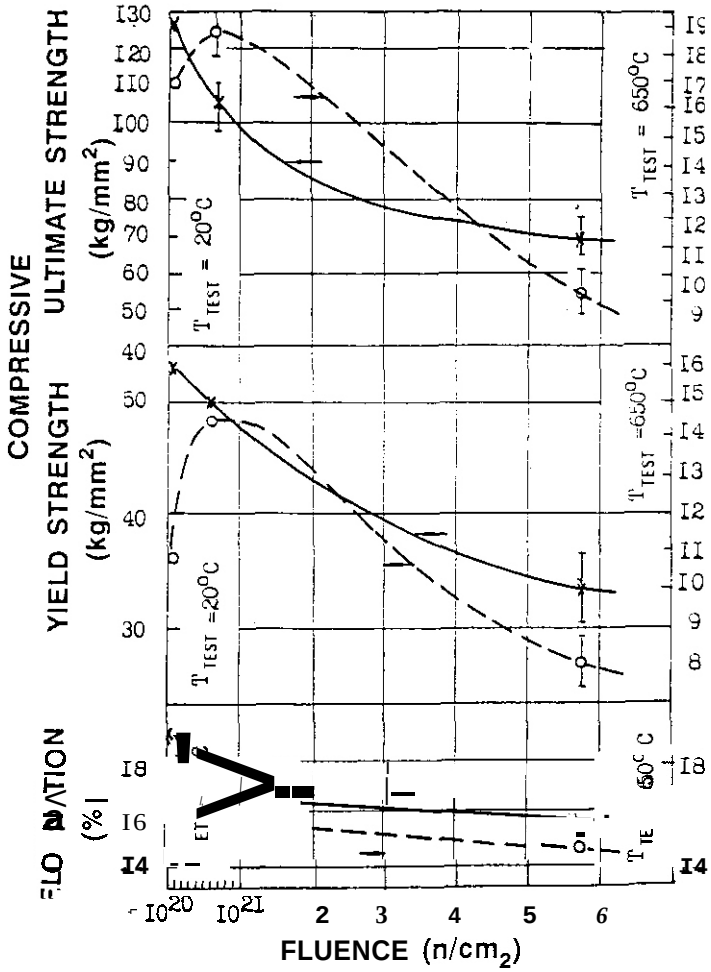

Fig. 2. Compressive Strength and Elongation as a Function of Fluence for Specimens Irradiated at 650°C (using the same notation as in Figure 1).

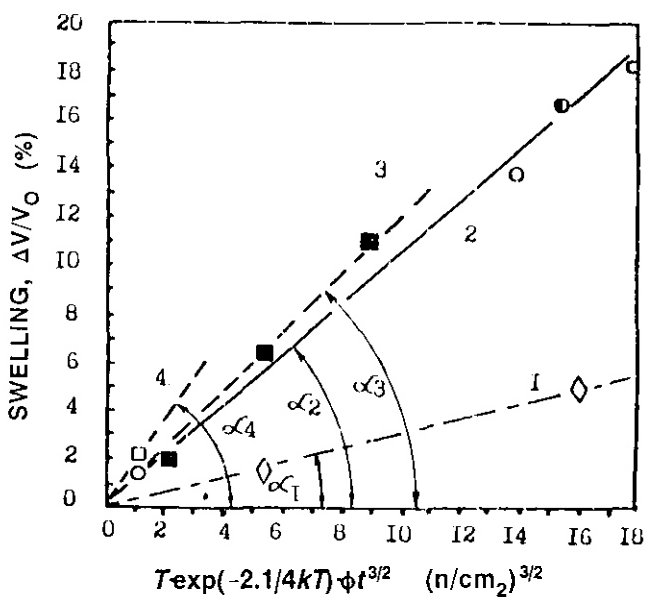

Fig. 4. Predicted Swelling as a Function of Fluence. (1) grain size (g.s.) 400 μm and 2.5 wt% O_2, (2) g.s. 56 μm and 2.8 wt% O_2, (3) g.s. 600 μm and 2.3 wt% O, and (4) g.s. 600 μm and 2.3 wt% O.

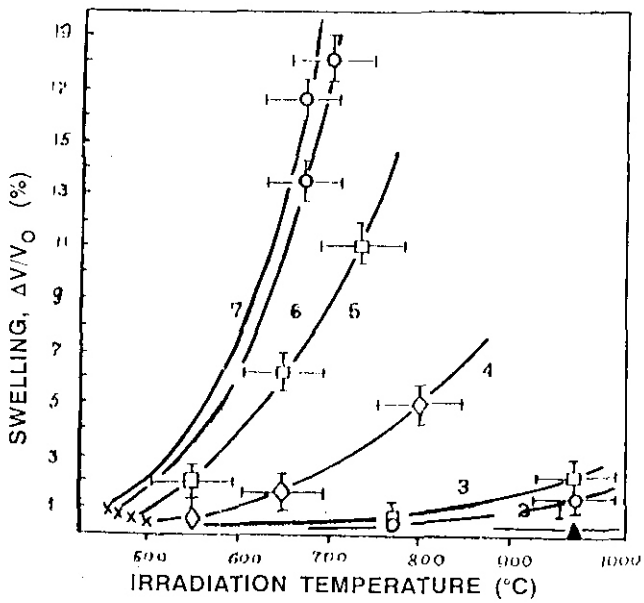

Fig. 3. Swelling as a Function of Irradiation Temperature. (1) is single crystal; (2, 6, 7) are hot pressed. main size (g.s.) 56 μm; (3,5) are hot pressed, g.s. 600 μm; (4) is thermally extruded, g.s. 400 μm. Also, (1-3) are at 6×10^{20}, (4,5) are at 5.7×10^{21}, (6) is at 8.9×10^{21} and (7) is at 1.02×10^{22} n/cm², E > 0.85 MeV.

Figure 4 was prepared to predict swelling as a function of fluence for the various material conditions. Figure 4 was labeled as follows: curve 1 corresponds to 400 μm grain size and 2.5 wt% O,, curve 2 corresponds to 56 μm grain size and 2.8 wt% O,, curve 3 corresponds to 600 μm grain size and 2.3 wt% O,, and curve 4 corresponds to 600 μm grain size and 2.3 wt% O,. From Figure 4, it is apparent that the 400 μm thermally extruded beryllium has a significantly lower slope than the hot pressed materials. From Figure 4. the parameter M that appears in equation (2) can be evaluated, giving $M_{1,2,3,4} \approx 0.31,\ 1.05,\ 1.17,$ and $1.65 \times 10^{-34}\ K^{-1}\ (n/cm^2)^{-3/2}$

Further evaluation determined that the grain size of the material, in and of itself, was not a significant factor for high temperature swelling. Instead, the differences between M_1 and M_3 were ascribed to differences in oxygen content. Furthermore, to reduce the swelling of beryllium, it appears that hot pressing should be replaced by extrusion and by introducing oxygen into the material.

The paper by Burmistrov et al.[6] provided experimental objectives similar to those of Sernyaev:[7] to determine swelling in beryllium following irradiation at several temperatures in a fission reactor, in order to predict swelling in a fusion reactor. Following irradiation at 40°C to 3.2×10^{22} n/cm² (E > 0.1 MeV) [or 1.6×10^{22} n/cm² (E > 0.8 MeV)], beryllium components with grain sizes from 100 to 500 μm from an MIR reactor were reported to retain shape and integrity and develop volumetric swelling <0.3%, in agreement with the predictions of Sernyaev. [Mechanical compression tests showed an

absence of plastic properties (6 = 0) and high strength (σ_u = 650 MPa)]. The authors note that cracking is not generally a problem to fluences of 10^{22} n/cm^2. However, cracking can be expected following irradiation in the SM-2 reactor at 2 x 10^{22} n/cm^2 (E > 0.8 MeV) for beryllium with a grain size of 70 μm, whereas cracking will not occur for a grain size of 20 μm until irradiation at 7.5 x 10^{22} n/cm^2.

Swelling was also reported for beryllium, with grain size of about 10 μm, irradiated in thermocouple monitored capsules in the SM-2 reactor over the temperature range 500 to 750°C. Fluences achieved were 2.8 to 3.7 x 10^{21} n/cm^2 (E > 0.1 MeV) or 3.4 to 5.8 x 10^{21} n/cm^2 (E > 0.68 MeV). These data are given in Figure 5 in which curve 1 corresponds to technical reactor grade beryllium with 30 μm initial grain size, curve 2 corresponds to technical reactor grade beryllium with 20 μm initial grain size, and curve 3 corresponds to beryllium with 8 to 13 μm initial grain sire. The doses for curves 1 and 2 are 5.7 x 10^{21}, and for curve 3 the dose is 3.5 x 10^{21} n/cm^2 (E > 0.1 MeV).

Tensile tests showed that the irradiated materials retained plasticity, about 4% following irradiation at 20°C, 13% following irradiation at 650°C, and 7% following irradiation at 750°C. Transmission electron microscopy revealed that at 700°C and above, gas bubbles 9 to 50 nm in diameter formed primarily along grain boundaries that were without inclusions of second phases. In addition, accumulations of defects of about 6 nm diameter were found, with a dark contrast zone around the accumulations, that was interpreted to indicate the presence of stress fields. These defects were assumed to be of vacancy type. Lattice parameter measurements based on x-ray diffraction indicated compressive strains, interpreted to indicate the presence of dissolved helium. The retention of dissolved helium was used to explain the retention of excellent mechanical properties despite the high fluence.

Based on available data, Barabash' has provided Figure 6 to show swelling in beryllium at 700°C as a function of fluence. Both density change and swelling ($\Delta V/V_o$) are plotted as a function of fluence in units based on E > 0.1 MeV. From this figure, swelling levels of about 15% are predicted for fluences on the order of 10^{22} n/cm^2. However, no details are provided regarding oxygen content or grain size.

Sernyaev' also studied the initiation and growth of helium gas bubbles in single crystal beryllium irradiated at 60°C to fluences of 2.6 and 5.1 x 10^{21} n/cm^2 (E > 0.8 MeV) and then annealed at temperatures of 100 to 1100°C. Techniques employed included small angle x-ray scattering (SAS), differential microcalorimetry (DMC), and transmission electron microscopy (TEM). The SAS measurements used isothermal step annealing in 50° increments with 1 h hold times from 100 to 650°C in air, whereas higher temperature annealing was conducted in a vacuum furnace. Irradiated samples gave SAS responses identical to that of the unirradiated samples, indicating the absence of bubbles larger than 2 nm. Scattering only increased after annealing at 450°C for the material irradiated to 2.6 x 10^{22} n/cm^2, but increases were noted after annealing at 400°C for the material irradiated to 5.1 x 10^{22} n/cm^2. With further increases in annealing temperature, scattering increased rapidly, as shown in Figure 7.

Figure 7 provides a plot of the overall bubble volume determined from SAS measurements as a function of annealing. Only at temperatures higher than 700°C did the rate of increase with temperature begin to slow.

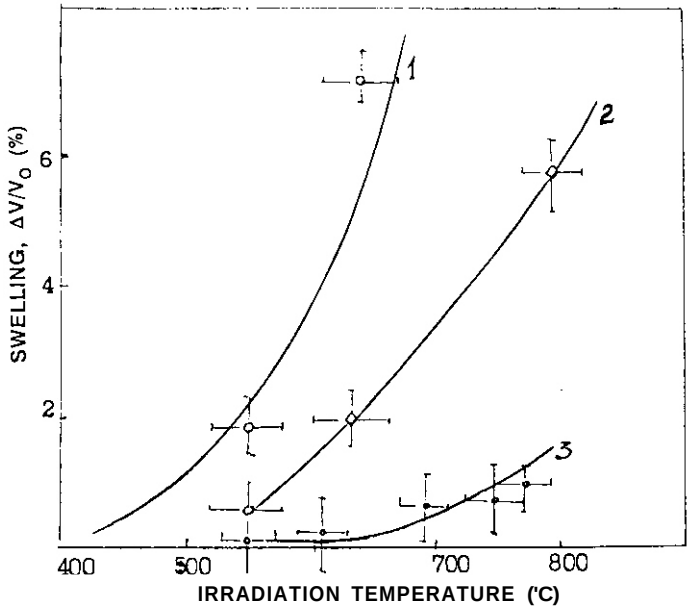

Fig. 5. Swelling as a Function of Irradiation Temperature. (1) grain size (g.s.) 30 μm, (2) g.s. 20 um, and (3) g.s. 8 to 13 μm and fluences for (1,2) 5.7 x 10^{21}, and for (3) 3.5 x 10^{21} n/cm^2 (E > 0.1 MeV).

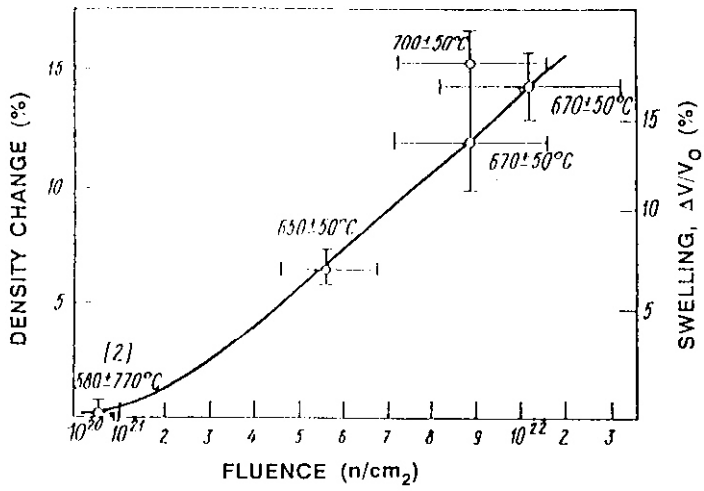

Fig. 6. Swelling in Beryllium at 700°C as a Function of Fluence.

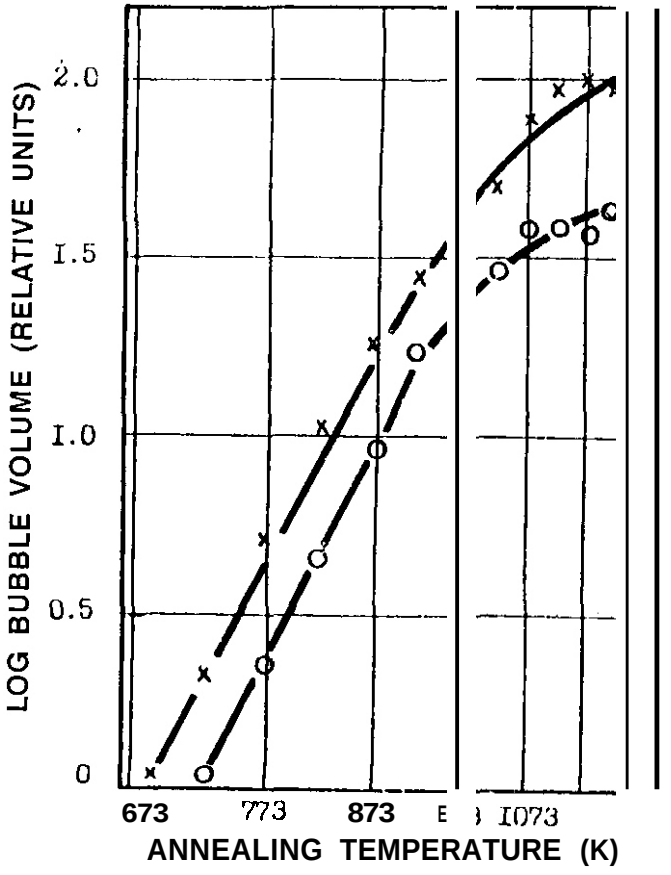

Fig. 7. Dependence of Total Bubble Volume in Beryllium with Annealing Temperature for Fluences of 2.6 x 10^{21} (o) and 5.1 x 10^{21} (x).

These scattering changes could be shown by TEM to correspond to the disappearance of dislocation loops and the nucleation and growth of bubbles. Derived from the data at 650°C and above in Figure 7, the measured activation energy was 75,100 ± 4,800 J/mole, whereas self-diffusion of beryllium is ≈161,700 J/mole, and diffusion of helium in beryllium is ≈214,900 J/mole. Therefore, bubble growth could not be ascribed to elementary processes. Higher fluence irradiation resulted in ≈2.3 times greater total bubble volume.

The data of Figure 7 were also analyzed to estimate mean bubble diameter (assuming spherical bubbles). The results are reproduced in figure 8. Although bubbles were initially larger in the material irradiated to higher fluence, growth during step annealing was slower, and bubble densities remained 1.3 times larger. However, computations for the number of gas atoms contained in bubbles compared to the number of vacancies composing them were found to give ≈0.17 for both fluence conditions.

The DMC results are reproduced in Figure 9. Heat was released at temperatures ranging from 150 to 350°C, absorbed in the range of 350 to 600°C and released at temperatures above 600°C. Comparison of Figures 8 and 9 provided the correlation that heat absorption corresponded to bubble nucleation, and heat release above 600°C corresponded to bubble growth. The lower regime was thought to correspond to preliminary diffusion processes.

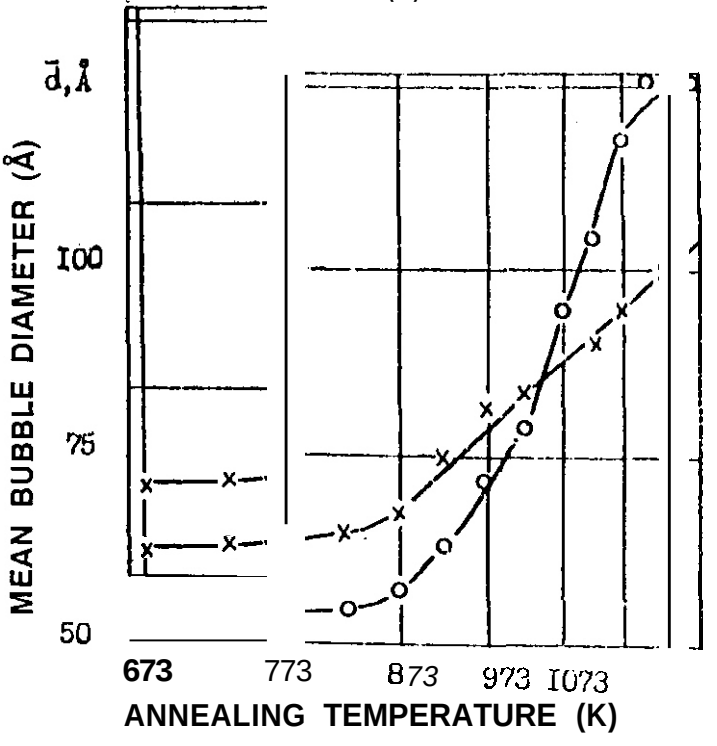

Fig. 8. Dependence of Mean Bubble Diameter with Annealing Temperature for Fluences of 2.6 x 10^{21} (o) and 5.1 x 10^{21} n/cm^2 (x)

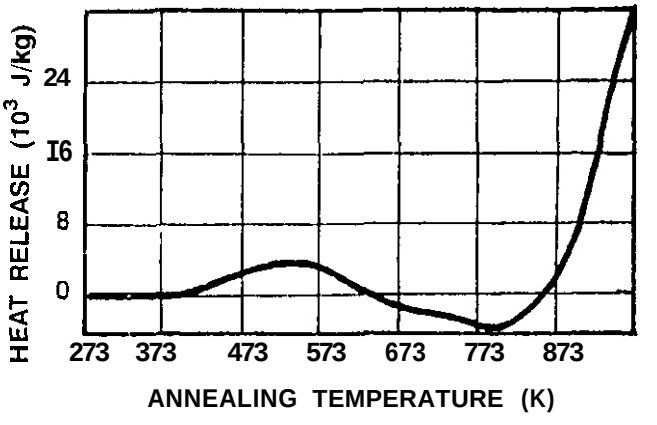

Fig, 9. Temperature Dependence of Heat Released (Absorbed) in Material irradiated to 5.1 x 10^{21} n/cm^2

CONCLUSIONS

Test results recently obtained from Russia demonstrate swelling in beryllium on the order of 15% following irradiation in the SM-2 reactor at 700°C to a dose of 10^{22} n/cm^2. Swelling is found to vary as a function of material condition, apparently dependent on oxygen content. Data are also provided for postirradiation mechanical strength and elongation in tension and compression, and for bubble growth during step annealing. These data provide quantitative descriptions of irradiation response of beryllium.

FUTURE WORK

This work will be continued as more information becomes available.

REFERENCES

1. C. E. Johnson, J. Nucl. Mater., 179-181 (1991) 42.

2. K. J. Dietz, J. Nucl. Mater. 155-7 (1988) 8.

3. P. -H. Rabut, "ITER: The Machine" reported at the ITER Joint Central Team Meeting held in San Diego, CA, August 20, 1992.

4. D. S. Gelles and H. L. Heinisch, J. Nucl. Mater., 191-194 (1992) 194.

5. V. Barabash, "Brief Review of Be Study for Plasma Facing Component in RF for ITER Reactor," presented at the US/RF Exchange Meeting, September 17-19, 1992 in St. Petersburg, Russia.

6. V. N. Burmistrov, Yu. D. Goncharenko, V. A. Kazakov, O. Yu. Shvedov, V. A. Gorokhov, and I. B. Kupriyanov, "Certain Aspects of the Radiation Stability of Beryllium with Application to Synthesis Reactor Conditions from Results of Tests in a Fission Reactor," presented at the Second International Conference on Effects of Irradiation on Materials for Fusion Reactors, held September 21-24, 1992 in St. Petersburg, Russia, PNL-TR-487.

7. G. A. Sernyaev, "Swelling of Beryllium in a Mode of High-Temperature Neutron Irradiation," Voprosy Atomnoi Nauki i Tekniki, No 2 (56), (1991) 16, PNL-TR-488.

8. G. A. Sernyaev, "The Formation of Helium Bubbles and Energy Phenomena in Beryllium," Voprosy Atomnoi Nauki i Tekniki, No 2 (56), (1991) 82, PNL-TR-490.

8.0 CERAMICS

MEASUREMENT OF ELECTRICAL AND OPTICAL PROPERTIES OF DIELECTRIC MATERIALS DURING NEUTRON IRRADIATION -- E. H. Farnum. F. W. Clinard Jr.. J. C. Kennedy 111, W. F. Sommer. and W. P. Unruh (Los Alamos National Laboratory)

OBJECTIVE

The objective of this experiment is to determine the extent of degradation during neutron irradiation of electrical and optical properties of candidate dielectric materials. The goals are to identify promising dielectrics for ITER and other fusion machines for diagnostic applications and establish the basis for optimization of candidate materials.

SUMMARY

An irradiation experiment was carried out during the summer of 1992 at the Los Alamos Spallation Radiation Effects Facility (LASREF). In ***situ*** measurements of electrical conductivity in alumina, sapphire and mineral-insulated electrical cables were made at 640 "C, 590 °C and 400 °C. Both DC and AC (100 Hz to 1 MHz) measurements were made to a fluence of approximately 2 x 10^{23} n/m^2. Optical absorption from 200 nm to 800 nm was measured in pure silica- and OH-doped silica-core optical fibers during the irradiation. A large number of passive samples were included in the irradiation, some at the furnace temperatures and some at ambient temperature. Data is being analyzed during the first quarter of FY93. All samples will be recovered for post-irradiation examination during the second quarter of FY93.

PROGRESS AND STATUS

The radiation source

This experiment was conducted at LASREF. This facility is located at the beam stop of the Los Alamos Meson-Physics Facility (LAMPF) and provides a source of spallation neutrons from an 800 MeV proton beam. The neutron energy spectrum of this source differs from both fission and anticipated fusion sources, but has some distinct advantages for conducting in ***situ*** irradiations. First, the Source has a very large volume available. Our single-width insert had interior dimensions of 14 x 17.4 x 50.8 cm. In our experiment, we used this volume to hold three furnaces, two irradiation capsules and one spool for fiber optic cables. In addition. we had five packets of activation foils to measure the neutron fluence and spectrum. The access to the volume is large enough that we were able to run 36 MI signal cables, 12 thermocouples, ***6*** furnace power leads and two furnace gas lines into the irradiation volume. Second, the proton beam is delivered in ms pulses with about ***8*** ms between pulses. We were able to see these pulses in the optical experiment and measure time response of radiation-induced absorption. The proton beam also turns off and on at irregular intervals. We were able to use this to measure transient radiation-induced conductivity (RIC) in the electrical measurements. Third, the spectrum, being of higher average energy than fission sources, generates spallation gasses (mostly H and He) at about the same rate (in copper) as a 14-MeV neutron source. We anticipate detecting the effects of this gas generation in our post-irradiation examinations. The source also has some disadvantages. First, because the beam stop is a quasi-point source of neutrons, the flux is very dependent on distance and varies by a factor of about 5 across the available irradiation volume. Positioning the samples thus becomes an important variable. We have been careful to measure the sample positions and have placed activation foils at locations that will allow us to map the fluence to try to overcome this problem. Third, the pulsed nature of the beam introduces electrical noise in all the ground planes. This noise substantially reduced the sensitivity of our measurements and will require double shielding in future experiments. Fourth, the fact that the proton beam has only about a 60%up-time factor reduces the effective fluence. During the summer experiments we were able to accumulate a fluence of about 3 x 10^{23} n/m^2s at the DC samples in 10 weeks of irradiation. A reactor running full power for these 10 weeks would need a flux of 5 x 10^{16}n/m^2s to achieve an equivalent fluence.

The furnaces

Three furnaces were inserted into the LASREF volume. The outside dimensions of each was 12.7 cm diameter x 17.4 cm long. The furnaces were powered by a proportional controller and a programmable DC power supply. Thermocouples were placed near the top, center and bottom of the heated zone and the center temperature was used for control., The furnace atmosphere was argon gas at a pressure of about 33 kpa (5 psi). The gas flowed at a low rate through the furnaces during the entire run. Each furnace contained three capsules for electrical measurements. two mineral-insulated (MI) cables, two foil wrapped alumina specimens for post-irradiation thermal conductivity measurements (supplied by D. White at ORNL) and two silica ampoules containing high purity copper TEM disks (supplied by F. Garner, PNL). Initial temperatures were set for 300 °C in furnace A, 400 °C in furnace B, and 500 °C in furnace C. When the LAMPF beam reached full power (about 11 days into the irradiation) the equilibrium temperatures of the furnaces was 640 °C for furnace A, 590 °C for furnace B, and 400 °C for furnace C. We maintained these temperatures for the remainder of the 70-day run.

The AC electrical measurements

Each furnace held two AC capsules. These were made of stainless steel and evacuated. Each capsule contained a single, thin sample with three electrical leads in a guard-ring capacitor configuration. One capsule in each furnace was designed and built at Los Alamos and contained an un-doped sapphire single crystal sample about 216 μm in thickness. A drawing of this capsule is shown in Fig 1. The second capsule in each furnace was designed and built by Tatsuo Shikama, Tohoku University. Japan, This capsule contained a 99.5-grade Sumitomo alumina sample, also about 100 μm in thickness. In addition to the capsules, a MgO-insulated cable passed through the hot zone of each furnace. About 25 cm length was in the hot zone. During the entire run. an AC electric field of about 1850 V/cm peak and 10 kHz was applied to all samples. This voltage was removed during measurement. The capsules and cable were scanned continuously with a computer-controlled switch and electrical impedance was measured from 100 Hz to 1 MHz. Impedance. time and proton-beam current were digitized and archived

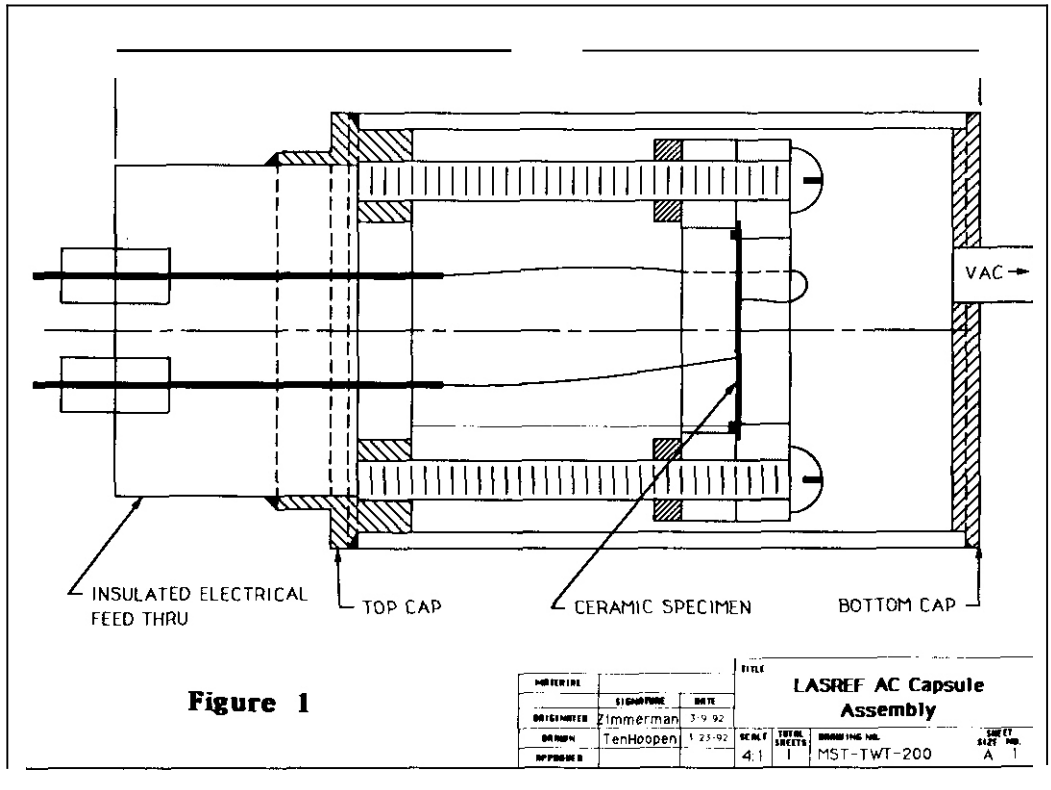

Figure 1

The DC electrical measurements

Each furnace held one DC capsule that was open to the argon furnace atmosphere. Each DC capsule contained two 1-mm-thick, 1.9-cm-diameter alumina disks and two 3-mm-thick disks. The disks were stacked with interleaved electrodes as shown in Fig. 2. An applied DC voltage of 150 V caused an electric field of 500 v/cm on the thick disks and 1500 V.cm on the thin disks. This voltage was applied continuously during the experiment. The alumina disks are part of the IEA round-robin 99.5 Wesgo alumina purchased by R. Stoller at ORNL. R. Stoller prepared and supplied the disks. Platinum thin-film electrodes 1.25-mm-diameter were evaporated onto the disks and platinum foil was sandwiched between the disks to form the electrodes. Each DC capsule had four electrodes. the high-voltage input, a thin-disk output. a thick-disk output, and a "dummy"-output that entered the capsule and hung down beside the samples but was not connected to any disks. The three "output" electrodes and one MgO-insulated cable in each furnace were scanned continuously with a computer-controlled switch and pico-ammeter. and sample current, time and proton-beam current were, digitized and archived.

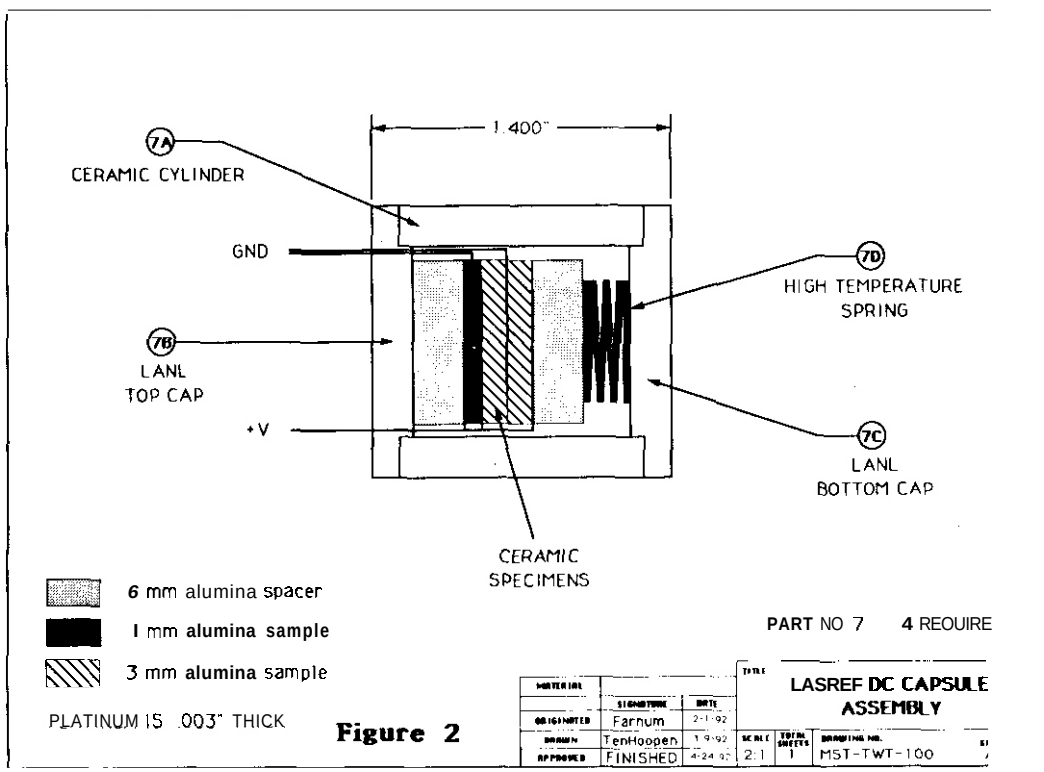

Figure 2

The Optical Fiber measurements

A 15-cm-diameter aluminum spool containing fiber optic cables was inserted outside the furnaces in the ambient environment. This environment was air at temperatures that reached a maximum of about 200 °C during maximum beam current. Both pure-silica-core and OH-doped-silica-core fibers were fielded. One fiber of each type had about 2 m length on the spool and one had only 1 turn on the spool. Optical density was measured from 200 nm to 800 nm wavelength during the experiment. A computer-controlled switch scanned the fibers continuously and the optical data, proton beam current and time were digitized and archived. A plot of initial darkening with approximate fluence (current fluence values are only approximate) is shown in Fig. 3.

Passive Experiments for Post-Irradiation Examination

In addition to the active electrical and optical experiments above, we have included a number of samples that will be examined later. As mentioned above, inside the furnace hot zones, we have alumina samples from ORNL for thermal conductivity measurements and copper disks from PNL for

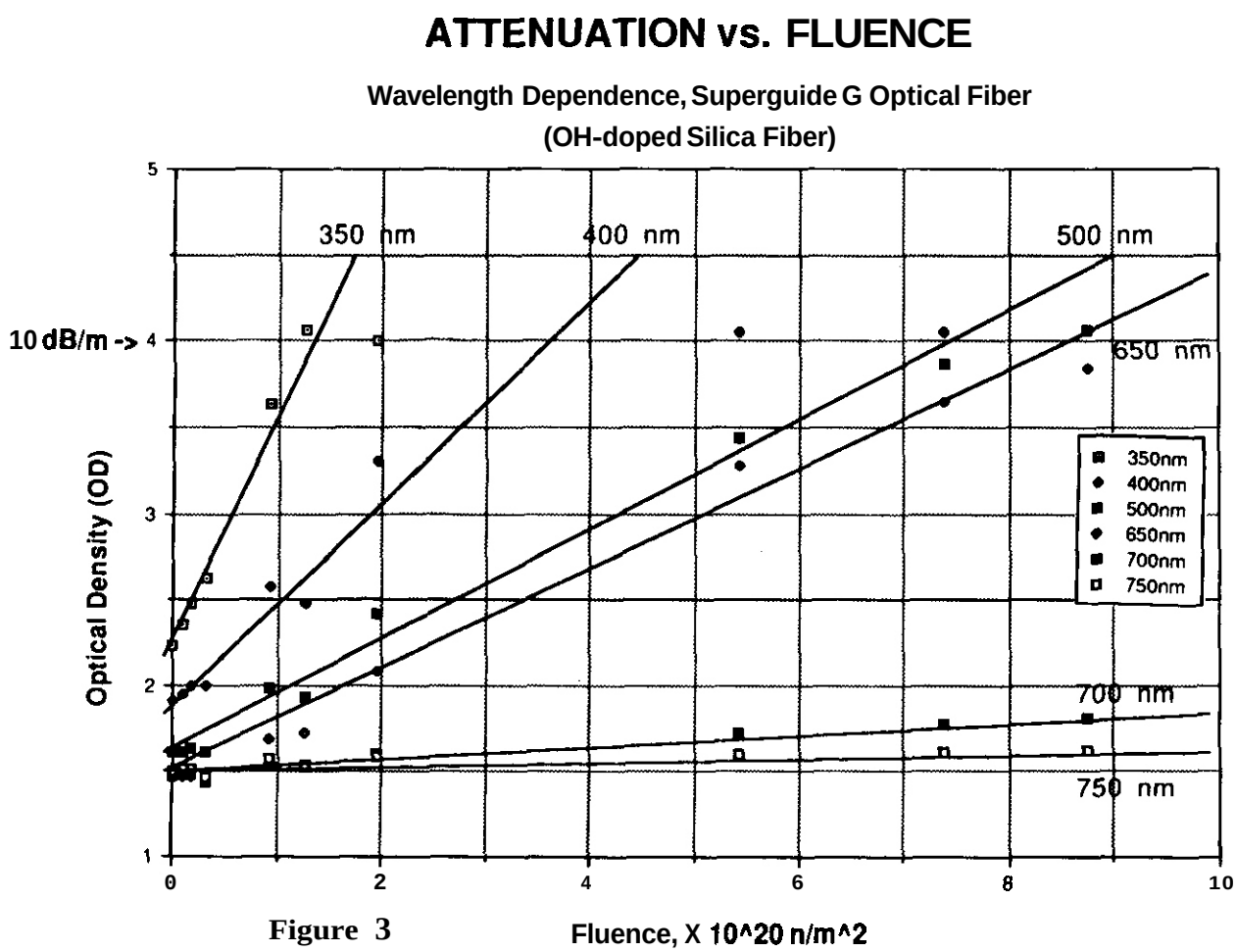

Figure 3

TEM examination. We also have two capsules at the top of the insert at ambient temperature. Ambient varied between 100 °C and 200 °C depending on beam current. Each capsule is stainless steel approximately 6 cm in diameter and 10 cm long welded under argon. A thermocouple passing through one end measures temperature at the capsule center. One activation foil packet was placed in each capsule to measure fluence. Samples include a number of materials of interest for fusion diagnostic applications. Layered Synthetic Microstructures (LSM) are carbon-molybdenum multilayers designed for soft x-ray mirrors. Lead-glass microchannel plates are used for x-ray and particle imaging, dielectric-coated silica mirrors are used for optical imaging within the tokamak chamber. Other materials included are for research interest. Nearly all of these samples are part of a collaboration with researchers from other laboratories. A list of the samples and collaborators is shown in Table 1

Contributions to MOTA-2C at EBRII

We submitted a number of samples for irradiation in MOTA-2C at EBRII. These materials were chosen Cor their potential importance for fusion applications. The materials were obtained in collaboration with researchers from other laboratories. A list of materials submitted, together with the collaborator and flux position is shown in Table 2.

Summary

The major in ***situ*** irradiation experiment at LASREF has been completed and data is being analyzed. We expect to recover the insert along with the active and passive samples in February, 1993 and will begin post-irradiation examination. Much of our experiment has been in collaboration with researchers from other labs involved in the fusion materials program. These collaborations have been very fruitful and rewarding and we hope to be able to continue such collaborations in the future.

Table I

PASSIVE SAMPLES FIELDED IN LASREF, SUMMER. 1992
(Material and Collaborator)

1) Four LSM mirrors (S. Regan, Johns Hopkins Univ.)
2) 24 oxide and mineral samples (D. Howitt, UC/Davis)
3) Samples of complex silicate mineral (W. Weber, PNL)
4) Alumina samples for PIE thermal conductivity (D. White, ORNL)
5) Lead glass microchannel plate (F. Clinard. LANL)
6) Cr-doped (2 levels) and undoped sapphire (J. Kennedy, LANL)
7) Cu and Fe samples from Japan (F. Garner, PNL)
8) Aluminum nitride disks (Farnum and Clinard)
9) Spinel disks (Farnum and Clinard)
10) Alumina and sapphire from IEA round robin (R. Stoller)
11) Zirconia-toughened alumina and spinel (J. Molla CIEMAT,Spain)
12) High-field permanent magnets (D. Barlow, LANL)
13) Lead indium phosphate glass samples (L. Boatner, ORNL)
14) Seven samples of various oxide ceramics (F. Cooper, LANL)
15) Five different dielectric-coated mirrors on silica substrates (B. Schunke, JET)

Table 2
Samples submitted for MOTA-2C at EBR-II
(Three capsules are fielded, each in a different flux location. All samples are disks.)

Collaborator	Material	Low Flux	Medium Flux	High Flux
Clinard:	$MgAl_2O_4$	X	X	X
(LANL)	AlN	X	X	X
Boody:	Al_2O_3	X	X	X
(USSR)	Sc_2O_3 / ZrO_2	X	X	X
	ZrO_2 / Y_2O_3			
Hull (ANL):	Y_2O_3	X		X
Schunke (JET):	Dielectric reflectors(3)	XXX		
Haggerty :	Si_3N_4 Colloidally pressed	X	X	X
(MIT)	si_3N_4 Die pressed	X		X

THE EFFECT OF VACANCIES ON THE THERMAL CONDUCTIVITY OF SINGLE CRYSTAL ALUMINA (SAPPHIRE) AT LOW TEMPERATURES – D.P. White (Oak Ridge National Laboratory)

OBJECTIVE

This work is intended to provide information on the changes expected in the thermal conductivity of single crystal alumina due to radiation produced vacancies at low temperatures.

SUMMARY

The effect of radiation on the thermal conductivity of alumina is an important design consideration in the development of microwave windows for ion cyclotron resonance heating (ICRH) systems for the heating of plamas in fusion reactors. Several recent papers [1,2,3] have addressed this question at higher temperatures and the present report extends the calculation of the effect of point defects to low temperatures. This extension of the calculations to low temperatures is of interest because it has been proposed to cool these windows to liquid nitrogen temperatures in order to take advantage of the much higher thermal conductivity of alumina at these temperatures.

PROGRESS AND STATUS

Introduction

The lattice thermal conductivity of crystalline material is given by the following expression due to Callaway [4],

$$k_l = \frac{(6\pi^2)^{1/3}}{2\pi^2}\frac{k_b^3}{\hbar^2}\frac{T^3}{\Theta a}\left[I_1 + I_2^2/I_3\right] \tag{1}$$

where k_b is the Boltzmann's constant, $\hbar$ is Plank's constant divided by 2π, Θ is the Dehye temperature of the material, a^3 is the volume per unit cell, and

$$I_1 = \int_0^{\Theta/T} \tau_c \frac{x^4 e^x}{(e^x-1)^2} dx$$

$$I_2 = \int_0^{\Theta/T} \frac{\tau_c}{\tau_n} \frac{x^4 e^x}{(e^x-1)^2} dx$$

$$I_3 = \int_0^{\Theta/T} \frac{\tau_c}{\tau_n \tau_r} \frac{x^4 e^x}{(e^x-1)^2} dx$$

Here $x = \frac{\hbar\omega}{k_b T}$, ω is the cirular phonon frequency, τ_n is the phonon relaxation time for normal processes, $1/\tau_c = 1/\tau_1 + 1/\tau_2 + \ldots$ and $1/\tau_r = \sum_j 1/\tau_j$, where the τ_j are the relaxation times of the various resistive phonon scattering processes, which include 3-phonon umklapp processes, boundary scattering, and point defect scattering.

This formulation of the thermal conductivity takes the effect of phonon-phonon normal processes into account which is particularly important in treating the low temperature case.

Calculation

In order to evaluate the expression in Eq. 1, a computer program was written to calculate the various integrals, given functional forms for the various phonon relaxation times. The forms used for the normal process relaxation time and umklapp process relaxation time are given in Eq. 2.

$$\tau_n^{-1} = b_n \omega T$$

$$\tau_u^{-1} = b_u \omega^2 T \exp\left(-\frac{\Theta}{\alpha T}\right) \tag{2}$$

for normal and umklapp processes respectively. The values of the parameters b_n and b_u for sapphire were obtained by de Goer [5] and are the values used in this case. These values were obtained by fitting the expression of Eq. 1 to experimental thermal conductivity data at high temperatures. The values obtained by de Goer are,

$$b_n = 2.7 \times 10^{-13} K^{-4}$$

$$b_u = 1.7 \times 10^{-18} s K^{-1}.$$

The parameter α is a numerical factor which depends on the details of the zone structure. de Goer found that $\alpha = 2$ gives a good fit to experimental data.

The boundary scattering relaxation time has the form.

$$\tau_b^{-1} = \frac{2}{L} \tag{3}$$

where v is the phonon velocity and L is a parameter on the order of the dimensions of the crystal and is dependent on the geometry of the sample. The point defect scattering relaxation time has the form.

$$\tau_p^{-1} = A\omega^4 \tag{4}$$

where **A** is a parameter which is proportional to the defect concentration and depends on the nature of the defect, which in pure unirradiated samples will include thermodynamic vacancies, and trace impurities.

For a pure, single crystal, cylindrical sample 50 mni long and 5 mm in diameter de Goer vaned the values of **A** and L to fit the calculated values of the thermal condnctivity to experimental values in the temperature range 2 to 100 K. It was found that a good fit was found for $L = 4.12 \times 10^{-3} m$ and $A = 4.08 \times 10^{-46} s^3$. These values will he used in the present calculations. It should be noted however that the thermal conductivity below the conductivity maximum is highly sensitive to the value of L, as will be demonstated later in this paper.

In order to determine the effect of radiation produced vacancies on the thermal conductivity of sapphire. another term dependent on the radiation produced vacancy Concentration. must be added to the point defect relaxation time. For vacancies it has been shown [6,7] that the phonon relaxation time is given by.

$$\tau_v^{-1} = C_v \Omega \left(\frac{3\Delta M}{M}\right)^2 \frac{1}{4\pi v^3} \omega^4 \tag{5}$$

where C_v is the vacancy concentration per unit cell. ΔM is the change in mass of the unit cell due to a vacancy. and M is the mass of the unit cell. In this case the unit cell is chosen to he the formula unit, Al_2O_3, with a mass of 102 and a volume of $42.6 \times 10^{-30} m^3$. The Debye temperature in this case is then 600 K, and the phonon velocity is $7 \times 10^3 m/s$. Thus the form of the point defect relaxation time is given by.

$$\tau_p v^{-1} = \left(4.08 \times 10^{-46} + C_v \frac{\Omega}{4\pi v^3} 0.79^2\right) \omega^4 \tag{6}$$

for aluminum vacancies. These relaxation times may now he substituted into **Eq.** 1 and the thermal conductivity calculated for a range of temperatures and radiation produced vacancy concentrations.

Results of Calculations

The results of the thermal conductivity calculations are **given** in Figs. 1-4. In Fig. 1 the calculated thermal conductivity versus temperature is plotted for several values of the radiation produced vacancy concentration. The largest reduction in the thermal conductivity due to these vacancies is in the region of the conductivity maximum at approximately 30 K. Figure 2 is a plot of the thermal conductivity versus vacancy concentration at 77 K. This plot shows the reduction in the thermal conductivity at liquid nitrogen temperatures, where it has been proposed to cool ICRH microwave windows to take advantage of the high thermal conductivity of alumina at these temperatures. In Refs. **1-3** the reduction in the thermal conductivity was expressed as the fractional change in the conductivity and Fig. **3** is a plot of the fractional change in the conductivity versus vacancy concentration at 77 K. Figure **4 is** a plot of the thermal conductivity versus temperature for several values of the parameter L of Eq. **3.** This plot shows that the boundary scattering has a much larger effect on the thermal conductivity at the lowest temperatures and the effect is not so great at liquid nitrogen temperature.

DISCUSSION AND CONCLUSIONS

The thermal conductivity of sapphire is significantly reduced by vacancies at low temperaures. From Fig. 1 it is seen that the major part of the reduction is in the area of the thermal conductivity maximum, which occurs at about 30 K. There is however significant reduction in the thermal conductivity at liquid nitrogen temperature, as can he seen in Figs. 2 and **3.** From Fig. **3** it can be seen that the fractional change in the thermal conductivity for a vacancy concentration of 0.01 per atom is expected to be about 90% at 77 K. This is a very large reduction in the lattice thermal conductivity and it raises the question as to whether or not this reduction negates the increase in the thermal conductivity gained by going to low temperatures.

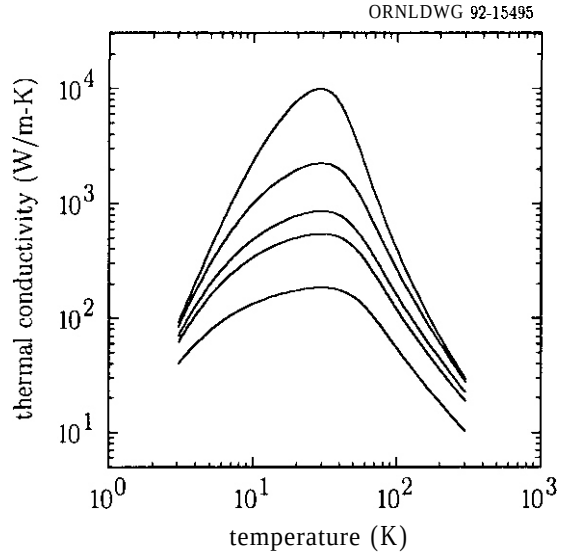

Figure 1: Plot of the thermal conductivity of single crystal alumina versus temperature. The different curves correspond to different vacancy concentrations with the top curve corresponding to no radiation induced vacancies, c=0, and the lower curves correspond to c=0.0002, c=0.001, c=0.002, and c=0.01 respectively, where c is the vacancy concentration per atom.

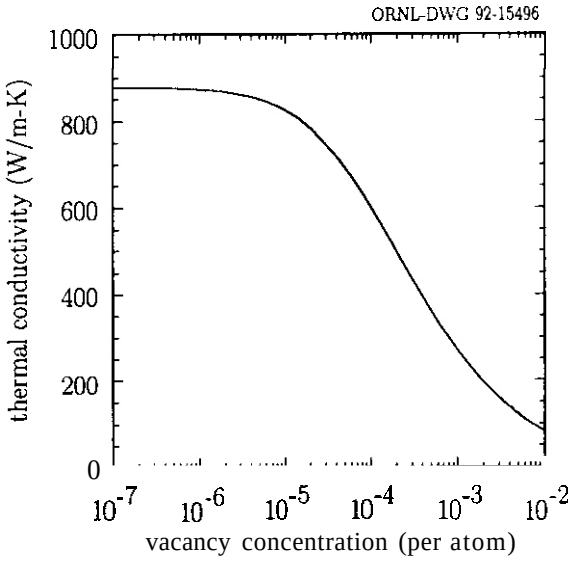

Figure 2: Plot of the thermal conductivity of single crystal alumina versus vacancy concentration at 77 K.

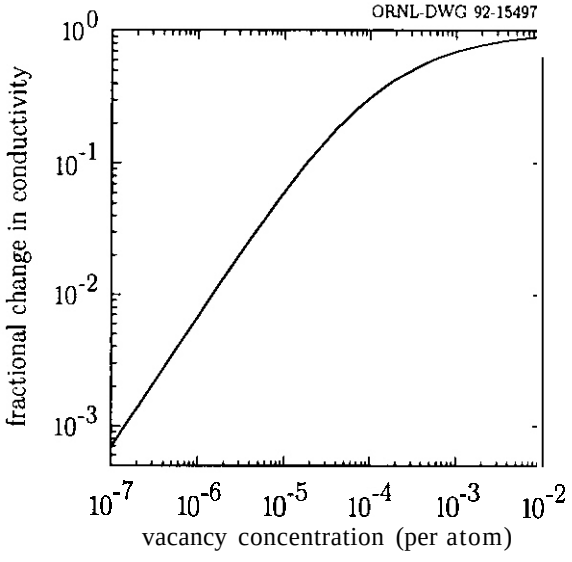

Figure 3 Plot of the fractional change in the thermal conductivity versus vacancy Concentration for single crystal alumina at 77 K.

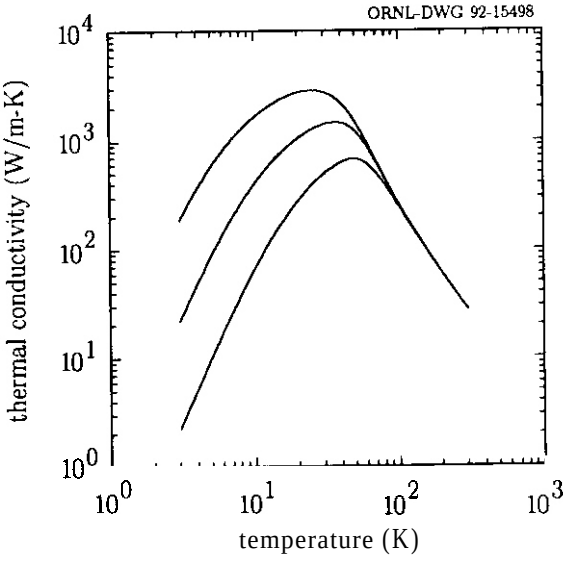

Figure 4: Plot of the thermal conductivity of single crystal alumina versus temperature, showing the effect of grain size. All curves have a radiation induced vacancy concentration of c=.0002 per atom. The different curves correspond to different values of the parameter L in the boundary scattering relaxation time in &. 3. The curves correspond to $L = 1 \times 10^{-2}, 1 \times 10^{-3}, 1 \times 10^{-4}$ from top to bottom respectively.

In Ref. 1 it was shown that at 400 K the fractional reduction in the thermal conductivity due to a vacancy concentration of 0.01 per atom would be expected to he approximately 39% which is a much smaller fractional decrease in the lattice thermal wnductivity compared to the 90% reduction expected with the same defect concentration at 77 K. The larger fractional reduction at low temperatures is due to the fact that the umklapp scattering is much weaker at low temperatures and allows the point defect scattering to he the dominant scattering mechanism at lower phonon frequencies, thus scattering a larger fraction of the phonon spectrum. However at 400 K a 39 % reduction in the thermal conductivity would result in a wnductivity of approximately 16 W/m-K, compared to an expected conductivity of 83 W/m-K after a 90 % reduction in the conductivity at 77 K. Thus even at defect concentrations as high as 0.01 per atom the thermal conductivity advantage gained by going to lower temperatures would he maintained. However the vacancy concentration depends on the thermal stability of the vacancies, if many of the vacancies recombine at 400 K but are immobile at 77 K, then the low temperature thermal conductivity could be less than the 400 K thermal conductivity for a given fluence of vacancy producing irradiation. This problem points to the need of performing in-situ cryogenic thermal conductivity tests.

From Fig. 4 it is seen that the effect of boundary scattering at 77 K is rather small. In decreasing L from 0.01 to 0.0001 m the thermal conductivity is reduced by only 16%. It is thus not likely that the window thickness will be of concern in the design of sapphire microwave windows.

FUTURE WORK

The calculation of the effects of other phonon scattering mechanisms at low temperatures is planned. Among the mechanisms to be studied are the scattering of phonons by conduction hand electrons, dislocation loops, and voids.

REFERENCES

1. D.P. White, DOE/ER-0313/11, 277, (1991).
2. D.P. White, DOE/ER-0313/12, 298, (1992).
3. D.P. White, J. Appl. Phys., submitted for publication.
4. J. Callaway, Phys. Rev., 113, 1046, (1959).
5. A.M. de Goer, J. Phys. (Paris), 30, 389, (1969).
6. P.G. Klemens, in *Solid State Physics*, eds. F. Seitz and D. Turnbull, Academic Press, New York, 7, (1958).
7. C.A. Ratsifaritana, in *Phonon Scattering* in *Condensed Matter*, ed. H.J. Maris, Plenum Press, New York, 259, (1980).

FATIGUE CRACK GROWTH OF SiC/SiC AT 1100°C - R. H. Jones and C. H. Henager, Jr., (Pacific Northwest Laboratory)'

OBJECTIVE

The objective of this study is to determine the effect of cyclic stresses on the high-temperature structural stability of SiC/SiC composites.

SUMMARY

Fatigue crack growth tests have been conducted on a SiC/SiC composite at 1100°C and a stress intensity ratio of 0.1. Tests were conducted in pure Ar and Ar + 2000 ppm O to determine the effects of an oxidizing environment. The crack growth rate-stress intensity relationship exhibits a K independent regime, stage II, which is not exhibited in monolithic ceramics. The crack velocity in this stage II regime ranged from a low of 10^{-8} m/s to a high of 10^{-7} m/s. Cyclic stresses were found to decrease the crack velocity relative to static loads while oxygen increased the crack velocity. Both effects are consistent with a model developed to describe the subcritical crack growth of these materials where the fibers bridging the crack wake produce crack closure forces which reduce the crack tip K value. The decrease in crack velocity with cyclic loading resulted primarily from the longer hold-times at a given K value without any apparent cyclic damage. Based on these tests and other published data, cyclic stresses may not pose a fatique concern for SiC/SiC if the stresses are below the proportional limit and the stress or-stress intensity-ratio is >0 and tension-tension. Further tests are in progress to evaluate the effect of hold-time on crack growth rates in SiC/SiC.

PROGRESS AND STATUS

Backuround

Structural Applications of Ceramic Composites in Fusion Reactors

Ceramic matrix composites (CMCs) such as SiC/SiC offer high-temperature performance with minimal nuclear activation and afterheat for structural applications in fusion reactors. Silicon carbide is a very hard and corrosion resistance compound and similar properties are expected for SiC/SiC composites although this must be demonstrated for specific fusion relevant environments. Composites such as SiC/SiC are considered "engineerable" because their properties may be optimized for a variety of performance requirements without the constraint of equilibrium phase diagrams.

A number of developmental issues have been identified(1) for these materials including: 1) hermetic and vacuum properties relative to coolant in-leakage and tritium out-leakage, 2) radiation stability, 3) joining technology, 4) chemical compatibility, 5) thermal conductivity, 6) thermal fatigue and thermal shock resistance and 7) redefinition of design codes for brittle matrix-fiber strengthened materials.

A broader list of required evaluations beyond the feasibility issues listed above include: 1) radiation stability including dimensional phase stability as a result of C burnout and effects solid and gaseous transmutants, 2) baseline physical and mechanical properties, 3) the long-term thermal stability of these baseline properties, 4) creep and subcritical crack growth behavior and 5) reactor safety issues associated with the use of CMC's as the primary structural components.

Thermal fatigue and shock will result from start-up/shut-down cycles and plasma discharges to the wall, respectively. Start-up and shut-down cycles will induce stress and temperature cycles with a frequency determined by the duty cycle of the reactor. The stress frequency resulting from start-up and shut-down cycles is expected to be low and to be more related to the type of data obtained from low-cycle fatigue rather than high-cycle fatigue testing. Stresses in CMCs will result from primary loads, thermal gradients, dimensional gradients, and differential coefficient of expansion between the fibers and the matrix. Thermal shock will induce high loading rates in very localized regions with the magnitude of the stress related to the energy deposition rate, thermal conductivity, coefficient of thermal expansion and elastic modulus. Both reactor cycles and plasma discharge will induce both stress and temperature cycles with stresses possibly having R (Pmax/Pmin) values ranging from -1 to a high of 1. Stress ratio values of -1 result in compressive loads which have been shown to be deleterious to composite materials (2-4).

'Pacific Northwest Laboratory is operated for the U.S. Department of Energy by Battelle Memorial Institute under Contract DE-AC06-76RLO 1830.

Fatigue Behavior of Composite Materials

Studies on the effects of compressive stress cycles on the failure of composite materials are limited to a study by Morrone et al. (2) for SiC whisker reinforced Al_2O_3, Suresh et al. (3) for SiC whisker reinforced Si_3N and to polymer matrix composites such as studies by Bakis and Stinchcomb (4) and Kunz and Beaumont (5). Morrone et al. (2) measured crack growth in Al_2O_3 reinforced with SiC whiskers at an R of 10 in compression-compression fatigue at room temperature. They found that the composite was highly susceptible to fatigue crack growth under these conditions and that the results were similar to unreinforced Al_2O (6) and SiC whisker reinforced Si_3N_4 (3). Cracks propagated in compression because anelastic effects produce tensile stresses at the crack tip. The effects of tension-compression cycles in composites with continuous fibers can be illustrated with glass or graphite fiber reinforced polymer composite materials. Bakis and Stinchcomb (4) demonstrated that delamination was a predominant failure process for graphite-epoxy composites with 0/45/90 degree Fiber alignment when stressed at R = -1 and frequencies of 1 to 10 Hz. Kunz and Beaumont (5) measured the fatigue crack growth behavior of graphite fiber-epoxy composite stressed with zero-compression cycles at frequencies of 1 to 3 Hz. They found that fatigue cracks propagated perpendicular to the compressive stress axis but that fiber-matrix cracking and microbuckling occurred behind the primary crack in a direction parallel to the stress. High Fiber-matrix bond strengths resulted in less axial cracking and microbuckling.

The available results on fatigue crack growth in composites where there is a compressive stress cycle indicate the possibility *of* axial cracking along fiber-matrix interfaces, microbuckling, delamination and crack growth perpendicular to the principal compressive stress axis. Important material parameters include interlaminar shear strength, fiber-matrix bond strength and fiber architecture. Strong fiber-matrix interfaces are desirable to reduce the effects of compressive fatigue stresses while weak fiber-matrix interfaces are desirable for fracture resistance in tension. Clearly, compressive stresses should be avoided or minimized wherever possible in the design of a fusion reactor blanket utilizing SiC/SiC.

Elevated temperature fatigue crack growth involves cyclic stresses at constant temperature while thermal shock involves cyclic stresses and temperatures. Thermal shock studies are generally performed by rapidly cycling the material through a thermal cycle with the low temperature of the cycle frequently being established by immersing the sample in water. An example of this type of study are the results of Lee and Case (7) who evaluated the thermal shock of SiC whisker reinforced Al_2O_3 by removing the materials from a furnace followed by immersion in water at 25°C. Tests were performed with ΔT's of up to 380°C at a frequency of 1 cycle per hour. The thermal shock damage was monitored from changes in the elastic modulus and internal friction as a function of thermal cycles. The decrease in the modulus and the increase in the internal friction with thermal cycles probably resulted from microcrack formation. Lee and Case (7) found that the thermal shock damage saturated with thermal cycles and that the damage level was a function of ΔT^5 for the temperature range studied. Saturation occurred in only 3 cycles for a A I of 380°C and 49 cycles for a AT of 270°C. In a related study, Tiegs and Becher (8) found that the thermal shock resistance of SiC whisker reinforced Al_2O_3 was excellent up to a AT of 900°C. They found no decrease in the flexural strength of the composite material up to this AT while monolithic Al_2O_3 exhibited a decrease in fracture strength for ΔT's less than 400°C.

Wang and Chou (9) have modeled the thermal shock resistance of a laminated SiC fiber reinforced glass composite which has a fiber architecture similar to that of the SiC/SiC composites of interest to fusion reactor technology. They found that the thermal shock parameter for CMCs cannot be expressed in as simple a form as for monolithic materials and that the maximum allowable temperature change, ΔT_{max}, is the best parameter to describe thermal shock resistance of CMCs. The coefficient of thermal expansion has a greater effect on ΔT_{max} than elastic modulus and thermal conductivity. The initial failure mechanism ranges from delamination to matrix microcracking depending on fiber orientation but CMCs retain their load carrying capacity in spite of thermal fatigue damage because of the R curve behavior of these materials.

Constant temperature-mechanical fatigue is in some ways less complex than thermal fatigue because only the stress is cycled; however, the effect of high-temperature, time-dependent processes are more important than for thermal fatigue. Elevated temperature fatigue crack growth measurements have been made by Holmes (10) on a unidirectionally reinforced SCS-6 SiC fiber-Si_3N_4 matrix composite at 1200°C. Tests were conducted in tension at a frequency of 10 Hz and for R values of 0.1, 0.3 and 0.5. While the Si_3N_4 matrix may exhibit more creep at 1200-C than will a SiC matrix at 800-1000°C, these results are perhaps the most relevant data available for estimating the possible fatigue behavior of SiC/SiC. Holmes found that there were no failures up to 5×10^6 cycles for peak stresses below the proportional limit of the composite (matrix microcracking stress) while the fatigue life decreased with decreasing R ratio for tests conducted at peak stresses exceeding the proportional limit, Figure 1. Creep was the dominant damage process at stresses below the proportional limit while fatigue and creep occurred at higher stresses. Holmes' observation of a decreasing fatigue life with decreasing R ratio is consistent with results observed for metallic materials but opposite that observed by Han and Suresh (11) for a SiC whisker reinforced Al_2O_3 tested at 1400°C. Han and Suresh found an increase in the fatigue life of this composite with decreasing R ratio. One explanation was that creep crack growth would be much more dominant in the SiC-Al_2O_3 composite at 1400°C than for the SiC-Si_3N_4 composite at 1200°C. Creep crack growth would be more extensive for high R values because a greater percentage of the test would be conducted at higher stresses than low R values. Consistent with this conclusion was the observation by Han and Suresh that crack growth in statically

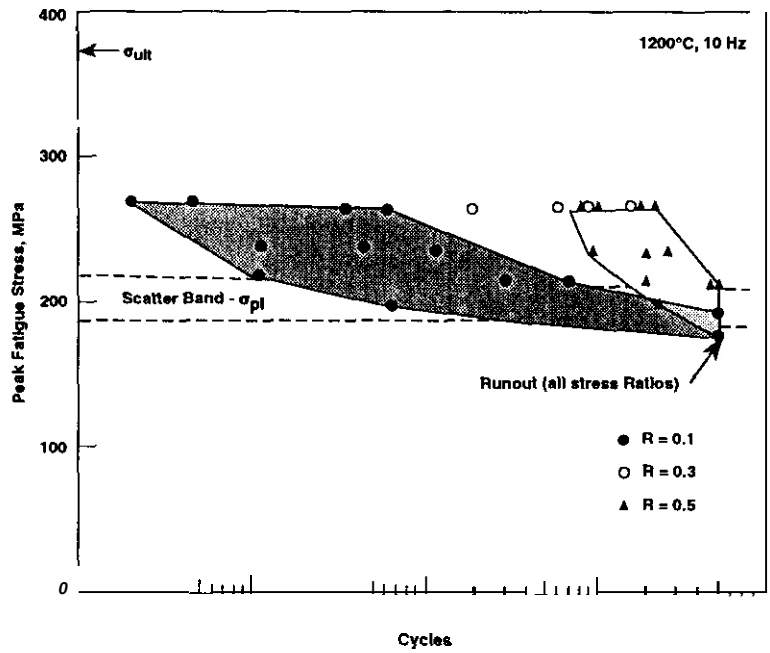

Fig. 1. Influence of stress ratio on the tensile fatigue life of unidirectional HP-SiC/Si_3N_4. At 180 MPa all specimens survived 5 X 10^6 cycles, independent of stress ratio (four specimens were fatigued at each stress ratio). Above the proportional limit, progressive fatigue failures were observed.

loaded specimens was faster than in cyclically loaded specimens. The primary damage mechanisms observed by Han and Suresh was the nucleation and growth of interfacial flaws. Oxidation of the SiC whiskers at the crack tip produced a silica glass phase which led to the viscous creep induced debonding of the interface. Fatigue crack growth rates of 10^{-1} mm/cycle were observed for **AK** values of 5 MPa/m while threshold $\Delta K's$ ranged from 1 to 4 for R values of **0.75** and 0.15, respectively.

Prewo (12) and Zawada et al. (13) measured the fatigue life of SiC fiber reinforced glass matrix composites and found, as did Holmes (10), that there was minimal fatigue damage below the proportional limit. Zawada et al. (13) further noted that for stresses above the proportional limit, the elastic modulus decreased for the first 10 cycles and then stabilized for unidirectionally reinforced material but that most of the damage occurred on the first loading cycle for 0/90 reinforced material. Zawada et al. tested their material at 25°C so these results only reflect fatigue damage without creep. Matrix microcracking and fiber/matrix debonding were the primary damage processes. Prewo (12) performed tests at 25, 600 and 900°C and noted the same dependence of fatigue damage on proportional limit.

Determining whether composite materials exhibit improved fatigue lives over unreinforced material is difficult because these comparisons have not been made for ceramic or glass matrix materials. However, these comparisons have been made for polymer matrix composites. For instance, Steinbrunner (14) found that glass fiber reinforced liquid epoxy resin cured with cycloaliphatic amine exhibited significant increases in the fatigue thresholds for tests conducted at an R value of 0.6 and frequency of 20 Hz. A shift in the threshold from 0.2 to 0.6 MPa/m resulted from the glass fiber reinforcement. It is expected that fiber reinforced ceramics will exhibit similar increases in the fatigue threshold and decreases in the fatigue crack growth rate under certain conditions. Thermal shock studies of CMCs are consistent wit this conclusion since it has been shown that the thermal shock resistance of CMCs exceed that of monolithic material (8,9). A high thermal shock resistance coincides with a reduced crack initiation and fatigue crack growth rates.

In summary, compressive stress cycles in composites can induce delaminations and microbuckling while tension-tension stress cycles produce little damage for stresses below the proportional limit. For stresses above the proportional limit the number of cycles to failure decreases as the R ratio decreases if matrix creep is small while the number of cycles to failure increases as the R ratio decreases if matrix creep is significant. The effect of fiber creep is presumably similar to matrix creep; however, this has not been demonstrated.

ExDerimental Approach

Cyclic stress effects on the static load crack growth rate of SiC/SiC was evaluated in order to simulate the effects of stress cycles from reactor start-up and shut-downs. The primary concern was the possible damage produced to the composites during these cycles and the subsequent crack growth rates during high-temperature operation. For these reactor conditions, high cycle fatigue tests are not appropriate so tests were performed where the effects of cyclic stress on the static load crack growth rate could be assessed.

Composites consisting of Nicalon fiber cloth (0/90°) and CVI β-SiC with a carbon interface, was tested. The composites were 4 mm thick, 8-ply material, fabricated by RCI of Whittier, CA and were supplied in the form of bars having dimensions of 4 mm x 13 mm x 50 mm. An interface of 0.4 μm C was deposited on the Nicalon fibers before the β-SiC CVI fabrication step. Single-edge-notched bend bars (SENB) specimens with dimensions of 4 mm x 5.5 mm x 50 mm were prepared from the larger bars. The SENB specimens were loaded in 4-point bending using a fully articulated SiC bend fixture. The tests were performed inside a sealed mullite ceramic tube using a split clamshell furnace. The fixture was supported at the mid-plane of the furnace by a SiC support tube.

Load was applied through a SiC pushrod attached to the top sealing flange of the sealed tube using a flexible metal bellows. A double-hole alumina tube, holding a Type K thermocouple, spring-loaded against the bottom midpoint of the bend specimen was used to measure the specimen midpoint displacement by deflecting a strain gage extensometer positioned beneath the SiC support tube. The strain gage extensometer provided the spring tension to load the alumina tube against the specimen. The total length of the alumina tube was about 30 cm. The thermocouple wires exited the tube just above the extensometer and were routed through an electronic ice point connector. This entire testing assembly is mounted on a load cell mounted on an Instron Model 2115 electromechanical test machine.

A gas mixing apparatus was used to establish and control the gas atmospheres during the test. Pure Ar and pure O_2 gas were mixed in the desired quantities using an MKS Type 1476 four channel mass flow/pressure programmer with an MKS Type 2508 pressure controller. A baratron pressure transducer mounted on the gas mixing manifold provided the feedback signal to the pressure controller. This allowed the mass flow programmer to set each of the two mass flow meters to the correct setting and maintain the correct flow rates. The gas mixing ratios were set using a Thermox oxygen analyzer, and the manifold pressure was controlled at a level that allowed the gas flow rate through the mullite tube to be held at -1.6×10^{-6} m^3/s.

The static load subcritical crack growth (SCG) studies were performed using stepped load tests with load holding carried out at 1100°C in Ar and Ar plus 2000 ppm O_2. Initially, SENB specimens were tested to failure at 1100°C in Ar at a strain rate of 1.6×10^{-5} s^{-1} to establish the matrix cracking and peak loads, Figure 2. The SCG SENB specimens were then loaded to just below the matrix cracking stress, typically at an applied stress intensity of 7-8 MPa$\sqrt{m}$, to begin the test. The specimens were held at each load for 1000 s and the load was then increased to correspond to a stress intensity increase of about 1 MPa$\sqrt{m}$. This continued until the specimens underwent a load drop and the test was stopped at that

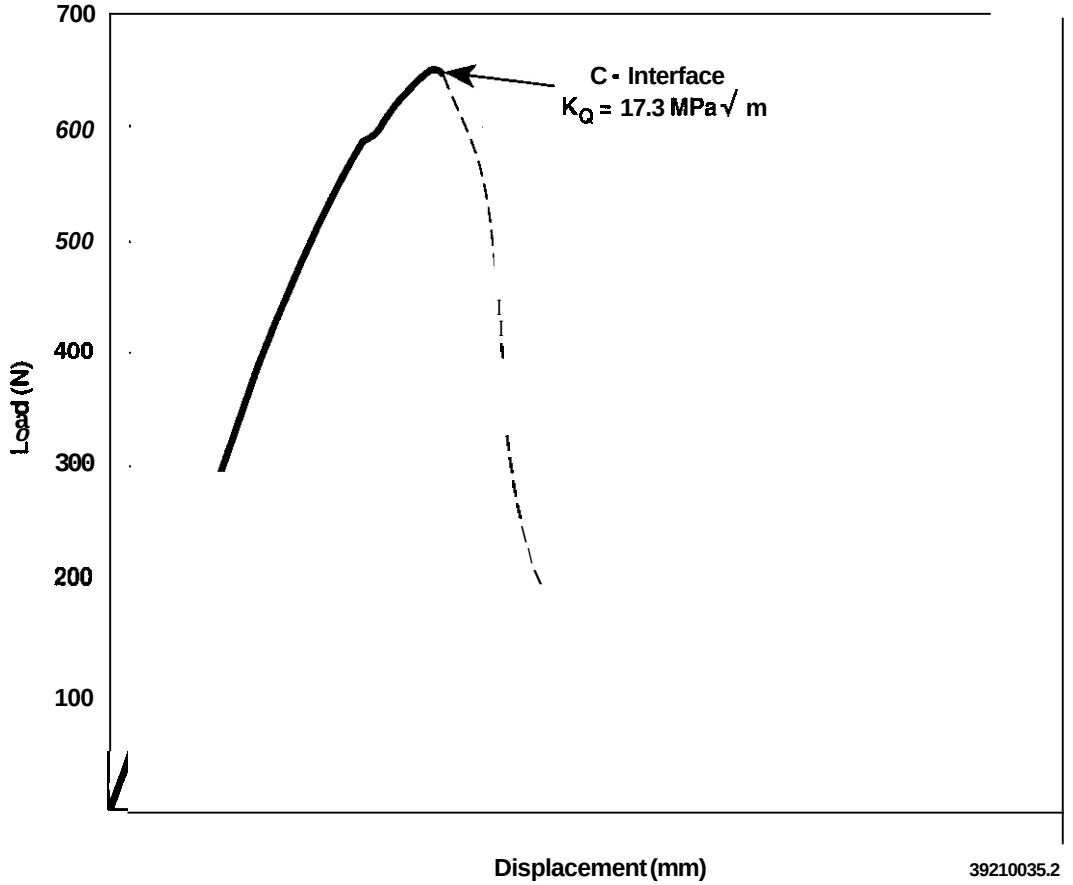

Fig. 2. Load-displacement curves at 1100°C in pure Ar for C-interface material. A peak load fracture toughness values of 17.3 MPa$\sqrt{m}$ is calculated for this material.

point. Some SCG tests included unloading-reloading steps to determine specimen compliance curves. SCG specimens that were tested in Ar plus O_2 were brought up to temperature in pure Ar and the gas mixture was switched over when the specimens were ready to be tested. An additional series of tests was performed on identical specimens using load holding for longer times to explore the transient nature of the crack velocity.

Fatigue crack growth tests were performed similarly to the static load subcritical crack growth tests with the load cycled 5 or 25 times at each of the constant loads used for the static load tests. The load was held for 1000s between each load cycle and the load ratio, R, was 0.1. Tests were conducted in both Ar and Ar plus 2000 ppm O_2. The crack velocity was determined during each of the 1000s hold periods between load cycles and compared to the crack velocity obtained with the statically loaded samples.

Test data was acquired using a Macintosh II computer equipped with analog-to-digital converter cards and data acquisition software (LabView™). Time, load, displacement, oxygen partial pressure, and temperature data were acquired at a total data throughput rate of 200 Hz. Thirty data points were averaged each second for each of these 5 signals and were written to disk and recorded on the computer screen at user selected time intervals ranging from 1 s to 30 s. The user selected time interval for data recording also represents the time over which the data were averaged. For example, the time interval was set to 30 s for recording the data during the 1000s load holding period and each data point represents the numerical average of 900 separate readings taken over that time. The data recording time interval was set to Is during the load increases and subsequent displacement transient. These data were then processed to give load-displacement and displacement-time curves for each load step.

Experimental Results

The presence of a crack growth regime which is weakly dependent on K (stage II) is common to both statically and cyclically loaded crack growth behavior in SiC/SiC composites as shown by the data in Figures 3 and 4. Crack growth in monolithic ceramics does not exhibit this stage as shown by the data for SiC and Si_3N_4 in Figure 5. This stage II behavior has been successfully modeled for SiC/SiC by Henager and Jones (16) using the crack closure forces applied to the crack tip from the fibers bridging the crack wake. Creep of the fibers and corrosion of the fiber/matrix interface of fibers bridging the crack wake can explain the fatigue and environmental effects, respectively, on crack growth of SiC/SiC.

Comparison of Figures 3 and 4 reveals that the cyclic crack velocities are lower than the static crack growth rates for Ar and Ar + 2000 ppm O_2. This effect is revealed by comparing the crack velocities after 1 cycle and after 25 cycles, figure 4c. Clearly, the crack velocity decreases with increasing number of cycles; however, the decrease in crack velocity is greatest at low K values at the beginning of the test

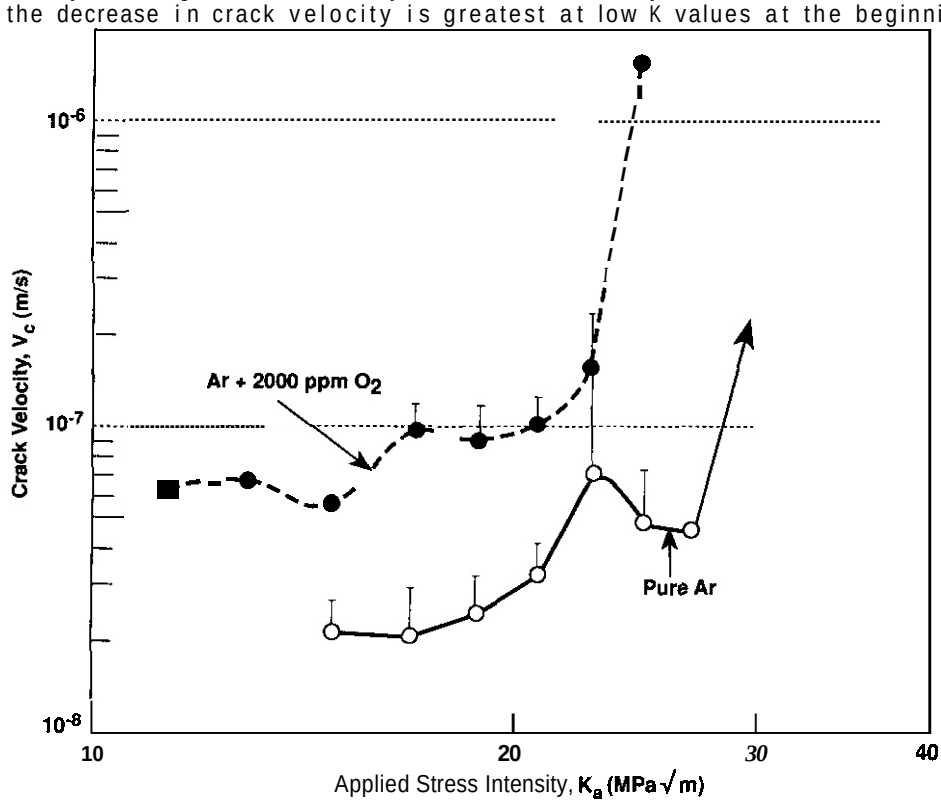

Fig. 3. Crack velocity as a function of applied stress intensity (V-K) data for C-interface material at 1100°C in pure Ar and Ar plus 2000 ppm oxygen. Data is averaged from several specimens and single-sided error bars are shown.

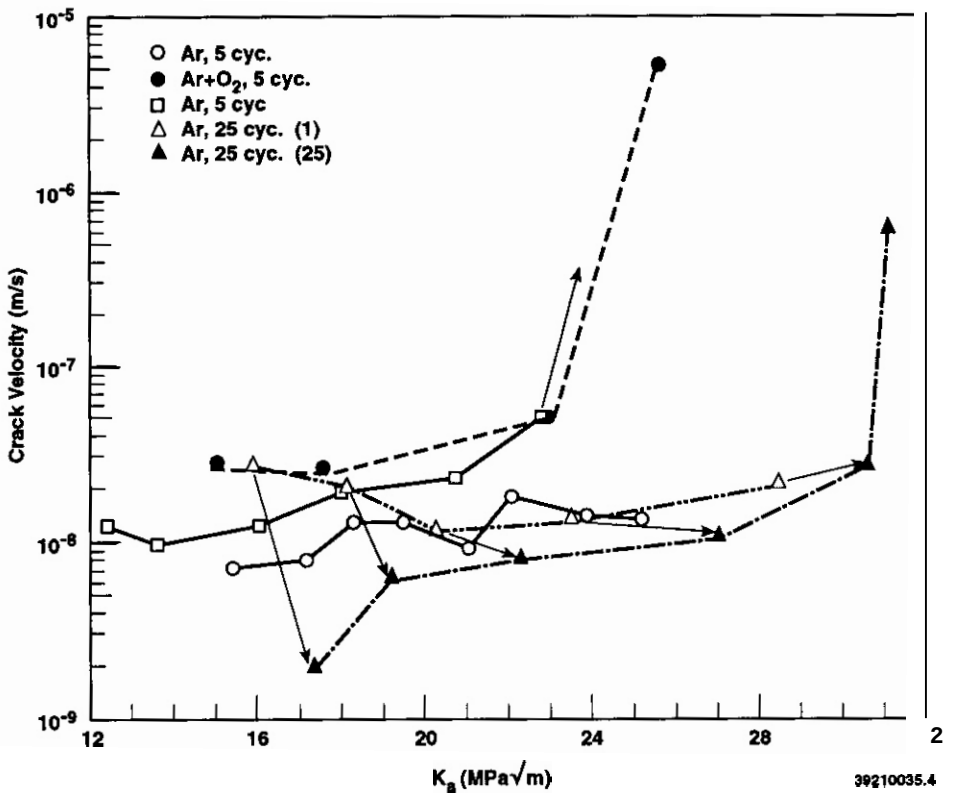

Fig. 4. Crack velocity as a function of applied stress intensity (V-K) for C-interface material at 1100°C in pure Ar and Ar t 2000 ppm oxygen and with cyclic stresses at a R of 0.1

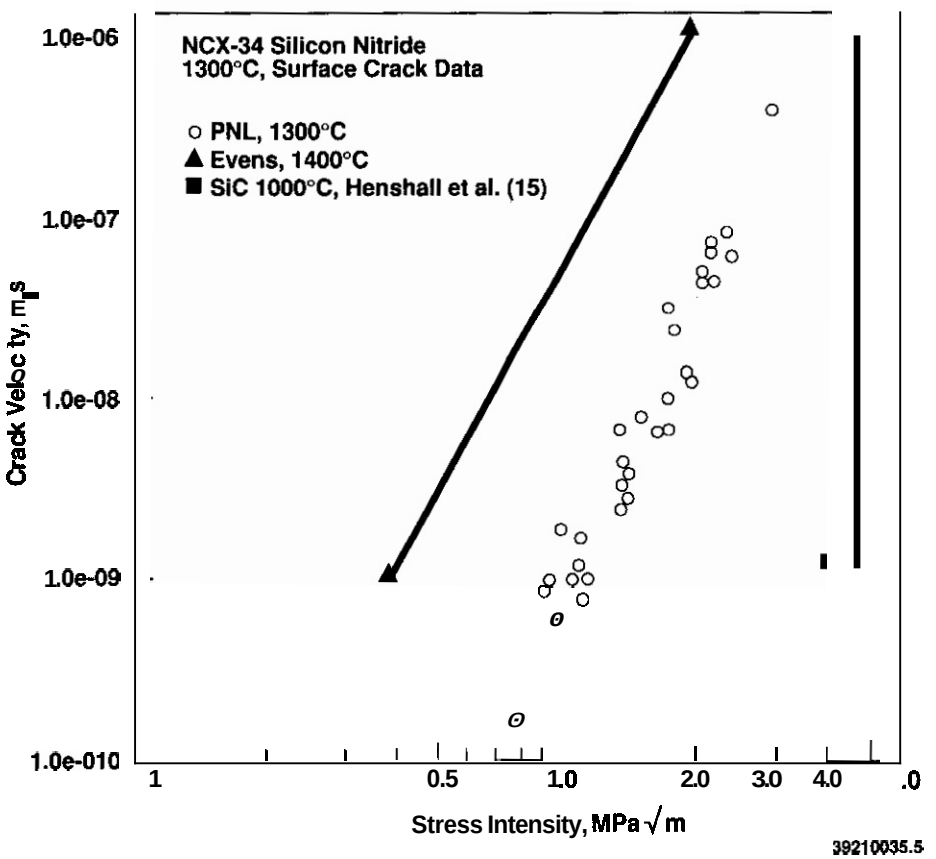

Fig. 5. Crack velocity as a function of stress intensity for monolithic Si_3N_4 and SiC

with less of a decrease at higher K values. Stage II crack velocities ranged from 2 x 10^{-9} to about 3 x 10^{-8} m/s in Ar and 3 x 10^{-8} to 1 x 10^{-7} m/s in Ar + 2000 ppm O_2. The stage II crack velocities in Ar would allow a crack to propagate between 0.06 to 0.1 m in one year of reactor operation.

The effect of cyclic stresses on the transition from stage II to rapid fracture, stage III, is difficult to identify with this data set. For the tests in Ar + O_2, the transition occurs at about the same K level for static and cyclic loading while the data for tests conducted in Ar is less conclusive. A transition from stage II to stage III occurred at about 28 MPa/m with static loading, Figure 3, but for two tests conducted with cyclic loading the transition occurred at about 24 MPa/m in one test while the other survived to 25 MPa/m without failing. The test was terminated at this stress intensity because of equipment failure. Apparently the time-dependent processes occurring at the crack tip and in the crack wake result in a time-dependent $K_0(t)$ which is greater than the time-independent K_0. This effect is presently the subject of a modeling effort but a quantitative explanation is not presently available.

Evidence for a stress intensity threshold below which crack propagation ceases, K_0, was not clearly demonstrated; however, the test with 25 cycles per load gives a slight suggestion of a threshold at about 16 MPa/m. If a K_0 exists, it would define a stress and flaw size limit for design since the stage II crack velocities are too high for extended life of a SiC/SiC component. The development of improved high-temperature SiC fibers which would reduce the stage II crack velocity is needed before these materials could be utilized for extensive periods at stress intensities in stage II. Much more data is needed before definite lifetime, stress or flaw length limits can be defined for these materials.

Discussion

Both the occurrence of stage II and the crack velocity in this stage have been modeled by Henager and Jones *(16)* by assuming the fibers bridge the crack wake and reduce the crack tip stress intensity because of crack closure forces. Using a definition for the equilibrium bridging zone, an expression can be derived for the velocity of a crack in a composite for the conditions of equilibrium, which results in a quasi-static approximation to the crack velocity. For this approximation, it is assumed that the bridging zone is in equilibrium by virtue of a balance between crack advance and relaxation of bridging zone stresses. As the crack advances, it bridges additional fibers which retards its growth. As the stresses in the bridging zone relax, the crack-tip screening is reduced and the crack tends to advance. This assumption does not require detailed information about the physical mechanism of crack advance and is valid only over the range of applied stress intensity that corresponds to the R-curve of the material, which is the region of stable bridging zone lengths. Also, it does not provide any information regarding the dependence of crack velocity on the applied stress intensity.

The quasi-static approximation assumes that the stress intensity at the crack-tip is a constant such that

$$K_{tip}(a,t) = C \Rightarrow dK_{tip} = 0 \qquad (1)$$

Therefore, one can write the total differential of K_0 as

$$dK_{tip} = \frac{\partial K_{tip}}{\partial a}\,da + \frac{\partial K_{tip}}{\partial t}\,dt \qquad (2)$$

which can be used to derive an expression for crack velocity, V_c, as

$$V_c = \frac{da}{dt} = -\left[\frac{\dfrac{\partial K_{tip}}{\partial t}}{\dfrac{\partial K_{tip}}{\partial a}}\right] \qquad (3)$$

where the crack velocity is expressed as the ratio between the time-dependence of K_{tip} due to crack advance, dK_{tip}/da.

Values for dK_{tip}/dt can be calculated from differentiating a polynomial fit to the K_{tip} data as a function of time due to fiber creep. The rate of change of K_{tip} with respect to crack length, a, is easily calculated from the bridging model by computing K_{tip} for incremental changes in crack length. For a given choice of model parameters, or material constants, this quantity is a constant.

Utilizing experimental creep data for Nicalon by Simon and Bunsell *(17)* and experimental interface shear strength data by Lowden (18), a crack velocity of 10^{-8} m/s is predicted for these SiC/SiC materials at 1100°C. The similarity between the experimental and predicted values of the crack velocity give confidence that the bridging zone model is correct. The transition from stage II to stage III occurs when the bridging zone cannot support further increases in the applied K and the K at the crack tip increases dramatically. A quantitative prediction of this limiting K has not been determined but it is a function of the fiber/matrix interface shear strength and fiber fracture strength. Further modeling of this effect is in progress.

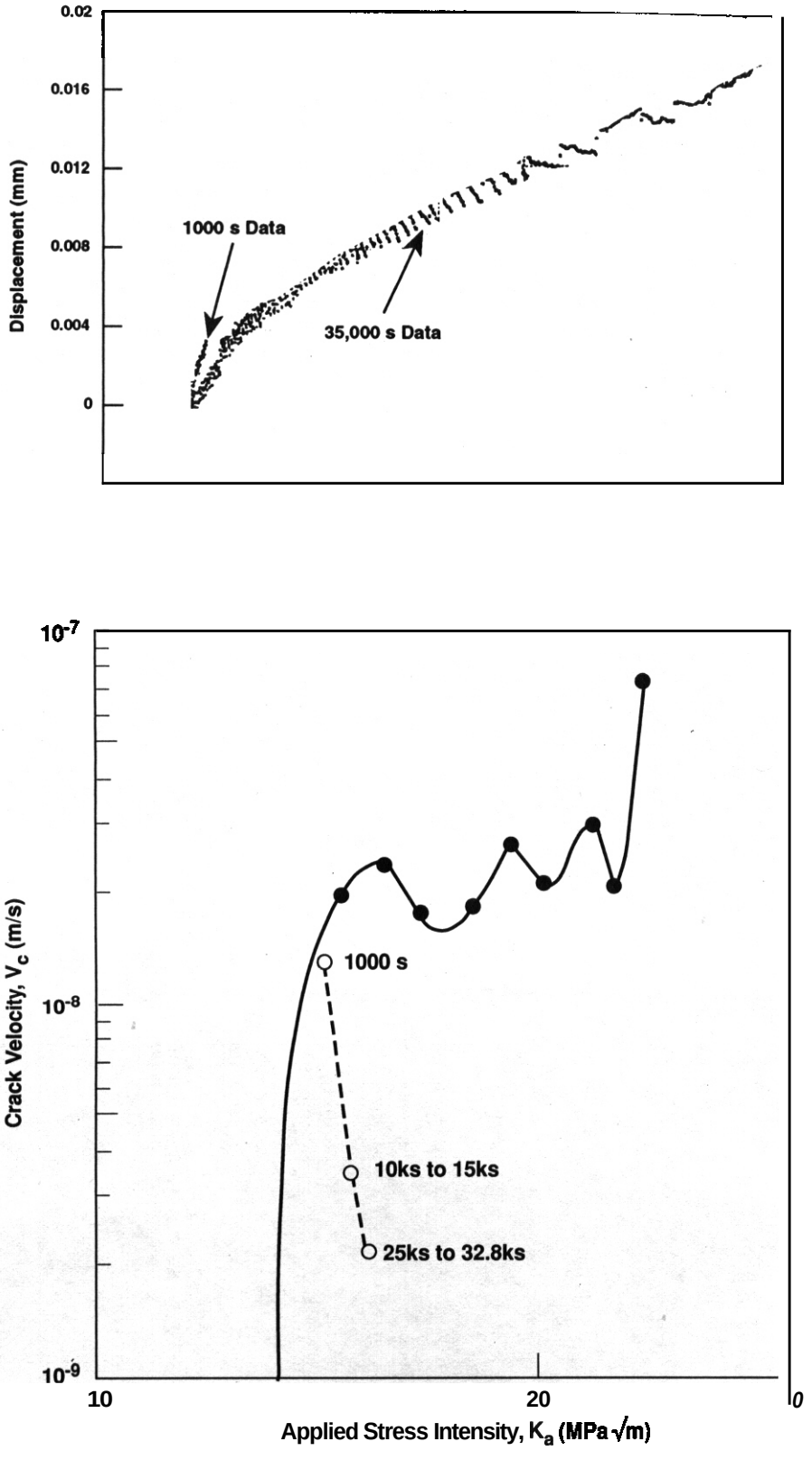

Fig. 6. Time dependence of a) crack opening displacement and b) crack velocity of SiC/SiC at 1100°C.

The present results indicate that the crack velocity is not increased by cyclic stresses under the conditions of these tests with R = 0.1. A similar conclusion was reached by Holmes (10) for high-cycle fatigue of SiC fiber reinforced Si_3N_4 and Prewo (12) and Zawada et al. (13) where they found no damage for stresses below the proportional limit or matrix fracture stress. In the present case, a crack is growing at a stress intensity which exceeds the time-independent K_0 which is equivalent to being above the proportional limit. However, as noted above the $K_0(t)$ appears to exceed K so it is not clear whether the tests were conducted at stresses exceeding the time-dependent proportional limit. However, not only was there no increase in the crack velocity there was an apparent decrease. This decrease can be explained by the absence of a cyclic stress damage process and the crack velocity retardation effect of increased hold time at each load level. This effect is illustrated by the data presented in Figure 6 where a comparison between a 1000 s hold time and a longer hold time and the crack opening displacement is shown in Figure 6a and the resulting crack velocity in Figure 6b. The static load tests were conducted with 1000 s hold times at each load or K level while the fatigue tests were conducted with 1000 s between each cyclic load. For a test with 5 cycles at each load or K level, the sample experienced a cumulative time of 5000 s at each load while for the test with 25 cycles per load or K level the sample experienced 25,000 s per load or K level. Therefore, in the absence of a cyclic stress damage process the crack velocity after 5 or 25 cycles (5000 or 25000 s) would be less than after a single hold period of 1000 s. This effect of hold time is consistent with the Nicalon creep behavior at 1100°C where it is in the transient creep regime after 1000 s so the creep rate decreases with increasing time. A decreasing fiber creep rate results in a decreasing dK_{tip}/dt and hence a decreasing da/dt according to equation 3.

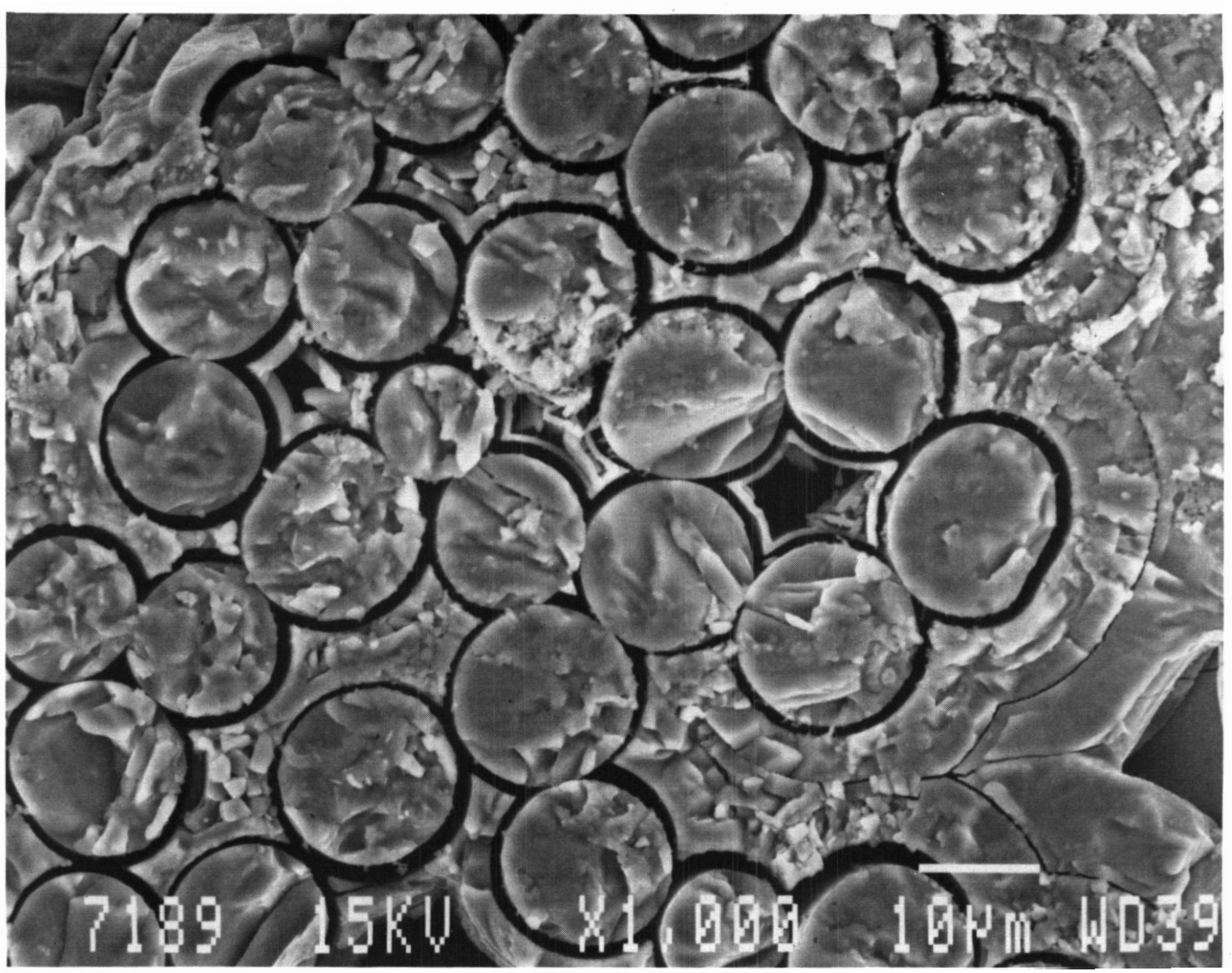

Fig. 7. Scanning electron micrograph of a Nicalon fiber reinforced SiC/SiC composite with a C fiber/matrix interface layer following exposure to Ar at 0.

Oxygen was found to increase the stage II crack velocity and reduce the transition from stage II to stage III. Carbon in the fiber/matrix interface reacts with O_2 during the subcritical crack growth, Figure 7, such that the interface pull-out stress is reduced. While the extent of corrosion has not been measured it is apparent that the interface is completely eliminated to some depth. A reduction in the fiber pull-out stress has the effect of increasing the stress on the fiber and increasing the fiber creep rate. An increase in the fiber creep rate increases dK_{tip}/dt in equation 3 and therefore, increases da/dt. The shift in the transition between stage II and stage III can also be explained by the reduced fiber pull-out stress causing a higher fiber stress. An increase in the fiber stress for a given $K_{applied}$ will result in a reduced bridging zone length and less crack tip shielding. Therefore, the K value at which the bridging zone can no longer shield the crack tip occurs at a lower value.

These preliminary fatigue crack growth results indicate that cyclic stresses from reactor thermal cycles or fluctuating loads with R values of 0.1 or above and stresses below the proportional limit are not necessarily a concern for SiC/SiC materials. Thermal cycles which induce compressive stresses could be a problem if SiC/SiC behaves like other composite materials. Delamination and micro-buckling can occur in continuous fiber composite materials for R values < 0. The effect of stresses above the proportional limit on SiC/SiC without a precrack has not been evaluated but again results similar to other continuously reinforced composite materials is expected. In high cycle fatigue tests, Holmes (10) found that the number of cycles to failure decreased with decreasing R values for maximum alternating stresses which exceed the proportional limit. Therefore, before the fatigue life of SiC/SiC in a structural application in a fusion blanket can be assessed, maximum and minimum thermal and mechanical stresses must be known. Sharafat et al. (19) determined that the maximum thermal and pressure stresses on the SiC/SiC first wall structure in ARIES I was 17 MPa with the maximum thermal stress being 44 MPa. A stress ratio of 0.4 results for the condition with the plasma off and the coolant pressure retained and an R value of 0 for the reactor in a total shut-down mode. Also, the maximum stress is below the proportional limit of 140 MPa for these materials. Therefore, these uniform stress ratios and stress magnitudes are not expected to produce a fatigue life concern for SiC/SiC. The presence of non-uniform stress at notches, holes, corners, etc. could produce stresses and R values which do induce fatigue crack growth but these effects are design specific and can be controlled by design.

FUTURE OIRECTION

Further measurements of the effects of hold-times on crack velocities will be conducted including constant K tests to evaluate creep-crack growth rates for extended periods of time. Crack growth rate measurements will also be conducted at more fusion relevant temperatures of 800-1000°C. These tests will be conducted in Ar and Ar + 2000 ppm O_2. Also, an assessment of the thermal shock behavior of SiC/SiC will also be completed.

ACKNOWLEDGEMENTS

The assistance of J. L. Humason in performing the crack growth experiments is gratefully acknowledged. This work was supported by the Office of Fusion Energy and the Office of Basic Energy Sciences of the U.S. Department of Energy under contract DE-AC06-76RLO 1830 with Battelle Memorial Institute which operates Pacific Northwest Laboratory for DOE.

REFERENCES

1. "Proceedings of the Office of Fusion Energy/DOE Workshop on Ceramic Matrix Composites for Structural Applications in Fusion Reactors", R. H. Jones and G. E. Lucas, eds., held at U.C. Santa Barbara, CA, May 21-22, 1990, PNL-SA-17843, CONF-9005225.

2. A. A. Morrone, S. R. Nutt and S. Suresh, J. of Mater. Sci., 23 (1988), p. 3206

3. S. Suresh, L. X. Han and J. J. Petrovic, J. Amer. Ceram. Soc., 71 (1988), p. C158.

4. C. E. Bakis and W. W. Stinchcomb, in Composite Materials: Fatigue and Fracture, ASTM STP 907, H.T. Hahn, ed., American Society for Testing and Materials, Philadelphia, PA., 1986, p. 314.

5. S. C. Kunz and P.W.R. Beaumont, in Fatigue of Composite Materials, ASTM STP 569, American Society for Testing and Materials, Philadelphia, PA., 1975, p. 71.

6. L. Ewart and S. Suresh, J. Mater. Sci., 22 (1987) p. 1173.

7. W. J. Lee and E. D. Case, Mater. Sci. and Engr. A119 (1989) p. 113.

8. T. N. Tiegs and P. F. Becher, J. Amer. Ceram. Soc. 70 (1987) p. C109.

9. Y. R. Wang and T.-W. Chou, J. of Mater. Sci., 26 **(1991)** p. **2961.**

10. J. W. Holmes, J. Am. Ceram. Soc., **74 (1991)** p. **1639.**

11. L. X. Han and S. Suresh, J. Am. Ceram. Soc., **72 (1989)** p. **1233.**

12. K. M. Prewo, J. of Mater. Sci., **22 (1987)** p. **2695.**

13. L. P. Zawada, L. M. Butkus and G. A. Hartman, J. Am. Ceram. Soc. **74 (1991)** p. **2851.**

14. D. L. Steinbrunner, in Advanced Composites III: Expanding the Technology, Proceedings of the Third Annual Conference on Advanced Composites, ASM Intl., Material Park, OH, **1988,** p. **329.**

15. J. L. Henshall, O. J. Rowcliffe and J. W. Edingtan, J. Am. Ceram. Sac., Vol. **62** (1979), **p.36.**

16. C. H. Henager, Jr and R. H. Jones, Ceramic Engineering and Science Proceedings, July-Aug **1992,** The American Ceramic Society, **735** Ceramic Place, Westerville, OH 43081-6136, p. **411.**

17. G. Simon and A. R. Bunsell, "Creep Behavior and Structural Characterization at High Temperatures of Nicalon SiC Fibers", J. Mater. Sci. **19** (1984), pp. 3658-3670.

18. R. P. Lowden, "Interface Effects and Fracture in Nicalon/SiC Composites", Fourth Conference on Fossil Energy Materials, May **1990,** Conf. **900 54612,** ORNL, Oak Ridge, Tennessee.

19. S. Sharafat, C.P.C. Wong and E. E. Reis, Fusion Technology, Vol. **19,** (1991), p. 901.

RADIATION ENHANCED CONDUCTIVITY IN SILICON CARBIDE MATERIALS — Lance L. Snead (Oak Ridge National Laboratory), Matthew Ohland (Rensselaer Polytechnic Institute), Roger A. Vesey (Rensseiaer Polytechnic Institute)

OBJECTIVE

The objective of this work is to gather preliminary data on the radiation enhanced electrical conductivity in silicon carbide based materials.

SUMMARY

The radiation enhanced conductivity (REC) in four types of silicon carbide based materials was measured. As expected, the material with the highest initial conductivity showed the lowest conductivity enhancement. Chemically vapor deposited material showed only a few percent change at ionizing fluxes of several Gy/s. Two materials with higher initial resistivities demonstrated significant REC, the highest resistivity of the two changing by more than a factor of thirty for a dose of **4.2**Gyls.

PROGRESS AND STATUS

Introduction:

The phenomenon of radiation enhanced conductivity (REC) of insulating materials has been known since the early fifties.' Ansbacher and Ehrenberg demonstrated in **1951** that thin films of Al_2O_3 and As_2S_2 acquired enhanced conduction during high-energy electron irradiation. Numerous studies have investigated the REC of various forms of alumina[2-4] and MgO.[5] One reason for the focus on these materials is due to their potential use as ohmic breaks, windows and other specialty applications in fusion reactors. In a typical fusion power reactor, these materials would be expected to receive operating ionizing doses ranging between **4.6** x 10^3 and 340 Gy/s, depending on whether they are at the first wall, or **1/2**m into the blanket region, respectively.

The first study on the electromagnetic radiation enhanced conductivity of alumina was published in **1967** by Huntley and Andrews[2] and followed by more comprehensive studies by Klaffky et. al[3] and Pells.[4] The latter work demonstrated an increase in room temperature ***DC*** conductivity of Vitox alumina from 10^{-17} to 10^{-10} $(ohm\text{-}cm)^{-1}$ under a **6** Gy/s dose of X-radiation (**60**keV peak) and a further increase to more than 10^{-8} under a **2.5** x 10^3 Gy/s dose of **20** MeV protons (original reference incorrectly quoted **56** Gy/s). This dramatic increase in the conductivity of alumina is generally attributed to the ionizing radiation generating electron-hole pairs in proportion to the ionizing dose rate. Once these electrons are excited they may contribute to the material conductivity. The REC in insulators has been described as having a power law dependence:

$$a = \sigma_0 + KR\sigma$$

where σ_0 is the unirradiated conductivity, K is a constant, R is the dose rate and δ is the dose rate exponent obtained from a log-log plot of the radiation induced conductivity-vs-dose. Both **K** and δ have been found to be temperature dependent.

Recently, the question of the effect of radiation on the conductivity of silicon carbide has come into question. This is of interest in that SiC has been proposed as a structural material by many fusion reactor studies, most recently by the ARIES study.6 One advantage SiC has when compared to metallics in fusion reactors is its relatively low electrical conductivity. During the current quench phase of a disruption, the collapsing plasma will drive current in the surrounding structure. As this induced current is proportional to the material conductivity, and the corresponding (JxB) forces are proportional to the induced current, it is desirable to have a highly resistive structure near the plasma. In near-term fusion systems, such a problem is mitigated by including insulating breaks between reactor segments to limit toroidal continuity. In the ARIES study it was assumed that such insulating breaks would not be required as the electrical conductivity of the candidate material (CVD SiC/Nicalon fiber) has relatively poor electrical conduction. The question of a radiation enhanced conduction would then be of primary importance.

Silicon carbide itself is made up of two general crystalline types. The most common form is the face centered cubic β crystal structure (E_b = **2.2**eV).[7] However, also common is the hexagonally close packed form of α SiC of which **109** polytypes have been identified, with the **6H** α structure (E_b = **2.66** eV) is the most prevalent. The electrical conductivity of single crystal α and β, like all semiconductors, is a strong a function of the impurity (dopant) levels

present. Ranges of electrical conductivity of commercially manufactured high purity single crystal α and β SiC manufactured by CREE for electronic purposes are:

$$\alpha SiC: 167 - 500(\Omega - m)^{-1}$$
$$\beta SiC: 1.3 - 20{,}000(\Omega - m)^{-1}$$

Polycrystalline forms of silicon carbide have an even larger range of conductivities. For example, hot-pressing of SiC powder into monolithic ceramic involves the addition of sintering aids to increase density. Takeda[8] has shown that the addition of 1 w% of different sintering aids can yield a 13 order of magnitude difference in electrical conductivity. The addition of 1 w% $AlPO_4$ prior to hot pressing yields an electrical conductivity of 142 $(\Omega\text{-m})^{-1}$ while the addition of 1 w% Be reduces the conductivity to 3.3 x 10^{-12} $(\Omega\text{-m})^{-1}$. Interestingly. the thermal conductivity of the 1 w% Be sintered sample is 260 W/m-K, while the higher electrically conducting sample has a thermal conductivity of only 60 W/m-K. The reason of the increased electrical resistivity of the beryllium sintered sample has been attributed to grain boundary formation of a highly resistive phase, while the increased thermal conductivity is explained by Be atoms dissolving in the matrix and acting as acceptors in the crystal lattice.

Experimental

Materials selected for this preliminary study are given in Table 1. The chemically vapor deposited SiC was made by the Thermoelectron Corporation and represents a commercial grade material with moderate impurity levels. The next two materials in Table 1 were prepared by pressureless sintering of alpha and beta silicon carbide powders, respectively. The final material is Nicalon continuous silicon carbide based fiber. This material is nominally beta silicon carbide with excess carbon and SiO_2. The density of Nicalon fiber is only 82% of theoretical SiC density.

Table 1. Silicon Carbide Information

Material	Supplier	Processing	Density (g/cc)	Room Temp. Electrical Conductivity $(ohm\text{-}m)^{-1}$
CVD SiC	Thermoelectron	Chemically Vapor Deposited (CVD)	3.1	162.0
Alpha SiC	Carborundum (Hexoloy)	Pressureless Sintered	3.1	1.32×10^{-4}
Beta SiC	Kyocera (SC-221)	Pressureless Sintered	3.0	unknown
SiC Fiber	Nippon Carbon (Nicalon)	Polymer Precursor Continuous Fiber	2.6	1×10^{-1}

The three monolithic materials were machined into discs of 1 mm thickness and approximately 20 mm in diameter. Each of these materials were plated with 50 nm of platinum and a thick (>300 nm) layer of gold in a three electrode (guarded electrode) configuration as shown in Figure 1. For each sample, an equal voltage was applied to the central electrode and the outer 'guard ring," thus eliminating the problem of surface currents affecting the results. Such a guard ring has been used extensively and is discussed elsewhere.[9] The bottom sample contact was held at ground. The Nicalon fiber was mounted in the form of a single tow of fibers suspended between two ceramic posts. Each end of the tow was painted with silver paint to make ohmic contact to the fibers. As the total cross sectional area of the tow was unknown the results presented are normalized to the unirradiated resistivity.

The resistance of the samples was found by measuring the voltage drop across known resistors which were in series with the specimens (Fig.1). A DC bias was then applied across the two series resistors and the resistance of the sample found by the relation:

$$R_{sample} = R_{known}\left(\frac{V_{applied}}{V_{measured}} - 1\right)$$

For each sample the applied voltage was varied from 1 to 20 volts to ensure ohmic behavior of the samples. The maximum applied field on the samples was then 20 V/mm, well below the breakdown field for these materials.

The volume resistivity for the three electrode system following Amey and Hamburger's analysis[9] is given by:

$$R_{sample} = pt / \pi(r_0 - \delta)^2$$

where **p** is the volume resistivity of the sample, t is the sample thickness, r_0 is the radius to the center of the gap between the center electrode and the guard ring, and δ is the fringing constant given by:

$$\delta = t[(2/\pi)\ln\cosh(\pi G/2t)]$$

where G is the half the width of the gap between the center electrode and the guard ring.

The radiation dose was produced by the Rensselaer L-band traveling wave electron accelerator. This linear accelerator was operated at approximately 60 MeV to produce packets of electrons which were accelerated onto a tantalum target yielding bremsstrahlung radiation. Figure 2 shows the shape of an individual electron pulse. The pulse width was 200 ns with a peak current of 1.75 amps. The resulting dose per pulse was measured using lithium borate TLD powder. The dose rate was varied by varying the linac repetitinn rate from 6.25 to 300 Hz For the electron pulse shown in Figure 1, this corresponds to a duty cycle of 1.25 x 10^{-6} to 6 x 10^{-5}. The corresponding average dose rate was 0.1 to 4.74 Gy/s.

ORNL-DWG 93-1522

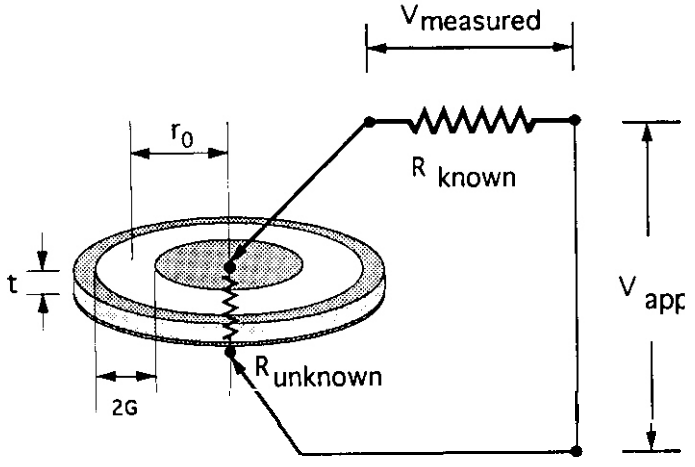

Fig. 1. Sample electrode configuration.

ORNL-DWG 93-1523

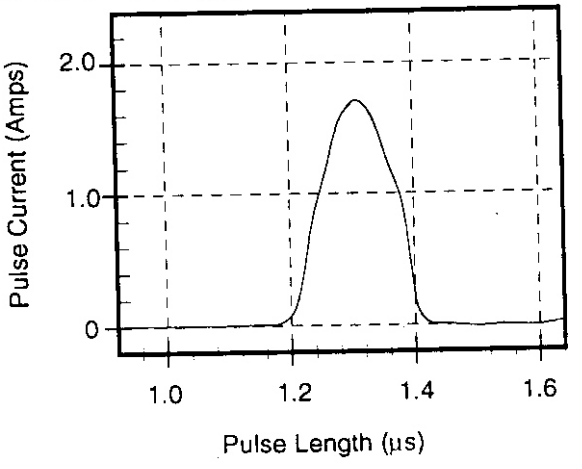

Fig. 2. Linear accelerator pulse shape.

RESULTS

The chemically vapor deposited SiC showed a 2.5% increase in conductivity at 0.15 Gyls. Any change in conductivity with increasing dose was within the scatter in the data. This small change in conductivity was not surprising given (Table 1) that the unirradiated conductivity was fairly high. The reason for the high conductivity is attributed to the moderate levels of impurities present which act as dopants.

Figure 3 shows the data obtained from the tow of Nicalon fibers. The data is presented as conductivity normalized to the unirradiated fiber conductivity and plotted on a log-log scale. The fiber showed a 4% increase in conductivity for the 0.098 Gy/s dose which increased to 10.5% at 4.73 Gy/s. By treating the data as following a power law (equation 1). the dose rate exponent is found to be 0.017.

Higher REC was seen in both the sintered β and ***a*** SiC. Figure 4 shows the plot of conductivity-vs-dose for Hexoloy ***a*** SiC. The material used in this study had an unirradiated conductivity of 1.32 x 10^{-4} $(\Omega\text{-m})^{-1}$. From the figure it is seen that the conductivity has a linear increase on a log-log plot to a maximum of 6.14 x 10^{-4} $(\Omega\text{-m})^{-1}$ at 3.05 Gy/s. The dose rate exponent for Hexoloy is found to 0.126 with the constant K = 4.32 x 10^{-4} $(\Omega\text{-m})^{-1}$ (s/Gy).

Similar behavior is seen in Figure 5 for the Kyocera SC-221 β SiC. The resistivity is given for both room temperature and 200°C measurements and is **seen** to linearly increase on both log-log plots over the range of **flux** studied. From the figure it is seen that the REC of the SC-221 has the largest increase of those materials studied, increasing for both the room temperature and 200°C irradiations by more than a factor of 30 in both cases from the dose rate of 0.086 to 4.2 Gy/s. That the SC-221 would have the largest fractional increase in conductivity is to be expected as it is also the sample with the highest initial resistivity of the sample studied.

ORNL-DWG 93-1524

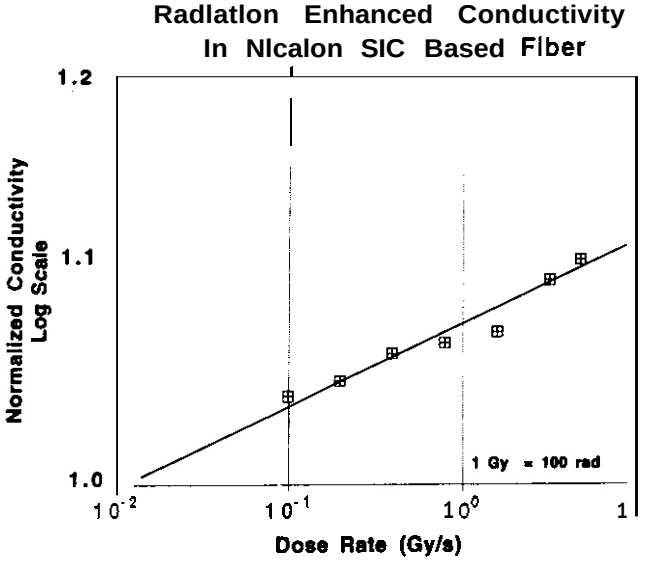

Fig. 3. Radiation enhanced conductivity in Nicalon fiber during X-ray irradiation.

ORNL-DWG 93-1525

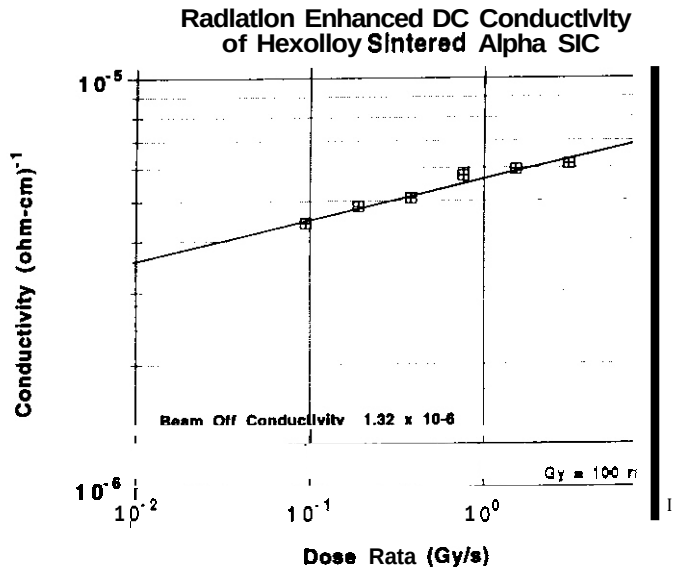

Fig. 4. Radiation enhanced conductivity in Hexolloy alpha SiC during X-ray irradiation.

ORNL-DWG 93-1526

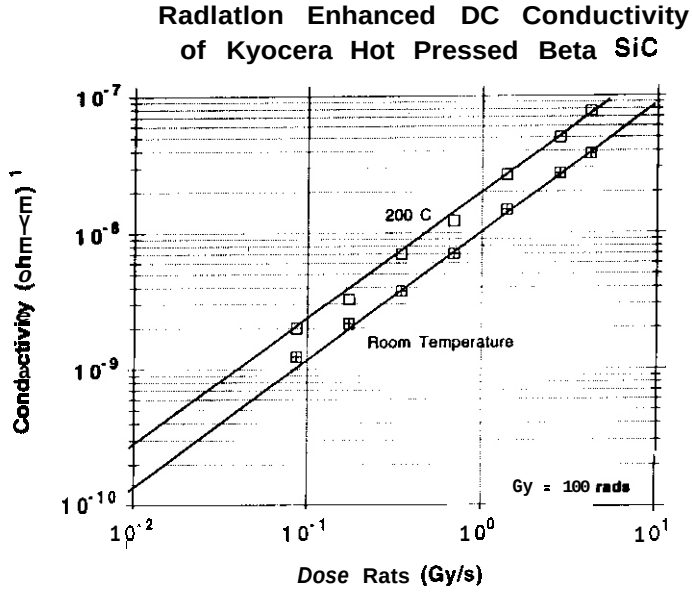

Fig. 5. Radiation enhanced conductivity in Kyocera Beta SiC during X-ray irradiation.

DISCUSSION

For the candidate material system for the **ARIES** reactor study, CVD SiC/Nicalon fiber, results have shown that the REC will be negligible for dose rates up to several Gy/s. For this material a change of 2.5% in conductivity was measured at a dose rate of several Gy/s. The Nicalon fiber likewise showed a small change, though larger than would have been seen in the composite matrix. The fiber which would make up 40 to 50 volume percent of the composite showed a 10.5% increase at 4.73 Gy/s. A third component typical for CVD SiC/Nicalon fiber composite systems is the fiber/matrix interfacial layer which can constitute a few percent of the composite volume fraction. The most widely used interfacial layer is carbon or graphite which should exhibit no REC unless in the form of diamond. which has a non-zero energy band. This was verified by including a sample of pitch based C/C composite into the test matrix. No change in conductivity was observed.

For reactor design, it is generally desirable to achieve as high an electrical resistivity and thermal conductivity as possible. As noted earlier, it is possible to engineer a silicon carbide material with such properties: resistivity of $>10^{11}$ R-m and thermal conductivity ~300 W/m-K. However, tailoring silicon carbide material for high electrical resistivity will yield the highest difference between the unirradiated conductivity and the REC. This has been evidenced by the five-fold change in the conductivity for Hexoloy SiC and more than a thirty-fold change in conductivity for Kyocera SC-221. For such highly resistive silicon carbides, this large increase in electrical conductivity will have to be taken into account in assessing disruption forces. It should be noted that the highest dose rate achieved in this study was 4.73 Gy/s which is three orders of magnitude less than would be seen in the ARIES first wall (operating at 2.5 MW/m^2). An ionizing damage rate of 4.73 Gy/s corresponds more to what would be seen in back of the blanket of a reactor operating at 1 MW/m^2.

FUTURE WORK

To complete this work, a larger range of ionizing dose rates should be studied. This could be achieved easily with the same facility simply by increasing or decreasing the distance the samples are located with respect to the tantalum target. By moving the samples in close proximity to the target an order of magnitude increase in the gamma flux would be achievable.

Identical samples to those in this experiment were included into the MOTA-26 capsule along with samples of SiC/Nicalon composite, two purities of CVD SiC, single crystal a-alumina, silicon nitride and aluminum nitride.[10] These samples should be available for REC measurements by mid-1993.

ACKNOWLEDGEMENTS

The authors would like to thank Don Steiner, Peter Brand, and Jim Howard as well as the guys who ran the linac at Rensselaer. We would also like to thank Marie Williams and Peter Ficalora for aid in the sample preparation.

REFERENCES

1. F. Ansbacher and W. Ehrenberg. "Proc. Phys. Soc. 64, (1951). p. 363.

2. D. J. Huntley and J. R. Andrews, "Gamma Photoconductivity of Al_2O_3," Can. J. Phys. 46, (1968), pp. 147-156.

3. R. W. Klaffky et. al, "Radiation-induced Conductivity in Al_2O_3: Experiment and Theory," Phys. Rev. B. 21 [8] (1980), pp. 3610-3634.

4. G. P. Pells, "Electrical Conductivity of Alumina in Radiation Field at Temperatures up to 700°C; Radiation Effects 97 (1986). pp. 39-47.

5. E. R. Hodgson and S. Clement, "Dose Rate Dependence of the Radiation-Induced Electrical Conductivity in MgO," J. Nucl. Mat. 155-157 (1988), pp. 357-360.

6. The ARIES-1 Tokamak Reactor Study. Final Report, UCLA-PPG-1323. Vol.2 (1991).

7. R. F. Davis et. al, "Thin Film Deposition and Microelectronic and Optoeiectric Device Fabrication and Characterization in Microcrystalline Alpha and Beta Silicon Carbide," Proc. of the IEEE 79 [5] (1991). pp. 677-700.

8. Y. Takeda, "Development of High-Thermal-Conductive SiC Ceramics." Ceram. Bull. 67 [12] (1988). pp. 1961-1963.

9. W. G. Amey and F. Hamburger, Jr.. "A Method for Evaluating the Surface and Volume Resistance Characteristics of Solid Dielectric Materials," Proc. Amer. Soc. Test Mat 49 (1949), pp. 1079-1091.

10. S. J. Zinkle and L. L. Snead, "Irradiation of Ceramics in FFTF," Fusion Reator Materials Semiannual, DOE/ER-0313/10, pp. 317-319 (1991).

Distribution

1-16. Argonne National Laboratory, 9700 South Cass Avenue, Argonne, IL 60439
M. C. Billone, O. K. Chopra, H. M. Chung, D. R. Diercks, R. Erck, A. K. Fisher, Y. Gohar, A. B. Hull, C. E. Johnson, F. Kassner, B. A. Loomis, R. F. Mattas, L. A. Niemark, J. H. Park, D. L. Smith, S. W. Tam, H. C. Tsai, H. Wiedersich

17-18. Argonne National Laboratory, EBR-II Division, P.O. Box 2528, Idaho Falls, ID 83403-2528
H. P. Planchon, D. L. Porter

19. Auburn University, Department of Mechanical Engineering, 201 Ross Hall, Auburn, AL 36849
B. A. Chin

20-33. Battelle-Pacific Northwest Laboratory, P.O. Box 999, Richland, WA 99352
J. L. Ethridge, F. A. Garner (5), D. S. Gelles, L. R. Greenwood, M. L. Hamilton, H. L. Heinisch, G. W. Hollenberg, R. H. Jones, W. W. Laity, O. D. Slagle

34. Carnegie Institute of Technology, Camegie-Mellon University, Schenley Park, Pittsburgh, PA 15213
W. M. Garrison, Jr.

35-36. EG&G Idaho, Inc., Fusion Safety Program, P.O. Box 1625, Idaho Falls, ID 83415-3523
D. F. Holland, S. J. Piet

37. GE Astrospace Division, San Jose Operations, 6834 via Deloro, P.O. Box 530954, San Jose, CA 95153-5354
Mike Kangilaski

38-41. General Atomics, P.O. Box 85608, San Diego, CA 92138
T. A. Lechtenberg, D. I. Roberts, K. R. Schultz, C. Wong

42. General Dynamics Corp., 5001 Kearny Villa Rd., San Diego, CA 92138
T. L. Cookson

43. Georgia Institute of Technology, Fusion Research Center, 0225, Atlanta, GA 30332
W. M. Stacey

44. Grand Canyon University, Department of Natural Science, 3300 W. Camelback Rd., Phoenix, AZ 85017
W. A. Coghlan

45-47. Lawrence Livermore National Laboratory, P.O. Box 808, Livermore, CA 94550
E.C.N. Dalder, M. Guinan, J. Perkins

48-55. Los Alamos National Laboratory, P.O. Box 1663, Los Alamos, NM 81545
J. L. Anderson, F. W. Clinard, E. H. Farnum, H. M. Frost, J. C. Kennedy, R. E. Siemon, W. F. Sommer, K. E. Sickafus

56. Manlabs, Inc., 231 Erie Street, Cambridge, MA 02139
D. Tognarelli

57-59. Massachusetts Institute of Technology, Department of Metallurgy and Materials Science, Cambridge, MA 02139
L. W. Hobbs, N. J. Grant, K. C. Russell

60-61. Massachusette Institute of Technology, Plasma Fusion Center Headquarters, Cambridge, MA 02139
H. D. Becker, D. B. Montgomery

62. McDonnell-Douglas Missile Systems Company, Mail Code 306 4204, P.O. Box 516, St. Louis, MO 63166
J. W. Davis

63-65 National Institute of Standards and Technology, Boulder, CO 80302
F. R. Fickett R. P. Reed
H. I. McHenry

66 National Materials Advisory Board, 2101 Constitution Avenue, Washington, DC 20418
K. M. Zwilsky

67-68 Naval Research Laboratory, Code 6506, Washington, DC 20375
D. L. Gibson J. A. Sprague

69-109 Oak Ridge National Laboratory, P.O. Box 2008, Oak Ridge, TN 37831

Central Research Library	R. H. Goulding	T. K. Roche
Document Reference Section	M. L. Grossheck	A. F. Rowcliffe (10)
Laboratory Records Department (2)	E. A. Kenik	R L. Senn
Laboratory Records-RC	R. L. Klueh	J. Sheffield
Patent Section	E. H. Lee	L. L. Snead
D. J. Alexander	A. W. Longest	R. E. Stoller
C. C. Baker	L. K. Mansur	K. R. Thoms
G.E.C. Bell	P. J. Maziasz	P. F. Tortorelli
J. Bentley	J. E. Pawel	D. P. White
E. E. Bloom	T. C. Reuther	S. J. Zinkle
T. D. Burchell		

110 Oregon Graduate Institute, Dept. of Materials Science & Engineering, 19600 N.W. Von Neumann Drive, Beaverton, OR 97006
J. M. McCarthy

111-113 Princeton University, Princeton Plasma Physics Laboratory, P.O. Box 451, Princeton, NJ 08540
C. Bushnell Long-Poe Ku
H. Furth

114. Reactor Materials Technology, 272 Baywood Avenue, Pittsburgh, PA 15228
A. Boltax

115-116 Rensselaer Polytechnic Institute, Troy, NY 12181
D. Steiner David Duquette

117. Rockwell International Corporation, NA02, Rocketdyne Division, 6633 Canoga Avenue, Canoga Park, CA 91304
D. W. Kneff

118-120 Sandia National Laboratories, Fusion Technology Dept., Dept. No 6531, P.O. Box 5800, Albuquerque, NM 87185-5800
M. J. Davis R. D. Watson
W. B. Gauster

121-122. Sandia National Laboratories, Livermore Division 8316, Livermore, CA 94550
W. Bauer W. G. Wolfer

123. San Diego State University, Mechanical Engineering Dept., San Diego, CA 92182-0191
L. D. Thompson

124. TSI Research, 225 Stevens Ave., #110, Solana Beach, CA 92075
E. T. Cheng

125-126. University of California, Dept. of Chemical and Nuclear Engineering, Santa Barbara, CA 93106
G. E. Lucas G. R. Odette

127-129 University of California, Dept. of Chemical, Nuclear, and Thermal Engineering, Los Angeles, CA 90024
M. A. Abdou N. M. Ghoniem
R. W. Conn

130. University of California, IPFR, 405 Hilgard Avenue, Los Angeles, CA 90024-1600
S. Sharafat

131. University of Michigan, Dept. of Nuclear Engineering, Ann Arbor, MI 48109
T. Kammash

132. University of Missouri, Department of Nuclear Engineering, Rolla, MO 65401
A. Kumar

133-134. University of Wisconsin, Nuclear Engineering Dept., 1600 Johnson Drive, Madison, WI 53706
J. B. Blanchard G. L. Kulcinski

135. Washington State University-Tr-Cities, 6012 W. Ridgecrest Drive, Spokane, WA 99208
D. G. Doran

136-139. Westinghouse Hanford Company, P.O. Box 1970, Richland, WA 99352
R. E. Bauer F. M. Mann
A. M. Ermi R. J. Puigh

140-142. Hokkaido University, Faculty of Engineering, Kita 13, Nishi 8, Kita-ku, Sapporo 060, Japan
Heischichiro Takahashi Akira Okada
Somei Ohnuki

143-144. Japan Atomic Energy Research Institute, Tokai Research Establishment, Tokai-mura, Naka-gun, Ibaraki-ken 319-11, Japan
Tatsuo Kondo Akimichi Hishinuma (3)

145. Kyushu University, Dept. of Nuclear Engineering, Faculty of Engineering, Kyushu University 36, Hakozaki, Fukuoka 812, Japan
C. Kinoshita

146. Kyushu University, Research Institute of Applied Mechanics, 6-1, Kasuga-Koen, Kasuga-Shi, Fukuoka-Ken 816, Japan
Takeo Muroga

147-148. Muroran Institute of Technology, Dept. of Metallurgical Engineering, 27-1 Mizumoto-cho, Mororan 050, Japan
Toshihei Misawa Akihiko Kimura

149. Nagoya University, Dept. of Nuclear Engineering, Furo-Cho, Chikusa-ku, Nagoya 464-01, Japan
Michio Kiritani

150-152. National Institute for Fusion Science, Furo-cho, Chikusa-ku, Nagoya 464-01, Japan
Osamu Motojima Chusei Namba Nobuaki Noda

153-155. National Research Institute for Metals, Tsukuba Branch, Sengen, Tsukuba-shi, Ibaraki-ken, 305, Japan
Fujio Abe Josei Nagakawa Haruki Shiraishi

156. Osaka University, Dept. of Nuclear Engineering, 2-1 Yamadaoka, Suita, Osaka 565, Japan
Tetuo Tanabe

157. PNC Oarai, 4002 Narita, Oarai, Ibaraki 311-13, Japan
Itaru Shibasaki

158. Science University of Tokyo, Dept. of Materials Science & Technology, 2641 Yamazaki Noda City, Chiba Prefecture 278, Japan
Naohira Igata

159. Teikyo University, Otsuka, Hachioji, Tokyo 192-03, Japan
Akira Miyahara

160. Tohoku University, Institute for Materials Research, Katahira 2-2-1, Sendai 980, Japan
Hideki Matsui

161-162. Tohoku University, Institute for Materials Research, Oarai Branch, Oarai, Ibaraki 311-13, Japan
Tatsuo Shikama Hideo Kayono

163. Tohoku University, Dept. of Nuclear Engineering, Tohoku University, Aoba, Aramaki, Sendai 980, Japan
Katsunori Abe

164-166. University of Tokyo, Dept. of Nuclear Engineering, 3-1, Hongo 7-Chome, Bunkyo-Ku, Tokyo 113, Japan
Shiori Ishino (2) Naoto Sekimura

167-168. University of Tokyo, Dept. of Materials Science, 3-1, Hongo 7-Chome, Bunkyo-ku, Tokyo 113, Japan
Akira Kohyama Yutaka Kohno

169. Commission of European Communities, Directorate-General for Research Science and Education, Fusion Programme RUE De La Loi 200, B-1049 Brussels, Belgium
J. Darvas

170-171. Chalk River Nuclear Laboratories, Atomic Energy of Canada, Ltd., Chalk River, Ontario KOJ 1J0, Canada
I. J. Hastings D. P. Jackson

172. Southwestern Institute of Physics, P.O. Box 432, Chenedu 610041, Sichuan, P.R. China
J. P. Qian

173. Institute of Atomic Energy, Academia Sinica, P.O. Box 275-51, Beijing, P.R. China
J. Yu

174 Riso National Laboratory, Materials Dept., P.O. Box 49, DK-4000, Roskilde, Denmark
B. N. Singh

175. Centre d'Etudes Nucleaires, Saclay, DLPC/SMCM, Commissariat a l'Energie Atomique, 91191 Gif-Sur-Yvette, Cedex, France
N. Roux

176. Commission for European Communities, Joint Research Centre, I.A.M. Ispra Establishment 21020 Ispra (Varese), Italy
P. Schiller

177. EURATOM/CIEMAT Fusion Association, Avenida Complutense 22,28040, Madrid, Spain
E. R. Hodgson

178. Paul Scherrer Institute, CH-5232 Villigen, Wuerenlingen PSI, Switzerland
M. Victoria

179. Harwell Laboratory, B393, Radiation Damage Dept., Oxfordshire, OX11 ORA, United Kingdom
C. A. English

180. Metallurgical and Nuclear Consultant, 9A Cumnor Rise Road, Cumnor Hill, Oxford OX2 9HD, United Kingdom
D. R. Harries

181. Culham Laboratory, U.K. Atomic Energy Authority, D5/117, Abingdon, Oxon OX14 3DB, United Kingdom
G. J. Butterworth

182. Hahn-Meitner-Institut fur Kernforschung Berlin, Glienicker Str. 100, D-1000 Berlin 39, Germany
H. J. Wollenberger

183. Institut fur Festkorperforschung der Kernforschungsanlage, D-5170 Julich 1, Postfach 1913, Germany
H. Ullmaier

184-185. Kernforschungszentrum Karlsruhe, Postfach 3640, 75 Karlsruhe 1, Germany
M. Dalle-Donne (INR) K. Erlich (IMF-II)

186. A. A. Baikov Institute of Metallurgy, USSR Academy of Sciences, Leninsky Prospect 49, Moscow, Russia
L. I. Ivanov

187. CRISM "Prometey," Naberezbnava r. Monastyrick 1, 193167, St. Petersburg, Russia
V. V. Rybin

188. D. V. Efremov Institute of Electro-Physical Apparatus, 189631, St. Petersburg, Russia
Yu. G. Prokofiev

189. Institute of Power Engineering, 218 M. Krasnosel's Kaji St., 107113 Moscow, Russia
G. M. Kalinin

190. Kharkov Physical-Technical Institute of Atomic Reactors, Kharkov, Academishen, 1, Moscow, Russia
I. M. Neckludov

191. V. I. Lenin Research Institute of Atomic Reactors, 433510 Dimitrovgrad-10, Ulyanovsk Region, Ukraine
V. K. Shamardin

192. Department of Energy, DOE Oak Ridge Field Office, P.O. Box 2008, Oak Ridge, TN 37831-6269
Assistant Manager for Energy Research and Development

193. Department of Energy, DOE Oak Ridge Field Office, P.O. Box 2008, Oak Ridge, TN 37831-6269
S. D. Frey

194. Department of Energy, Ofice of Basic Energy Sciences, Washington, D.C. 20585
J. B. Darby

195-201. Department of Energy, Office of Fusion Energy, Washington, D.C. 20585

S. E. Berk	N. A. Davies	F. W. Wiffen
M. M. Cohen	T. R. James	
D. H. Crandall	R. E. Price	

202. Department of Energy, Richland Operations Office, Federal Bldg., MS-A590, Richland, WA 99352
D. Segna

203-252. Department of Energy, Ofice of Scientific and Technical Information. Office of lnformation Services, P.O. Box 62, Oak Ridge, TN 37831
For distribution as shown in DOE/TIC-4500, Distribution Categories UC-423 (Magnetic Fusion Reactor Materials) and UC-424 (Magnetic Fusion Energy Systems)